Dust Near Galactic H II Regions

by

Gopika Krishnan Sreenilayam

A thesis
presented to the University of Waterloo
in fulfillment of the
thesis requirement for the degree of
Doctor of Philosophy
in
Physics

Waterloo, Ontario, Canada, 2012

I hereby declare that I am the sole author of this thesis. This is a true copy of the thesis, including any required final revisions, as accepted by my examiners.

I understand that my thesis may be made electronically available to the public.

Abstract

The distributions of physical properties, such as the temperature, mass, or density of the dust grains in molecular clouds near Galactic massive star forming regions are relatively poorly understood. These properties are significant in characterizing the early stages of high-mass star formation. The major goal of this thesis is to study the dust properties using continuum emission to learn about the effect on the dust of the extreme environments around high-mass star formation. For this we estimate mass, temperature and luminosity of the hot ($\geq$ 100 K), cool (20-40 K) and cold ($\leq$ 20 K) dust in the environs of Galactic H II regions using Infrared Astronomy Satellite (IRAS) and James Clerk Maxwell (JCMT) Submillimeter Common User Bolometer Arrays (SCUBA & SCUBA-2) data.

A total of 83 clouds has been examined using IRAS data. A two-component model Spectral Energy Distribution (SED) of hot and cool dust is used to fit the IRAS data. A three-component model SED is fitted to combined SCUBA and IRAS data for 15 clouds near H II regions to measure the cold dust component. Surprisingly, the ratio of the bolometric luminosity of the cool dust to the hot dust appears to have the same value 2.8 in virtually all objects. The cool dust has typically four to five orders of magnitude greater mass than the hot dust. However, the mass in cold dust is much greater than the mass in cool and hot dust. These results may prove useful for using IR observations for estimating gas masses in extragalactic systems with active high-mass star formation.

The clouds in the environments of H II regions are modelled assuming a thermal equilibrium in large grains, ignoring small grains and polycyclic aromatic hydrocarbons (PAHs). A number of different models having varying density distributions and external stellar radiation are compared to the IRAS SEDs. The model results suggest that the assumptions are not valid. We need a larger amount of dust at 30 K than the models produced and in this thesis we propose a solution to this problem, which we have not yet tested.

The JCMT Submillimeter Common User Bolometer Array-2 (SCUBA-2) data of six complexes is used to analyze the cold dust near Galactic H II regions. Dust physical property maps such as the temperature, optical depth, column density and visual extinction are constructed from the SCUBA-2 data at 450 and 850 μm wavelengths. All of the molecular cloud cores are found to be at very low temperatures, down to 6 K at the centres, with increasing values toward the periphery. This is surprising because we expected some internal heating at the centre. The column densities at the centres of the clouds exceed 10^{23} cm^{-2} and the derived peak visual extinction values of most of the cloud cores are above 100, indicating a highly opaque cloud centre. The observed clouds are massive with gas masses ranging from 10^2 to over 10^4 $M_\odot$. All of these properties together suggest that the cores are high-mass starless cores (HMSCs), which are not hosting any massive stars at the centre. Note that there are only a few such observations, on these potential precursors of high-mass proto-stellar objects, by others. From the derived physical properties such as

high column densities, high visual extinction and the cold temperatures toward the centres of the cores, we speculate that the all the sample cores are in a state of collapse. Note that the Jeans masses of the clouds are much less than their real cloud masses and the free fall times range from 10^3 to 10^4 years, confirming the potential state of the cores.

Acknowledgments

I would like to thank my supervisor Dr. Michel Fich for giving me an excellent opportunity to do my research in Canada. His pleasant attitude and positive approach during all my Ph.D days were always inspiring. I am thankful for his guidance and support in research during all these years.

I also express my gratitude to my departmental committee members, Drs. Walter Duley, Gretchen Harris and James Taylor. Many thanks to Dr. Duley for very useful suggestions about my research; Dr. Harris for providing feedback that enabled me to improve; Dr. Taylor for advising me how to write a good proposal.

I acknowledge Drs. Marshall McCall and Jeffrey Shallit, for carefully reading my thesis and for making invaluable comments.

I remember and thank my grandmother for her support during all the years of my studies until my Master's degree. This thesis is a dedication to her for she was the one and the only one who wished the best out of my studies. I am grateful to my parents because this thesis would not have been possible without them. Special thanks to my mother for being my best friend in all the hard times. I thank my brother, Gopee, for introducing me to astronomy, for directing me in my studies, and for helping me to get through tough times. I thank my better half, Denys, for supporting me in times I needed encouragement. Thank you for being always there for me, and for making me an optimistic and confident person.

I am thankful to Drs. Carolyn McCoey, Michael Balogh, Brian McNamara, Michael Hudson, Helen Russel, David Gilbank, and Sylvie Beaulieu for their constructive suggestions and feedbacks, during my PhD days. Special thanks to Dr. Carolyn McCoey, whose door was always open for me and I gratefully acknowledge her valuable input at every stage of this thesis.

I extend my sincere thanks to my teachers from SPAP, especially Dr. K. Indulekha, and late Dr. G.V. Vijayagovindan who helped me to reach here. I cannot forget to mention Sam uncle and Mercy aunty who were like my guardian for some important period of my life.

Good moments with colleagues and friends including Ting Lu, Miok Park, Mina Rohanizadegan, Yeongyoon Kim, Farbod Kamiab, Robbie Henderson, Samuel Tisi, Stephen Turnbull and Aida Ahmadzadegan are also happily acknowledged.

Finally, I am indebted to the Graduate Secretary, Judy McDonnell, for her congeniality and helpfulness all throughout the past years.

Dedication

to my grandmother
(muthassi)

Contents

List of Tables

List of Figures

Chapter 1

Introduction

1.1 Interstellar Dust

The presence of interstellar dust was first noticed as dark patches in the bright sky—the "holes in the heavens"—by Sir William Herschel at the end of the 18th century. But scientific evidence of the presence of interstellar dust took one and a half centuries to be found. The existence of interstellar dust was first confirmed in 1930 by Trumpler during his studies of open clusters [Trumpler, 1930a,b] and the results were published in two momentous papers entitled "Preliminary results on the distances, dimensions and space distribution of open star clusters" and "Absorption of Light in the Galactic System." In his studies, Trumpler found an inconsistency in the photometric and diameter based distances of the open clusters, which led him to the finding of the space absorption of light by interstellar dust. The interstellar dust obscures starlight by absorption and scattering, and this is generally called the interstellar extinction. Moreover, dust is also responsible for selective absorption, i.e., wavelength-dependent absorption. The dust is found to obstruct at shorter wavelengths more than at longer wavelengths. For example, the light obscuration by dust is much more for UV and blue wavelengths than for IR or red wavelengths. This feature is also known as interstellar reddening since the light after passing through the intervening dust grains, appears more reddish coloured than bluish coloured due to the selective nature of the extinction. Such an attribute guided scientists to surmise that the dust grains are fine particles and their sizes are comparable to the shorter wavelengths. Even eight decades after the authentication of its existence, the field of interstellar dust is still one of the most intriguing areas of astronomy.

The interaction of dust with electromagnetic radiation yields plenty of information on the physics and chemistry of the interstellar medium (ISM). Dust grains exist in a wide variety of astrophysical environments including star forming regions, molecular clouds,

circum-stellar envelops, galactic nuclei, and planetary nebulae. It is responsible for majority of the absorption, scattering, polarization and re-radiation of UV and visible light from stars. Dust is the major repository for the chemical components required to build terrestrial planets and henceforth life. The study of interstellar dust is of fundamental importance because the dust grains indirectly help in collapsing a molecular cloud by carrying away excess heat, aiding in the formation of stars. The star formation process in low-mass stars is relatively well understood, but this is not true of high-mass stars. Dust in different environments is different in physical properties such as temperature, mass, size, composition, shape and structure.

1.1.1 Dust grains in the ISM

The most important observational evidence for the presence of interstellar dust grains in the ISM is the interstellar extinction curve. Other observational evidence includes polarization of starlight, scattering of starlight, microwave emission, infrared (IR) and sub-millimeter (sub-mm) emission, as well as polarization of IR and sub-mm emission. Together, the observational evidence constrains grain properties such as composition, structure, and size.

Interstellar dust material (both in solid and gaseous form) becomes part of the ISM in a variety of processes. It is well known that oxygen-rich asymptotic giant branch (AGB) stars contain grains composed of silicates in their wind, and carbon-rich AGB stars are the sources of carbonaceous materials. Note that these carbon-bearing AGB stars are also the source of one silicon-rich dust component—silicon carbide (SiC). Aside from the winds from these evolved stars, ejection of dust from core collapse supernovae is yet another source responsible for the return of dust mass into the ISM [Kozasa et al., 2009]. Another production site of dust grains is the metal-rich winds of novae [Ney and Hatfield, 1978]. Other Galactic birthplaces of dust include planetary nebulae, O-B stars, and Wolf-Rayet stars. See Figure 1.1 [Jones, 2004] for a schematic diagram showing the life cycle of dust grains in the ISM. Note that most of the material from all these sources ejected into the ISM is in gaseous form. Dust grains in the solid (also called stardust) form from all these stellar sources listed above account for only 4% of the total mass of the dust in the ISM, and most of the dust grains are grown in the ISM by the depletion of condensible elements from the gas phase by means of chemical processes such as thermal desorption, hydrogenation, and UV photolysis [Draine, 2009].

All elements are in the plasma phase in stellar atmospheres. In interstellar clouds the gas phase abundance of the elements such as C, N, O, Mg, Si, Fe, etc., is much less compared to their abundance in stellar atmospheres. The presence of heavy elements in dust is therefore deduced from the abundance of these condensible elements in stellar atmospheres and their observed depletion in the interstellar gas. For example, scientists determine the solar system abundance and depletion by spectroscopically analyzing the

elements in the atmosphere of the Sun and then compare it with the laboratory inspection of meteorites [Whittet, 2003]. It is also interesting to note that the heavy elements—C, N, O, Mg, Si, and Fe—are also the primary constituents of all terrestrial materials. Figure 1.2 shows a bar diagram of the ratio of the mass density of each of the depleted element C, O, Mg, Si, and Fe to the total mass density of all the depleted elements in the diffuse clouds (for solar reference abundances), indicating the dominance of these elements in the total depleted mass. The portion of the bars with filled black colour in Figure 1.2 represents elemental proportions that may be locked up in silicate compounds especially in a mix of Mg and Fe silicates, such as olivine and pyroxine, with a Mg to Fe ratio of $\approx 5/2$ [Whittet, 2003].

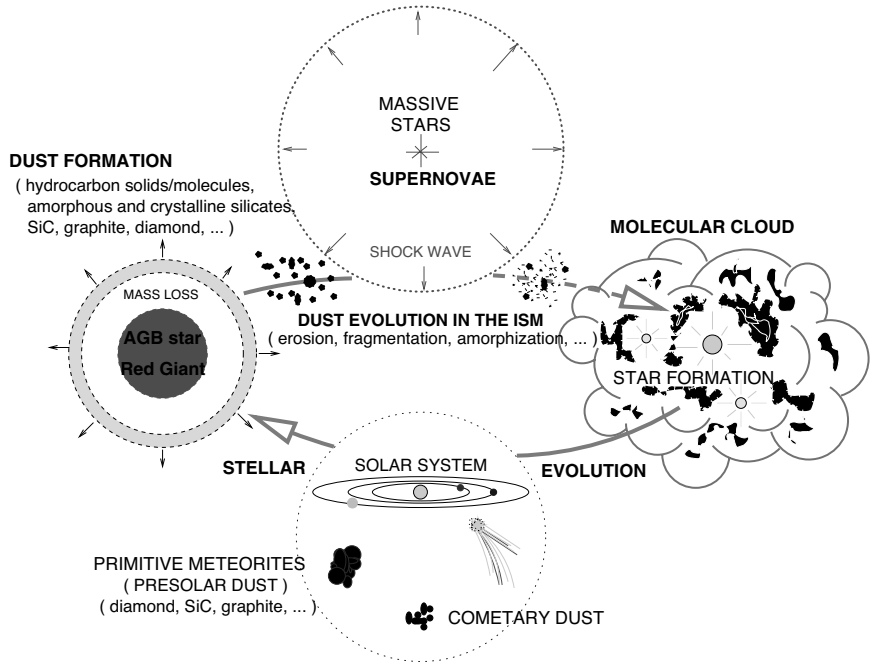

Figure 1.1: (Reprinted from Jones [2004]. Copyright (2004) by the ASP.) A schematic diagram showing the life cycle of dust grains in the ISM.

One of the two most important interstellar grain components is the silicates, which are ejected into the ISM as a result of mass loss from the oxygen-rich AGB stars and supergiants. Silicates are compounds made up of silica tetrahedron [SiO_4] units and in general have two structures: amorphous and crystalline. Crystalline silicates are those with an ordered lattice structure whereas amorphous silicates have a disordered lattice structure. The

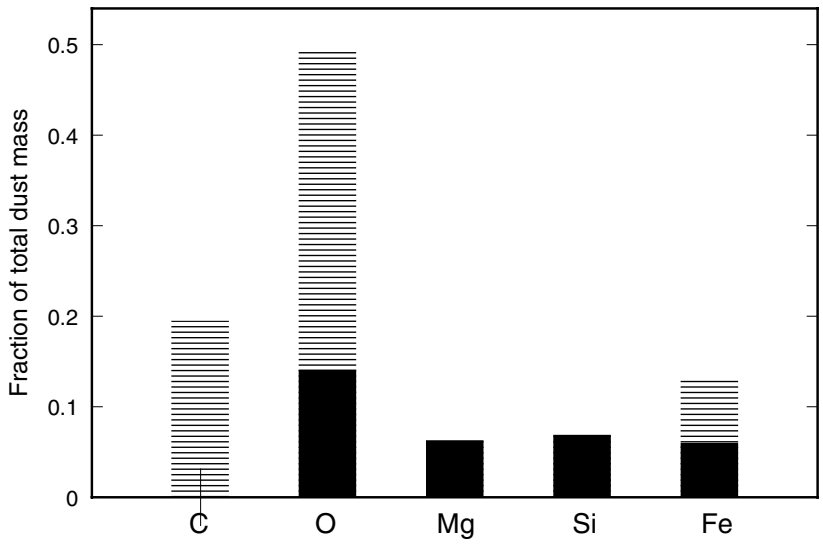

Figure 1.2: (Reprinted from Whittet [2003]. Copyright (2003) by IOP Publishing Ltd.) Fraction of the mass abundance of the five major elements depleted into the dust grains in diffuse interstellar clouds relative to the total depleted mass, for the five most predominant condensible elements in the ISM. Note that the portion of the bars shown in black colour represents possible elemental mass proportions in Mg-and Fe-rich silicate compounds with Mg:Fe $\approx$ 5:2.

compounds such as Olivines, Pyroxines, and Quartz are examples of crystalline silicates. Crystalline silicates are commonly found in the circum-stellar environments of pre-main sequence and post-main sequence stars, while the diffuse ISM is devoid of any crystalline silicates [Kemper et al., 2004]. Their studies show a silicate mass fraction (crystalline to crystalline+amorphous) of less than 1% in the ISM and the low abundance of crystalline silicates is attributed by their destruction in the diffuse ISM [Draine, 2009]. Amorphous and crystalline silicates differ in the width of their absorption or emission peaks. Amorphous silicates show broad emission and absorption signatures, characteristic of large degree of lattice defects, in the near-mid infrared wavelengths, whereas the crystalline silicates show much narrower and stronger resonances at the respective wavelengths. Emission features of silicate grains, which peak at 9.7 μm (corresponding to Si-O stretching mode) and 18 μm (corresponding to O-Si-O bending mode), are observed [Stein and Gillett, 1969; Ney et al., 1973] when a silicate grain is heated to a temperature above 200 K near to luminous young stars in the Orion Trapezium region. Furthermore, silicate absorption features are observed at 9.7 and 18 μm in the 16-30 μm studies along the line of sight toward the galactic centre [McCarthy et al., 1980].

Graphite grains were first proposed by Hoyle and Wickramasinghe [1962] as a potential candidate for the interstellar grain component since their theoretical interstellar reddening curve using graphite spheres satisfied the observed interstellar reddening law. A strong bump in the interstellar extinction curve at λ^{-1}= 4.4 μm^{-1} was first noted by Stecher [1965] in the UV region of the spectrum, and later the carrier of the peak was suggested as graphite flakes by Stecher and Donn [1965]. Graphite grains are also distinguished by their broad feature from 1-20 μm and a broad peak near 30 μm in the absorption efficiency depending upon dust temperature in the near and mid IR wavelengths [Draine and Lee, 1984]. Polycyclic aromatic hydrocarbons (PAHs) with emission features at 3.3, 6.2, 7.7, 8.6, and 11.3 μm and very small grains (VSGs) with continuum mid IR emission features are two other vital components in the ISM. The existence of PAHs in the ISM was proposed first and foremost by Platt [1956].

Large grains are responsible for most of the long wavelength emission, namely the far-infrared and sub-mm part of the emission, and carry most of the mass of the dust. Grain sizes range from approximately a hundredth of a micron up to around a tenth of a micron. Since their sizes are comparable to visible light wavelengths, they produce most of the extinction of the visible light. Although most of the mass is in large grains, most of the absorption cross section is in small grains because of their major contribution to the total surface area available for absorption. They radiate mostly at mid-infrared wavelengths, and their sizes are about a thousandth of a micron. Whenever a very small grain absorbs an interstellar photon, it can undergo very large fluctuations in temperature in comparison with large grains and this can raise the small dust grain temperatures to approximately a 1000 K for a short while before cooling by the emission of infrared radiation.

1.2 Dust Models

The observed interstellar extinction curve of a specific region can be used to constrain the size distribution, composition, and physical structure of the dust grains at that region, and thereby can provide details about the grain population of a selected environment. For example, to explain the average interstellar extinction curve of our own galaxy, one requires many grain components with varying sizes. Based on the observed interstellar extinction curve, the first popular size distributions of interstellar grains were developed in 1977 [Mathis et al., 1977] by using a dust model composed of bare graphite and silicate grains of varying sizes, later known as the MRN distribution of grains. Since the observed extinction curve of the diffuse ISM spans from IR to UV, the authors required grains with different sizes to reproduce the observations, with large particles in the IR and small ones in the UV. The size distribution of MRN grains have approximately a power law nature as

shown below;

$$\frac{dn}{da} = An_H a^{-3.5} \tag{1.1}$$

where a is the grain radius, ranging generally from 5 nm to about 0.25 μm, and n_H is the number density of hydrogen nuclei. The MRN model was later extended by Draine and Lee [1984] using graphite and "astronomical silicate" dielectric functions synthesized from laboratory and astronomical data. They calculated the absorption efficiencies of spherical silicate and graphite grains for a wide range of wavelengths. Figure 1.3 shows $\frac{\lambda Q_{abs}}{a}$ for $\lambda > 1$ μm for silicate and graphite grains of the Draine & Lee dust model, where

$$Q_{\nu abs} = \frac{C_{abs}}{\pi a^2} \tag{1.2}$$

is the absorption efficiency factor, which is the ratio of absorption cross section, C_{abs}, to the geometric cross section of a grain.

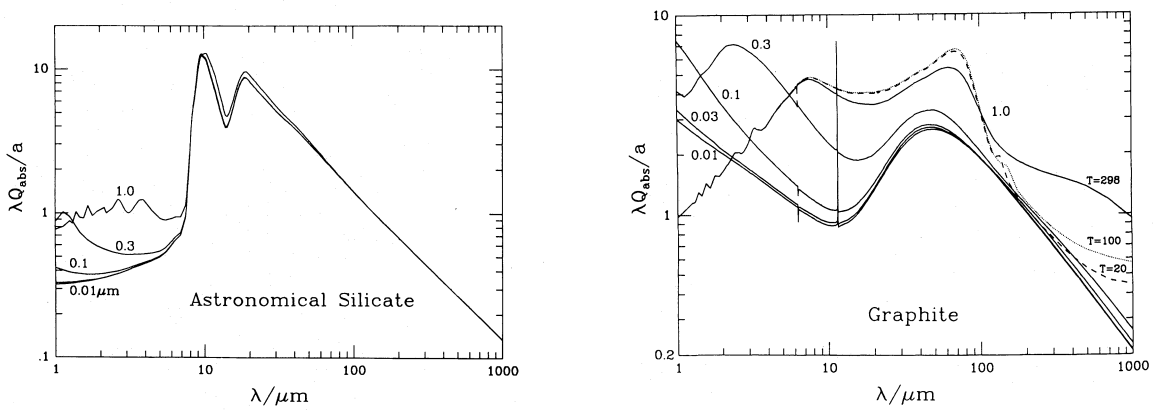

Figure 1.3: (Reprinted from Draine and Lee [1984]. Copyright (1984) by IOP Publishing Ltd.) Plot showing the $\frac{\lambda Q_{abs}}{a}$ for $\lambda > 1$ μm for spherical silicate (left) and graphite (right) of the Draine & Lee dust model. Different curves in each plot represent different grain radii in μm.

The absorption efficiency of the graphite grains dominates at wavelengths less than 10 μm. At wavelengths between 10-40 μm, the silicate grains dominate the absorption efficiency. Beyond 40 μm, the contributions from both grains to the absorption efficiency are almost equal. Different curves in each plot represent grains with different radii in μm.

The absorption efficiencies of the silicate and graphite grains in the UV visible range is shown in Figure 1.4. Graphite grains with radii greater than 0.1 μm more or less maintain a unit efficiency in absorption in the UV visible regime. The case is similar for silicate grains of radii 0.1 μm, 0.3 μm (especially at wavelengths below 2000 Angstrom) and 1 μm.

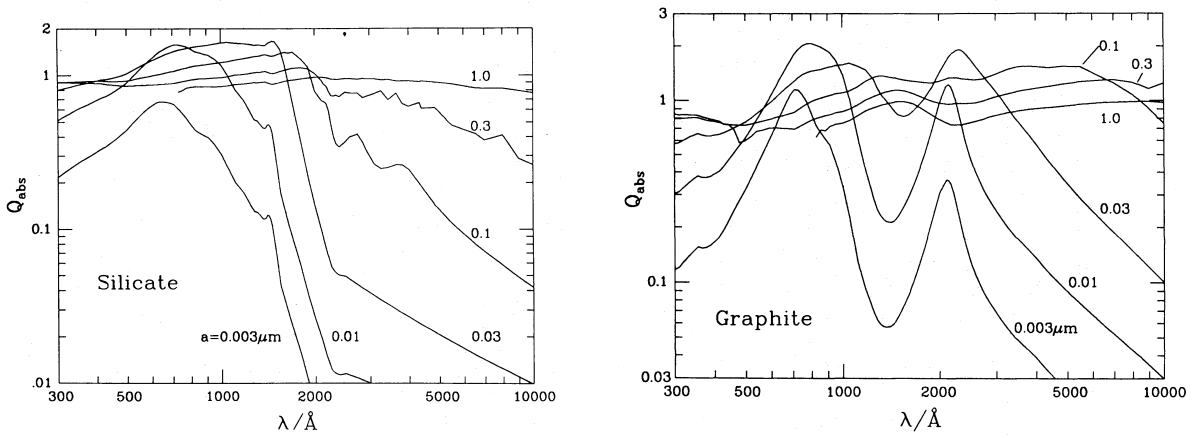

Figure 1.4: (Reprinted from Draine and Lee [1984]. Copyright (1984) by IOP Publishing Ltd.) Plot showing the absorption efficiencies in the UV-visible range for spherical silicate (left) and graphite (right) of the Draine & Lee dust model. Different curves in each plot represent different grain radii in μm.

1.3 Background Theory

Radiative transfer:

As radiation propagates through an absorbing or emitting medium, the intensity of radiation varies and the "radiative transfer" is simply a description of this phenomenon. If I_ν is the intensity when the radiation hits a medium, and if I_ν changes by dI_ν due to emission or absorption as the radiation proceeds through a very small distance dl (path length) of the medium, then we can write the infinitesimal change in I_ν—the dI_ν, as a sum of the contributions from absorption and from emission. The term due to absorption is $-\kappa_\nu I_\nu dl$ and the term due to emission is $j_\nu dl$, where κ_ν is called the absorption coefficient or absorptivity, which has units of m^{-1}, and j_ν is the emission coefficient or emissivity, which has units of $Wm^{-3}Hz^{-1}sr^{-1}$. Using the above two terms, the equation for radiative transfer can be written as

$$\frac{dI_\nu}{dl} = -\kappa_\nu I_\nu + j_\nu. \tag{1.3}$$

If we consider pure emission (when $\kappa_\nu = 0$), the solution to the radiative transfer equation becomes

$$I = I(0) + \int_0^l j(r)\, dr. \tag{1.4}$$

Note that $I(0)$ is the intensity at which $l = 0$. When there is only absorption ($j_\nu = 0$) and the solution becomes

$$I = I(0)e^{-\int_0^l \kappa(r)\,dr}\ . \tag{1.5}$$

The term $\int_0^l -\kappa(r)\,dr$ is called the optical depth τ. Whenever the value of $\tau \gg 1$, then the absorbing medium is said to be optically thick and whenever the value of $\tau \ll 1$, then the absorbing medium is said to be optically thin. We can rewrite the absorption term using the optical depth as:

$$I = I(0)e^{-\tau_\nu}. \tag{1.6}$$

Whenever the emitting and absorbing media are in local thermodynamic equilibrium, i.e., at an equilibrium temperature, then the situation is different; it is applicable to emission from large dust grains and this is explained in the next section.

1.4 Dust Emission

Apart from extinction and reddening, dust grains are also responsible for emission at mainly infrared and sub-mm wavelengths. As the grains absorb short wavelength radiation, they heat up and re-emit the energy in the IR and sub-mm wavelengths. Large grains reach a steady state with little fluctuations in temperature due to their large heat capacity and very short time between photon absorptions. We can use Kirchoff's law, which states that at local thermodynamic equilibrium (LTE), the emissivity (j_ν) of a dust grain is equal to the absorptivity (κ_ν) of a dust grain, to explain the dust emission by a classical dust grain, i.e.,

$$\frac{j_\nu}{\kappa_\nu} = B_\nu(T_d), \tag{1.7}$$

where

$$B_\nu(T_d) = \frac{2h\nu^3}{c^2}\frac{1}{exp(\frac{h\nu}{kT_d}) - 1} \tag{1.8}$$

is Planck's function and T_d is the equilibrium dust temperature. Under LTE, there is a balance between the radiation absorbed and the radiation emitted by the large grains as given by the Kirchoff's law. If we consider spherical grains with radius a, then

$$Q_{\nu em}(a) = Q_{\nu abs}(a), \tag{1.9}$$

where $Q_{\nu abs}$(a) is the absorption efficiency factor, which is the ratio of absorption cross section, C_{abs}, to the geometric cross section of a grain. Similarly, $Q_{\nu em}$(a) is the emission efficiency factor with a corresponding emission cross section C_{em}.

We can calculate $Q_{\nu_{abs}}$ from Mie theory:

$$Q_{\nu_{abs}} \simeq \frac{8\pi a}{\lambda} Im\{\frac{m^2-1}{m^2+2}\} = aQ_0\nu^\beta \tag{1.10}$$

and at infrared wave lengths where the radius of the dust grain is much less than the wavelength of the radiation, the above equation becomes:

$$Q_{\nu_{abs}} = 10^{-23} a\nu^\beta \tag{1.11}$$

where β is known as dust emissivity index, and can have different values (e.g., 0, 1, 2, or 3), depending on various factors, although the preferred value at far-infrared wavelengths is 2 (see [Krügel, 2003] chapter 8).

At longer wavelengths (e.g., far-infrared and sub-mm) a dust grain emits less than a blackbody. Let's consider a cloud consisting of N spherical dust grains with geometric cross section σ, at a distance D, temperature T_d, and with an absorption efficiency which varies like ν^2, then the emission from dust can be expressed as

$$F_\nu = \frac{N\sigma Q_\nu B_\nu(T_d)}{D^2}; \tag{1.12}$$

[Hildebrand et al., 1977; Hildebrand, 1983]

Thermal emission from dust grains can be described by the Planck law modified by an emissivity. Figure 1.5 shows how a black body emission differs from a grey body (modified black body) emission by a silicate grain of 0.6 μm radius. The dashed curve corresponds to emission from a silicate grain with an absorption efficiency calculated from equation (1.11). The broken curve represents emission for a silicate grain with an absorption efficiency calculated from Mie theory with silicate optical constants. Near the Rayleigh-Jeans regime, the grey bodies have lower intensities compared to the black bodies of the same size. As shown in the figure, the peak intensity of the emission varies with the location (and temperature) of the dust particles. Also note that at high temperatures, we can see the spectral features, which are absent at low temperatures. Dust emission also depends on the value of β. Figure 1.6 shows modified blackbody emission from dust with different β for constant column density at $T = 20$ K (solid lines) and $T = 5$ K (dashed lines). Note that $\beta = 0$ corresponds to blackbody emission. As the value of β increases from 0 to 3 at a constant dust temperature, the wavelength of maximum emission shifts towards shorter values and the peak flux increases by a factor of 1000. Dust emission depends on the temperature of the grains at the same value of β: as the dust temperature increases by a factor of 4, the peak flux increases by around three orders of magnitude.

Dust emissivity varies as $\lambda^{-\beta}$ [Hildebrand, 1983], where the value of β, the emissivity index, varies with environment, wavelength, temperature, and structure (composition) of

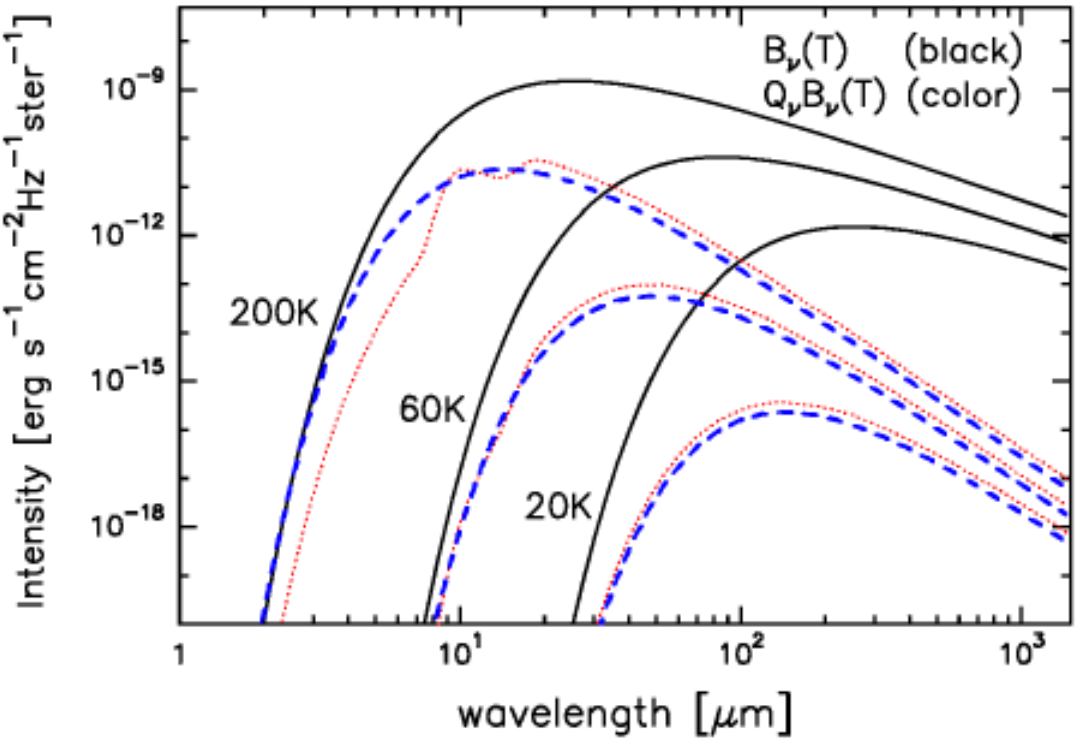

Figure 1.5: (Reprinted from Krügel [2003]. Copyright (2003) by IOP Publishing Ltd.) Plot showing the blackbody and grey body emissions for three different temperatures. The solid curve corresponds to blackbody emission. The dashed curve corresponds to emission from a silicate grain (of 0.6 μm radius) with an absorption efficiency calculated from equation (1.11). The broken curve represents emission by a silicate grain with absorption efficiency calculated from Mie theory with silicate optical constants.

dust grains. In the FIR and sub-mm, the value of β changes from ~ 1, for wavelengths less than 200 μm, to ≤ 2, for wavelengths from 200 μm-1000 μm [Hildebrand, 1983]. The dust emissivity index alters with respect to the structure (crystalline, amorphous or layered), chemical nature (dielectric or conductor), and the morphology (dimension, shape or clustering) of the dust grains [Mennella et al., 1995]. From the 20 μm-2 mm laboratory studies of the mass absorption coefficient of cosmic carbonaceous analogue grains, they found a value of 2 for graphite grains while amorphous grains displayed a value of 1.

Several studies found a steeper value of spectral index in cold regions than in the warm zones. A spectral index close to 2, which is the most common value of β in cold cores, is obtained in the studies of starless core TMC-1C using data from FIR to mm wavelengths [Schnee et al., 2010]. Compatible results are observed in the studies on the pre-protostellar core L1498 using SCUBA 450 and 850 μm data [Shirley et al., 2005] and the derived value of β for an assumed dust temperature of 10.5$\pm$ 0.5 K is 2.44$\pm$ 0.62. However, an anti-correlation between temperature and β is observed in different astrophysical environs in the Galaxy [Dupac et al., 2003] using PRONAOS where the spectral index increase from 0.8 to 2.4 when the temperature falls from 80 K to 11 K. Similar features of inverse correlation, although slightly steeper in comparison to the values observed by [Dupac et al., 2003], between the dust temperature and β, are noticed in a sample of local luminous infrared galaxies [Yang and Phillips, 2007]. One of the possible explanations that consolidates their results is the presence of different grain populations at different temperatures, i.e., formation of ice mantles on grains by accretion at low temperatures giving rise to strong long wavelength emission and hence a higher β, while the same process is absent in small grains which undergo transient heating. An alternative explanation that the line-of-sight density as well as temperature variations and noise uncertainties plausibly cause the observed relationship between dust temperature and β [Shetty et al., 2009a,b], nevertheless, is disproving the anti-correlation to some extent. Recent studies of Galactic starless cores using *Herschel* data [Juvela et al., 2011] also indicate an anti-correlation of β with temperature where the median values of β range from 1.9 to 2.2, and their radiative transfer models demonstrate that the line-of-sight temperature variations are the cause of this specific correlation.

1.5 Massive Young Stars

Most of the high mass stars, with mass $> 8\ M_{\odot}$, are located very far away ($\approx$ a couple of kpcs) from us. Note that massive stars are deeply buried inside their parent dust cloud during their lifespan and therefore we cannot detect them in visible wavelengths. Furthermore, high-mass stars do not usually form in isolation like lower mass stars. Due to these reasons, the star formation processes for massive stars are not very well understood

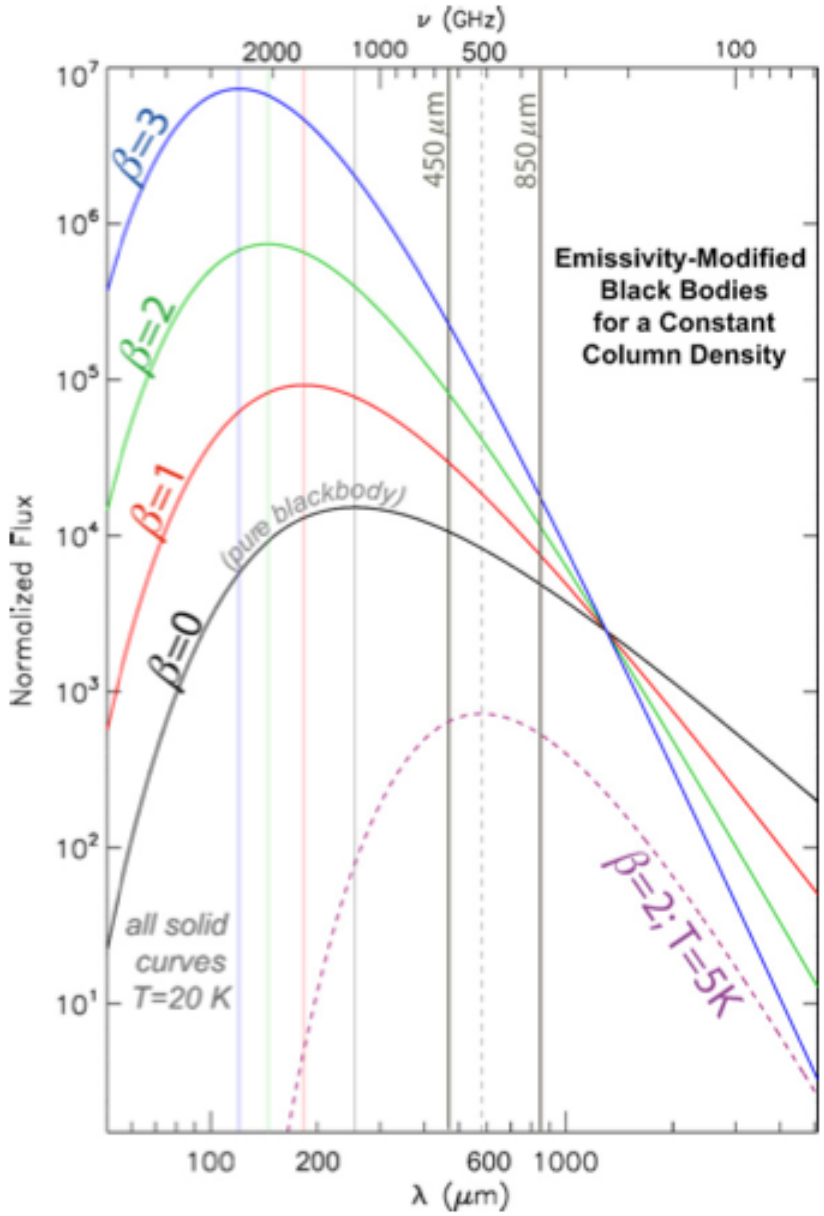

Figure 1.6: (Reprinted from Shetty et al. [2009b]. Copyright (2009) by IOP Publishing Ltd.) Plot showing the modified blackbody emission with different β for constant column density at T=20 K (solid lines) and T=5K (dashed lines).

compared to low mass star formation, which is more common and well studied. However, the dust envelopes of massive stars are strong re-radiators of UV light and hence the presence of massive stars can be revealed through the dust regardless of their enormous distance from us. The strong UV radiation from massive stars leads to the ionization of dense molecular gas surrounding them forming an ionized hydrogen region—generally called the H II region. The ionization of the atomic hydrogen is primarily through the absorption of Lyman continuum radiation from the central massive star (such as type O and B stars) with wavelength < 912 Å, photon energy > 13.6 eV.

Depending on the size of the ionized area, the H II regions are mainly classified into four classes: (a) Compact H II regions: These regions contain a small area of ionized hydrogen around the central star with a range of size from 0.1 to 0.5 pc. (b) Ultra compact H II regions: These are smaller areas of ionized hydrogen around the central massive star with sizes ranging from 0.01 pc to 0.1 pc. (c) Hyper-compact H II regions: If the H II region is smallest, associated with youngest massive stars, it is called a hyper-compact H II region with sizes $\leq$0.01 pc. (d) Classical H II regions: These are evolved H II regions with sizes ranging from 1 - 30 pc [Habing and Israel, 1979]. See the table [Kurtz, 2002] below for a detailed classification of H II regions. Column 1 represents the class of H II regions and column 2 lists the size of the H II regions in parsecs. Columns 3, 4 and 5 are respectively the density, emission measure (EM) and ionized mass of the corresponding classes of H II regions. In this thesis, I deal only with clouds associated with classical H II regions in the Milky Way.

Class of Region	Size (pc)	Density (cm^{-3})	EM ($pc\ cm^{-6}$)	Ionized Mass ($M_\odot$)
Hypercompact	$\lesssim 0.05$	$\gtrsim 10^6$	$\gtrsim 10^9$	$\sim 10^{-3}$
Ultracompact	$\lesssim 0.1$	$\gtrsim 10^4$	$\gtrsim 10^7$	$\sim 10^{-2}$
Compact	$\lesssim 0.5$	$\gtrsim 5 \times 10^3$	$\gtrsim 10^7$	~ 1
Classical	~ 10	~ 100	$\sim 10^2$	$\sim 10^5$
Giant	~ 100	~ 30	$\sim 5 \times 10^5$	10^3 – 10^6
Supergiant	>100	~ 10	$\sim 10^5$	10^6 – 10^8

Figure 1.7: (Reprinted from Kurtz [2002]. Copyright (2002) by the ASP.) Table showing the classification of H II regions.

1.6 Dust Destruction

Dust destruction depends primarily on the environs, chemical composition, and the size of the dust grains. Destruction in shocks is a dominant method of dust disintegration. Shocks can form in a wide variety of environments such as supernovae, H II regions, and in stellar winds. The shocks associated with stellar winds, H II regions or supernova remnants can also destroy dust grains by shattering. The velocity of the shock determines the mechanism for dust destruction. For example, if the shock velocity is less than 200 km/s, then the grains undergo shattering. However shattering conserves the total grain mass. In an H II region, atoms can be ejected from the surface of a grain by collision with ionic or neutral gas particles in shocks (sputtering) and by photons (photodesorption). If the shock velocity is much greater than 200 km/s, then the prominent method of erosion is sputtering [Jones, 2004]. Note that the photodesorption is due to the UV photons from the OB stars and is either by physisorption or by chemisorption from the surface of a grain. Besides, close to hot-massive young stars, dust grains also undergo sublimation in addition to sputtering and shattering [Jones, 2004], and this is considered to be the most dominant method of dust disintegration near H II regions.

Because of the many dust destruction processes, there can be only a very small amount of dust inside the H II regions. But even if the dust inside H II regions is small in amount, it could be bright due to its high temperature. Transient heating of very small dust grains in or near H II regions [Greenberg, 1968; Duley, 1973; Draine and Anderson, 1985] by the absorption of UV photons from the central star can raise the temperatures up to $\sim$ 1000 K for a short while before gradual cooling by emission of IR radiation. On the other hand, large grains always tend to be close to a steady-state equilibrium temperature [Draine, 2003]. Since H II regions are associated with a central high-mass star and peripheral natal molecular clouds, the temperature of the dust in regions associated with H II regions span from as much as 1000 K near to the star to under 10 K in deeply embedded molecular cloud cores. We may also find dust between 10 K and 1000 K inside H II regions because of the rapid cooling of small dust grains after the absorption of starlight. Note that the maximum temperature a dust grain can reach is limited by its sublimation temperature which depends on the composition and size of the dust particles. For example, most volatile components sublime at moderate temperatures. H_2O ice sublimes at 90 K, other ice mantles can sublime at $\sim$ 200 K, and the least volatile compounds sublime around 2000 K. Large grains carry most of the mass of the dust, and near massive young stars, due to their efficient cooling, the maximum value of the equilibrium temperature of large dust grains is limited to $\sim$ 100 K [Tielens, 2005].

1.7 Physical Properties of Dust

Dense molecular clouds are the prospective locations of star formation. The knowledge of the physical conditions in such clouds is highly essential to develop insight into the comprehensive evolutionary stages that lead to star formation. The physical properties such as mass, temperature, luminosity, and density of the dust in molecular clouds are powerful tools that can provide us the knowledge of the detailed state of the clouds. These properties can be derived using a wide variety of methods.

1.8 Dust Mass from Dust Emission

Mass estimation of molecular clouds from dust emission:

Dust grains surrounding stars are primarily heated by absorption of light from stars and subsequently cooled by emitting long wavelength radiation in the infrared and sub-millimeter wavelengths. Dust is a reliable mass tracer because this dust emission is optically thin at sub-millimeter wavelengths, is finely mixed with the gas, and represents typically 1% of the gas mass although this probably depends somewhat on metallicity. However, measured dust masses depend strongly on the dust temperature determined for each cloud. The distribution of the dust mass with temperature depends on environmental factors such as radiation field, and geometry, but is further complicated by variations due to size, composition, and structure of the dust grains themselves. Whenever the size of a dust grain is comparable to the wavelength of the incident light, then the grain-radiation interaction will be the highest. Since most of the dust grains in the ISM have sizes less than a micron, the UV and optical radiation suffers most of the extinction, while for the IR-sub-mm regime, the dust emission is optically thin. Therefore, long wavelength radiation can trace most of the mass of the dust. In cases of optically thin emission, the specific intensity and Planck function can be related as follows:

$$I_\nu = B(\nu, T_d)(1 - \exp(-\tau_\nu)) \approx B(\nu, T_d)\tau_\nu, \tag{1.13}$$

where τ, the dust optical depth, can be expressed as $\tau = n_d C_{ext} L$ where C_{ext} is the extinction cross section, n_d is the number density of dust grains, and L is the length of the dust column. Flux is the integral of specific intensity over a solid angle Ω, i.e.,

$$F_\nu = \int_\Omega I_\nu \, d\Omega \; = \frac{1}{D^2} \int_A B(\nu, T_d)\tau_\nu \, dA. \tag{1.14}$$

Using the mass absorption coefficient, κ ($\mathrm{cm^2 g^{-1}}$) $= \frac{n_d C_{ext}}{\rho_d}$ where ρ_d is the dust mass density, we can rewrite the above equation as;

$$F_\nu = \frac{1}{D^2} \int_V B(\nu, T_d)\rho_d \kappa_\nu \, dV. \tag{1.15}$$

For constant mass absorption coefficient and dust temperature, one can obtain a relation between flux and the dust mass of the observed region as follows:

$$F_\nu = \frac{B(\nu, T_d)\kappa_\nu M_d}{D^2}. \tag{1.16}$$

Note that, κ (cm^{2}g^{-1}) $= \frac{n_d C_{ext}}{\rho_d} = \frac{Q_{ext}\pi a^2}{m} = \frac{3Q_{ext}}{4a\rho}$ where a, m, and ρ are respectively the radius, mass and density of an individual dust grain. The mass of an ideal cloud with spherical dust grains of fixed size, composition, and temperature along with the above value of κ can therefore be expressed as follows:

$$M_d = \frac{4a\rho}{3Q(\nu)} \frac{F_\nu D^2}{B(\nu, T_d)}. \tag{1.17}$$

(See also Hildebrand et al. [1977] and Hildebrand [1983]).

1.9 Dust Temperature

Dust grain temperatures are controlled by many environmental factors including the shape of the interstellar radiation field, the thermal coupling between the gas and the dust, and the composition of the grains.

Dust temperatures are also strongly dependent on grain optical properties. Figure 1.8 below shows the dust temperature distribution as a function of optical depth for silicate and graphite grains inside a spherical dense interstellar dust cloud heated by interstellar radiation fields [Leung, 1975]. Different numbers on the right side of the solid curve represent clouds with different optical depths. For clouds with the same optical depth, graphite grains are a factor of two hotter than the silicate grains. Note that for optically thin clouds, the dust grains are heated by the UV and visible components of the starlight. When the cloud becomes moderately optically thick, not many UV and visible photons can penetrate the innermost regions of the clouds and the major heating in the interiors of such clouds is contributed by near-infrared emission from stars. As the cloud becomes highly optically thick, there is severe attenuation of all the components of starlight; not even near-infrared components of the starlight can reach the innermost regions of the clouds, and in such cases, thermal emission from dust grains is the only mechanism that contributes to heating. Due to the infrared heating in the interiors of the clouds, the dust temperature does not drop to zero at places where the optical depth is the highest.

Large grains (classical dust grains with radii $a > 0.03\ \mu m$) maintain a steady temperature by balancing radiative heating and cooling. For large grains near a massive star, the

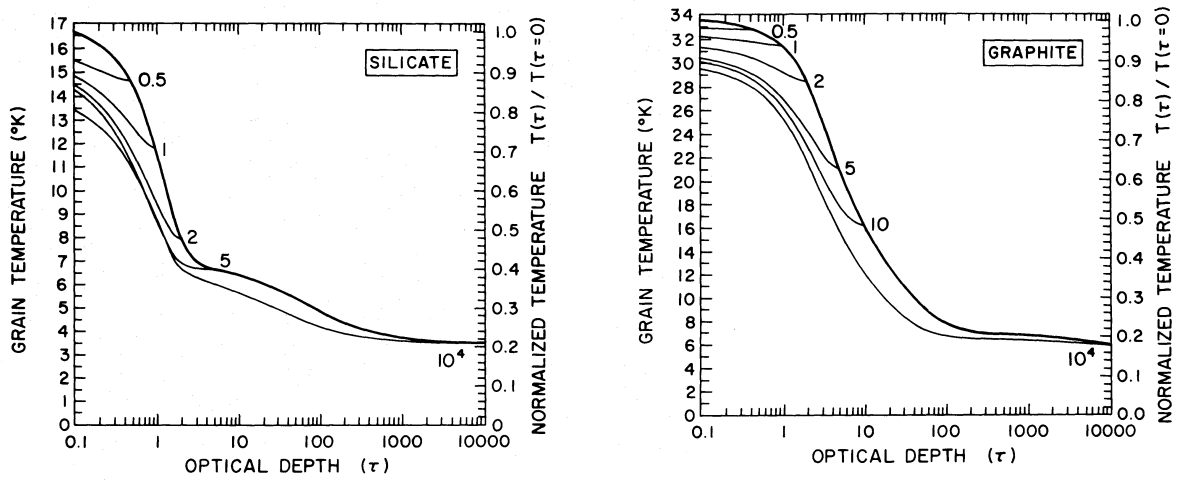

Figure 1.8: (Reprinted from Leung [1975]. Copyright (1975) by IOP Publishing Ltd.) Dust temperature distribution of silicate and graphite grains as a function of optical depth inside spherically dense interstellar dust clouds heated by interstellar radiation fields. The numbers on the right side of the solid curve represent optical depth of different clouds.

radiative heating is mainly due to the stellar radiation and the cooling is by emission of IR radiation. The figure below (Figure 1.9) shows large dust grain temperatures as a function of distance from a B1V star. Some studies have modelled dust emission from low mass pre-stellar cores and found very low dust temperatures at high column densities and visual extinction [Evans et al., 2001] for different input density distributions. See Figure 1.10 for more details.

Dust temperatures are typically estimated from broadband flux measurements, particularly from the ratio of flux densities at any two adjacent wavelengths. The dust temperature thus obtained is widely called the colour temperature. For example, if $F_{\lambda 1}$ is the flux obtained at wavelength $\lambda 1$ and if $F_{\lambda 2}$ is the flux obtained at wavelength $\lambda 2$, then one can get the colour temperature (single temperature) by solving the equation

$$\frac{F_{\lambda 1}}{F_{\lambda 2}} = \left(\frac{\lambda 2}{\lambda 1}\right)^{-\beta} \frac{B_{\lambda 1}(T_d)}{B_{\lambda 2}(T_d)}, \tag{1.18}$$

where $B_{\lambda 1}$ is Planck's function at wavelength $\lambda 1$, and $B_{\lambda 2}$ is Planck's function at at wavelength $\lambda 2$, T_d is the dust colour temperature, and β is the dust grain spectral index.

If at least three flux measurements are available, a spectral energy distribution (SED) can be fitted to evaluate the dust temperature. With more flux data points, one can

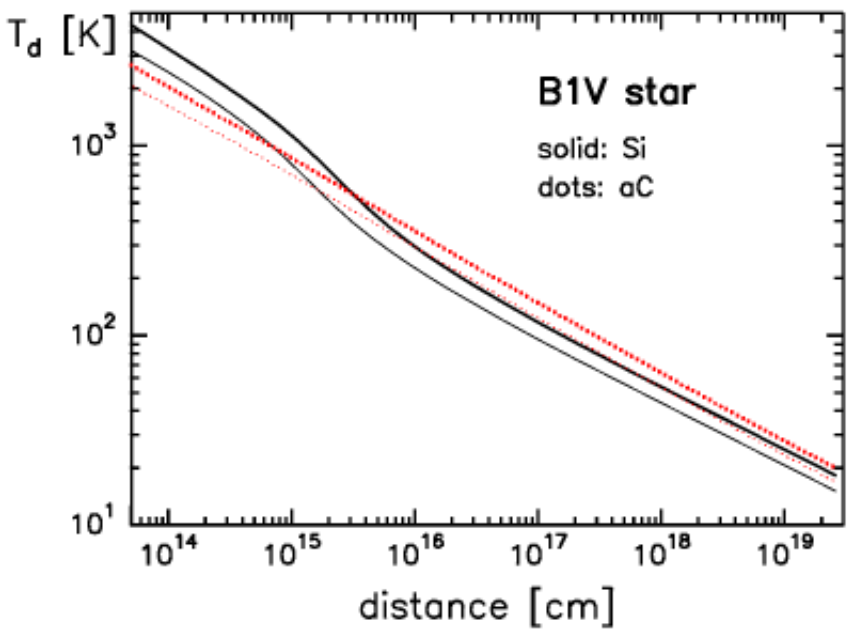

Figure 1.9: (Reprinted from Krügel [2003]. Copyright (2003) by IOP Publishing Ltd.) Plot showing the dust temperature with distance from a B1V star.

often find a better fit by including more than one temperature in the fit. A wide range of dust temperatures are expected in the ISM since the dust is not likely to be at a single temperature.

Subject to the availability of many flux measurements, more detailed modelling can be done by fitting the mass as a function of temperature directly. There are a number of inversion techniques capable of reproducing mass distribution of dust such as the analytical method [Xie et al., 1993], maximum entropy method [Hobson and Padman, 1994], and Fourier inversion method [Li et al., 1999]. In the analytical method, the observed source spectra are fitted with a function of the form $F_\nu = A\nu^\beta e^{-B\nu^{0.5}}$ (A, B, and β are free parameters), and then solved for the dust mass distribution analytically using a modified Möbius inversion theorem [Chen, 1990] and the inverse Laplace transform. One artefact of the analytical method is that the temperature distribution shows negative values below the cut-off temperature. Another downside of this method is that it uses extrapolated values outside the frequencies of available discrete data points and thus generates fluxes at points where there are no observed data values. The maximum entropy method, on the other hand, uses only available measured fluxes to reconstruct the dust temperature distribution, and unlike the analytical method, the mass distribution shows a smooth rise at the low temperature side. In the Fourier inversion method, a well-sampled dust emission

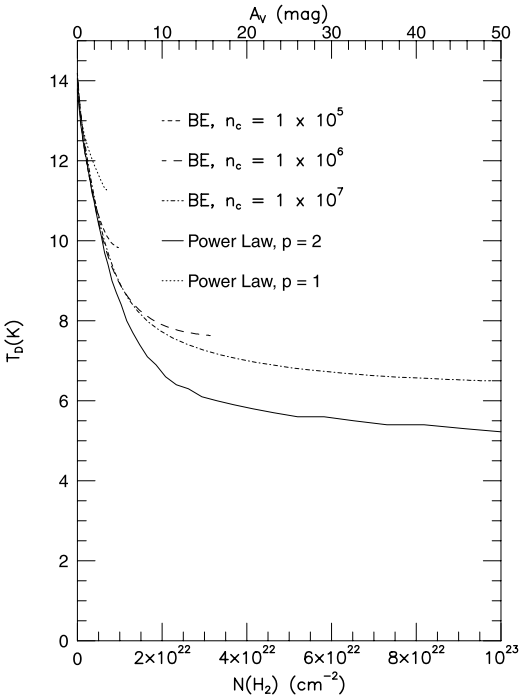

Figure 1.10: (Reprinted from Evans et al. [2001]. Copyright (2001) by IOP Publishing Ltd.) Plot showing the relation between the dust temperature, T_D, column density, $N(H_2)$, and visual extinction, A_v for different density distributions.

spectrum is used to create the mass distribution of dust and the authors [Li et al., 1999] studied a number of pre-stellar cores in Bok globules using the method, finding a good agreement with results obtained from grey body fitting. Moreover, the general shape of the dust temperature distribution, which displayed more mass in cold dust than in the hot dust, was the same in all three methods.

Employing many flux measurements, one can also do a more detailed modelling by varying parameters to find a possible source model that fits the observed SED. One such example is the modelling software DUSTY [Nenkova et al., 2000], which uses dust radiative transfer to model the physical system. Dust radiative transfer models like DUSTY are capable of producing dust temperature as a function of distance from the central external source. Another advantage of radiative transfer models is that they can provide certain parameters of the physical system like dust optical depth, density of the dust shell, and size of the dust shell, etc. One big caveat in all these methods, often ignored, is that the flux densities predicted in many models must be colour corrected before comparison with the observations, especially in the near- and mid-IR.

1.10 Results on Dust

A number of papers have focused on the reprocessing of photons by dust near young massive stars. It has been suggested that the dust near massive young stellar objects is well fit by two different dust components, namely hot (100-144 K) and cold (28-41 K) [McCutcheon et al., 1995], and that different dust emission components (warm and cold) originate from different heat sources [Sievers et al., 1991]. According to a study by Hobson and Ward-Thompson [1994], the hot dust (108±5 K) emission of the M17SW region originates either from the ionized gas region or from photodissociation regions (PDRs). Employing the 60 and 100 μm data, the dust temperature derived in the environs of the H II region Sh2-205 is $\approx$ 29 K [Romero and Cappa, 2008] and in the region surrounding the H II region of S173, the dust temperature obtained is 30±5 K [Cichowolski et al., 2009]. All the studies mentioned above have used Infrared Astronomy Satellite (IRAS) data. However, IRAS was insensitive to dust at temperatures below 20 K. The detection of colder dust ($\leq$20 K) requires sub-millimeter observations.

There are very few existing analyses of cold dust in the environments of H II regions. Mezger et al. [1987] using mm and sub-mm observations found dust at 20 K near S106. In addition, according to their studies, dust in S106 has three different temperatures, viz. hot, warm, and cold and the three components stem from three different regions with the hot dust emission (146 K) arising from the dust associated with the ionized gas, the warm dust emission (44 K) being exterior to the ionized gas, and the cold dust emission ($\sim$20 K) being from the extended molecular cloud. According to some analyses, the clouds connected to some H II regions are warmer (S151; 25-40 K) [Brand and Wouterloot, 1998] than nearby dark clouds (20-25 K) [Wood et al., 1994], which may indicate the existence of embedded stars in the clouds that heat up the dust surrounding them. However, other studies have shown that giant molecular clouds (GMCs) with and without H II regions display a fairly small disparity in the mean dust temperatures [Scoville and Good, 1989] (31.6±0.4 K compared with 25.4±1.5 K).

Regions with temperatures less than 20 K represent the coldest and densest regions of molecular clouds. There are a number of studies that examined the dust in isolated pre-stellar clouds. For example, from the observed SED of the low-mass pre-stellar core L1544, Andre et al. [2000] obtained a dust temperature of 13 K for $\beta = 2$. Similarly, an average dust temperature of 7.6 $\pm$ 0.5 K is found in the low-mass pre-stellar core of L183 [Pagani and et al., 2003]. Further studies of the same cloud by Pagani and et al. [2004] confirmed this result and came to a conclusion that the coldest temperature in the inner core could be as low as 6.7 K.

1.11 Recent Results on Dust near H II Regions

The Balloon-borne Large Aperture Submillimeter Telescope (BLAST; [Pascale et al., 2008]) observations of the Aquila, a high-mass star forming region, show dust temperatures of $\sim$ 35-40 K in the clumps for a dust emissivity index of 1.5 [Rivera-Ingraham et al., 2010]. Similarly, infrared and sub-mm studies on an OB forming complex, Cygnus-X, using BLAST provide about 22 K as the median temperature distribution value of the sources in the field with some sources approaching temperatures as warm as $\sim$ 40 K, and some other sources, as cold as $\sim$ 10 K [Roy et al., 2011b]. In their further studies, Roy et al. [2011a] analyzed BLAST maps of two molecular cloud complexes, namely K3-50 and IC5146, using improved image restoration methods, and found that K3-50 harbours warmer dust zones with dust temperatures ranging from 20 to 35 K as opposed to much colder dust in IC5146 ($T_d \sim$ 12 to 16 K).

Recent observations of massive star forming regions made with *Herschel Space Observatory* [Pilbratt et al., 2010] as a part of "Herschel imaging survey of OB Young Stellar objects (HOBYS)" program [Motte et al., 2010] have provided unprecedented details of clouds associated with H II regions. The Rosette molecular cloud, excited by a cluster of OB stars at the centre, exhibits a gradient in temperature with temperatures of around 30 K at the molecular cloud-H II region interface and around 10 K in the direction away from the H II region [Schneider et al., 2010]. The obtained dust temperatures using aperture photometry on *Herschel* data towards S104, a well known Galactic bubble H II region, are between 17.3 $\pm$0.4 K and 35.7$\pm$2.1 K (for β =2) and between 17$\pm$2 K and 47$\pm$15 K (for free β) [Rodón and et al., 2010].

Using data from *Herschel*, SPITZER MIPS, and APEX LABOCA, the dust temperature map of the Galactic bubble H II region RCW 120 derived by Anderson et al. [2010] shows regions with temperatures as low as 10 K towards local infrared dark clouds (IRDCs) including cold filaments and $\sim$ 30-35 K in the direction of the RCW 120 interiors. According to their study, the photodissociation region of RCW120 is at a temperature of $\sim$ 20 K. One of the GMC on the Galactic disk, Vela-C, which is also a site for both low- and high-mass star formation, shows warmer protostellar sources with mean dust temperatures of 12.8 K compared to starless sources with mean dust temperatures of 10.3 K [Giannini et al., 2012]. A number of bubble Galactic H II regions are recently studied by Anderson et al. [2012] and their results confirm mean dust temperatures of 26 K along PDRs and H II regions with colder dust having temperatures of 15 K at locations of IRDCs and 19 K at filamentary regions. The dust temperatures of the Galactic H II region W5-E observed with *Herschel* range from 17.5 K, in dense regions to 31 K, close to H II regions [Deharveng et al., 2012].

1.12 Specific Goals of This Thesis

This thesis is an observational as well as modelling study to derive the physical properties of dust associated with Galactic H II regions in order to understand the impact on the dust of the extreme conditions close to massive stars. The principal aim of this thesis is to provide the breadth of the temperature and mass distribution in clouds associated with H II regions since these properties are relatively poorly understood in Galactic H II regions, although such properties are known in many different regions.

Stars form in "cores", cold dense condensations of gas and dust within molecular clouds. Cores that produce low-mass stars are very well studied due to their proximity, abundance, and solitary conditions. However, the high-mass star formation is one of the least studied area in the field of star formation since birth places of massive stars are buried within large amounts of dust and gas. Furthermore, most of the GMCs that harbour massive star forming sites are at least a kpc away and we require high spatial resolution instruments to probe such locations.

The densest cores in molecular clouds are believed to be the most favourable sites for massive star formation. But what are the physical properties of these cores? Are there cold cores exist near H II regions? How do these cores turn into stars? These questions are still open in the field of star formation. We address these questions in this research. Since cores within molecular clouds produce stars, the nature, properties, and environment of the cores should regulate the initial conditions for star formation.

In order to derive the global physical properties of H II region clouds, at first, we selected a large number of GMCs in the Galaxy which were observed at IRAS mid-infrared wavelengths. By selecting the mid-infrared observations, we aim to characterize the properties of the dust grains, which are emitting at 12, 25, 60, and 100 μm, such as the temperature, mass, and bolometric luminosities. Dust grains that are emitting at shorter wavelengths such as 12 and 25 μm can be hotter than the grains that are emitting at longer wavelengths such as 60 and 100 μm.

Another goal of this thesis is to determine the internal gas density distribution of Galactic H II region clouds using the observed flux densities at IRAS wavelengths. Note that the giant molecular clouds selected in this thesis are associated with massive stars and therefore it is significant to study the effect of the stellar radiation on the molecular clouds. By using the conditions of thermal equilibrium in large grains, we model the gas density, dust emissivity, and temperature distribution. By analyzing the observed and modeled flux density distributions, we aim to show whether there are any standard density structure exist in the clouds associated with Galactic H II regions.

One of the major aims of this thesis is to search for the existence of very cold dust components near to very hot massive star forming conditions. The coldest regions of the

molecular clouds are located deep within the clouds and are shielded from any UV radiation sources. Since massive star forming regions are deeply embedded within large amounts of gas and dust, we require optically thin tracers to explore such coldest and densest regions. Sub-mm thermal continuum emission by cold interstellar dust probes the very early stages of star formation, by tracing the high column densities and low temperatures within star-forming cores. So we can use sub-mm observations to measure core masses. To understand the initial conditions of star formation, we need to determine the nature as well as the influence of internal and external forces on the cores; this means that we also want to measure temperature as well as density to establish the stability of cores.

Are the cloud cores harbour proto-stellar objects? or the observed cores at sub-millimeter wavelengths are pre-stellar cores? If the cores are not hosting a massive proto-star at the centre, what are their characteristic physical properties? Using the sub-mm continuum emission by interstellar dust, we aim to answer these questions by finding out whether there are any temperature gradients in clouds near Galactic H II regions. If the temperature is increasing towards the centre of the cloud core, then this may imply the presence of a heating source at the centre. However, if the cloud cores are cold with increasing dust temperatures toward the outer cloud envelope, this may imply a centrally cold cloud without any internal heating. In such cases, the envelope heating is provided by the external radiation field. The analysis can help identify the presence of any internal heating sources associated with our clouds.

Another plan of this thesis is to quantify the influence of dust emissivity index on the temperature and densities. The value of dust emissivity index depends on many different factors such as environment, composition, and structure of the grains. However, in the far-infrared and sub-millimeter, the value varies from 1 to 2. We aim to examine how the dust temperature and density distribution can change as we increase the emissivity index from 1 to 2.

In this thesis I also aim to analyze the effect, if any, of spectral line contamination to the SCUBA-2 bolometer band-passes. Continuum flux, especially at 850 μm SCUBA-2 wavelength, can be contaminated by molecules such as CO(3-2), SO and SO_2. We search for any change in the density and temperature distribution after the removal of the line contamination to the SCUBA-2 fluxes. However, note that we do not have any clouds observed at the above molecular lines and are uncertain about the presence of line contamination in our sample clouds. Therefore, we assume line contamination in one of our target clouds and test the effect of contamination removal on the cloud's physical properties.

The coldest and densest sites in GMCs are precursors to massive star formation. Densest regions of the molecular clouds have high visual extinction, high column densities, and high mass. At such conditions, the regions may favour an infalling state over an equilibrium state if thermal pressure is the only force that balances against gravity. However, if other

forces such as the force due to magnetic field, and the turbulence counteract gravity, the densest regions may support against gravity. With the use of sub-millimeter dust emission maps from the sample clouds, we probe the present state of the cloud cores.

The last goal of this thesis is to provide a schematic diagram of the Galactic H II region clouds using the knowledge from both the observations and modelling.

1.13 Structure of This Thesis

In this thesis I present the physical properties of dust such as mass and temperature in molecular clouds associated with H II regions in order to learn about the effect on the dust of the harsh environments around high-mass stars. Chapter 2 of this thesis deals with the physical properties of dust derived from IRAS observations of 83 clouds near H II regions. The motivation for this thesis is described in this chapter along with cloud selection criteria and calculation as well as presentation of the obtained physical properties. The dust properties derived from archival SCUBA observations of a subsample of 15 clouds are also presented in the same chapter. In Chapter 3, I analyze the properties of the clouds obtained from Chapter 2. Chapter 4 contains model calculations of H II region clouds based on the IRAS observations. Chapter 5 is a detailed study of the cold dust in a subsample of 6 molecular cloud complexes associated with Galactic H II regions, the data of which were obtained from the new SCUBA-2 camera. Chapter 6 includes the analyses of the results obtained from the SCUBA-2 observations. Chapter 7 concludes this thesis by discussing and summarizing the major results of this thesis and by providing a synopsis of subsequent research. The SPITZER mid-infrared view of some of the Galactic H II regions observed with SCUBA-2 and the morphology of the cold dust and ionized hydrogen regions are also presented in Chapter 7.

Chapter 2

Physical Properties of Galactic H II regions from IRAS and SCUBA observations

In this chapter, I study the properties of dust, such as the temperature, masses (note that in this chapter, I present only the dust masses; however, in Chapter 3, I also discuss the gas masses) and bolometric luminosities, associated with Galactic H II regions to learn about the effect on the dust of the extreme environments around high-mass stars. We present calculated properties of dust near Galactic H II regions, primarily based on Infrared Astronomical Satellite (IRAS) data [Chan and Fich, 1995]. Our study does not utilize any Spitzer data since the coverage of Galactic H II regions by Spitzer is very limited and the angular extent of molecular clouds associated with H II regions is very small in already existing Spitzer data, although this may change as various Spitzer survey programs release their data. This study utilizes the large, reduced data set from Chan and Fich [1995] that had not yet been analyzed in any detail. A two temperature dust model is used to fit IRAS data for 83 clouds in the vicinity of Galactic H II regions. The total bolometric luminosities of hot and cool dust in these regions are calculated separately. To find the amount of cold dust, I used Submillimeter Common User Bolometric Array (SCUBA) data of 15 molecular clouds near H II regions. A three-component dust model is used to fit both the IRAS and SCUBA data of these regions (see section 2.2 for details).

In this chapter I show that the dust grains in clouds near Galactic H II regions are not at uniform temperatures. The temperatures in these clouds may span a wide range but with the use of only IRAS data we can employ only two temperature components in our models. With the inclusion of SCUBA data points we can use, and in fact need, a third temperature component. The coldest component is likely to be located in the interior of the cloud and the cloud may be warmer towards the exciting star and may be the hottest

near to the star. Furthermore, there is another component between the hottest and the coldest regions of a cloud—the cool dust. We demonstrate that this cool dust dominates the bolometric luminosity while the cold dust dominates the mass of clouds. Note that the material in this chapter and in Chapter 3 is adapted from the paper entitled "Hot and Cold Dust Near H II Regions" [Sreenilayam and Fich, 2011].

2.1 The Data

We used measured flux densities from Chan and Fich [1995] to calculate emission properties of hot and cool dust in the H II regions. In their survey of H II regions, Chan and Fich used the Infrared Processing and Analysis Center (IPAC) Full Resolution Survey CO-adder (FRESCO) image products at four (12, 25, 60 and 100 μm) Infrared Astronomy Satellite (IRAS) bands. All of the images of H II regions in their study have an angular size of $1^\circ \times 1^\circ$, and a pixel size of $15'' \times 15''$. We selected the IRAS flux densities of 83 objects from Chan and Fich [1995], beginning with 50 clouds that have known distances [Chan and Fich, 1995] obtained from the measurements of distances to H II regions [Fich and Blitz, 1984]. The objects with a 'C' at the end of their names in Table 2.2 are complexes that contain multiple resolved or unresolved IR peaks. If the distance to a cloud in a complex is known, then I use that value as the distance to all of the clouds in the complex; there are 30 such clouds. In complexes with two or more distance estimates, e.g., BFS15C, the average distance to the clouds is taken as the distance to the clouds without any distance measurements; there are two such clouds). In our study, we updated the distances of 30 clouds using revised distance information that is based on UBV photometric and spectroscopic data of the exciting stars [Russeil et al., 2007; Caplan et al., 2000]. An uncertainty of 20% in distance is assumed for clouds without any distance uncertainty quoted in their spectrophotometric distance measurement. We included the H II region BFS8 in to our list of clouds because of a recent distance measurement [Russeil et al., 2007]. If the difference between a complex's flux density and the sum of its clouds' flux density is less than 10% of the complex's flux density at 12 μm, then the complex is discarded from this study. We establish this criterion for the selection of the complexes in order to avoid duplication of the results, because, if a complex satisfies the above criterion, then the emission from the complex becomes identical to the sum of its clouds' emission, and hence the flux is counted twice. IRAS 12 μm is chosen for setting up the above criterion since all the complexes and clouds are best resolved at 12 μm compared to all other IRAS wavelengths. Consequently, the total number of objects in our study is 83 (including complexes and their individual clouds), and of these, 13 are solely complexes. The total number of H II regions associated with the clouds is 66.

Most of the clouds in this study are giant molecular clouds typically with a single H II region. But a few clouds harbor two, three or as many as five H II regions. For example,

the complex S99/100C contain two H II regions—S99 and S100—whereas S147-9 is a single molecular cloud with three H II regions: S147, S148, and S149. The complex S254-8C accommodates five H II regions: S254, S255, S256, S257, and S258. Clouds that are not resolved in the 100 μm images are not included in this study. For example, the peaks of clouds BFS57C$_a$, BFS57C$_b$, BFS57C$_c$ are unresolved at 100 μm, and therefore, I avoided these individual clouds in our investigation.

2.1.1 Error estimation

The uncertainty values in IRAS flux densities of 83 clouds are taken directly from Chan and Fich [1995].

2.1.2 SED fitting

We cannot fit IRAS observations by a one-component model since a model reproducing the four IRAS flux density measurements required at least two temperature components. By the same token, IRAS and SCUBA observations cannot be fitted by models with one or two temperature components; at least three temperature components are required to explain these observations. The Spectral Energy Distributions (SEDs) of the clouds near H II regions were fit using an MRN distribution [Mathis et al., 1977] of grains with 50% silicate and 50% graphite. A two-component model SED is fitted with the IRAS data for 83 H II regions. The two-component model produces a fit with a cool component, with temperature ranging from 20 to 40 K, and a hot component with temperature above 100 K. In order to determine the cold component (T$\leq$20 K), the 450 and 850 μm SCUBA data for 15 H II regions are included along with IRAS data and a three-component model SED is fitted. It must be noted that in this study I do not fit for PAHs and VSGs mainly because to include these components we need near IR flux density measurements or even hotter higher spectral resolution observations, which are currently unavailable. In addition, the contributions from these components are limited to only the 12 μm IRAS wavelength.

For spherical grains of radius a, the modeled flux density F_ν can be written as

$$F_\nu = \frac{3Q_{em}}{4a\rho}\frac{B(\nu, T_{dust})M_{dust}}{D^2}, \tag{2.1}$$

where ρ is the density of the dust grains, M_{dust} is the mass of dust grains, $B(\nu, T_{dust})$ is the Planck function and D is the distance to the object. All our calculations adopted a value of $\rho = 2\frac{g}{cm^3}$. The dust grain emission efficiency is Q_{em}, given by

$$\frac{Q_{em}}{\frac{4}{3}a} = \frac{C}{V}, \tag{2.2}$$

where C is the emission cross section and V is the volume of dust [Fich and Hodge, 1991]. C/V values of silicate and graphite spherical grains were obtained from Dr.Peter G. Martin (private communication) and are similar to the C/V values of Draine [1985]. The term $\frac{4}{3}a$ is derived from the projected geometrical surface area and the volume of a spherical dust grain of radius a, and is different for grains having different shapes. Figure 2.1 shows the $\lambda Q_{em}/a$ vs. λ corresponding to 50% silicate and graphite (solid red line), silicate (dashed green line), and graphite (dashed blue line), plotted using the C/V values of silicate and graphite.

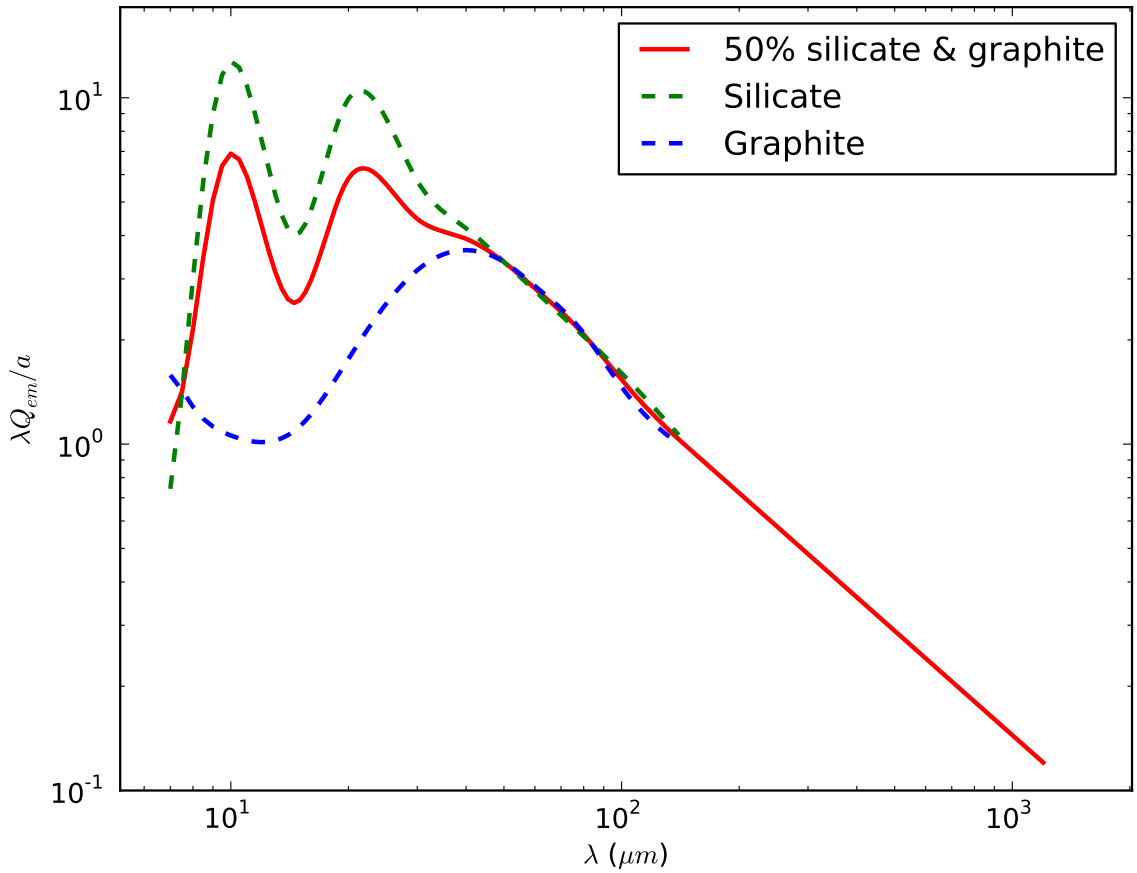

Figure 2.1: Plot showing $\lambda Q_{em}/a$, for silicate (dashed green line) and graphite (dashed blue line). The solid red line represents 50% silicate and graphite as used in this study.

2.1.3 Uncertainties due to the fitting procedure

The two dust components are entirely independent of each other in the two-component fit. Independently performing a one component fit to the 12 and 25 μm flux densities and an additional one component fit to the 60 and 100 μm flux densities, we observe that the results of these fits match very well with the solutions collected from the two-component "joint" fit. The average relative difference between the two-component and one component models is 4% in the mass of the cool and hot dust, 0.6% in temperature of the hot dust, and 0.8% in the temperature of the cool dust.

In the two-component model, there are four flux density measurements and four unknown parameters (M_{hot}, T_{hot}, M_{cool}, T_{cool}) while the three-component model consists of six flux density measurements and six unknown parameters (M_{hot}, T_{hot}, M_{cool}, T_{cool}, M_{cold}, T_{cold}). In principle, an exact fit is possible for the above cases, but the fits may be not well constrained because of the uncertainties in the flux density measurements. This is not important for the two-component model; but it is critical for the three-component model.

In order to obtain the limited values of the parameters bounded by our adopted dust components present in the SED, we employed the following method: Within the given temperature ranges of the hot ($\geq$ 100 K), cool (20 K-40 K), and for objects with SCUBA data—the cold ($\leq 20K$) dust, the masses and temperatures of each dust component are found by minimizing the chi-square weighted by the measurement error associated with the observed flux density. The same minimization procedure is also applied to the two-component model. The fitting uncertainties in the masses and temperatures of the hot and cool dust components, obtained as the values corresponding to a chi-square less than two, are much smaller than the uncertainties due to the errors in the measured flux densities. Nevertheless, the fitting uncertainties in the parameters for the cold dust far exceed the uncertainties due to the errors in the measured flux densities. The obtained fitting uncertainties in the cold dust parameters, which correspond to a chi-square less than two, are discussed in detail in Section 2.2.3.

2.1.4 Color correction

We model the measured flux density at each effective wavelength of the IRAS bands convolved with the wavelength dependent instrument response and the SED to get a prediction of the observed flux density to directly compare to observations. Our SED modelling code yields a colour correction factor (K-correction; [Beichman et al., 1988]) and a flux density at each IRAS wavelengths along with the masses and temperatures of the two dust components. The predicted flux density is multiplied by the K-correction to get the observed (measured) flux density of clouds near H II regions at the four effective wavelengths of the IRAS bands.

Table 2.1: Color correction

Wavelength (μm)	Minimum K	Maximum K	Mean K
12	0.74 (S138C$_b$)	1.07 (BFS53)	0.88
25	0.93 (S138C$_b$)	1.26 (BFS53)	1.13
60	0.88 (S233C$_a$)	1.16 (S266C$_c$)	0.91
100	0.95 (S266C$_c$)	1.03 (S138C$_b$)	1.00

For all clouds, except BFS53, BFS58, S201C$_c$, S208C$_b$, and S259C$_c$, the K-correction increased the observed flux density at 12 μm. The K-correction reduced the observed flux density at 25 μm for all objects except BFS15C$_c$, BFS57C, S138C$_b$, S233C$_b$, and S247C$_c$. At 60 μm, the K-correction increased the observed flux density of all the H II regions with the exception of S266C$_c$. In the case of 100 μm, each behaviour is almost equally observed: the K correction increased the observed flux densities of 47 objects while it reduced the observed flux densities of 36 clouds. The minimum and maximum values of K factors and the clouds that show these extreme values at four IRAS wavelengths are given in Table 2.1. In addition, Table 2.1 also provides the mean K values of all the clouds at each IRAS wavelengths.

2.1.5 Calculated Results

We calculated the the mass, temperature, and bolometric luminosity of the hot and cool dust from the two-component model SED fitted to the IRAS data. As an attempt to calculate the amount of cold dust, we continued the study with 15 H II regions which also had archival SCUBA data. We also compared our results to clouds not associated with an H II region, using IRAS data of 13 isolated low mass pre-stellar clouds. It must be emphasized that the derived masses in this study are masses of dust except in section 3.3, where we converted the dust mass to the gas mass to compare our results with those obtained in previous studies.

Table 2.2: Calculated masses, temperatures, and bolometric luminosities of H II regions.

Name	$\mathbf{M}_{cool}$ $(M_\odot)$	$\mathbf{M}_{hot}$ $10^{-6}(M_\odot)$	$\mathbf{T}_{cool}$ **(K)**	$\mathbf{T}_{hot}$ **(K)**	$\frac{M_{cool}}{M_{hot}}$ $\times 10^3$	$L_{Bol_{cool}}$ $10^3(L_\odot)$	$L_{Bol_{hot}}$ $10^3(L_\odot)$
BFS6	10±1	40±10	28.7±0.4	210±10	250±60	34±5	9±3
BFS8	60±20	100±25	25±1	230±15	630±260	80±40	30±13
BFS10	5±2	26±7	30±1	210±10	190±80	20±9	5±2
BFS15C							
a	12±1	930 ±50	36.4±0.4	174±2	13±1	170±15	75±6
b	9±1	115±20	33±1	216±7	80±16	72±12	27±6
c	1.2±0.8	≤2902	36±4	140±40	0.40[1]	≤33	76[4]
d	1.1±0.6	20±5	34±3	190±10	50±30	10±8	3±1
BFS31	1.6±0.2	12±1	30.8±0.5	217±6	135±20	8±1	2.7±0.4
BFS34	1.06±0.07	21 ±2	33.8±0.4	198±5	50±6	10±1	3.2±0.5
BFS53	0.6±0.1	1.0±0.2	28±1	300±20	600±200	1.6±0.5	1.0±0.3
BFS54	23±2	90±10	29.6±0.4	260±8	270±40	100±10	46±9
BFS57C	0.9±0.2	310 ±70	36±1	142±6	3±1	12±4	9±3
BFS58	6±1	6±2	27±1	280±30	930±340	13±3	4±2
BFS62	0.10±0.02	18.3±0.5	36±1	159±1	5±1	1.3±0.4	0.95±0.03
BFS64C	8.2±0.7	36±6	30.3±0.4	240±10	230±50	41±5	14±3
S99/100C							
a	130±40	12000±2000	38±2	170±6	11±4	2500±1100	910±220
b	≤129	≤281	27±10	200±100	459[2]	299[3]	46[4]
S104	8±3	150±40	32±2	200±10	55±25	55±30	21±8
S107	0.4±0.2	9 ±2	33±3	180±10	40±25	3±2	0.9±0.3
S120	4±1	190±10	35±1	182±3	20±4	43±13	19±2
S121	13±4	130±30	30±1	200±10	100±40	60±20	19±7
S127	13±2	250±40	33±1	191±6	50±10	100±20	31±7
S128	12±1	750±140	35±1	163±6	17±4	130±20	44±12
S138C							
a	1.4±0.3	120±13	36±1	167±4	12±3	19±6	8±1
b	0.15 ±0.03	70±20	38±2	123±8	2.2±0.9	3±1	1.0±0.5
S141C	14±4	53±13	28±1	240±10	300±100	40±15	21±7
a	10±3	33±14	27±1	220±20	300±160	23±10	9±6
c	2.5±0.5	10±5	28±1	260±30	250±130	7±2	6±4.0
S146	4.1±0.1	340±20	36.3±0.2	174±3	12.0±0.8	59±3	27±3

Continued on Next Page...

Table 2.2 – Continued

Name	$\mathbf{M}_{cool}$ $(M_\odot)$	$\mathbf{M}_{hot}$ $10^{-6}(M_\odot)$	$\mathbf{T}_{cool}$ **(K)**	$\mathbf{T}_{hot}$ **(K)**	$\frac{M_{cool}}{M_{hot}}$ $\times 10^3$	$L_{Bol_{cool}}$ $10^3(L_\odot)$	$L_{Bol_{hot}}$ $10^3(L_\odot)$
S147-9	19±2	120±25	31±1	230±12	160±40	100±20	40±10
S152C	4.5±0.5	65±3	32.3±0.5	234±2	69±9	33±5	22±1
S159	8±2	690±80	34±1	158±4	11±3	80±30	35±6
S168	20±13	50±14	27±2	230±20	400±300	50±40	15±6
S172	2.4±0.7	11 ±3	30±1	240±15	210±90	11±4	4±2
S175C	0.8±0.1	4.0±0.6	29±1	234±9	190±40	3.0±0.7	1.3±0.3
a	0.4±0.1	2.9 ±0.4	31±2	220±7	120±50	2±1	0.7±0.1
b	0.4±0.2	1.2±0.7	27.±2	220±30	300±200	0.9±0.7	0.29±0.27
S186	1.4±0.5	13 ±5	33±2	230±25	110±60	11±6	4±2
S192-4	9±4	20 ±3	28±2	250±10	500±200	26±14	9±2
S196C							
c	3.1±0.5	320±25	34±1	158±2	10±2	29±6	16±2
a+b	5±2	16 ±6	28±2	240±20	350±180	17±8	6±4
S201C	25±6	390±80	33±2	200±7	60±20	200±70	60±20
a	15±3	110±20	33±1	225±8	140±30	120±30	30±7
b	4±2	460±170	34±3	151±9	9±5	40±24	19±9
c	9±6	≤18	26±2	300±100	476[1]	15±14	16[4]
S208C	13±5	110±20	31±2	220±10	120±50	80±40	29±8
a	9±1	60±30	30±1	220±30	140±70	43±8	15±11
b	0.3±0.2	2.0±1.9	32±4	290±70	≤317	≤4	≤4
c	3.8±1.3	41±7	31±2	217±8	90±40	23±10	10±2
S209C							
a	130±10	9600±1200	35±1	160±4	13±2	1600±200	520±90
b	≤90	≤787	32±8	≤896	114[2]	642[3]	165[4]
S211C	15±2	600±200	33±1	170±7	25±7	130±20	44±15
a	12±2	100±20	31±1	210±9	120±30	70±20	20±6
S233C	4.4±2.2	40 ±4	30±2	194±5	110±60	20±13	6±1
a	0.6±0.4	≤16	35±4	240±50	41[1]	6.9±6.8	5.70[4]
b	2.2±1.6	80±50	30±3	140±15	27±26	10.2±9.6	2.2±1.8
S237C	1.29±0.04	25 ±2	34.3±0.2	213±3	52±4	13.5±0.6	5.3±0.5
S242C	4.6±0.2	17 ±2	29.8±0.2	246±6	270±30	20±1	7±1
a+b	4.5±0.4	18±3	30±1	240±10	250±40	19±3	7±1
S247C							
a	8.5±1.0	280±20	33±1	179±2	31±4	70±10	26±2
b	4.7±0.6	200±100	33±1	160±15	21±9	41±7	13±8

Continued on Next Page...

Table 2.2 – Continued

Name	$\mathbf{M}_{cool}$ ($M_\odot$)	$\mathbf{M}_{hot}$ $10^{-6}(M_\odot)$	$\mathbf{T}_{cool}$ **(K)**	$\mathbf{T}_{hot}$ **(K)**	$\frac{M_{cool}}{M_{hot}}$ $\times 10^3$	$L_{Bol_{cool}}$ $10^3(L_\odot)$	$L_{Bol_{hot}}$ $10^3(L_\odot)$
c	2.0±0.2	320 ±60	36±1	145±6	6±1	29±3	10±3
S253	1.5±0.5	2 ±1	27±1	260±40	800±600	3.5±1.5	0.90±0.85
S254-8C	16±1	260±10	33.0±0.3	202±3	62±4	130±10	43±4
S259C							
a	7±2	180 ±40	33±2	181±8	40±10	60±30	18±6
b	1.5±1.1	≤31	33±4	200±70	48[1]	≤25	5.2[4]
c	4±1	7±3	28±1	300±30	600±300	11±4	7±4
S266C							
a	42±6	300±50	31±1	223±9	139±31	220±40	80±20
c	40±30	10±5	21±2	230±20	4200±4100	20.3±20.0	3±2
S269	6.1±0.5	170±15	35.0±0.4	190±3	36±4	72±8	22±3
S270	4±1	540±90	35±1	151±5	7±2	45±12	22±5
S271	7±1	32±9	30±1	230±10	220±70	31±7	9±4
S283	3.1±0.6	20±2	31±1	224±5	160±40	18±5	5.4±0.8
S285	5.0±0.4	18 ±2	29.6±0.3	248±7	280±40	21±2	8±1
S286	10±1	20 ±6	27±1	240±14	500±200	26±5	7±3
S288	0.72±0.05	58 ±3	38.1±0.4	173±2	12±1	14±1	4.6±0.3
S294	5.3±0.6	12±2	27.4±0.4	250±10	430±80	14±2	5±1
S297	0.98±0.09	6 ±1	32±1	240±10	160±30	6.1±0.8	2.4±0.7
S299/300C							
a	3.8±0.6	11±5	29±1	240±20	340±150	15±3	4±2
b	3±1	13 ±5	30±1	230±20	220±100	13±5	4±2
S305C	29±1	580±40	31.2±0.2	190±3	50±4	170±10	72±7
S307C							
c	1.2±1.1	1.4±0.8	26±3	250±30	≤1745	≤5	0.6±0.5
a+b	1.2±0.5	29±4	33±2	185±3	40±20	9±5	3.2±0.5

[1]Using the upper limit of the mass of hot dust
[2]The upper limit of M_{cool}/M_{hot}
[3]Upper limit of the bolometric luminosity of cool dust
[4]Upper limit of the bolometric luminosity of hot dust

Hot and Cool dust

The model SED of the H II region S104 is shown in Figure 2.2. The cloud S104 is selected as a representative cloud primarily because this is the only cloud with a large area scan map at 850 μm, and the image clearly reveals most of the extended features of the cloud. The SED shows one peak around 10 μm corresponding to the silicate emission and a peak around 30 μm indicating the broad graphite feature. The masses of hot and cool dust in S104 are $150\times10^{-6}M_{\odot}$ and 8 $M_{\odot}$, respectively. In S104, the hot dust is at a temperature of 200 K, whereas the cool dust is at 32 K. The properties of the cold dust in S104 are described in Chapter 3.

The estimated masses and temperatures of hot and cool dust of all the 83 clouds near H II regions, derived from IRAS flux densities, are listed in Table 2.2. The first column of Table 2.2 lists the name of each cloud. The masses of the cool (M_{cool}) and hot dust (M_{hot}) components are given in columns two and three, and the temperatures of the cool (T_{cool}) and hot dust (T_{hot}) are in the following two columns. The sixth column gives the ratio of the mass of cool dust to the mass of hot dust. We included the bolometric luminosities of cool and hot dust in the seventh and eighth columns. The bolometric luminosities of the clouds are calculated by integrating the continuum emission from 7 μm to 1000 μm using the SEDs. Emission outside the above mentioned range does not contribute significantly to the total bolometric luminosity. The bolometric luminosities due to hot and cool dust are each calculated separately.

The uncertainties in the masses and temperatures of the hot and cool dust shown in Table 2.2 are associated with the measurement uncertainties of the flux densities at the four IRAS bands. Not included in Table 2.2 are the uncertainties in the derived parameters associated with the distance uncertainty to the clouds. Some clouds show a very large uncertainty in the distance, for example, the distance to the cloud BFS62 is uncertain by 56%, while the cloud S270 shows a 47% uncertainty in the distance. The uncertainty in distances to H II regions contributes largely to the observed flux densities of clouds in the four IRAS bands. In all clouds, the average uncertainty contribution due to distance to the observed flux densities is $\approx$ 43%.

A few clouds exhibit a very large uncertainty in the calculated masses of both dust components. Cloud S99/100C$_b$ has a substantial uncertainty in the masses of cool (the upper limit of M_{cool} is 129 $M_{\odot}$ while the lower limit of M_{cool} is 1.34 $M_{\odot}$) and hot (with the mass of hot dust ranging from 5×10^{-6} $M_{\odot}$ to 281×10^{-6} $M_{\odot}$) dust due to the large uncertainties in the IRAS flux densities. In the case of cloud S209C$_b$, the upper bound to the mass of cool dust is 90 $M_{\odot}$, and that of the hot dust is 787 $\times10^{-6}$ $M_{\odot}$. Certain clouds, such as BFS15C$_c$, S201C$_c$, S233C$_a$, and S259C$_b$, show a significant uncertainty only in the mass of one dust component—the hot dust. For these clouds, the upper limit of the mass of the hot component is considered. For those clouds that have only upper limits of

the mass, the values of M_{cool}/M_{hot}, $L_{Bol_{cool}}$, and $L_{Bol_{hot}}$ are calculated using these upper mass limits (see Table 2.2 for more details), and such clouds are not included in further discussions.

Figure 2.3 shows the range of the mass of the cool dust and the mass of the hot dust of our sample clouds. The two objects at the right side edge of Figure 2.3 are S99/100C$_a$ and S209C$_a$ and are the most massive in the hot and the cool dust among all the objects. Clouds S99/100C$_a$ and S209C$_a$, being the most massive in the cool dust, contains 130 $M_\odot$ of the total cool dust and 0.01 $M_\odot$ of the total hot dust. Cloud BFS62 is the least massive (0.10 $M_\odot$) object in cool dust amongst all our sample clouds. The cool-to-hot dust mass ratio M_{cool}/M_{hot}, denotes the fractional mass in the cool and the hot dust. Since both M_{cool} and M_{hot} are proportional to the distance in the same manner, the ratio, M_{cool}/M_{hot} is not affected by any uncertainties in the distance. For most of the H II regions in our study, M_{cool}/M_{hot} is found to be above 10^4. The ratio M_{cool}/M_{hot} ranges from 2.2×10^3 (S138C$_b$) to 4.2×10^6 (S266C$_c$) with a mean value of 2.2×10^5. The cool dust masses that we derived span from 0.10 $M_\odot$ to 130 $M_\odot$, with the mean mass around 11.3 $M_\odot$. From the IRAS 100 and 60 μm flux densities, Scaife and et al. [2008] calculated the dust temperatures of fourteen Galactic H II regions. Our studies have 9 H II regions in common and the cool dust temperatures are similar. The average difference between our values of the dust temperature is 1.60 K with an rms uncertainty of 0.96 K.

The luminosity vs. mass of the cool component of the dust in the clouds examined in this paper is plotted in Figure 2.4. The IR luminosities given in Figure 2.4 are calculated from the colour corrected flux densities at the four IRAS wavelengths. The clouds near H II regions on the plot have been categorized based on three temperature ranges of the cool dust component. The three different colours on the plot represent the three different temperature ranges. Blue denotes a temperature range of 20 K to 29 K; likewise, Cyan and Red represent temperature ranges of 29 K to 33 K and 33 K to 39 K respectively. Cloud S266C$_c$ has the lowest value (21 K) of the temperature of the cool dust, and the cloud S288 shows the maximum value of the temperature of the cool dust, which is 38.1K. Likewise, clouds BFS53 and S201C$_c$ are the hottest among all our sample clouds with the hot dust temperature of 300 K, while cloud S138C$_b$ has the lowest value for the temperature of the hot dust (123 K).

2.2 SCUBA Observations of H II Regions

2.2.1 SCUBA

The Submillimeter Common User Bolometer Array (SCUBA) [Holland et al., 1999] is a continuum array receiver at submiliimeter wavelengths. SCUBA has a field of view of

2.3′and it consists of two arrays of bolometers, whose FWHM beam sizes at 850 μm and 450 μm are 14″and 7.5″, respectively. The long wavelength array which operates at 850 μm has 37 pixels and the short wavelength array which operates at 450 μm has 91 pixels. The SCUBA archival data, which were acquired from 1997 to 2004, are used for calculating the properties of cold dust near H II regions. The SCUBA data have been retrieved from the Canadian Astronomical Data Centre (CADC) and processed using ORACDR data reduction pipeline [Jenness and Economou, 1999] and the SCUBA User Reduction Facility-SURF software package. Out of the three different observing modes (scan, jiggle, and photometry) of SCUBA, the scan mode is used for mapping objects larger than the array and the jiggle mode is for mapping objects smaller than the array. The bolometers (pixels) are arranged in a hexagonal close packing structure. Due to the spacing between the adjacent array pixels, the source image will be under-sampled. To avoid this and to fully sample the source image, the telescope secondary is jiggled in a 64 point pattern. The sky variability on the signal (due to the thermal radiation from the atmosphere) is reduced by means of chopping the secondary mirror and nodding the telescope. During the chopping, the secondary mirror is drifting between the source position and the sky position at a frequency of 7 Hz to cancel the temporal and spatial fluctuations in the sky. Scan mapping uses a raster technique of surveying the required field and repeating the rasters to get the intended result. Note that in jiggle mapping, which is a "stare" mapping, the bolometer array is positioning towards the intended sky location and integrating to the required depth to get the proper result [Jenness et al., 1998]. Most of the data are primarily small area jiggle maps except for the region S104, where larger area scan maps were used. Out of 83 IRAS H II region clouds, I found SCUBA data for 15 objects. For comparison, we have also selected 10 isolated pre-stellar clouds analyzed by Kirk et al. [2005] using 450 and 850 μm SCUBA data. The IRAS data for the pre-stellar molecular clouds are obtained from SkyView [McGlynn et al., 1996] for the comparison of calculated properties of clouds with and without H II regions. Some of the IRAS pre-stellar clouds showed a peak emission position which is different from their peak position according to Kirk et al. [2005]. The maximum emission position of the cloud L1512 at IRAS 100 μm is offset from the maximum emission position of the same cloud at 450 and 850 μm by 18.3′and, therefore, we are not certain whether both peaks are parts of the same cloud.

2.2.2 Error estimation

The uncertainty values in IRAS flux densities of 83 clouds are taken directly from Chan and Fich [1995]. For the SCUBA data, the uncertainties in the absolute flux calibration are 20% at 850 μm and 50% at 450 μm because of the fluctuations in the optical depth of the atmosphere and due to the uncertainties in the beam-shape during observations and calibration [Di Francesco et al., 2008]. The integrated flux densities are obtained

by summing the flux densities within an irregular area around the extended emission of the cloud. The size of the area differs for different clouds but is always large enough to cover the extended emission down to a 3σ detection limit. We calculated the integrated flux densities from clouds by defining different boundaries since the clouds lacked any well defined boundaries. We then estimated the uncertainties due to the scatter in these flux densities measured with different boundaries, which represents the boundary uncertainty of the clouds. We considered both the boundary and the background uncertainty in calculating the total uncertainty of the SCUBA measurements. The flux density obtained from all of the SCUBA observations of H II regions is always a lower limit to the real submillimeter flux density in our study mainly because the area the SCUBA object covers is smaller than the area the IRAS object encloses. Moreover the SCUBA images were made with large scale emission removed due to chopping in the observation and this certainly reduces the measured fluxes.

2.2.3 Cold dust

IRAS cannot trace cold dust since the low temperatures of these grains mean that they primarily radiate at longer wavelengths, beyond the IRAS limit of 100 μm. For this reason, the total of hot and cool dust mass is a severe underestimation of the total mass of dust in clouds near H II regions. Most of the mass of interstellar dust probably dwells in the densest and coldest conditions. Thus in order to accurately measure the mass of the clouds, we need to analyze the cold dust. Fifteen clouds from our sample (see Figures 3.10 to 3.34 for the surface brightness maps of the target clouds) are analyzed at 850 μm and twelve at 450 μm as well, using SCUBA data. The results of the measurements and analysis are summarized in Table 2.3. Column one shows the names of clouds, columns two & three give the integrated flux density in Jy at 450 and 850 μm, columns four & five provide the mass of cool and cold dust obtained from three-component model fitting, and column six lists the temperature of cold dust. The ratio M_{cold}/M_{cool} of the clouds is shown in column seven. Of the fifteen clouds which have SCUBA data, seven clouds show a good three-component (hot, cool and cold dust) fit. The clouds near H II regions BFS15C$_a$, S104, and S146 have no 450 μm data available for the calculation of the cold dust. For these clouds, a temperature of 10 K is used to estimate the mass in cold dust.

It is found that even though the temperature of the cold dust is well constrained, the mass of the cold dust is poorly constrained. For five clouds (S247C$_c$, S254-8C, S138C$_a$, S196C$_c$, and S242C), a good three-component fit cannot be found. The 450/850-μm flux ratios of all these five clouds are found to be above 10. We require higher large grain dust temperatures, above 30 K, to fit such a larger ratio. Note that for a lower β, ($\beta = 1$), dust temperatures attain very high values (above 500 K), greater than those found for the hot dust, at a lower 450/850-μm flux ratio ($\sim$7). Such high values of dust temperatures are very

unlikely for the large grains at long wavelengths. Also, these results are not consistent with the IRAS 12 μm observations. Future investigations are needed for clarifications. Figure 2.5 shows the SCUBA 850 μm scan map of S104 with different complexes of the same molecular cloud. A DSS image of S104 is also given for comparison (2.6). Note that these complexes are not resolved in the IRAS data. Therefore, to calculate the total flux density from S104 at 850 μm, we add up the integrated flux density contribution from all six individual molecular cloud complexes. We compared the flux densities of Complex 1 and Complex 6 obtained from SCUBA 850 μm observations with that of the UC H II and PDR 1 of Rodón and et al. [2010] obtained from *Herschel*. The flux densities of the above mentioned regions obtained from SCUBA measurements are significantly ($\approx$ 3-4 times) higher compared with the 850 μm flux densities acquired from the extrapolation of the SED fitted to *Herschel* observations. These variations are likely caused by the difference in the size and shape of the apertures used to calculate the integrated flux densities of the regions in the two studies.

The three-component SED of S104 is shown in Figure 2.2. The mass and temperature of the cold dust component are not well constrained for this cloud because of the absence of 450 μm data. A slight change in the temperature of the cold dust affects the mass of the cold dust to a great extent, since temperature appears in Planck function non-linearly. We assume a probable temperature for the cold component of the cloud to find the mass. For example, in S104, the mass of the dust at 10 K is 497 $M_{\odot}$, but if the dust temperature is 15 K, its mass would be 242 $M_{\odot}$. Clouds with both 450 and 850 μm SCUBA flux data points show a much better fit. As an example, the SED of S201C$_b$ is given in Figure 2.7. The modelled masses of hot, cool, and cold dust in S201C$_b$ are $400\times10^{-6} M_{\odot}$, 1.3 $M_{\odot}$, and 107 $M_{\odot}$, respectively. In S201C$_b$, the hot dust is at a temperature of 154 K, whereas cool dust is at 40 K. The cold dust component of S201C$_b$ has the temperature of 17 K.

Out of the ten clouds with good cold dust measurements, the most massive in cold dust is cloud S266C$_a$ ($M_{cold} = 810 \pm 60 M_{\odot}$), and the least massive is S233C$_a$ ($M_{cold} = 7.4 \pm 5.4 M_{\odot}$). The greatest value of M_{cold}/M_{cool} is found in BFS15C$_d$ (260) and the lowest value in S233C$_a$ (12.3) with an average value of 71. Note that we discarded the cloud S233C$_b$ from calculating the average M_{cold}/M_{cool} because this ratio is obtained with an upper limit in the mass of cool dust. The maximum and minimum values of the temperature of the cold dust are 21 K (S269) and 6.2 K (BFS15C$_d$). The masses and temperatures of the cold dust are underestimated since the SCUBA observations do not cover the entire area in which IRAS emission is seen (except for S104, where the SCUBA observation overlaid the entire area of IRAS emission). The SEDs of the clouds S233C$_a$, S233C$_b$, BFS15C$_d$, S266C$_a$, S269, and S159 are shown below (See Figures 2.8, 2.9, 2.10, 2.11, 2.12, and 2.13). The SEDs of all the clouds near H II regions contain a peak at 60-100 μm, emitted primarily by the cool dust. Although the emission is dominated by the cool dust, the mass is dominated by the cold dust in all the cases.

For some clouds, the values of the temperature and mass of the cool and hot dust in the two- and the three-component fits agree very well. For example, clouds S266C$_a$, S159, S233C$_a$, and BFS15C$_d$ show a good matching of the fitted parameters of the hot and cool dust components in the two and three-component fit. However, certain clouds like S269 and S201C$_b$ show large deviations in the values of the fitted parameters of the hot and cool dust. For example, in cloud S269, the two-component modelling gives M$_{cool}$ of 6.1 $\pm$ 0.5 $M_{\odot}$, while the three-component modelling provides M$_{cool}$ of 1.1 $\pm$ 0.5 $M_{\odot}$. Similarly, the temperature of the cool dust in S269 is 35.0 $\pm$ 0.4 K according to the the two-component modelling, while it is 46 $\pm$ 4 K from the three-component modelling.

The uncertainties listed in Table 2.3 are those associated with the flux densities. The uncertainties due to fitting contributes to the uncertainties of the fitted parameters to a great extent. The fits do not provide any useful information on the upper mass limit and the lower temperature limit of the cold dust in most of the clouds. But, there is a well-determined value for the lower mass limit and the upper temperature limit of the cold dust in most of the clouds. For example, the upper limit of the temperature of cloud S266C$_a$ is 12 K and the lower mass limit of this cloud is 480 $M_{\odot}$. The upper mass limit and lower temperature limit of cloud S266C$_a$ are not useful for further analysis. However, the mass and temperature of cloud S269 is well bounded: the upper and lower mass limits of the cold dust in this cloud are 57 $M_{\odot}$ and 41 $M_{\odot}$, respectively, with 23 K as the highest and 18 K as the lowest values of the temperature of the cold dust.

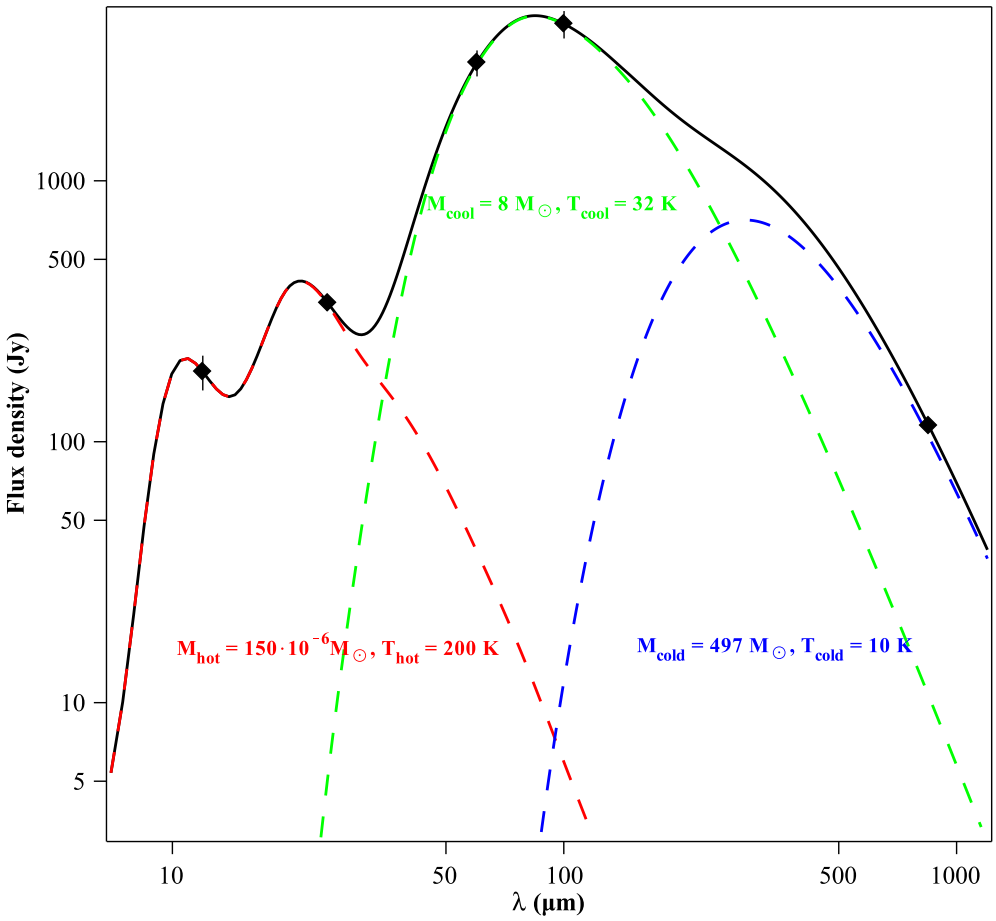

Figure 2.2: Illustration of the Spectral Energy Distribution of the Galactic H II region S104 from both the IRAS and SCUBA observations (solid diamonds mark the observed flux densities) along with the three-component-optimal model fit. The red dashed line shows the contribution from hot dust, the green dashed line represents the contribution from the cool dust, and the blue dashed line displays the contribution from the cold dust, whereas the black solid line denotes the combined spectrum of all the three components. The cold component is assumed to be at a temperature of 10 K. The double peak in the hot component corresponds to silicate features at 9.7 μm and 18 μm arising from respectively the Si-O stretching and O-Si-O bending modes.

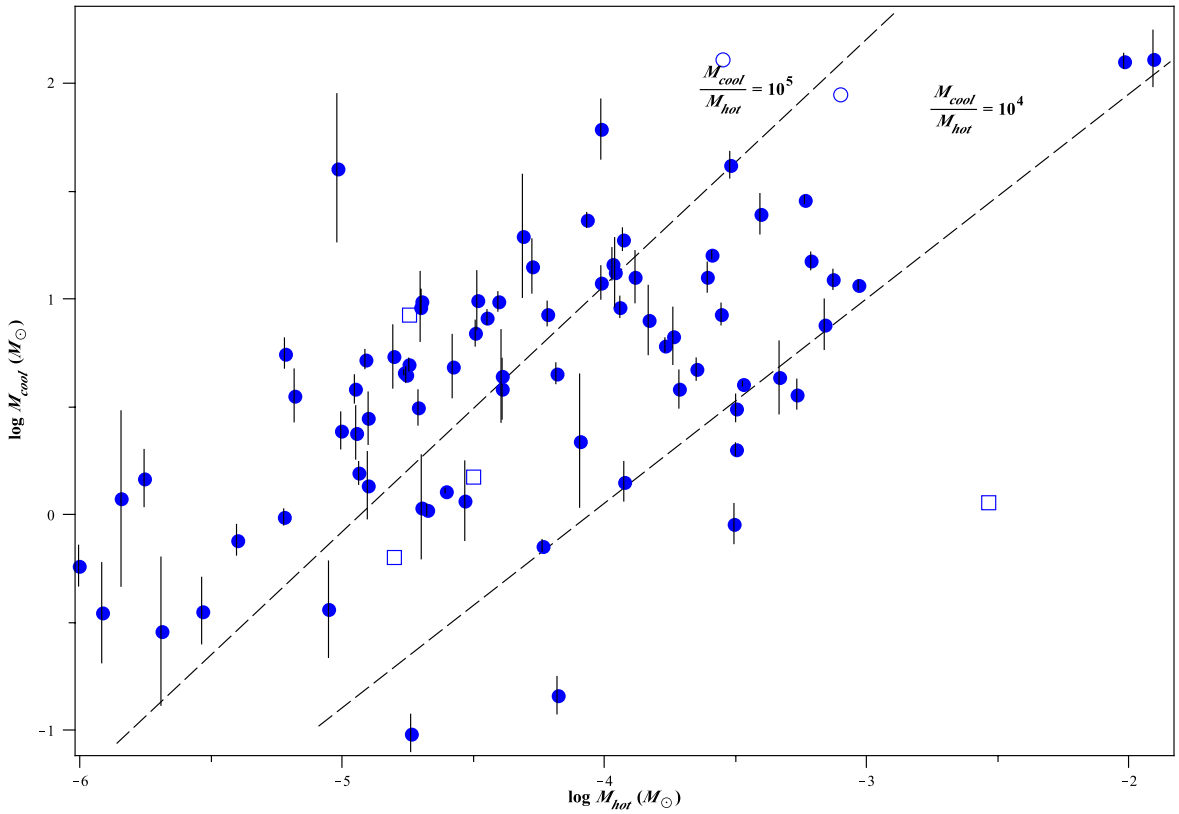

Figure 2.3: Diagram showing the cool dust mass vs. hot dust mass of clouds near H II regions examined in this paper. Solid circles mark all clouds with explicit uncertainties in masses. Note that the horizontal error bars are so small that they are not visible in the diagram. The clouds marked by open boxes are those with an upper limit of M_{hot}. The open circles represent clouds with upper limits of both M_{cool} and M_{hot}. In most H II regions, the mass in cool dust is 10^4 to 10^5 times higher than the mass in hot dust. The two black dashed lines through the plot are the loci where M_{cool}/M_{hot} is 10^4 and 10^5, respectively.

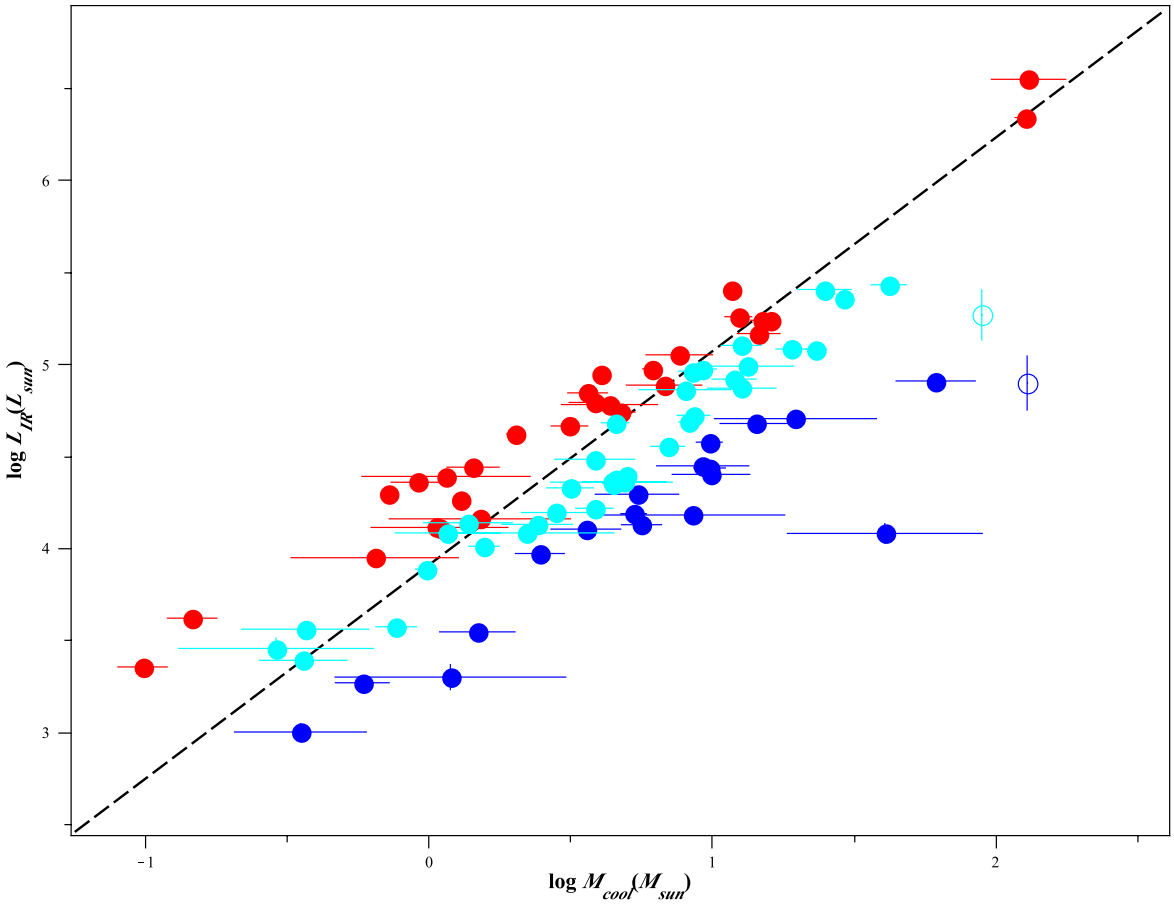

Figure 2.4: The IR luminosity of 83 clouds near H II regions based on the IRAS data is plotted as a function of the mass of the cool dust component. There are 81 clouds with explicit uncertainties in masses and luminosities, shown in solid circles. The two clouds shown in open circles are those with only an upper limit in the mass of cool dust. The three different colours on the plot represent three different temperature ranges. Blue denotes a temperature range of 20 K to 29 K. Likewise, cyan and red represent temperature ranges of 29 K to 33 K and 33 K to 39 K respectively. The black straight line represents the best fit to all the 81 data points.

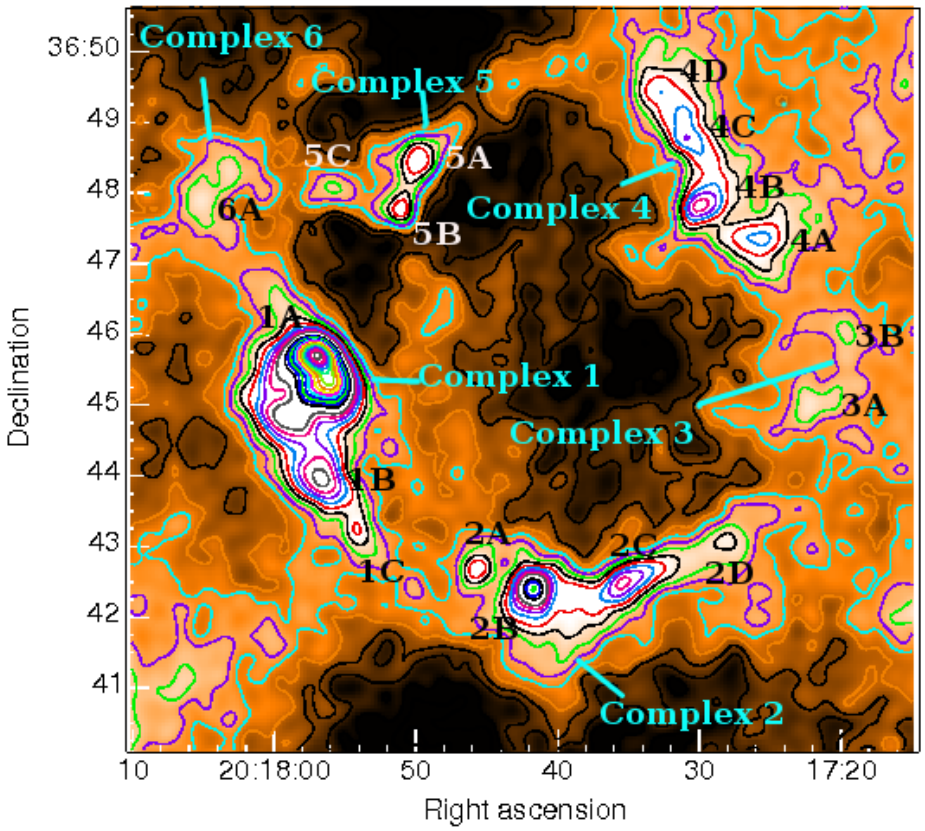

Figure 2.5: Different complexes and clumps of S104 at 850 μm.

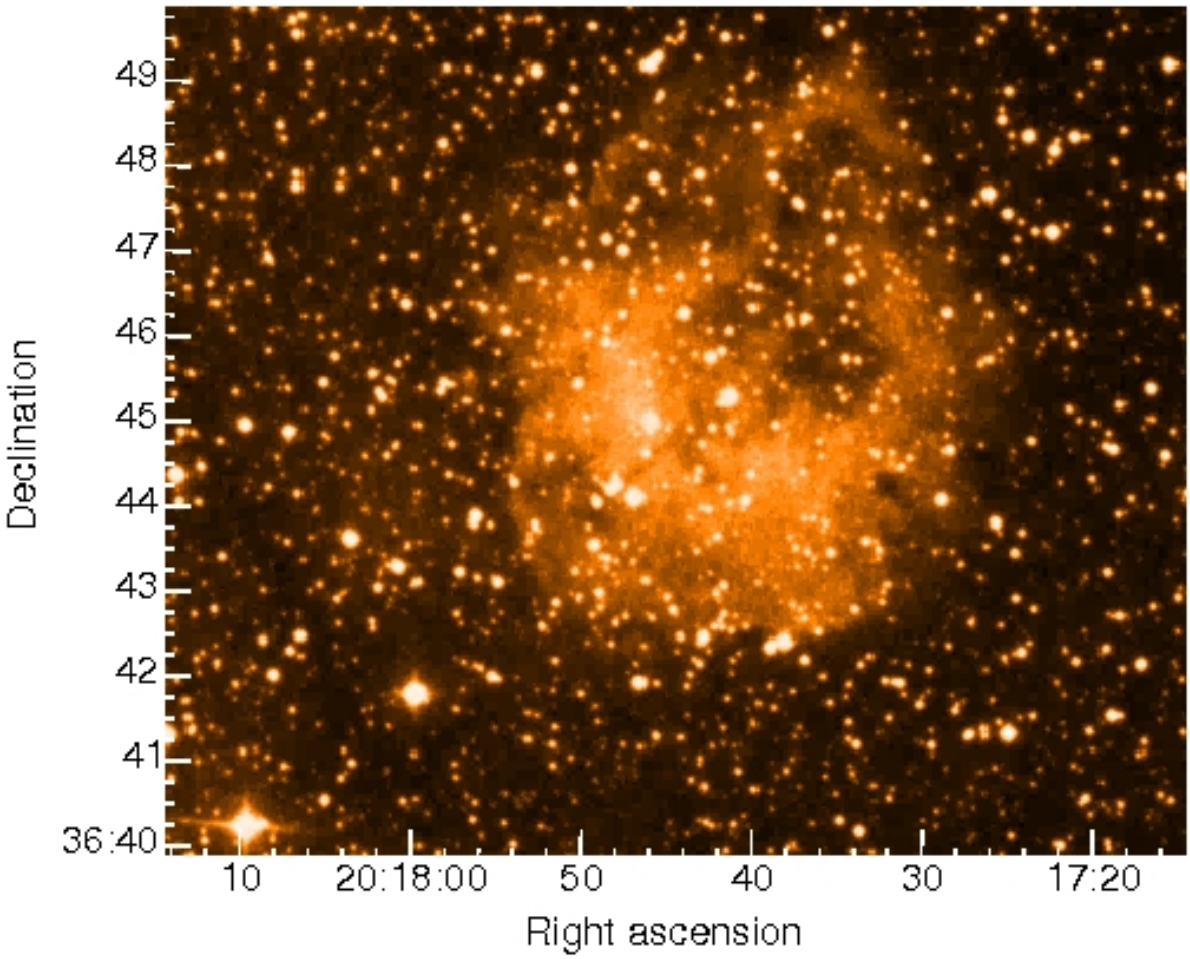

Figure 2.6: DSS image of S104.

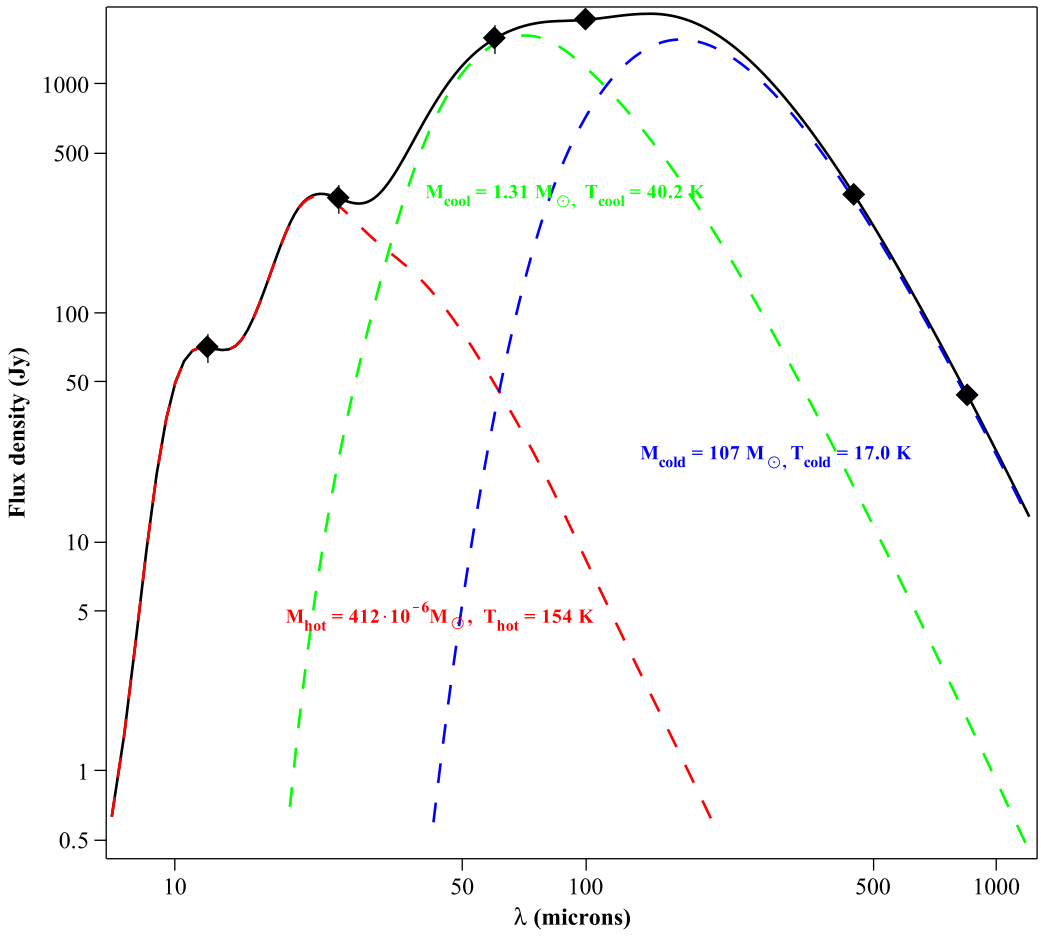

Figure 2.7: Dust emission spectrum of S201C$_b$. The red dashed line shows the contribution from hot dust, the green dashed line represents the contribution from the cool dust, and the blue dashed line displays the contribution from the cold dust, whereas the black solid line denotes the combined spectrum of all the three components.

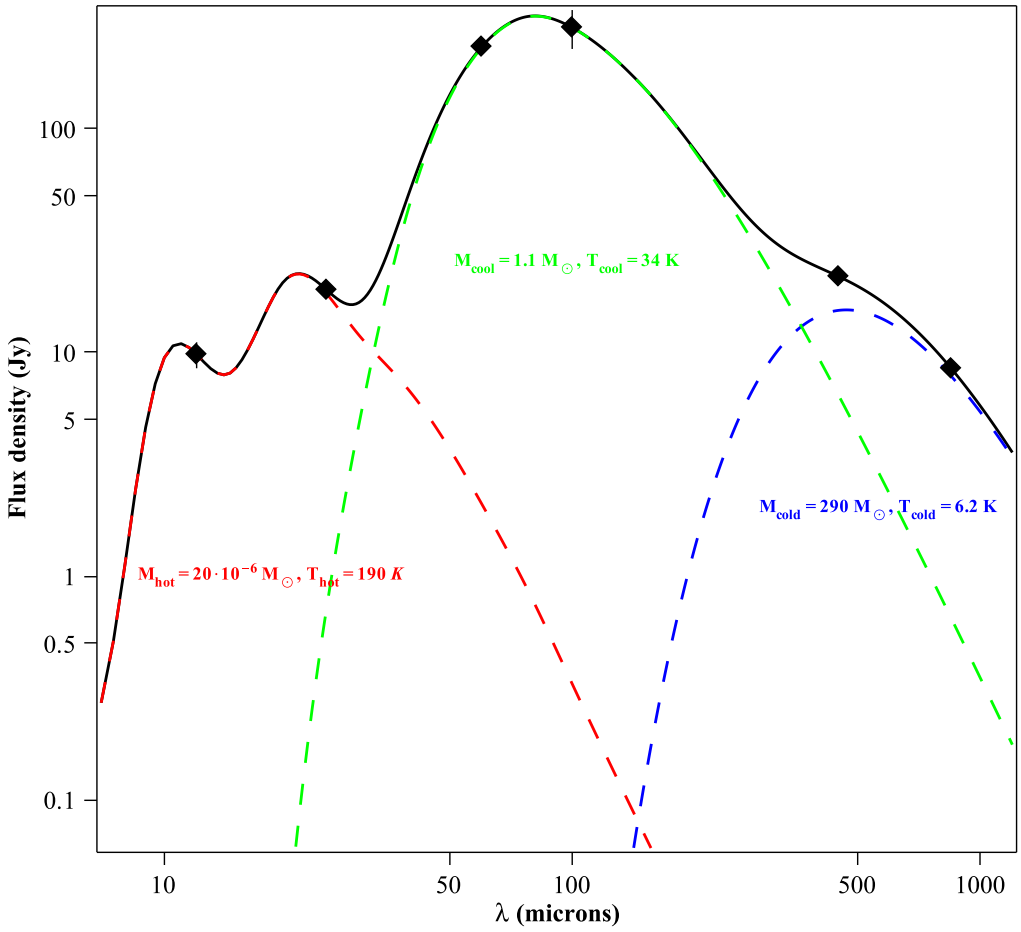

Figure 2.8: Dust emission spectrum of BFS15C$_d$. The red dashed line shows the contribution from hot dust, the green dashed line represents the contribution from the cool dust, and the blue dashed line displays the contribution from the cold dust, whereas the black solid line denotes the combined spectrum of all the three components.

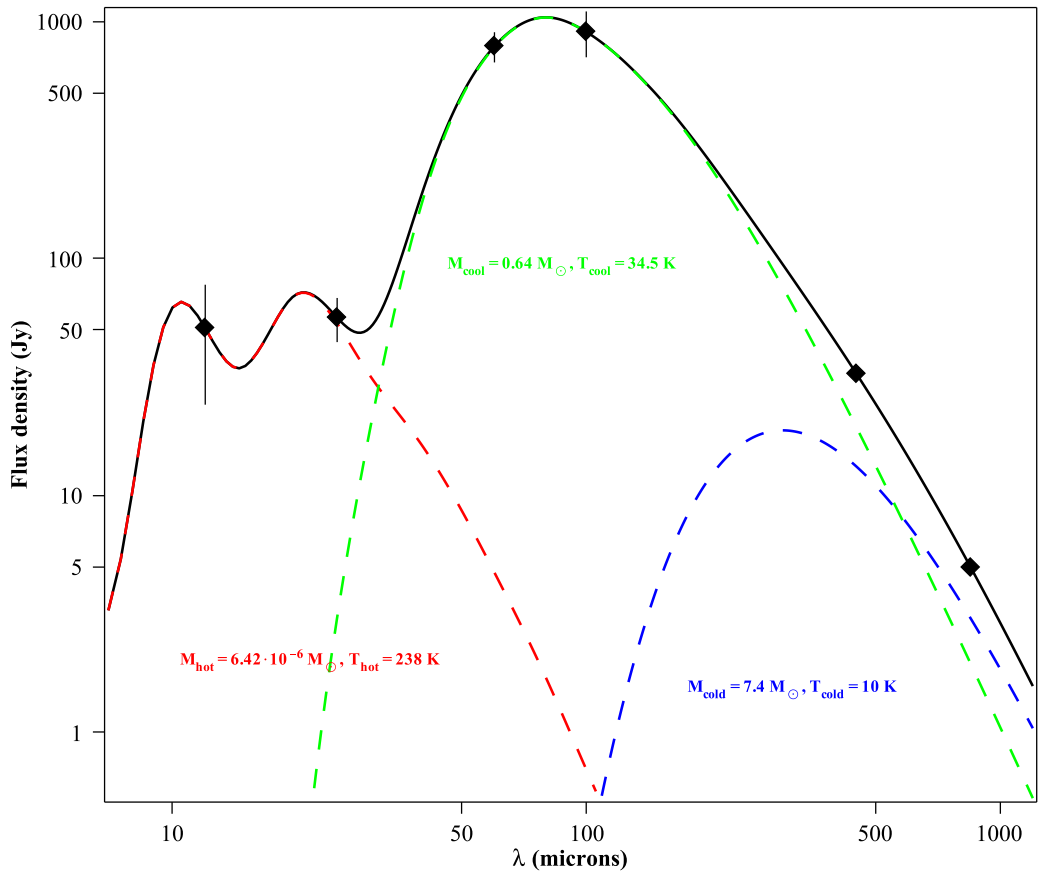

Figure 2.9: Dust emission spectrum of S233C$_a$. The red dashed line shows the contribution from hot dust, the green dashed line represents the contribution from the cool dust, and the blue dashed line displays the contribution from the cold dust, whereas the black solid line denotes the combined spectrum of all the three components.

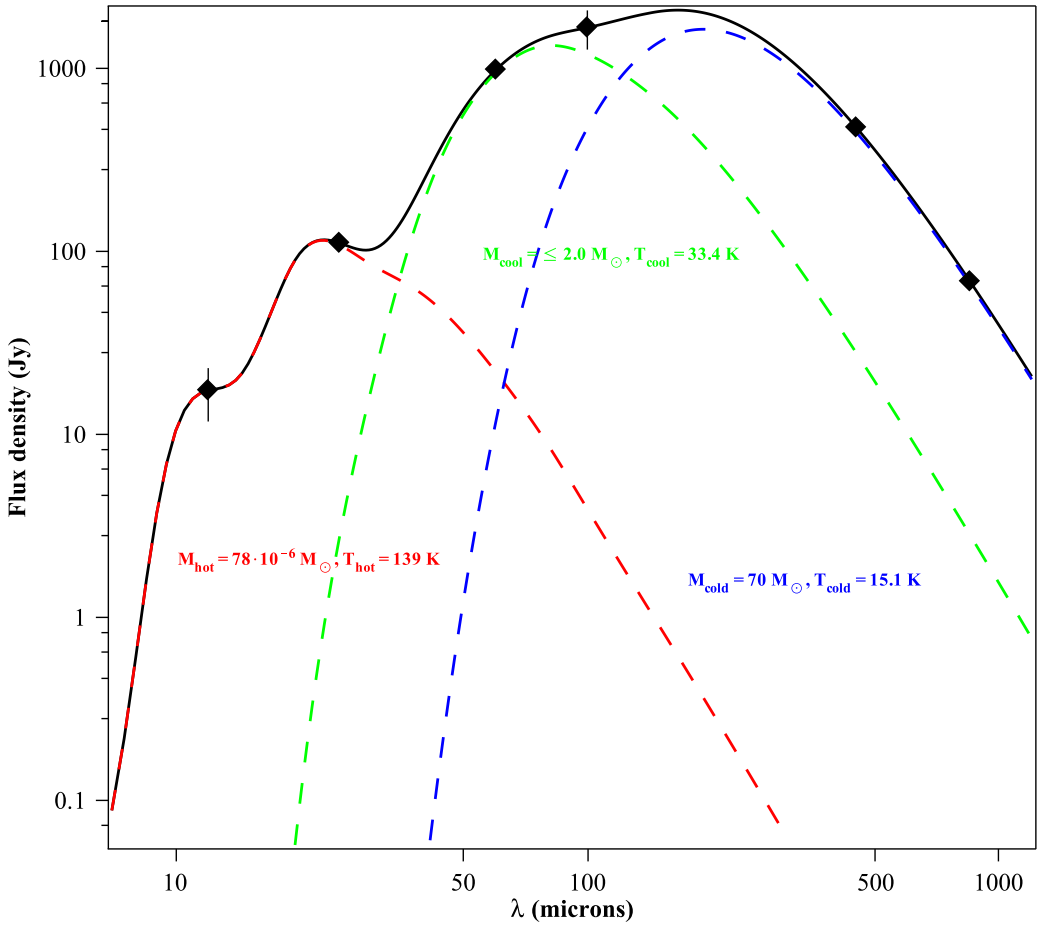

Figure 2.10: Dust emission spectrum of S233C$_b$. The red dashed line shows the contribution from hot dust, the green dashed line represents the contribution from the cool dust, and the blue dashed line displays the contribution from the cold dust, whereas the black solid line denotes the combined spectrum of all the three components.

Table 2.3: SCUBA flux densities, cold masses and temperatures of H II regions

Name	Integrated flux density (Jy)		Mass ($M_\odot$)		Temperature (K)	Mass ratio
	450 μm	850 μm	M_{cool}[1]	M_{cold}	T_{cold}	$\frac{M_{cold}}{M_{cool}}$
BFS 15C$_a$	–	25±1	12±1	357	10	30
BFS 15C$_d$	21.8±0.2	8.5±0.1	1.1±0.6	290±40	6.2±0.4	260±150
S 104	–	115.0±0.2	8±3	497	10	62
S 138C$_a$	346±7	27.3±0.3	–	–	–	–
S 146	–	30.3±0.2	4.0±0.1	303	10	76
S 196C$_c$	165±1	11.61±0.02	–	–	–	–
S 201C$_b$	327±7	43.6±0.2	1.3±0.9	107±6	17±1	80±60
S 233C$_a$	33±2	5.0±0.1	0.6±0.4	7.4±5.4	10±3	12.3±12.2
S 233C$_b$	473±8	68.2±0.5	≤ 2	70±3	15.1±0.6	35[2]
S 242C	278±4	24.2±0.5	–	–	–	–
S 247C$_c$	328±2	32±1	–	–	–	–
S 254-8C	1170±10	100±1	–	–	–	–
S 266C$_a$	75±1	13.4±0.2	42±5	810±60	9.2±0.4	19±3
S 269	242±1	28.5±0.2	1.1±0.5	47±1	21.1±0.6	40±20
S 159	233±4	58±1	8±2	500±100	6.5±0.6	60±20

[1]Obtained from the three-component model fit.
[2]Using the upper limit of the mass of cool dust.

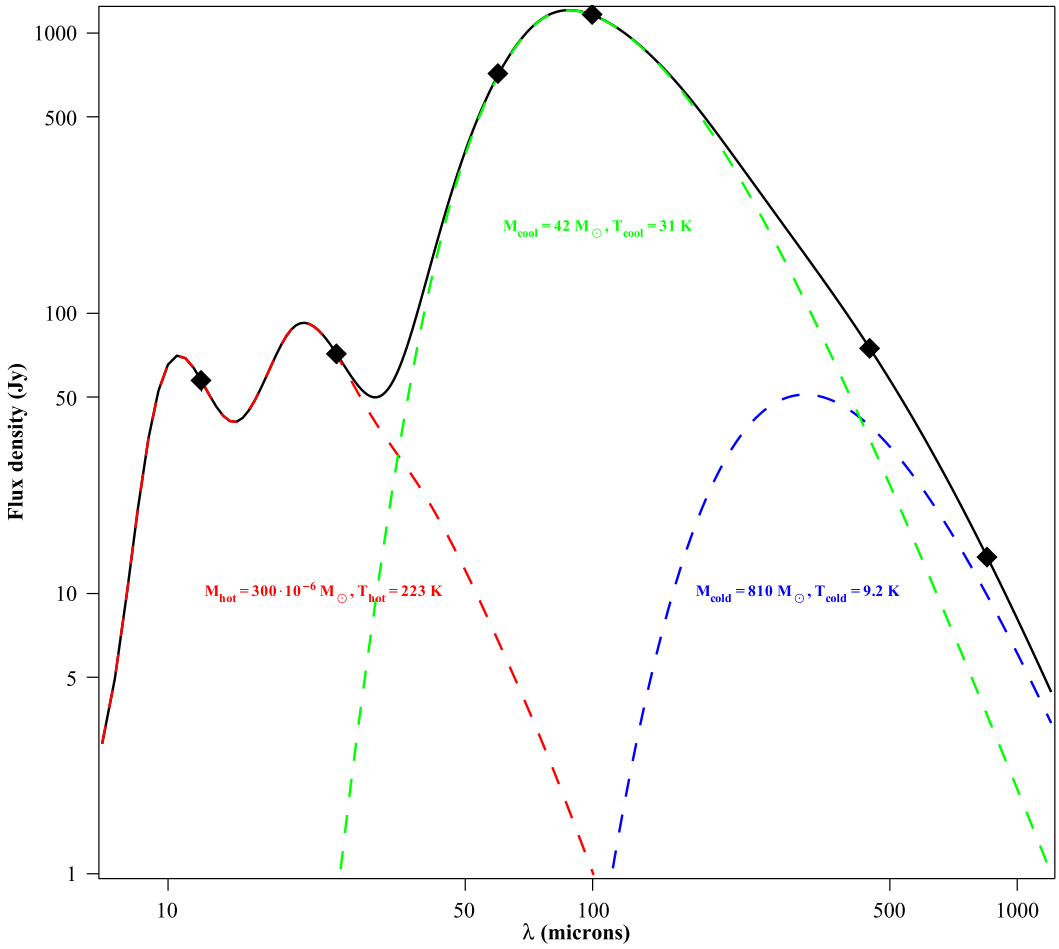

Figure 2.11: Dust emission spectrum of S266C$_a$. The red dashed line shows the contribution from hot dust, the green dashed line represents the contribution from the cool dust, and the blue dashed line displays the contribution from the cold dust, whereas the black solid line denotes the combined spectrum of all the three components.

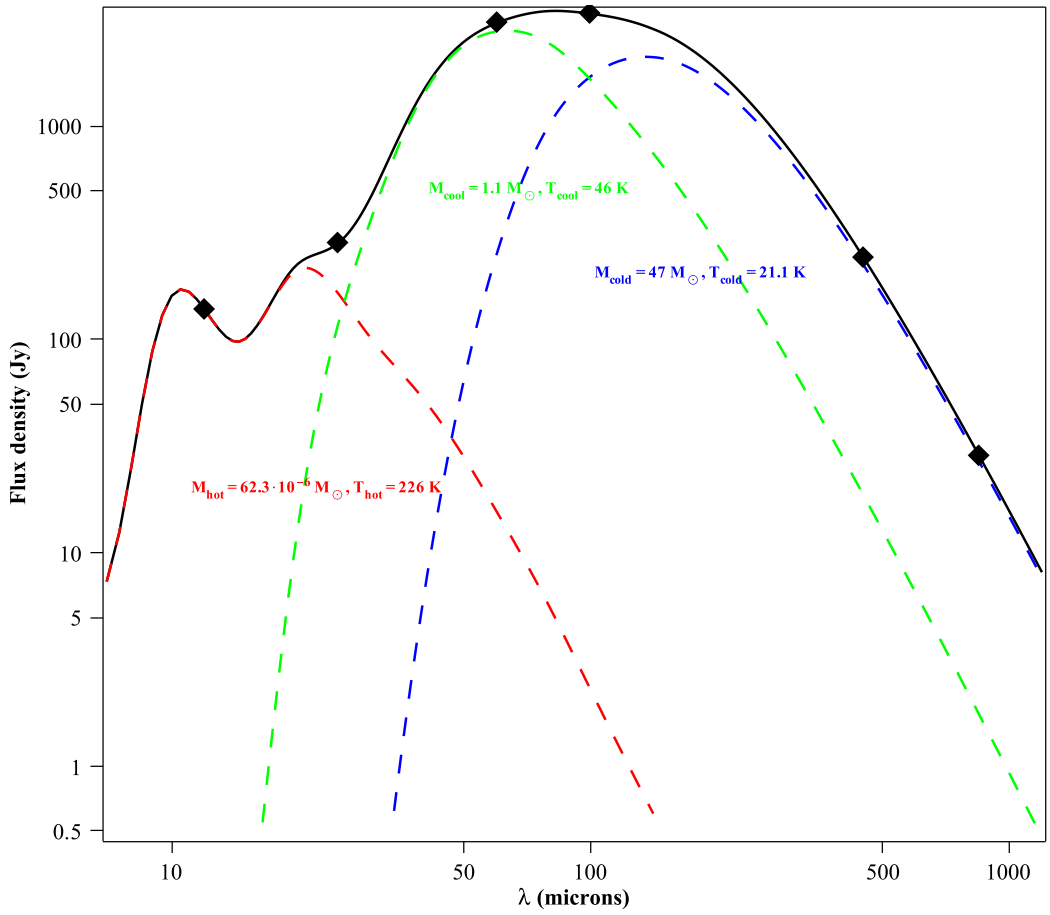

Figure 2.12: Dust emission spectrum of S269. The red dashed line shows the contribution from hot dust, the green dashed line represents the contribution from the cool dust, and the blue dashed line displays the contribution from the cold dust, whereas the black solid line denotes the combined spectrum of all the three components.

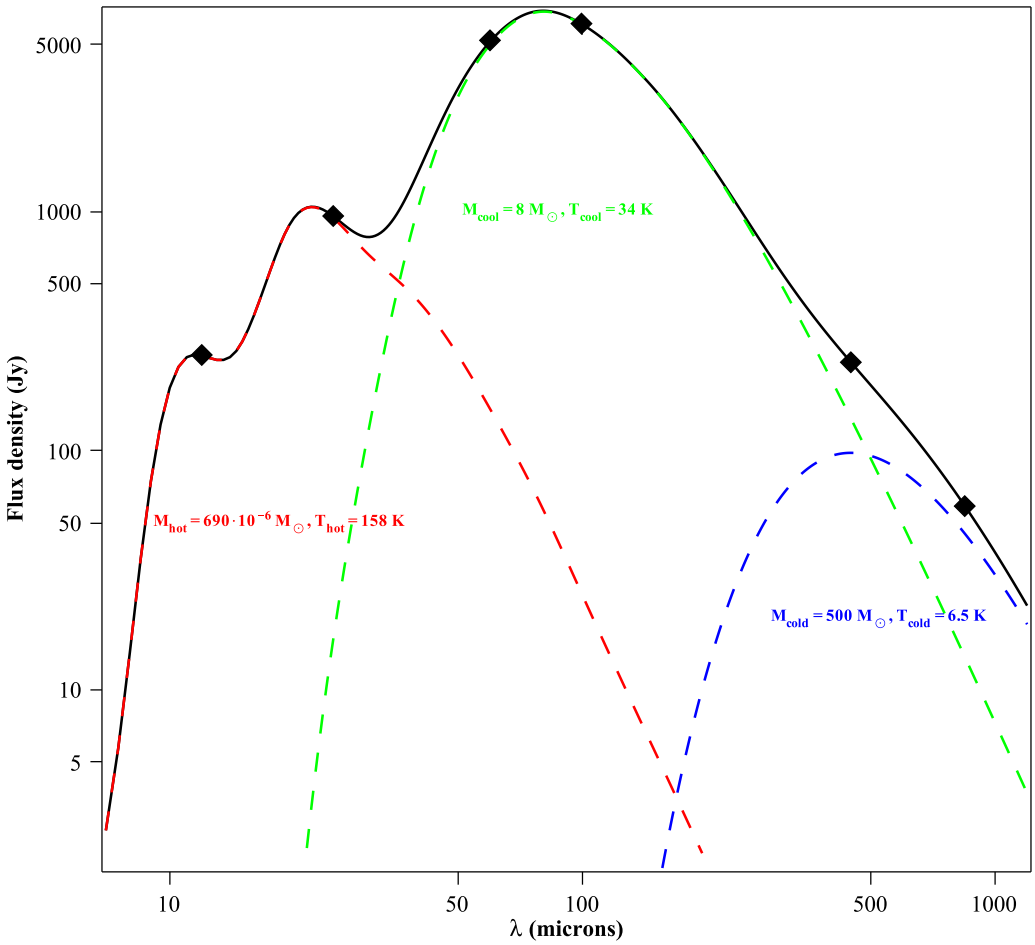

Figure 2.13: Dust emission spectrum of S159. The red dashed line shows the contribution from hot dust, the green dashed line represents the contribution from the cool dust, and the blue dashed line displays the contribution from the cold dust, whereas the black solid line denotes the combined spectrum of all the three components.

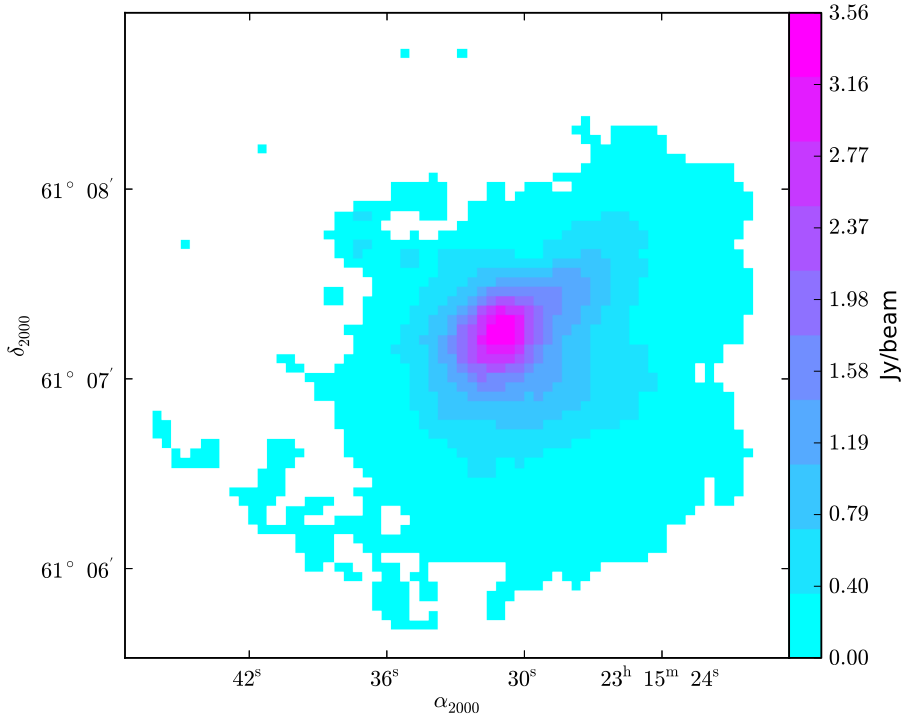

Figure 2.14: S159 at 850 μm.

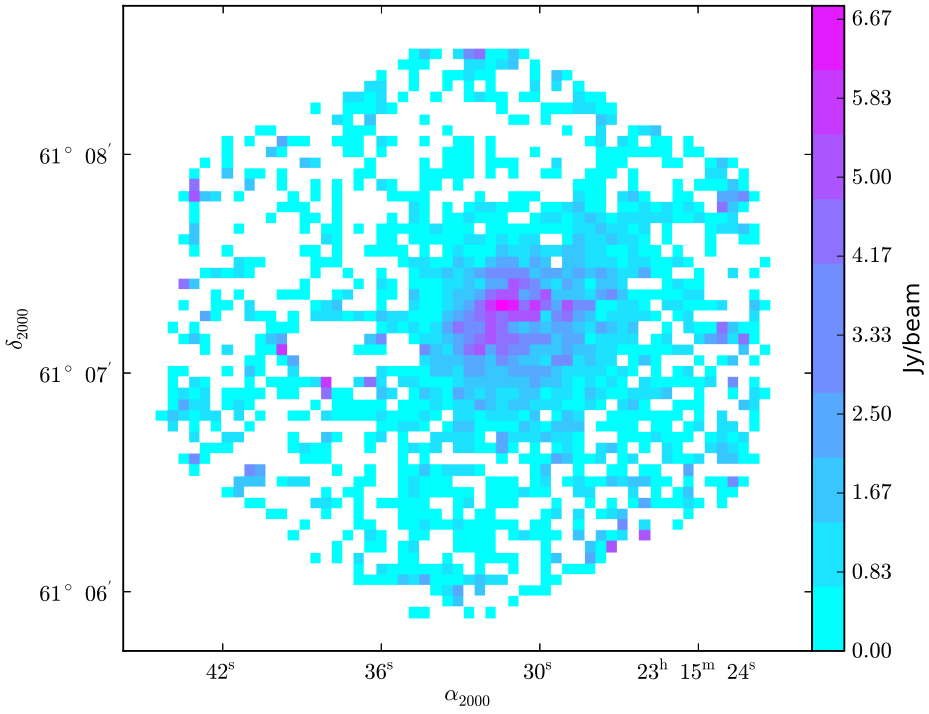

Figure 2.15: S159 at 450 μm.

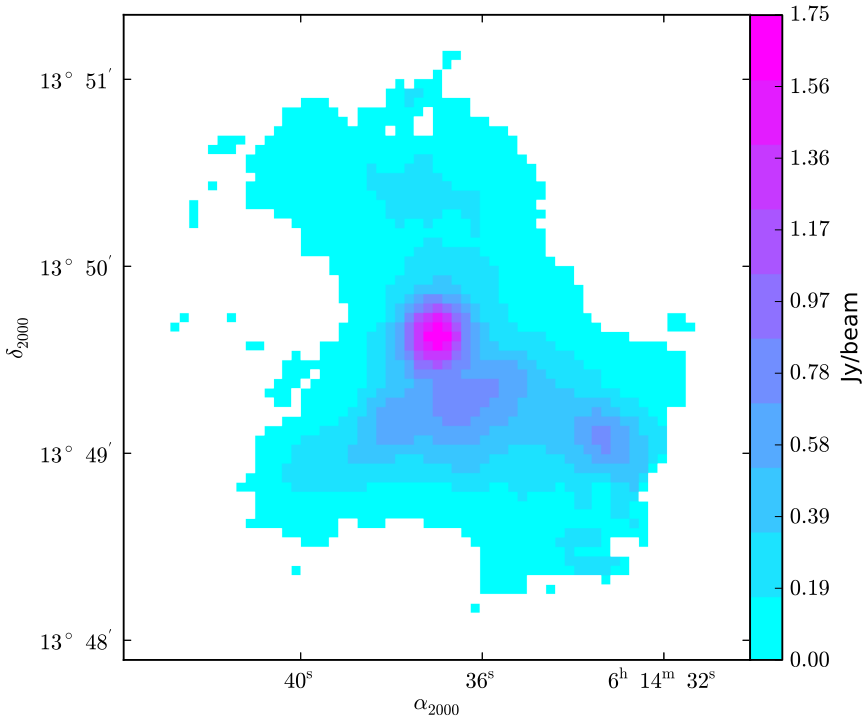

Figure 2.16: S269 at 850 μm.

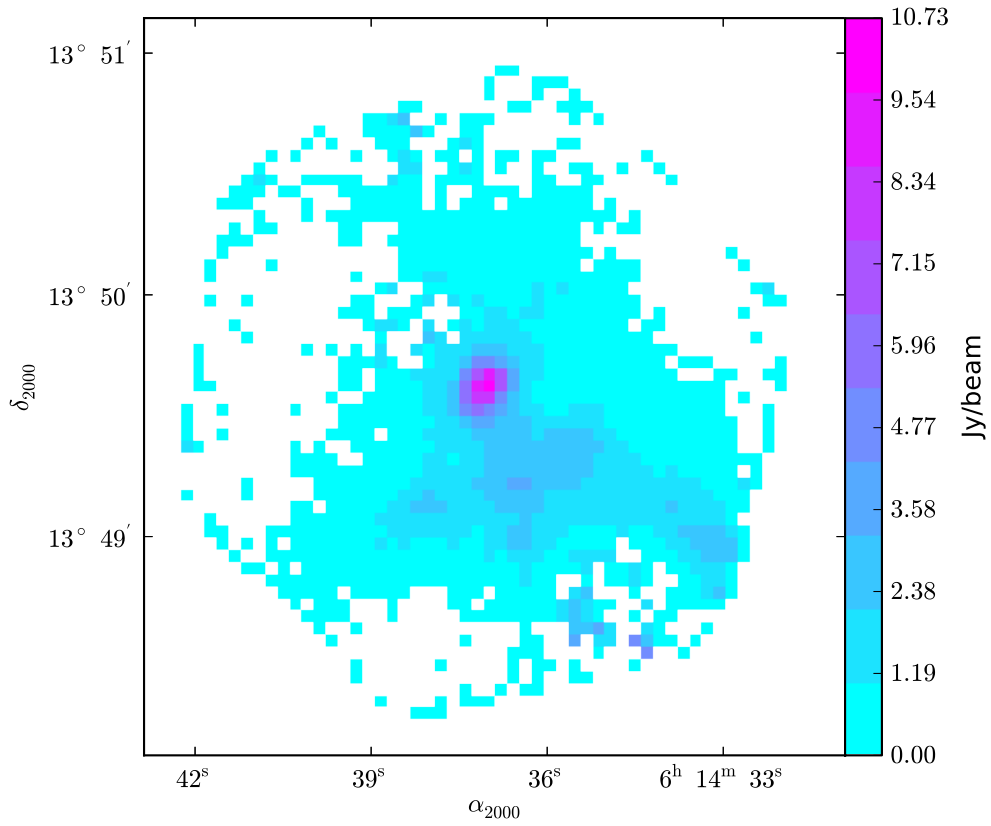

Figure 2.17: S269 at 450 μm.

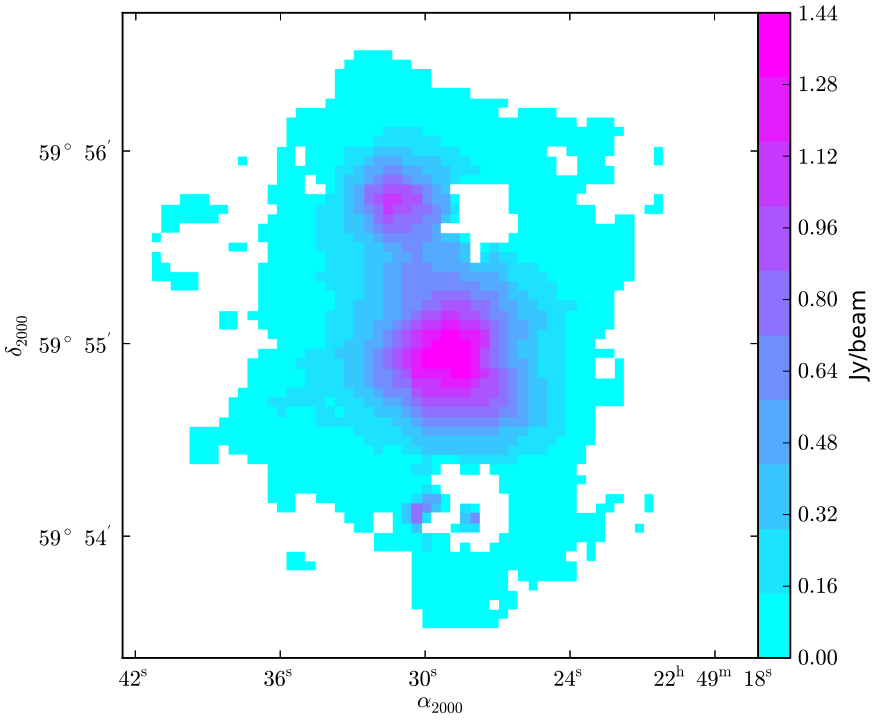

Figure 2.18: S146 at 850 μm.

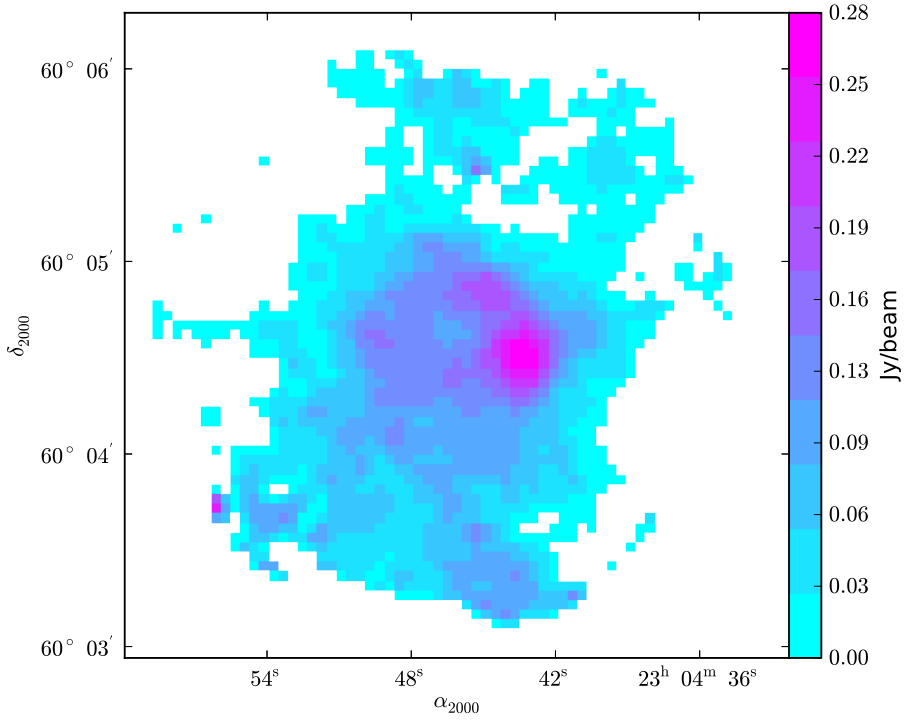

Figure 2.19: BFS15C$_d$ at 850 μm.

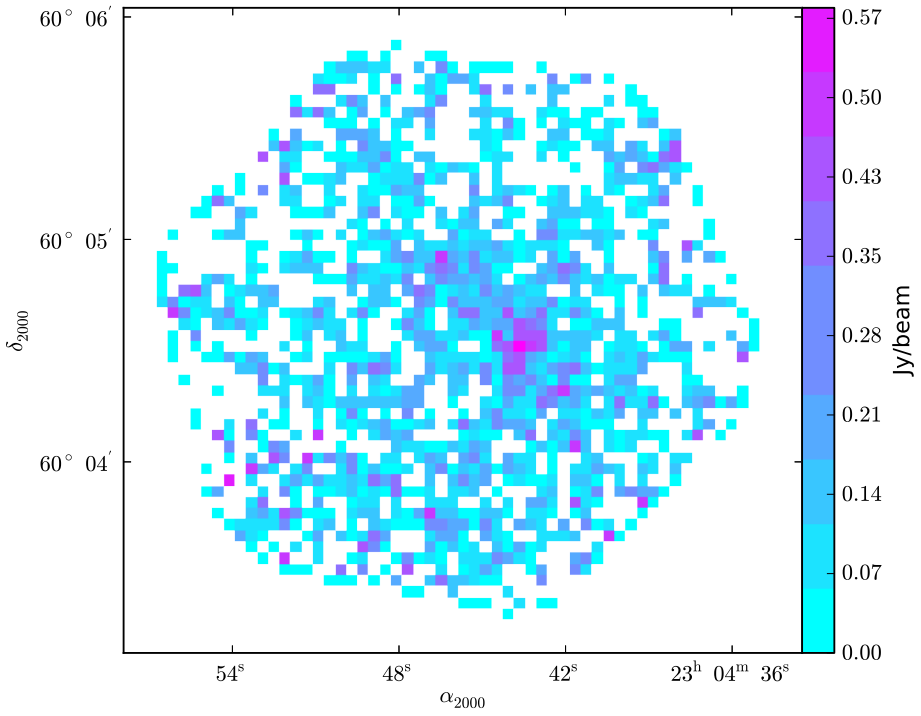

Figure 2.20: BFS15C$_d$ at 450 μm.

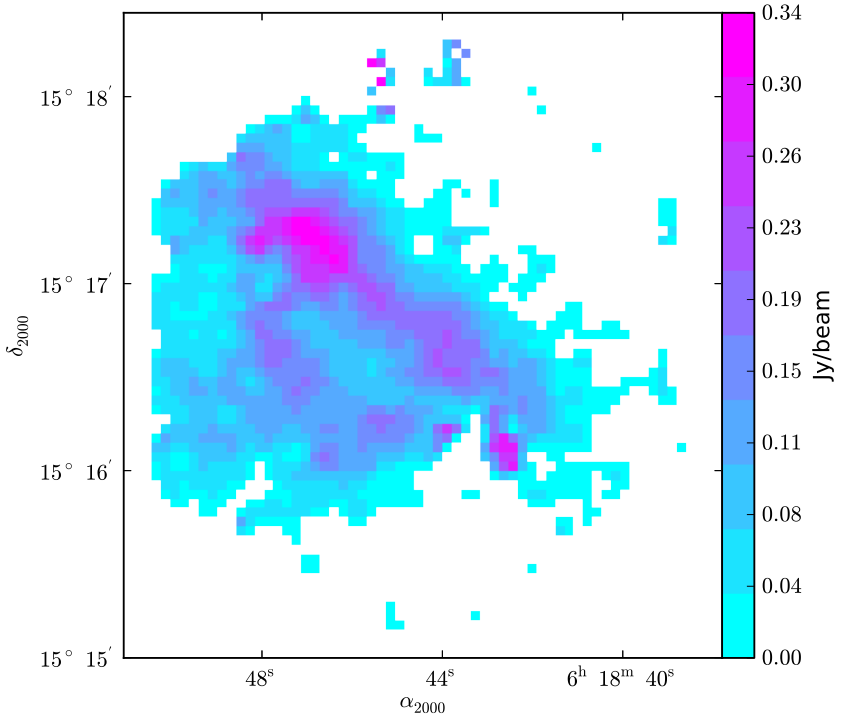

Figure 2.21: S266C$_a$ at 850 μm.

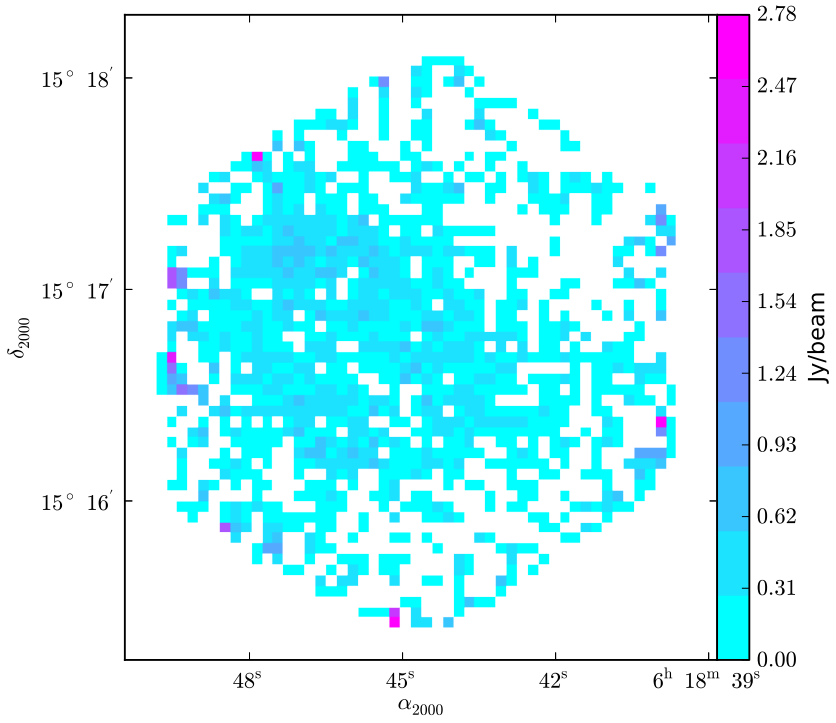

Figure 2.22: S266C$_a$ at 450 μm.

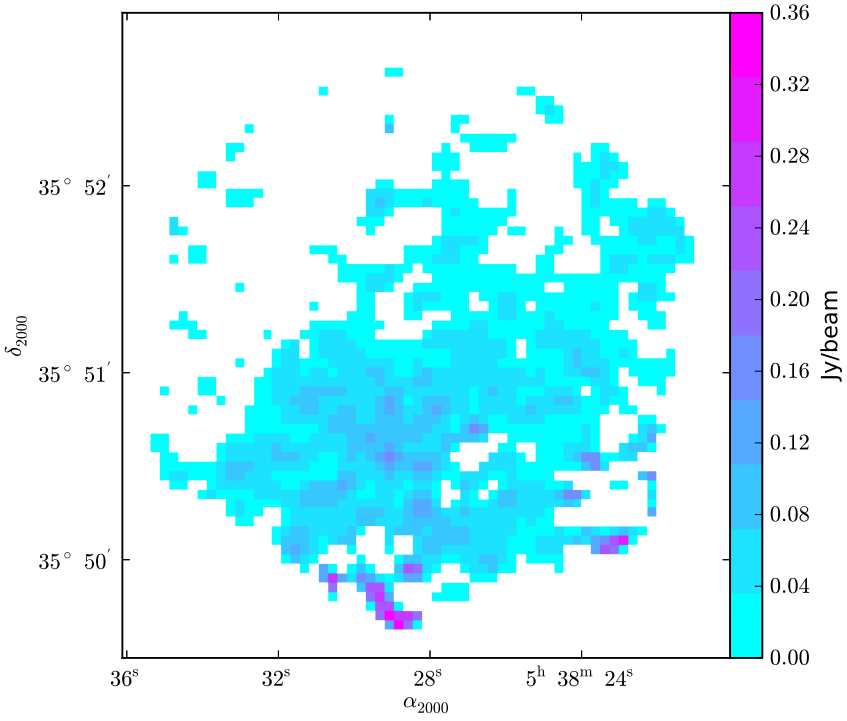

Figure 2.23: S233C$_a$ at 850 μm.

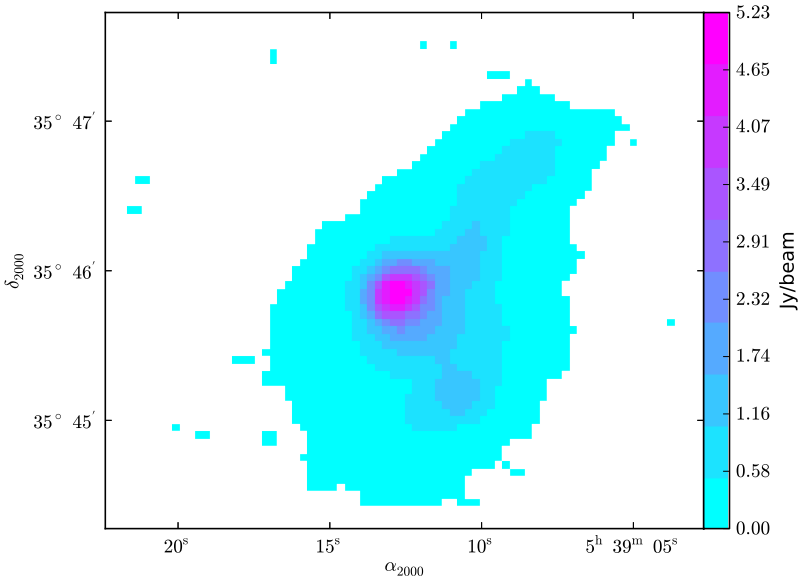

Figure 2.24: S233C$_b$ at 850 μm.

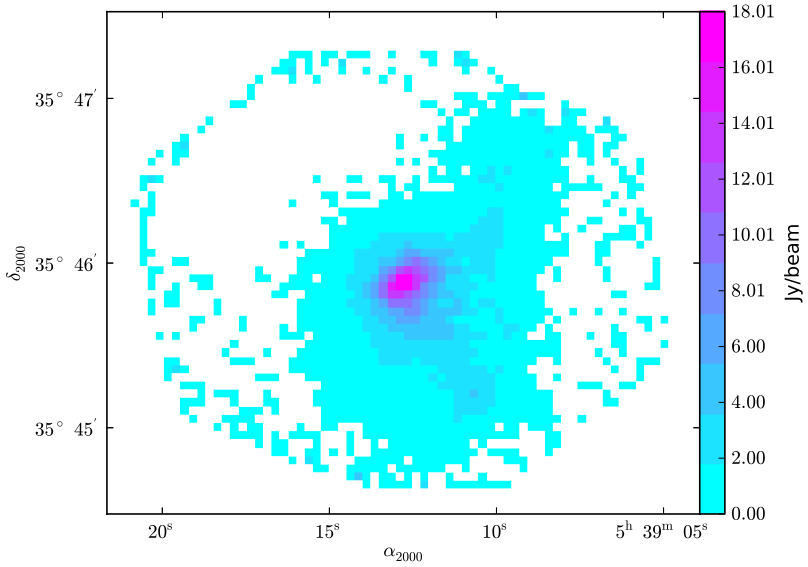

Figure 2.25: S233C$_b$ at 450 μm.

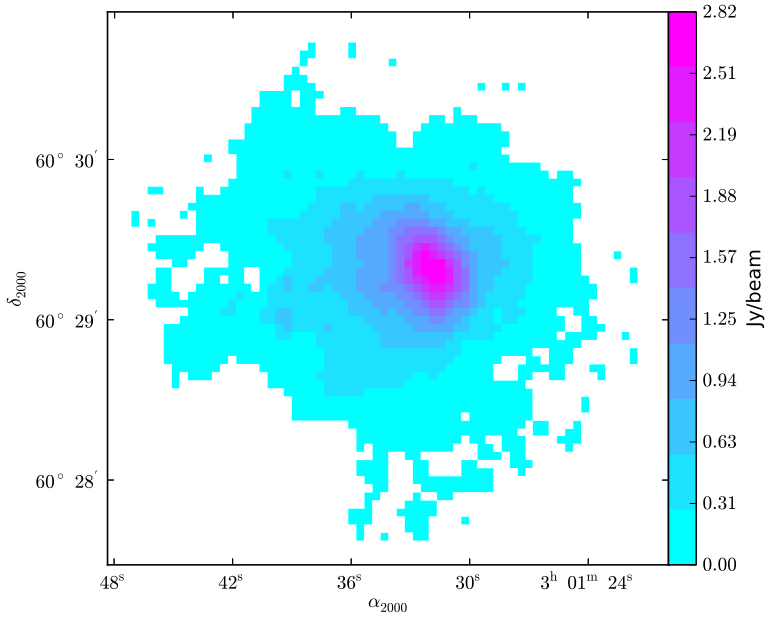

Figure 2.26: S201C$_b$ at 850 μm.

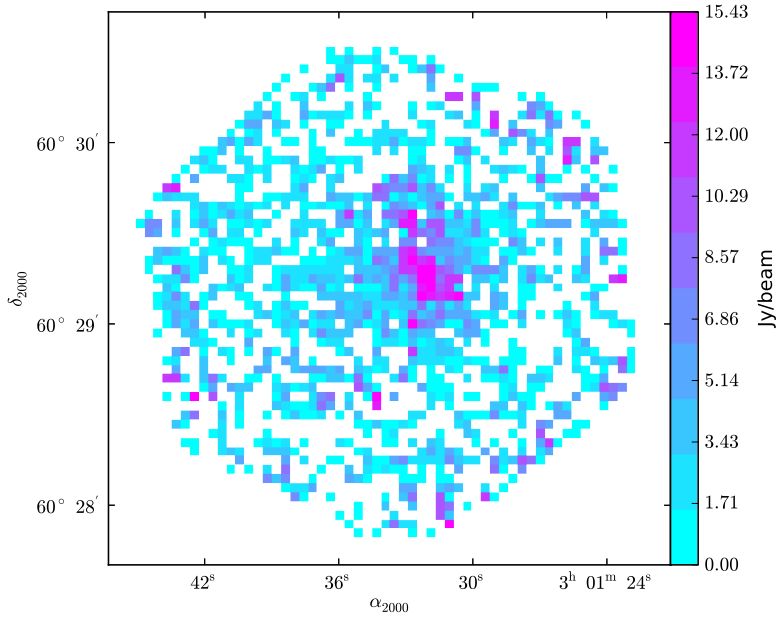

Figure 2.27: S201C$_b$ at 450 μm.

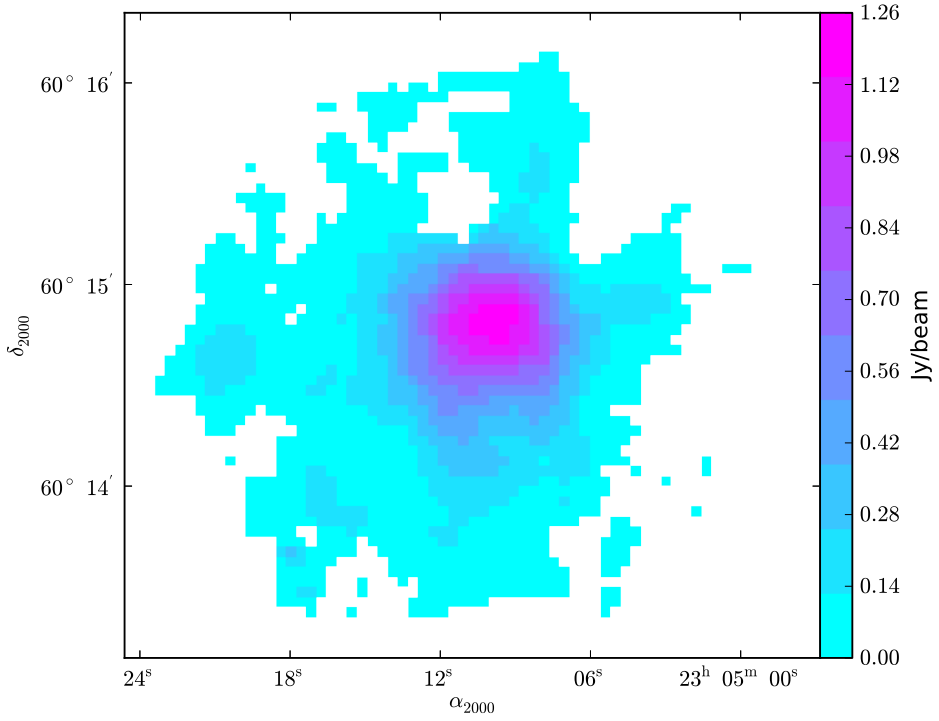

Figure 2.28: BFS15C$_a$ at 850 μm.

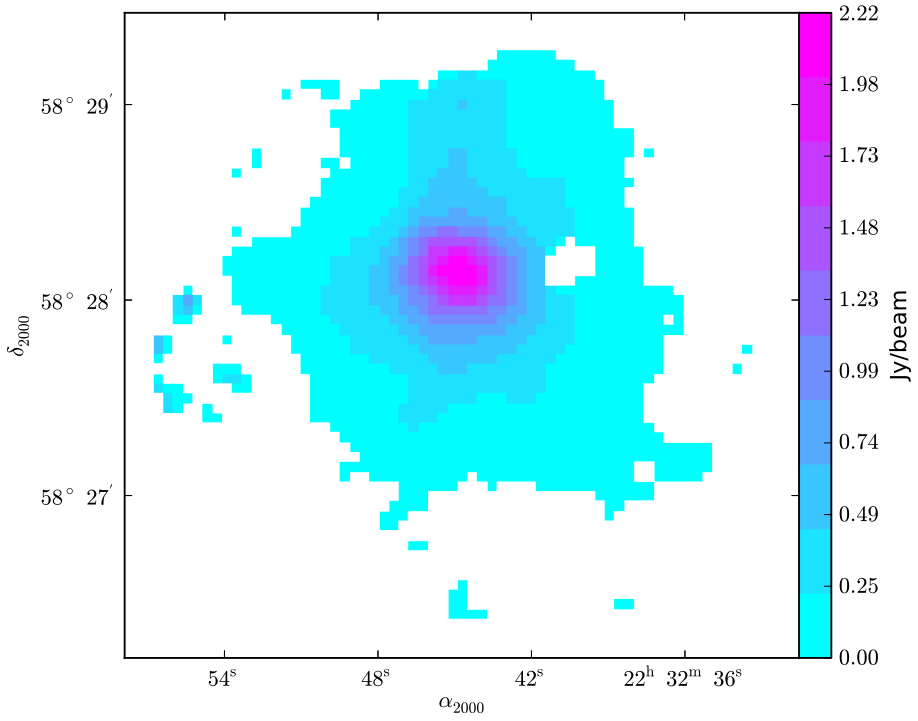

Figure 2.29: S138C$_a$ at 850 μm.

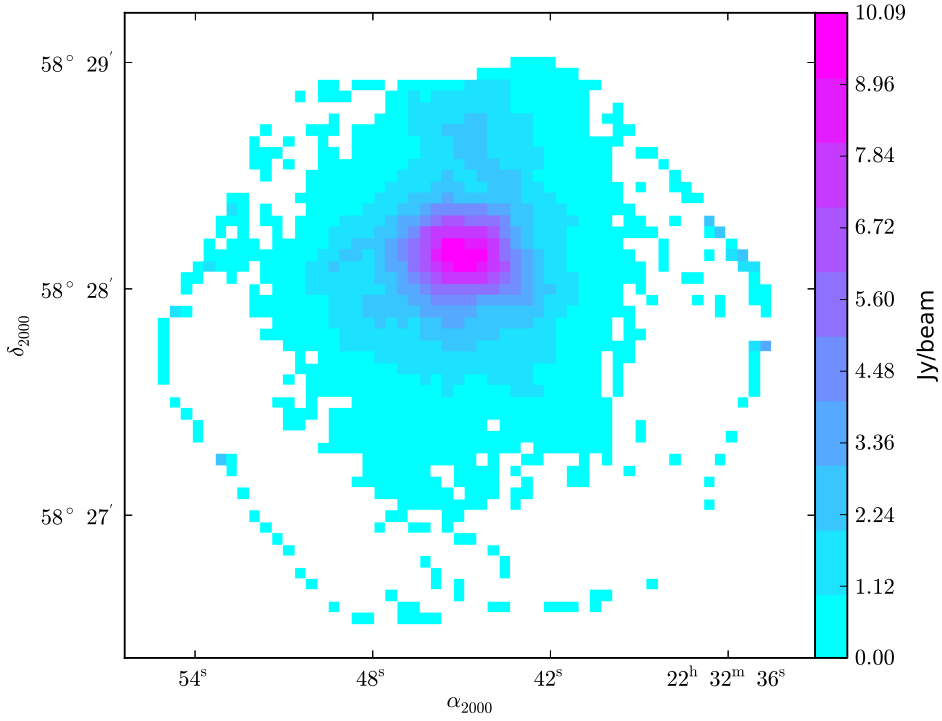

Figure 2.30: S138C$_a$ at 450 μm.

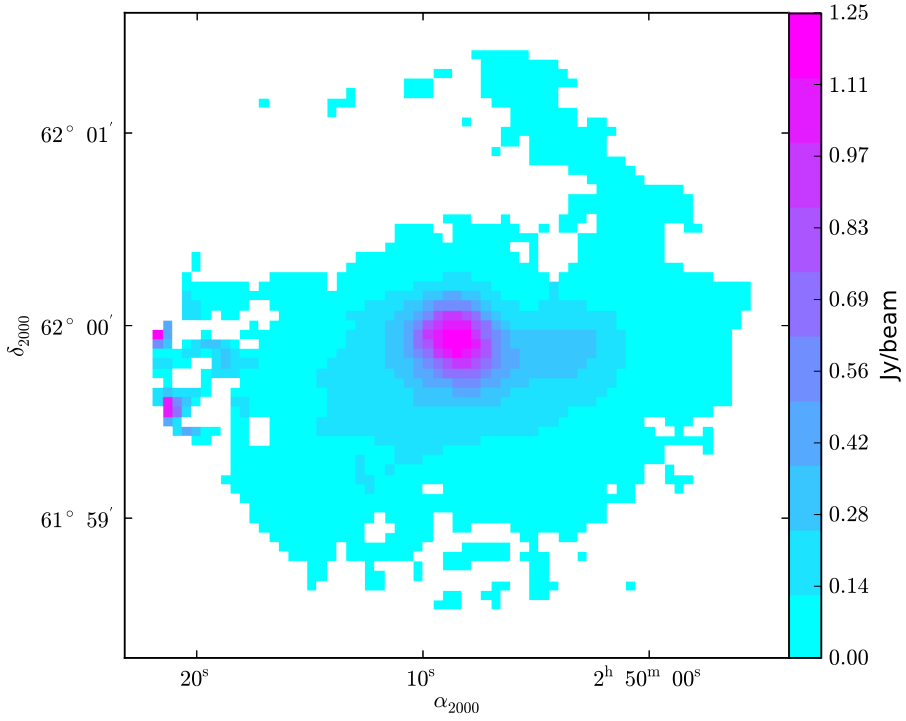

Figure 2.31: S196C$_c$ at 850 μm.

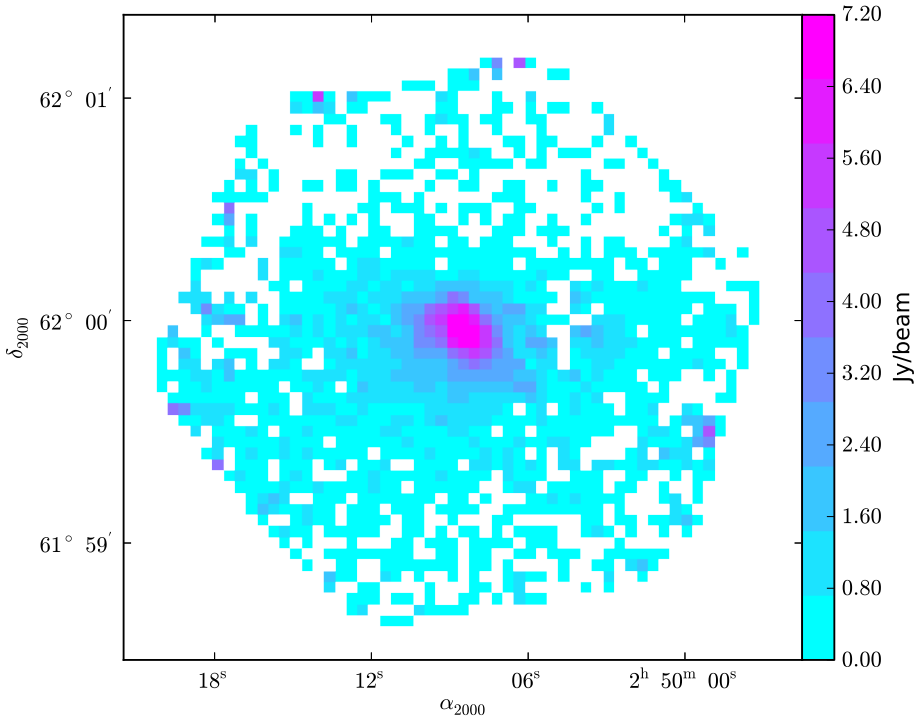

Figure 2.32: S196C$_c$ at 450 μm.

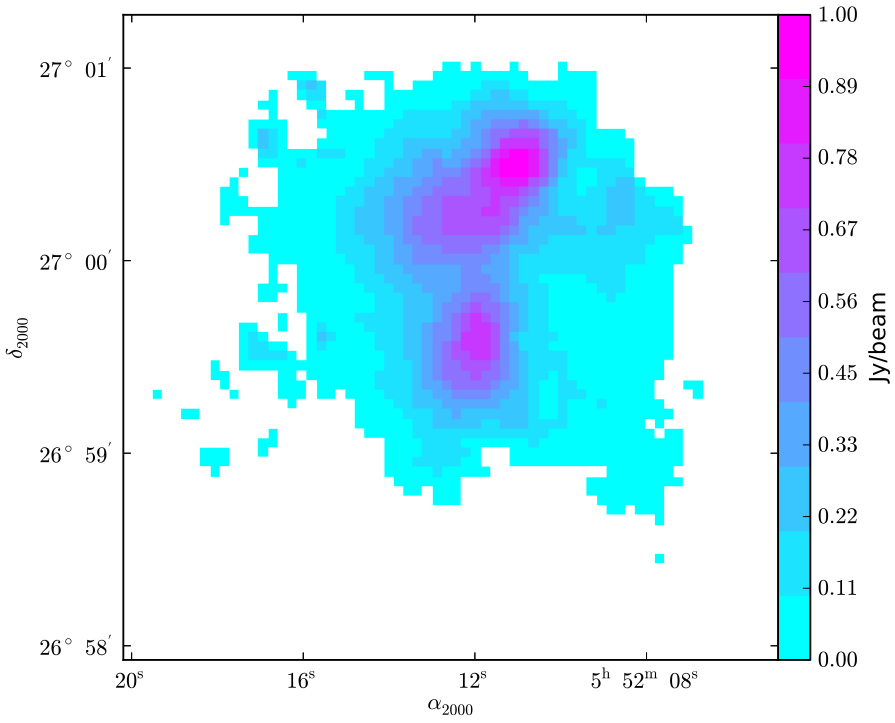

Figure 2.33: S242C at 850 μm.

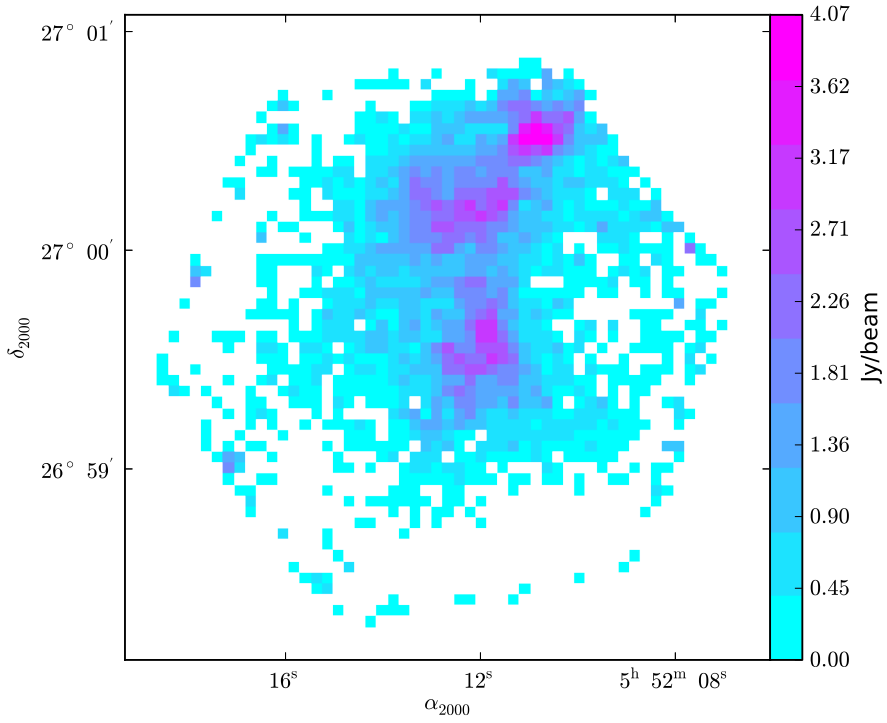

Figure 2.34: S242C at 450 μm.

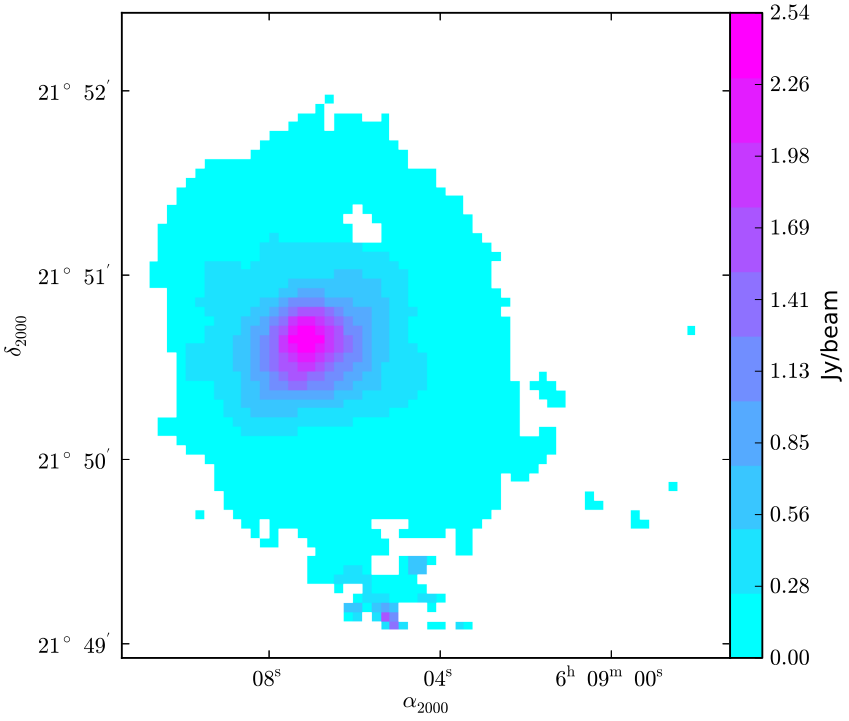

Figure 2.35: S247C$_c$ at 850 μm.

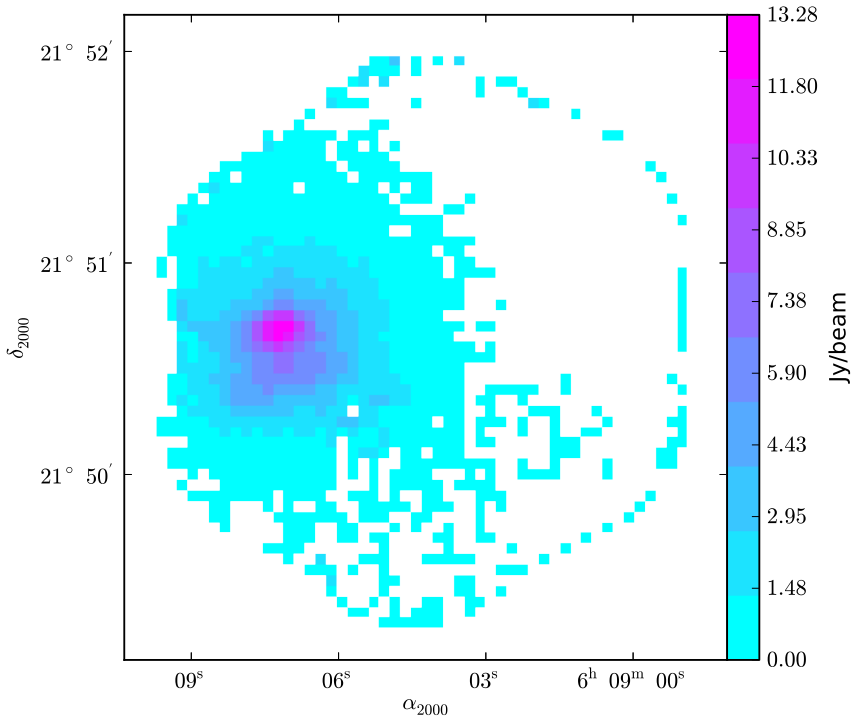

Figure 2.36: S247C$_c$ at 450 μm.

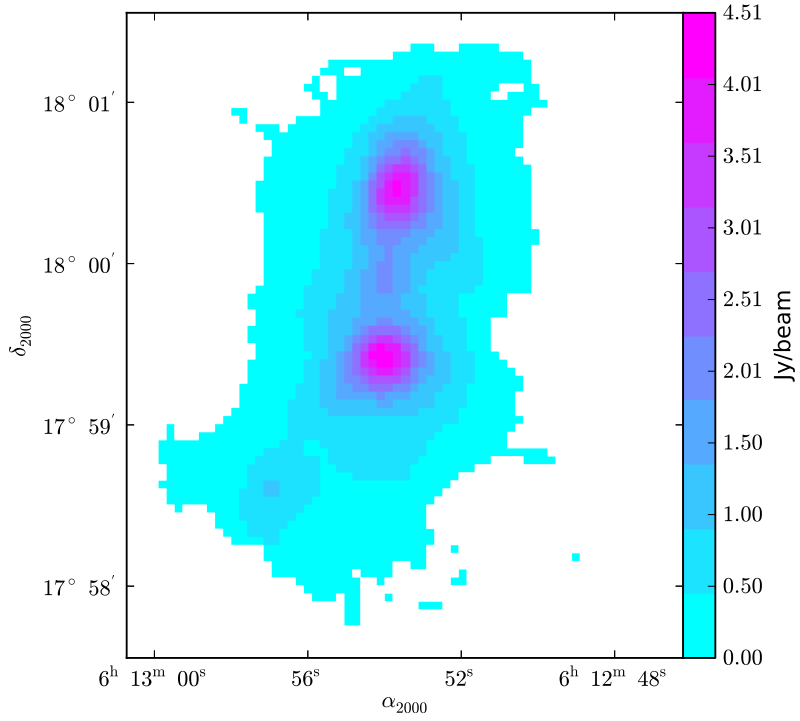

Figure 2.37: S254-8C at 850 μm.

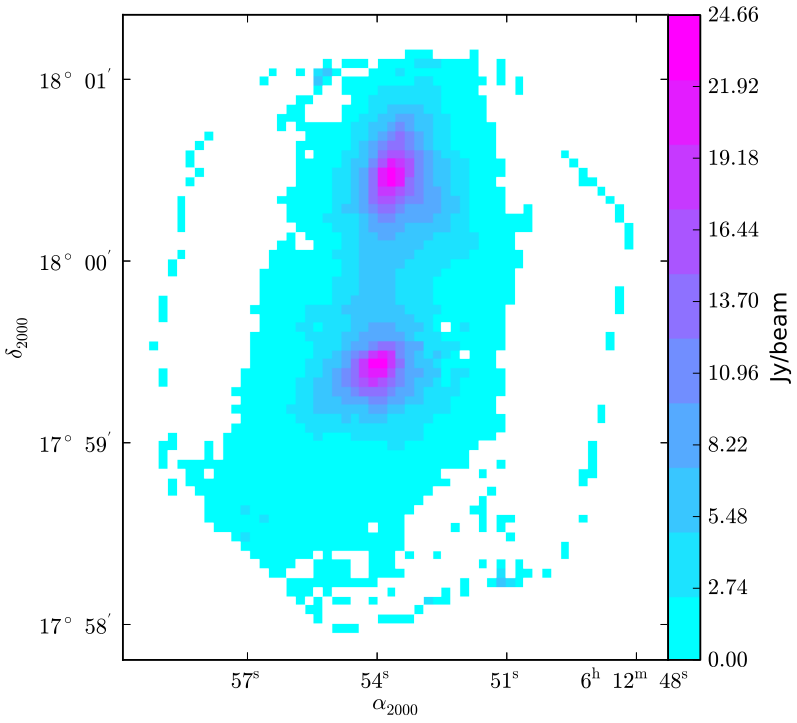

Figure 2.38: S254-8C at 450 μm.

2.3 Chapter Summary

We have performed a comprehensive study of dust in clouds near Galactic H II regions based on IRAS, and SCUBA data products. The physical properties of these dust clouds are derived by fitting SEDs to the IRAS and SCUBA data. The results obtained are compared with clouds without any potential H II regions.

Chapter 3

Analysis: Hot, Cool and Cold Dust

3.1 Bolometric Luminosity Ratio & Flux Density Ratio

We examined the ratio of the bolometric luminosities ($L_{Bol_{cool}}/L_{Bol_{hot}}$) due to the cool and the hot dust. While the luminosities vary by greater than a factor of 1000 from object to object, it is apparent from Figure 3.1 that the values of $L_{Bol_{cool}}/L_{Bol_{hot}}$ for all the clouds show very little scatter; the average value of $L_{Bol_{cool}}/L_{Bol_{hot}}$ = 2.8 ± 0.1, i.e., there is a 4% uncertainty in the mean (the standard deviation is 0.8). In other words, in all of the objects, the cool dust produces approximately 75 % of the total bolometric luminosity.

The calculation of this ratio requires several steps including an automated fitting procedure. However there is a simple test; directly using the data, that helps lend confidence to this result.

The 12 and 25 μm radiation is emitted only from the hot dust and the bolometric luminosity of the hot dust is proportional to the 12 and 25 μm fluxes. If the 100 μm emission arises only from the cool dust, if the bolometric luminosity of the cool dust is proportional to the 100 μm fluxes, and if the ratio $L_{Bol_{cool}}/L_{Bol_{hot}}$ is a constant as found above, then the ratio $F_{100}/(F_{12}+F_{25})$ should also be a constant. This is because the in-band luminosity is proportional to the flux density times the bandwidth of the corresponding IRAS wavelength band. We find that the $F_{100}/(F_{12}+F_{25})$ ratio has only a slightly wider scatter than the expected value. The $F_{100}/(F_{12}+F_{25})$ ratio on average is 9.0 ± 0.4 with ∼4 % uncertainty in the mean (the standard deviation is 4), for all the clouds in the neighbourhood of Galactic H II regions presented here. Note, the larger value of the flux density ratio with respect to the bolometric luminosity ratio is a consequence of the difference in bandwidth.

The slightly broader scatter in the value of $F_{100}/(F_{12}+F_{25})$ reflects the fact that the flux density at 100 μm is not only contributed by the cool dust, but also by the cold dust. There may also be a slight contribution from the cool dust to the 25 μm flux densities. The distribution of $F_{100}/(F_{12}+F_{25})$ ratios is plotted as a histogram in Figure 3.2.

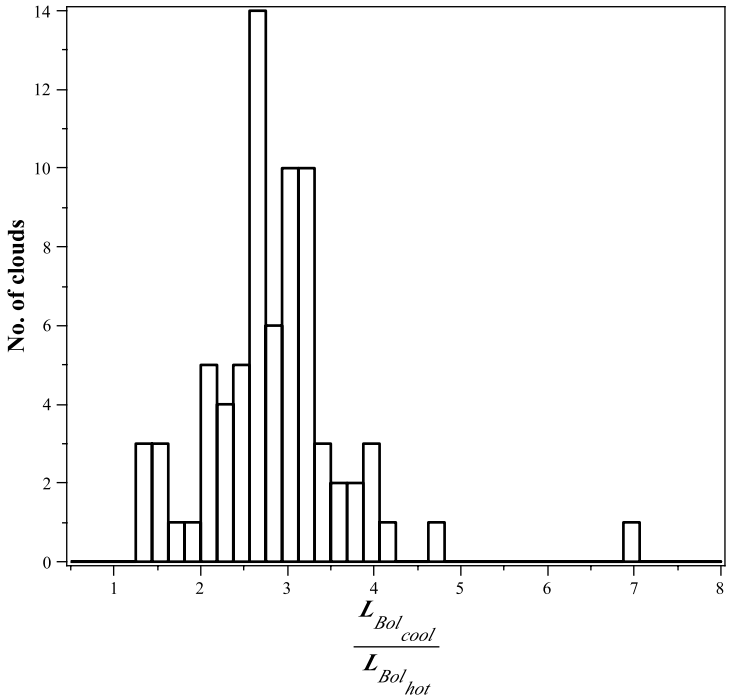

Figure 3.1: The histogram showing the ratio of the bolometric luminosity of the cool dust to the hot dust of all the H II regions in our study. Note the small scatter in the ratios of bolometric luminosity.

We also compared the flux density ratio of clouds surrounding H II regions with that of objects in the IRAS Point Source Catalogue (PSC). All the entries in the IRAS PSC with a good and moderate flux quality in all four IRAS bands were used and their ratio $\frac{F_{100}}{F_{12}+F_{25}}$ was calculated. Figure 3.3 shows the histogram of log $\frac{F_{100}}{F_{12}+F_{25}}$ of all the objects in the IRAS PSC. Note that the log of $F_{100}/(F_{12}+F_{25})$ is used because the distribution of IRAS PSC objects spans more than four orders of magnitude. All the clouds associated with H II regions of our study are found in a limited region of this histogram, marked as 'H II regions.' This characteristic shows that the flux density ratios of all our clouds in the vicinity of H II regions are confined to a very narrow band as compared to all the objects in the IRAS PSC, and even narrow as compared to objects in the ISM.

A few studies of H II regions [Wood and Churchwell, 1989a; Hughes and MacLeod, 1989; Chan and Fich, 1995; Kerton, 2002] have used an IRAS colour-colour diagram to define

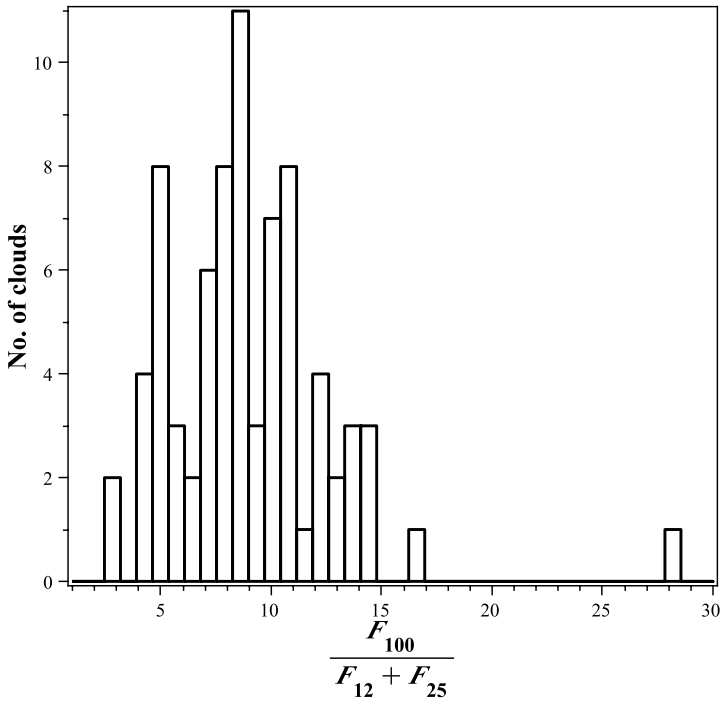

Figure 3.2: Histogram showing the $F_{100}/(F_{12} + F_{25})$ ratios of H II regions. The ratio seem to be varying only a little around the mean value 9.

the objects of their sample. We compare our result with the results obtained from IRAS colours of ultra compact H II regions [Wood and Churchwell, 1989a], by deriving the mean $F_{100}/(F_{12} + F_{25})$ ratio from the 100/60, 60/25, and 25/12 flux density ratios of 30 UC H II regions. We find the average of $F_{100}/(F_{12} + F_{25})$ of their sample of UC H II regions to be 12 ± 8. The average value of the flux density ratio found for all the H II regions of our study ($\frac{F_{100}}{F_{12}+F_{25}}$=$9 \pm 4$) is within the uncertainty limits of the value obtained for the UC H II regions. This similarity suggests that both the extended and the UC H II regions may have the same value for the ratio of the luminosities of the cool to the hot dust.

Dust in clouds in the environs of H II regions is very unlikely to be at a uniform temperature. The portion of the cloud that is closest to the exciting star should be the hottest, and the portion of the cloud that is least affected by the radiation field of the star, probably the cloud's interior making up most of the cloud's mass, will be at the lowest temperature. There must be a continuous change in temperature between these hottest and coldest regions of the cloud. Using the six flux density measurements available in this study, we find that we need at least three different temperature components across the cloud to fit the observations: hot, cool, and cold. Note that a two-component model does not fit the objects with five or more measured flux densities spanning from mid-IR to sub-mm

wavelengths and fits with more than three temperature components do not provide any additional meaningful insights (because we do not have enough data to fit them) into the physical properties of the regions.

Although the clouds most probably receive very different amounts of radiation from their exciting stars, a nearly constant value for the ratio of the bolometric luminosity of the cool dust to the hot dust is found in all these clouds. However, the mass ratio of the cool dust to the hot dust ranges over approximately three orders of magnitude and the luminosities vary by greater than a factor of 1000. This suggests that the luminosity ratio is dependent on some properties of the dust and the structure of the interface region and not on the intensity of the radiation field of the exciting star or the size of the clouds. Also note that the cold dust dominates the mass while the cool dust dominates the bolometric luminosity in all the clouds in the environs of Galactic H II regions of our study. Therefore the hot and the cool dust emission are probably from the surface layer of the cloud, which is the interface between the H II region and the molecular cloud.

3.2 Clouds without H II Regions

A molecular cloud which has a star forming in it or which contains a young star, differs significantly from an isolated molecular cloud without any star formation. Near H II regions, the surface layers of a cloud are exposed to radiation from its star. However, for clouds without any H II regions, the surface layers are heated by the diffuse interstellar light and not by any nearby direct radiation sources. In both cases mentioned above, the volume of dust deep within clouds is shielded from any radiation. In order to better understand the differences in dust clouds due to the presence and absence of a nearby star, we inspected 13 isolated low-mass pre-stellar clouds [Kirk et al., 2005] that are not associated with any H II regions. We calculated the $F_{100}/(F_{12}+F_{25})$ value of these pre-stellar clouds using IRAS data and compared this result with the $F_{100}/(F_{12}+F_{25})$ value obtained from the H II regions.

The $F_{100}/(F_{12}+F_{25})$ distribution of isolated cloud cores shows a slightly higher mean value than that of clouds with associated H II regions. The average value of $F_{100}/(F_{12}+F_{25})$ for these clouds is 15 ± 2. This higher value suggests that the surface layers of these clouds are cooler than the H II region clouds. It is also found that all the isolated clouds on average have IR luminosities about three orders of magnitude lower than that of H II region clouds indicating the presence of a less intense heating environment. Another possible reason for the low values of the IR luminosities of these isolated clouds is their lower masses in comparison with the masses of giant molecular clouds associated with the H II regions.

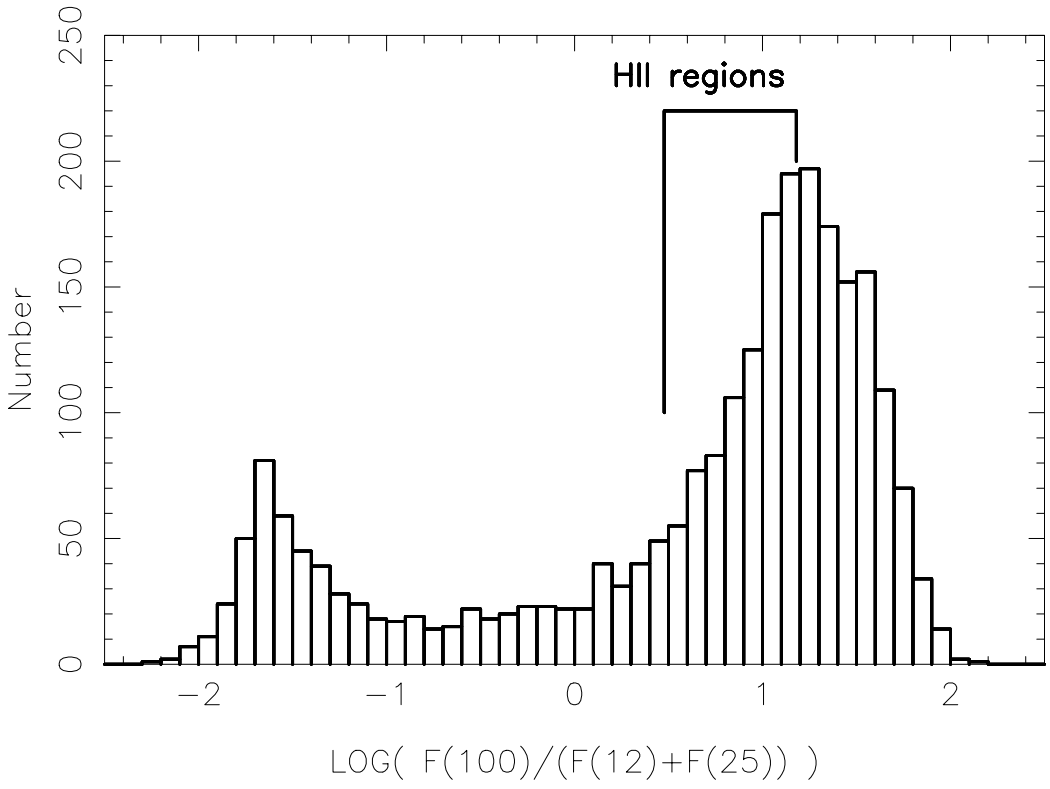

Figure 3.3: Histogram showing the log of $F_{100}/(F_{12} + F_{25})$ ratios of all the point sources in the IRAS PSC. From comparison with various catalogs, the left side peak of the histogram contains mostly stars, and the right side peak corresponds to objects in the interstellar medium. The loci of all the H II regions of our sample are marked as 'H II regions.'

3.3 Luminosity-Mass

The mass of the cool dust in clouds near H II regions shows a relationship with the IR luminosity as presented in Chapter 2, Figure 2, i.e.,

$$L \propto M_{cool}^{1.16\pm0.01} \tag{3.1}$$

Similar mass-luminosity relations were derived observationally for a sample of 66 compact H II regions by Chini et al. [1987], and for a sample of 15 intermediate SFRs by Arvidsson et al. [2010], where the gas mass is strongly related to the luminosity.

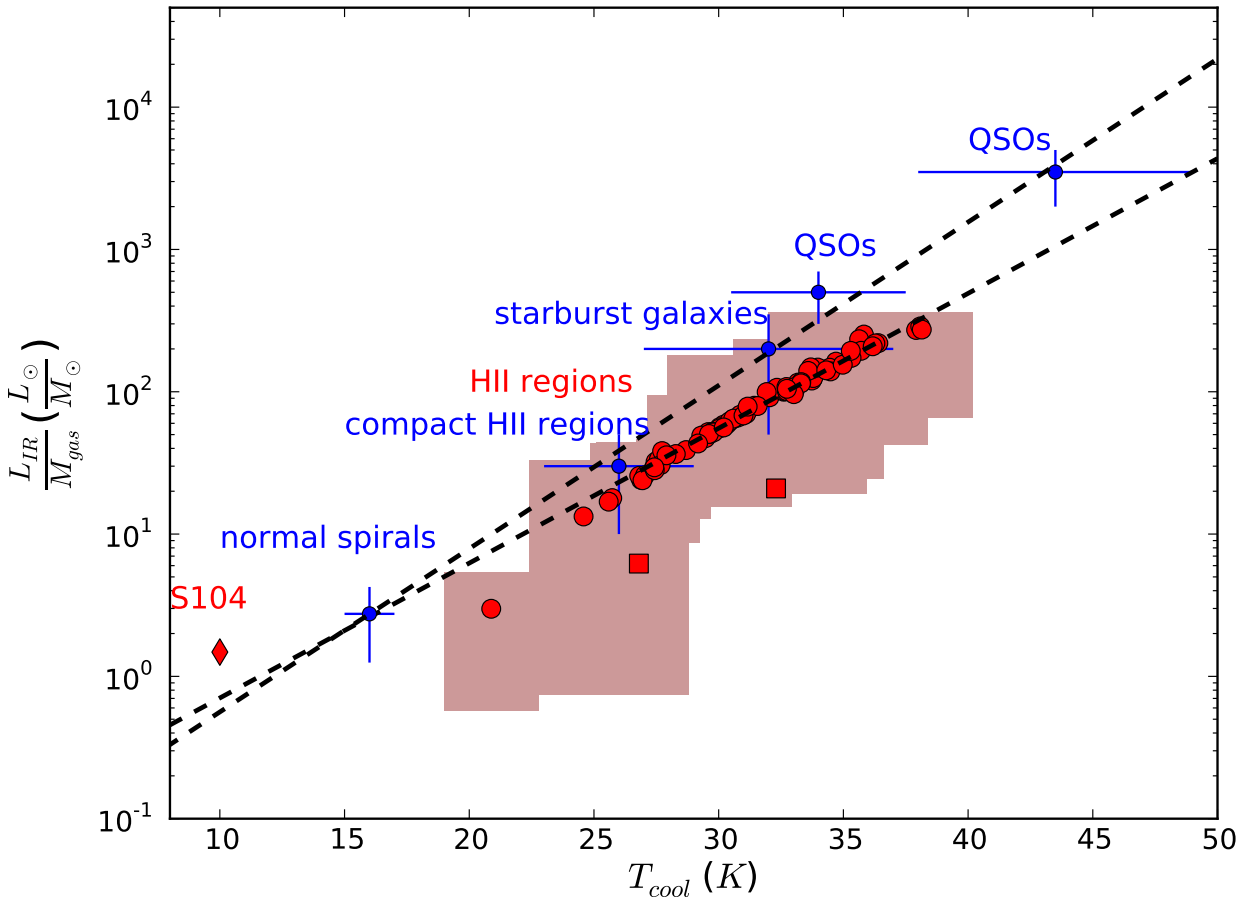

Figure 3.4: L/M vs. temperature T_{cool} of the dust component for different classes of objects. The data in solid red circles are the H II regions of our study and can be fitted by a relation $\log(L/M_{gas}) = -1.10 + 0.09 \cdot T_{cool}$. The shaded area corresponds to the uncertainty associated with this data. The solid red squares represent the (L/M) values with an upper limit of the mass of cool dust, and are not included in the fit. The solid red diamond stands for the cloud S104 with cold dust mass at a temperature of 10 K. The data in solid blue circles are taken from Chini et al. [1989] and corresponds to L/M vs T of the coldest dust component for different classes of objects. The two black dashed lines show the best fit for our values and those of Chini et al. [1989].

We converted the dust mass to gas mass by assuming a gas to dust mass ratio of 100, and the ratio of the total IR luminosity to the gas mass is calculated and plotted against

the cool dust temperature of all the H II regions of our study. We found that the L/M_{gas} of all H II regions is well correlated with the cool dust temperature. These L/M_{gas} values of H II regions are compared with the L/M_{gas} of dust embedded sources such as compact H II regions, normal spirals, starburst galaxies and QSOs studied by Chini et al. [1989]. The results are plotted in Figure 3.4. The luminosities of H II regions are calculated from the colour corrected flux densities from 12 to 100 μm, while for the other objects shown in blue, the energy distribution from 0.3 to 1300 μm contributes to the luminosity. The data of all H II regions in Figure 3.4 can be fitted by a relation:

$$\log(L/M_{gas}) = -1.10 + 0.09 \cdot T_{cool} \tag{3.2}$$

where L/M_{gas} is the ratio of the embedded luminosity to the mass of interstellar material.

The above equation is consistent with the equation $\log(L/M) = -1.44 + 0.12 \cdot T_d$ [Chini et al., 1989], which states that dust temperature at sub-millimeter wavelengths can be used to estimate the ratio of the embedded luminosity to the gas mass of different classes of objects. Similar to the result of Chini et al. [1989], our finding indicates that the L/M_{gas} of a cloud near an H II region can be determined from the cool dust component of the cloud, i.e., if we know the cool dust temperature of a cloud, we can derive the L/M_{gas} of that cloud by using the above relation. Figure 3.4 also shows the L/M_{gas} value of the cold dust in S104 for an assumed T_{cool} of 10 K. The point corresponding to S104 is consistent with the above relation of H II region clouds.

The IR luminosity-to-gas mass ratio of molecular clouds is an important parameter since it is often used to obtain the star formation rate per unit mass. If we consider only the mass of cool dust, the average ratio L/M_{gas} of all the H II regions of our study is 100 ± 70 $\frac{L_\odot}{M_\odot}$, but the ratio varies by almost a factor of 100. The minimum value of the ratio is 3 $\frac{L_\odot}{M_\odot}$ found for S266C$_c$, and the maximum value is 288 $\frac{L_\odot}{M_\odot}$ obtained for S138C$_b$. According to some studies, low values of L/M_{gas} such as ≤ 1 $\frac{L_\odot}{M_\odot}$ [Mooney and Solomon, 1988], ≤ 1.8 $\frac{L_\odot}{M_\odot}$ [Deane et al., 1994], ≤ 0.5 $\frac{L_\odot}{M_\odot}$ [Paradis and et al., 2011] denote quiescent clouds and higher values are found for clouds with star formation activity.

The L/M_{gas} ratio falls to low values if we consider the cold dust mass. For example, when considering only the cool dust mass, the L/M_{gas} value of the cloud S104 is 92 $\frac{L_\odot}{M_\odot}$. But, if we also take into account the cold dust mass in calculating L/M_{gas}, the ratio falls to 1.5 $\frac{L_\odot}{M_\odot}$. The cause of this variation in L/M_{gas} is because most of the mass is in cold dust and the cold dust's contribution to the total bolometric luminosity is negligible. An increase in the mass therefore decreases the value of the L/M_{gas}. The obtained value of L/M_{gas} of the cloud S104 is most likely showing its star formation activity since this value is above the limit for quiescent clouds in most cases. Furthermore, no correlation between L/M_{gas} and M_{gas} is seen in clouds near H II regions like in the studies of dust in LMC molecular clouds [Paradis and et al., 2011].

3.4 Hot Dust

The PAHs and VSGs radiating at the near- and mid-IR wavelengths can affect the temperature and mass of mainly the hot dust. Such a conclusion is suggested by the observation that the equilibrium temperatures of the hot dust, obtained in our study, are higher than 100 K, and large grains are unlikely to be at such high temperatures. Therefore, these unusually high temperatures could be evidence for the presence of VSGs and PAHs. It must be emphasized that VSGs and PAHs are by no means in radiative equilibrium with their surroundings since they undergo temperature spikes. The masses of the hot dust have been obtained by assuming that the dust is in the thermal equilibrium with its environment. Thus, the inclusion of stochastic heating of PAHs and VSGs is likely to change the values of these masses. However, the luminosity is not affected by the PAHs and VSGs since we are concerned only with the total contribution from all the grains. Unfortunately, the influence of VSGs and PAHs on the hot dust cannot be determined in the current paper due to the lack of required observations.

3.5 Cold Dust and Cool Dust

The masses of the cold dust were determined for seven clouds by fitting the three-component SED using IRAS and SCUBA data. Having only five data points for the other three clouds, we calculate the masses of the cold dust by assuming the temperature of the cold dust to be 10 K. The masses of cold dust and cool dust of these ten clouds are plotted in Figure 3.5. The probability that a relationship exists between M_{cold} and M_{cool} is more than 90%. It is clear that most of the mass of the dust in the clouds near H II regions are at temperatures below 20 K.

The mass ratio, M_{cold}/M_{cool}, ranges from 12 to 260 with an average value of 71 and hence there is a large uncertainty in the mass ratio attributed by the lower number of data points. If this mass ratio is accurate, then the mass of cold dust can be readily calculated once the value of the mass of cool dust is known. Note that the mass of cold dust, obtained in such a way, will always be underestimated because the SCUBA observations have not covered as large area as the IRAS observations have. Hence, to provide a more accurate value for M_{cold}/M_{cool}, the sub-mm observations ought to cover a larger area. If more sub-mm flux were measured from the bigger area, then the value of M_{cold} as well as M_{cold}/M_{cool} would increase. Also note that the very cold dust temperatures, obtained by fitting our model to the IRAS and SCUBA data for a number clouds (see Table 2.3 for details), are very low (≈ 6 K). Since it is physically difficult to have very low equilibrium temperatures for big grains, the hypothesis of the presence of large amounts of very cold dust grains in clouds near H II regions sounds less plausible.

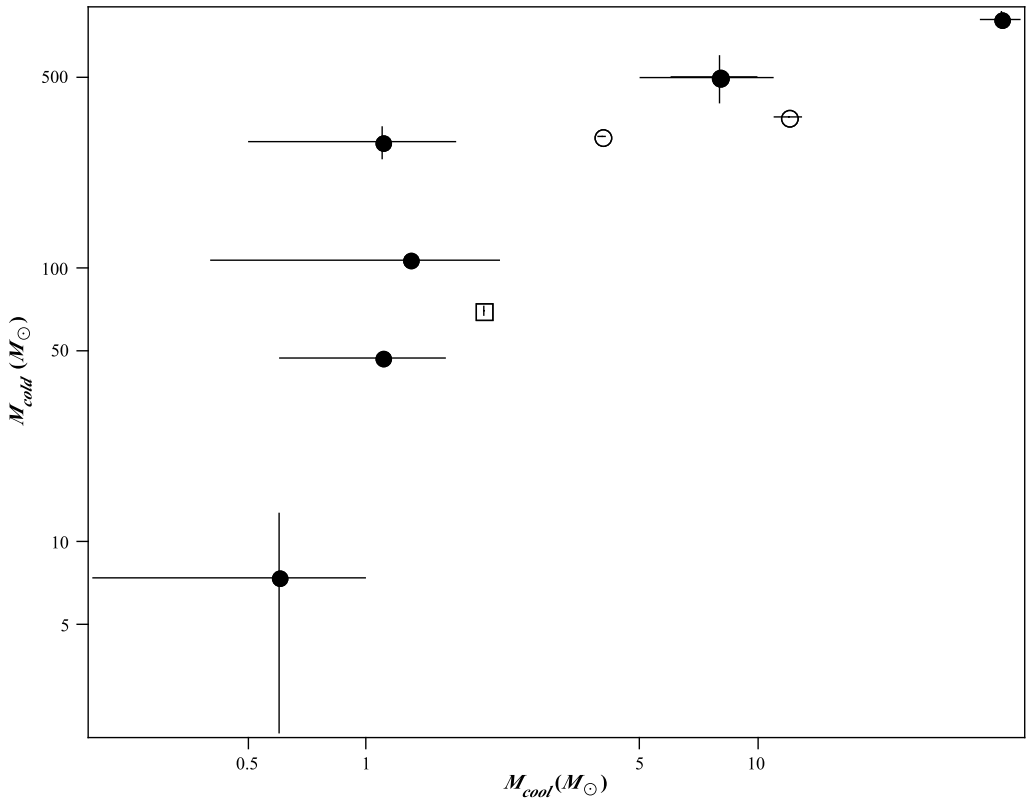

Figure 3.5: Mass of cold dust vs. mass of cool dust near 10 H II regions. The solid circles mark the clouds that show a good three-component fit, the clouds shown in open circles are those with an assigned temperature of 10 K for the cold dust, and the open box represents the cloud S233C$_b$ with an upper limit in the mass of cool dust in the three-component fit.

Let us list alternative explanations for the very low temperature. Foremost, there may be a contribution in emission from very small spinning dust grains to the flux density at sub-mm wavelengths. Although the Galactic spinning dust emission peaks are observed between 20-40 GHz, the peak emission can vary depending on the cloud environment and grain composition [Bot et al., 2010]. Due to this reason, there could be some contamination from the spinning dust emission to the flux density at 450 and 850 μm in these clouds. Another possibility is variations in the dust emissivity spectral index at sub-mm wavelengths perhaps due to temperature, structure and composition effects on the dust. Several laboratory experiments [Mennella et al., 1998; Bösch, 1978; Boudet et al., 2005] and astronomical observations [Dupac et al., 2003; Désert and et al., 2008] have pointed out an increase in the spectral index with a decrease in temperature in sub-mm and mm wavelength ranges. A third possibility is contamination in emission from molecules like CO at SCUBA 450 and 850 μm. In addition to the continuum emission from dust, CO(3-2)

and CO(6-5) transitions can contribute to emission at 850 and 450 μm respectively as discussed in Seaquist et al. [2004]. Near strong radiation fields like H II regions, we can expect such contamination from molecules. Similar CO features are also found in the data of UC H II region G29.96-0.02 obtained from *Herschel* SPIRE FTS SLW [Kirk and et al., 2010]. We briefly explain the effect of the spectral line contamination on the sub-millimeter flux in Chapter 6 where the SCUBA-2 data are analyzed.

The mass and temperature of the cold dust strongly depend on the lower limits of the SCUBA flux densities. In order to determine the effect of the lower limits on the physical properties of the cold dust, we calculated changes in the values of the masses and temperatures induced by increasing the flux densities. First, we doubled the values of only the 450 μm flux densities and good three-component fits were found only for clouds S159 and BFS15C$_d$, which yielded an 86% decrease of the mass and a 174% increase of the temperature of the cold dust in S159 and a 72% decrease of the mass and a 70% increase of the temperature for BFS15C$_d$. Second, we doubled the values of only the 850 μm flux densities and good three-component fits were obtained for all the clouds except S159 and BFS15C$_d$. A drastic increase (by a factor of eight, on average) of the mass of the cold dust and a drop (by half, on average) of the temperature were observed (e.g., the mass of the cold dust in S269 became ten times its initial value while its temperature reduced by 61%). And finally, we doubled the values for both the 450 μm and 850 μm flux densities and valid three-component fits were computed for all the clouds but S269. The mass of the cold dust in S159 increased by a factor of 1.3 (the mass of cold dust in all the clouds rose by a factor of 1.7, on average); the temperature increased by 23% in all the clouds except BFS15C$_d$, S201C$_b$, and S233C$_b$, where the increases were 6.3%, 0.1%, and 2.4% respectively. In summary, doubling the values of only the 450 μm flux densities decreased the mass moderately, and increased the temperature significantly. However, doubling only the values of 850 μm flux densities increased the mass dramatically and decreased the temperature moderately. Surprisingly, doubling both the values of 450 μm and 850 μm flux densities showed only a moderate increase in the mass and a slight increase in the temperature.

3.6 Total IR Luminosity

We have measured the average values of the ratios of colour corrected flux densities ($F_{25}/F_{12} = 2.1 \pm 1.7$, $F_{60}/F_{25} = 9.5 \pm 3.0$, and $F_{100}/F_{60} = 1.7 \pm 0.8$) of all our sample clouds near H II regions. Since we know the average value of the bolometric luminosity ratio, we can derive the total IR luminosity with the help of the above flux density ratios. In this way, we can estimate the total IR luminosity from flux densities at each wavelengths. For example, if we consider a cloud near an H II region with a distance D (kpc), and a

flux density F (Jy) at a particular wavelength, then the total IR luminosity (L$\odot$) can be estimated as;

$$L_{IR} = (30 \pm 20) D^2 F_{12} \tag{3.3}$$

$$L_{IR} = (16 \pm 5) D^2 F_{25} \tag{3.4}$$

$$L_{IR} = (1.7 \pm 0.7) D^2 F_{60} \tag{3.5}$$

$$L_{IR} = (1.0 \pm 0.6) D^2 F_{100} \tag{3.6}$$

i.e., if one has flux density measurements at any one wavelength, such as 12, 25, 60 or 100 μm, and the distance to the cloud, then one can estimate the total IR luminosity of the cloud by using the above equations.

3.7 Chapter Summary

Dust ranges in temperature from a few hundred K, probably at the edge of the molecular cloud near to the H II region, to $\approx$ 10 K, probably at the centre of the cloud. The cool dust component which is in the temperature range 25 K-40 K, located between the hottest and coldest regions of the cloud, dominates the luminosity. If we can calculate the total IR luminosity, we can estimate the gas masses and these results may prove useful for IR observations for estimating masses in extragalactic systems with active high-mass star formation. A high value of L/M_{gas} due to the cool dust indicates high star formation activity, but the addition of cold dust mass reduces this value. We also present a new relation connecting total IR luminosity and flux density at a particular wavelength, and that will be beneficial if we have only one flux density measurement. Studies of dust mass often do not include the coldest dust that emits most strongly at sub-mm wavelengths. We found that in all cases the dust mass is dominated by this cold dust, even in the hot regions studied here.

Chapter 4

Modeling Clouds Associated with Galactic H II regions

The dust grains in clouds associated with massive star-forming regions absorb the short wavelength radiation from these stars, heat up, and then re-radiate at far-infrared and sub-millimeter wavelengths. For this reason, clouds near H II regions are good sources of thermal emission. Since thermal radiation from dust is optically thin at far-infrared wavelengths, it is a good tracer of the temperature and density structure of the clouds. A standard density distribution, which reproduces the observed dust emission in molecular clouds associated with our sample Galactic H II regions, is yet to be developed. It is therefore important to construct a model which simulates the observed emission from clouds near Galactic H II regions to constrain the physical properties of our sample molecular clouds.

Many studies have been conducted over the past decades on developing various models of the dust in and around H II regions. According to models of spherical uniform density dust clouds illuminated by a central star [Natta and Panagia, 1976], grains in H II regions can have two different sizes. Such models favour a cavity in the density distribution and, without the presence of this central dust-free cavity, the models could not be fitted with observations (particularly IRAS observations). These models also indicate that all the mid-infrared radiation arises from inside the H II regions. Infrared emission from clouds near OB stars generating blister H II regions has been model by Leisawitz [1991] and the derived models agree with observations.

Giant molecular clouds host massive star-forming sites. However, a large fraction of these massive stars are not embedded at the centres of the parent molecular cloud [Wood and Churchwell, 1989b]. Massive stars are more often located at the edges or the surfaces of the giant molecular clouds, rather than at the centres [Lada, 1978]. Furthermore in the case of evolved or classical H II regions, there may be a dust-free space surrounding the massive star. Note that spherical radiative transfer models using DUSTY have been

tested on molecular clouds associated with our sample Galactic H II regions and they failed to reproduce the observed dust emission. Therefore, we model a non-spherical geometry in our clouds, in particular, a plane parallel geometry, which best suits the idea of the formation of massive stars at the edges of molecular clouds and a region devoid of dust close to the star.

In this chapter, we present models of dusty molecular clouds associated with Galactic H II regions, heated by a source of energy (a massive star), employing radiative transfer through a plane parallel dusty slab. Using these models, we aim to understand the infrared continuum emission from dust clouds with a slab geometry accompanied by a variety of density distributions. The model results are also compared with observations in order to deduce the impact of stellar flux and cloud density structure on the grain temperature and the overall star formation process.

The general cloud geometry considered in all the models is described below: The massive star which illuminates the cloud is on the left, and there is no stellar illumination on the right side of the cloud (see Figure 4.1 for a cartoon showing the geometry of the sample cloud). Internal heating (such as from cosmic rays) is present at all points of the cloud. The optical depth of the cloud is τ, and r is the distance from the left edge of the cloud in parsecs.

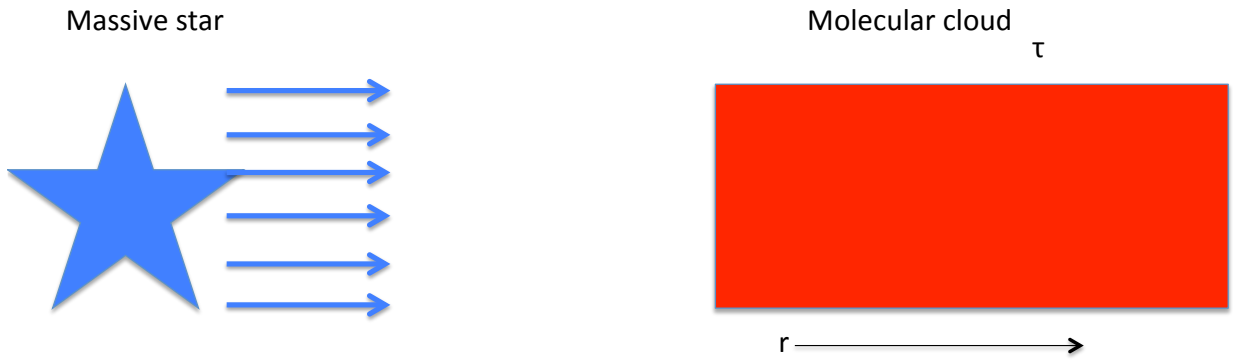

Figure 4.1: Schematic view of a cloud with plane parallel geometry used in the models.

In order to construct a reference cloud, flux density distributions (FDDs) of all our sample clouds near to Galactic H II regions are considered and the median value is taken to represent the theoretical cloud. Figure 4.2 shows the flux density distribution normalized to the flux density at 100 μm for all of our 83 clouds near H II regions. The median values of all the normalized fluxes at the three IRAS wavelengths are 0.044±0.011 (at 12 μm),

0.064 ± 0.030 (at 25 μm), and 0.656 ± 0.211 (at 60 μm). Except at 60 μm, the H II region sample clouds of our study show very similar FDDs to those of complex sources that are combinations of both interstellar clouds and star forming regions [Fich and Terebey, 1996]. The median value of the normalized flux at 60 μm is 0.467 ± 0.026 [Fich and Terebey, 1996] and the lower limit of this value is not within the uncertainty limits of the 60 μm normalized median flux density values of the Galactic H II regions. The median SED of the reference cloud is constructed (using a two-component model SED of hot and cool dust components) and is shown in Figure 4.3: the hot dust is at a temperature of 216 K and the cool dust is at 30 K.

A number of radiative transfer models are tested and compared with the clouds' mean observed flux density ratio ($\frac{F_{100}}{F_{12}+F_{25}}$) of 9.0 $\pm$ 3.0 (see Chapter 3 for details) using the equation of dust thermal equilibrium. The reference models are established by considering a constant stellar flux as well as different gas density distributions of the clouds, and include: (1) constant stellar flux; (2) constant gas density; (3) linear gas density distribution; (4) power law density distribution I; (5) power law density distribution II; (6) step function density distribution.

The major goal of this chapter is to explore the structure of the interface region, which we speculate as the possible cause of the constant luminosity ratio (see Chapter 3). The selected model scenarios are therefore, partly motivated by the quest for finding a probable density structure that can exist in our target clouds near H II regions. All our target clouds are exposed to different amount of incident radiation fields, nevertheless, the constant flux density ratio and bolometric luminosity ratio imply that these parameters are not dependent on the intensity of the radiation field. We therefore test the influence of incident stellar flux on the observed flux density distributions.

Large dust grains in molecular clouds are in local thermodynamic equilibrium where, in a simple model, radiative heating due to the absorption of short wavelength radiation from the star balances the cooling by re-emission of this radiation. Therefore, the large grain temperatures can be calculated in a simple way. For spherical grains with absorption efficiency Q_ν, radius a, and temperature T_d in a radiation field J_ν, the equilibrium condition can be expressed as follows:

$$\int Q_\nu J_\nu \, d\nu. \; = \int Q_\nu B(\nu, T_d) \, d\nu. \tag{4.1}$$

[Krügel, 2003]

The dust grains are exposed to plane parallel radiation from massive stars, whose spectral energy distribution peaks at the UV-visible frequency range. At such frequencies (where $\lambda \approx a$), the radiation field is hard for the dust grains; the grains absorb well at these

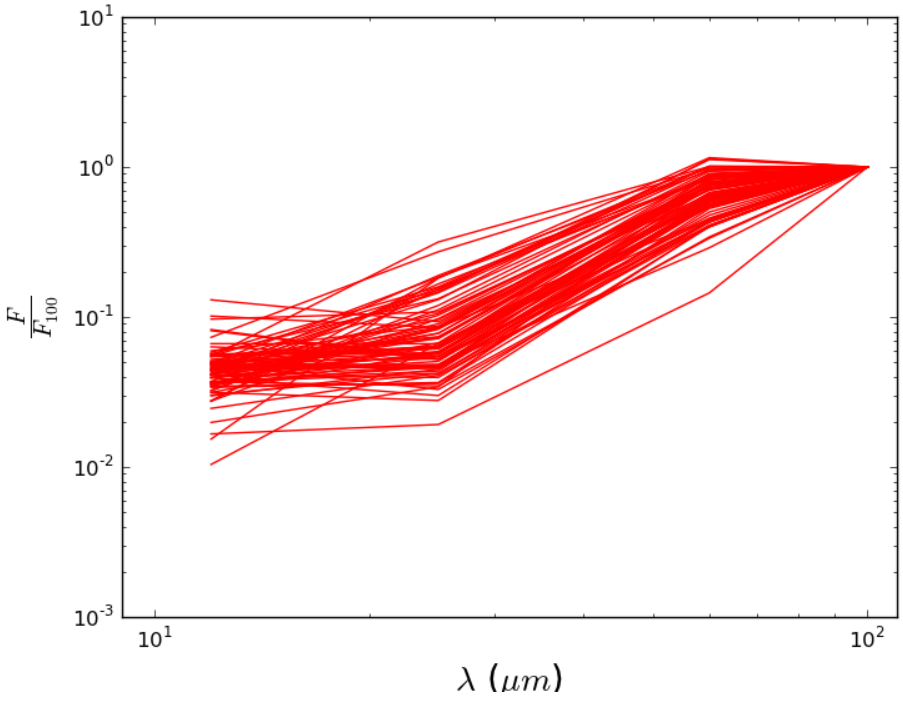

Figure 4.2: Normalized flux density distribution of all the observed clouds.

wavelengths, and therefore the absorption efficiency factor, $Q_{abs} \simeq 1$. Let's consider a dust grain at a distance x from a massive star (with an effective temperature T and radius R), then the star will subtend a solid angle $\frac{\pi R^2}{x^2}$ at the location of the grain providing a mean intensity,

$$J_\nu = \frac{1}{4\pi} B(\nu, T) \frac{\pi R^2}{x^2} \tag{4.2}$$

[Krügel, 2003]
The grains are also exposed to Galactic interstellar radiation field. See Figure 4.4 for the diluted radiation field experienced by a dust grain separated by 0.1 pc from a massive star having an effective temperature of 50000 K and a radius of 10 $R_\odot$ (in blue). The mean Galactic background radiation field at the site of the grain is given in green (selected from Black [1994]). Most of the UV, visible, and near IR radiation from the massive star will be absorbed within the surface layers, at very shallow optical depths, of the clouds facing the star. The stellar radiation field has negligible effect at larger optical depths and other long wavelength radiation fields dominate at deeper regions of the cloud.

In this chapter, we use a sample dust cloud with a slab geometry, which is illuminated by

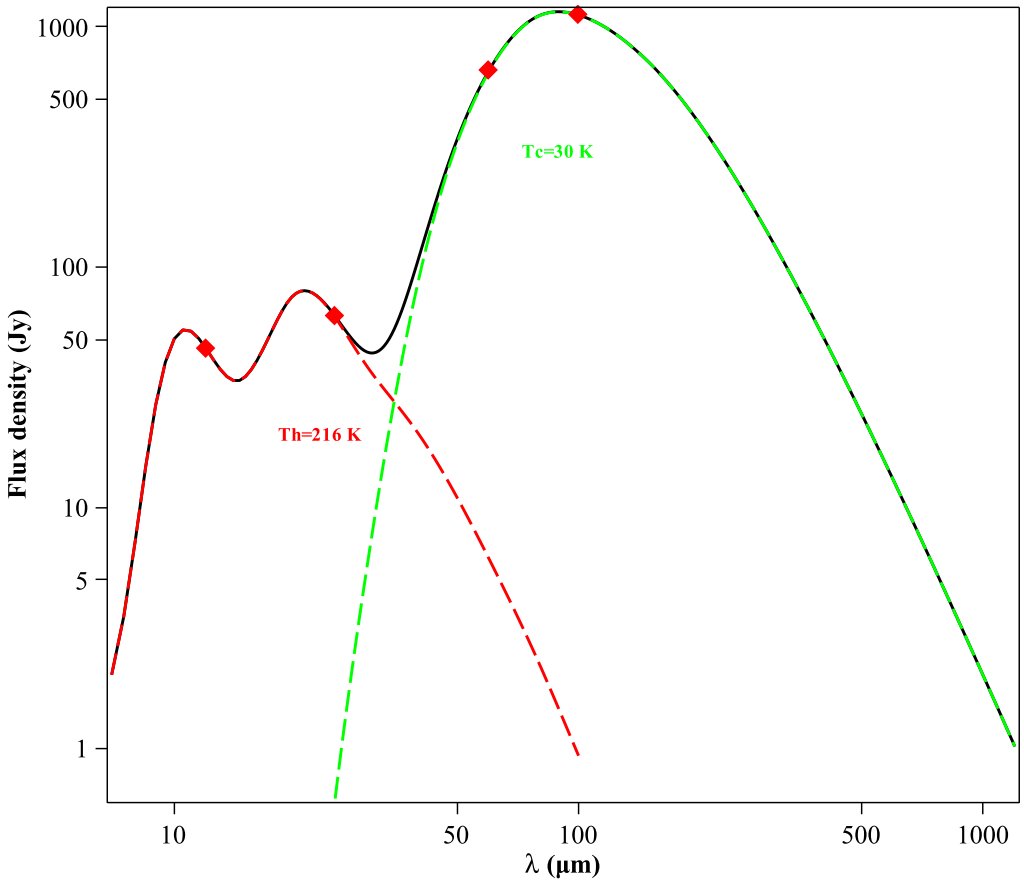

Figure 4.3: Median two-component model SED of the reference cloud. T_h and T_c are respectively the hot and cool dust temperatures obtained from the two component model fit.

plane parallel radiation from a massive star from the left side. Grains are also considered to be uniformly heated internally by for example cosmic rays. Cosmic rays are able to penetrate exceedingly opaque regions of the molecular clouds and are believed to be the principal heating mechanism in dense regions of the clouds. Other mechanisms such as heating due to the interstellar radiation field (ISRF) will not affect the high extinction regions of the cloud.

We consider only the heating by the exciting star and the internal heating and ignore all other heating mechanisms such as grain-gas collisions and shocks. The Lyα radiation resulting from recombination within the H II region is also ignored because it has little effect on the parental cloud. The cloud is regarded as optically thin at IRAS and sub-mm

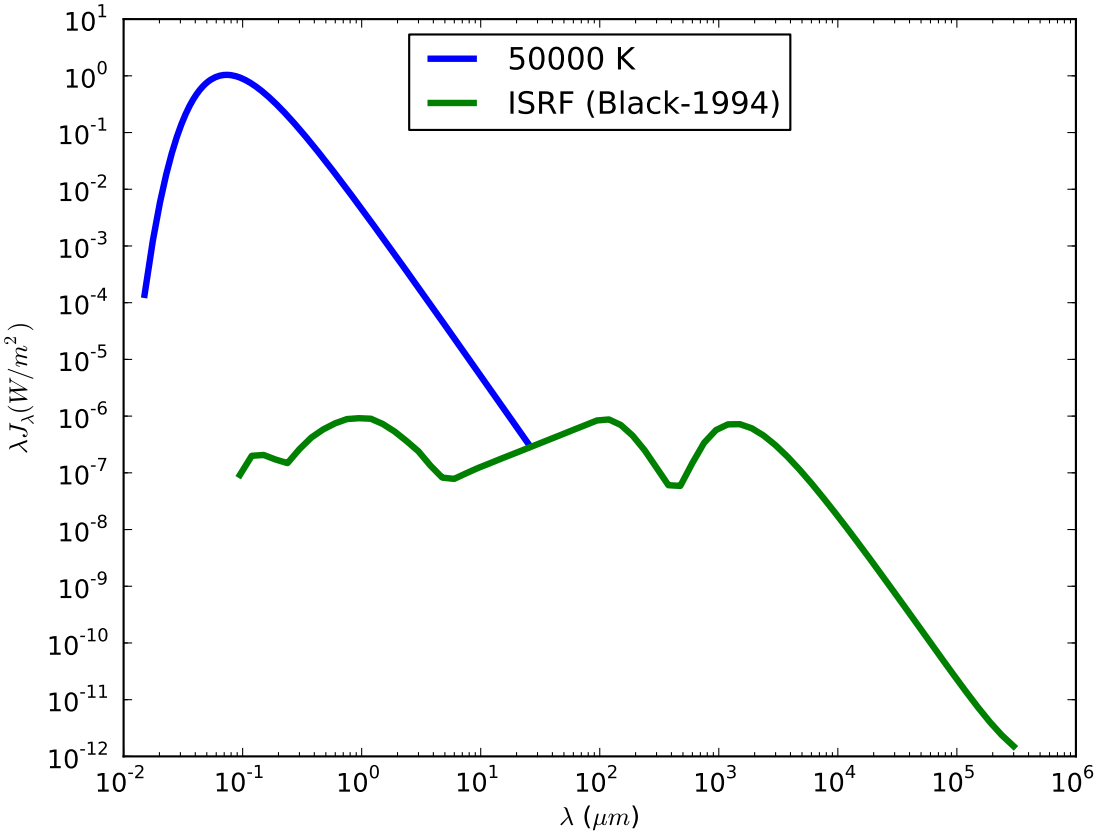

Figure 4.4: Radiation field from the massive star and the galactic background radiation field experienced by a grain at the edge of the cloud facing the star.

wavelengths and therefore the re-radiated long-wavelength photons are not re-absorbed by the grains as the photons propagate through the cloud. The cloud (at the left edge) receives a flux F from the star along with a uniform flux from the internal heating and these two mechanisms heat up the cloud and the condition for thermal balance can be re-written as:

$$n_d \pi a^2 F \exp(-\tau) + n_d \pi a^2 F_{internal} = n_d 4\pi a^2 \int Q_\nu \pi B(\nu, T_d)\, d\nu. \tag{4.3}$$

where $B(\nu, T_d)$ is Planck function and Q_ν is the efficiency factor for emission. The term on the left hand side represents radiative heating experienced by the grains, caused by absorption of a flux F from the massive star (first term on the left hand side) and the

absorption of radiation due to internal heating mechanisms (second term on the left hand side). The term on the right hand side represents the radiation emitted by grains (radiative cooling) per unit volume of dust with n_d and a, the number density and radius of dust grains, respectively. The cloud is assumed to have only single sized classical dust grains. A value equal to the average for a MRN grain size distribution (0.1 μm) is adopted as the radius of the dust grain. The term τ represents the optical depth of the cloud, defined as:

$$\tau = \int n_d(r)\pi a^2 Q_{abs}\, dr. \tag{4.4}$$

A mixture of 50% silicate and 50% graphite is adopted as the composition of the reference cloud with an MRN grain size distribution. The selected $\frac{\lambda Q_{em}}{a}$ of the grain is shown in Chapter 2 (Figure 2.1). The values follow a power law emissivity index, $\beta = 2$, at sub-mm wavelengths. In order to test the effect of flux on the temperature of the left edge of the cloud, at first, we consider the flux dependence of the temperature, and a temperature distribution is plotted as a function of incident flux on the left edge of the cloud as shown in Figure 4.5. From Figure 4.5, it is obvious that the left side temperature of the cloud increases with the incident flux and the temperature can be well described by a power law ($T \propto F^{1/4}$) up to a temperature of $\approx$ 300 K or up to $\approx$ 100 Wm^{-2}. As the incident stellar flux rises beyond 100 Wm^{-2}, the slope of the curve changes. This is because, as the temperature exceeds 300 K, the emission starts to fall in the optical regime and the grains cannot undergo efficient cooling although they are being heated by much higher stellar flux. At this stage, the condition for the balance between the cooling and the heating breaks down.

The infrared (IR) volume dust emissivity (which is the power emitted by unit volume of the dust at a specific frequency in unit frequency interval to a unit solid angle and has the unit $\mathrm{Wm^{-3}Hz^{-1}sr^{-1}}$) is given by

$$j_\nu = n_d \pi a^2 Q_\nu B(\nu, T_d). \tag{4.5}$$

The IR emissivities are calculated at each effective wavelength of the IRAS wave bands using the C/V values at respective IRAS wavelengths. The specific intensity at each point r of the cloud can be written as follows:

$$I_\nu = \int_r j_\nu\, dr, \tag{4.6}$$

or in other words,

$$I_\nu = \tau_\nu B(\nu, T_d), \tag{4.7}$$

which has the units of power per unit area per unit frequency bandwidth per unit solid angle ($\mathrm{Wm^{-2}\ Hz^{-1}sr^{-1}}$). The total monochromatic flux F_ν ($\mathrm{Wm^{-2}Hz^{-1}}$) from the whole cloud is given by:

$$F_\nu = 4\pi I_\nu \tag{4.8}$$

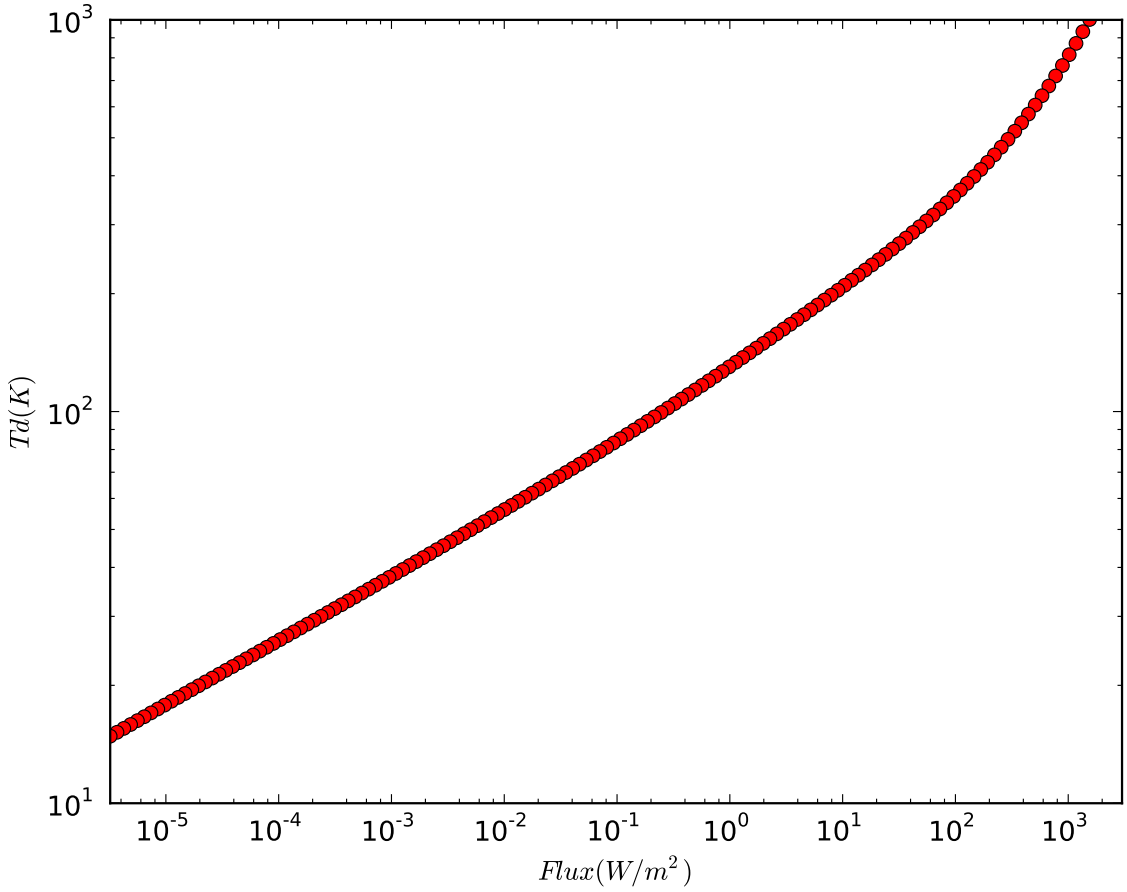

Figure 4.5: Dust temperature (T_d) at $r = 0$ vs. incident flux at the edge of the cloud facing the star.

As a next step, we considered a cloud with a constant flux on the left edge of the cloud for different number densities. In all the cases considered below, the maximum size of the cloud selected is 10 pc. This selection is based on the maximum diameter of a cloud from a sample of 10 clouds associated with Galactic H II regions obtained from CO observations [Azimlu and Fich, 2011].

4.1 Case 1: Constant Flux for Uniform Gas Densities

The simplest case for a cloud in the environments of an H II region is that of a cloud of uniform gas density exposed to a constant stellar flux. As a first step, we examine three clouds with uniform gas densities (n_{H_2}) of 10^3, 10^5, and 10^7 cm^{-3}, which encompass the range of typical gas densities found in the diffuse and dense regions of a molecular cloud. A constant flux of 10 W/m^2 is incident on the left edge of the clouds. We calculated the temperature as well as the IR emissivity distributions of the dust grains in the clouds for each value of n_{H_2}.

4.1.1 Temperature distribution

Dust temperature distributions (T_d) within the clouds are plotted as a function of distance from the left edge of the cloud (see Figure 4.6). The distance, r, along the cloud is rescaled to r', which is r(pc) $\times$ n_{H_2} cm^{-3}. All three density cases fall on the same curve in the T_d vs r' diagram. This is because as we increase the density by two orders of magnitude, the path length of the photons decreases by the same order of magnitude along the cloud. Since we scale the distances by the densities, all the three cases provide homologous emissivity distribution curves. The maximum temperature of the cloud is 208 K, on the envelope facing the star. The maximum temperature value stays constant irrespective of the gas density because the dust is heated primarily by the incident stellar flux on the left edge. The temperature of the dust grains falls to 13 K at an r' of 10 and beyond, where the internal heating dominates the stellar heating.

4.1.2 IR emissivity distributions

IR dust emissivity distributions j'_{12}, j'_{25}, and j'_{100} are plotted as a function of the scaled distance r' through the cloud (see Figures 4.7, 4.9, and 4.11) and dust temperature (see Figures 4.8, 4.10, and 4.12) for three effective IRAS wavelengths: 12 μm, 25 μm and 100 μm, respectively. The scaled unit j'_λ is j/n_{H_2}.

For the densest cloud, the 12 μm emissivity reaches a value of 3.2×10^{-26} Wm^{-3}Hz^{-1}sr^{-1} at the hot surface layer. The emissivity (j) scales with the gas density and therefore decreasing the gas density values will decrease the values of emissivity. Consequently, as we reduce the gas density to 10^5 cm^{-3}, the peak value of 12 μm emissivity also decreases by two orders of magnitude. However in the scaled units, the emissivity distributions at different number densities follow the same curve. The scaled emissivity distributions take off the dependency of the density on the emissivities. As the density of the cloud increases, the photons undergo attenuation much faster, and scaling the distance along the cloud by

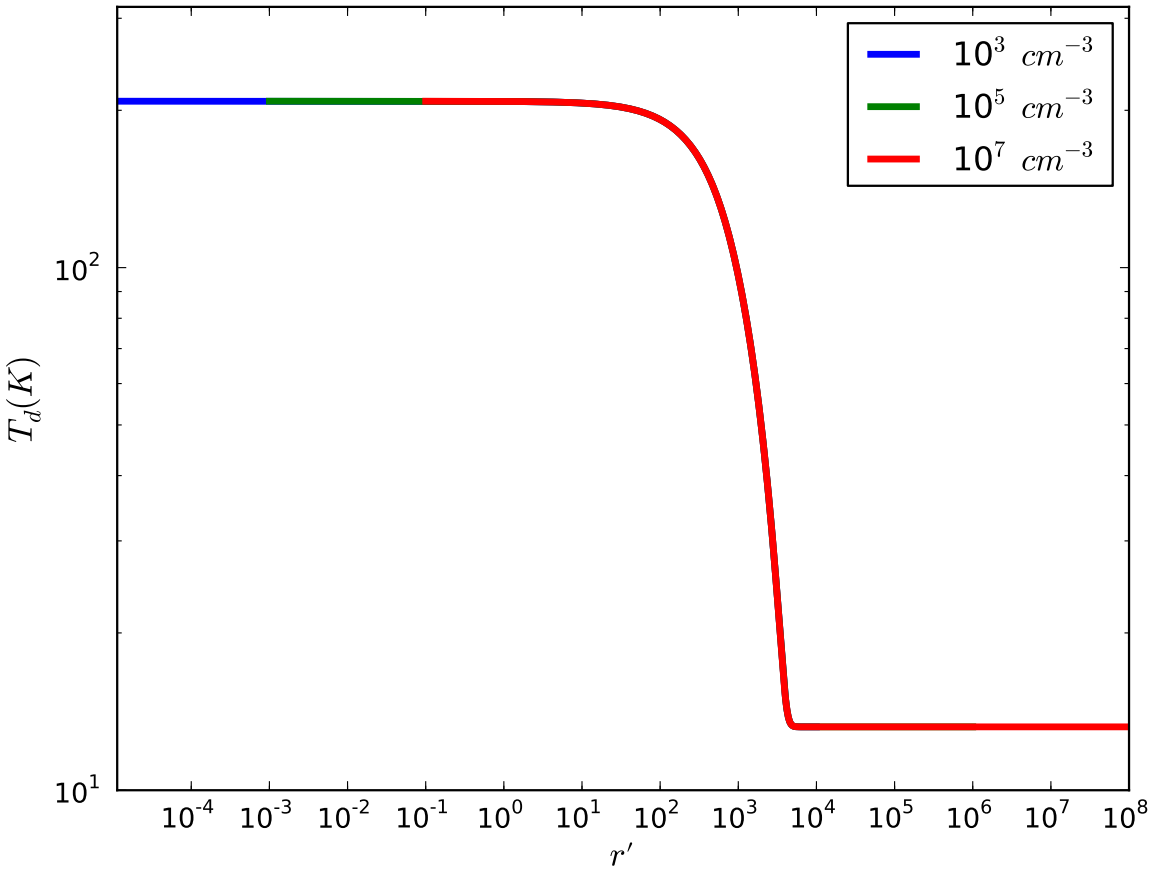

Figure 4.6: Dust temperature distribution: T_d vs. r'—constant flux case, for three different number densities of the hydrogen molecule, H_2.

the density values cancels this dependence and all the emissivity distributions lie on the same curve.

Since the left edge of the clouds receive the same stellar flux, all the modeled clouds possess the same peak temperature value regardless of the gas density. All the emissivity plots display a conspicuous trend—the emissivity of the dust peaks at the cloud edge facing the star, i.e., the highest value of the emissivity is reached at regions of peak dust temperature.

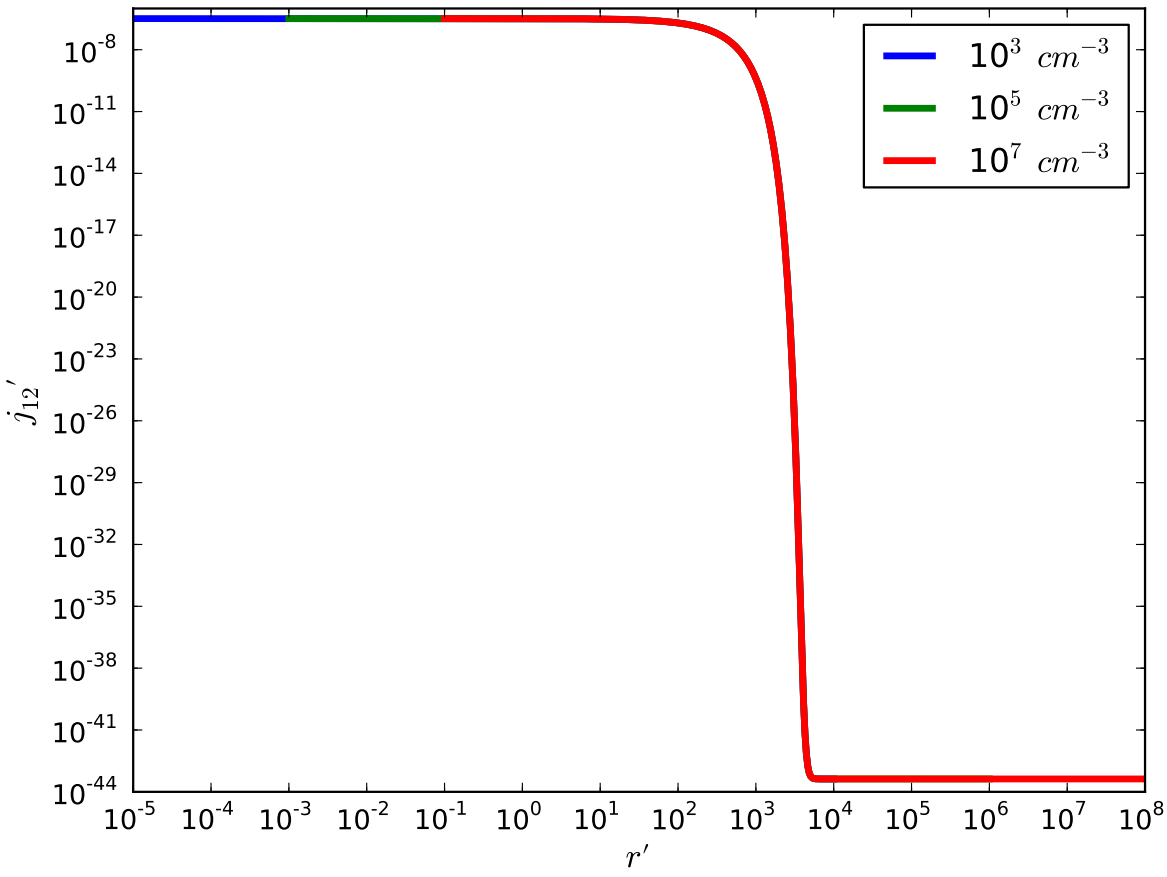

Figure 4.7: Plot showing the j'_{12} distribution along the cloud—constant flux case, for three different number densities of H_2.

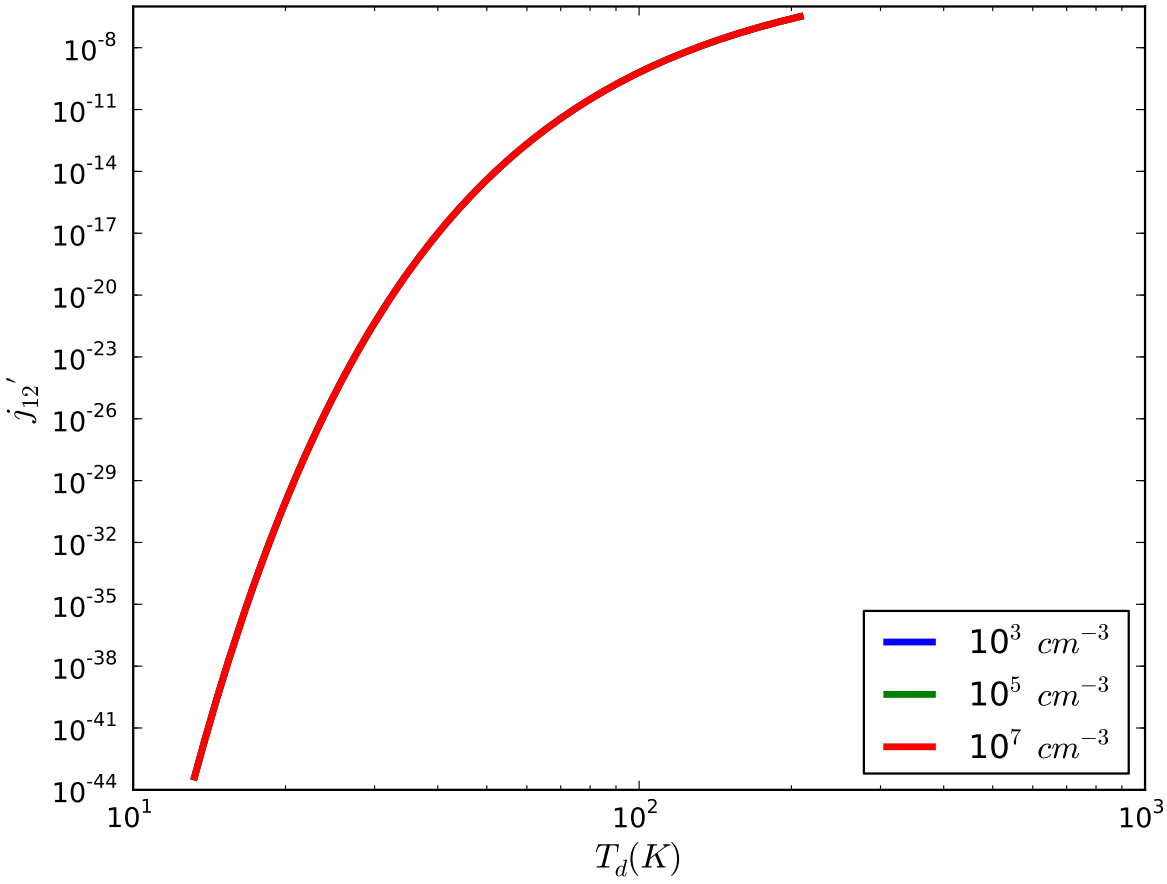

Figure 4.8: Plot showing the j'_{12} distribution as a function of T_d—constant flux case, for three different number densities of H_2.

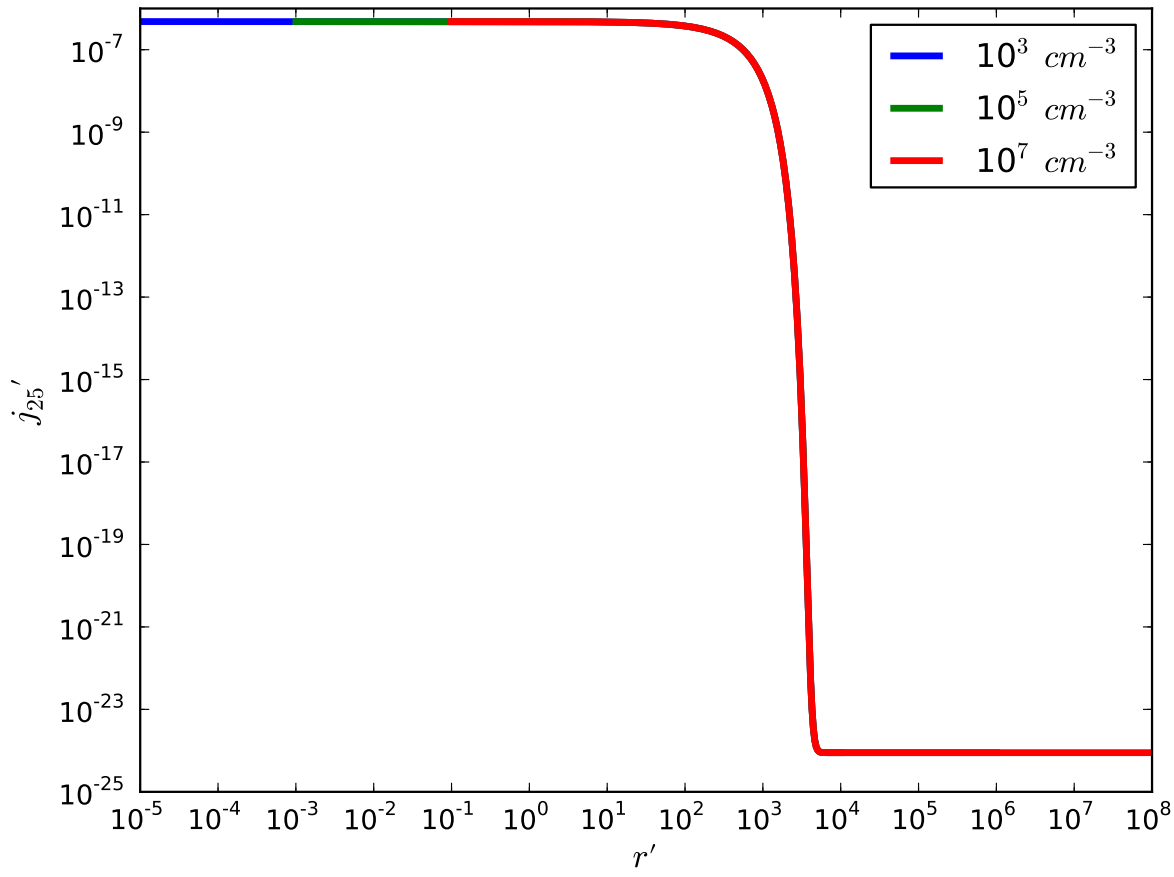

Figure 4.9: Plot showing the j'_{25} distribution along the cloud—constant flux case, for three different number densities of H_2.

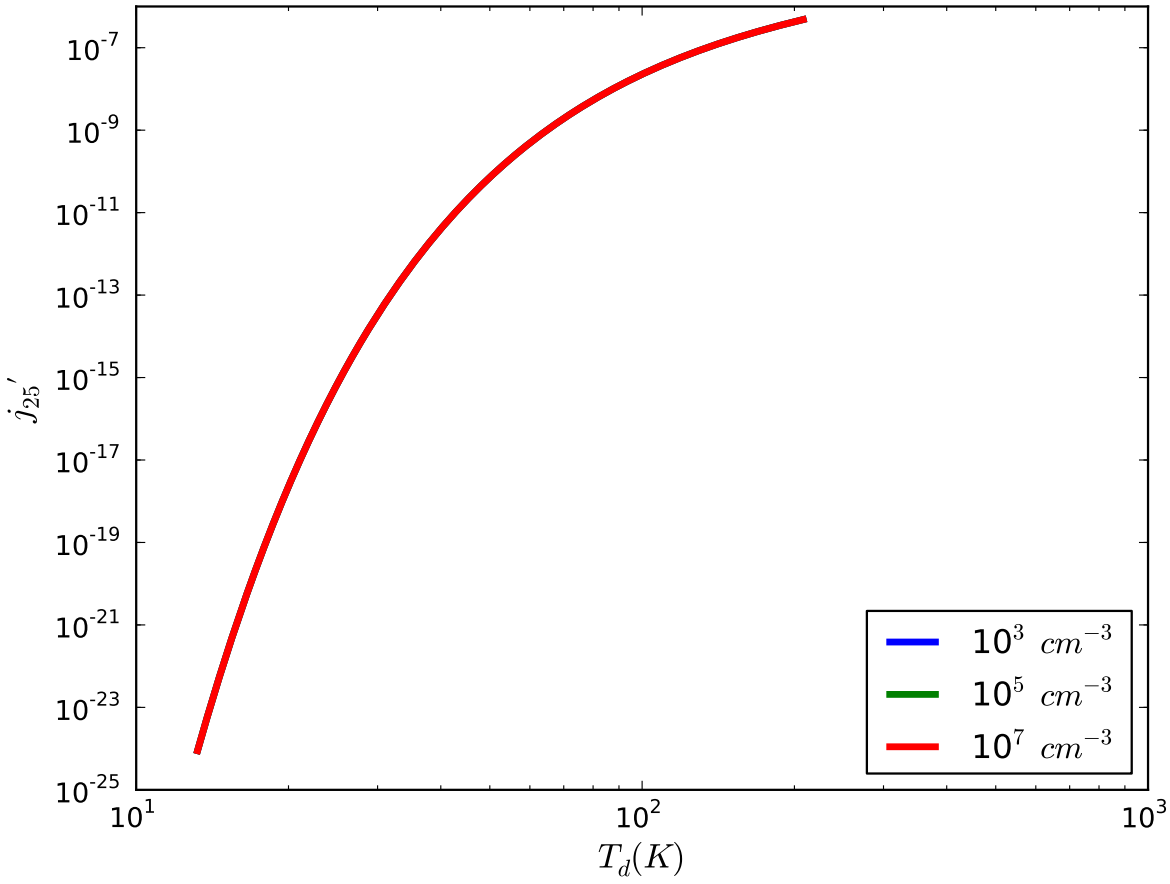

Figure 4.10: Plot showing the j'_{25} distribution as a function of T_d—constant flux case, for three different number densities of H_2.

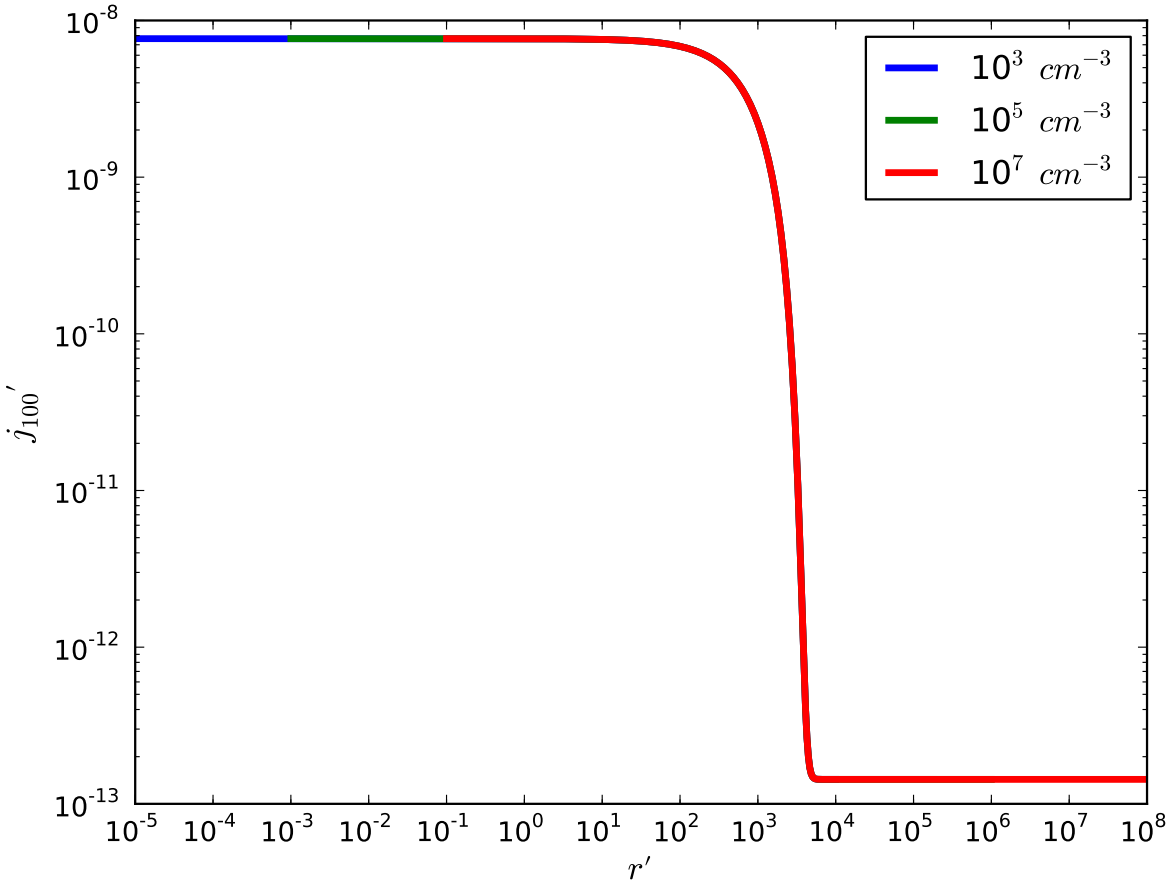

Figure 4.11: Plot showing the j'_{100} distribution along the cloud—constant flux case for three different number densities of H_2.

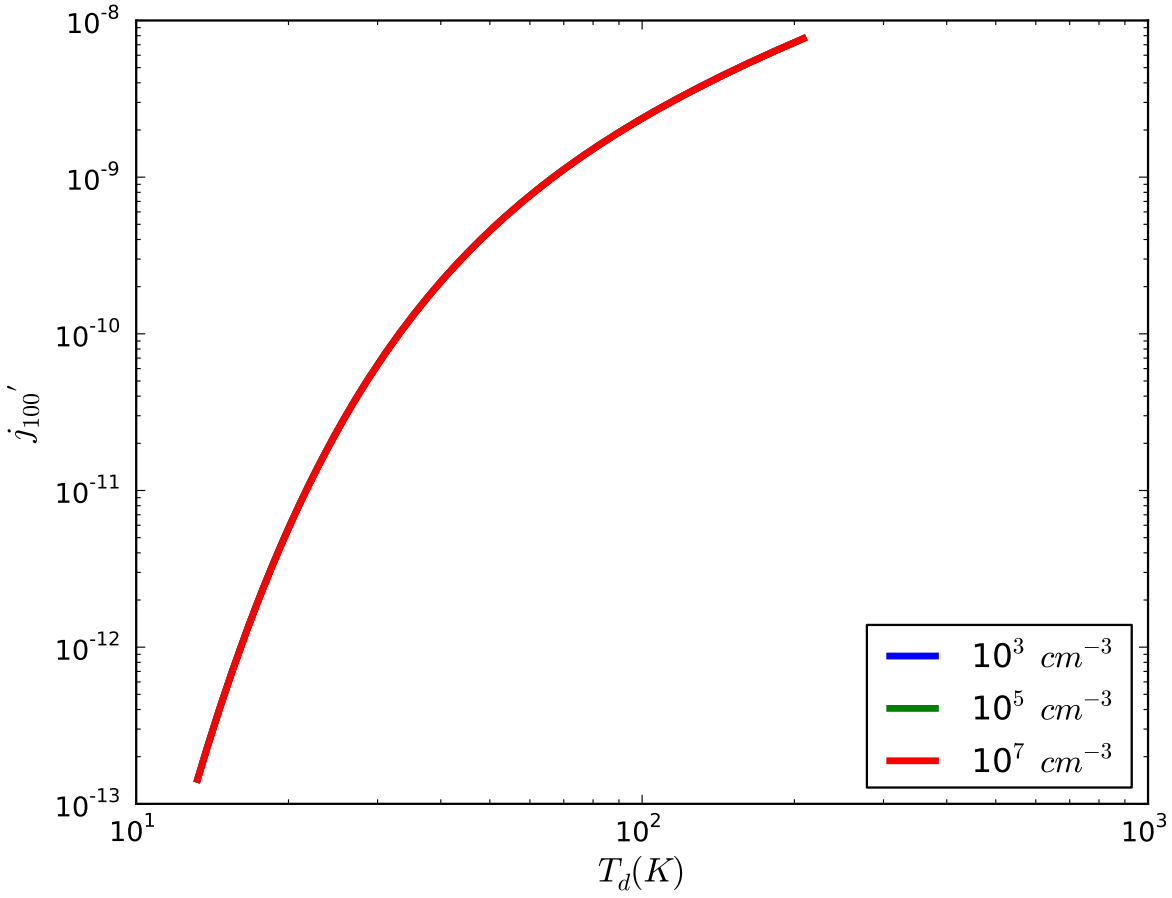

Figure 4.12: Plot showing the j'_{100} distribution as a function of T_d—constant flux case for three different number densities of H_2.

4.1.3 Case 1: Analysis

The temperature distribution of interstellar dust in three different test clouds with the same incident flux reveals that the temperature gradually decreases up to some distance from the hottest cloud layer as shown in Figure 4.6. In the scaled units, temperature distributions corresponding to all the densities follow the same curve. Note that the internal heating dominates the high extinction regions of the cloud. The temperature of the densest cloud drops much faster than other clouds. This is expected since at such high densities, the cloud becomes optically thick within a very short distance from the edge. In the case of the 10^3 cm^{-3} cloud, a radial distance of 0.26 pc corresponds to an optical depth of 1. Similarly, for the 10^5, and the 10^7 cm^{-3} clouds, the optical depth reaches a value of 1 at 2.6 $\times 10^{-3}$ pc and 2.6 $\times 10^{-5}$ pc respectively. All the stellar photons are consumed by the cloud at around 5 pc from the hot surface layer in the lowest density case. A two-order of magnitude increase in the cloud density decreases the path length of the photons by two orders of magnitude. However, in the scaled units, the three cases behave the same way, since increasing the density by two orders of magnitude decreases the photon mean free path along the cloud by the same order of magnitude. Since we scale the distances by the densities, all three cases follow the same curve.

The scaled dust emissivity distributions as a function of distance and temperature disclose the effect of the number densities on the emissivities. At all three densities, the scaled emissivities follow the same distribution, indicating that a change in the density will have little influence on the emissivity distribution. Similarly, at all three densities, the emissivity distributions with dust temperature also follow the same curve. If we compare emissivity distributions as a function of dust temperature at the three different (12, 25, and 100 μm) IRAS wavelengths, it is apparent that the short-wavelength emissivities have higher values than the long-wavelength emissivities near the surface facing the star, at the peak temperature. These properties indicate that the re-emission of the unattenuated flux at 12 and 25 μm exceeds the re-emission of the attenuated stellar flux at 100 μm.

The normalized flux density distributions of the modeled clouds are shown in Figure 4.15. The flux density distributions of clouds with gas densities 10^8, 10^9, and 10^{10} cm^{-3} are also presented in Figure 4.15 to demonstrate the behaviour of the model at high densities. Although dust emissivity scales with number density of dust, the FDD shapes behave in a more complex way. At low densities, dust grains re-radiate immensely at 12 and 25 μm. As the density increases, the 12 and 25 μm emission reduces due to the increased surface layer optical depth at respective wavelengths. At a density of 10^9 cm^{-3}, the modeled FDD at 12 μm matches up with the observed value. However, at such high optical depths, the stellar photons are incapable of penetrating too deep in to the cloud, and therefore dust emission at other wavelengths is reduced.

Consequently, for the single flux and multiple density case, high densities are able to

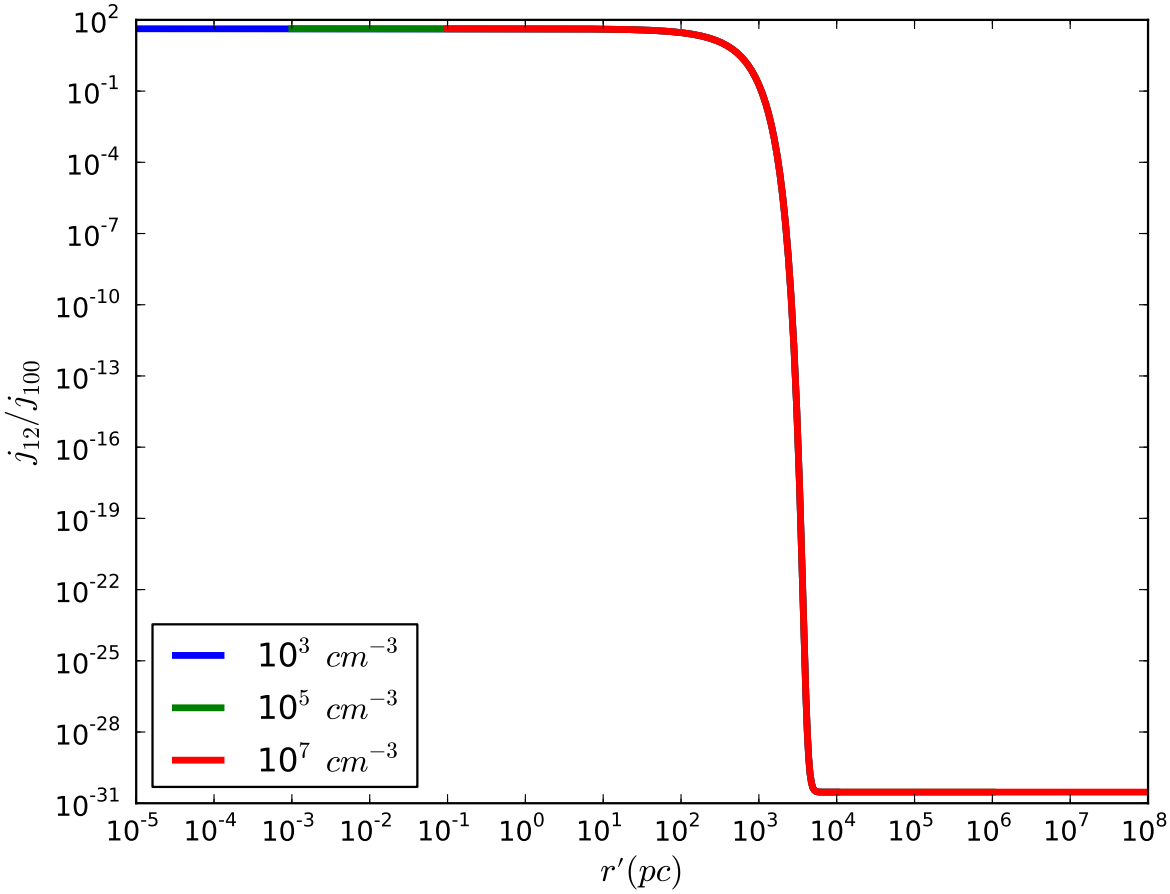

Figure 4.13: Plot showing the (j_{12}/j_{100}) distribution as a function of r'—constant flux case for three different number densities of H_2.

reproduce the observed normalized fluxes at 12 and 25 μm, however they fail to simulate the long-wavelength fluxes. Lower densities generate much better matching between the observed and modeled values at 60 and 100 μm, but these models produce higher short wavelength fluxes and therefore do not complement observations. None of the modeled FDDs match the observed FDDs in this case.

A possible explanation for the mismatch is that the clouds near Galactic H II regions are most likely exposed to a different incident stellar flux. In the next section we examine the influence of different incident stellar fluxes on a uniform gas density cloud and the resultant model predictions.

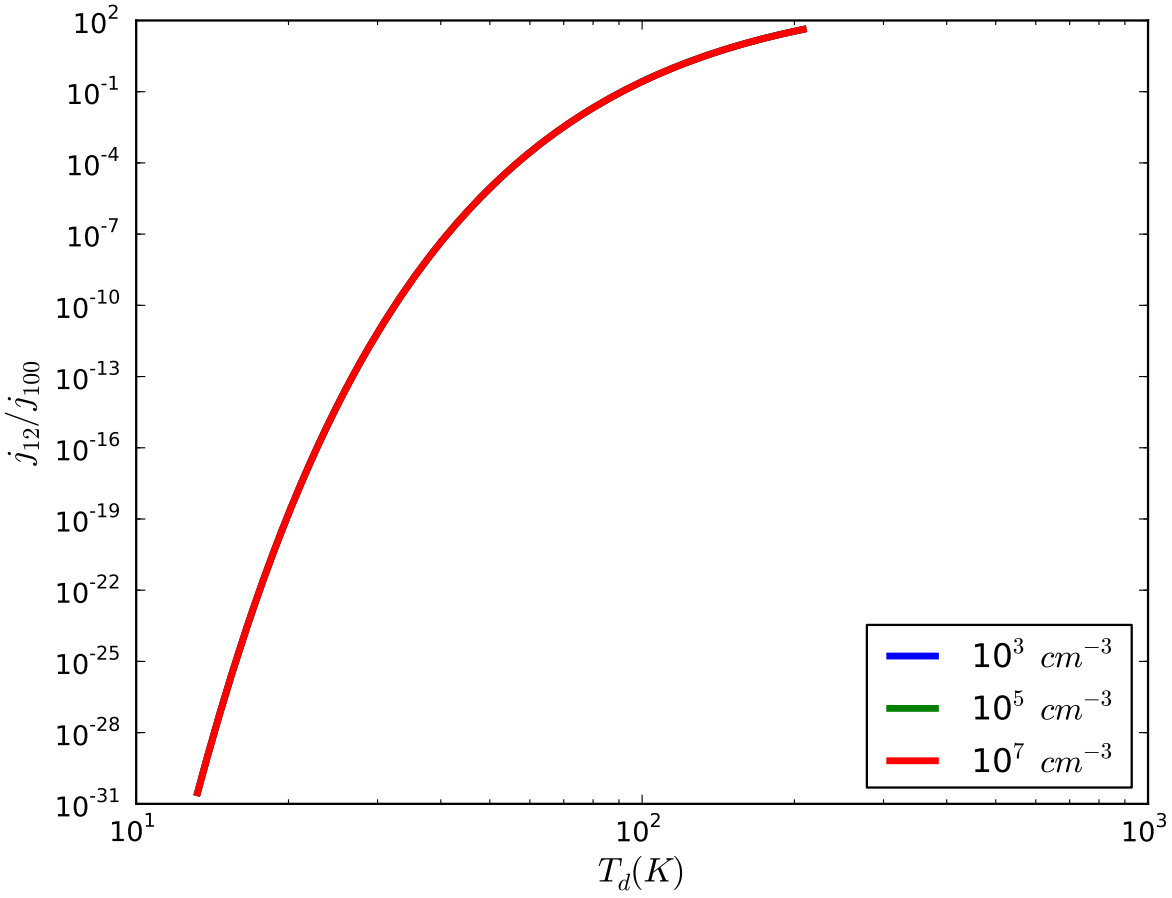

Figure 4.14: Plot showing the (j_{12}/j_{100}) distribution as a function of dust temperature—constant flux case for three different number densities of H_2.

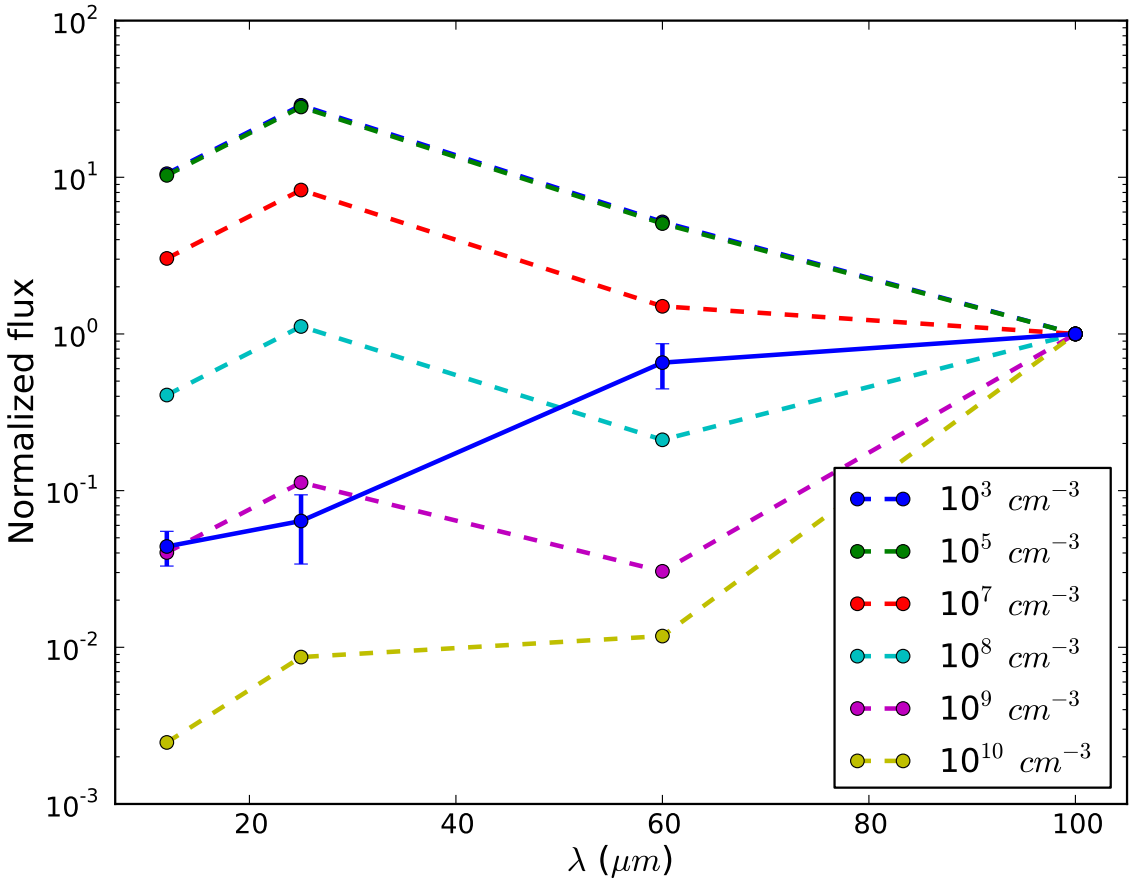

Figure 4.15: Median value of the normalized FDD of the observed clouds (blue solid line) and the modeled FDD corresponding to six different number densities (dashed lines)—constant flux case.

4.2 Case 2: Constant Number Density for Different Incident Fluxes

In this case, we consider a single cloud exposed to five different incident fluxes. The value of n_{H_2} is a constant throughout the cloud (for example, 10^6 cm^{-3}). Five different models are constructed corresponding to five different incident stellar fluxes, say, 0.01, 0.1, 1.0, 10.0, and 100 Wm^{-2}. Uniform internal heating is present in addition to the stellar heating in this case too.

4.2.1 Temperature distribution

Dust temperature distribution within the cloud is plotted as a function of distance from the left edge of the cloud (see Figure 4.16). Note that Figure 4.16 is different from Figure 4.5. In Figure 4.5, we presented the stellar flux incident on the left edge of the cloud facing the star and the corresponding temperatures on the left layer. However, in Figure 4.16, we present the temperature through the length of the cloud when the cloud is exposed to different values of stellar fluxes. For a stellar flux of 100 Wm^{-2}, the temperature on the left cloud edge rises to 358 K. At 0.01, 0.1, 1.0, and 10.0 Wm^{-2}, the left cloud edge heats up to 56 K, 84 K, 130 K, and 208 K respectively. There exists five different temperature distributions in a single cloud corresponding to five different fluxes. All the temperature curves start to fall off quickly at a distance of 2.6×10^{-4} pc from the hot left edge.

4.2.2 IR emissivity distributions

The 12 μm emissivity distribution as a function of distance along the cloud is plotted in Figure 4.17. The maximum value of j_{12} is 3.7×10^{-26} Wm^{-3}Hz^{-1}sr^{-1}, at 100 Wm^{-2}. A factor of 10 decrease in the stellar flux on the left cloud envelope reduces the emissivity by a factor of $\approx$12. Likewise, a flux reduction by two, three, and four orders of magnitude leads the emissivity to diminish by two, four, and seven orders of magnitude respectively. Identical behaviours are observed in the j_{25} (Figure 4.19) and j_{100} (Figure 4.21) distributions. The distribution of j_{12} with respect to the dust temperature (see Figure 4.18) lies on the same curve for all the incident fluxes. However, the temperatures corresponding to the peak emissivities are distinct for all the incident fluxes. The 25 (Figure 4.20) and 100 μm (Figure 4.22) dust emissivity curves follow shapes similar to the one for j_{12}.

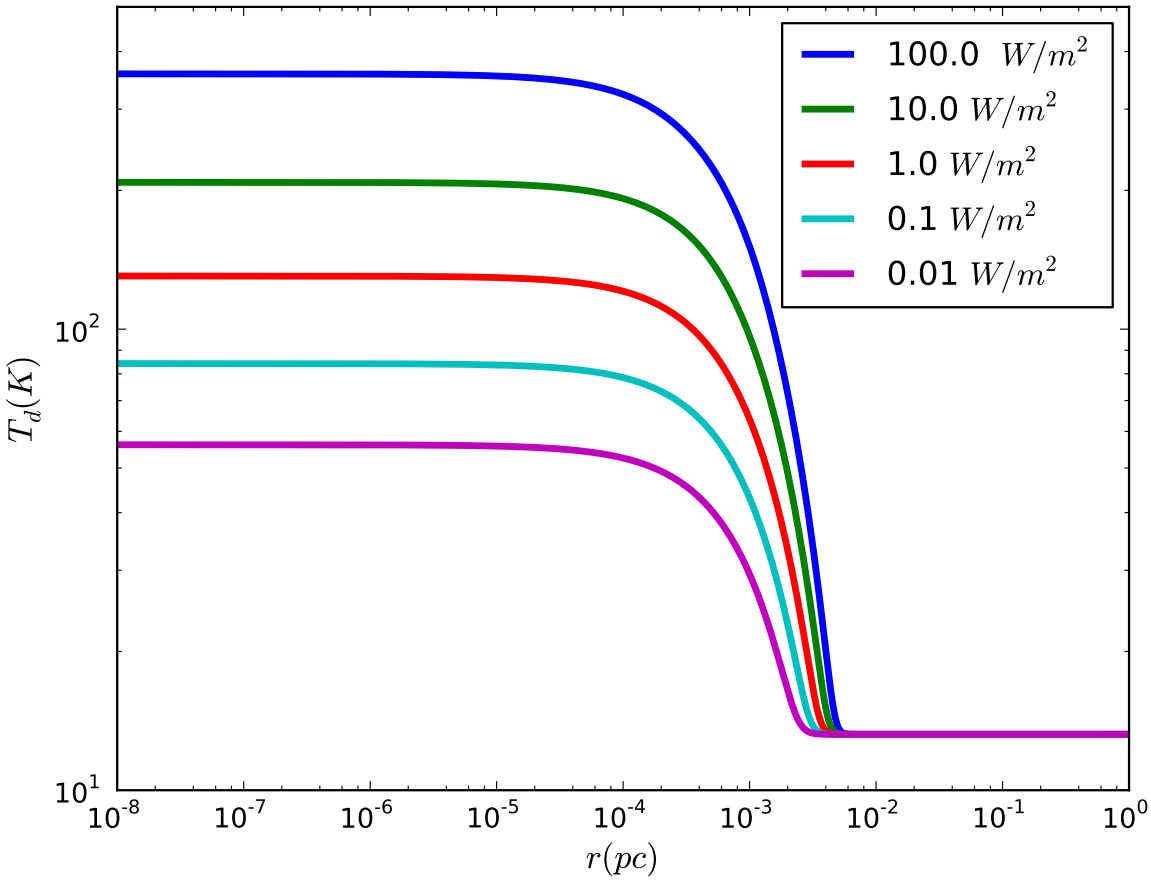

Figure 4.16: Temperature distribution: T_d vs. r—constant density case for five different incident fluxes.

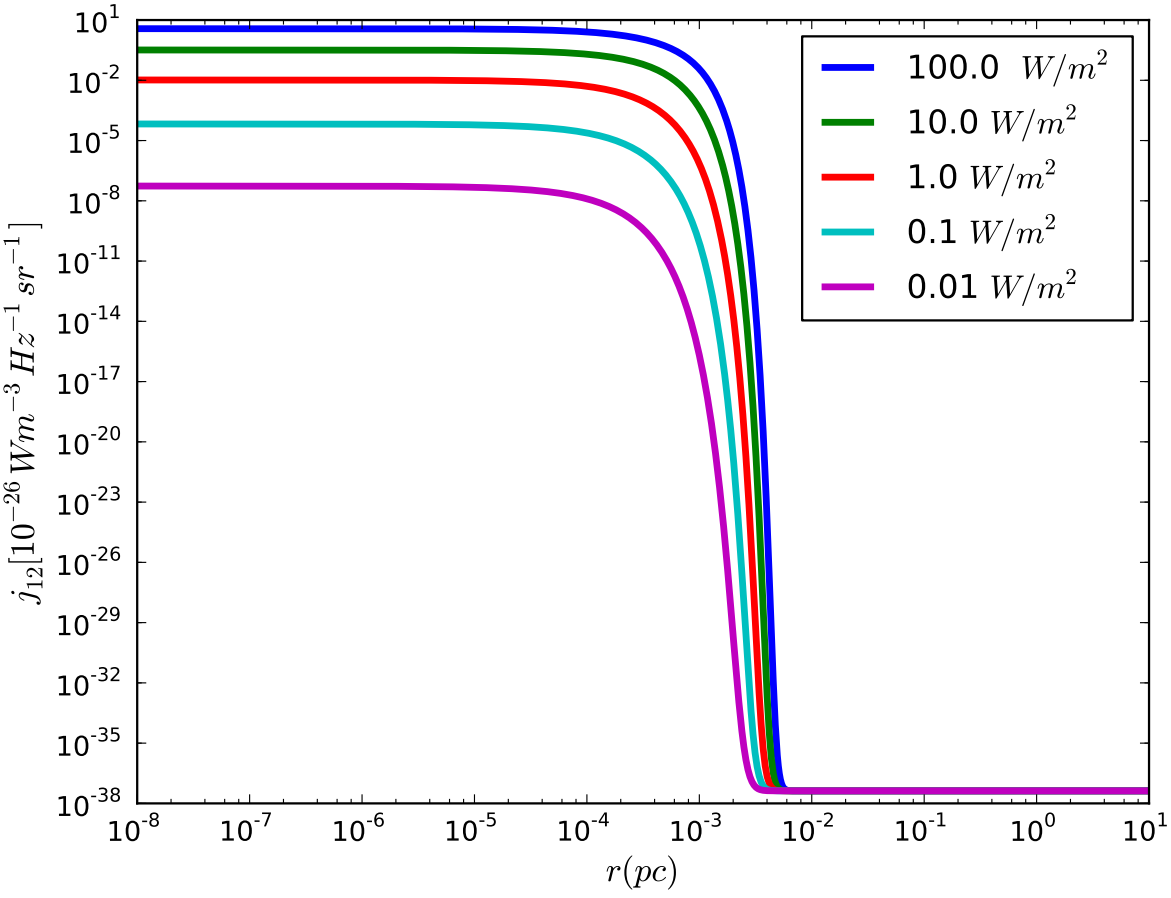

Figure 4.17: j_{12} vs. r—constant density case for five different incident fluxes.

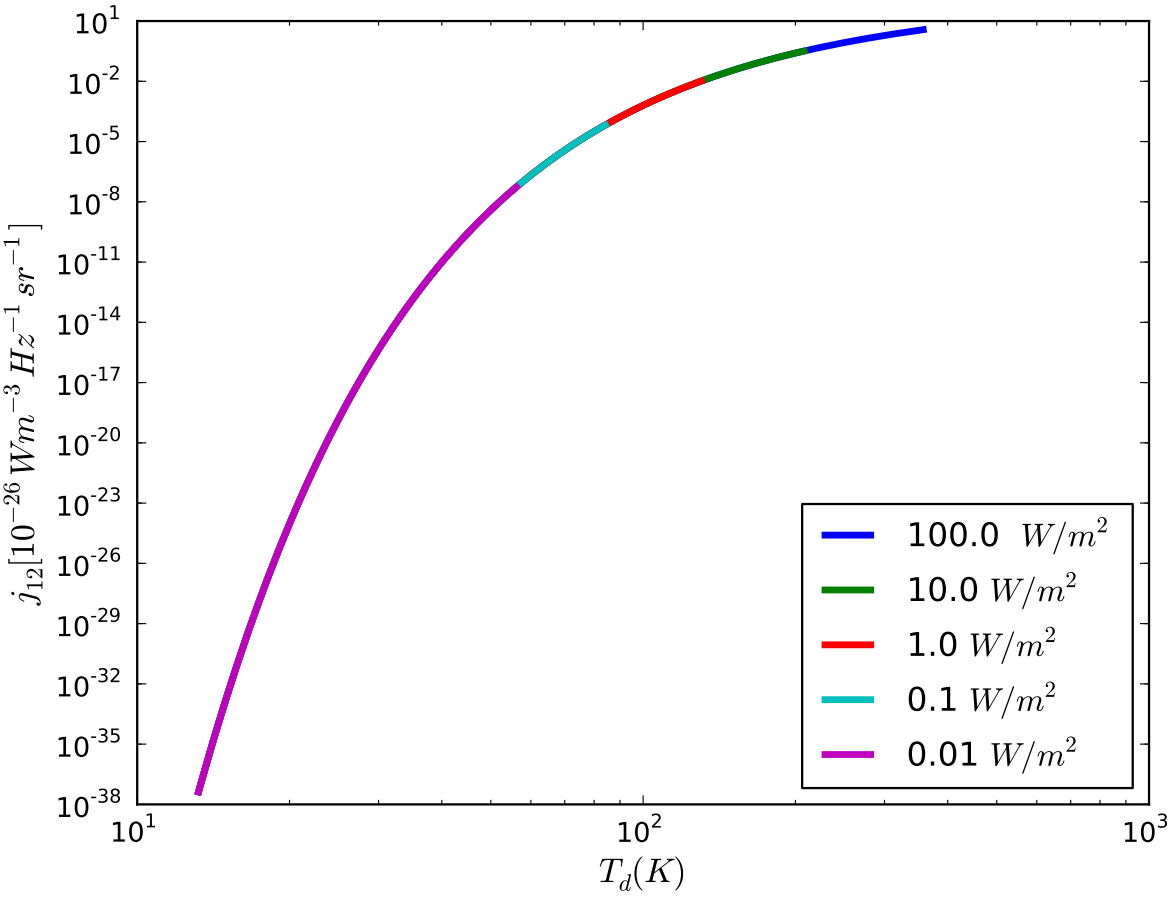

Figure 4.18: j_{12} vs. T_d—constant density case for five different incident fluxes.

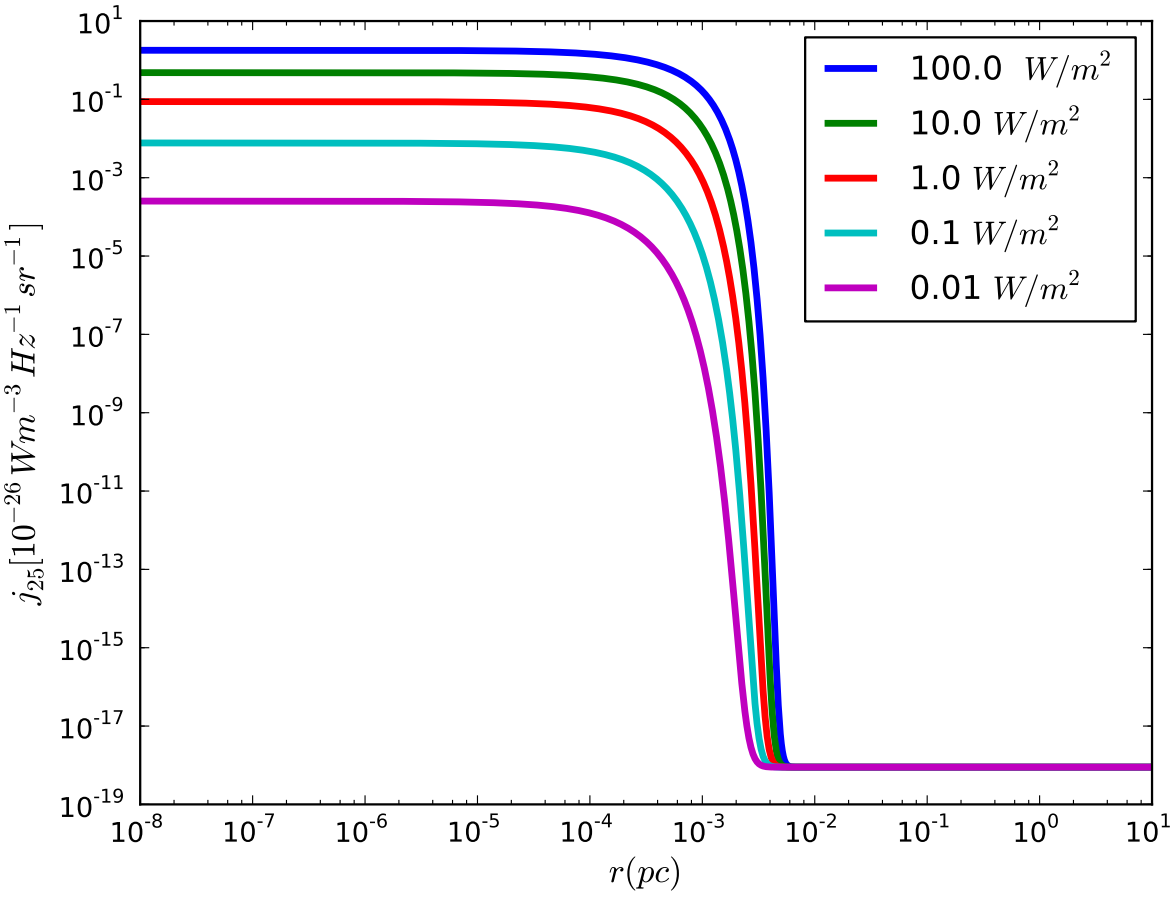

Figure 4.19: j_{25} vs. r—constant density case for five different incident fluxes.

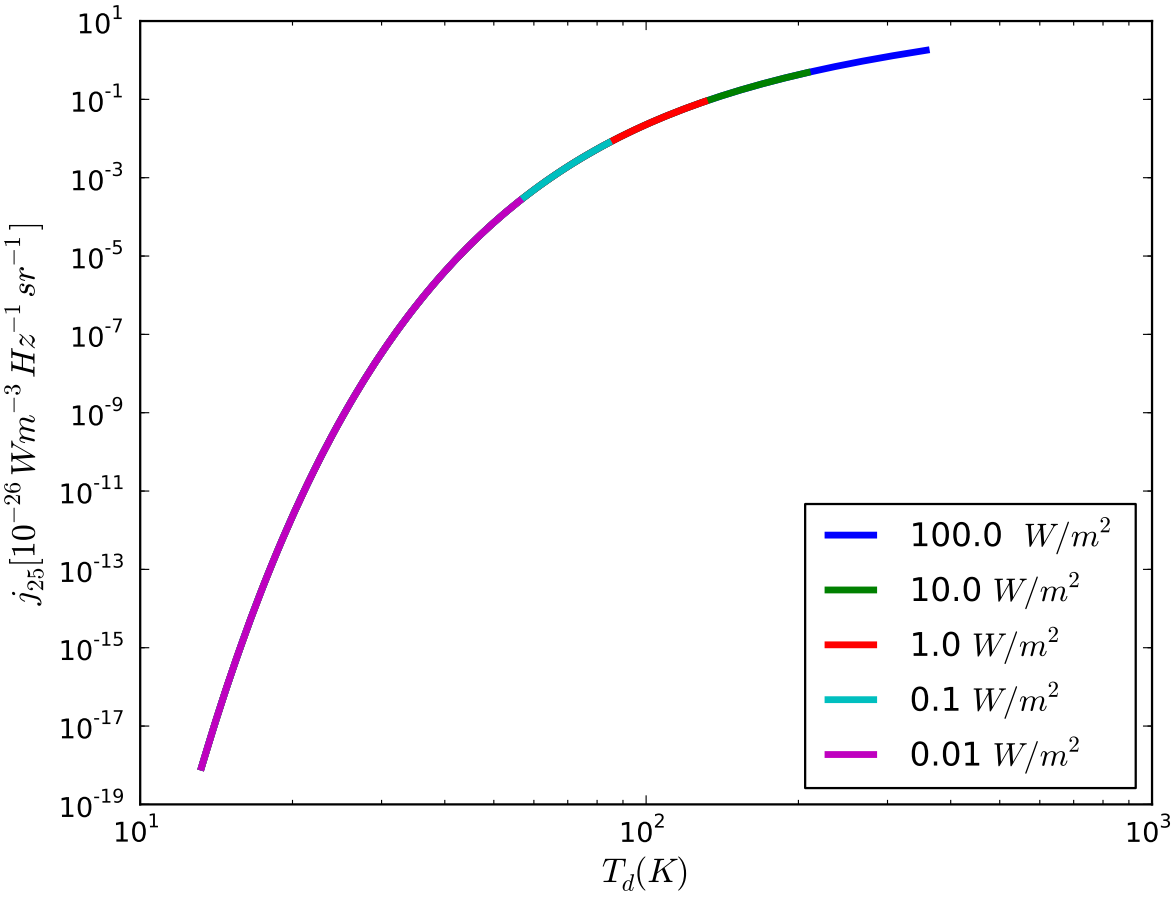

Figure 4.20: j_{25} vs. T_d—constant density case for five different incident fluxes.

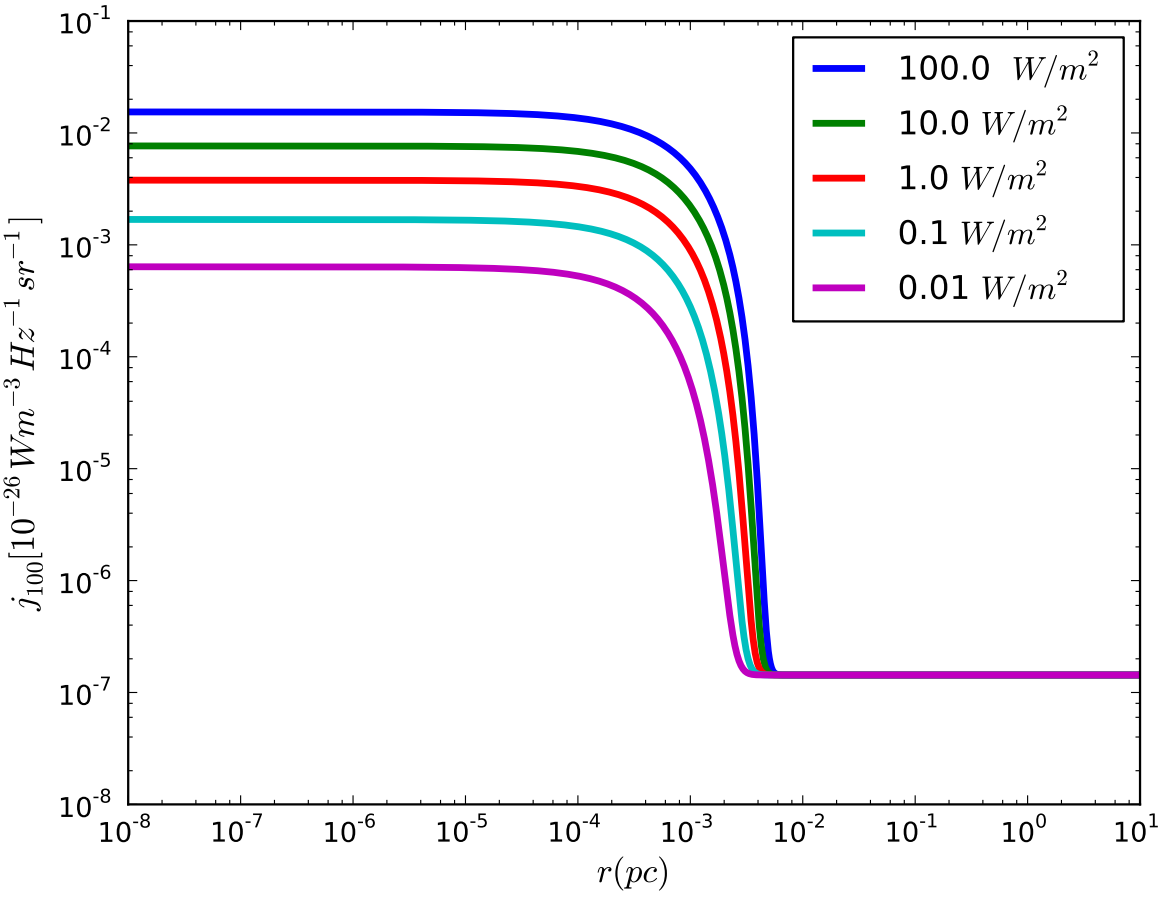

Figure 4.21: j_{100} vs. r—constant density case for five different incident fluxes.

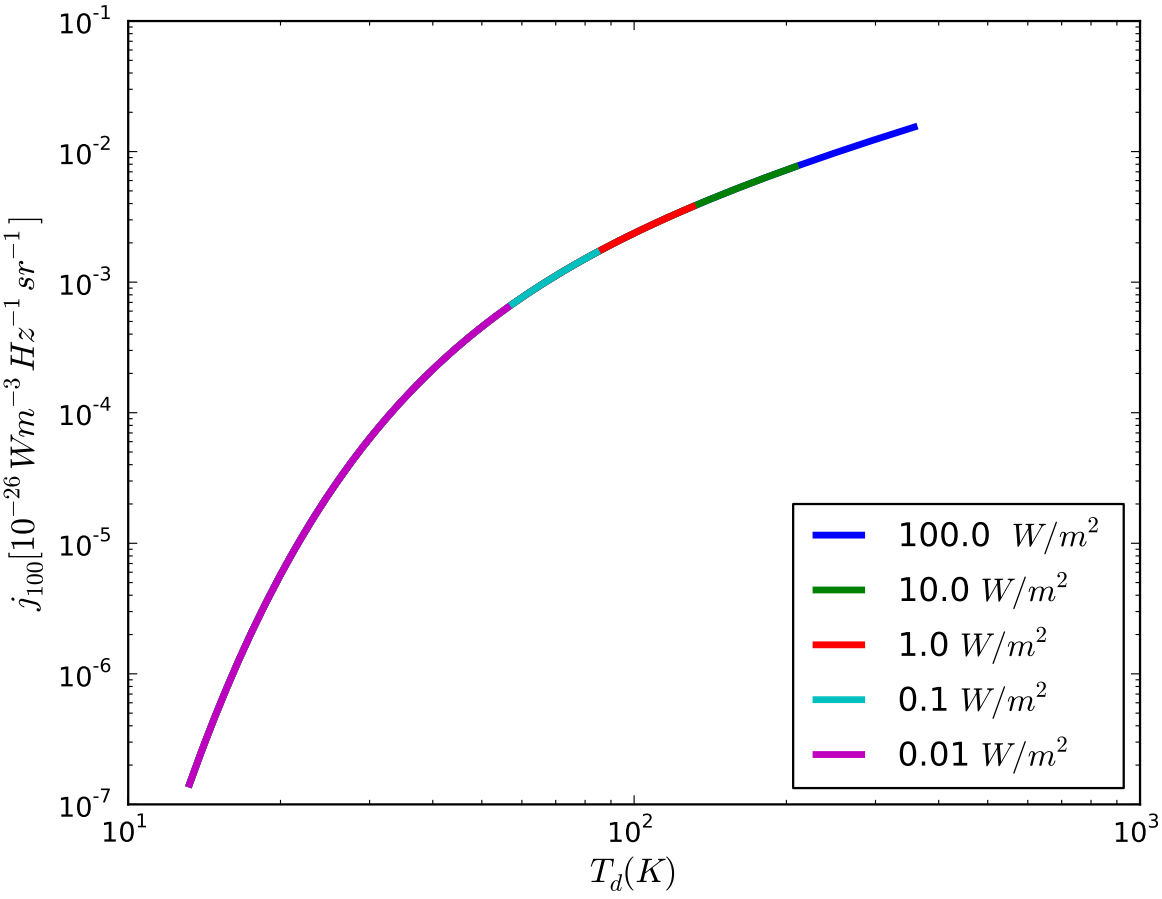

Figure 4.22: j_{100} vs. T_d–constant density case for five different incident fluxes.

4.2.3 Case 2: Analysis

In the temperature distribution (Figure 4.16), all the curves show the same drop-off distance, they all have different temperatures at the plunging position. This is because the path length of the photons will be the same even if we supply different stellar fluxes at the hot edge due to constant density of the cloud. However, as the stellar flux is different, we get different temperatures at the dropping distance: higher stellar fluxes provide higher temperatures.

The emissivities are dependent on the incident stellar flux. The effect of the stellar flux on the 12, 25, and 100 μm dust emissivities at the left cloud edge is plotted in Figure 4.23. Most of the 12 and 25 μm emissivity contribution is at higher stellar flux, above 0.5 W/m^2 whereas the the contribution of 100 μm emissivity dominates at fluxes below 0.02 W/m^2. However, at such low incident flux from the stars, the value of the 100 μm emissivity is very low. If the incident stellar flux drops below 0.02 W/m^2, the contribution from 12 μm diminishes more quick than does 25 μm, which in turn is below the 100 μm emissivity contribution.

As the incident flux increases, the emissivity value also increases due to the increased absorption of stellar photons. The j_{12}/j_{100} profile (Figure 4.24) for all the incident fluxes indicates an increased contribution of 12 μm dust emissivity on the hot surface layer while the 100 μm emissivity contributes significantly at the cold cloud edge. The flux density distribution of the modeled cloud is shown in Figure 4.25. At 0.01 W/m^2, the 12 μm dust emission drops to very low values since the the cloud envelope facing the star fails to receive sufficient flux to re-radiate efficiently at 12 μm. At higher fluxes of 10 W/m^2 and 100 W/m^2, dust grains consume a large number of visible photons and re-emit this energy efficiently at 12 and 25 μm.

At lower stellar fluxes, we are able to reproduce the ratio ($\frac{F_{100}}{F_{12}+F_{25}}$), but too little 12 μm emission, which makes the FDD fail to match with the observed data. At high stellar fluxes, the 12 and 25 μm dust emission is too high although the 60 and 100 μm emission is more close to the observed normalized flux values, and therefore, we are unable to reproduce the ratio.

Varying the incident flux could not reproduce the observations. The discrepancy between the observations and the models suggests the absence of uniform gas densities in clouds near Galactic H II regions. The simplest case for a non-uniform gas density distribution is a linear distribution and in the next section, we investigate the effect of a linearly varying density on the final flux density distribution.

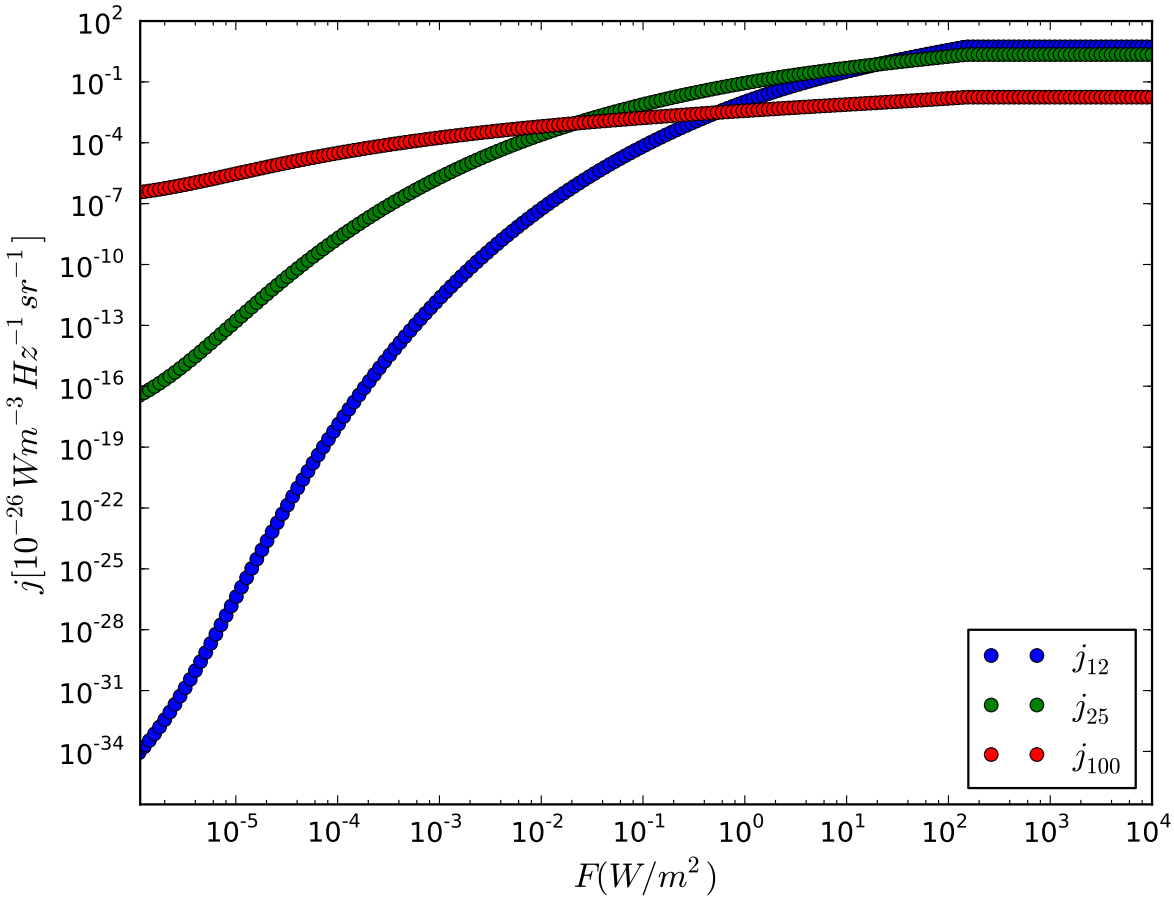

Figure 4.23: j at the left cloud edge vs. F—constant density case.

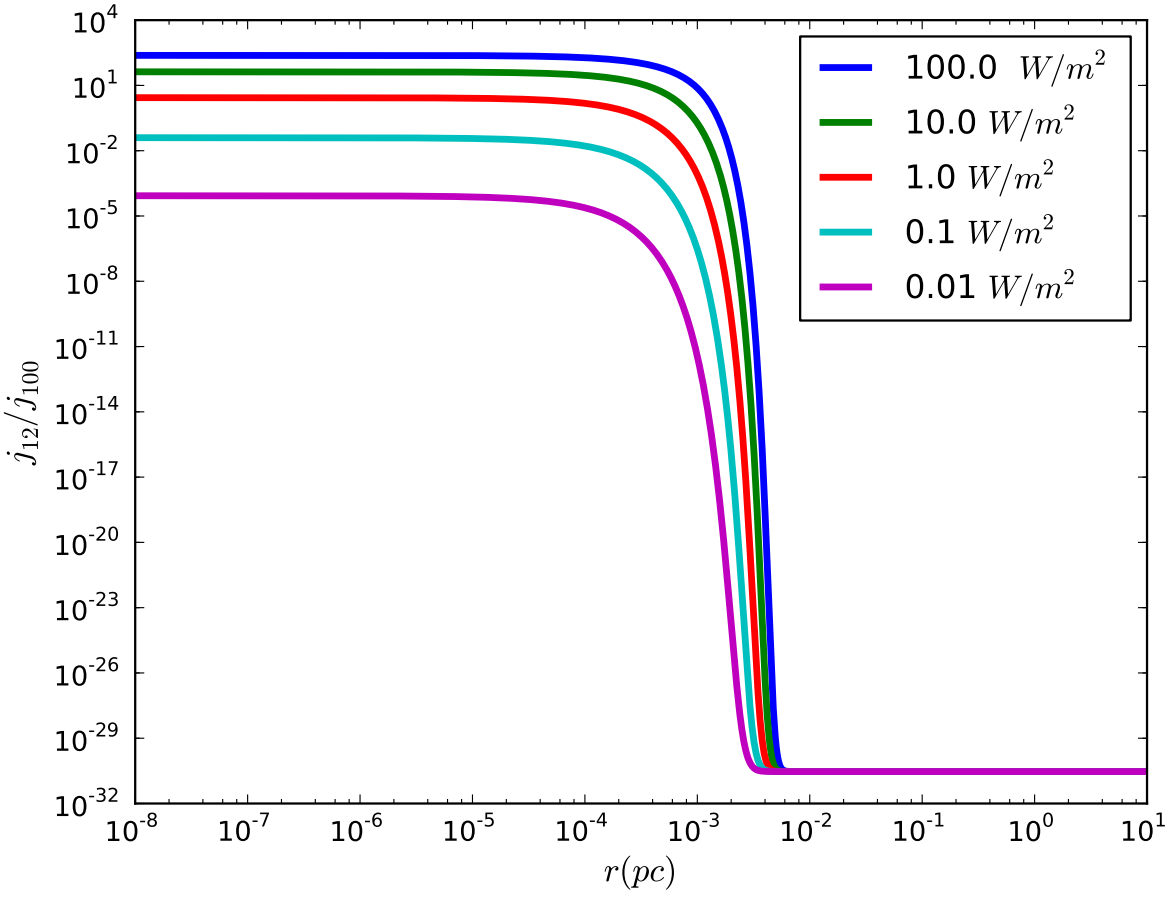

Figure 4.24: j_{12}/j_{100} vs. r—constant density case for five different incident fluxes.

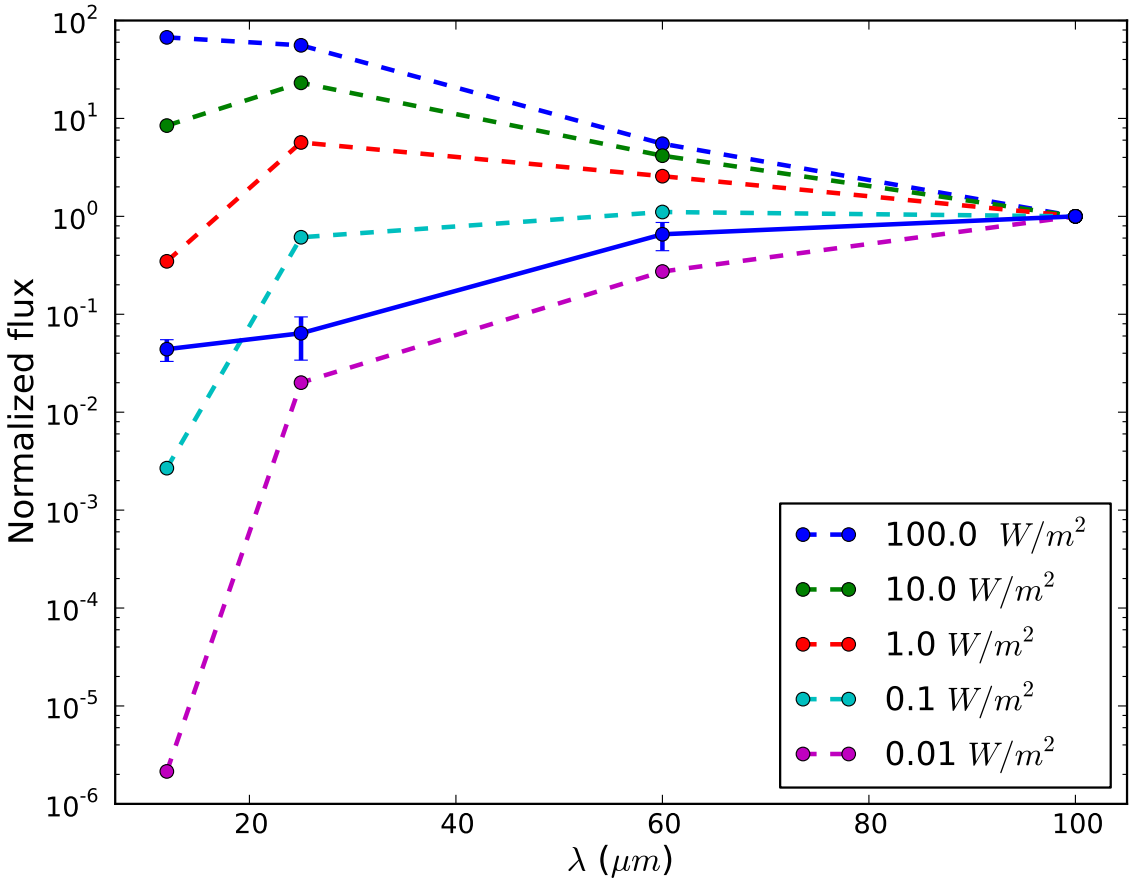

Figure 4.25: Median value of the normalized FDD of the observed clouds (blue solid line) and the modeled FDD corresponding to five different fluxes (dashed lines)—constant density case.

4.3 Case 3: Linear Density Profile

In case 3, we examine a single cloud having a linear gas density distribution with density increasing into the cloud and with a flux of 10 W/m^2 impinging on the left edge of the cloud. The role of a linear gas density distribution on the temperature as well as the IR emissivities of the dust grains is explained below. The effect of different slopes of the linear gas density distribution on the FDDs is compared in the final FDD plot.

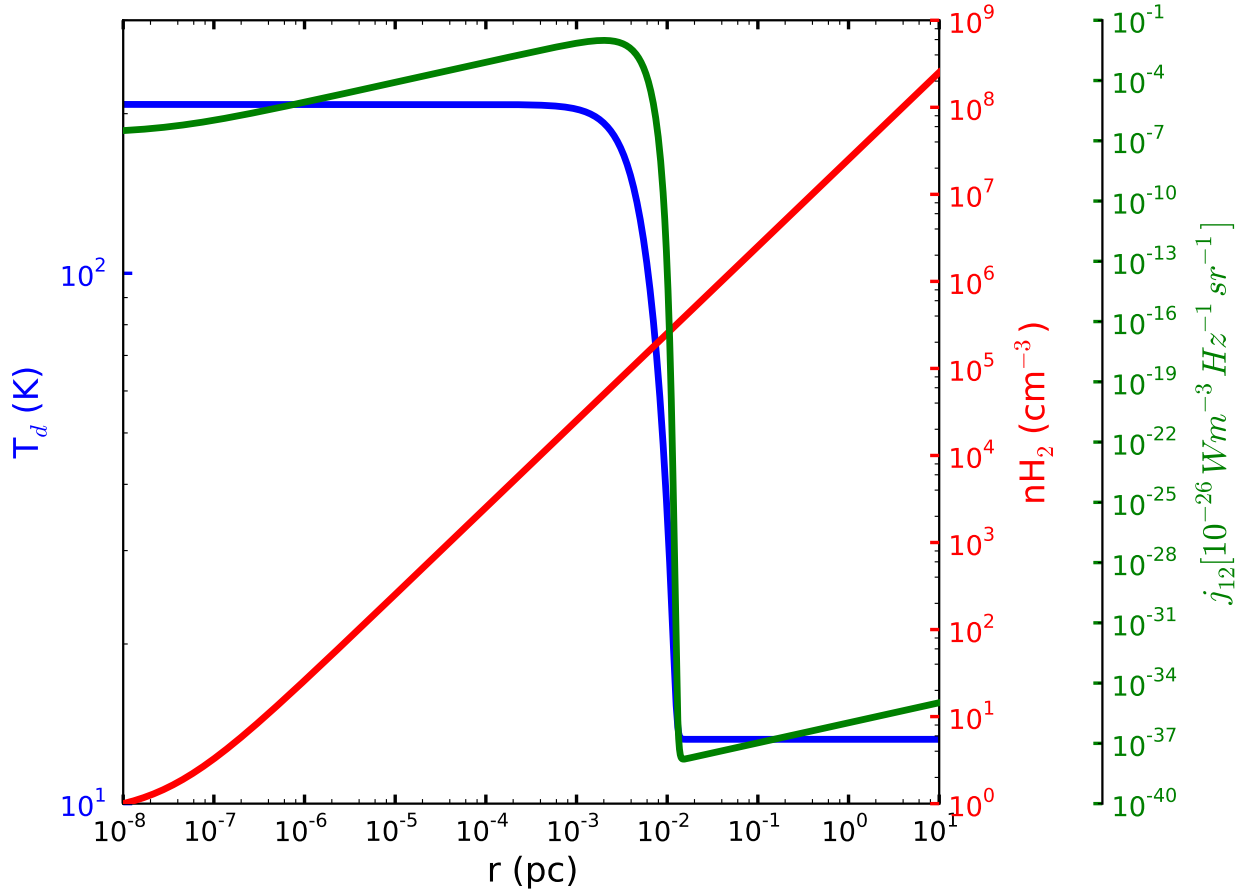

Figure 4.26: j_{12} vs. r—linear gas density distribution.

4.3.1 Temperature and IR emissivity distributions

The dust temperature and j_{12} distributions for a sample linear gas density profile, with a slope of 100 m^{-3}/pc, are shown in Figure 4.26. The red solid line denotes the distribution of the model linear gas density along the cloud starting from the left edge. The blue solid curve represents the temperature distribution, and the green solid curve stands for the emissivity distribution through the cloud as a function of distance.

As the number density increases, the emissivity initially increases and then begins to fall off due to the effect of dropping grain temperature. When the grains drop to a temperature of 13 K, which is the supplied value of the internal heating, the emissivity begins to rise up to the right cloud edge. The 25 μm emissivity, j_{25}, (see Figure 4.27 for the 25 μm dust emissivity distribution) and the 12 μm emissivity, j_{12}, show slightly higher values for the peak emissivity compared to j_{100}. The 100 μm dust emissivity distribution is shown in Figure 4.28. Note that j_{100} shows the lowest value of emissivity at the hottest side of the cloud (see Figure 4.29). The contribution of the 12 and 25 μm emissivities to the colder side of the cloud is negligible. However, their contribution predominates the hotter cloud edge. On the other hand, the influence of 100 μm emissivity prevails at the right edge of the cloud. A jump in all the j values at the start of the j vs. T_d curves (Figure 4.29) is due to the increase in the j values as a result of increase in the densities at the regions where the constant internal heating is dominant (ie., at the coldest and the deepest regions of the cloud).

4.3.2 Case 3: Analysis

The linear density distribution affects the emissivity and temperature values at the three effective wavelengths of the IRAS band. Due to the influence of linearly increasing density, the emissivity distributions vary in a complex way along the cloud distance.

In order to analyze the contribution of 12 and 100 μm emissivities along the cloud, we plotted the ratio j_{12}/j_{100} as a function of distance (Figure 4.30). Near the left edge of the cloud, re-radiation takes place mostly at 12 μm than at 100 μm, whereas re-radiation at 100 μm is the only source of dust emission at the cold edge. Six clouds with a single intercept and varying slopes in the gas density profile are modeled and compared with the observed FDD (see Figure 4.31). Lower values of the slopes are responsible for higher dust emission primarily at 12 and 25 μm. As the value of the slope increases, most of the visible photons are consumed at smaller distances and the 60 μm emission drops. By increasing the intercept values from 10^2 to 10^6 cm^{-3}, a factor of two increase is observed in the normalized flux. However, altering the values of intercepts plays only a minor role in changing the shape of the FDD curves (see Figure 4.32 and Figure 4.33). The outcome is that a cloud with a linear gas density distribution does not reproduce the observed FDD.

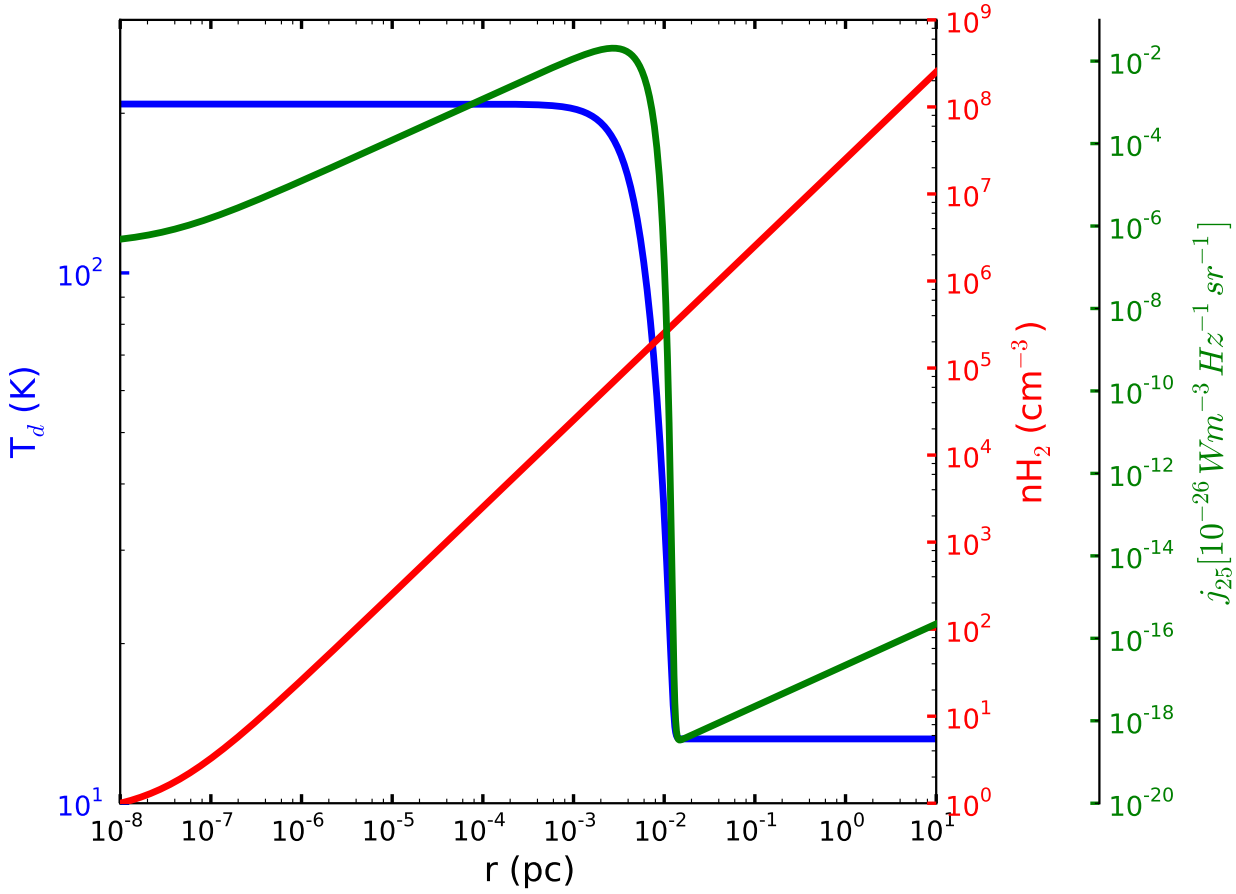

Figure 4.27: j_{25} vs. r—linear gas density distribution.

Clouds with linearly increasing density distribution from the hot edge to the interior of the cloud could not explain the IRAS observations. We therefore search for the presence of an alternate density distribution in our sample clouds such as a power law profile. Clouds near H II regions may possess a gradient in density up to some distance from the hot edge and then the density can be constant toward cooler regions. This type of density structure is favoured in the photodissociation regions of molecular clouds [Habart et al., 2005]. We therefore inspect the presence of a power law density profile in our sample clouds in the next section.

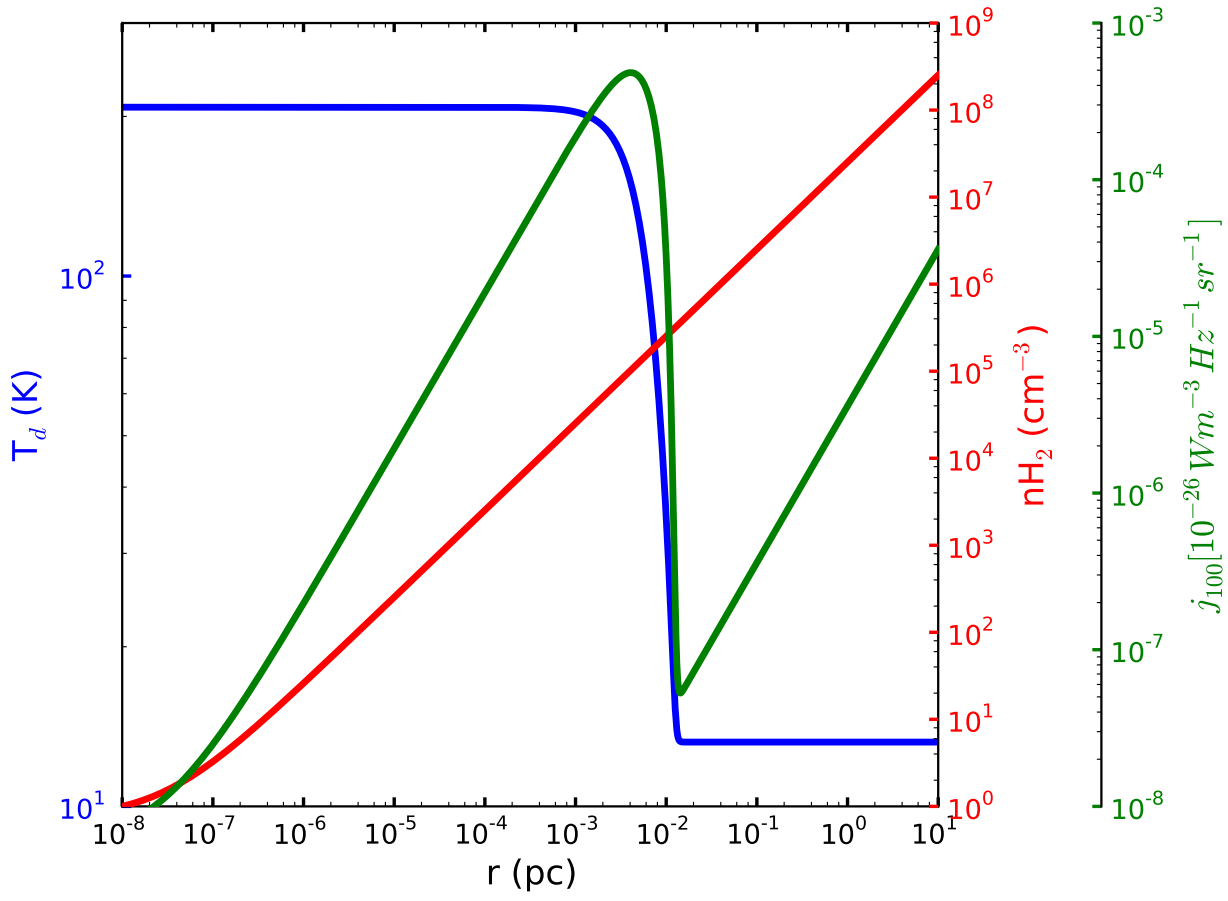

Figure 4.28: j_{100} vs. r—linear gas density distribution.

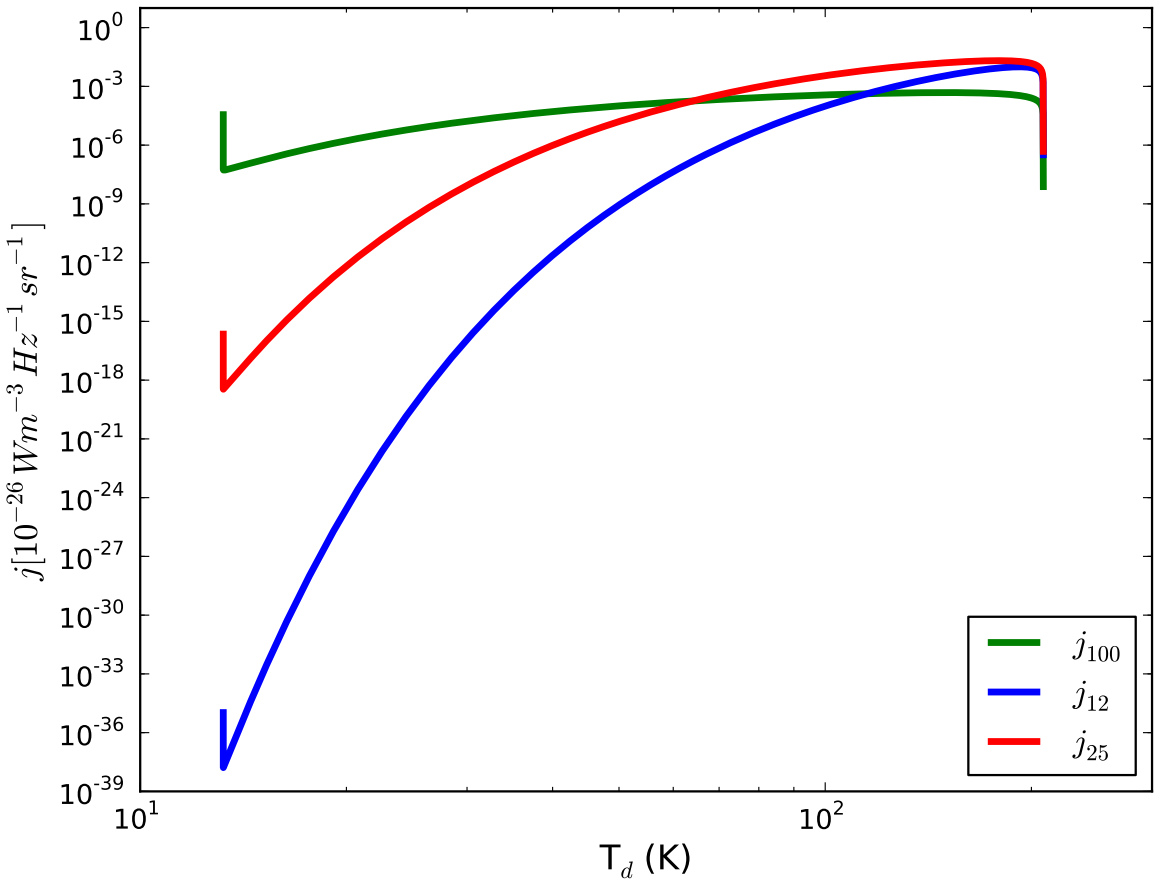

Figure 4.29: j vs. T_d—linear gas density distribution.

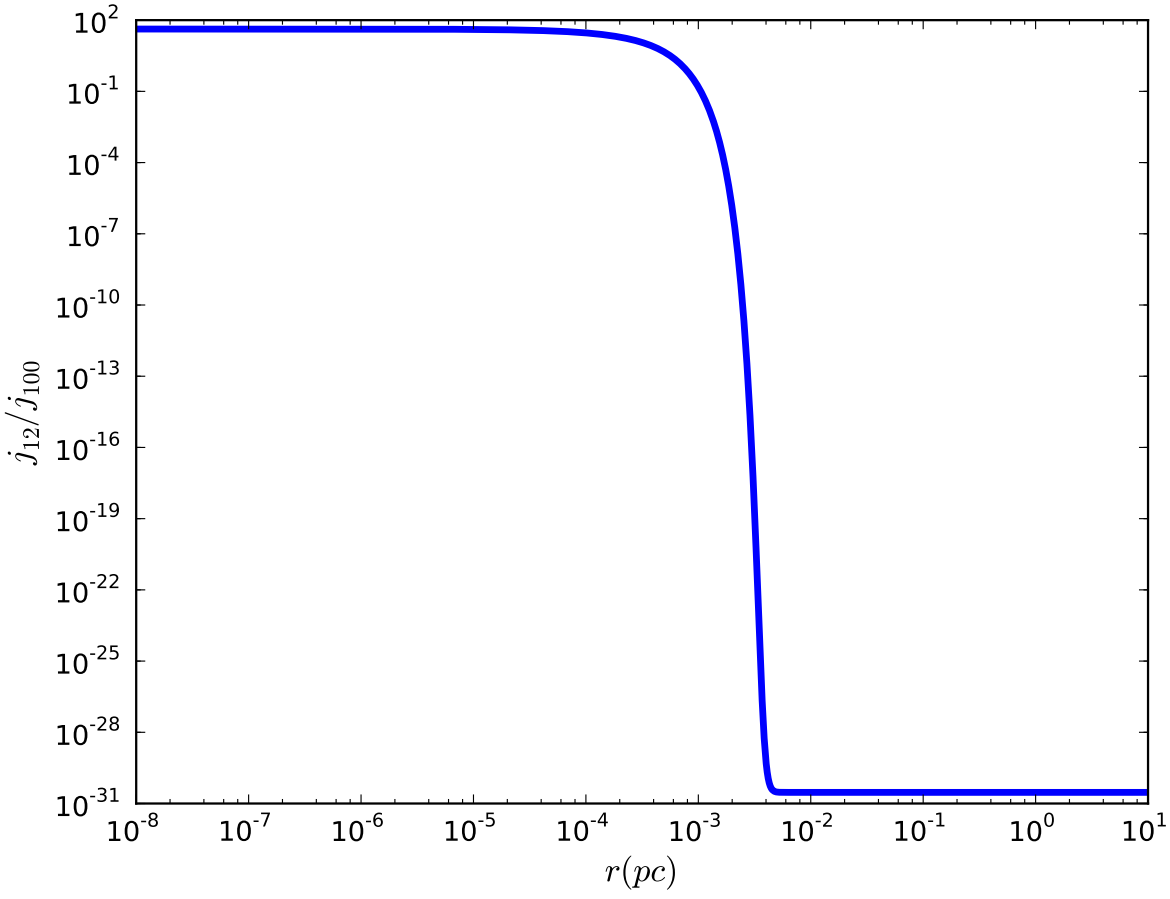

Figure 4.30: j_{12}/j_{100} vs. r—linear density distribution.

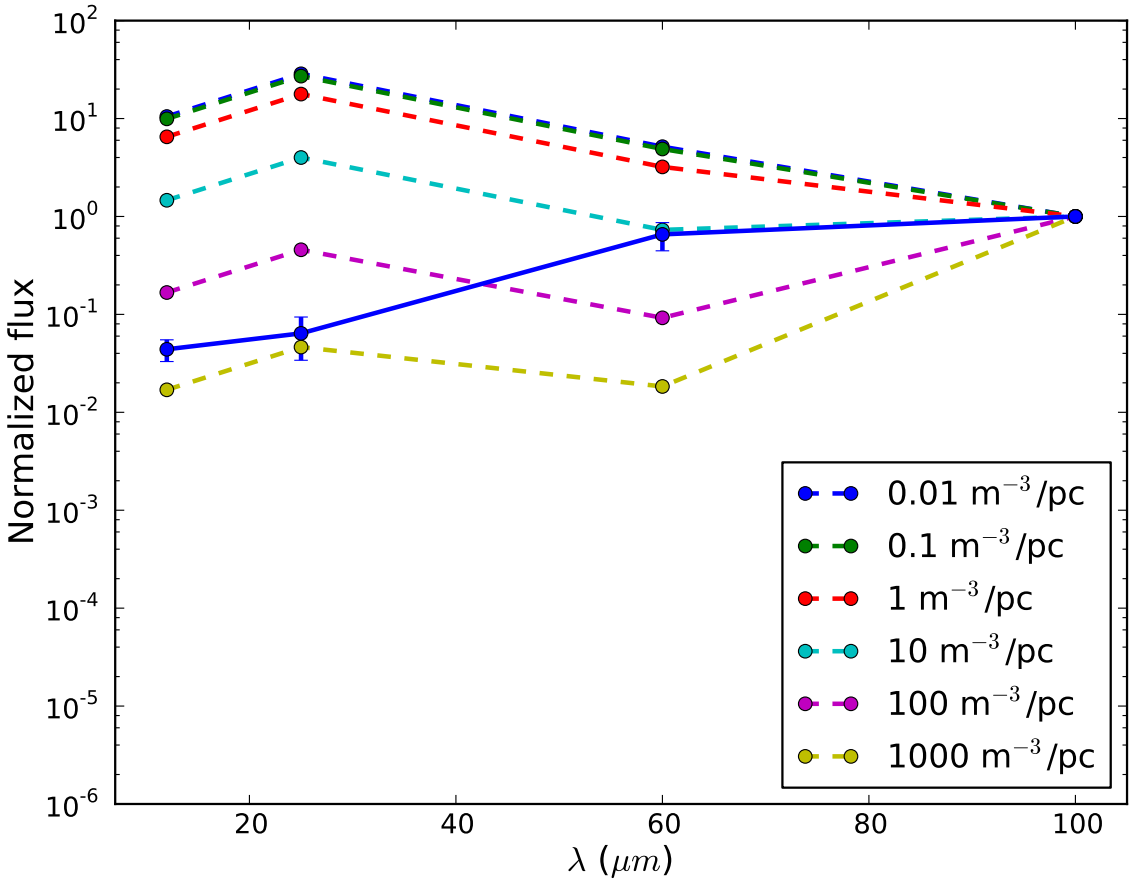

Figure 4.31: Median value of the normalized FDD of the observed clouds (blue solid line) and the theoretical FDDs corresponding to linear density distributions with different slopes (dashed lines) but a single gas density intercept (1 cm^{-3}).

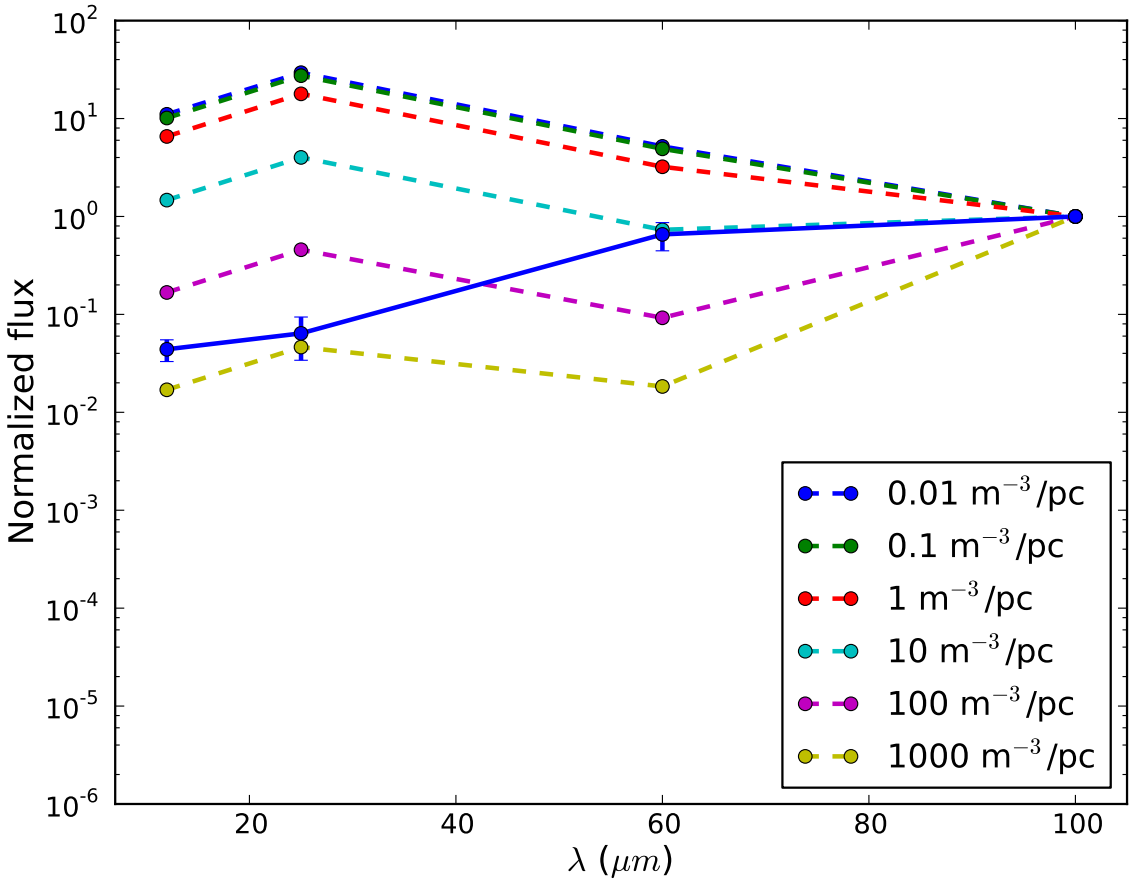

Figure 4.32: Median value of the normalized FDD of the observed clouds (blue solid line) and the theoretical FDDs corresponding to linear density distributions with different slopes (dashed lines) but a single gas density intercept (100 cm^{-3}).

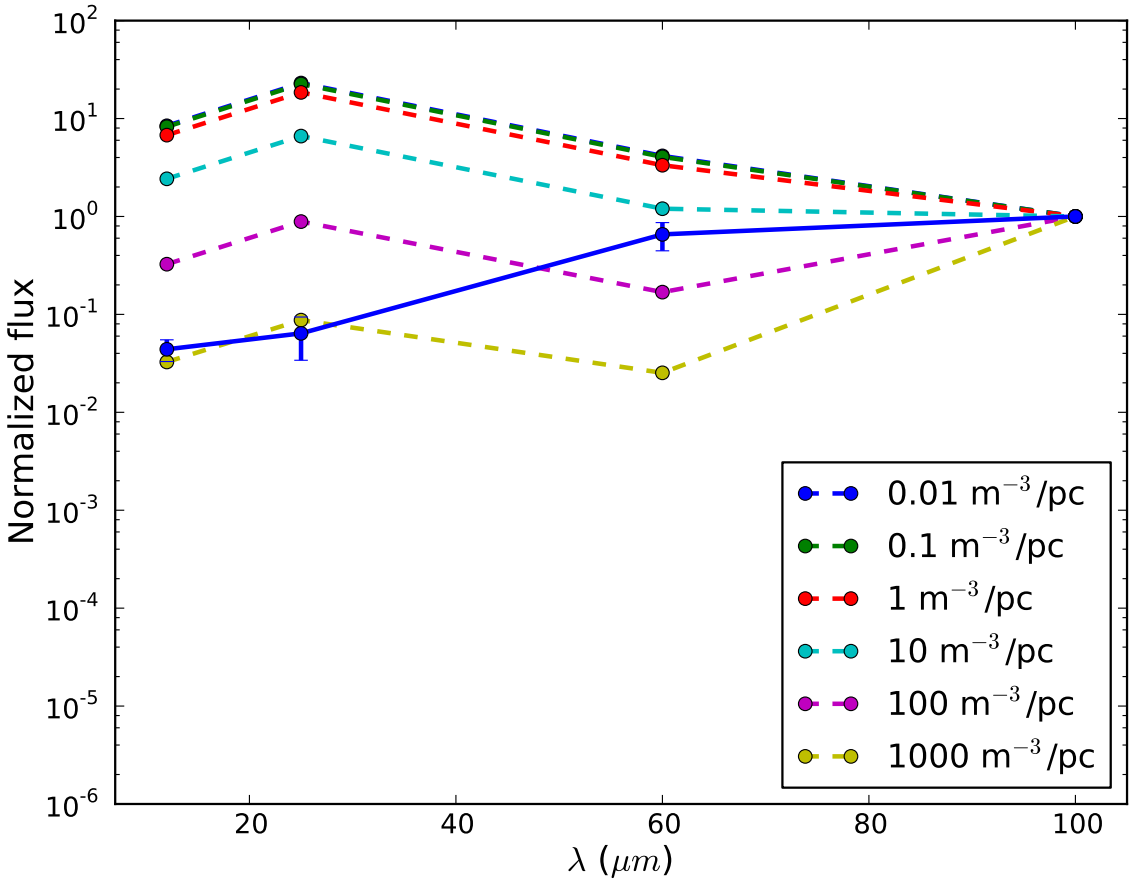

Figure 4.33: Median value of the normalized FDD of the observed clouds (blue solid line) and the theoretical FDDs corresponding to linear density distributions with different slopes (dashed lines) but a single gas density intercept (10^6 cm^{-3}).

4.4 Case 4: Power Law Profile I

In case 4, we examine models with a gas power law profile defined as:

$$n_{H_2}(r) = \begin{cases} n^0_{H_2}, & \text{if } r > r_0 \\ n^0_{H_2}(r/r_0)^\beta, & \text{if } r \leq r_0 \end{cases}$$

where r is the distance from the left edge of the cloud and r_0 is the distance at which the gas density attains a peak value $n^0_{H_2}$. β is the power law index. In the region where $r > r_0$, between r_0 and the outer edge, the cloud has a uniform gas density $n^0_{H_2}$. At regions where $r \leq r_0$, the gas number density is modified by $(r/r_0)^\beta$. The parameters r_0, $n^0_{H_2}$, and β are allowed to vary for a constant illuminating flux of 10 W/m^2 on the left cloud edge. The power law index is varied from 0.05 to 8.0 and the gas density is varied from 10^3 to 10^9 cm^{-3}. A number of r_0 values are considered between 10^{-5} pc and 5 pc, for a single $n^0_{H_2}$ and β.

4.4.1 Temperature and IR emissivity distributions

The model predictions of temperature and IR emissivities as a function of depth into the cloud for a sample β of 2.0, peak gas density $n^0_{H_2}$ of 10^7 cm^{-3}, and r_0 of 0.1 pc, are shown in Figures 4.34, 4.35, and 4.36. The gas density $n^0_{H_2}$(r) ranges over 14 orders of magnitude along the cloud. The 12 μm dust emissivity (Figure 4.34) increases from the left edge of the cloud, due to the effect of increasing density, up to a depth of ≈0.01 pc, and then begins to drop as a result of the falling temperature at that depth. At regions where the internal heating predominates, j_{12} remains approximately constant. There is a negligible contribution from the colder regions of the cloud to j_{12}. The j_{25} distribution (4.35) shows a trend similar to the j_{12} distribution. The dust emissivity at 100 μm has only a very minor contribution at the left edge of the cloud. However, as we move deeper into the cloud, j_{100} increases due to the effect of density and then declines rapidly by approximately 4 orders of magnitude at around 0.02 pc. The 100 μm emissivity, j_{100}, thereafter rises by a factor of 10 and then stays constant (see Figure 4.36). The dust emissivity variations as a function of temperature in a power law density distribution are displayed in Figure 4.37. As seen in all the previous models, virtually all the emission at the cold part of the cloud comes from the dust which is re-radiating the attenuated external flux and the flux due to internal heating at 60 and 100 μm whereas 12 and 25 μm emission dominates the hot edge of the cloud.

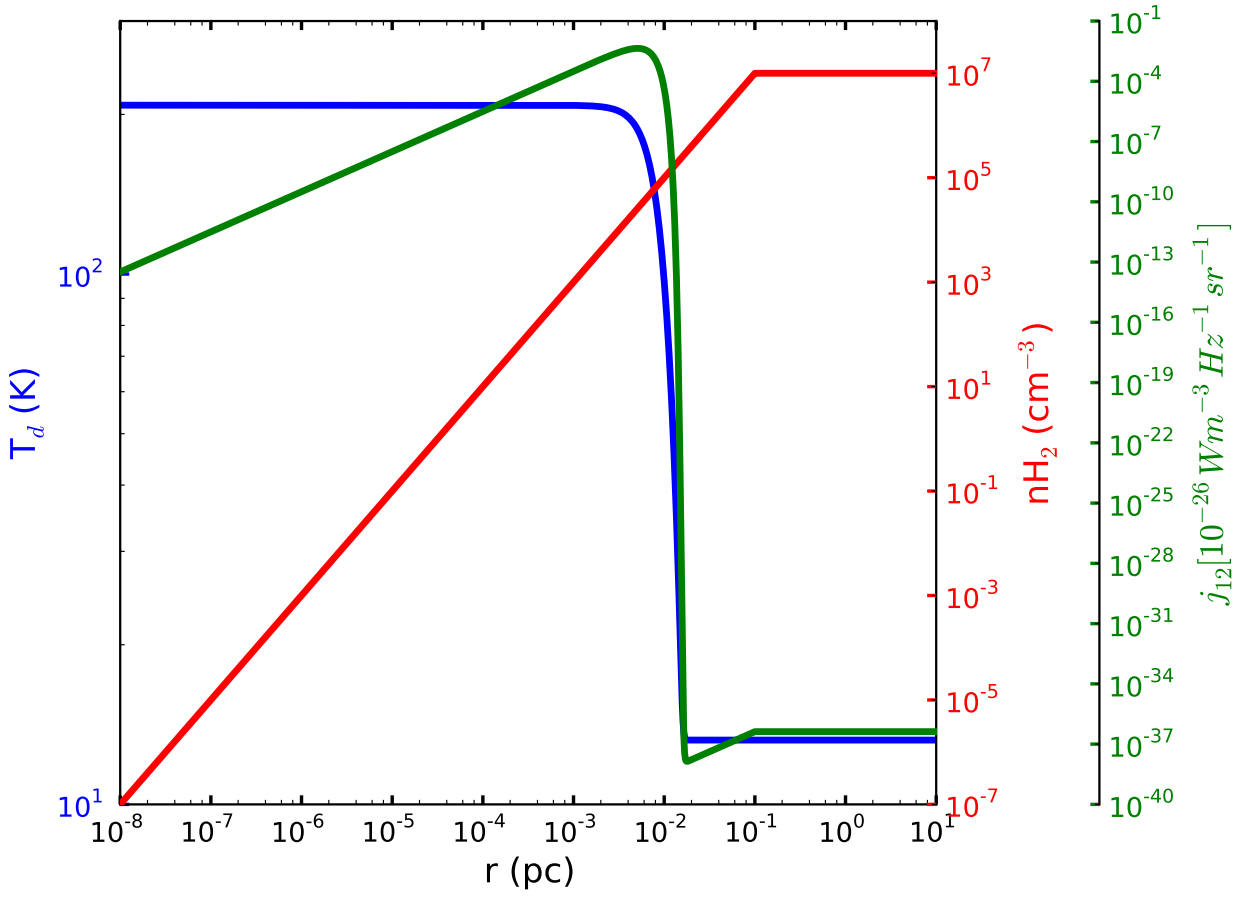

Figure 4.34: Temperature, density and j_{12}—power law profile I.

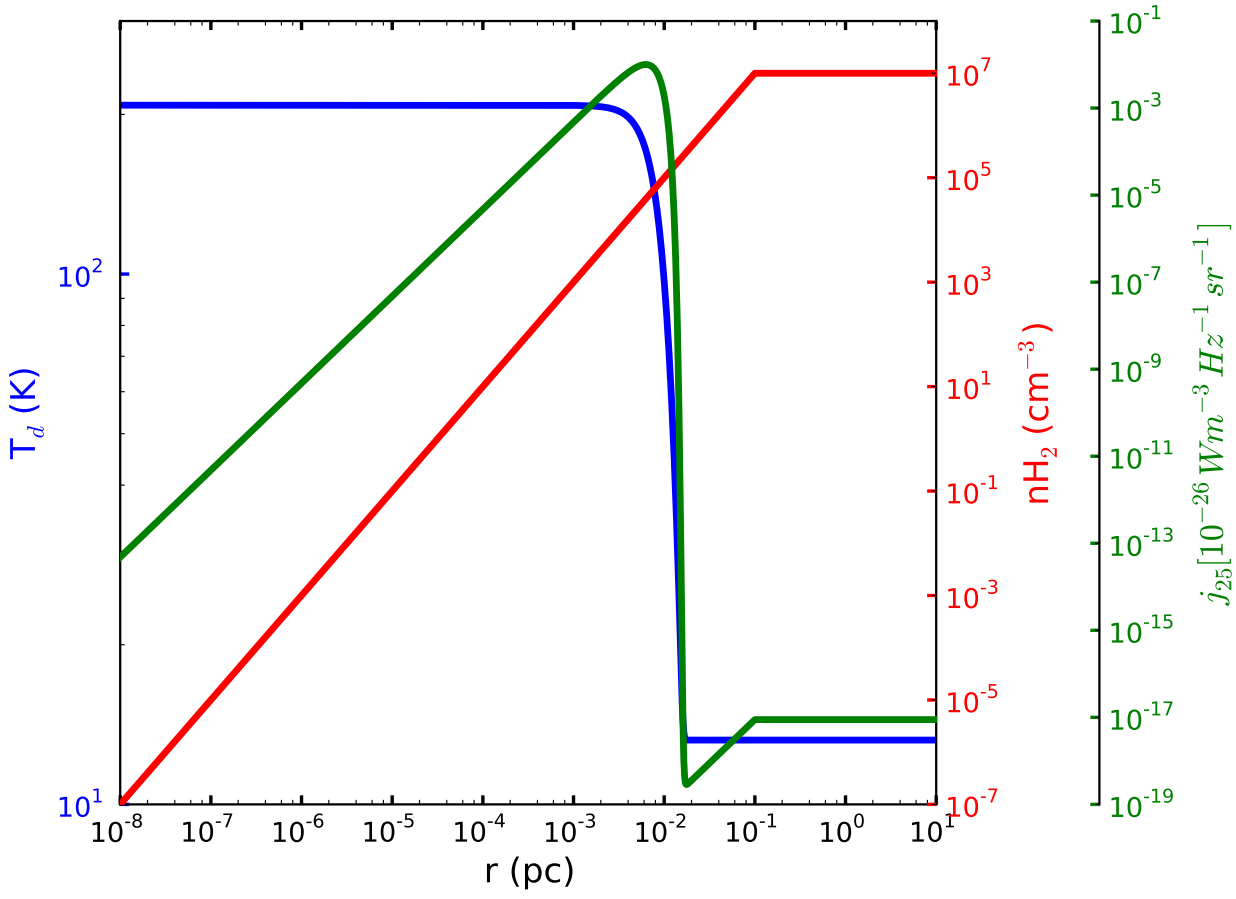

Figure 4.35: Temperature, density and j_{25}—power law profile II.

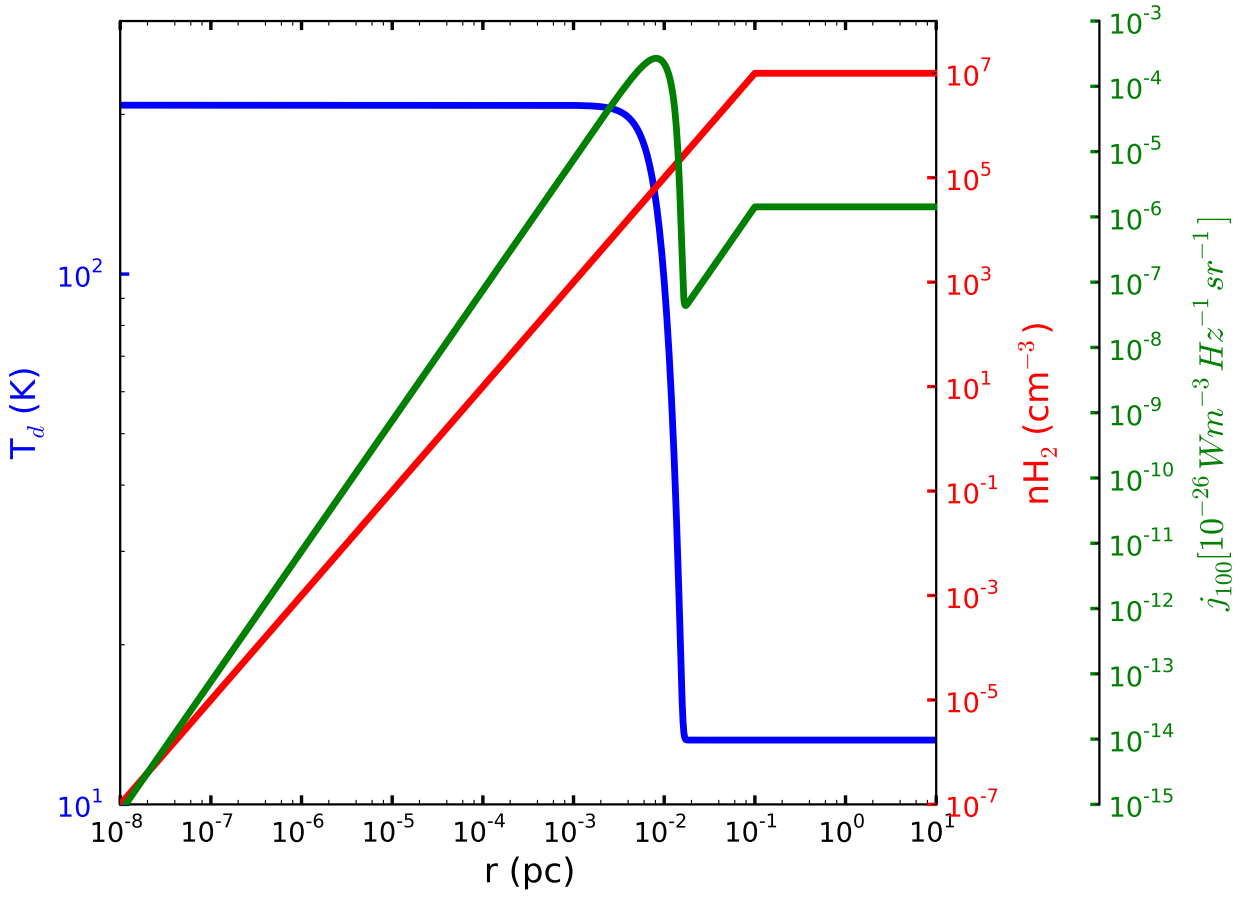

Figure 4.36: Temperature, density and j_{100}—power law profile I.

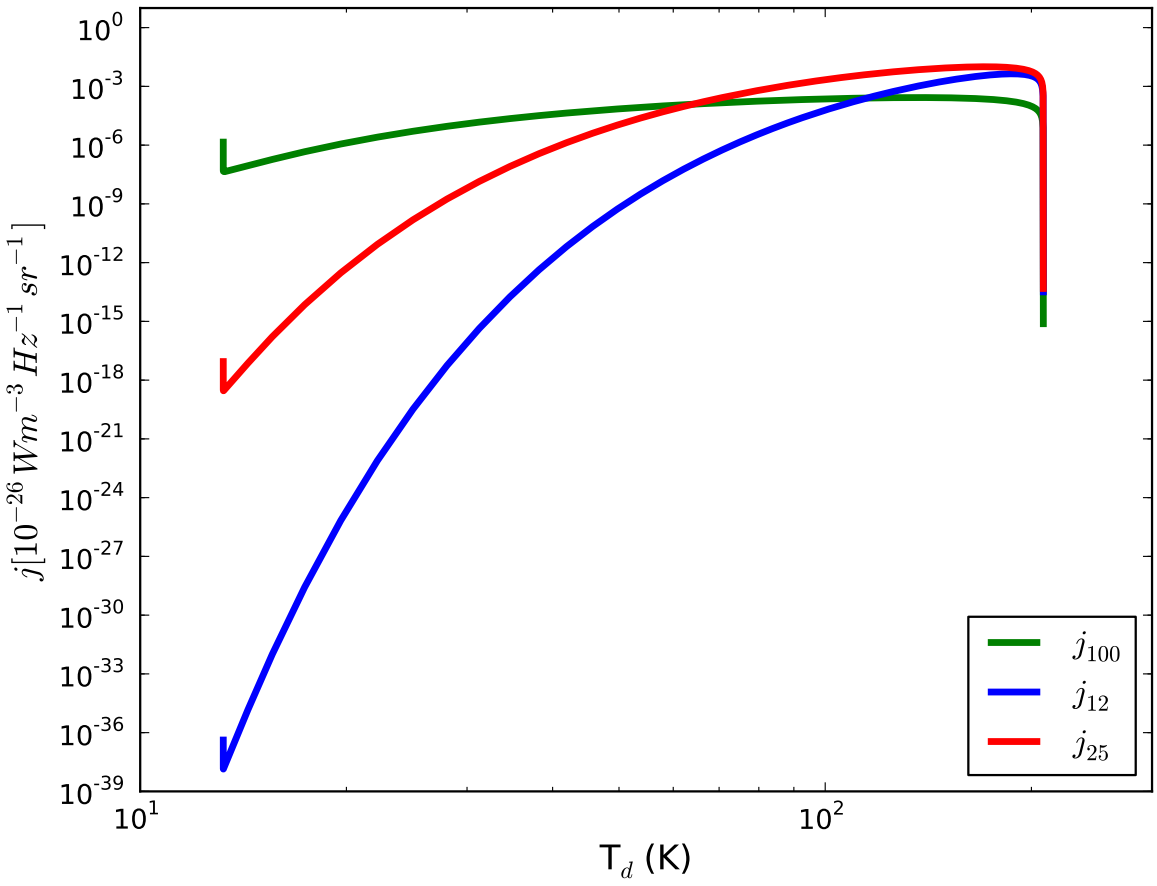

Figure 4.37: j vs. T_d—power law profile I.

4.4.2 Case 4: Analysis

In this section, we test a number of different power law profiles to study the impact of each parameter on the flux density distribution. At first we allow the power law index β to vary between 0.05 and 8.0 for a single value of $n^0_{H_2}$ and r_0. Figure 4.38 represents the resultant theoretical FDDs corresponding to power law distributions (dashed lines) with different values of β. All the modeled dust emission at 12 and 25 μm fails to match with the observed emission. However when the value of β is 2.0, the modeled dust emission coincides with the observed emission at 60 μm. As we increase β, the gas density decreases drastically at the left cloud edge, with little or no contribution from the dust emissivity at 12 and 25 μm to the edge. The effect of variations in the peak gas density on the FDD, for a single value of β and r_0, is plotted in Figure 4.39. As we increase the peak density from 10^3 to 10^9 cm^{-3}, the theoretical FDD curve shifts down by $\approx$ three orders of magnitude. A variation in the value of r_0 has little effect on the FDD especially at 12 and 25 μm (see Figure 4.40). Whenever the value of r_0 is very low, say, 10^{-5} pc, the cloud attains the peak density within a very short distance from the left edge and thereby produces an increase in dust emission at short wavelengths. On the other hand, at a larger r_0, say 5 pc, the portion of the cloud that emits the short wavelength radiation is comparably higher, and as a result, the total flux at these wavelengths again rises.

The modeled flux density distributions show inconsistencies with the observed flux density distribution, demanding a modification of the adopted model. Therefore, in the next section, we choose a second power law density distribution having a uniform density up to a short distance from the hottest cloud edge and increasing densities deeper into the cloud. If there is an interface between the H II region and the molecular cloud, the presence of such a density distribution is also feasible.

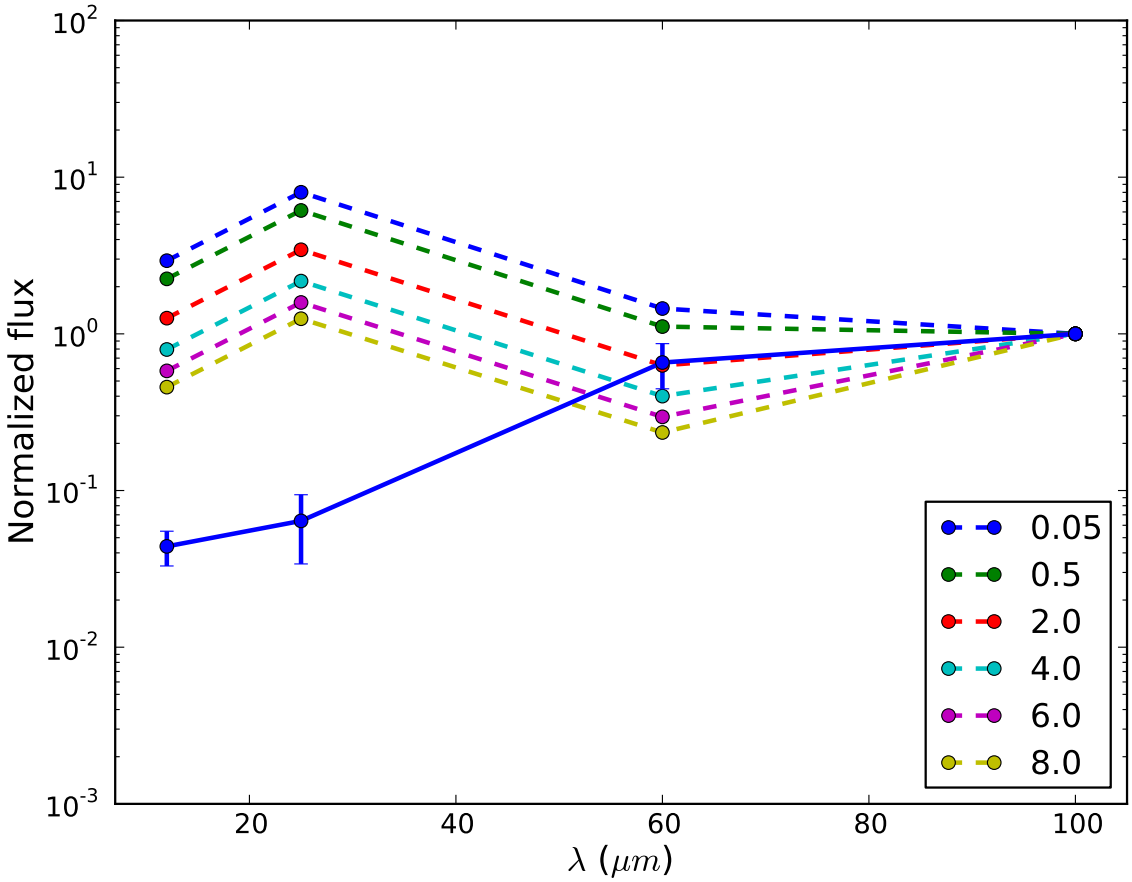

Figure 4.38: Median value of the normalized FDD of the observed clouds (blue solid line) and the theoretical FDDs corresponding to power law distributions (dashed lines) with different values of β.

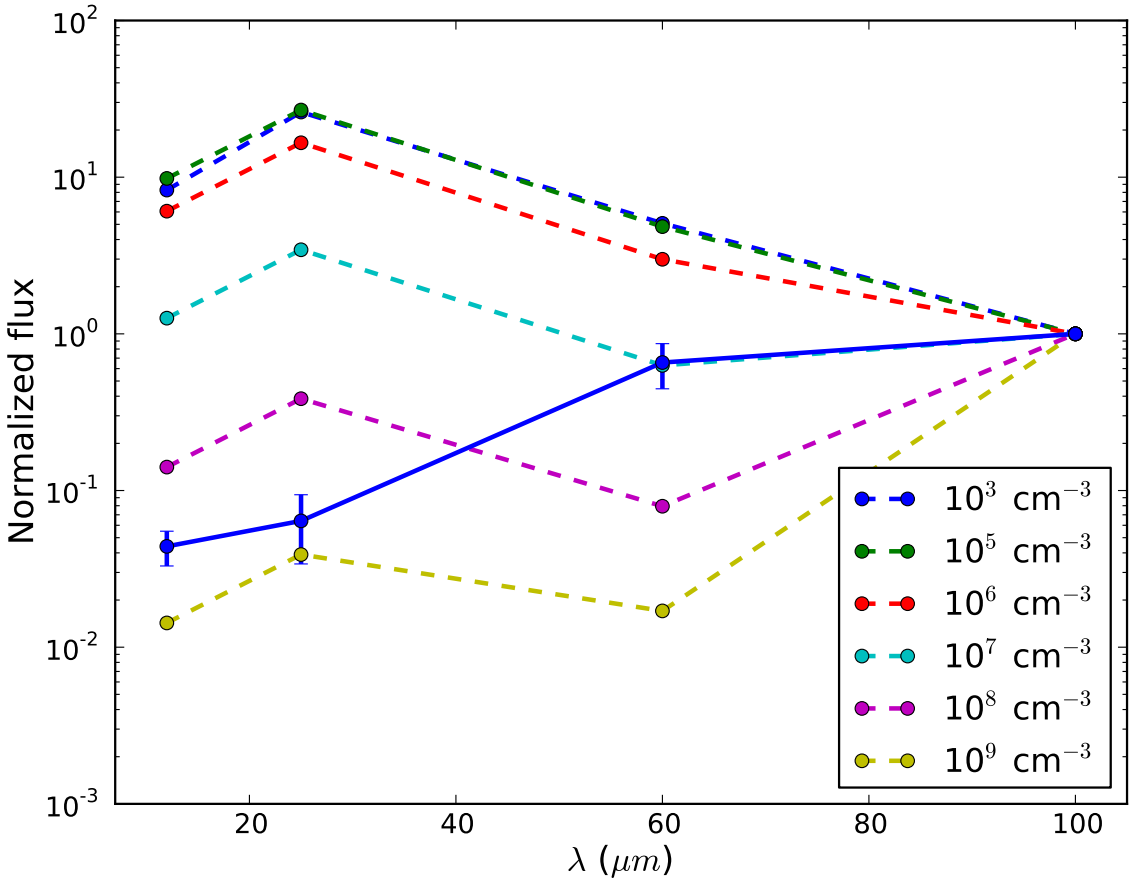

Figure 4.39: Median value of the normalized FDD of the observed clouds (blue solid line) and the theoretical FDDs corresponding to power law distributions (dashed lines) with different values of peak gas density.

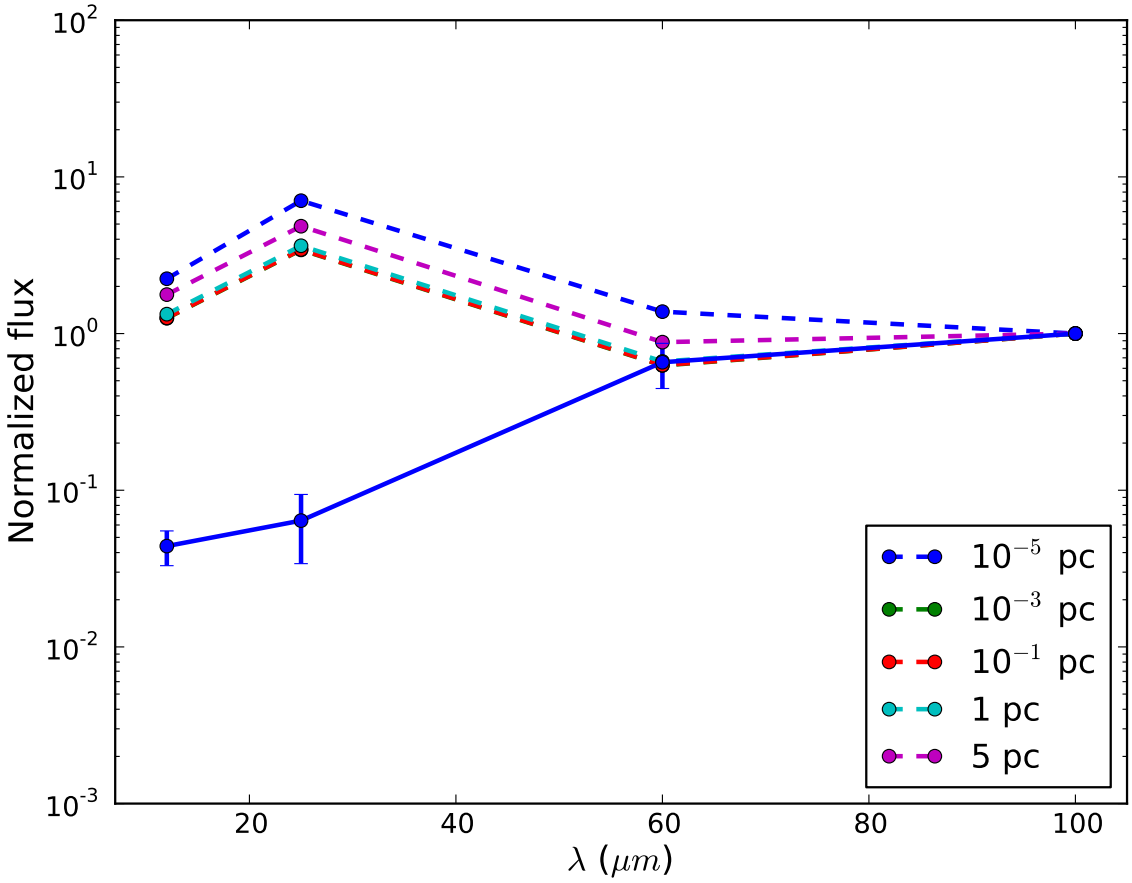

Figure 4.40: Median value of the normalized FDD of the observed clouds (blue solid line) and the theoretical FDDs corresponding to power law distributions (dashed lines) with different values of r_0.

4.5 Case 5: Power Law Profile II

The power law density profile used in case 5 is given below:

$$n_{H_2}(r) = \begin{cases} n^0_{H_2}, & \text{if } r < r_0 \\ n^0_{H_2}(r/r_0)^\beta, & \text{if } r \geq r_0 \end{cases}$$

where r is the distance from the left edge of the cloud. r_0 is the distance at which the gas density begins to rise from the value $n^0_{H_2}$. β is the power law index. In the region where $r < r_0$, between r_0 and the left edge, the cloud has a uniform gas density $n^0_{H_2}$. At regions where $r > r_0$, the gas number density is modified by $(r/r_0)^\beta$. Note that in Case 4, the density is increasing into the cloud up to a distance $r = r_0$, and then the density stays constant. However in the present case (Case 5), density stays constant as the photons move in to the cloud up to a distance $r = r_0$, and then the density increases into the cloud.

The parameters r_0, $n^0_{H_2}$, and β are allowed to vary for a constant illuminating flux of 10 W/m^2 on the left cloud edge. The power law index is varied from 2.0 to 3.5 and the gas density is varied by three orders of magnitude from 10^{-2} to 10 cm^{-3}. Six different r_0 values are considered between 5×10^{-3} pc and 10^{-1} pc, for a single $n^0_{H_2}$ and β.

4.5.1 Temperature and IR emissivity distributions

Modeled dust temperature distributions and IR emissivity distributions along with the gas density profiles for the power law profile II are shown in Figures 4.41, 4.42, and 4.43. The model distributions use an $n^0_{H_2}$ of 1 cm^{-3} on the left edge of the cloud up to a depth of 0.02 pc. After 0.02 pc, the gas number density is modified by a power law index of 3. The value of j_{12} remains constant until 10^{-2} pc, and then starts to rise due to the soaring gas density. But at around 0.1 pc, j_{12} is controlled by the dropping temperature and the emissivity thereby begins to drop. However, by slightly boosting the emissivity, the density takes dominance at 0.3 pc (see Figure 4.41). A similar effect can be seen in the distribution of 25 μm emissivity (Figure 4.42). At 100 μm, the cloud has a lower emissivity at the hot edge in comparison with the short wavelength emissivities. Due to the effect of dust temperature and gas density, j_{100} attains a higher value at the exterior cold cloud edge (Figure 4.42). The emissivity distribution as a function of dust temperature at all three wavelengths shown in Figure 4.45 illustrates that emissivity at 12 and 25 μm is greater than the emissivity at 100 μm, primarily beyond 100 K, close to the left cloud edge. Below a temperature of 100 K, j_{100} exceeds j_{12}, and under 60 K, j_{100} outstrips both the short wavelength contributions.

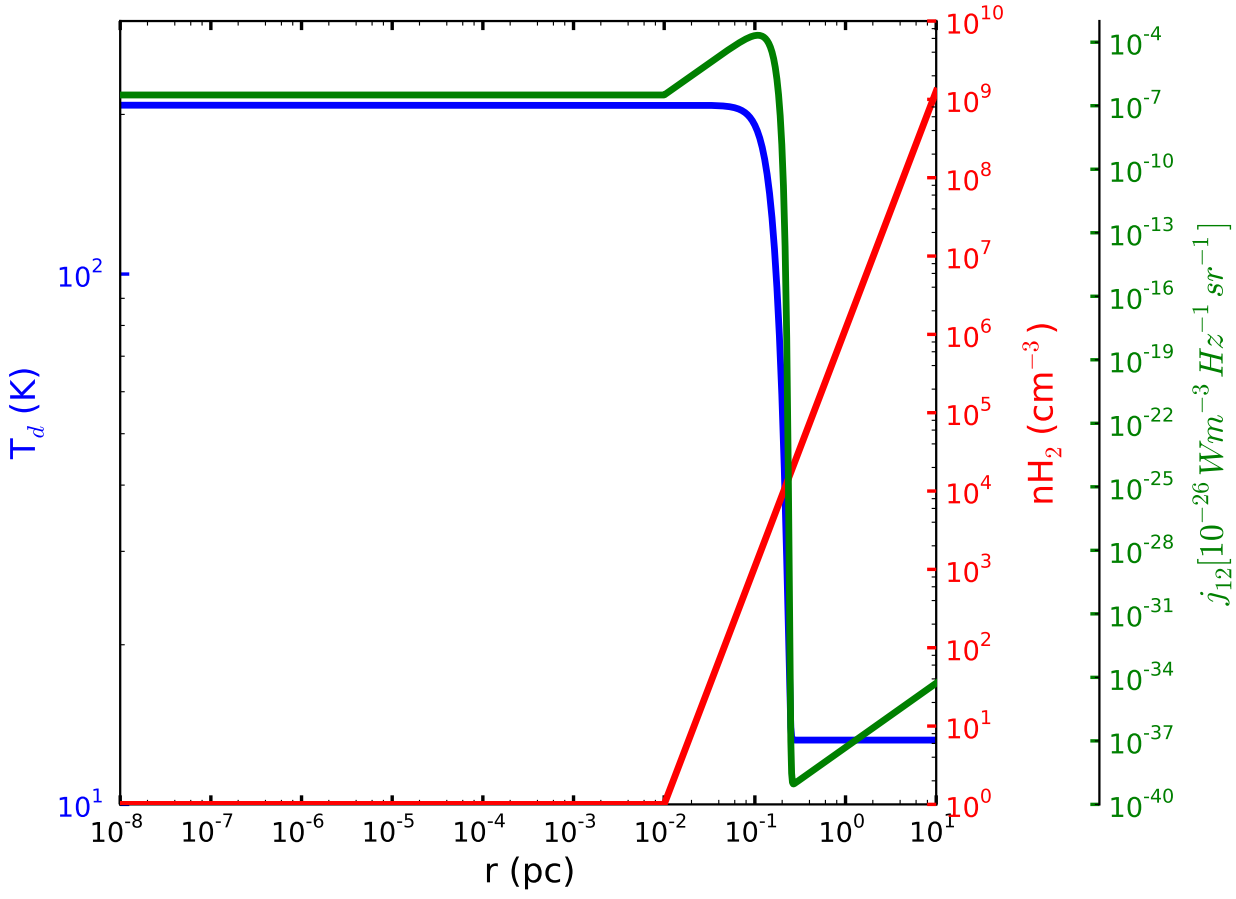

Figure 4.41: Temperature, density and j_{12} vs. r—power law profile II.

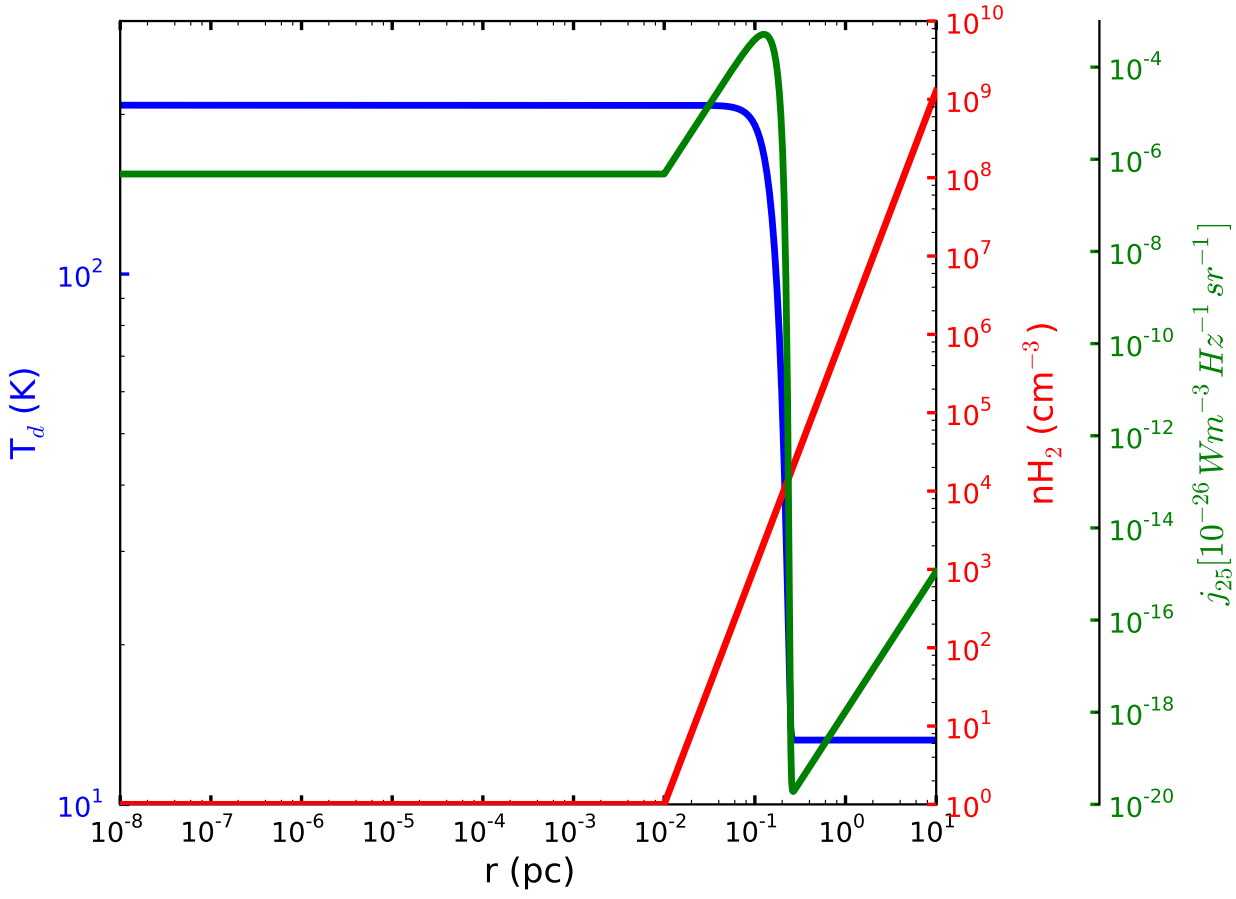

Figure 4.42: Temperature, density and j_{25} vs. r—power law profile II.

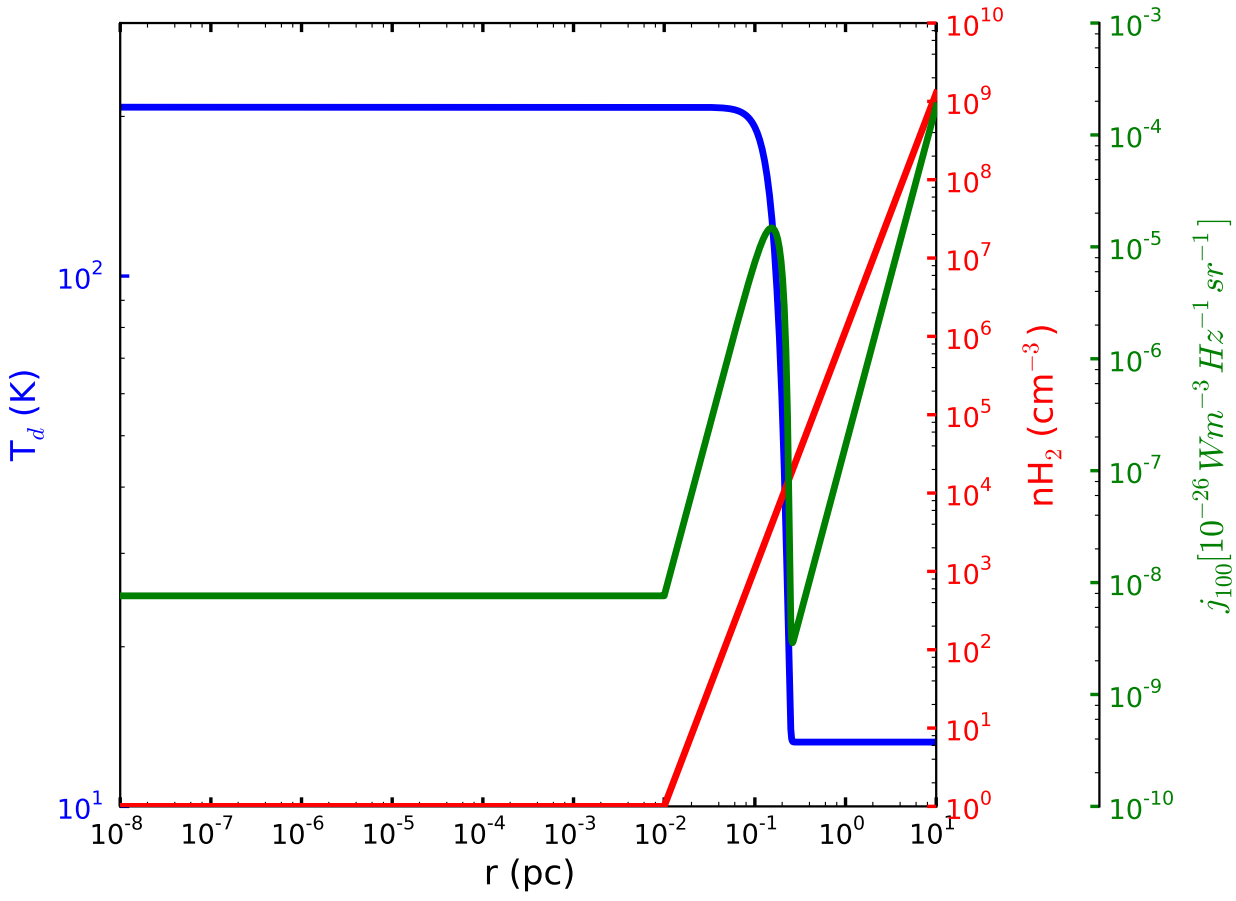

Figure 4.43: Temperature, density and j_{100} vs. r—power law profile II.

4.5.2 Case 5: Analysis

Several power law II profiles are tested to follow the response of each free parameter on the FDD curve. At first, different density profiles are constructed by varying the power law index between 2.0 and 3.5 for an $n^0_{H_2}$ of 1 cm^{-3} and r_0 of 0.01 pc. The resultant model FDDs (dashed curves) along with the observed FDD (blue solid curve) are shown in Figure 4.46. Raising β from 2.0 to 3.5 decreased the 12 and 25 μm by $\approx$ four orders of magnitude. However at 60 μm, the changes are less pronounced. As β decreases, the peak gas density as well as the gas density values along the depth of the cloud, beyond 0.01 pc, decrease and are thus responsible a lower number of dust grains to emit at all wavelengths. As we reduce the value of $n^0_{H_2}$ from 1 to 0.01 cm^{-3} for a β of 3.0 and r_0 of 0.01 pc, the cloud will be hotter in the deeper regions, and thus produce significant amount of emission at short wavelengths (see Figure 4.47). Changing the distance at which the density begins to rise also has a considerable influence on the infrared dust emission. Extending the value of r_0 by just a factor of 10 causes the infrared fluxes to jump by over a factor of 100 (Figure 4.48). As a result, models with the power law profile II do not agree with the infrared emission from dust grains.

As all the selected density profiles failed to replicate the IRAS emission simultaneously at all the wavebands, we search for alternate plausible density distributions that can exist in clouds near H II regions. The gas densities of molecular clouds especially at the surface layers can form a step (a sharp jump) in their distribution if there is an interface between the H II region and the molecular cloud. So we select a step function density distribution to examine whether such a distribution can reproduce the observed flux densities and is explained in the next section.

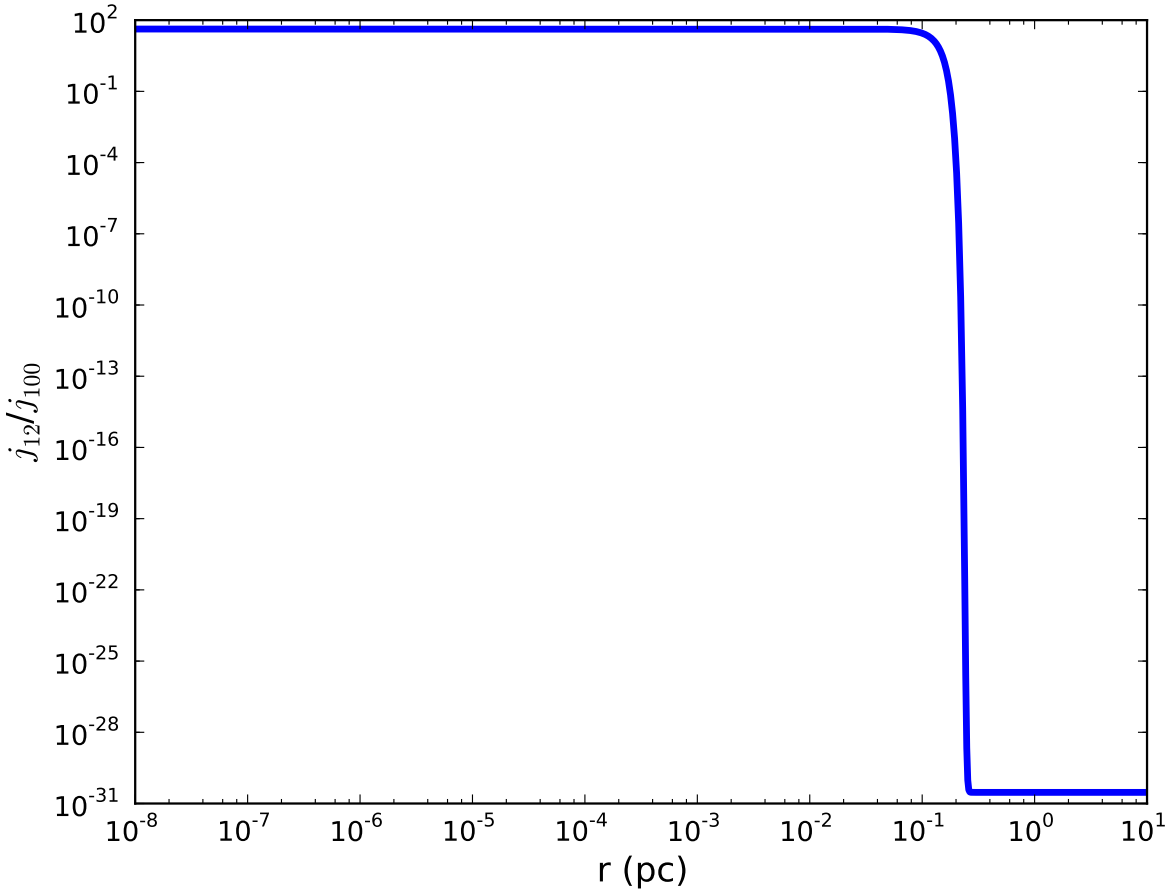

Figure 4.44: j_{12}/j_{100}—power law profile II.

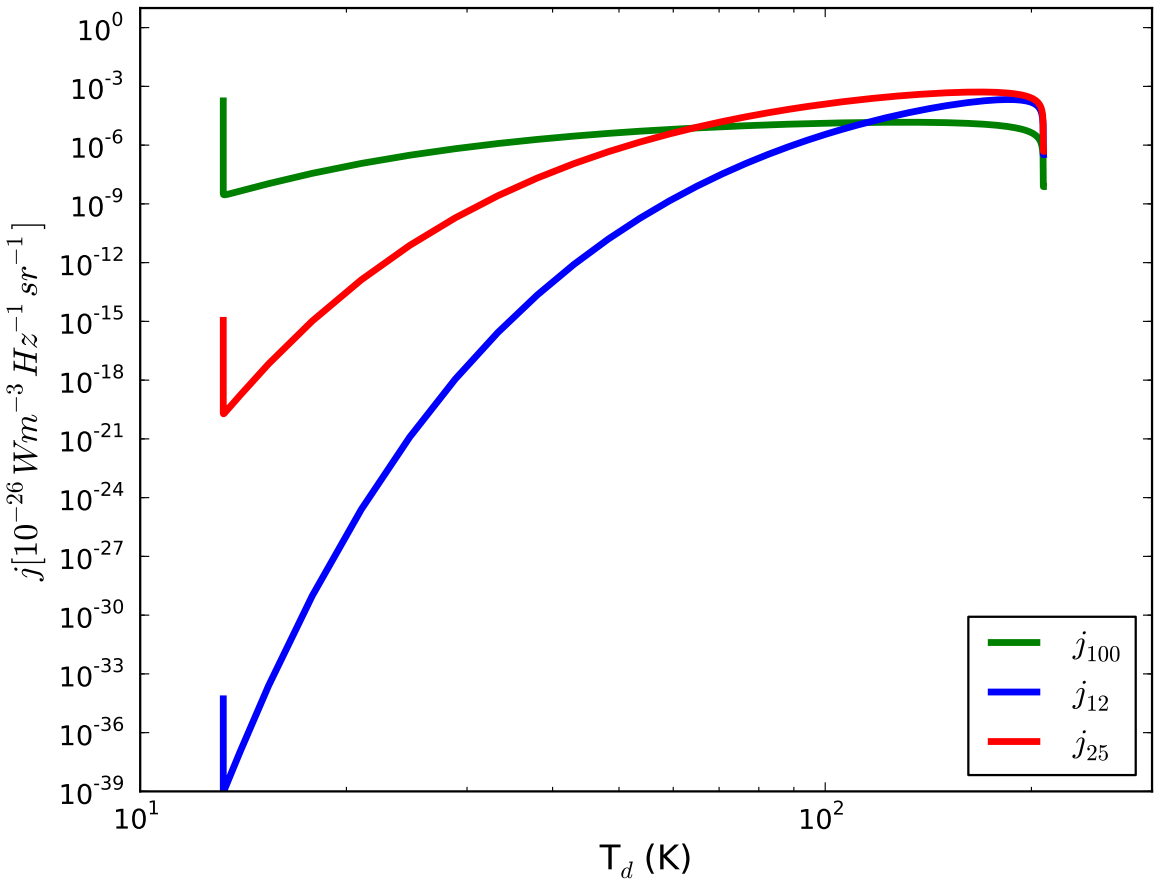

Figure 4.45: j vs. T_d—power law profile II.

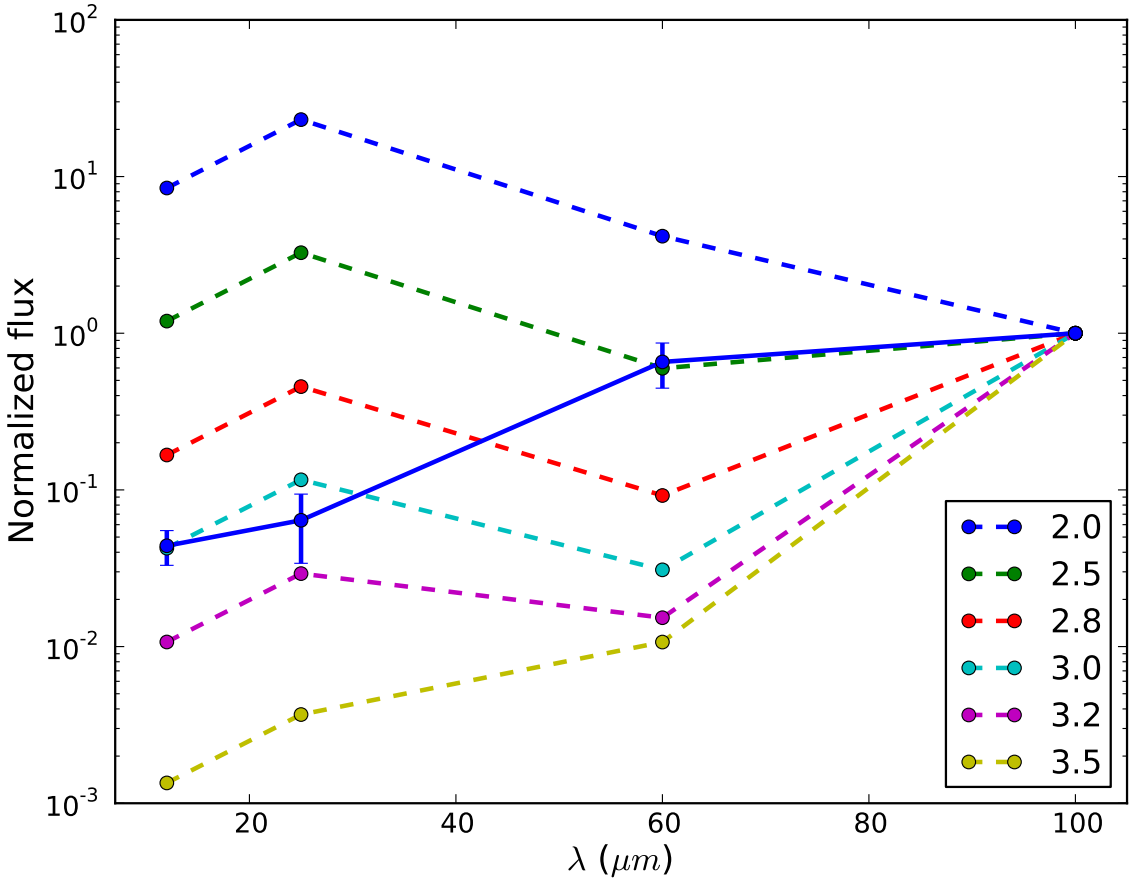

Figure 4.46: Median value of the normalized FDD of the observed clouds (blue) and the theoretical FDDs corresponding to power law profile II (red) for β ranging from 2.0 to 3.5.

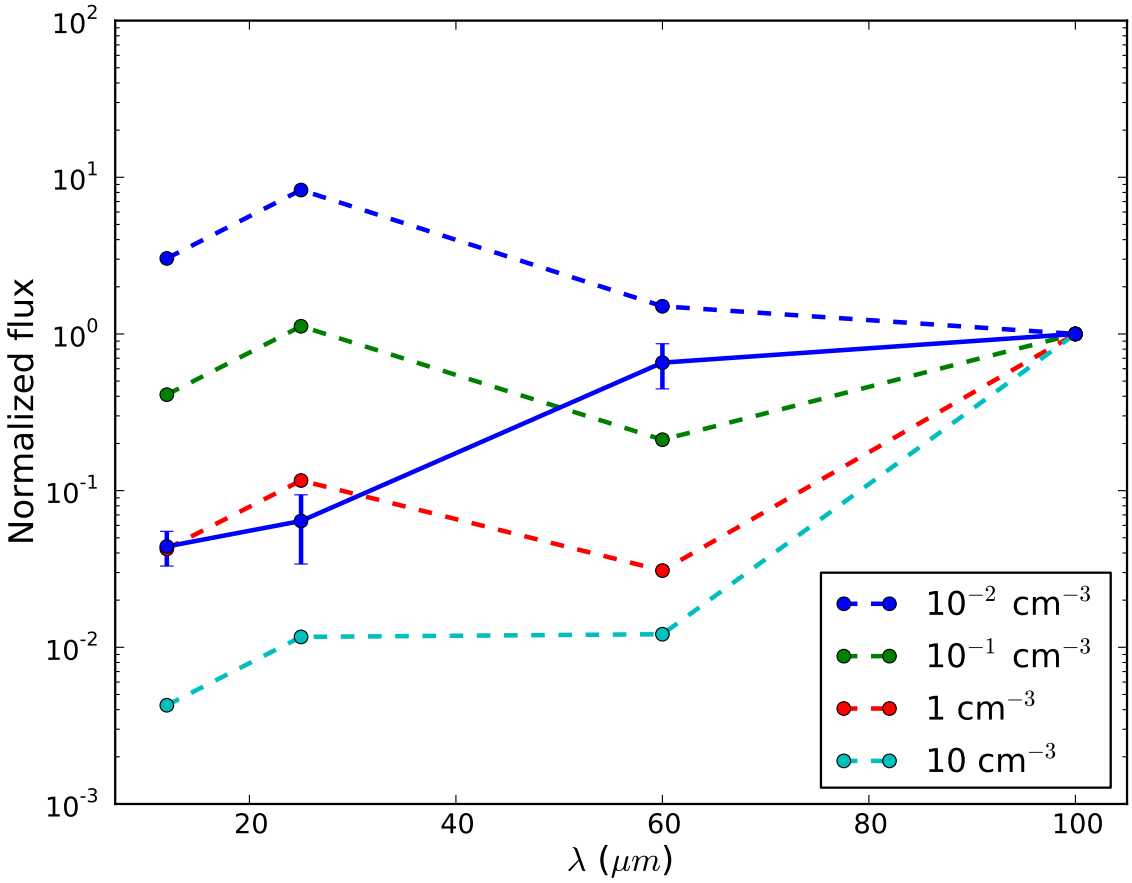

Figure 4.47: Median value of the normalized FDD of the observed clouds (blue) and the theoretical FDDs corresponding to power law profile II (red) for $n^0_{H_2}$ ranging from 10^{-2} cm^{-3} to 10 cm^{-3}.

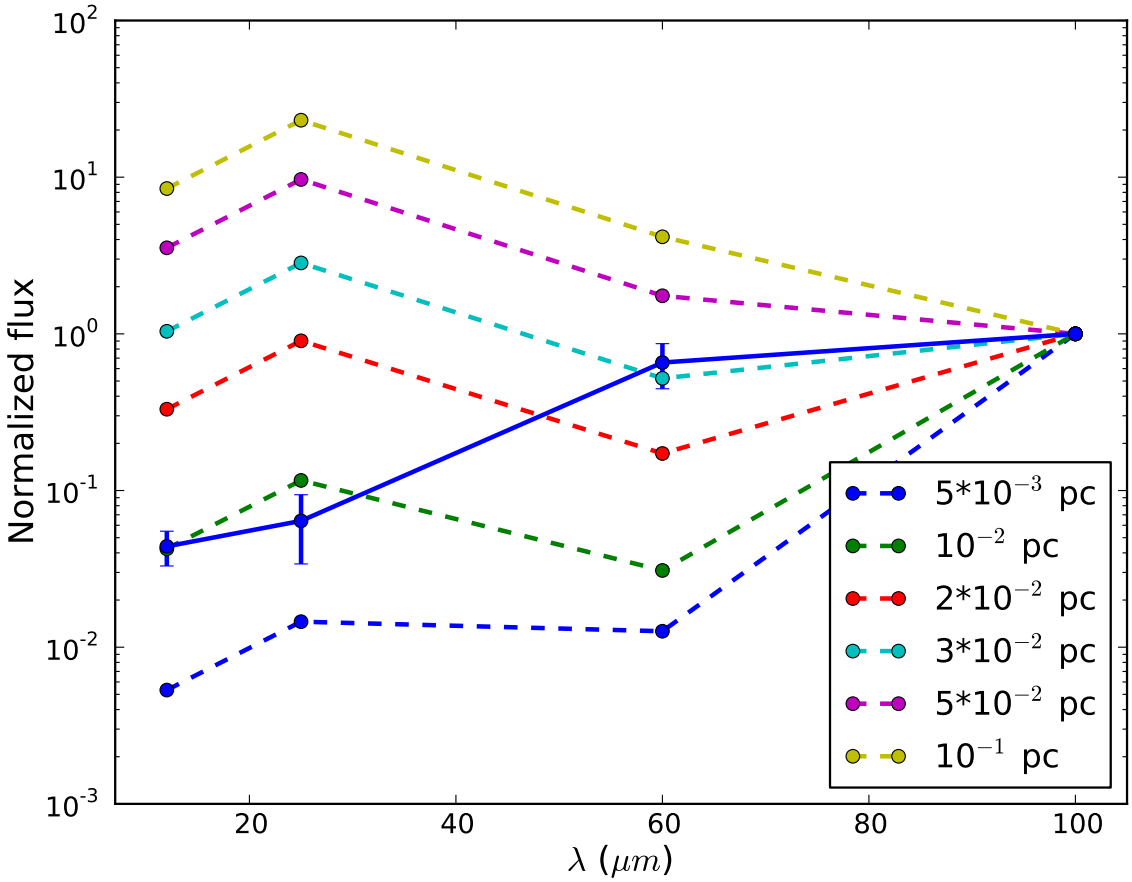

Figure 4.48: Median value of the normalized FDD of the observed clouds (blue) and the theoretical FDDs corresponding to power law profile II (red) for r_0 ranging from 5×10^{-3} pc to 0.1 pc.

4.6 Case 6: Step Function Density Profile

In case 6, we model a step function gas density distribution of the form:

$$n_{H_2}(r) = \begin{cases} n^0_{H_2}, & \text{if } r \geq r_0 \\ a n^0_{H_2}, & \text{if } r < r_0 \end{cases}$$

where r is the distance from the left edge of the cloud and r_0 is the distance at which the gas density obtains a peak value $n^0_{H_2}$. In the region where $r \geq r_0$, between r_0 and the right cloud edge, the cloud retains a uniform peak gas density $n^0_{H_2}$. At regions where $r < r_0$, the gas number density is modified by the height a of the step. The parameters r_0, $n^0_{H_2}$, and a are allowed to vary for a constant illuminating flux of 10 W/m^2 on the left cloud edge. The value of a is varied from 10^{-3} to 10^{-7} for a constant value of gas density and r_0. Similarly $n^0_{H_2}$ and r_0 are also varied independently by keeping the other two free parameters a constant, and the behaviour of the final FDD is studied.

4.6.1 Temperature and IR emissivity distributions

In order to show the distribution of IR emissivities and dust temperatures along the cloud depth, we selected a model cloud with a peak gas density of 10^7 cm^{-3} on the right side. The gas density at the left edge of the cloud is 10 cm^{-3}. At a distance of 0.2 pc from the left edge, the cloud shows an abrupt jump in the gas density. Figures 4.49, 4.50, and 4.51 display the temperature and the emissivity distributions of a cloud having such a distribution in the gas densities. The temperature drops from 208 K to 13 K at 0.2 pc where the step in the density distribution is located. In the same way, infrared emissivities at all wavelengths exhibit a step in their spatial distribution.

4.6.2 Case 6: Analysis

Foremost, we varied the peak density at the step for a constant r_0 and a. The resultant model FDDs are plotted in Figure 4.53. At lower peak densities the stellar photons traverse more distance through the cloud enabling the absorption and re-emission of photons deep inside the cloud. At higher peak densities due to a higher optical depth, emission drops at all wavelengths. The FDDs obtained from changing r_0 values for a constant peak density and step height are shown in Figure 4.54. As the optical depth depends on the distance along the cloud, increasing this distance increases the optical depth for a constant gas density and causes the emission to drop. Figure 4.55 illustrates the effect of step height on the SED. Note that we maintained a constant peak gas density and r_0. For a peak gas density of 10^7 cm^{-3}, and a r_0 of 0.2 pc, we varied the step height and the resultant FDDs

show an increase in the flux with a decrease in the step height. For example, if the cloud has a density of 10^4 cm^{-3} up to 0.2 pc from the left cloud edge, then grains emit much more infrared radiation mainly because emission scales with number density of dust grains. However, at low initial gas densities, the cloud emits less effectively at all wavelengths.

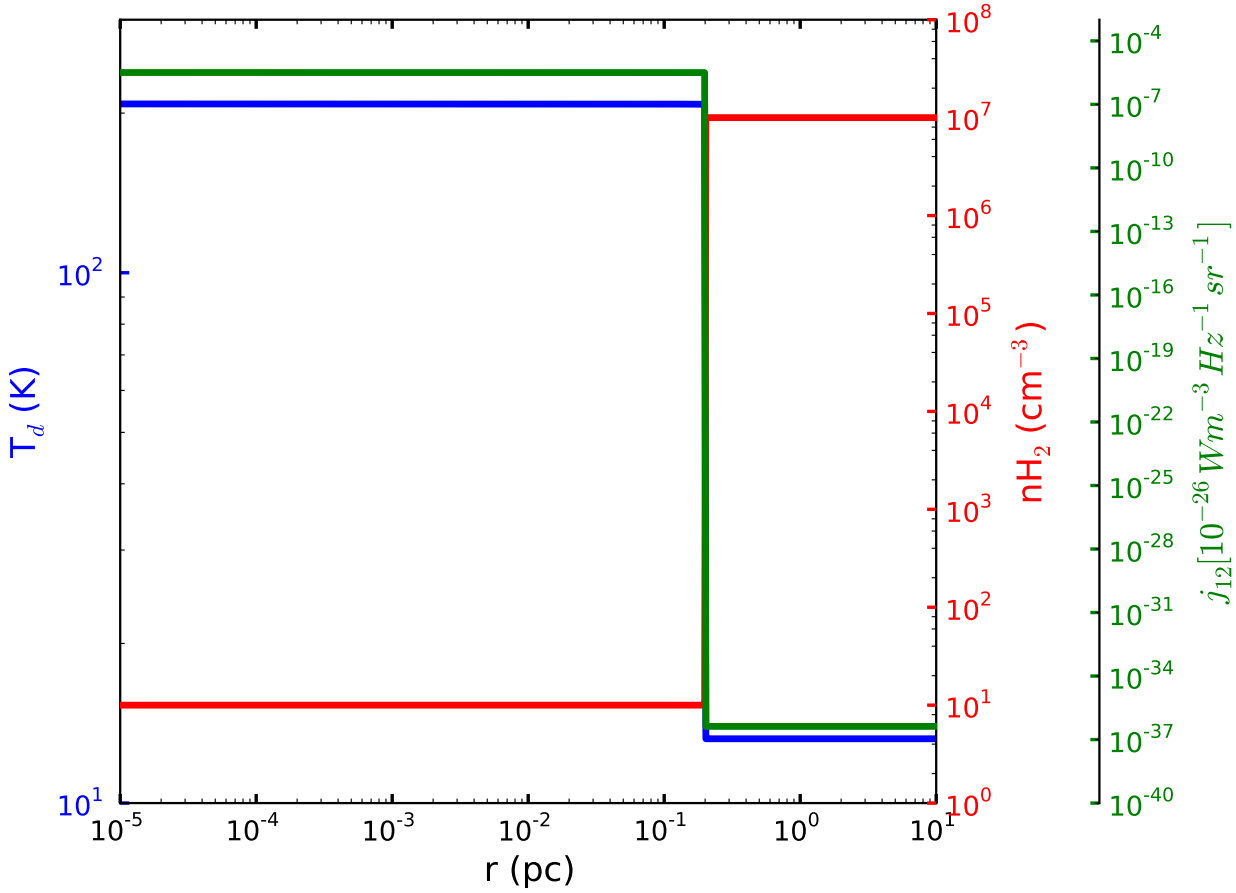

Figure 4.49: Distribution of temperature, density, and j_{12} in the case of a step function density profile.

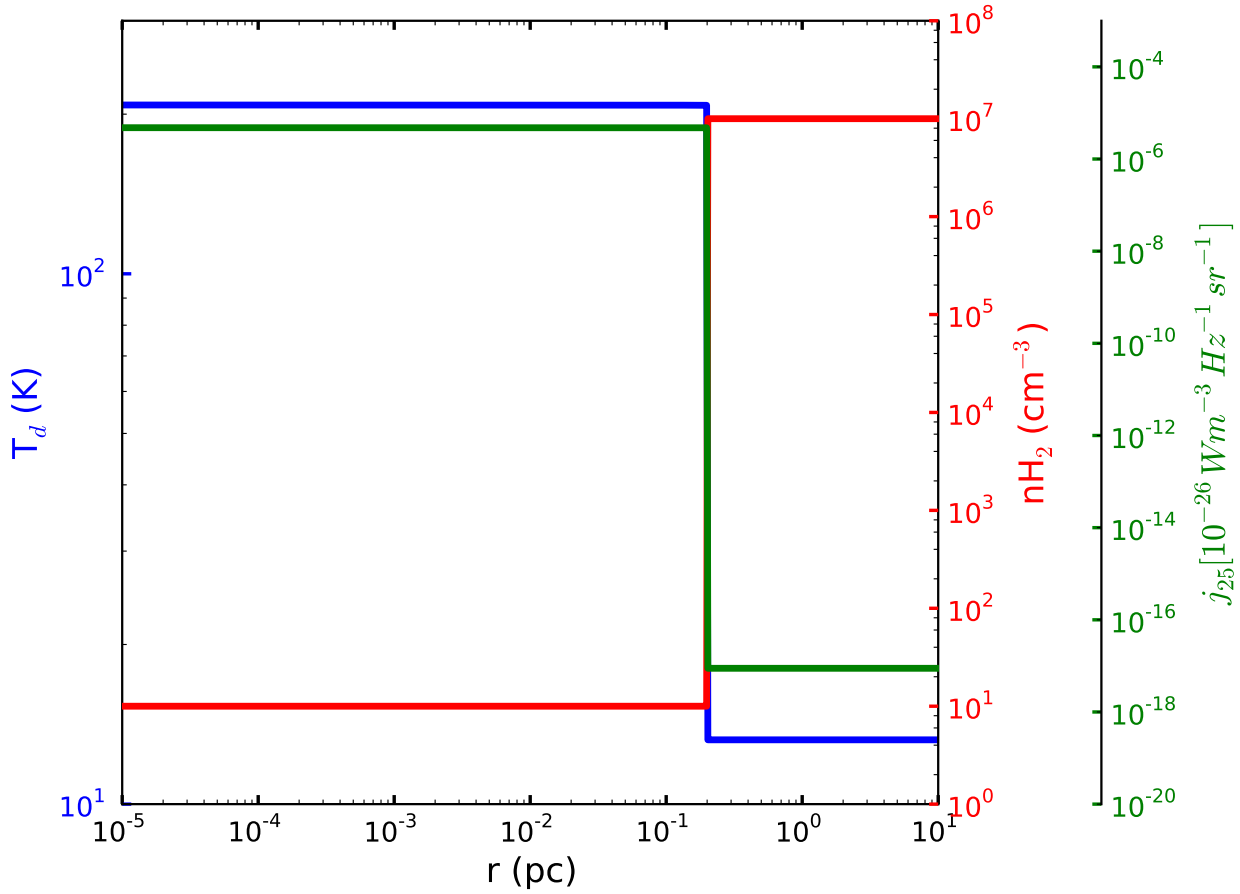

Figure 4.50: Distribution of temperature, density, and j_{25} in the case of a step function density profile.

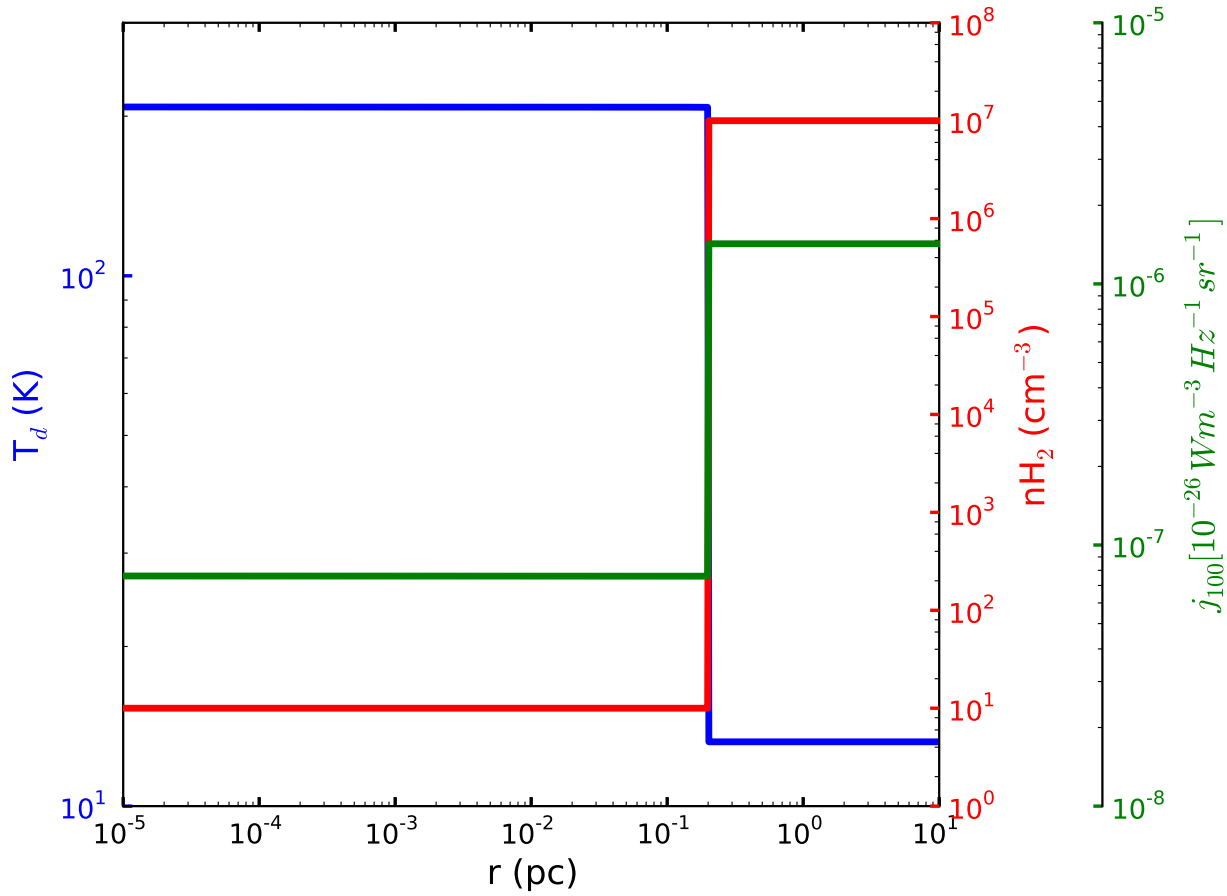

Figure 4.51: Distribution of temperature, density, and j_{100} in the case of a step function density profile.

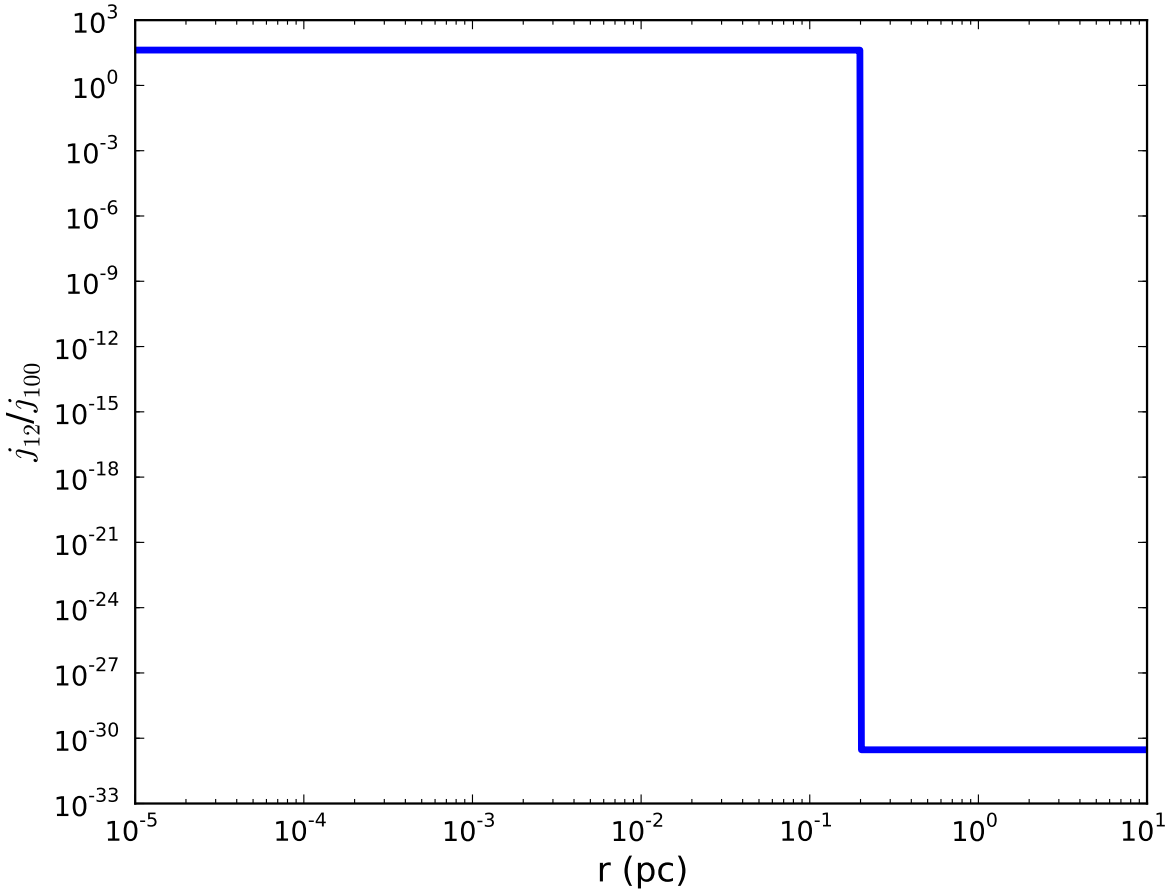

Figure 4.52: j_{12}/j_{100}—step function density profile.

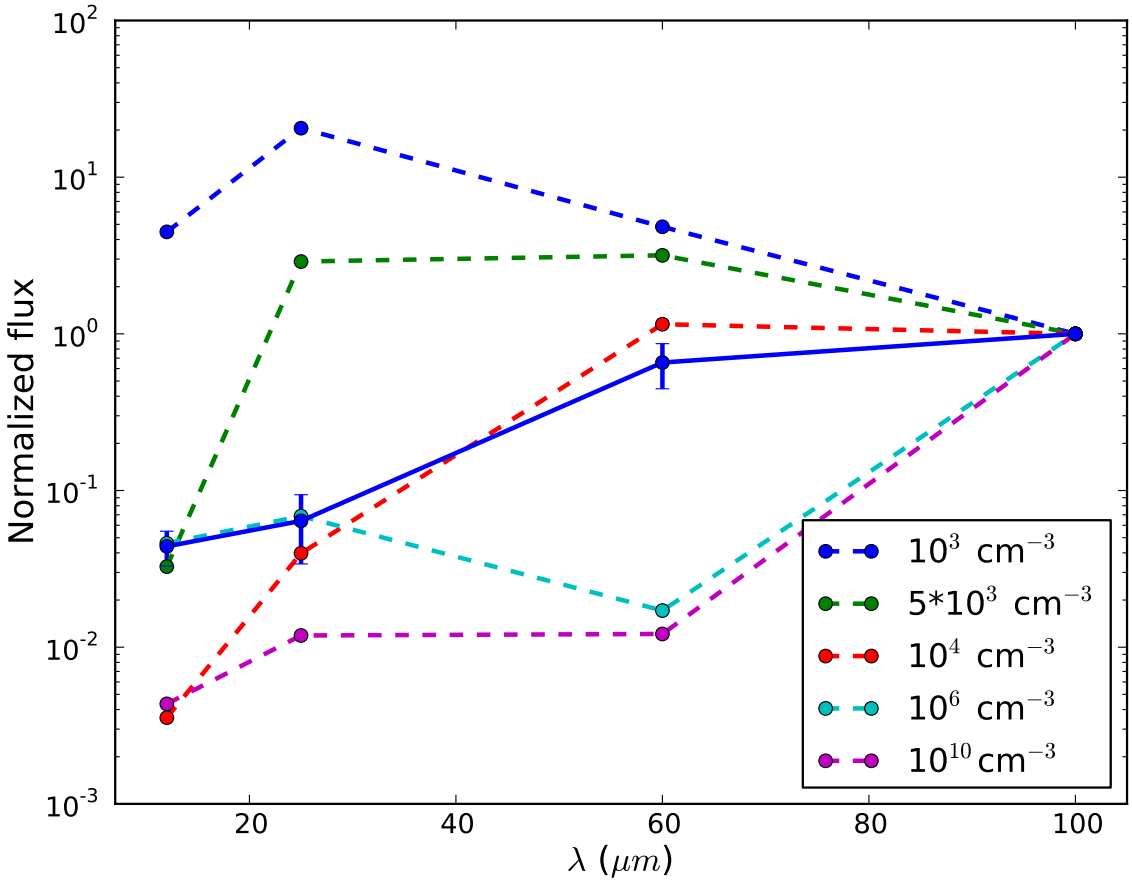

Figure 4.53: Median value of the normalized FDD of the observed clouds (blue) and the theoretical FDD corresponding to a step function density profile. SEDs are plotted for different initial densities but constant step height and constant radius at the step.

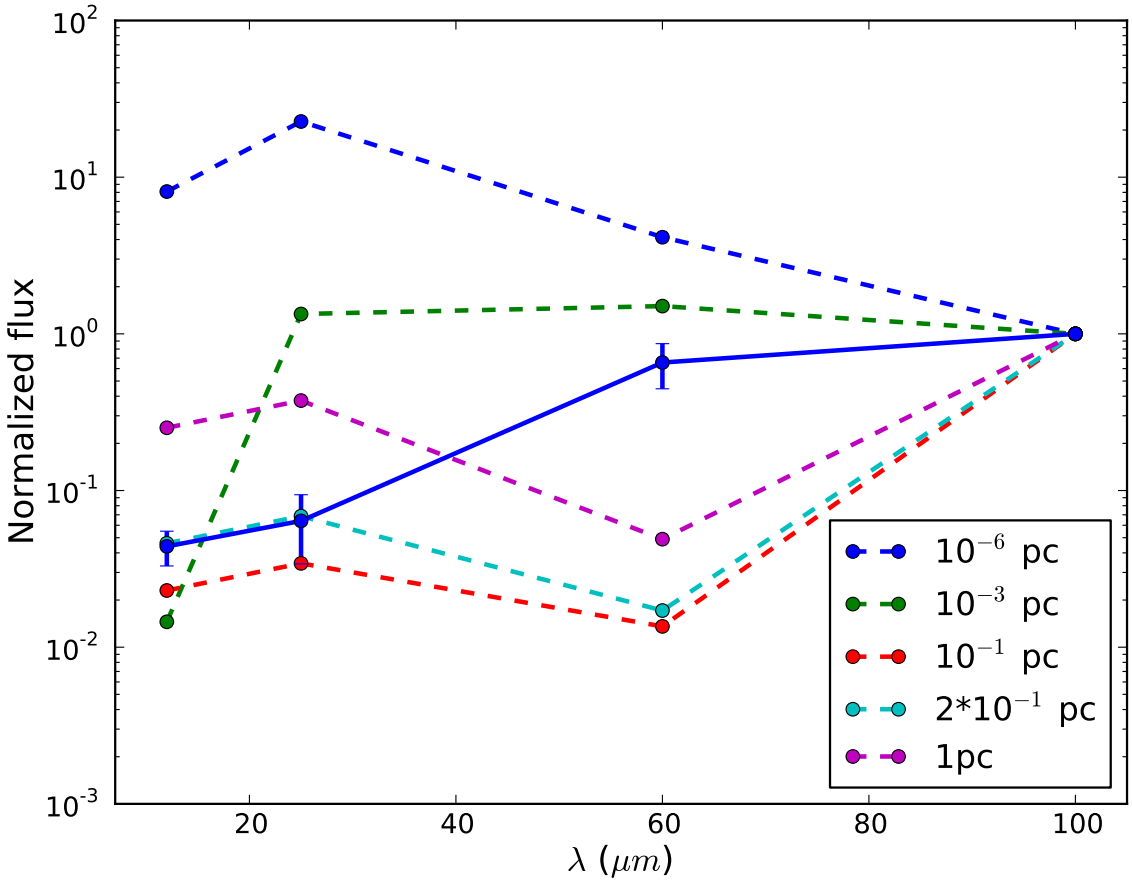

Figure 4.54: Median value of the normalized FDD of the observed clouds (blue) and the simplest theoretical FDD corresponding to a step function density profile. SEDs are plotted for different radius at the step but constant density and step height.

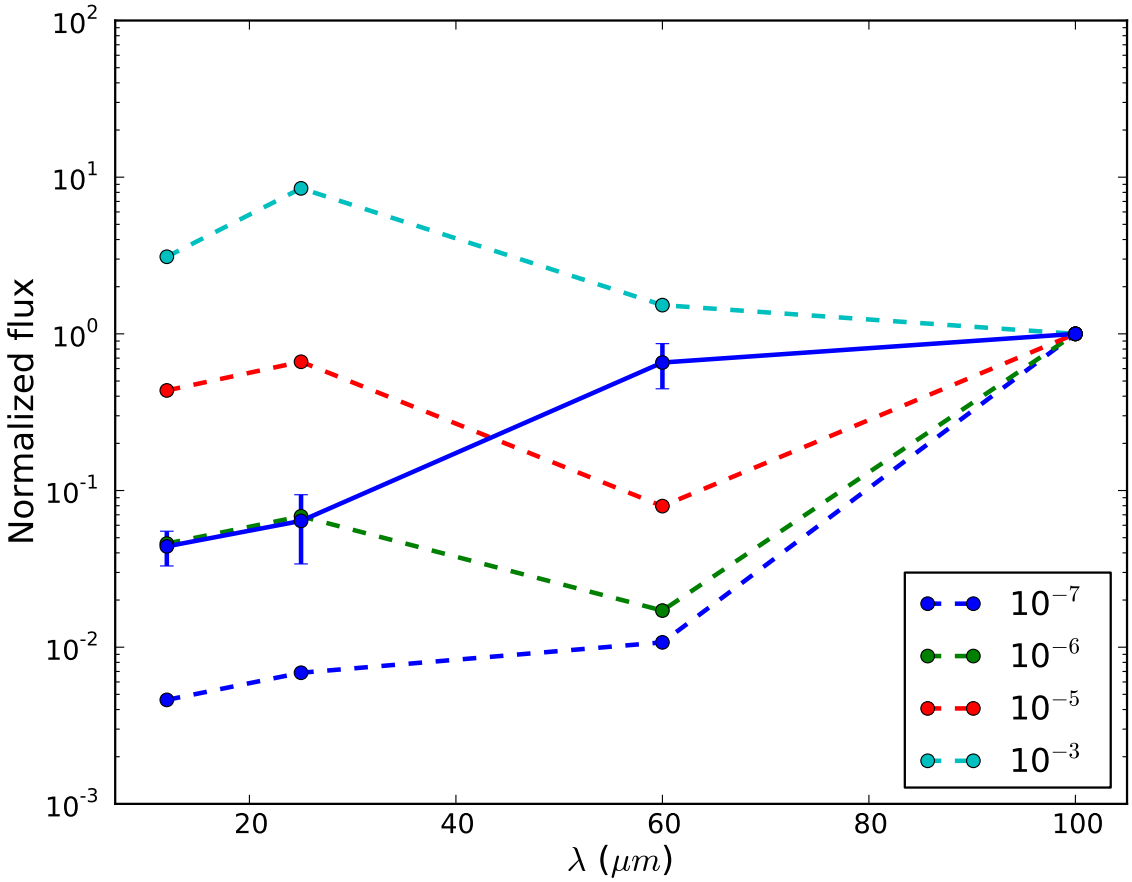

Figure 4.55: Median value of the normalized FDD of the observed clouds (blue) and the simplest theoretical FDD corresponding to a step function density profile. SEDs are plotted for different step height but constant density and step radius.

4.7 Discussion

In this section, we compare all our constructed models and then examine the prospect of a model step function density distribution with a slightly higher internal heating and stellar flux than the value used in other models. Furthermore, we discuss the feasibility of such a model and its significance on the observational data and on the overall star formation processes.

Infrared flux density distribution is very sensitive to gas densities. In the first model scenario, three different uniform gas density clouds are illuminated by a constant stellar flux from one side. The resultant dust temperature distributions for the three clouds follow the same distribution in the scaled units. The scaled dust emissivity distributions show identical curves irrespective of the gas density of the clouds. The observed normalized flux density distribution demands a longer path length for the photons, to produce sufficient far-infrared flux, concomitant with a lower mid-infrared flux. Nevertheless, the formulated models do not match the observed data as the decreasing gas densities shift the modeled FDDs in the same fashion.

Changing the incident stellar flux has a direct impact on the shape as well as the position of the normalized infrared fluxes in the FDD diagram. At a fixed density, a very low flux does not heat up the dust grains to the level that is required to match up with the observations. On the other hand, a high stellar flux heats up the grains to a high temperature, yielding a substantial flux at all wavelengths. Such a tendency in the heating failed to reproduce the observed normalized FDD.

Different gas density distributions along the cloud were tested to simulate the observations, as the first two cases were unsuccessful in reproducing the FDD. A linear density distribution is tested and we found that varying the slopes and intercepts is barely helpful in obtaining the required FDD. The behaviours of two different power law density profiles are investigated by varying free parameters such as the peak gas density, distance at the peak gas density, and the power law index. The modeled FDDs in both cases failed to follow the observed FDD. In all the above trial cases of density distribution, the modeled clouds were unsuccessful in re-radiating effectively at far-infrared wavelengths while keeping a lower mid-infrared contribution. Therefore, we examined the possibility of a step function density distribution by changing the density at the step, distance to the step and the height of the step. The models revealed a completely different and more promising trend in the shape of the FDD curves in comparison with other models. However, none of the models was satisfactory in producing realistic emission from a Galactic H II region cloud.

In all the cases a uniform internal heating of $\approx$13 K is an input parameter to the models. The internal heating contributed most of the long-wavelength flux. If the cloud maintains

a very cold temperature at the interior, it cannot emit effectively at 60 μm and 100 μm from the interior. As a result, flux at 60 and 100 μm will be lower relative to corresponding flux in the real cloud. In order to test whether the internal flux has some influence on the FDD, we artificially varied the flux that provides the internal heating in the step function density distribution. We also examined models that have slight variations in the stellar flux from the adopted value of 10 W/m^2.

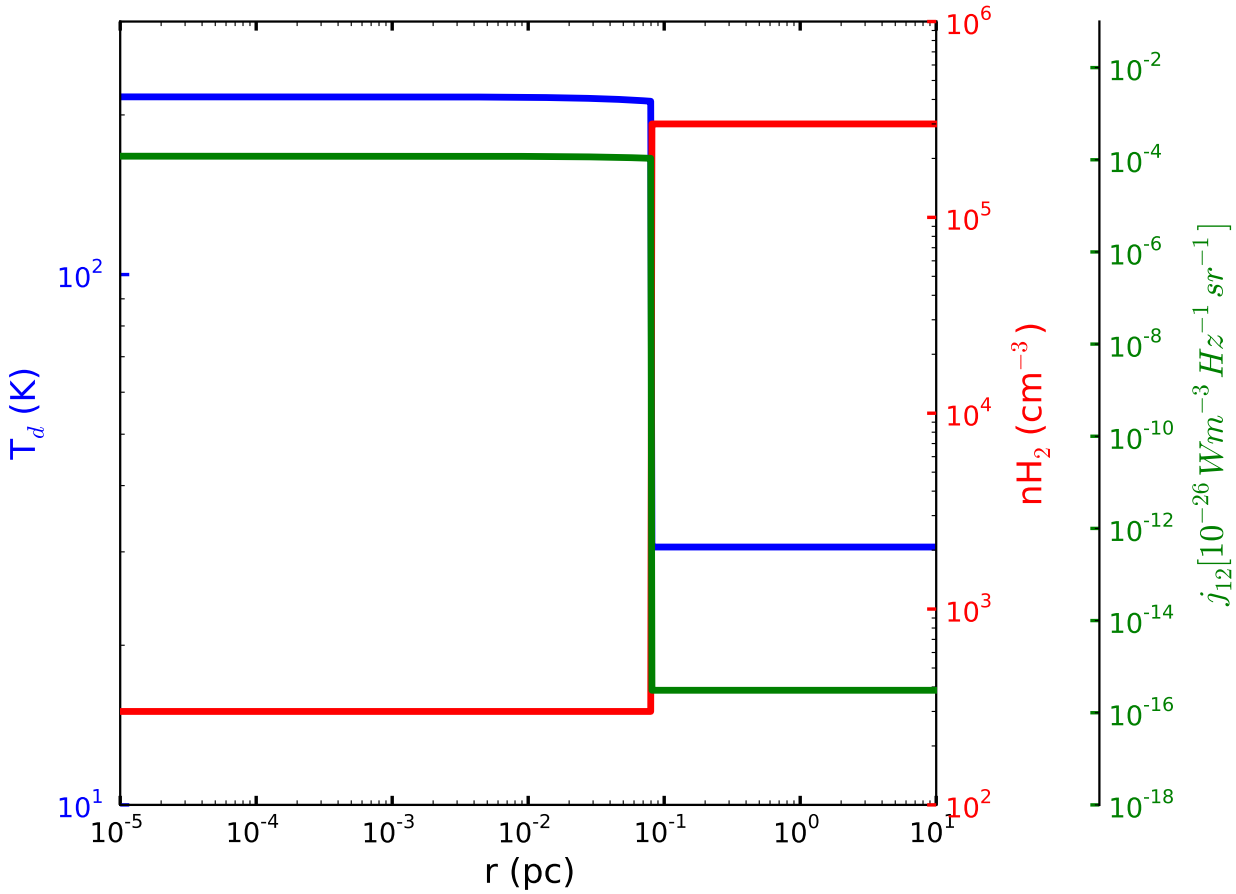

Figure 4.56: Temperature, density and j_{12} plotted against the distance from the cloud edge facing the star.

We adopted a step function gas density distribution with a value of 3×10^5 cm^{-3} at the right cloud edge. The density rises sharply at a distance of 0.08 pc from the hottest cloud layer and then remains constant up to the exterior cool edge. The gas density at

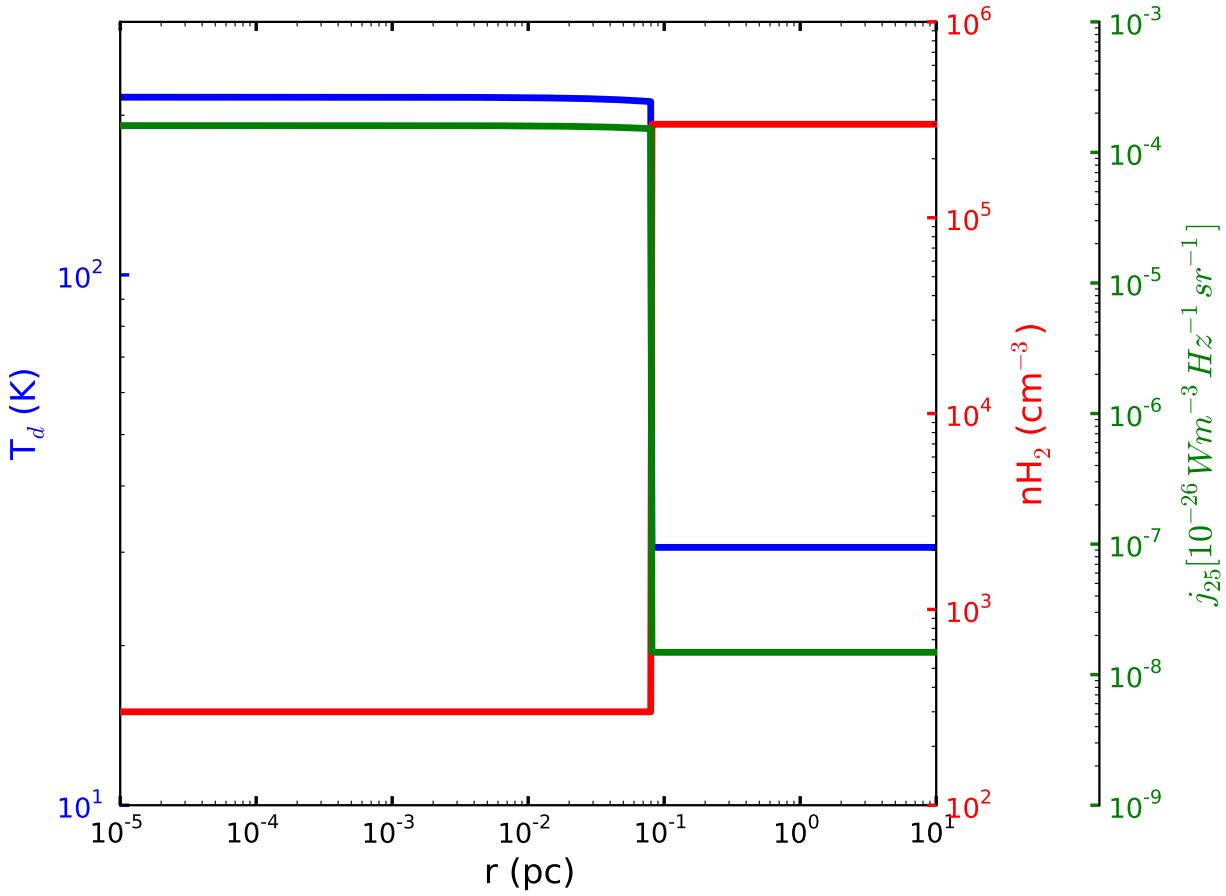

Figure 4.57: Temperature, density and j_{25} plotted against the distance from the cloud edge facing the star.

the hot side of the cloud is lower by three orders of magnitude compared to the density at the cool side. A stellar flux of 12 W/m^2 is impinging on the left side of the cloud and the internal heating contributes a dust temperature of 30.6 K on the right side. The highest temperature attained by the dust grains in this model is 216.4 K. The emissivity distributions at 12, 25 and 100 μm along with the gas density and temperature distributions obtained from this model are shown below (see Figures 4.56, 4.57, 4.58).

One remarkable difference from other models (Cases 1 to 6) is the shape of the 100 μm emissivity distribution. Unlike most other models, the value of j_{100} peaks at high densities (Figure 4.58), indicating more long-wavelength dust emission at deeper regions of the cloud

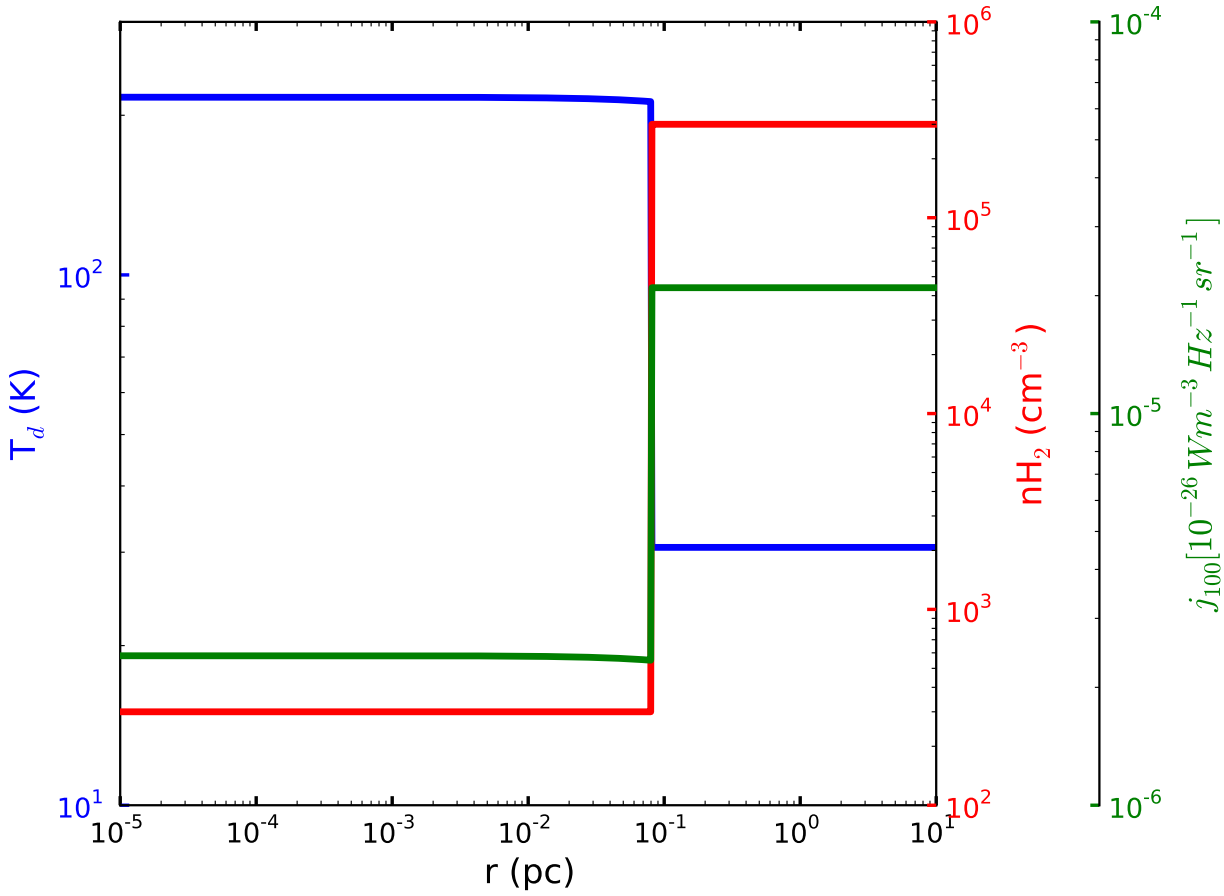

Figure 4.58: Temperature, density and j_{100} plotted against the distance from the cloud edge facing the star.

compared to the less dense hot surface layer. Furthermore, j_{12} and j_{25} do not plunge to very low values in the deeper regions of the cloud as in other models.

The normalized FDD obtained from the model is given in Figure 4.59, along with the observed normalized FDD. From the diagram, we find that the normalized model FDD agrees well with the observed normalized FDD. The modeled step function density distribution is able to provide a reliable estimate of the hydrogen number density, temperature structure and accompanying emissivity profiles in clouds associated with Galactic H II regions.

Increasing the internal heating up to 30 K is in fact artificial; however, this choice

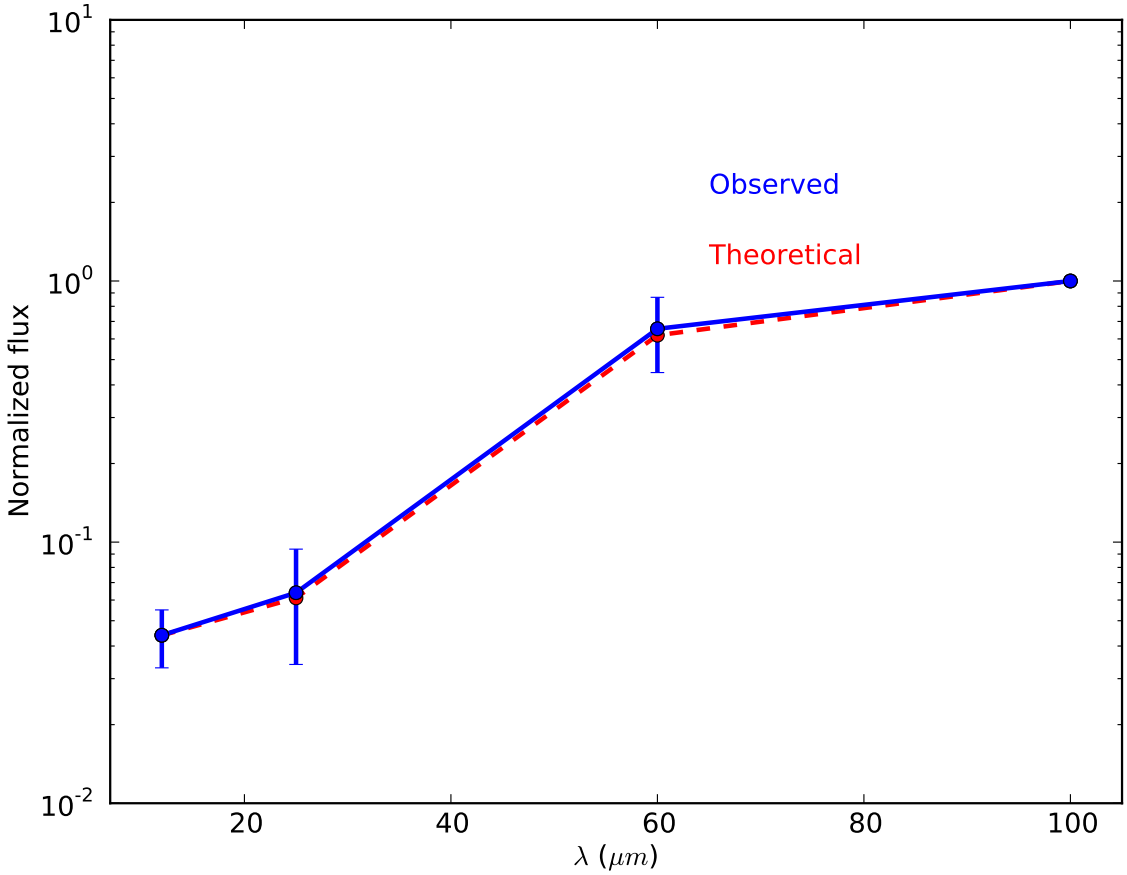

Figure 4.59: Median value of the normalized FDD of the observed clouds (blue solid lines) and the modeled FDD corresponding to a step function density profile with a higher internal heating (red dashed lines) than the one used in other models (Cases 1 to 6).

best matched the IRAS observations. We expect much colder dust than 30 K at the cloud interiors. Nevertheless, the IRAS observations could be reproduced only with a higher internal heating. The presence of some other mechanism which can raise the 60 μm emissivities at the moderately shielded regions of the cloud is speculated.

Grain sizes may have an effect on the model results. The generated models employed the standard MRN distribution which uses spherical grains having sizes ranging from 5 nm to 0.25 μm to calculate the absorption cross sections of silicate and graphite grains. The very small grains responsible for short wavelength infrared emission, shorter than

5nm—the lowest cut-off of the MRN grain size distribution, are not included in the models used in this study. To better represent the short wavelength IRAS emission, we may require grains with sizes down to $\sim$ 0.3 nm [Clayton et al., 2003]. In order to reproduce the infrared emission from PAHs and very small grains, Weingartner and Draine [2001] developed size distributions that account for very small carbonaceous and silicate grains. Size distributions by Weingartner and Draine [2001] reproduce observed extinctions and infrared emission towards regions with different R_v.

The MRN grain size distribution reproduces the observed extinction corresponding to the diffuse regions of the clouds ($R_v \approx 3.1$). Towards, denser regions of the ISM, R_v has a higher value, for example $\sim$ 5.5. The grain size distributions can vary with environments. For example, the small grains present in dense regions of the clouds can coagulate to form large grains. The grains in cold and dense conditions can also form ice mantles, which in turn can change the optical properties of the grains. The size distribution can therefore be modified by the mantle formation and coagulation. The upper cut-off of the Weingartner and Draine [2001] size distributions is $\sim 0.4\ \mu m$ for silicate grains and ranges from around 1 to 10 μm for carbonaceous grains, with more number of large grains toward higher R_v.

A number of other grain size distributions are later developed accounting different observed properties of dust grains. Grain size distributions presented by Zubko et al. [2004] satisfy interstellar extinction, diffuse infrared emission, and interstellar abundance limits. Their model constituents include bare silicates and graphites, PAHs, amorphous carbon, a blend of water ice, organic refractory materials, voids, and different proportions of silicates. Their models are composed of several different combinations of the above components and the lower cut-off grain size in all their models is 0.00035 μm—for PAHs, and the upper cut-off is $\sim 0.9\ \mu m$—for composites. The Weingartner and Draine [2001] size distribution is later revised by Draine and Li [2007] further considering the infrared emission from the Spitzer Space Telescope. Recently developed grain size distributions using PAHs, non-spherical (spheroidal) silicate and graphite grains reproduce the observed interstellar extinction and polarization [Draine and Fraisse, 2009].

The dust grain opacities can be modified in connection with the adopted grain properties such as the chemical composition and the grain size distributions. For example, adding larger dust grains at the upper cut-off of the size distributions can increase the opacity and hence the mass of the clouds since most of the mass of a cloud is located in large grains. Integrating very small grains and PAHs on the lower cut-off levels may result in an increase in the short wavelength IRAS emission.

4.8 Chapter Summary

Knowing the key physical properties such as the gas densities and the dust temperatures is crucial to determining the overall structure of the molecular clouds as well as the influence of such properties on the formation of new stars. In order to compute these parameters, a set of infrared emission models of dusty molecular clouds associated with Galactic H II regions, using radiative transfer through a plane parallel slab geometry, was constructed. The consequences of variations in gas density, impinging stellar flux, and internal heating on the temperature, emissivity, and flux density distribution in the infrared have been inspected. From the study, we can draw the following conclusions:
Clouds near Galactic H II regions are not at uniform densities. Variable values of the external flux in a uniform density cloud cannot simulate the observations. Moreover, clouds with a linear, power law, and step function density distributions are insufficient to reproduce the observed flux density distribution. All the above models could not replicate adequately 60 μm emission, which arises from the moderately shielded cloud interiors. Raising the value of the internal flux, which dominates the opaque interior regions of the cloud, remarkably improved the model and did reproduce the requisite far-infrared flux. It is noted that the role of internal heating is significant in H II region clouds. The physical mechanism which could be responsible for this higher internal heating is considered in Chapter 7.

Chapter 5

SCUBA-2 Observations of Clouds Near Galactic H II Regions

Understanding the physical conditions of the clouds is significant since these clouds are the sites of probable star formation as well as chemical evolution. Sub-millimeter wavelengths are suitable for tracing such conditions. Dust emission at sub-millimeter wavelengths is optically thin and is determined not only by the grain column density and the mass, but also by the grain temperature. In order to derive these physical properties, we use sub-millimeter continuum observations of a sub-sample of Galactic H II region clouds at 450 μm and 850 μm wavelengths with the SCUBA-2 camera.

5.1 Submillimeter Common User Bolometer Array-2 (SCUBA-2)

SCUBA-2 [Holland et al., 2006] is the world's largest sub-millimeter array camera operating on the James Clerk Maxwell Telescope (JCMT), Hawaii, with $8' \times 8'$ square field of view. SCUBA-2 consists of 8 bolometer arrays and each bolometer array consists of 40×32 pixels, with 4 at 450 μm and 4 at 850 μm. Both arrays together constitute 10,240 bolometers. Each SCUBA-2 bolometer element is a new generation sub-millimeter detector—the superconducting transition edge sensor (TES), which measures the temperature rise by absorption of radiation from the astronomical object. The amplification of the detected signals is accomplished by the use of a superconducting quantum interference device (SQUID) coupled to the TES [Robson and Holland, 2007].

SCUBA-2 is different from its predecessor SCUBA in many respects. The primary one is mapping speed: SCUBA-2 can map the sky approximately two hundred times faster

than SCUBA. The detecting (TES) and multiplexing (SQUID) technologies of SCUBA-2 are cutting-edge in the field of sub-millimeter astronomy. SCUBA-2 does not employ any sky chopping and thus does not restrict the size of the sky source. Moreover, SCUBA-2 does not use bolometer feed horns and the presence of a large format array containing thousands of closely packed bolometers moving very fast helps to preserve the large scale structure of the sky source. SCUBA-2 also offers the possibility of different styles and coverages in mapping that best suit the structure of the sky source.

SCUBA-2 employs two main types of mapping modes: Daisy and Pong patterns [1]. If the size of the source to be observed is compact, i.e., less than or equal to $3'$, then a Daisy scan pattern (Figure 5.1) is used. To map larger areas, there are four different Pong patterns available: (1) Pong900 (Figure 5.2), (2) Pong1800 (Figure 5.3), (3) Pong3600 (Figure 5.4), and Pong7200 (Figure 5.5). Each pattern will fully scan a square area in the sky and the scan patterns are named according to their capability to map different areas: a Pong900 scan pattern is able to map $900''\times 900''$ (or $15'\times 15'$) square field on the sky. Similarily, Pong1800, Pong 3600, and Pong7200 patterns can map respectively $1800''\times 1800''$ (or $30'\times 30'$), $3600''\times 3600''$ (or $1^\circ\times 1^\circ$) and $7200''\times 7200''$ (or $2^\circ\times 2^\circ$) square areas in the sky. The figures on the left side represent the telescope track for the respective scan pattern and the figures on the right side denote the exposure time map for a standard observation. The DRA (X axis) and DDEC (Y axis) on the left side maps are respectively the right ascension and declination offset from the map centre in arcsec.

All the Pong maps differ from each other by their scan spacing—the gap between consecutive rows of the telescope tracks on the sky, telescope velocity, and the number of rotations of the field within one integration, which is ≈ 40 minutes. The scan spacing of Pong900 maps is $30''$, whereas Pong1800, Pong3600, and Pong7200 have respectively 60, 180, and 360 arc second spacings in their scan. The telescope velocities for Pong900, Pong1800, Pong3600, and Pong7200 are $280''$/s, $400''$/s, $600''$/s, and $600''$/s respectively. A Pong pattern is rotated after each pass through the pattern which, in turn, increases the number of angles we scan across the source. Thus increasing the number of rotations helps the map maker to produce superior quality maps. However, the number of passes around the pattern within one integration is different for different Pong maps. Within a single integration of ≈ 40 minutes, there are 11 rotations of the field during the $15'$ Pong mapping. The $30'$ and 1° mapping modes make use of 8 rotations of the field. During a 2° scan mapping, the Pong pattern is repeated roughly 4 times.

[1] http://www.jach.hawaii.edu/JCMT/continuum/scuba2/scuba2_obsmodes.html

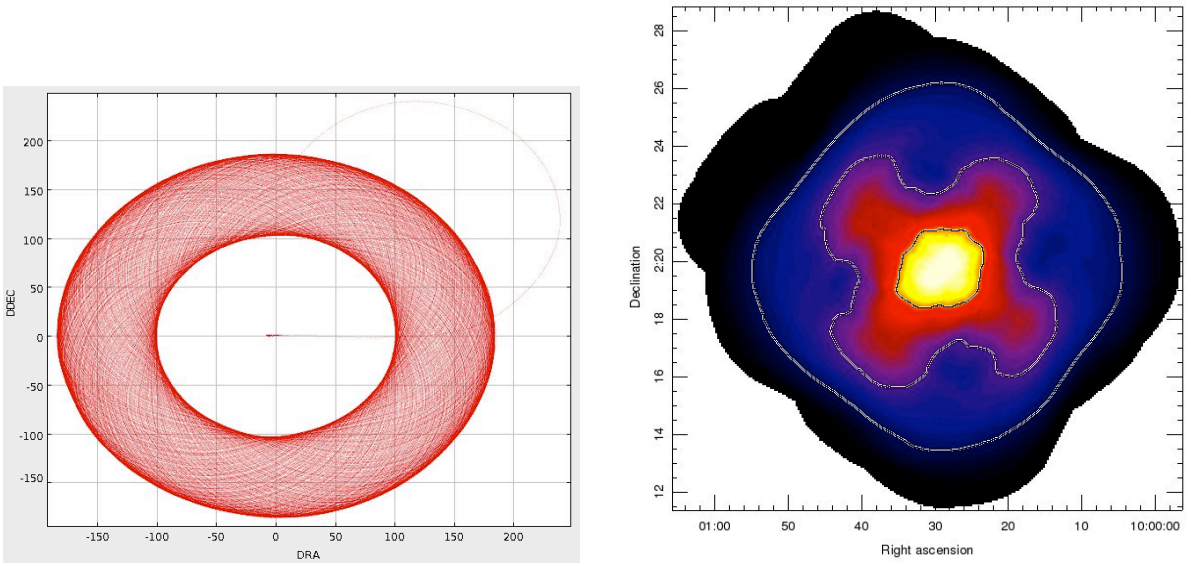

Figure 5.1: SCUBA-2 Daisy Scan pattern [*Courtesy: SCUBA-2 Support Information*[1]].

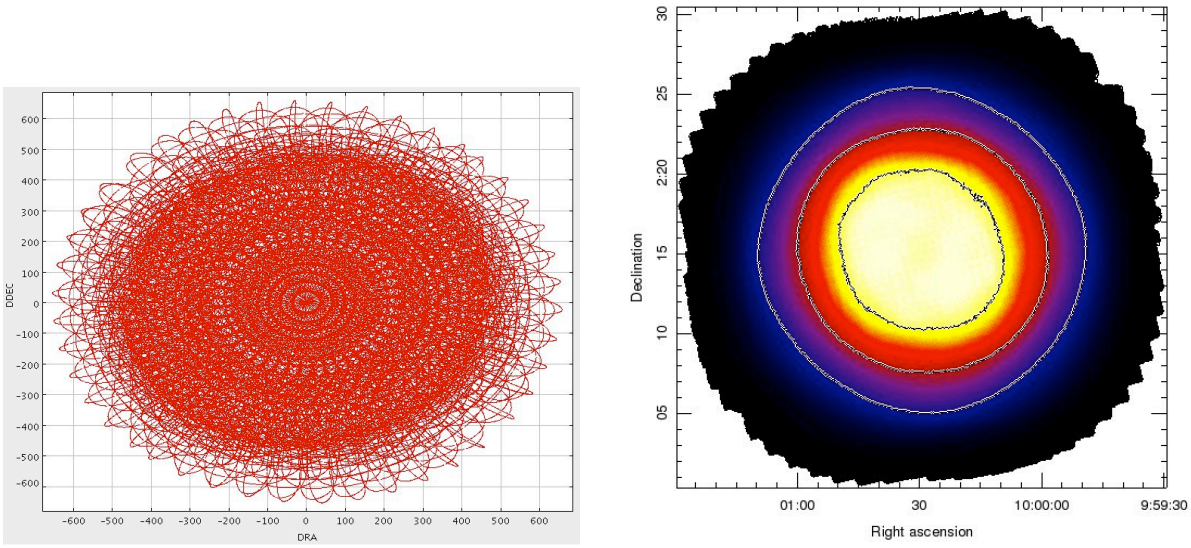

Figure 5.2: SCUBA-2 Pong 900 Scan pattern [*Courtesy: SCUBA-2 Support Information*[1]].

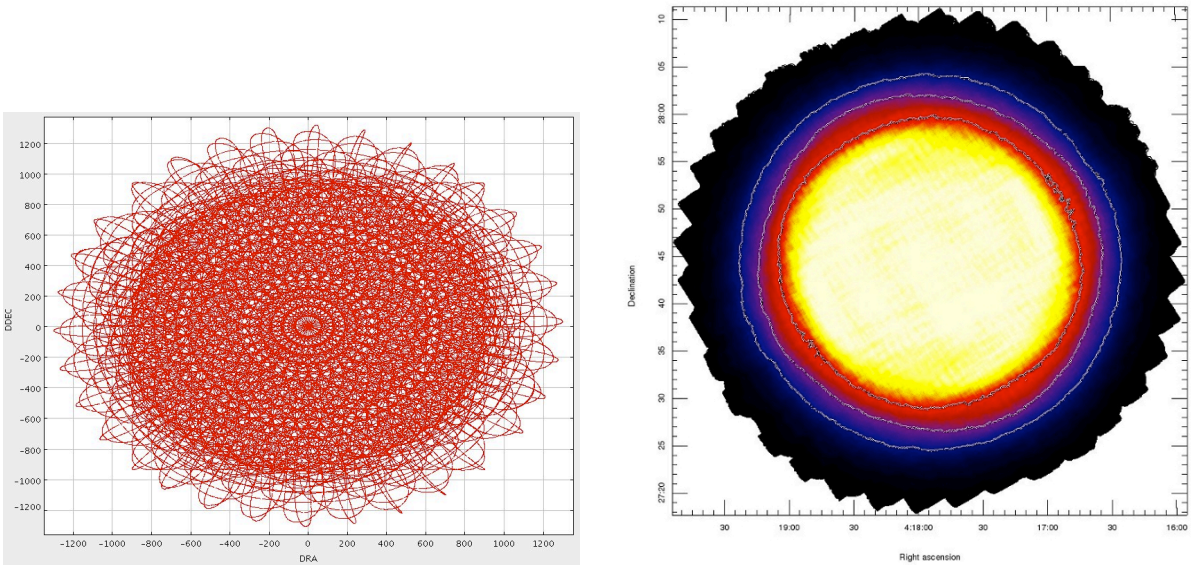

Figure 5.3: SCUBA-2 Pong 1800 Scan pattern [*Courtesy: SCUBA-2 Support Information*[1]].

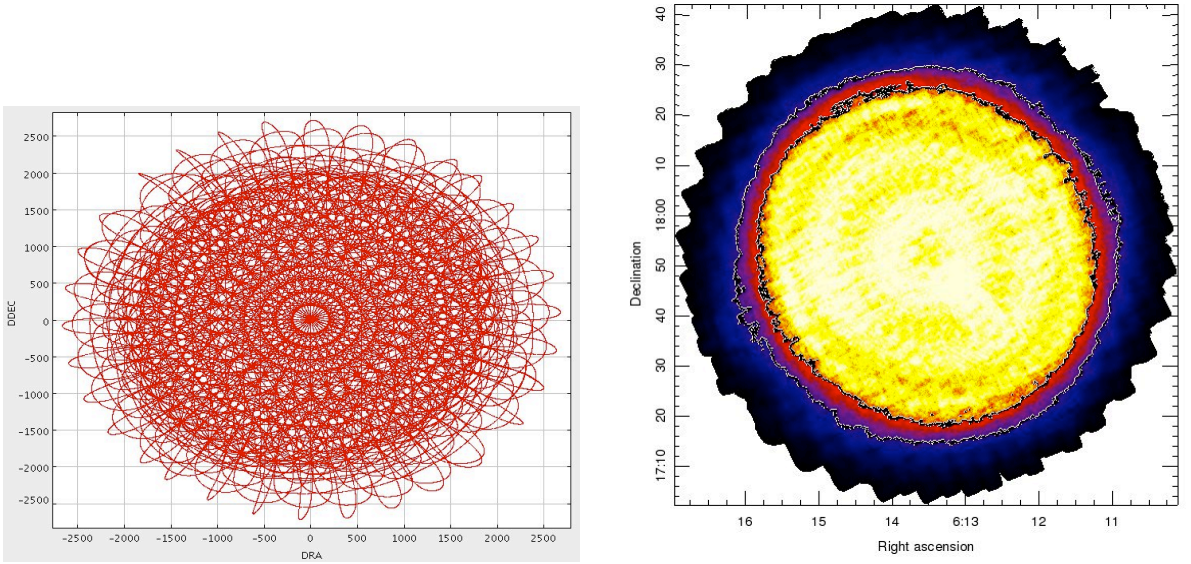

Figure 5.4: SCUBA-2 Pong 3600 Scan pattern [*Courtesy: SCUBA-2 Support Information*[1]].

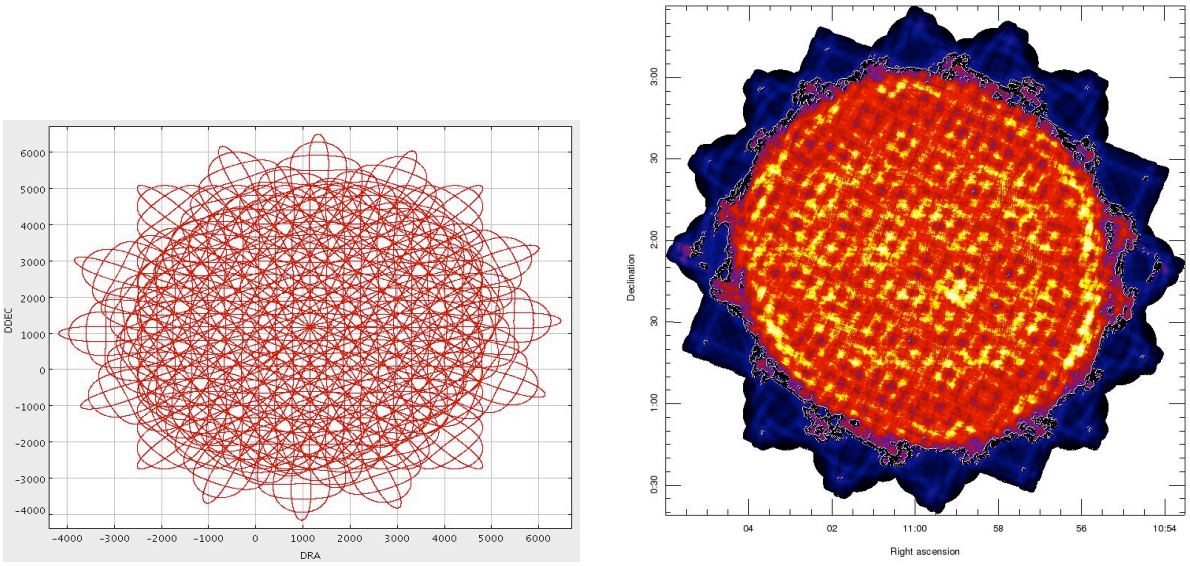

Figure 5.5: SCUBA-2 Pong 7200 Scan pattern [*Courtesy: SCUBA-2 Support Information*[1]].

5.2 Sample H II Region Clouds

In this chapter, we present six sample complexes near Galactic H II regions: (1) S159, (2) S148, (3) S156, (4) S305, (5) S254, and (6) S128. These objects are generally known as Sharpless H II regions and were first discovered and catalogued by Stewart Sharpless [Sharpless, 1959]. Note that all the selected Galactic H II regions are optically visible in the Palomar Observatory Sky Survey (POSS) prints. Since our sample objects are located in the outer Galaxy, there is very little confusion and contamination with foreground or background cold cores along the line of sight. The distances to our target objects are all well measured and are generally a few kiloparsecs away from the Sun. The target objects are all very bright and could be easily mapped using SCUBA-2 since their angular sizes are small. The target objects have been observed at the four IRAS bands and have also been observed at other wavelengths from the optical to centi-meter radio.

5.2.1 S159

S159 is an H II region located in the Cepheus region of the Perseus spiral arm in the outer Galaxy. The kinematic distance to the S159 H II region estimated using CO velocities of the accompanying nebulae and the CO rotation curve of the outer Galaxy is 5.19±0.87 kpc [Fich and Blitz, 1984]. Employing spectrophotometric observations of the star ionizing the H II region S159 [Chini and Wink, 1984] and considering the measured distance of 3.1±1.2 [Fich et al., 1989], the distance to this complex is re-evaluated as 3.10 ±1.20 kpc [Brand and Blitz, 1993]. According to a recent revised distance measurement based on the UBV photometric and spectroscopic data of the exciting star of the S159 H II region, the refined distance to this complex is 2.97 ± 0.31 kpc [Russeil et al., 2007]. In this thesis, we adopt the distance of 2.97 kpc in our further analyses because the latest study [Russeil et al., 2007] utilized high quality spectroscopic and photometric data in their distance measurements. The ionizing star of the S159 H II region is classified as O8.5 Ve [Chini and Wink, 1984] and as O9 V [Russeil et al., 2007].

The cloud is observed in 21 cm continuum radiation and a compact region in S159 is detected [Israel et al., 1973] which is located in roughly the same spot as its optical counterpart from the Red Palomar Sky Survey plates. The cloud has detected emission in CS representing zones of dense molecular gas [Zinchenko et al., 1994]. A comprehensive study of this H II region was carried out simultaneously in atomic, molecular and in radio regimes by Lebrón et al. [2001] who propose that the ionized component is excited by an O9 star. Using neutral hydrogen absorption and emission spectra of the region, the kinematics of the HI envelope were also obtained [Kothes and Kerton, 2002].

5.2.2 S148

The S148 (or S147-9) complex contains three H II regions S147, S148, and S149. These H II regions are excited by three stars with three different spectral types (a) the exciting star of S147 is an A4V star; however this exciting star cannot produce an H II region and therefore S147 is most likely ionized by a star of a different spectral type (b) the exciting star of S148 is an O8V star, and (c) S149 is ionized by a BOV star [Crampton et al., 1978]. All the H II regions are approximately at the same distance of 5.5 kpc. According to a recent spectrophotometric distance estimation [Caplan et al., 2000], the H II regions S148 and S149 are at a distance of 5.6±0.3 kpc away from the sun. In the red Palomar Sky survey plates, S148 and S149 appear as two bright nebulosities: one compact circular nebulosity situated north east, and another extended nebulosity in the south east location separated by less than 2 arc minutes [Felli and Harten, 1981].

The S148 region, exhibiting significant internal motions due to the expansion of the H II region, is the youngest of the three H II regions [Recillas-Cruz and Pismis, 1979] which are evolved from the same parent cloud. The S148 complex is observed in the near-infrared wavelengths, displaying the presence of three near-infrared point sources, and in the IRAS wavelengths, revealing the emission from dust grains [Pismis and Mampaso, 1991]. All the three H II regions of the complex are detected in low resolution radio observations [Felli and Churchwell, 1972] and the H II region S148 has a diameter of 45″ in high resolution radio observations [Fich, 1986; Felli and Harten, 1981] displaying an extended, centrally peaked circular emission.

5.2.3 S156

S156 is an extensive star formation complex located in the Perseus spiral arm, and the field includes the H II regions S156, BFS15 and BFS18. Of these three, S156 is the most studied object. In the red Palomar Sky Survey plates, the S156 nebulosity spans around 2′ in diameter [Cox et al., 1987]. The S156 nebula has a spectacular horseshoe shape in the optical, particularly in the H_α, H_β, [O III] , He I , [N II] [Heydari-Malayeri et al., 1980], and in the radio wavelengths [Fich, 1986; Israel, 1977].

From spectrophotometric observations, the distance to the H II region S156 is calculated as 6.40 kpc [Crampton et al., 1978] and is consistent with the distance of 6.4±2.0 obtained by Brand and Blitz [1993]. The exciting star in S156 is of spectral type O7V ([Heydari-Malayeri et al., 1980] and references therein). The distances to this complex compiled by Chan and Fich [1995] show that the H II region BFS15 is at a distance of 5.11 kpc. However, according to a recent study [Russeil et al., 2007], the photometric distance to the S156 H II region is estimated as 2.87±0.75 kpc and is found to be excited by an O8V star. Note that the complex 110.1+0.0 [Russeil et al., 2007], which is at a distance of

3.0±0.7 kpc and contains the H II region S156, harbours other H II regions such as BFS15 and BFS18. Therefore we select the distance to the complex as the distance to the H II regions BFS15 and BFS18.

Most of the research has focused on the central S156 region and there are only a very few existing observations of the large scale structure of the complex. One is a large area observation covering most of the S156 complex [Joy et al., 1984] in the near, far and millimeter wavelengths tracking down four additional regions of star formation, namely IRS2, IRS3, CO Peak B, and CO Peak C. CO Peak B, C and IRS3 are close to the H II regions BFS15 and BFS18, and BFS16 respectively. Spectrophotometric studies of this complex by the same authors provided the spectral types of the illuminating stars which are several early B stars for CO Peak B and single B0 stars for CO Peak C and IRS3.

5.2.4 S305

The H II region S305 is the least studied object of our sample clouds and is located in the southern outer Galaxy at a distance of 5.20 ±1.4 kpc [Fich et al., 1989]; which is a recalculated distance based on spectrophotometric observations of exciting stars by Chini and Wink [1984]. The cloud associated with this H II region has noticeable CO emission [Blitz et al., 1982], and the region is also identified in the H_α observations of Galactic H II regions [Fich et al., 1990]. An off-centre peaked strong circular emission in the radio wavelengths with a diameter of a $7'$ makes it a bright, more or less round H II region [Fich, 1993]. The associated molecular clouds in S305 also show the presence of four infrared point sources near four CO emission peaks [Hunter et al., 1990] implying the presence of star formation in clouds. Two exciting stars are present in the S305 region [Russeil et al., 1995] and are of spectral types O8.5 V and O9.5 V.

5.2.5 S254

The Sharpless region S254, one of the most studied star forming complexes of our sample, incorporates five individual H II regions: S254, S255, S256, S257, and S258, which are close together in the sky. The complex is the closest of all the six target clouds with a spectrophotometric [Pismis and Hasse, 1976; Moffat et al., 1979] and a kinematic [Fich and Blitz, 1984] distance of 2.5 kpc. The recent revised photometric distance to the S254 complex is 2.46±0.16 kpc [Russeil et al., 2007] and is consistent with distance measurements by other studies. The massive star exciting the H II region S254 is of spectral type O9.5 V and the ionizing stars of H II regions S255, and S257 are of spectral type B0 V [Pismis and Hasse, 1976; Moffat et al., 1979]. However, a recent comprehensive study of the S254 complex in the near- and mid-infrared wavelengths has helped to improve the overall picture

of this star forming complex [Chavarría et al., 2008]. The authors recalculated the exciting star's spectral type and found that S254, S255, S256, and S258 are ionized by stars with spectral types O9.6 V, B0.0 V, B0.9 V, and B1.5 V respectively. The youngest of all these H II regions is S258, which has an age of 0.1 Myr, and the oldest H II region is S254, which was formed around 5.1 Myr ago [Chavarría et al., 2008].

A vast molecular cloud is associated with the S254 H II region complex and is observed in the mid-infrared wavelengths as well as in the radio lines of CO and its isotopes [Evans et al., 1977]. The complex's far-infrared emission peaks are correlated with positions of H_2O maser activity [Wright et al., 1981]. Different physical properties derived from the far-infrared and millimeter line emission [Heyer et al., 1989] suggest the presence of ongoing star formation in the S254 complex. The massive star forming complex of S254 also harbours a large number of young stellar objects, which were detected for the first time in wide area near- and mid-infrared observations [Chavarría et al., 2008]. Using high angular resolution multiline CO data, Bieging et al. [2009] proposed the possibility of a sequential star formation scenario to describe the obtained molecular cloud morphology. A more recent comprehensive multi-wavelength study of the sub-region S255 and S257 [Ojha et al., 2011] laid out the evolutionary stages of the young stellar objects and the nature of the star formation associated with the region.

5.2.6 S128

Located in the Perseus spiral arm in the outer Galaxy [Heske and Wendker, 1982] at a distance of 8.40±1.68 kpc [Caplan et al., 2000], S128 is the most distant member of our six target complexes. The H II region is formed primarily due to the ionization by a very hot central O7V star [Caplan et al., 2000] and has a small round structure. S128 is a very well studied H II region from optical to radio. The DSS red image of the region displays a small round nebulosity. The first radio continuum observations of S128 revealed two radio components [Felli and Churchwell, 1972]: one extended continuum object and an adjacent compact continuum structure. Three different star formation sites are located in the S128 region according to a comprehensive study [Ho et al., 1981] using the Very Large Array (VLA) and the Westerbork Synthesis Radio Telescope (WSRT). In their studies, they discovered an H_2O maser source close to the compact radio source, north of the extended radio structure and indicative of OB star formation. Note that the authors named the compact radio source as S128N and found that this component has a high electron density, excited by an O9.5 zero age main sequence star. In addition, they found a coincidence in location between the extended radio and the optical emission and resolved the extended radio emission into two major components, named S128A and S128B. The S128 nebula, also known as KR23, is also mapped in the high resolution outer Galaxy VLA survey [Fich, 1986], providing a better view of the extended and compact radio sources.

More detailed studies of the S128 region [Haschick and Ho, 1985] using spectral line emission from CO, NH_3 and maser emission from H_2O, disclosed interesting features of the region. The authors noticed a pair of H_2O masers in the vicinity of the S128N. The S128N and the H_2O maser sources were sited on the peak ^{12}CO position. A near-infrared survey of the S128 region [Mampaso et al., 1984] showed two infrared sources, one of which excites the extended radio component and the other one near to S128N but distinct from the S128N's ionizing star. A small area of the complex (part of S128N) is mapped in the dust continuum at 350 μm using Submillimeter High Angular Resolution Camera (SHARC) and the H_2O maser emission is found close to the peak 350 μm dust emission [Hunter et al., 2000; Mueller et al., 2002]. The neutral material towards the peak position of the compact H II region in S128 was studied by analyzing HI absorption and emission spectra [Kothes and Kerton, 2002] and suggests the presence of an expanding atomic hydrogen envelope. Further imaging and photometry of the cloud in the near-infrared combined with spectroscopy and narrow band imaging in the optical regime proposed that both the extended and compact components are evolved from a single natal cloud at two different points in time [Bohigas and Tapia, 2003].

The physical properties of all the sample H II regions are summarized in Table 5.1. The first column lists the names of the H II regions. The second and third columns give the positions of the H II regions. The distances to the H II regions are tabulated in column four. The fifth and sixth columns give the angular and physical diameters of the H II regions. The last column provides the details of the ionizing stars of the respective H II regions. Typical errors on the cloud linear diameter are around 13%, primarily due to the uncertainty in the distance to the H II region.

Table 5.1: Properties of the chosen H II regions: H II region name, distance, angular diameter, physical diameter, and exciting star.

Name	RA (J2000)	Dec (J2000)	d (kpc)	Diameter (″)	Diameter (pc)	Exciting star
S159	$23^h15^m31.2^s$	61°06′55.5″	2.97±0.31	15	0.22	O9 V
S156	$23^h05^m10.6^s$	60°14′57.6″	2.87±0.75	40	0.56	O8 V
BFS15	$23^h04^m42.6^s$	60°04′56.1″	3.0±0.7	–	–	–
BFS18	$23^h05^m47.3^s$	60°24′06.8″	3.0±0.7	–	–	–
S147	$22^h55^m40.6^s$	58°28′02.0″	5.50±0.89	90	2.44	A4 V?
S148	$22^h56^m05.7^s$	58°30′55.4″	5.60±0.3	90	2.44	O8 V
S149	$22^h56^m22.3^s$	58°31′57.1″	5.60±0.3	120	3.30	BO V
S305	$07^h30^m07.0^s$	-18°31′33.5″	5.20±1.40	420	10.6	O8.5 V, O9.5 V
S254	$06^h12^m20.3^s$	18°02′32.5″	2.46±0.16	540	6.44	O9.6 V
S255	$06^h13^m09.5^s$	17°58′40.6″	2.46±0.16	300	3.58	B0.0 V
S256	$06^h12^m39.3^s$	17°56′48.1″	2.46±0.16	120	1.43	B0.9 V
S257	$06^h12^m49.1^s$	17°58′46.1″	2.46±0.16	240	2.86	B0 V
S258	$06^h13^m33.6^s$	17°55′39.7″	2.46±0.16	59	0.7	B1.5 V
S128S	$21^h32^m09.8^s$	55°51′32.2″	8.40±1.68	80	3.26	O7 V
S128N	$21^h32^m13.4^s$	55°53′38.3″	8.40±1.68	14.2	0.58	O9.5

5.3 Observations and Data Reduction

5.3.1 SCUBA-2 data

We observed the complexes S159, S148, S156, S305, and S254 as a part of SCUBA-2 guaranteed time project M11BGT01. A sixth complex S128 was observed as a part of the project M12AC10 entitled 'Cold Dust Near Hot Environs'. The first three observations employed a $15' \times 15'$ area in the PONG900 mapping mode in the band 1-2-3 weather. The last two observations made use of the $30' \times 30'$ PONG1800 mapping mode in order to capture their extended features. There were 3 integrations of the S159 field simultaneously at 850 and 450 μm whereas the complexes S148 and S156 had only 1 integration each. Note that one integration corresponds to ≈ 40 minutes of mapping time without overheads. The JCMT beam sizes at 850 μm, and 450 μm are $14.24''$ and $9.39''$ respectively. At 450 μm in particular, optical effects of the telescope show that the error beam is large and is not gaussian. Consequently, this results in an effective full width at half maximum (FWHM) of $9.39''$ that is much broader than the standard FWHM at 450 μm—$7.5''$, which is the approximate FWHM of the fit to the centre of the beam (diffraction limit of the beam at 450 μm wavelength). For S305, S254, and S128, we used the standard JCMT beam sizes.

The SCUBA-2 data were reduced using the dynamic iterative map maker, DIMM [Chapin et al., in prep] which is a part of the sub-millimeter user reduction facility, SMURF [Jenness et al., 2011] software package.

Unusually large negative valued areas (negative bowls) were present around the bright extended regions of the observed clouds. These are most likely software artifacts and underline a fundamental lack of sensitivity to large scales by SCUBA2. Note that all our target clouds' bright extended areas suffer from the presence of negative bowls. The negative bowls around sources were reduced by supplying an externally generated zero mask, which is a S/N based masking. To provide an external zero mask to the mapmaker, we first processed the data using the mapmaker and then created a mask based on thresholding the SNR map. For all our sources except S148, we employed a SNR threshold of 3.0. We used a SNR threshold of 2.0 for S148 in order to retrieve its weak 450 μm emission. The resultant maps were smoothed using a FWHM gaussian of $5''$. From the smoothed mask we took off extra pixels by visually selecting the value of the faintest pixel. The resultant map, known as the zero mask, is used to re-process the data, and is found to diminish the presence of negative bowls.

The final maps obtained after zero masking were calibrated using flux calibration factors (FCFs) obtained from planet data of the respective observation dates. We derived the FCF using SMURF and the pipeline for combining and analyzing reduced data, PICARD[2],

[2]http://www.oracdr.org/oracdr/PICARD

which is part of the ORAC-DR [Jenness and Economou, 1999] pipeline and has the same infrastructure.

5.3.2 Primary calibrators—Mars and Uranus

The FCFs for the object S156 were derived at both wavelengths using the primary calibrator Mars on the same night of the science observation. Uranus was also available as a primary calibrator on the observation date. Due to severely bad focusing and atmospheric effects in the Uranus observation in the early evening hours of the observation date, we selected a late night Mars observation to derive the FCF. The maps of Mars obtained from the observations are shown below (See Figure 5.6 for the 850 μm and Figure 5.7 for the 450 μm Mars images). The images display some features due to surface imperfections of the JCMT dish; the focal length of the dish and panels are not exactly the same. The large ring visible in both maps is due to scalloping of the panels. The patches in the scalloping ring could be artifacts due to the scanning and also would indicate some azimuthal patterns in the dish.

Note that there are also standard peak FCF values available from nearly 500 observations at both wavelengths, derived from the arcsecond FCF and the empirical beam area [Dempsey et al., 2012]. The FCFs for S159 and S148, which were observed on the same day, obtained from both Mars and Uranus, disclose large variations from the standard value especially at 450 μm. For the calibration particularly at 450 μm, the diurnal variation due to temperature changes is a factor. The 450 μm beam shape therefore is highly susceptible to changes in focus and atmospheric instability. Spherical aberrations due to thermal gradients will cause the peak flux to drop. However, the integrated flux should be less variable. These features arise specifically early in the night and a bit after sunrise. We therefore selected the standard FCFs to calibrate S159 and S148 data.

In finding the FCFs of S305 and S254, we considered two different observations of the planet Mars acquired on the same night. We adopted the FCF derived from the early night Mars observation for calibrating the short wavelength data. For calibrating the long wavelength data, we chose a Mars observation near midnight. Note that we selected two separate observations of the same calibrator mainly because each calibrator observation failed to supply both the FCFs within the standard limits. For the cloud S128, we selected the standard value at 450 μm and used early morning Uranus observations to derive the long wavelength FCF. We excluded the early morning observation of Uranus at 450 μm as well as the late night observations of Mars and secondary calibrator CRL2688 at both wavelengths since they were ineffective in reproducing the FCF within the standard limits.

The complexes S159 and S148 were observed on November 14, 2011 and the complex S156 was observed on January 28, 2012. The total integration time of S159 was about

2.22 hr. For the complexes S148 and S156, the integration times were 44.45 minutes each. The optical depth at 225 GHz (τ_{225}) obtained from CSO (Caltech Submm Observatory) at the start and the end of the observation of S159 indicated that the observation was in the weather band 1. The 186 GHz optical depth from JCMT water vapour monitor (WVM) ranged from 0.06 to 0.08 between the start and end of the observation of S159. The S148 observation shared the same τ_{225} value as that of the S159 observation and the 186 GHz JCMT WVM value varied between 0.08 and 0.09. For S156, the CSO τ values were 0.13 and 0.07 respectively at the start and the end of the observation, and the JCMT WVM retained a constant value of 0.06. All the maps at 850 μm (see Figures 5.12, 5.14, 5.16) show a 3σ detection. At 450 μm, the detection of large scale features is determined entirely by the integration time employed in the observation as well as the weather band at the time of observation. Note that in weather band 2/3, the optical depth of the atmosphere on the line of sight is large and variable especially at 450 μm. For example, see the difference in the large scale structures (Figures 5.13, 5.15, 5.17) due to different integration times and variations in the weather band. Moreover, the 450 μm maps also show some large scale structures not associated with the source, especially at the edges, and probably caused by the large scale surface errors of the dish.

The complexes S305 and S254 were observed on the night of 14th March 2012 with a total integration time of 2.06 hr for S305. The observation of S254 was incomplete, but found to contain important information about the astronomical object, and therefore we included this object in this thesis. Both observations employed $30' \times 30'$ PONG1800 mapping mode with τ_{225} and 186 GHz JCMT WVM value of 0.03 at the start and the end of the observations. Cloud S128 was observed on 23rd May 2012 for 1.4 hours in weather band 1 in the PONG1800 mapping mode.

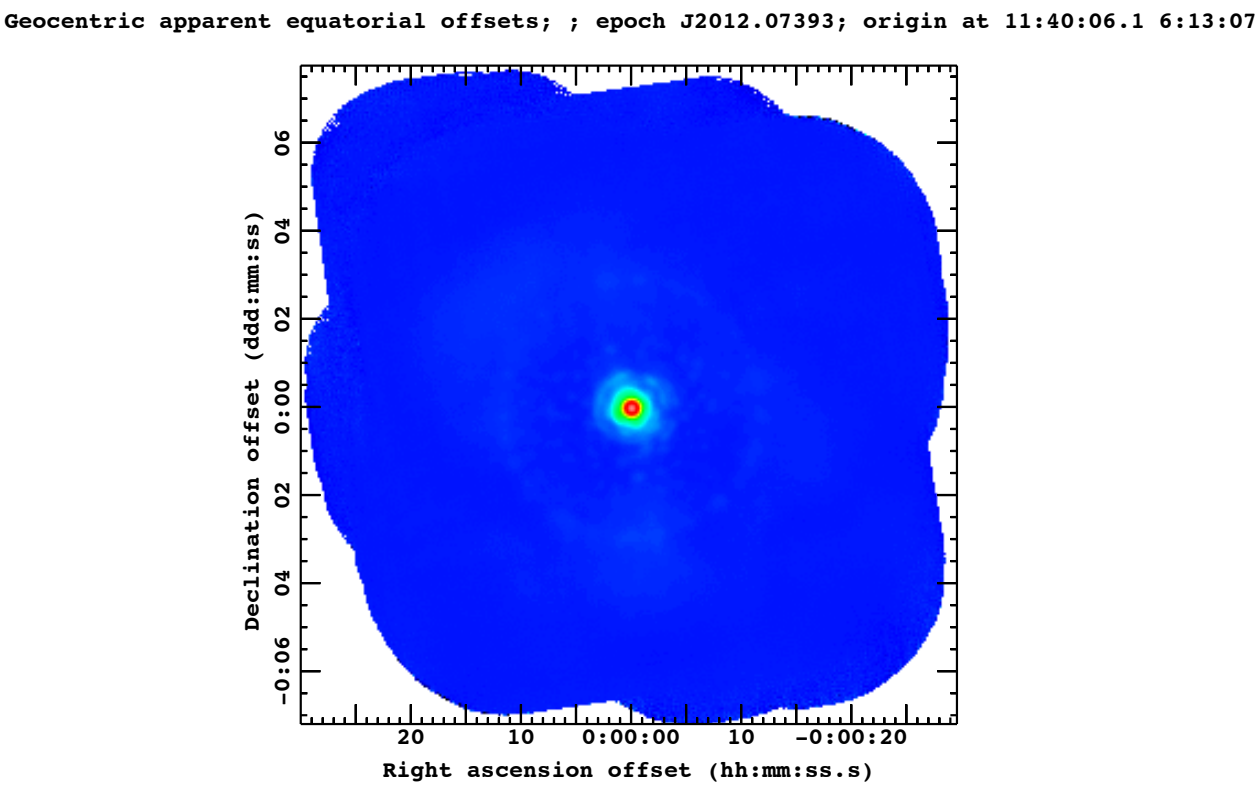

Figure 5.6: Primary Calibrator Mars; SCUBA-2 850 μm image.

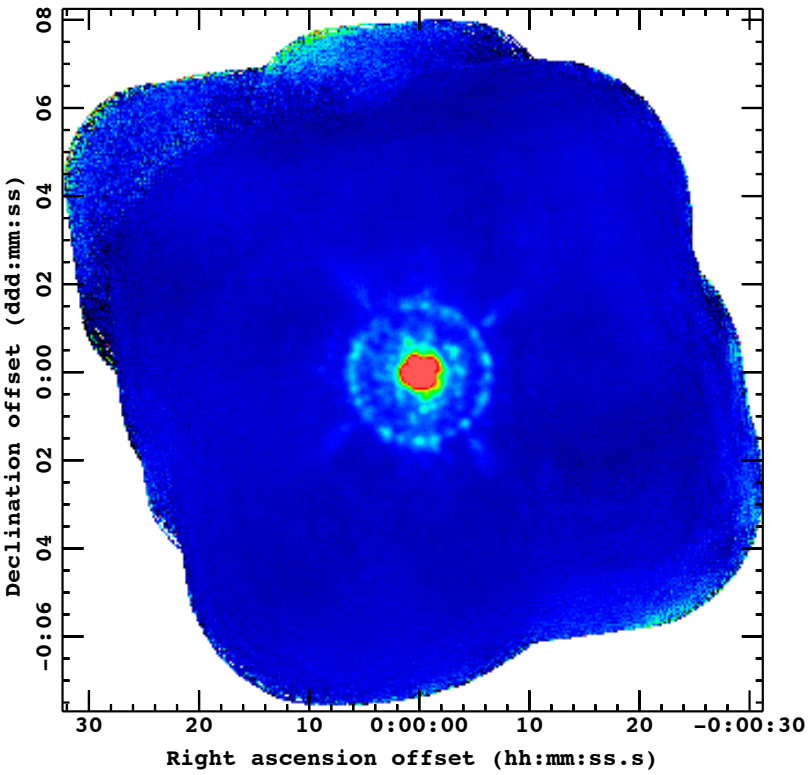

Figure 5.7: Primary Calibrator Mars; SCUBA-2 450 μm image.

5.3.3 Background

In this section we examine the role of background on the SCUBA-2 data. We selected the large area PONG1800 map of the cloud S305 at 850 and 450 μm to analyze the contribution of the background flux on the S305 emission. Moreover, being a large area map, the S305 P1800 mapping field could provide sufficient regions without any source emission, although large-scale filamentary structures were visible in parts of the map.

The mean background distribution of the S305 map field at 850 μm is shown in Figure 5.8 (left). The X-axis of the figure represents the mean distance from the map centre in arc minutes and the Y-axis represents the mean background value in Jy/beam. Near the map centre, a spike in the flux is seen and is probably due to contamination of the background flux by parts of the source flux. Note that there were pixels with negative values randomly distributed in the map that could be caused by artifacts in the data reduction. Many of the apertures selected for background calculation therefore yielded values below zero. When we move towards larger distances from the map centre, the mean background fluxes approach positive values. At the edges of the maps, especially near $25'$, the background emission is the highest and is most likely due to reduced integration time. Since each Pong map is defined to be a square, the edges are poorly integrated and therefore are noisy. Thus, on average, the background emission values are close to zero and therefore, we did not take in to account the contribution due to background in the S305 source emission. The background standard deviation distribution at 850 μm for the same cloud is plotted in Figure 5.8 (right). The error retains a constant value up to around $20'$ from the map centre and then begins to increase till the edge. The mean background values at 450 μm show much more variability than the corresponding values at 850 μm (see Figure 5.9-left). The background standard deviation, however, maintains a constant value up to around $20'$ from the map centre, and then increases (Figure 5.9-right) up to the map boundary.

In all the target fields of our study, the contribution from the mean value of the background on the source flux is computed to be very low and is neglected in further calculations. Typical on-source signal, especially at the fainter extended regions of S305, is 0.06 Jy/beam at 850 μm and 0.21 Jy/beam at 450 μm. Note that the absolute value of the mean background emission in S305 is a factor of around 22 (at 850 μm) and 24 (at 450 μm) times smaller than the faint extended on-source emission. For all the target objects, the ratio of the faintest on-source signal to the mean background on average is around 22 at 850 μm and 10 at 450 μm.

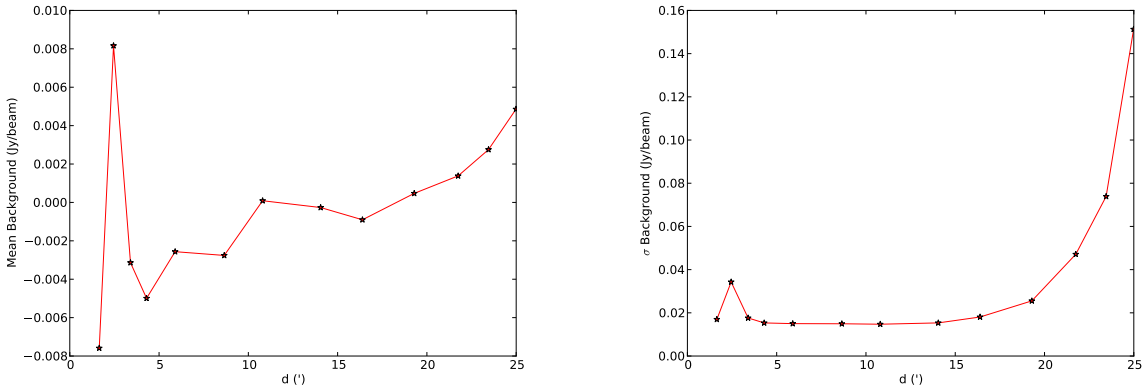

Figure 5.8: S305–Background mean (left) and standard deviation (right) distributions at 850 μm.

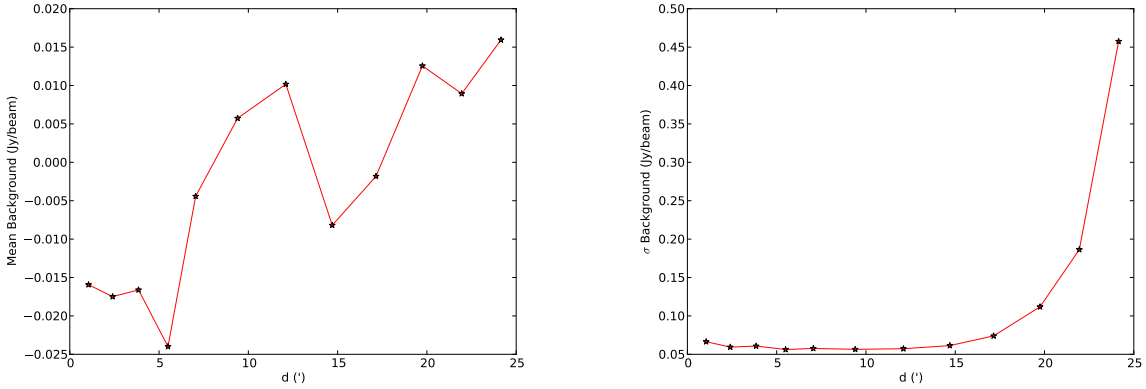

Figure 5.9: S305–Background mean (left) and standard deviation (right) distributions at 450 μm.

5.4 Properties of the Dust

Since dust emission at sub-millimeter wavelengths is optically thin, it is a good tracer of the mass which in turn is dependent on the grain temperature. In order to derive these physical properties, we made use of the obtained surface brightness maps of the clouds from SCUBA-2 at 450 μm and at 850 μm. In this section we describe the physical properties of the clouds that can be derived using the observed sub-millimeter dust emission maps.

5.4.1 Temperature distribution

One can derive a pixel-to-pixel dust colour temperature map of the clouds by taking the ratio of 450 and 850 μm observed surface brightness maps. Before constructing the ratio maps, we first smoothed the 450 μm SCUBA-2 map to the 850 μm resolution of the JCMT beam using a symmetrical Gaussian point spread function to roughly match the Gaussian main beams at both the wavelengths. The error beams, however, are not taken into account in matching the fluxes at two wavelengths. The ratio of the 450 and 850 μm data is calculated using the formula

$$\frac{S_{450}(Jy/beam)}{S_{850}(Jy/beam)} = \left(\frac{850}{450}\right)^{3+\beta} \frac{\exp(17K/T_{dust}) - 1}{\exp(32K/T_{dust}) - 1} \tag{5.1}$$

[Kramer et al., 2003].

The above flux ratio is derived from the 850 μm emission map and the beam smoothed emission map at 450 μm, assuming that the measured flux at both wavelengths is due to thermal emission from optically thin dust grains and is dependent on the dust emissivity index and temperature. In all the temperature maps, the distribution is derived by assuming a constant value for the dust emissivity index β. Note that the cloud S148 lacked a good detection at 450 μm and so we were unable to provide a detailed dust temperature map for this cloud. To derive the dust physical properties, we considered a β value of 2, which is considered to be the standard value at sub-mm and mm wavelengths [Draine and Lee, 1984]. The effect of varying emissivity index is discussed in Chapter 6 in order to learn about the influence of β on the physical properties of the clouds.

The variations in the dust temperature with the flux ratio values for different values of β, are plotted in Figure 5.10. A 20% uncertainty is added to the flux ratio values and the shaded regions represent the errors in the resulting temperatures. Note that the errors are very rapidly growing with increasing dust temperature, which causes convergence problems in the numerical algorithms of error estimation. The shaded regions are truncated at the point where the errors could not have been numerically calculated. For the highest β ($\beta = 2.0$), the temperatures vary slowly with the flux ratio. However, when the flux ratio

attains a value of 10.6, the resultant upper limit on the dust temperature exceeds 10^3 K. For a lower value of β, this trend occurs at even much lower flux ratio values: below 7.7 (for $\beta = 1.5$ case) and below 5.6 (for $\beta = 1.0$ case).

If $\beta = 1$, then the flux ratio values must be below 5 to get dust temperatures less than ∼20 K—the temperatures expected for colder dust. For higher flux ratios, we require higher values of β to achieve temperatures below 20 K. For a β of 1.5, the grains attain temperatures of 20 K at around a flux ratio of 7. If the flux ratio values are again high (for example, 10) we must use still higher values of β (for example, 2) to get temperatures of any dust. If the 450/850 flux ratio values exceed ~ 11, we require β values above 2 to get any dust temperature.

The mean flux ratio values of all the observed complex fields range from around 3 to 8 with a small scatter. For example, the observed flux ratio values of one of the mapped field S305 is shown in Figure 5.11, which has a mean of 3 and a standard deviation of 0.8.

5.4.2 Optical depth distribution

Cloud optical depth is calculated by assuming that the dust emission is optically thin at SCUBA-2 wavelengths. The 850 μm map (which is in units of Jy/beam) is selected to calculate the beam averaged optical depth. The beam solid angle can be derived from the FWHM beam width of the telescope. The JCMT telescope has a gaussian beam profile, and the gaussian function can be related to the FWHM beam width by the equation

$$G(x) = \exp\left(-x^2/2x_0^2\right). \tag{5.2}$$

The quantity x_0 is related to the FWHM beam width (x_b) by the relation

$$x_0 = \frac{x_b}{\sqrt{8\ln(2)}}, \tag{5.3}$$

and the solid angle of the beam can be written as:

$$\Omega_b = 2\pi \int_0^\infty G(x) x \, dx, \tag{5.4}$$

i.e.,

$$\Omega_b = 2\pi {x_0}^2 = \frac{\pi x_b^2}{4\ln(2)}. \tag{5.5}$$

The beam area in steradians can therefore be written as

$$\frac{\Omega_b}{sterad} = \frac{\pi}{4\ln(2)} \frac{{x_b}^2}{''^2} 2.350 \times 10^{-11} \tag{5.6}$$

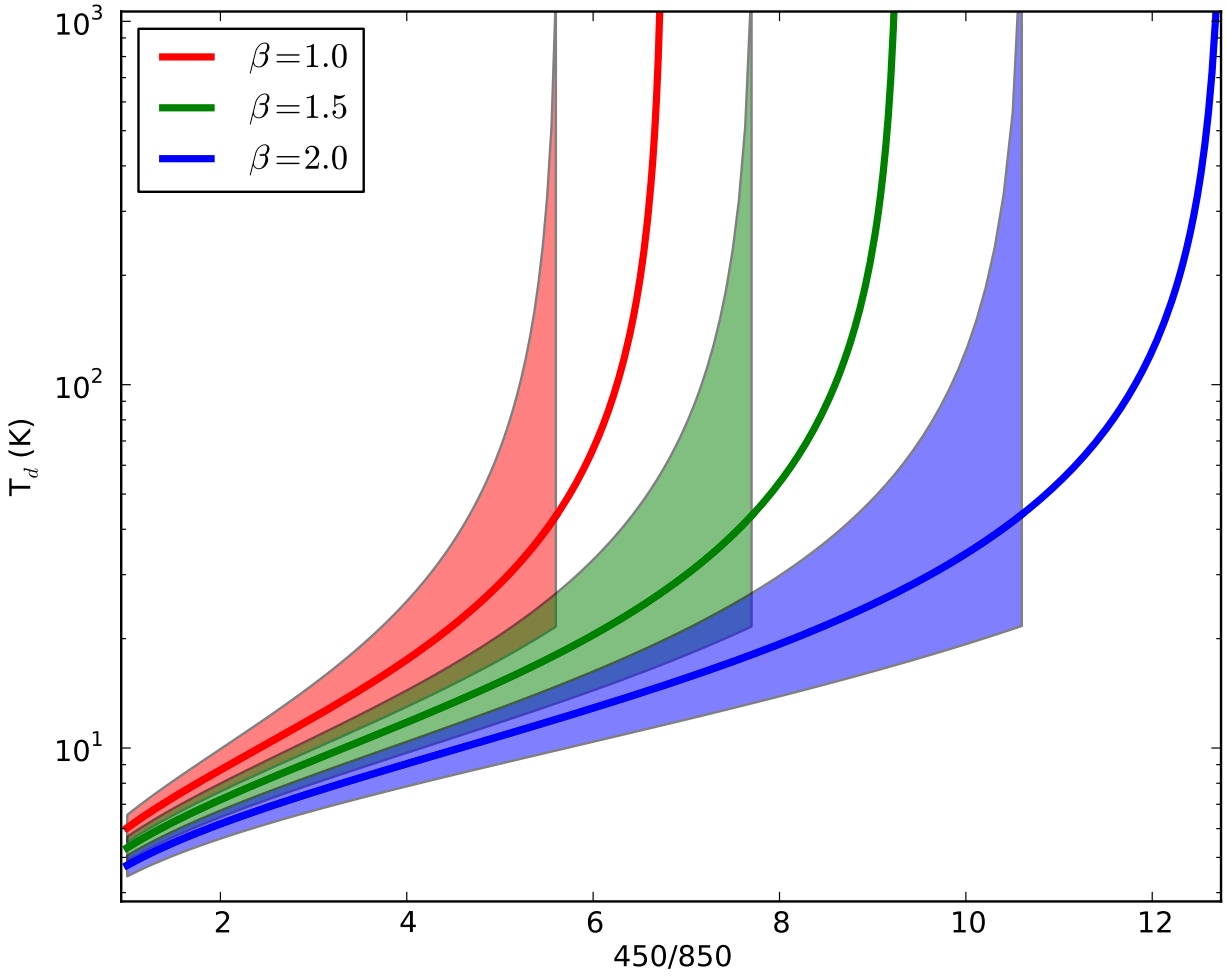

Figure 5.10: The relationship showing the dust temperature vs. 450 to 850 μm flux ratio for different values of β. The red, green, and blue solid lines correspond to the cases where $\beta = 1.0, 1.5$ and 2.0 respectively. The shaded regions represent the respective uncertainties in the dust temperatures.

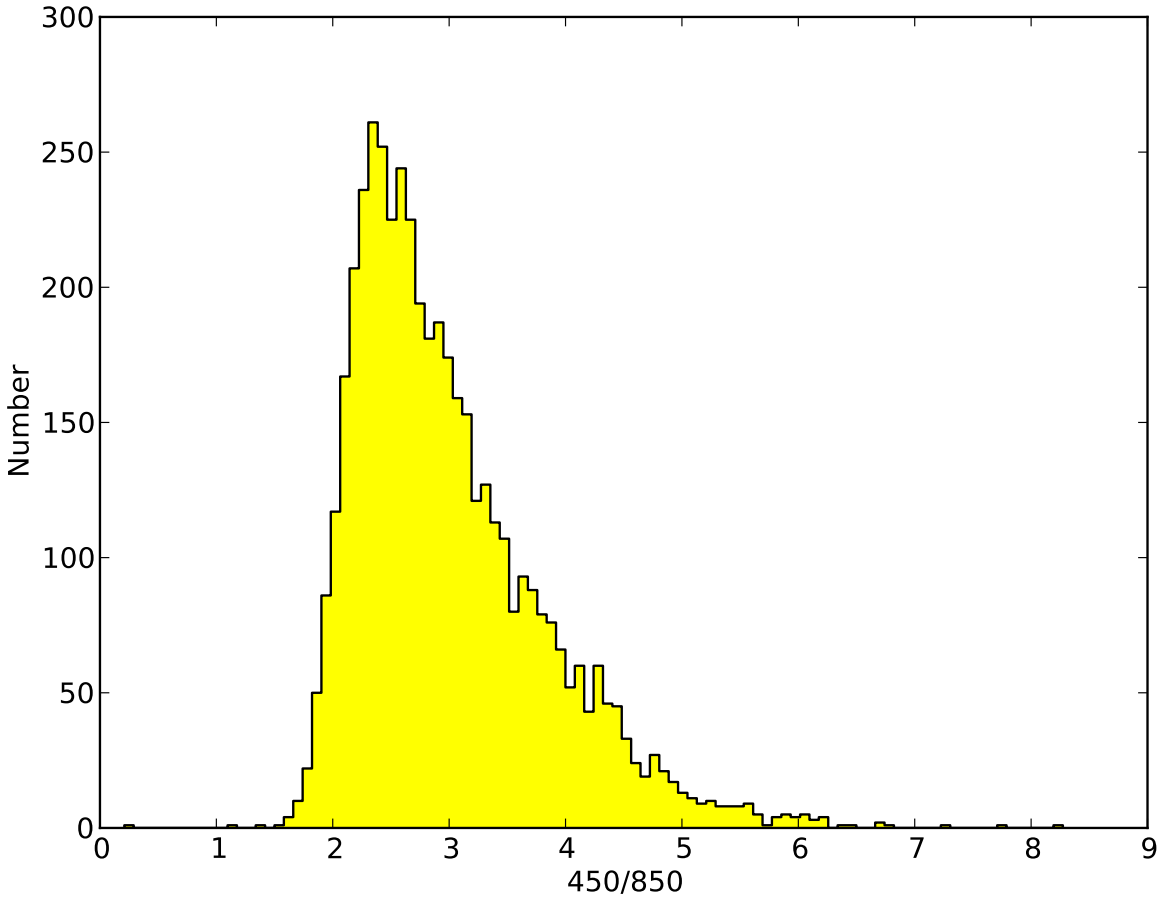

Figure 5.11: The observed 450/850 flux ratio histogram of one of the mapped field, S305. Y-axis represents the number of pixels in the mapped field.

where the last term is obtained from the conversion of $1''$ to radians.

Using the 850 μm flux density, the beam area at 850 μm, and Planck function at 850 μm ($B_{850\mu m}$), we can derive the optical depth at 850 μm (τ_{850}):

$$\tau_{850} = \frac{F_{850\mu m}}{\Omega_b B_{850\mu m}(T_d)}. \tag{5.7}$$

5.4.3 Column density and visual extinction distribution

Since thermal emission from dust at sub-millimeter wavelengths is optically thin, due to the declining dust opacity with λ, sub-millimeter dust emission can follow high column densities and the column density of hydrogen (H) from 850 μm observations can be derived directly from the optical depth using the formula

$$N_{H\,850} = \frac{\tau_{850}}{\kappa_{850} \mu m_H}, \tag{5.8}$$

where κ_{850} is the mass absorption coefficient, the opacity per unit mass column density, at 850 μm. We adopt κ_{850} =0.01 cm$^2/g$ (which includes the assumed gas-to-dust ratio of 100) in the column density calculations of all our target objects. The quantity μ is the mean molecular weight of the cloud material, and m_H is the mass of a hydrogen atom. The measured column density is proportional to the flux at a particular wavelength and the temperature of the dust.

The standard value of the gas-to-dust mass ratio in the Milky Way ISM is approximately 100, however, this ratio depends on the metallicity. Towards the outer Galaxy, the gas-to-dust ratio approaches higher values due to lower metallicity. Note that in low metallicity galaxies, the ratio reaches $\sim 10^3$- 10^4 [Draine et al., 2007]. Properties of the distant clouds, such as S128, will be affected by such variations in the metallicity; a higher gas-to-dust ratio in S128 can increase the gas mass of the whole complex. However, we do not have the exact values of the gas-to-dust ratios at the sample cloud locations, and therefore, we selected the standard Galactic ISM value in all our calculations.

The column density of the interstellar material is a measure of the visual extinction A_v, which is the photometric V band extinction at 0.55 μm, along the line of sight. Furthermore, A_v is connected to the optical total-to-selective extinction ratio R_v by:

$$R_v = \frac{A_v}{E(B-V)} \tag{5.9}$$

R_v is the term connecting the extinction and reddening, and is dependent on the environmental conditions such as the dust grain properties, along the line of sight. For example,

sight lines through diffuse, low density, ISM in the Milky Way are characterized by an R_v of 3.1, while those through dense clouds are usually represented by R_v from 4 to 6 [Mathis, 1990]. The term $E(B-V)$ is called the colour excess and is related to the total hydrogen nuclei column density, N_H, which is in fact the sum of the column densities due to atomic, $N(HI)$, and molecular, $2N(H_2)$, hydrogen, i.e.,

$$\frac{N_H}{E(B-V)} = 5.8 \times 10^{21} atoms/cm^2/mag. \tag{5.10}$$

[Bohlin et al., 1978]

Rewriting equations 5.9 (using an R_v of 3.1) and 5.10, we get the ratio of total gas column density and the visual extinction:

$$\frac{N_H}{A_v} = 1.87 \times 10^{21} atoms/cm^2/mag. \tag{5.11}$$

Note that the above equation uses the widely accepted value of R_v in the Milky Way and the value of A_v is determined by the selected value of R_v. Any change in R_v, therefore, changes the value of visual extinction. For example, if we adopt an R_v of 6 in our calculations, the the visual extinction of the clouds will be modified by a factor $\sim$2.

5.4.4 Mass determination

Thermal emission from dust at sub-millimeter wavelengths is a measure of the total mass of the cloud. The total mass of a cloud depends upon several factors such as the total flux, the distance to the dust cloud, the dust opacity per unit mass at the sub-millimeter wavelengths, and Planck function, which in turn is a function of dust temperature. For example, the equation for total dust mass (M_d) at 850 μm can be written as follows:

$$M_d = \frac{F_{850} D^2}{\kappa_{850} B_{850}(T_d)}, \tag{5.12}$$

[Hildebrand, 1983],
where F_{850} is the flux density at 850 μm, D is the distance to the cloud, κ_{850} is the opacity constant at 850 μm, and $B_{850}(T_d)$ is Planck function at 850 μm.

By assuming a gas to dust ratio of 100, one can get the total gas mass from the calculated dust mass.

Gas masses can also be determined from the hydrogen column density maps of the clouds, i.e.,

$$M_g = \mu m_H N_H A, \tag{5.13}$$

where μ and m_H are, respectively, the mean molecular weight and mass of hydrogen, N_H is the hydrogen column density in cm^{-2}, and A is the pixel area in cm^2.

5.5 Dust Emission Morphology

In this section we describe the sub-millimeter dust emission morphologies of the sample clouds at 450 and 850 μm SCUBA-2 wavelengths. The observed SCUBA-2 maps of the six clouds at both wavelengths are displayed in Figures from 5.12 to 5.23. In all the maps presented here, north is up and east is to the left with map coordinates in J2000. From all the maps at 450 and 850 μm excluding S148, pixels with S/N values less than 3 as well as negative valued pixels—possibly image reconstruction artifacts—are clipped and removed. A S/N of 2 is used for clipping the S148 map field in order to try to retrieve its very faint 450 μm emission. In all the H II region clouds presented here, it is apparent that the 450 μm maps more or less resemble their 850 μm counterparts in the absence of substantial sky variations.

5.5.1 S159

The surface brightness maps of the cloud at 850 and 450 μm SCUBA-2 wavelengths are shown in Figures 5.12 and 5.13 respectively. The sub-millimeter thermal emission at 850 μm in the cloud associated with the H II region S159 is peaked at right ascension 23h 15m 30.7s and declination 61° 07′ 14.8″. The 850 μm dust emission map shows a centrally peaked cometary morphology along with an extended outer envelope with the tail of the cometary structure inclined towards the north-west direction. An isolated but nearby small low surface brightness dust cloud is visible in a direction west of the central peak dust emission. A wisp of dust envelope is oriented in the north-east direction, and is connected to the central major dust cloud (see Figure 5.12). The position of the peak dust emission at 450 μm coincides with that of the peak 850 μm dust emission. However, at short wavelengths, the neighbouring clouds are slightly fainter in comparison with their long wavelength counterparts (see Figure 5.13).

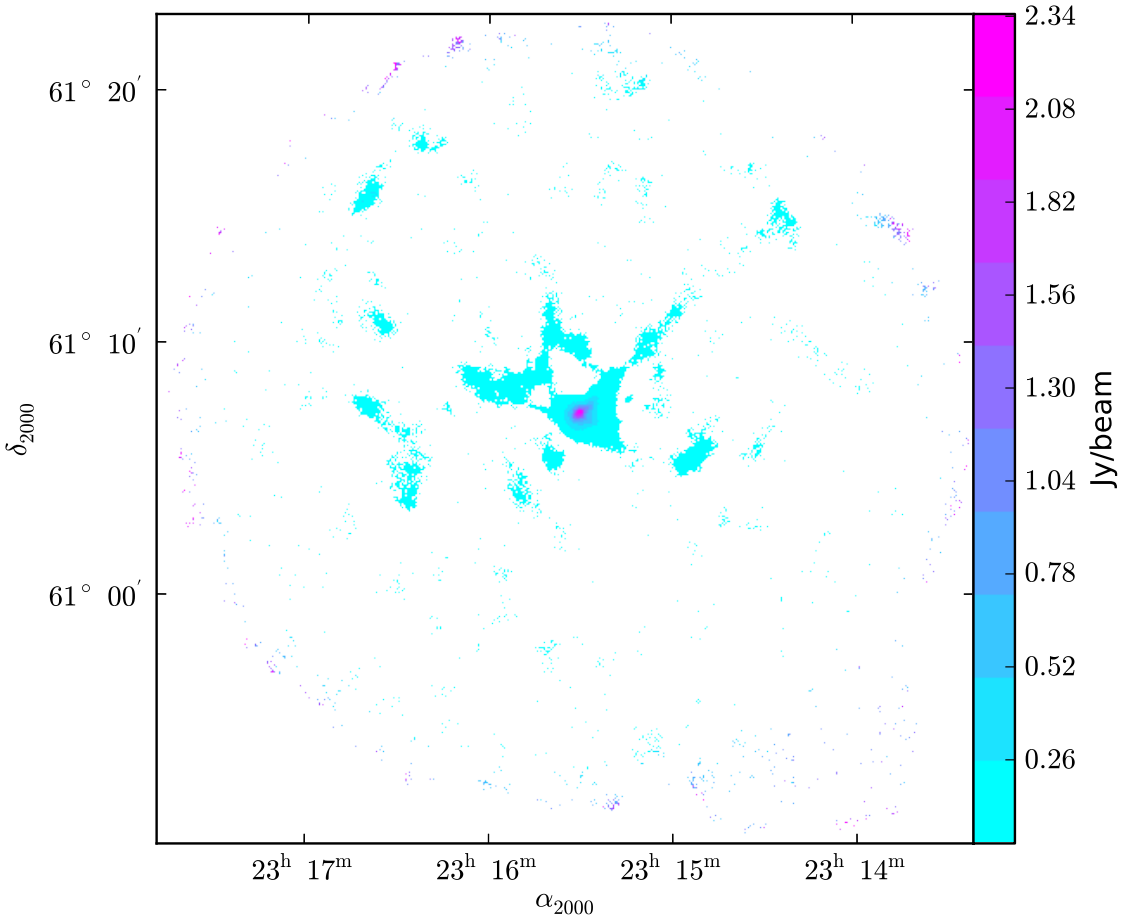

Figure 5.12: S159 surface brightness map at 850 μm.

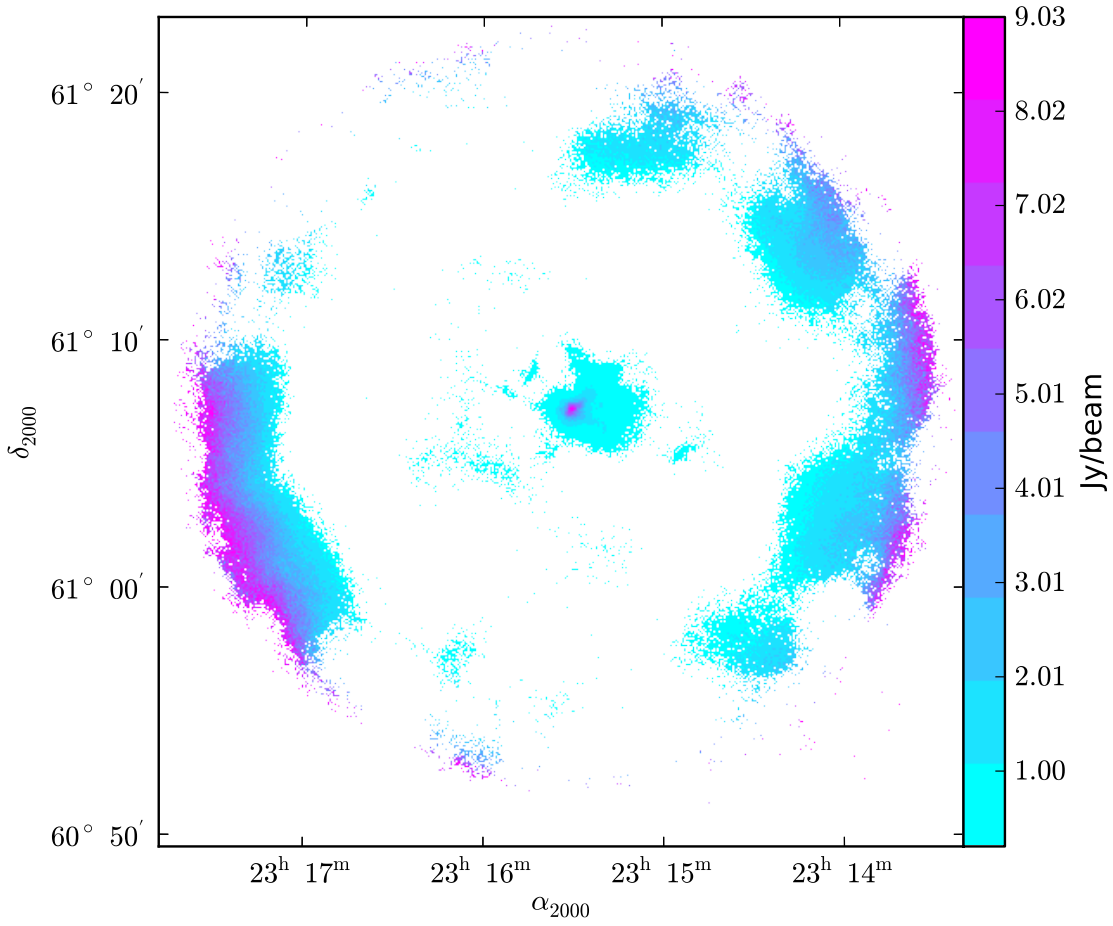

Figure 5.13: S159 surface brightness map at 450 μm.

5.5.2 S148

The surface brightness map of S148 at 850 μm (Figure 5.14) shows the presence of three different clouds. The map contains positive-valued pixels with S/N greater than 2. However, due to large-scale variations in dust emission at 450 μm (Figure 5.15), we discarded the 450 μm map from further analysis. The cloud present at the map centre is associated with H II regions S148 and S149 and has two different peaks: a stronger peak at RA 22h 56m 17.2s, Dec +58° 31′ 1″, and a fainter peak at a distance of 27″ in the north (see Figure 5.14) from the stronger peak. An extended bar-like structure is present in the north-east direction from the map centre. The cloud associated with S147 is either faint or not observable at 450 and 850 μm wavelengths. A long cloud whose strongest emission is located at 22h 56m 45.8s RA and +58° 30′ 00″ Dec, aligned in the north-south direction, is visible in the south-east direction of the cloud associated with the H II regions S148 and S149 and has two other peaks in the south-east direction. A third cloud is present in the S148 field at a distance of 6′ 45″ from the map centre to the north. Please note that there are no visible optical counterparts for these two unknown clouds in the DSS red image, and therefore these two clouds are most likely some dark clouds along the line of sight or associated with the centre cloud. Since the identity and the distances to these clouds are uncertain, we are not taking these two clouds into account in further studies.

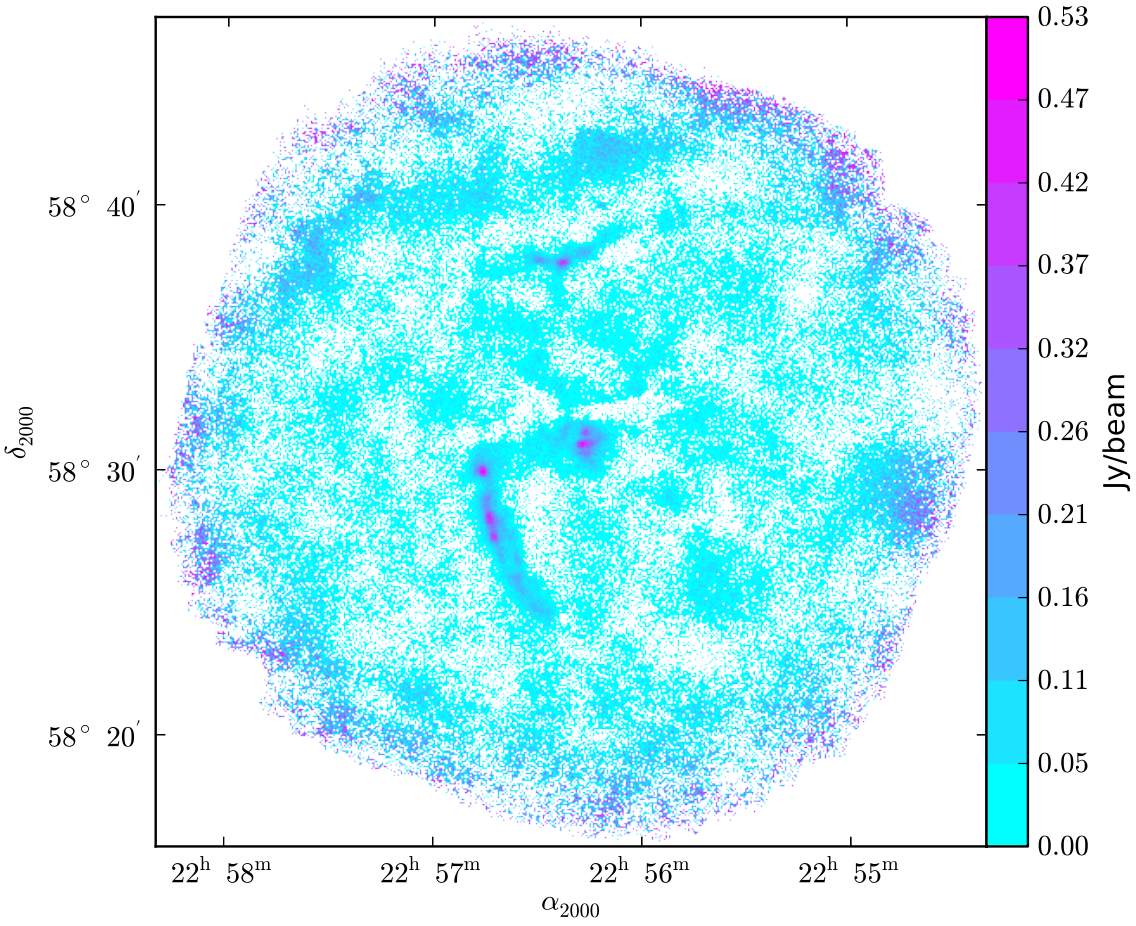

Figure 5.14: S148 surface brightness map at 850 μm.

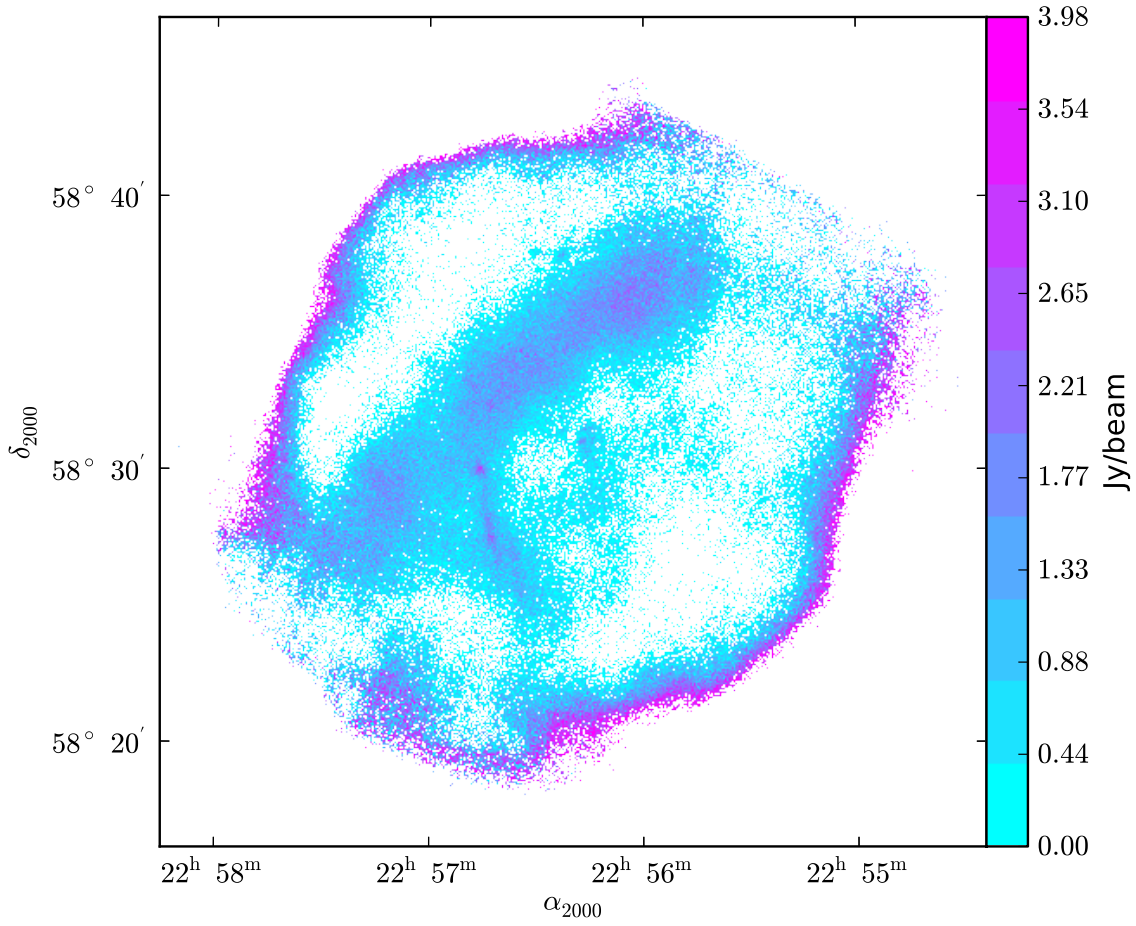

Figure 5.15: S148 surface brightness map at 450 μm.

5.5.3 S156

The observed S156 field consists of many H II regions such as S156, BFS15, BFS17, and BFS18. The surface brightness maps of the cloud at 450 μm and 850 μm are shown in Figure 5.17 and Figure 5.16 respectively. The cloud at RA 23h 05m 08.9s and Dec +60° 14′ 49″ is coincident with the the H II region S156. A bright cloud core is present to the south at a distance of 7′ 36″ from the cloud associated with the H II region S156. An H II region BFS15 is detected [Blitz et al., 1982] close to this cloud, and most likely this southern cloud is linked to the BFS15, which in turn probably is related to S156. The cloud, present in the north-east edge of the map is most likely associated with the H II region BFS18 since the H II region BFS18 is detected very close to this position by the same authors. A faint cloud is visible midway between the S156 and the BFS18 clouds, located very close to the H II region BFS17. None of the BFS H II regions are detected in the radio wavelengths except BFS15, which is a very weak radio source with a radio flux of merely 5mJy [Fich, 1993]. However, all of these BFS H II regions are detected in CO and their antenna temperatures are higher than 10 K [Blitz et al., 1982], ensuring a good detection in CO. There is no identified CO or radio emission towards any other faint clouds in the map, and most likely all the fragments are part of the same large nebula of S156. Note that many faint clouds that are visible at the 850 μm are absent at 450 μm due to large scale variations in the sky at 450 μm.

5.5.4 S305

In S305, there are a number of small nebulosities aligned roughly along a circular ring around the map centre with the brightest sub-millimeter source in the south-east direction (see Figures 5.18 and 5.19). The S305 complex has a very good detection at both 850 and 450 μm wavelengths. Many of the cloud cores are nearly circular in nature, connected by faint filamentary structures; the strongest sub-millimeter peak is at RA 07h 30m 16.5s and Dec -18° 35′ 15.9″ (hereafter S305S). The bright nebulosity in the north-west direction is at RA07h 29m 56.2s and Dec -18° 27′ 53.9″ and is also associated with the H II region S305 (hereafter S305N). All other faint cores near the map centre are also part of the parental cloud associated with S305. Two bright cores are visible at about 18 arc minutes south from the S305 cloud, and probably are not related to S305. Note that no distance information is available toward these two cores and no further analysis is performed on these two unknown cores.

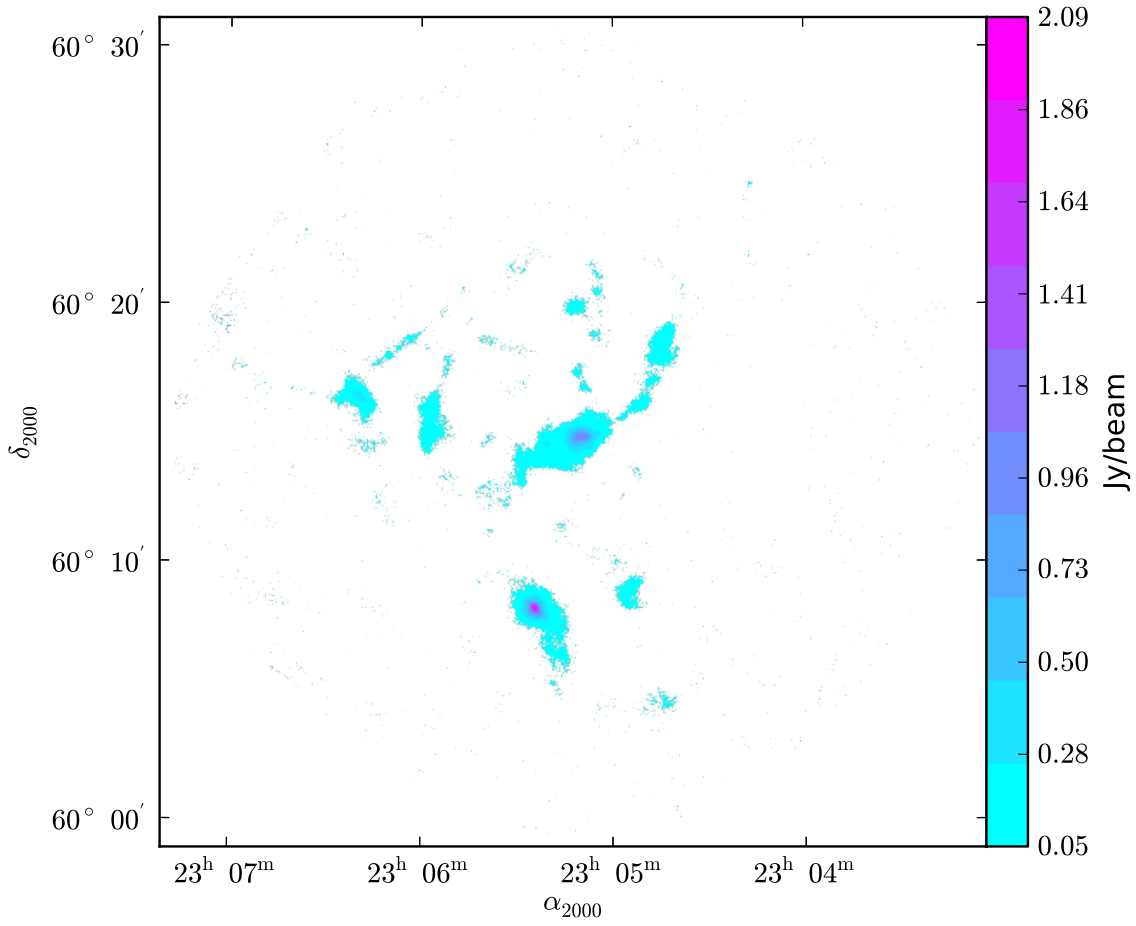

Figure 5.16: S156 surface brightness map at 850 μm.

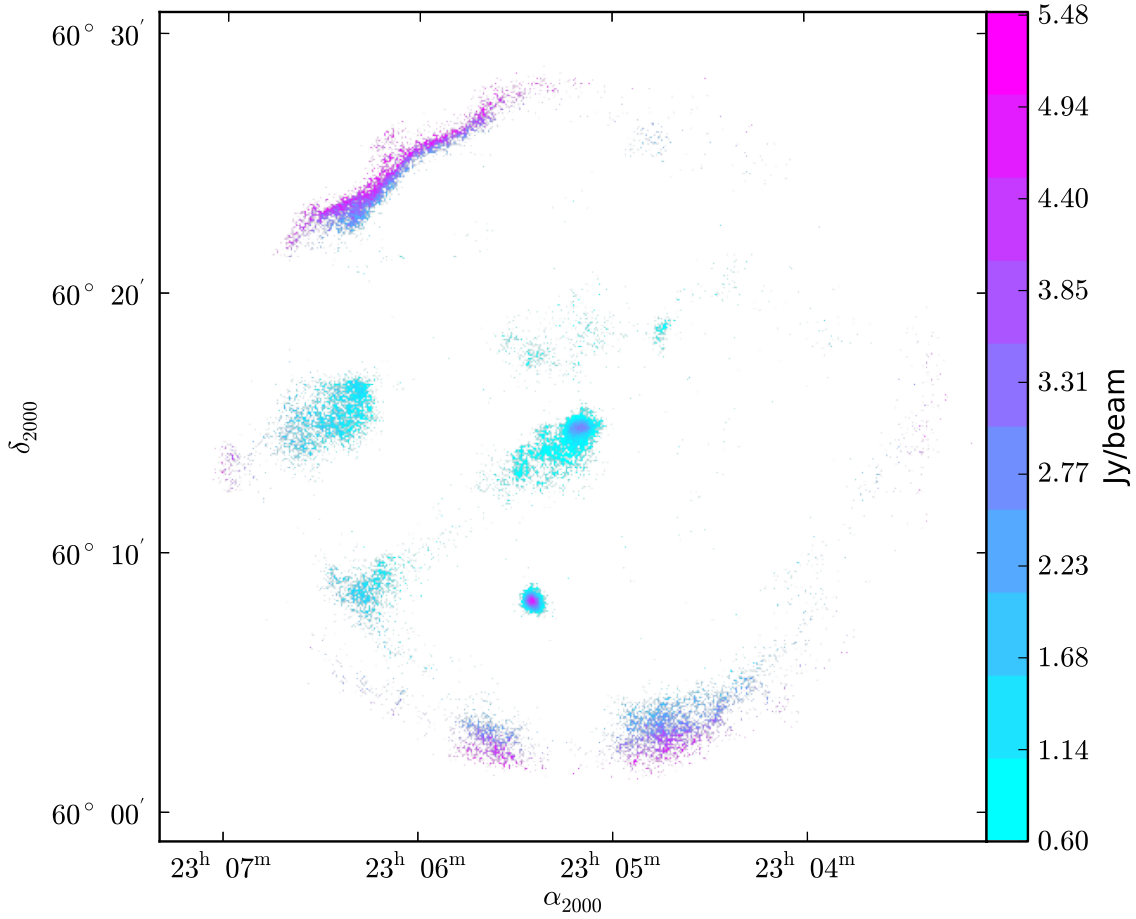

Figure 5.17: S156 surface brightness map at 450 μm.

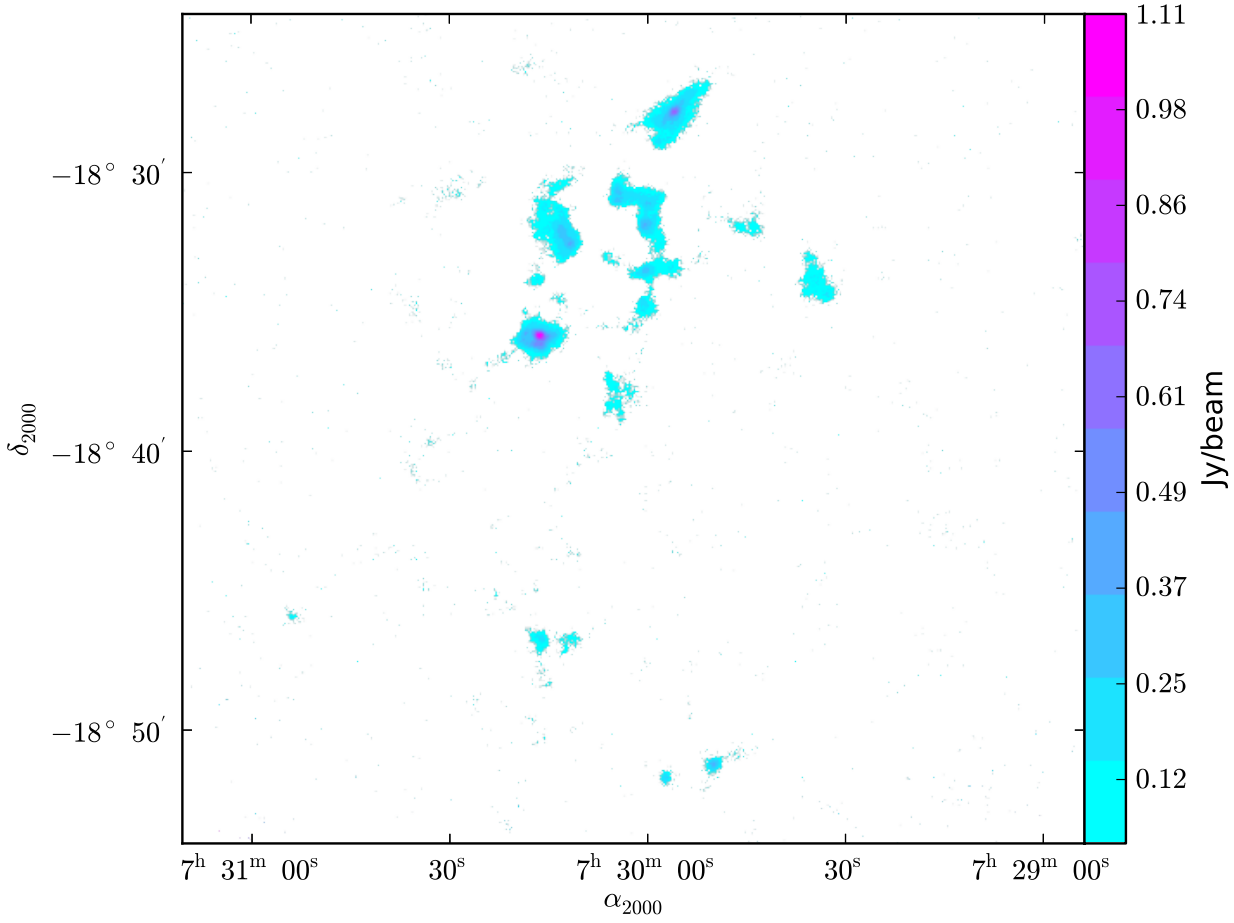

Figure 5.18: S305 surface brightness map at 850 μm.

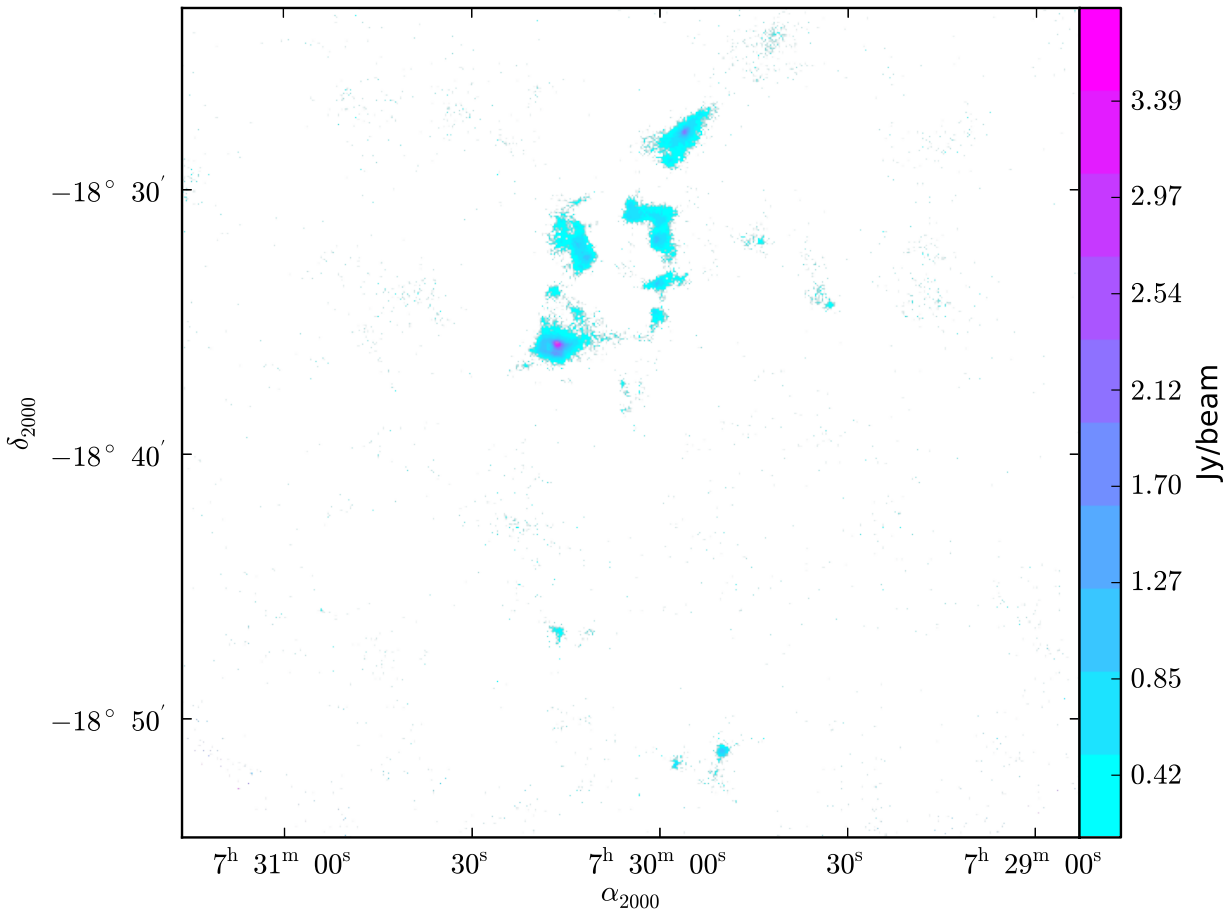

Figure 5.19: S305 surface brightness map at 450 μm.

5.5.5 S254

The observed field of S254 includes the optical H II regions S254, S255, S256, S257, and S258. Maps of sub-millimeter dust continuum emission at 850 and 450 μm SCUBA-2 wavelengths from the molecular cloud associated with H II regions S254 to S258 are presented in Figures 5.20 and 5.21 respectively. The morphology of the cloud reveals a central elongated structure with a pair of embedded cores: the most luminous of these two is located at RA 06h 12m 53.8s and Dec +17° 59′ 24.7″ (hereafter S254S), and is separated by about 1 arc minute from the other core located in the north direction (hereafter S254N). Note that these two sub-millimeter bright cores lie between the H II regions S255 on the east and and S257 on the west. A number of faint cloud fragments are visible in the south-east and south-west directions, and are associated with the S254 complex. The cloud fragment on the south-east direction, at RA 06h 13m 29.2s and Dec +17° 55′ 30.8″, is connected to the H II region S258. The fragment located south-east of this cloud may also be a part of S258 and the fragment found near the central bright cloud on the east, is part of the H II region S255. Similarly, the fragment on the south-west direction from the main cloud could be a part of H II region S256. The most interesting feature of the S254 complex is the shape of the central cloud containing the cores S254N and S254S: the morphology of the cloud indicates that it is squeezed by the H II regions S255 and S257.

5.5.6 S128

The observed 850 and 450 μm dust emission maps of S128 are shown in Figures 5.22 and 5.23, respectively. The cloud present in the map centre is associated with the H II region S128. The cloud associated with S128 has its strongest peak at RA 21h 32m 12.3s and Dec +55° 53′ 43.8″ and an association with S128-N, the compact S128 H II region, is found for this source (hereafter S128N). There are two additional cores closely connected to the S128 H II region towards the south. Note that these two cores are connected to the extended H II region in S128 (hereafter S128S1 and S128S2—for respectively the northern and southern cloud core associated with S128). Another fainter cloud is present in the far south-west direction from the centre cloud complex, and is probably not a part of the H II region S128.

The observed characteristics of the clouds are tabulated below (see Table 5.2). The name of each cloud in the complexes associated with Galactic H II regions is presented in the first column. The second and third columns provide the peak positions of the sub-millimeter emission from these clouds in RA and Dec(J2000). The fourth and fifth columns give the peak values of the 850 and 450 μm fluxes in units of Jy/beam. Since SCUBA has uncertainties in the absolute flux calibration of 20% at 850 μm and 50% at 450 μm because of the fluctuations in the optical depth of the atmosphere and due to the uncertainties in the beam-shape during observations and calibration [Di Francesco et al.,

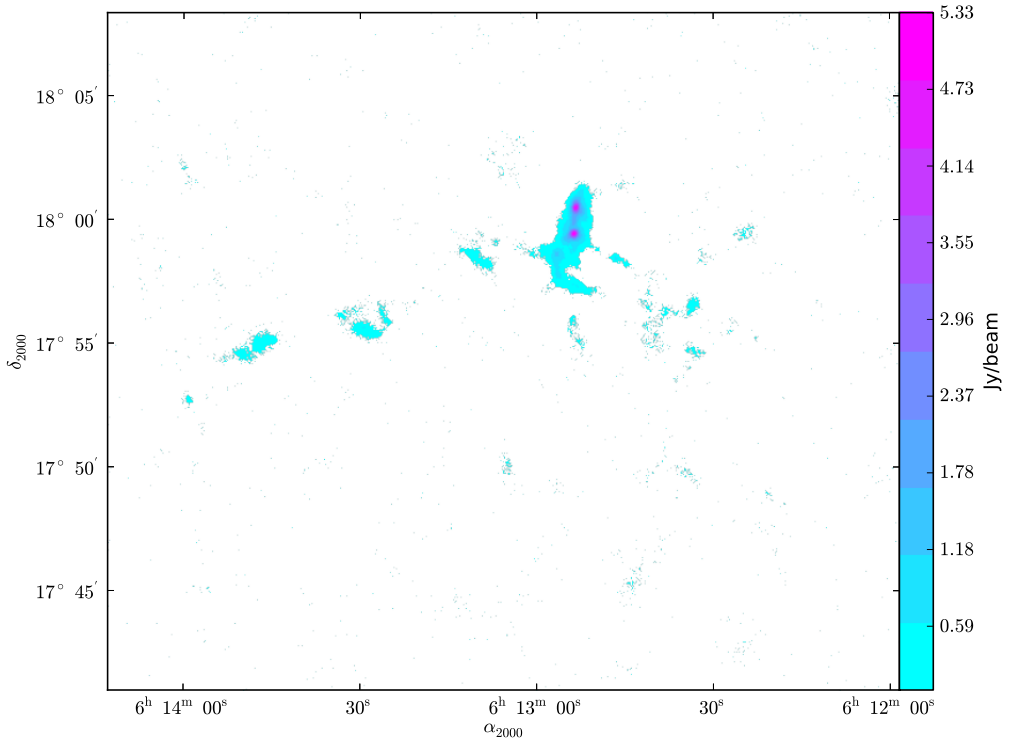

Figure 5.20: S254 surface brightness map at 850 μm.

2008], we expect similar calibration errors for SCUBA-2 and we do not know about any additional calibration errors in SCUBA-2 data. We therefore consider 20% calibration errors at 850 μm and 50% calibration errors at 450 μm SCUBA-2 fluxes.

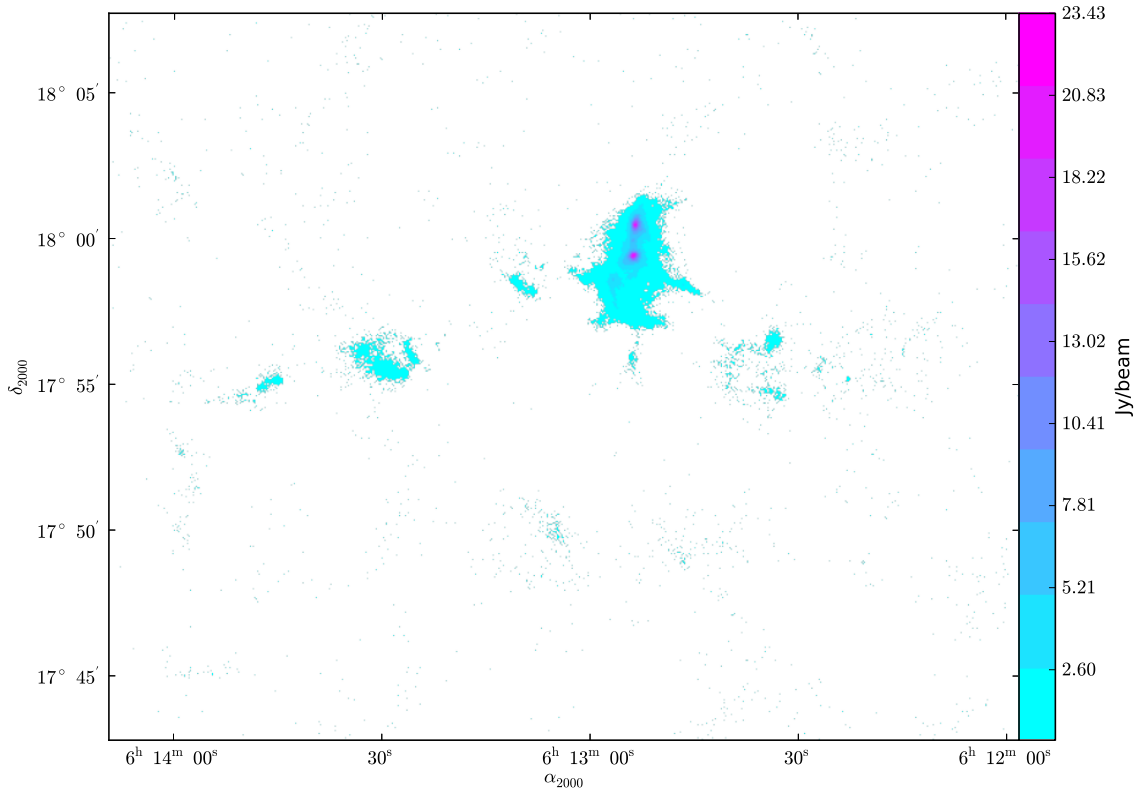

Figure 5.21: S254 surface brightness map at 450 μm.

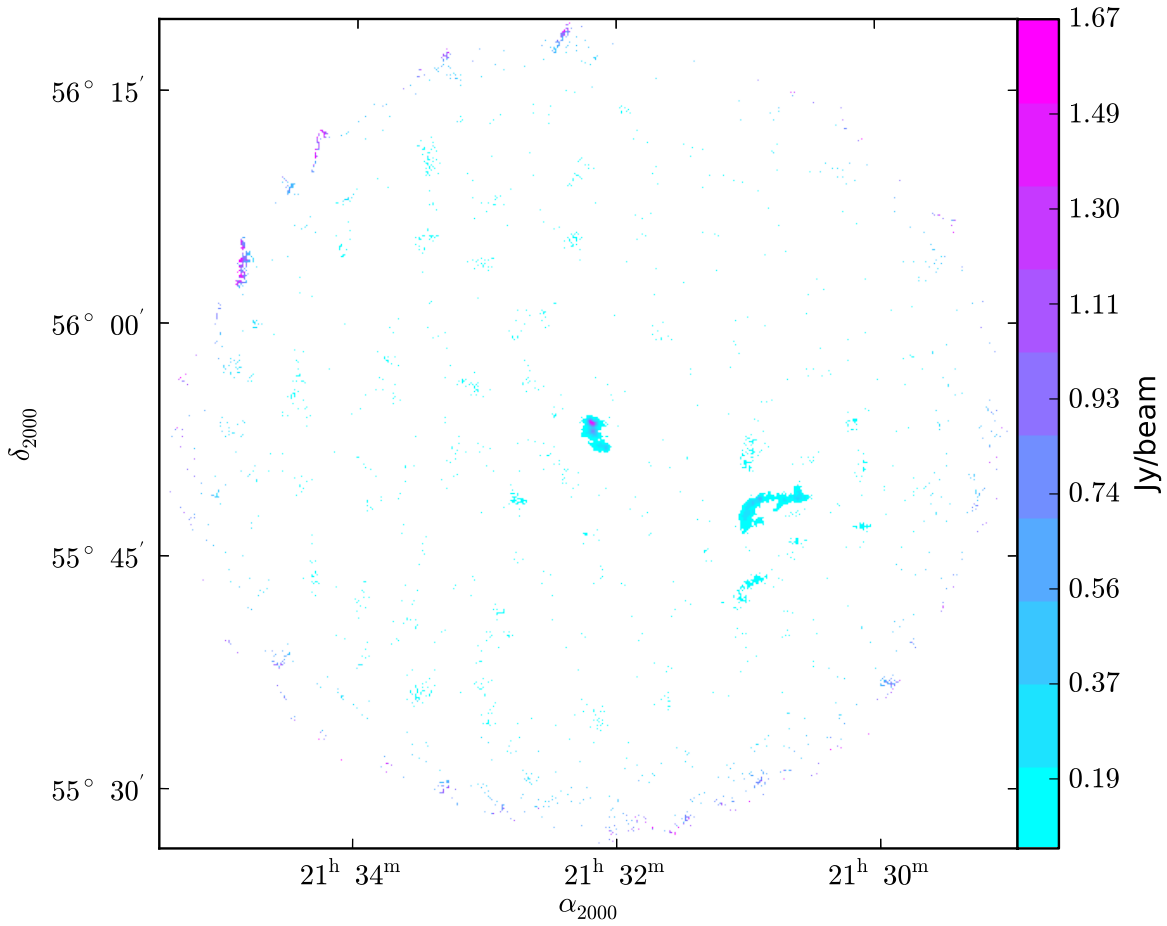

Figure 5.22: S128 surface brightness map at 850 μm.

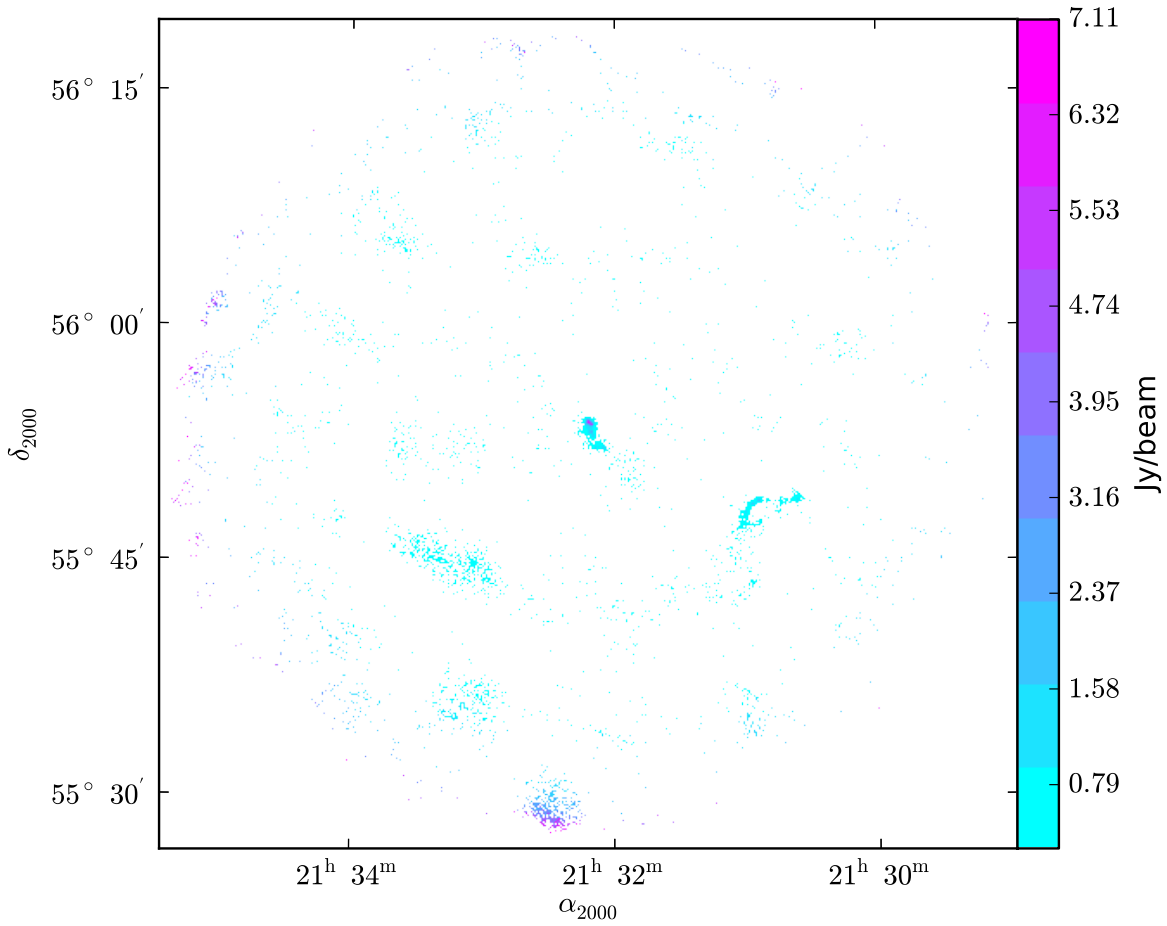

Figure 5.23: S128 surface brightness map at 450 μm.

Table 5.2: Observed parameters: object names, peak positions, and 850 and 450 μm peak flux densities of the 11 cores detected in the SCUBA-2 observations of Galactic H II region complexes.

Source	RA (J2000)	Dec (J2000)	S_{850}^{peak} (Jy/beam)	S_{450}^{peak} (Jy/beam)
S159	$23^h15^m30.7^s$	$61°07'14.8''$	2.34	9.03
S156	$23^h05^m08.9^s$	$60°14'48.9''$	1.09	3.49
BFS15	$23^h05^m24.6^s$	$60°08'12.8''$	2.09	5.48
S148	$22^h56^m17.2^s$	$58°31'01.0''$	0.50	1.86
S305S	$07^h30^m16.5^s$	$-18°35'51.2''$	1.10	3.82
S305N	$07^h29^m56.2^s$	$-18°27'54.2''$	0.71	2.22
S254S	$06^h12^m53.8^s$	$17°59'24.7''$	5.33	23.4
S254N	$06^h12^m53.6^s$	$18°00'27.7''$	4.97	21.7
S128N	$21^h32^m12.3^s$	$55°53'43.6''$	1.66	7.04
S128S1	$21^h32^m11.3^s$	$55°53'10.6''$	0.75	2.87
S128S2	$21^h32^m05.5^s$	$55°52'07.6''$	0.44	1.34

5.6 Dust Physical Property Maps

In this section we present two dimensional dust maps of our target complexes associated with Galactic H II regions showing different physical properties explained above. The maps reveal the evidence of local and global variations in individual dust characteristics. All the maps presented below have the resolution of the 850 μm SCUBA-2 data. In subsection 5.6.1, we describe dust temperature maps of all the target complexes. Detailed maps of dust emissivity variations in individual complexes are presented in subsection 5.6.2. Subsections 5.6.3, 5.6.4, and 5.6.5 show complexes' pixel-to-pixel variations in the optical depth, column density, and visual extinction respectively, at 850 μm.

5.6.1 Dust temperature maps

Dust temperature maps of the clouds are calculated using a single dust emissivity index: $\beta = 2.0$, and assuming that SCUBA-2 emission at 450 and 850 μm are solely originating from dust grains. Besides this, the derived temperatures most likely stand for the average of the observed temperatures along the line of sight through the cloud depths. The derived temperature maps of all the clouds are shown in Figures 5.24 to 5.28.

In each cloud, a gradient in temperature is observed from the cloud centre to the periphery. Temperature variations are high in the S159 cloud with some of the pixels at the main cloud's outer boundary reaching around 30 K. However, the cloud centre is at very low temperature ($T_d = 6$ K). Outer parts of the core retain a temperature between 10 and 16 K. All the fragments located in the south-west and north-east directions of the primary cloud more or less maintain a very low temperature between 6 and 8 K. The minor fragments visible in the south-east direction are significantly warmer: the temperature of these regions are found to be above 10 K (see Figure 5.24).

Temperatures are not derived for the cloud S148 due to a low signal to noise map at 450 μm. We assume a steady temperature of 10 K throughout S148 to derive the rest of the dust characteristics at sub-millimeter wavelengths. Most of the sources in the BFS15 field also show dust temperature gradients identical to that of S159 (see Figure 5.25). The core of S156 is cold with temperatures less than 8 K. The extended region of S156, located in the south-east direction, is relatively warm—reaching beyond 15 K close to the the outer layers. Note that the cloud BFS15, located in the south, is nearly at a single temperature and is very cold (less than 8 K). The cloud BFS18, on the other hand, displays variations in dust temperature with an increased temperature towards the edges of the cloud (see Figure 5.25).

The S305 complex shows a very small range in the dust temperatures, from 5.8 K to 14 K, making the bulk of this complex colder than most other sample complexes (except

S128). The cloud on the south-east is the warmest among all other nebulosities, with grain temperatures reaching 8 to 12 K at the boundary. All other components of the complex are at temperatures below 8 K (Figure 5.26). The clouds associated with the S254 complex, primarily S254S and S254N, are also at low temperatures, however, they are warmer than the S305 clouds. The centres are at temperatures around 7 K and there is a 14-21 K layer, enclosing both the S254S and S254N cores, at the exterior boundary (Figure 5.27). This layer is most likely attributed to the presence of two hot H II regions on either side of the clouds. The cloud surrounding the H II region S258 shows similar characteristics with around 12 K dust at its external border. Similar to all other clouds, S128 also has a warmer (10-13 K) dust ring, which encloses the colder interior. However, note that the temperature fluctuations in S128 from the centre to the outer envelope are the least amongst all the complexes. The core centres connected to the H II regions S128N, and S128-extended (S128S1 and S128S2) are cold with temperatures 6.3 K, 6.3 K. and 5.9 K respectively (see Figure 5.28).

The average value of the dust temperatures at the centres of all the clouds is 6.7 K. The lowest dust temperature is at the centre of the core S128S2 (5.9 K). The warmest core is BFS18 with a dust temperature of 8.8 K at the centre.

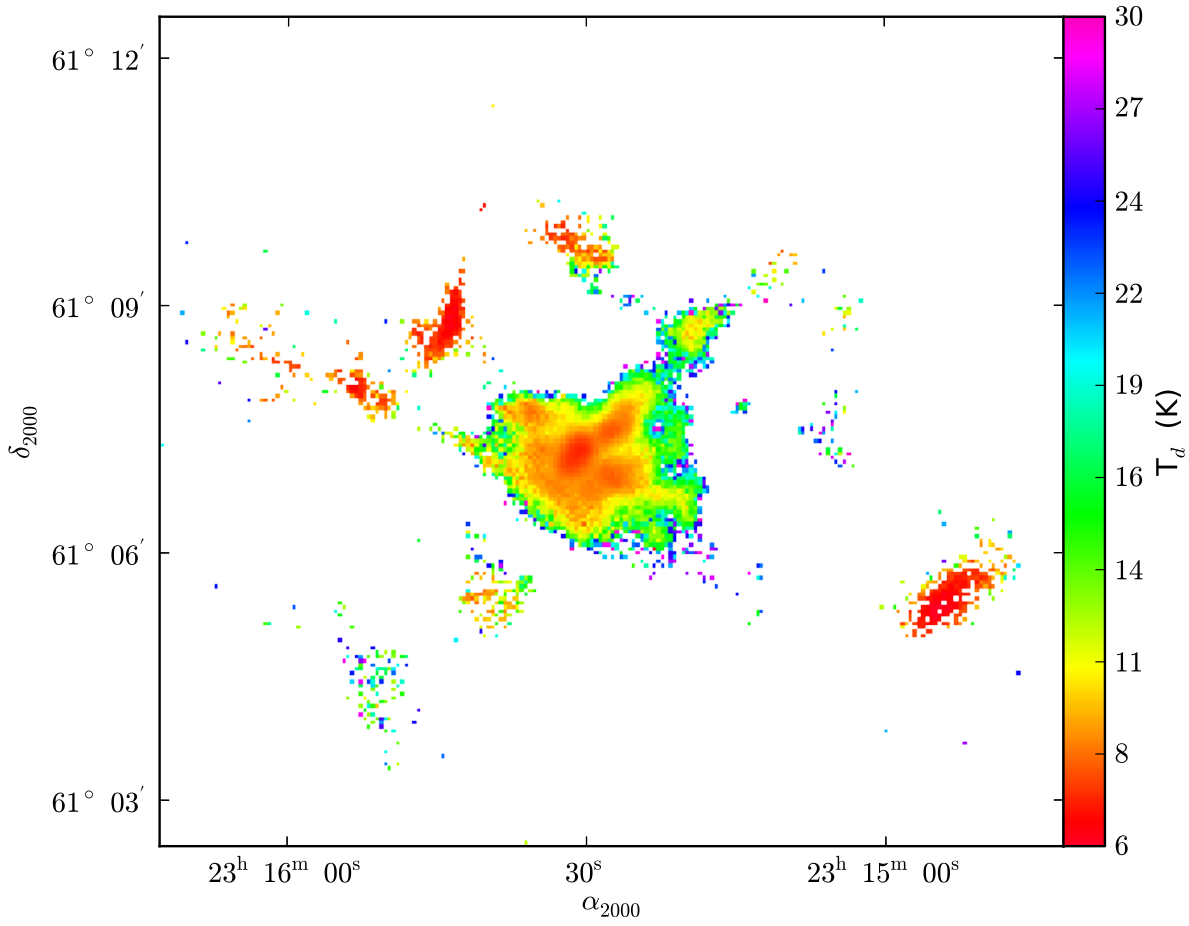

Figure 5.24: Derived dust temperature using SCUBA-2 450 and 850 μm maps of S159 with a β value of 2.0.

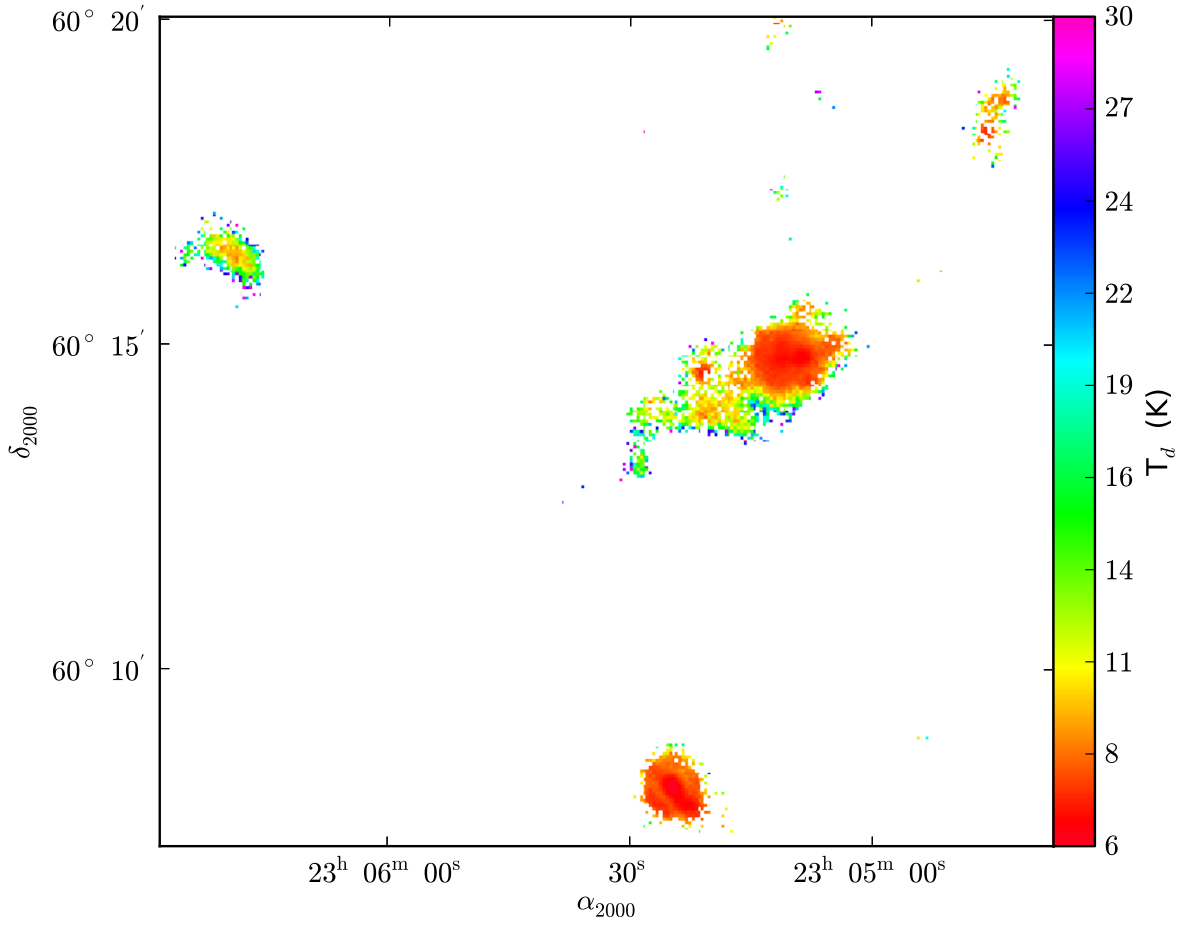

Figure 5.25: Derived dust temperature using SCUBA-2 450 and 850 μm maps of S156 with a β value of 2.0.

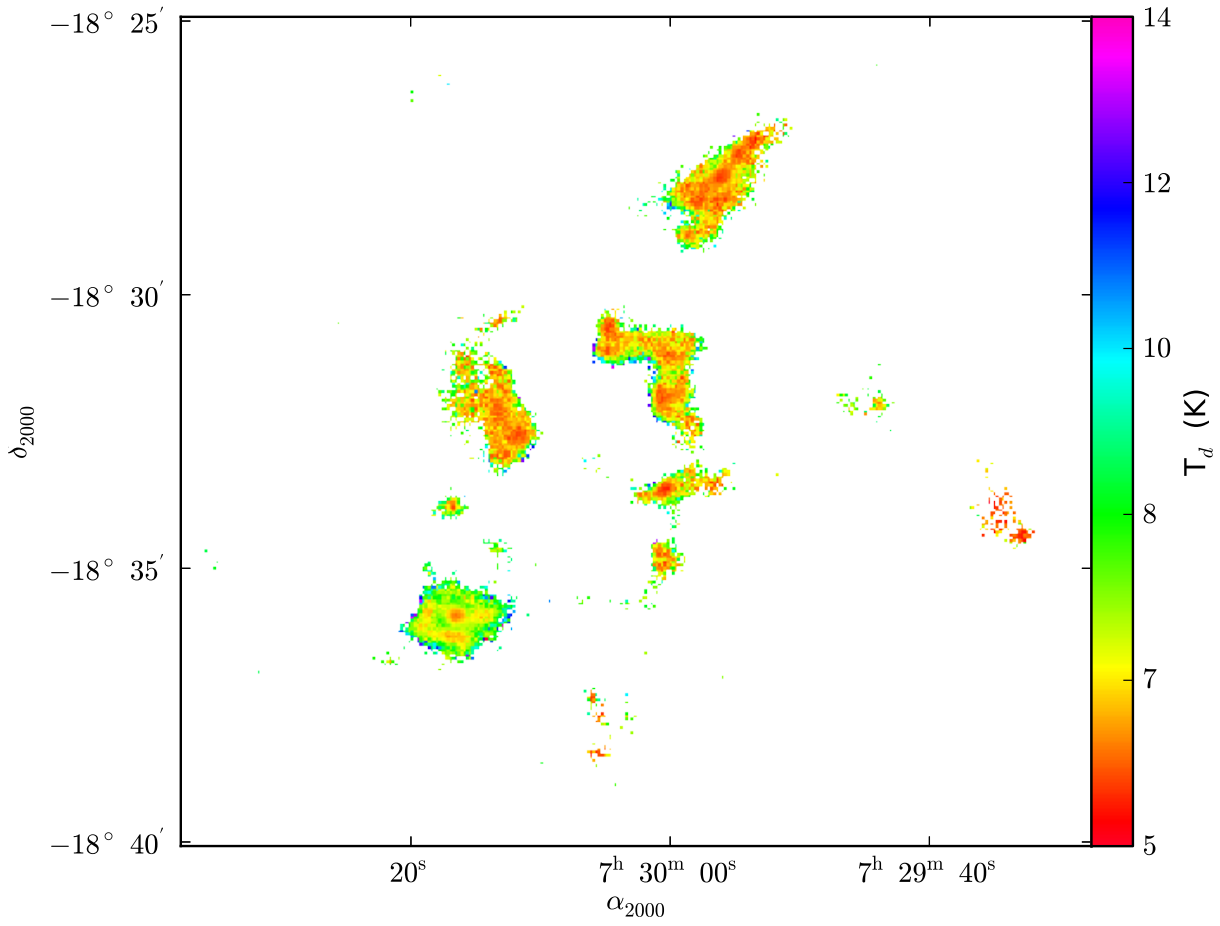

Figure 5.26: Derived dust temperature using SCUBA-2 450 and 850 μm maps of S305 with a β value of 2.0.

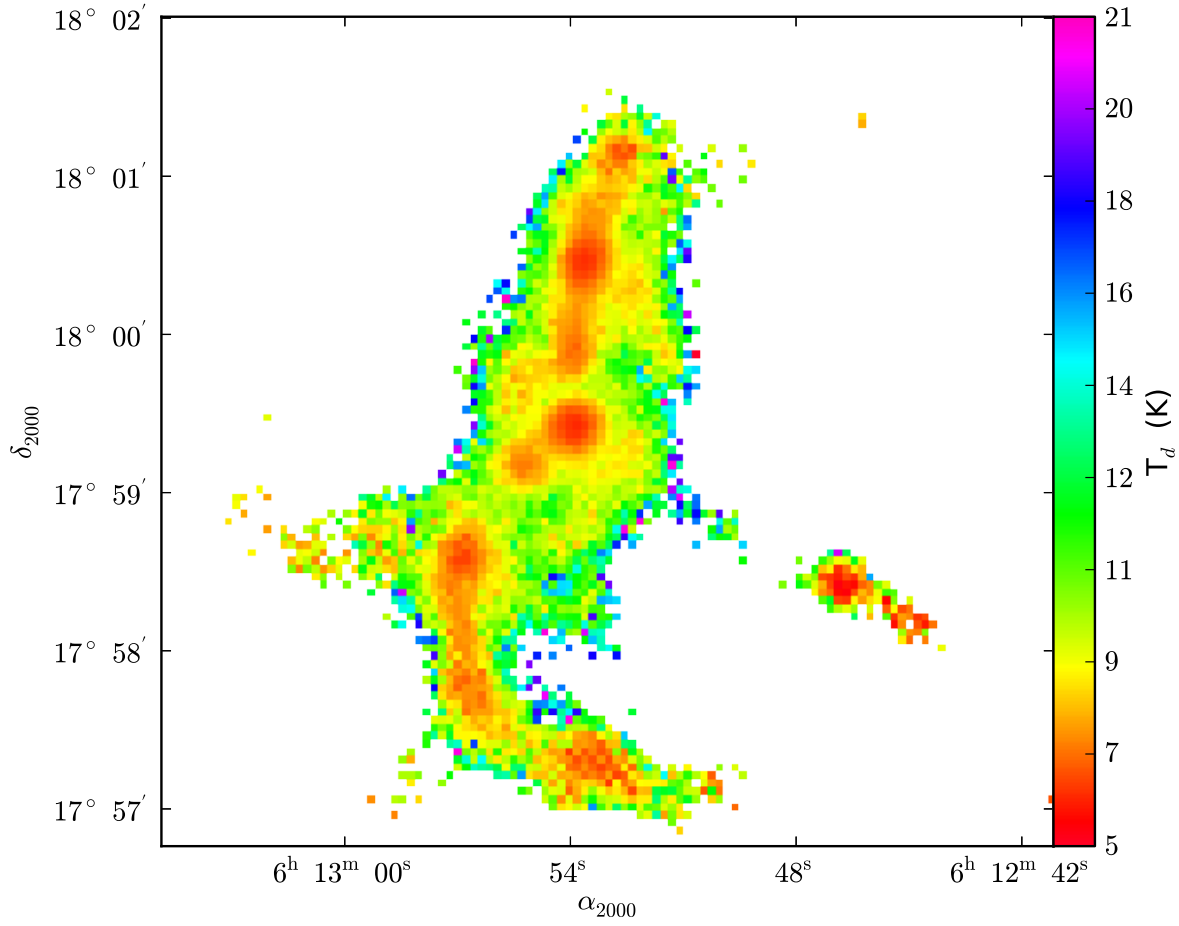

Figure 5.27: Derived dust temperature using SCUBA-2 450 and 850 μm maps of S254 with a β value of 2.0.

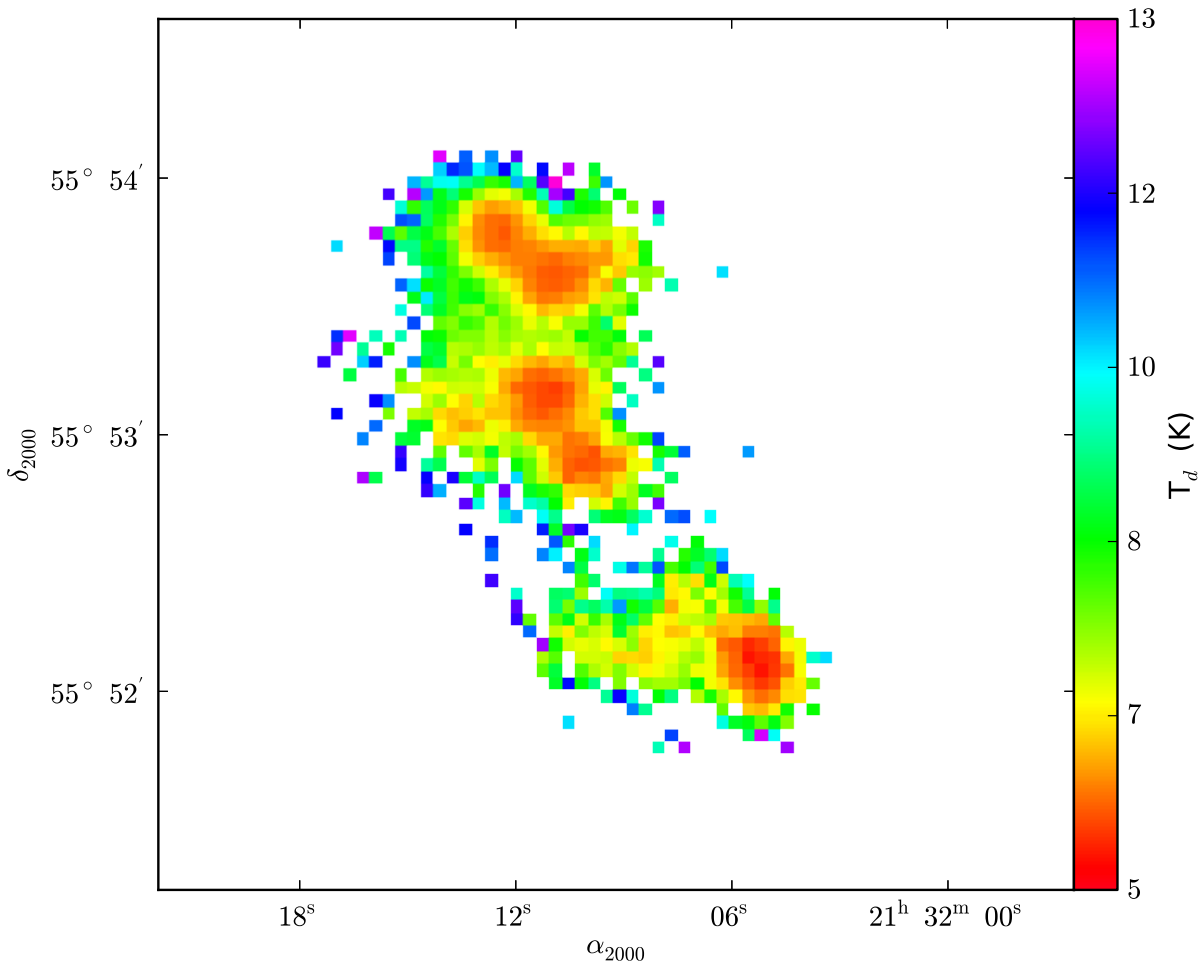

Figure 5.28: Derived dust temperature using SCUBA-2 450 and 850 μm maps of S128 with a β value of 2.0.

5.6.2 Dust emissivity index maps

The dust temperature and emissivity index cannot be simultaneously calculated using data from merely two wavelengths. We require data from a third sub-millimeter wavelength for this calculation. For this reason, using emission from only two wavelengths, we computed the value of the dust emissivity index at each pixel by assuming a constant temperature throughout the cloud, say 10 K. The assumed temperature is considered to be the typical temperature found in cold giant molecular clouds. Note that finding the values of the dust emissivity index in molecular cloud cores is significant especially because these values are dependent on different physical and chemical properties of the cores such as the grain size, composition and environment. In other words, the value of β reflects the overall physical properties of the clouds.

Dust emissivity index maps of the target cores are displayed in Figures 5.29 to 5.33. The value of β for the most part ranges from 0.5 to 3.5 and such a range is pronounced in S159 and S254. The β values span from 0.5 to 3.0 in BFS15 and S128 complexes and thus have a slightly lower range compared with S159 and S254 complexes. However, in S305, the upper limit of β is 2.9, and is the lowest among all the clouds. Note that a change in the line-of-sight temperature or the optical depth of the dust grain can modify the obtained values of β. Bear in mind that further physical properties of the clouds such as the optical depth, column density and visual extinction are calculated using a β of 2.0, which normally holds at sub-mm wavelengths.

Increasing the dust temperature has some effect on the β map. For example in S159, raising the dust temperature from 10 K to 15 K decreases the values of the dust emissivity indices (see Figure 5.34). At the centres of the fragments associated with the central cloud, the β values drop to negative.

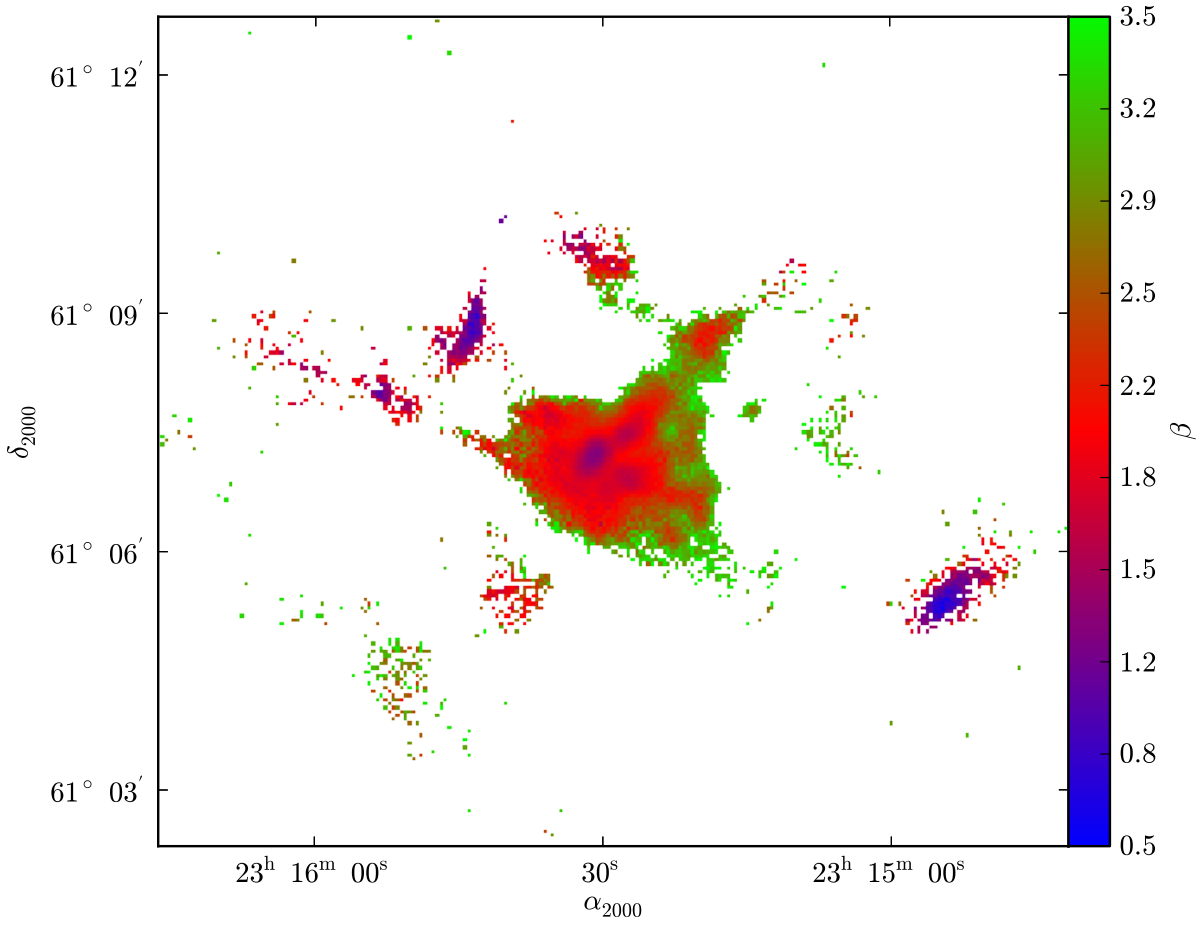

Figure 5.29: Dust emissivity index β derived from SCUBA-2 450 and 850 μm maps by assuming a constant dust temperature of 10 K throughout S159.

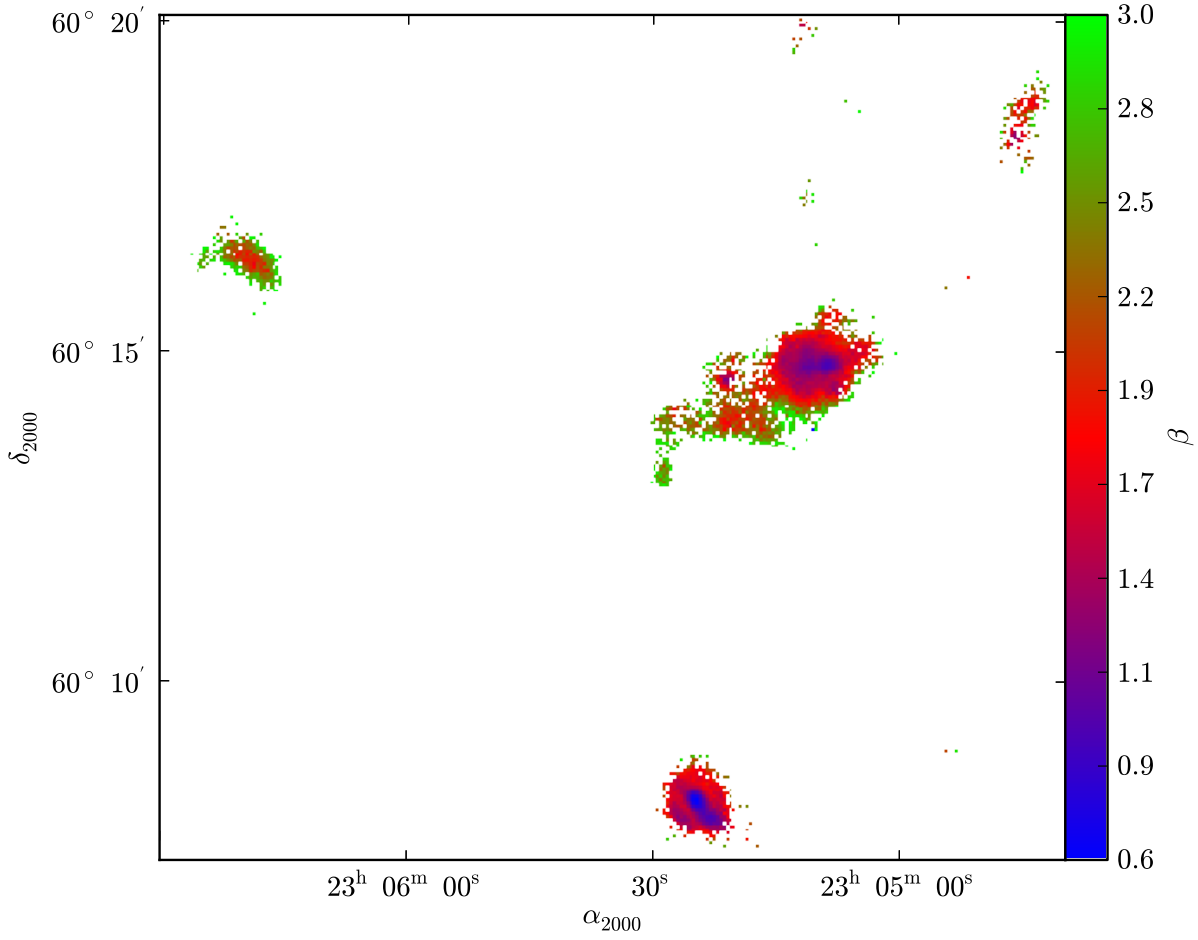

Figure 5.30: Dust emissivity index β derived from SCUBA-2 450 and 850 μm maps by assuming a constant dust temperature of 10 K throughout S156.

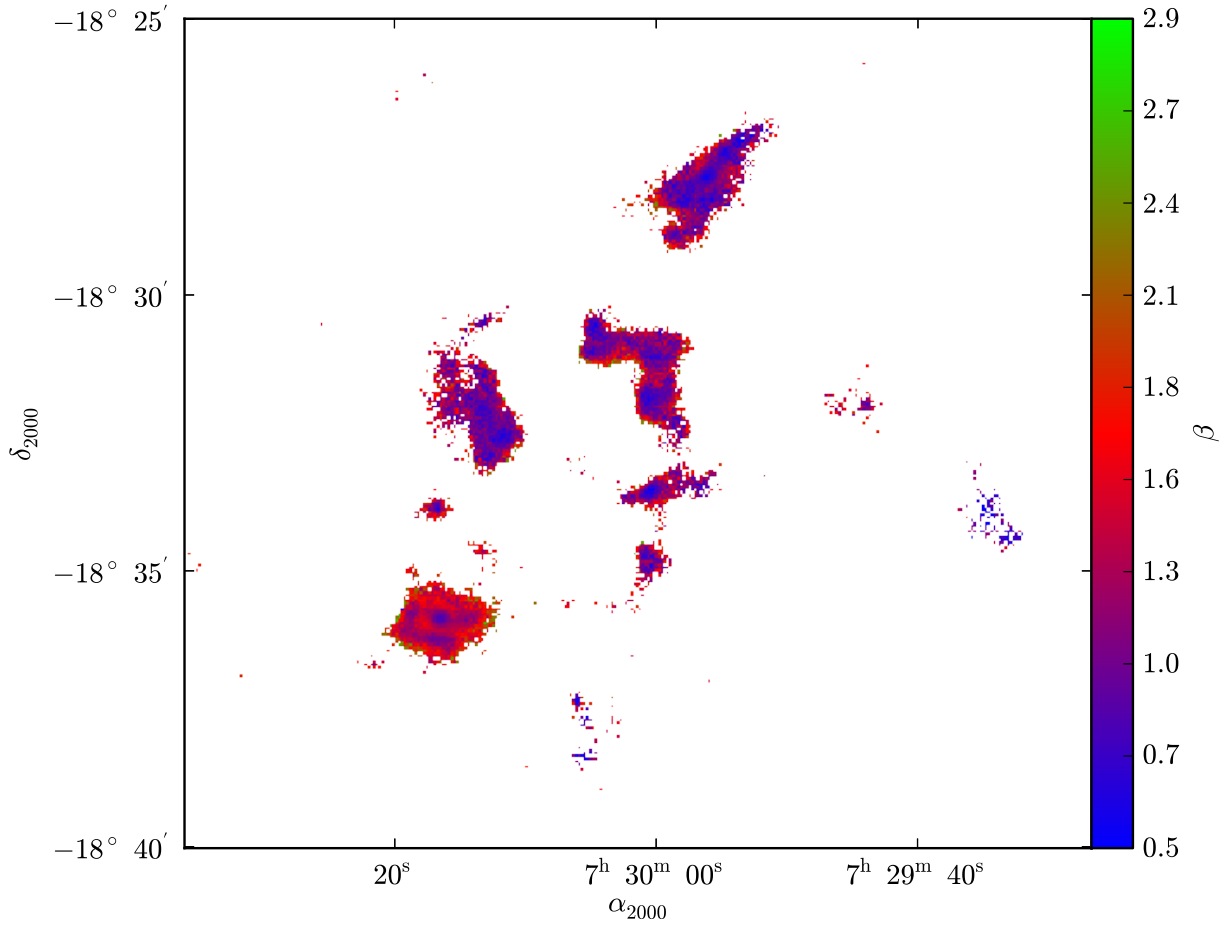

Figure 5.31: Dust emissivity index β derived from SCUBA-2 450 and 850 μm maps by assuming a constant dust temperature of 10 K throughout S305.

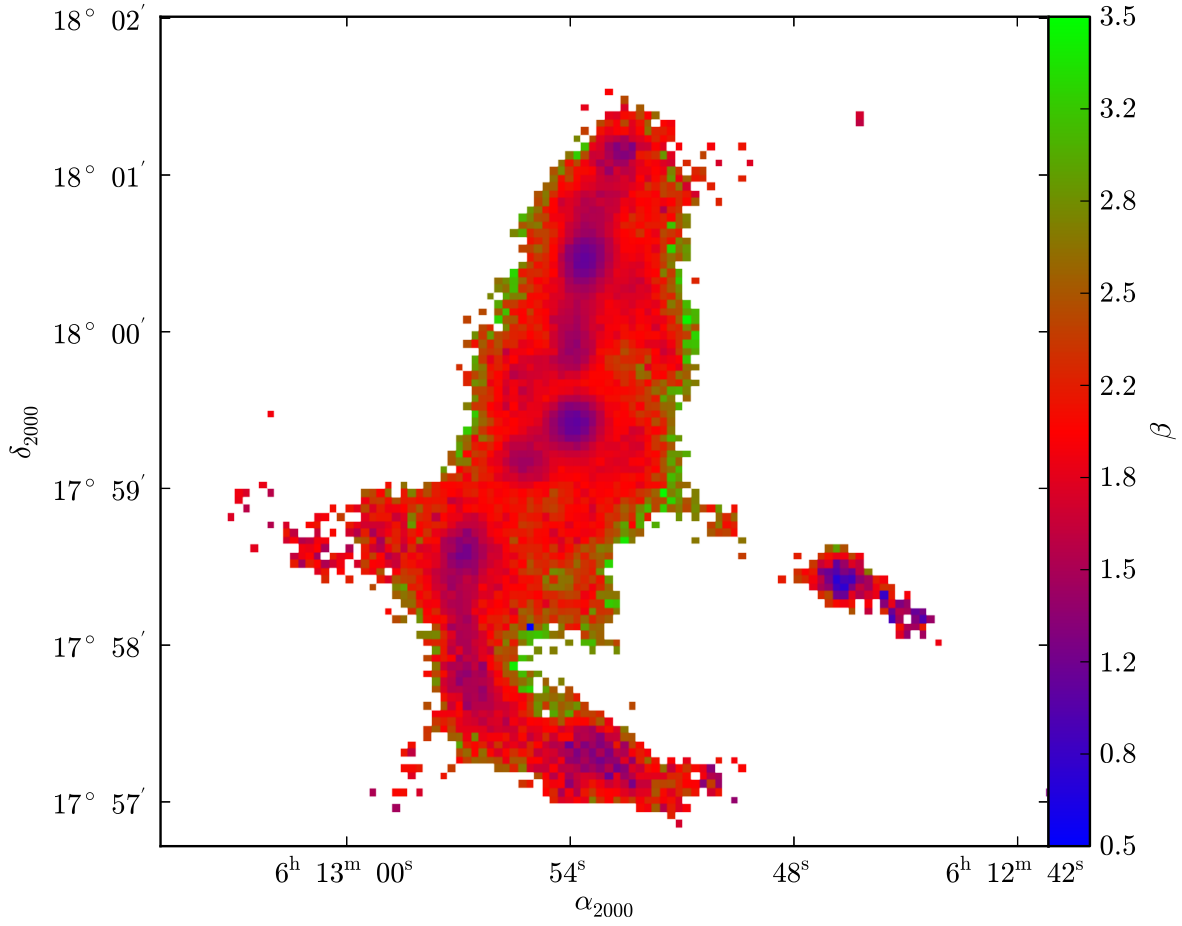

Figure 5.32: Dust emissivity index β derived from SCUBA-2 450 and 850 μm maps by assuming a constant dust temperature of 10 K throughout S254.

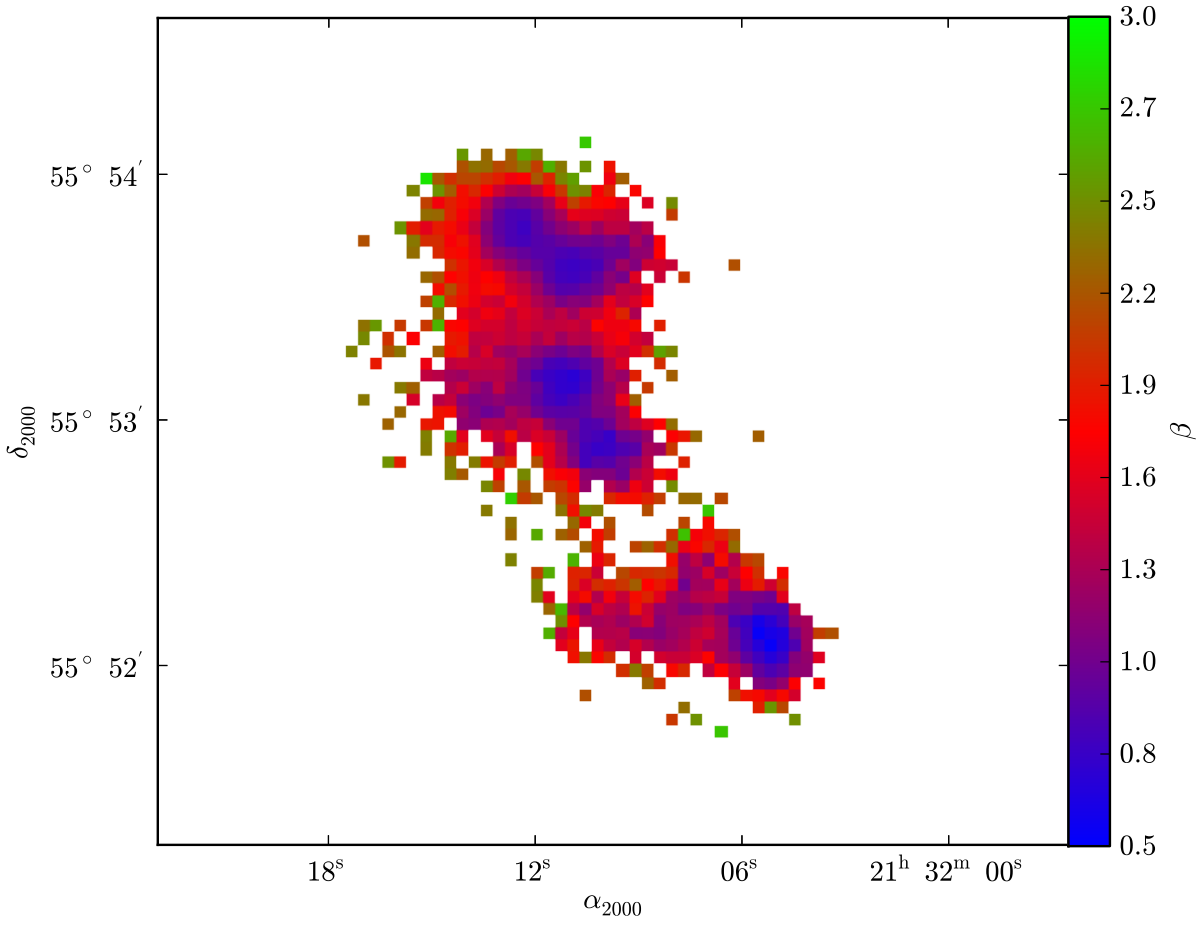

Figure 5.33: Dust emissivity index β derived from SCUBA-2 450 and 850 μm maps by assuming a constant dust temperature of 10 K throughout S128.

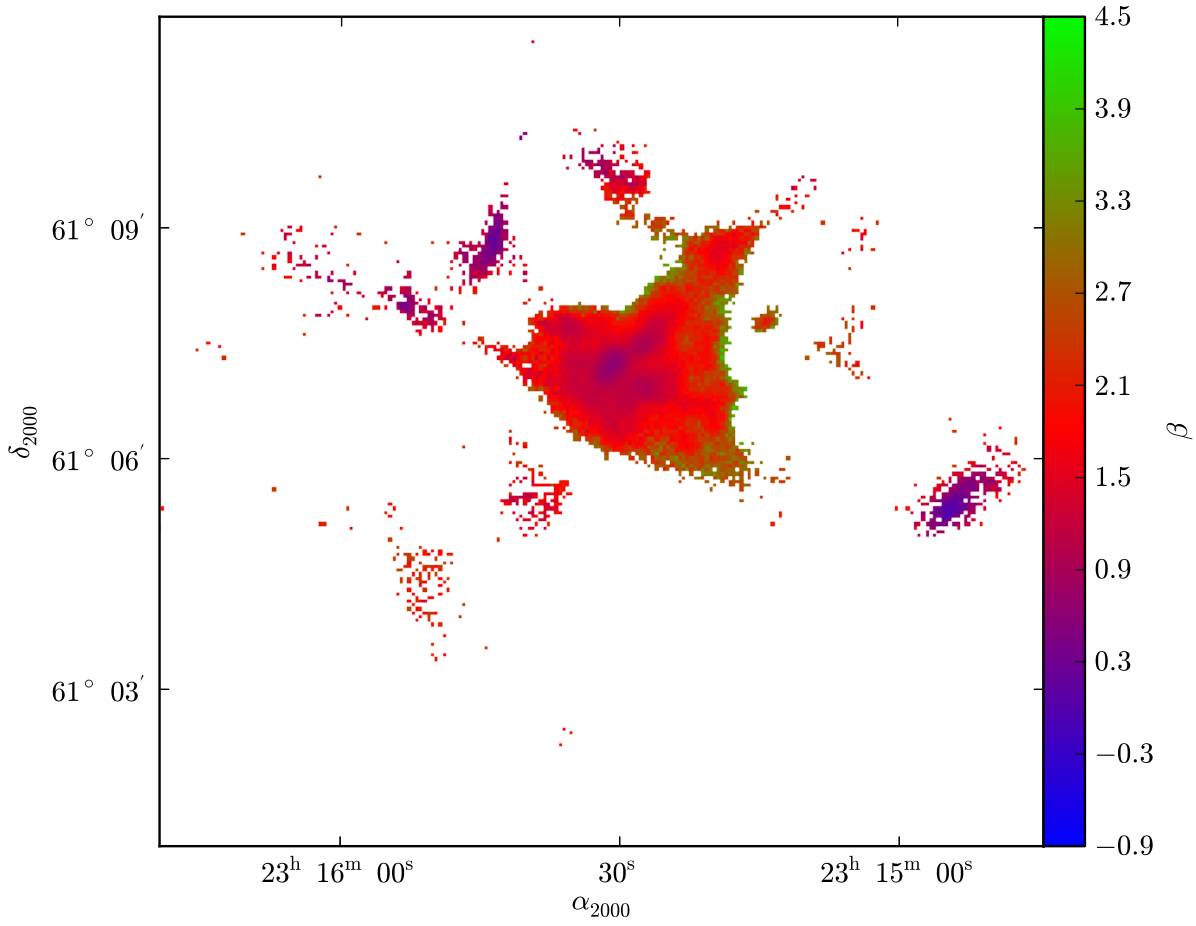

Figure 5.34: Dust emissivity index β derived from SCUBA-2 450 and 850 μm maps by assuming a constant dust temperature of 15 K throughout S159.

5.6.3 Optical depth maps

Dust optical depth maps are constructed from the derived temperatures using the surface brightness maps at 850 μm. The two-dimensional maps showing the spatial distribution of the dust optical depths in the sample clouds are shown in Figures from 5.35 to 5.40. All the cloud cores show a general tendency that the dust optical depth increases toward the cloud core centres where the dust temperatures usually show a minimum value. However, this is not true if we consider all the fragments associated with individual cloud complexes. The peak optical depths in most of the complexes are often not associated with the lowest temperatures. For example in S159, the maximum value of the optical depth is found toward the central cloud core, whereas the minimum values of the dust temperatures are in the fragments located in the south-west direction of the main core (see Figure 5.35 and 5.24) .

Similar features are observed in the complexes S305, S254 and S128. In S305, the brightest submillimeter core, the S305S, retains the optical depth maximum, however, the fragments located on the north-west direction have the lowest temperatures among all the cores of S305 complex (see Figures 5.38 and 5.26). Likewise in S254, the optical depth peaks at the central S254S core, even though the lowest values of temperatures are in the neighbouring cloud fragment close to S255 (see Figures 5.39 and 5.27). The coldest region in the S128 complex is associated with the diffuse H II region S128, particularly S128S2, despite the fact the zone of highest optical depth is close to the compact H II region S128N (see Figures 5.40 and 5.28). The cores connected to the H II regions S156 and BFS15, however, do not show such properties: the sites of minimum temperature and the maximum optical depth are nearly the same (see Figures 5.37 and 5.25).

If we compare all the cores in individual complexes, the optical depth is found to be highest in the core S254S with a τ value of 0.17 at 850 μm. S254N holds the second highest value in optical depth, which is 0.15. The cloud core associated with the compact H II region S128N possesses remarkably high optical depth (0.14) compared to the cores incorporated with the diffuse H II region S128 in the same complex. Lowest values of optical depths are found in the complex S148, where the values are derived by assuming a uniform temperature of 10 K throughout the cloud. Note that peak optical depth values are less than 0.07 in S148, S159, BFS15, and S305.

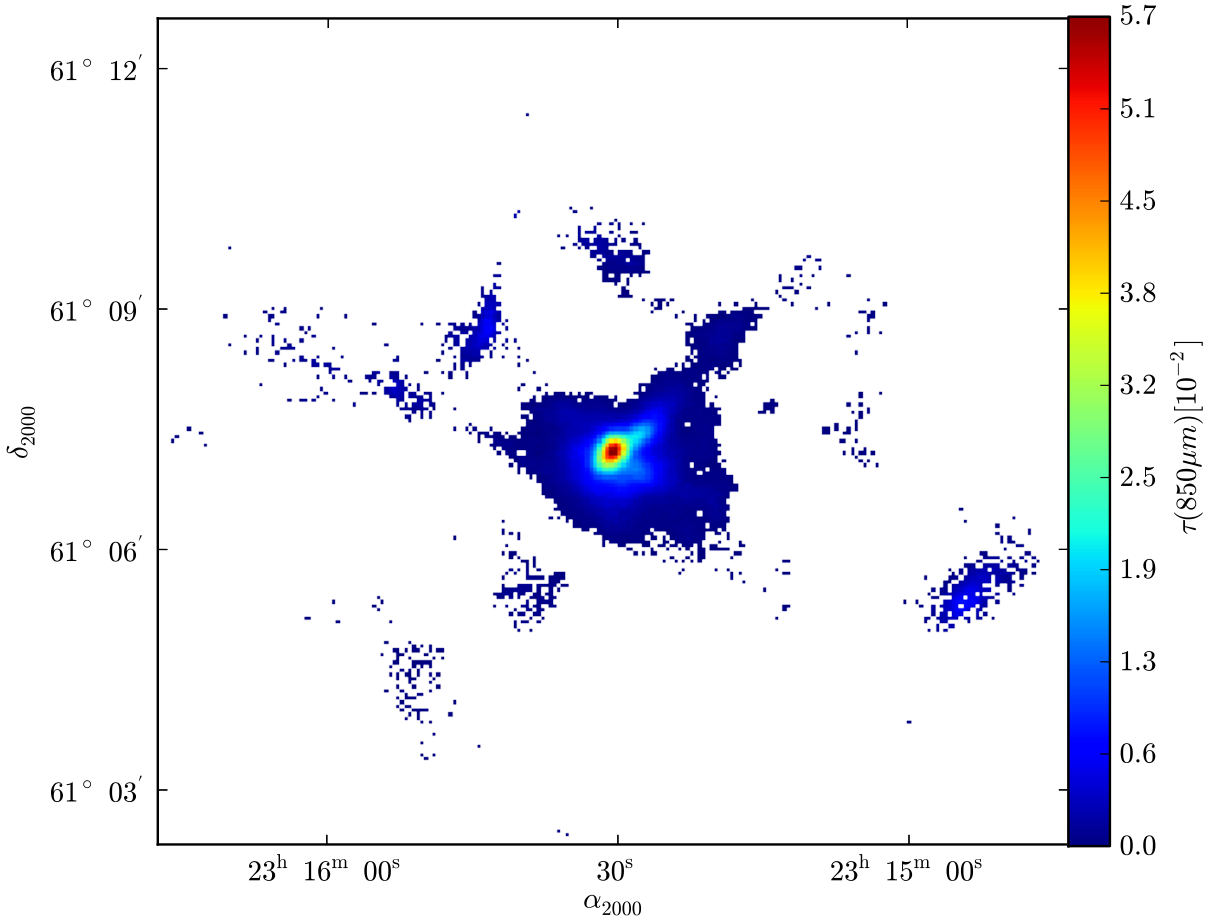

Figure 5.35: Optical depth plot of S159 at 850 μm using temperature derived from the assumption of a β of 2.

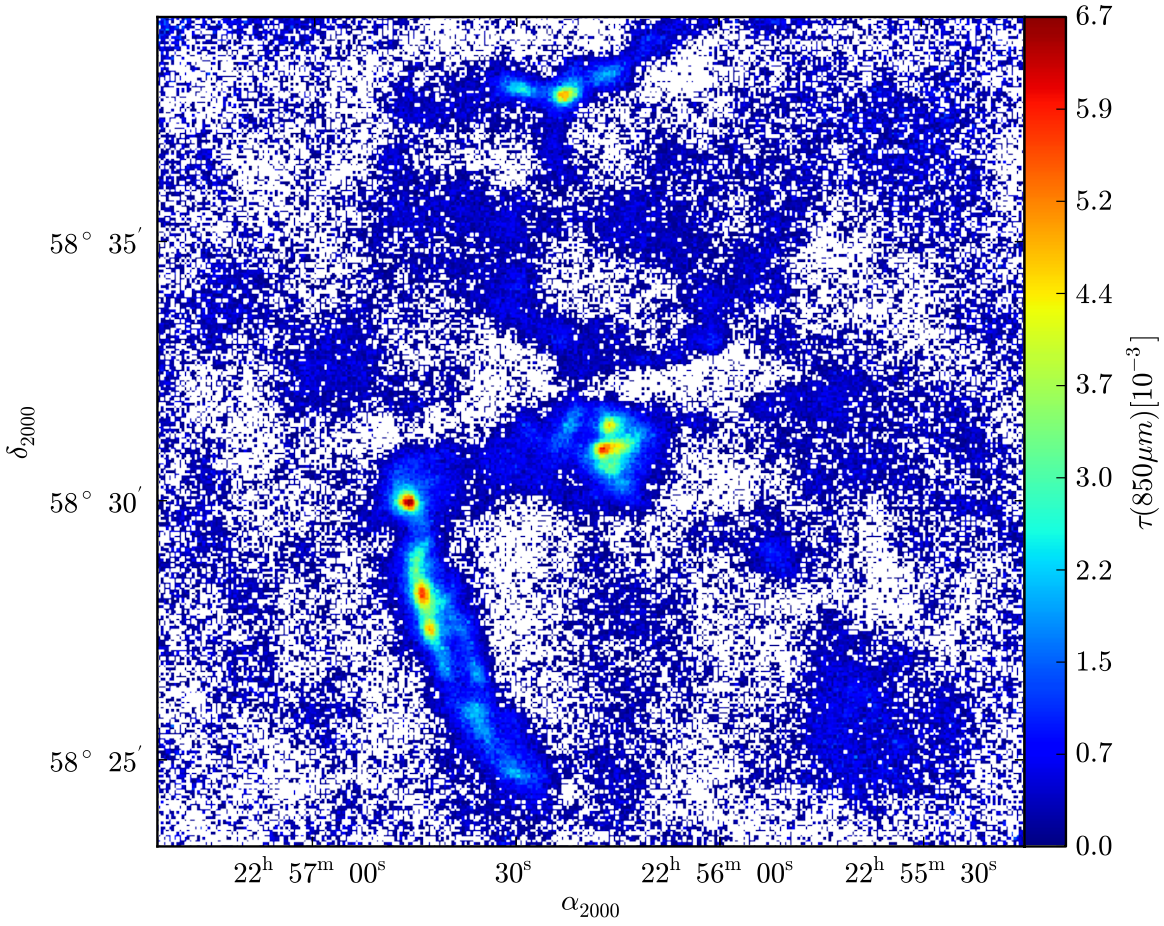

Figure 5.36: Derived optical depth of of S148 with an assumed T_d of 10 K.

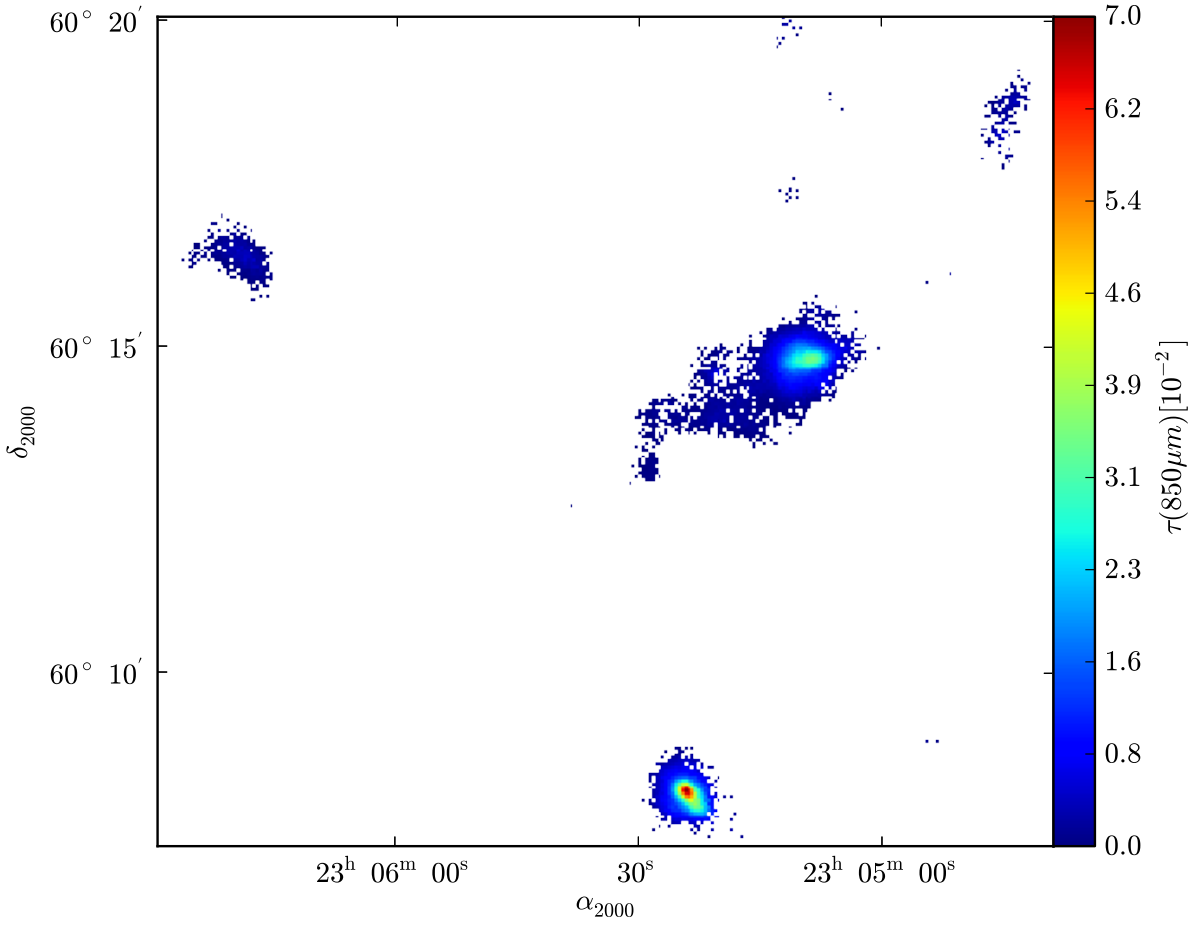

Figure 5.37: Optical depth plot of S156 at 850 μm using temperature derived from the assumption of a β of 2.

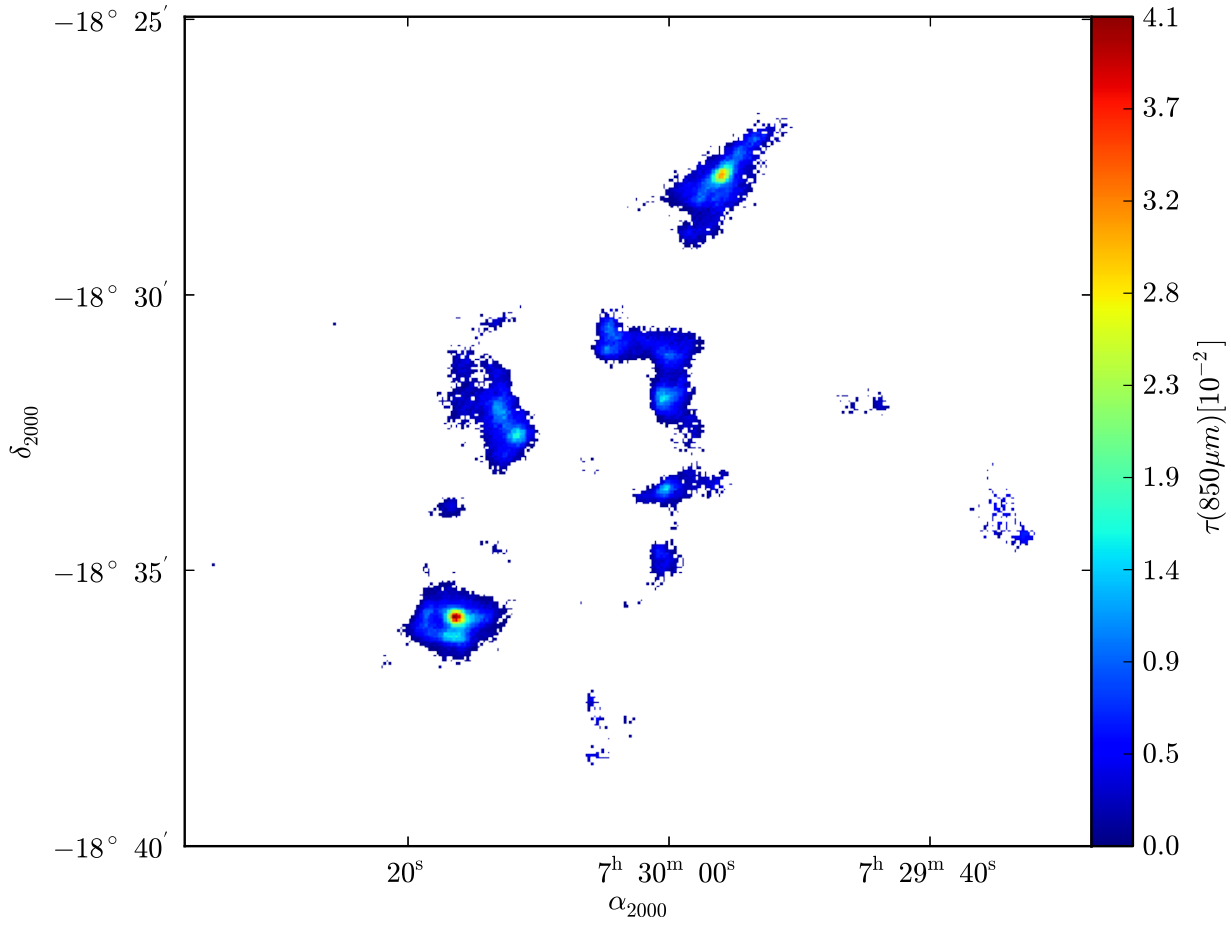

Figure 5.38: Optical depth plot of S305 at 850 μm using temperature derived from the assumption of a β of 2.

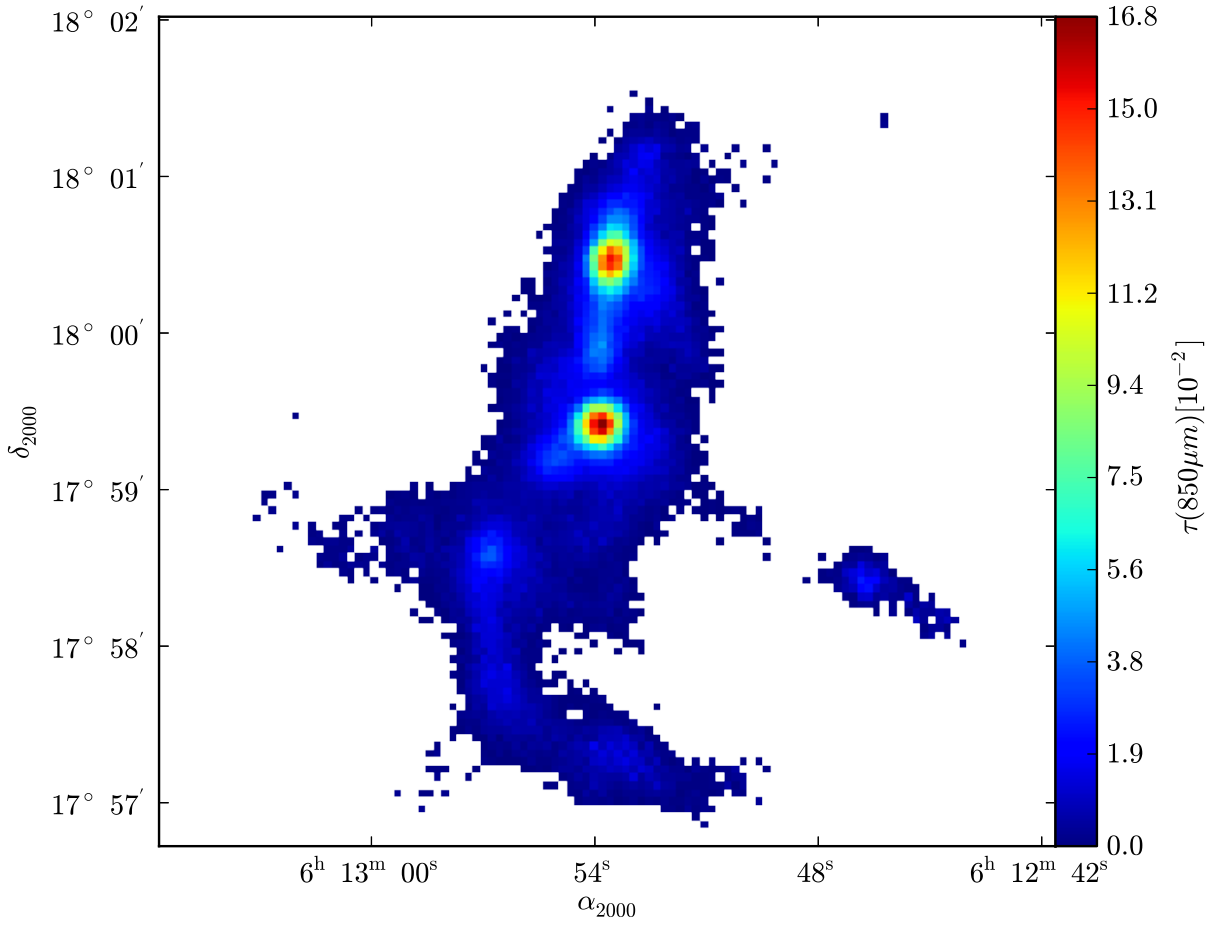

Figure 5.39: Optical depth plot of S254 at 850 μm using temperature derived from the assumption of a β of 2.

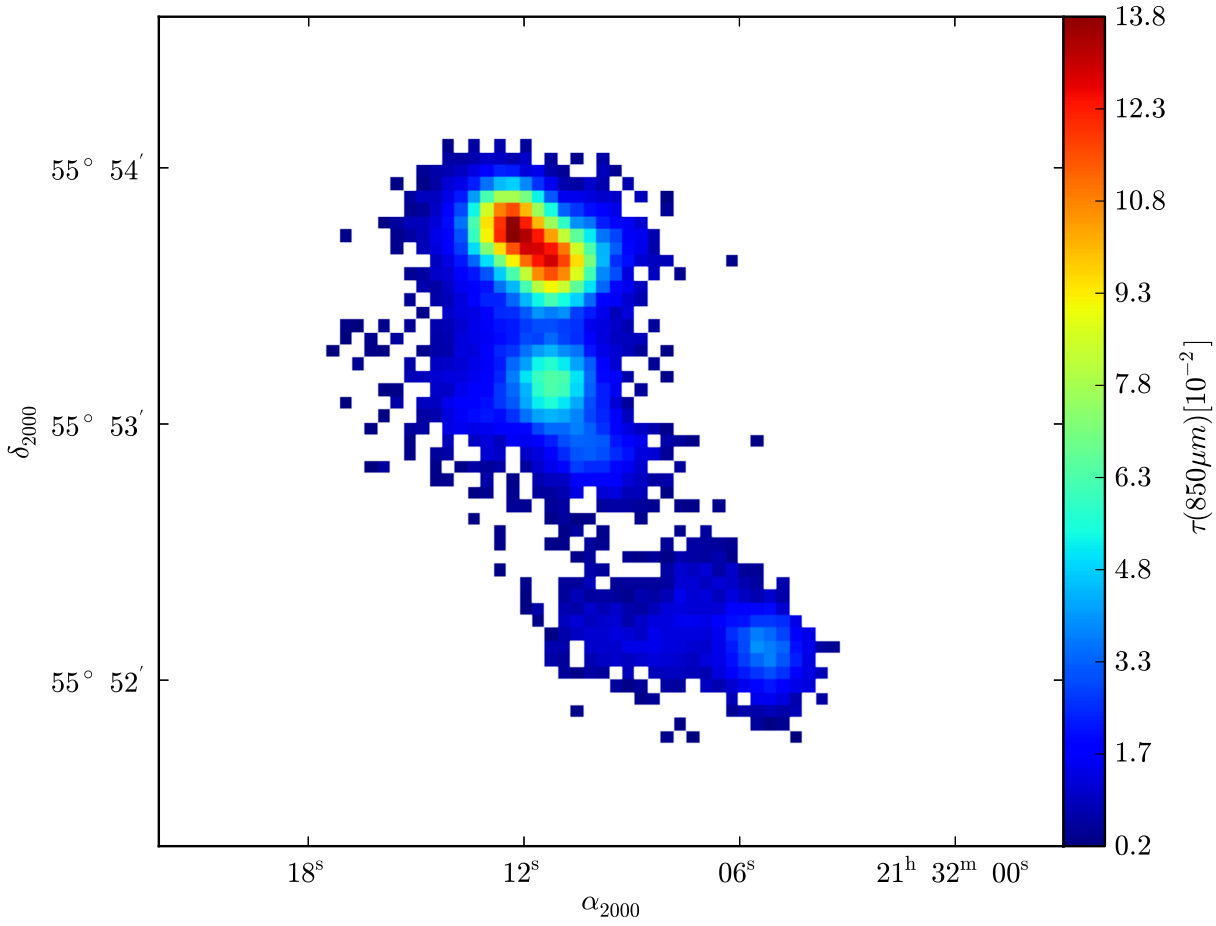

Figure 5.40: Optical depth plot of S128 at 850 μm using temperature derived from the assumption of a β of 2.

5.6.4 Column density maps

The maps of the hydrogen column density N_H derived from the 850 μm optical depth maps are shown in Figures 5.41 to 5.46. The value of N_H at the outer cloud boundary is close to zero and is analogous to the results from the optical depth maps. The column densities approach highest values towards the centres of the cores. The innermost region of S254S displays the highest column density, which is 4.3 $\times 10^{24}$ cm^{-2}. Note that S254N is also comparably dense with a column density of 3.9 $\times 10^{24}$ cm^{-2}. Column density maps of the other cloud cores such as S159, BFS15, S305S, and S128N also demonstrate peak column densities higher than 10^{24} cm^{-2} at the centres.

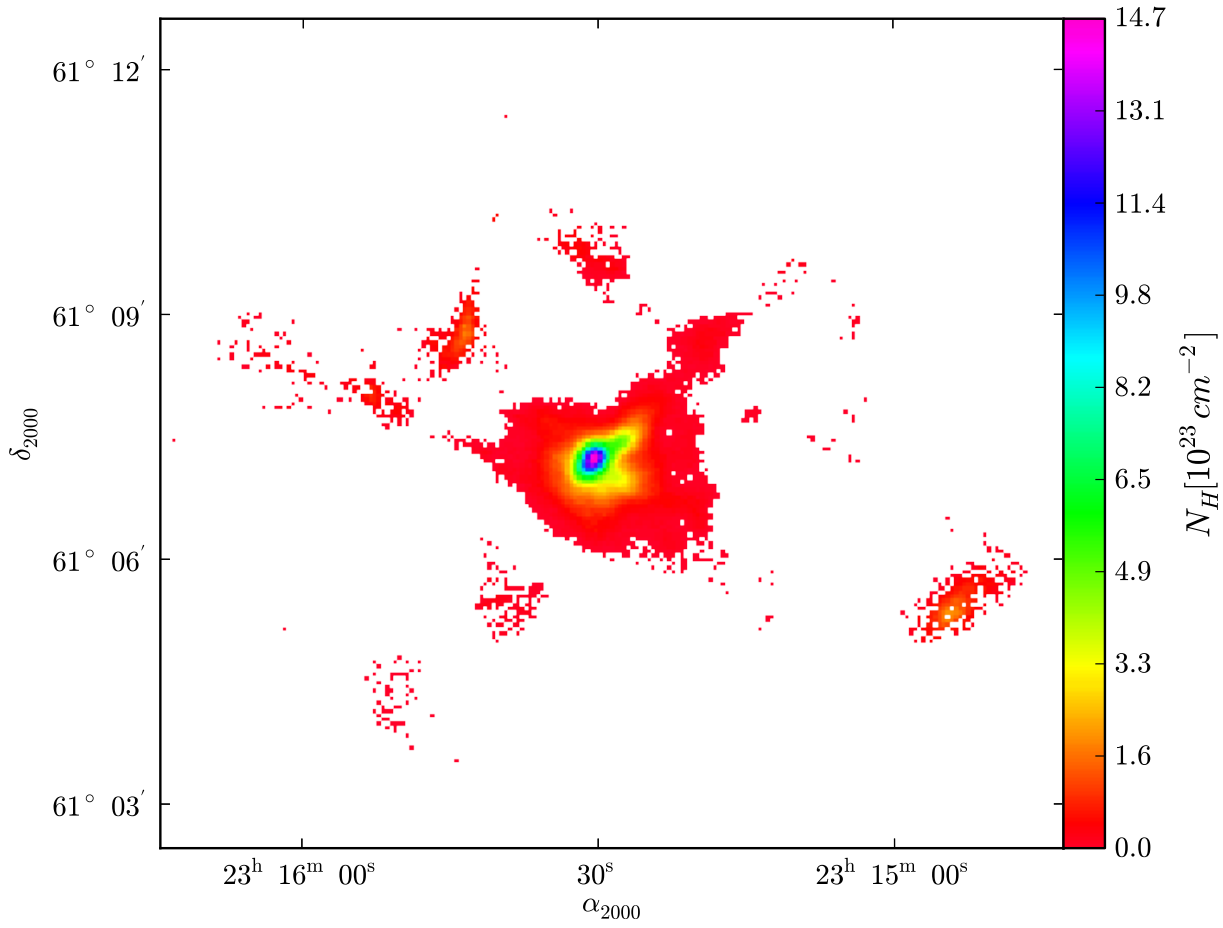

Figure 5.41: Column density plot of S159 obtained from 450 and 850 μm SCUBA-2 observations by assuming a β of 2.

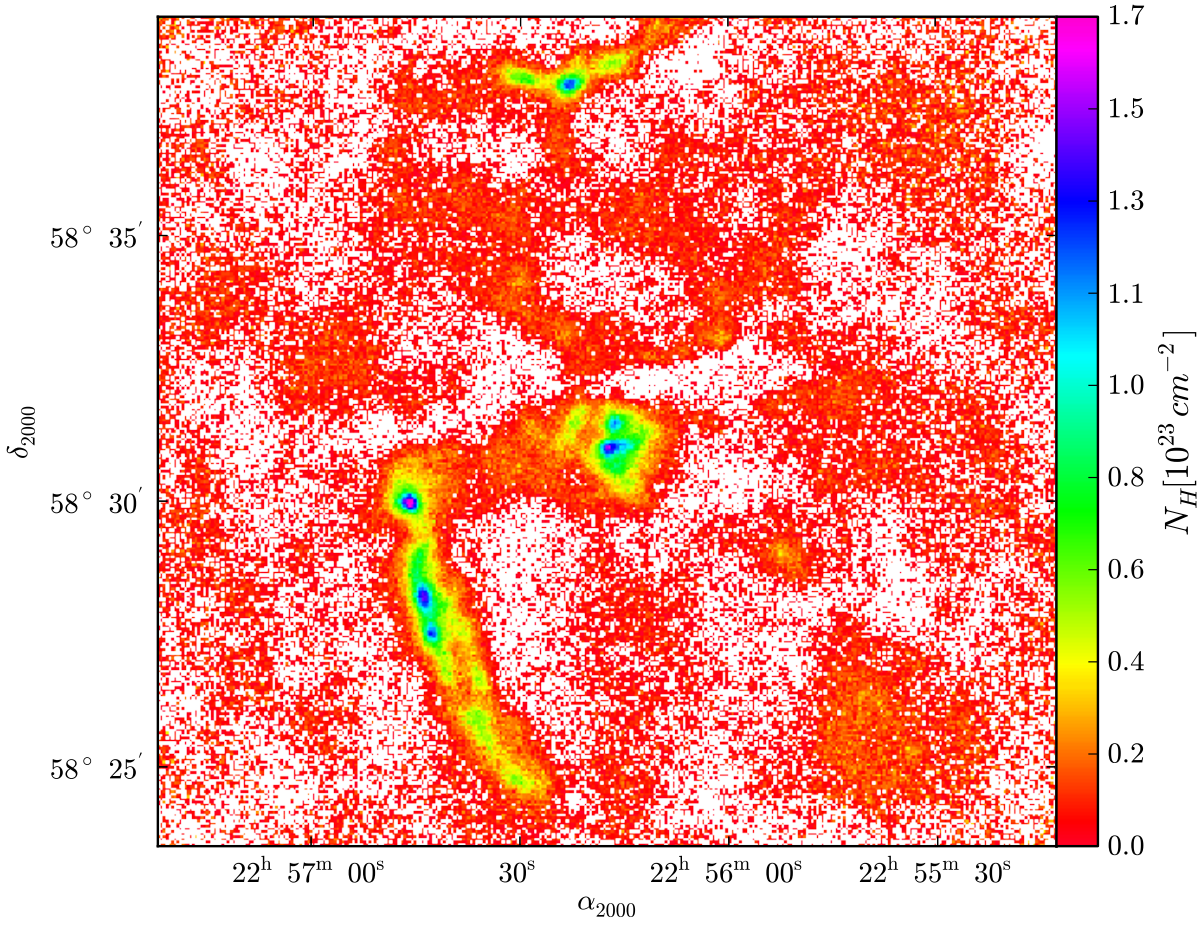

Figure 5.42: Column density plot of S148 at 850 μm using temperature derived from assuming a T_d of 10 K.

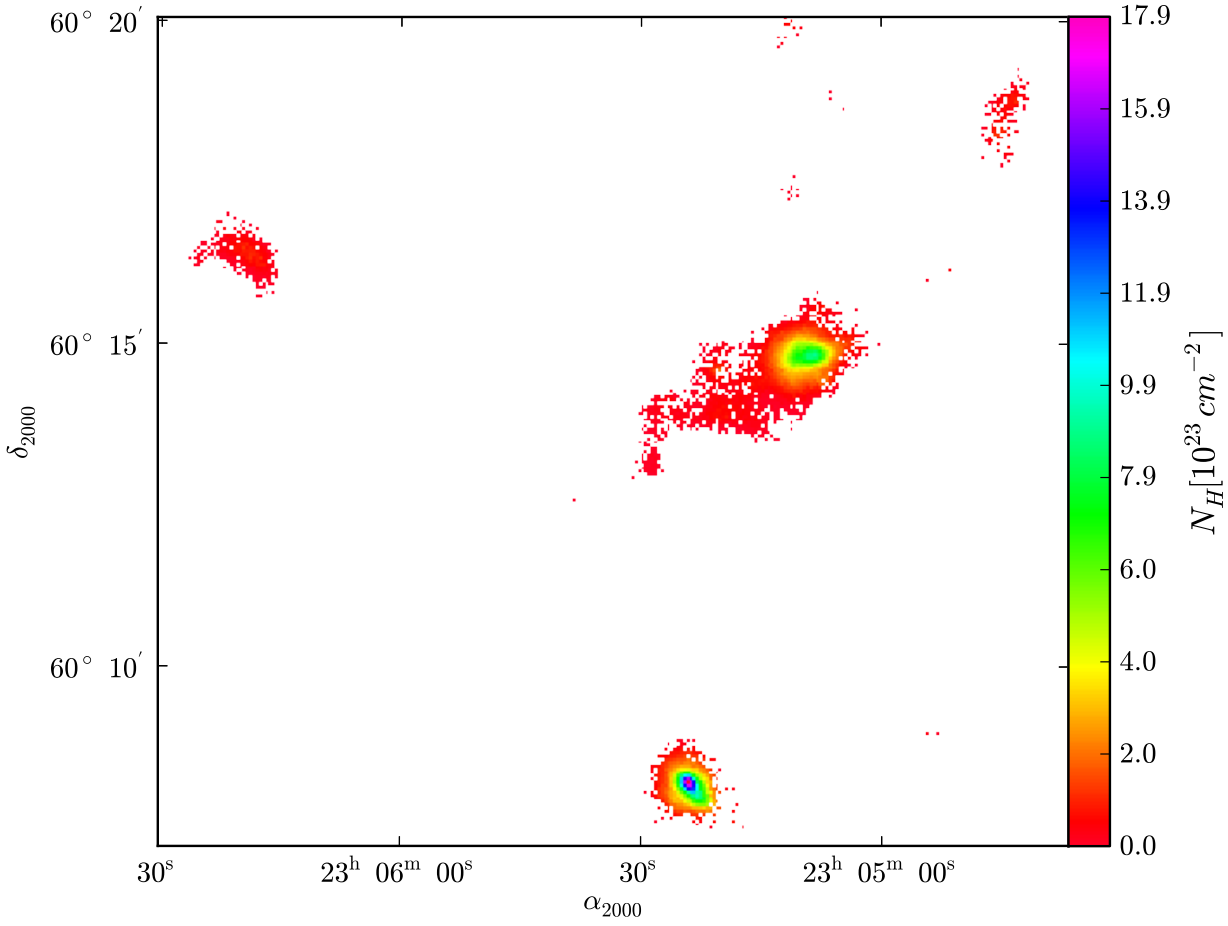

Figure 5.43: Column density plot of S156 obtained from 450 and 850 μm SCUBA-2 observations by assuming a β of 2.

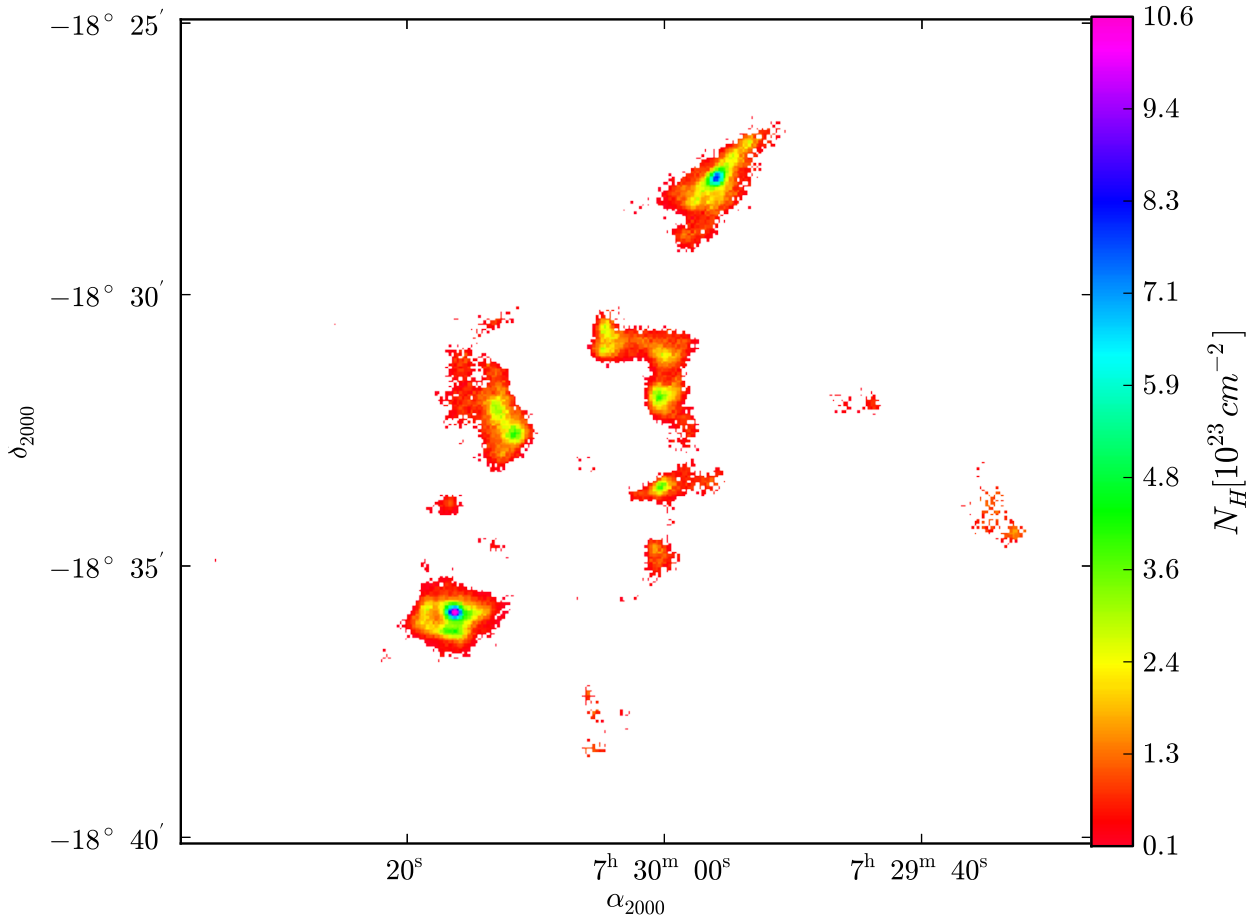

Figure 5.44: Column density plot of S305 obtained from 450 and 850 μm SCUBA-2 observations by assuming a β of 2.

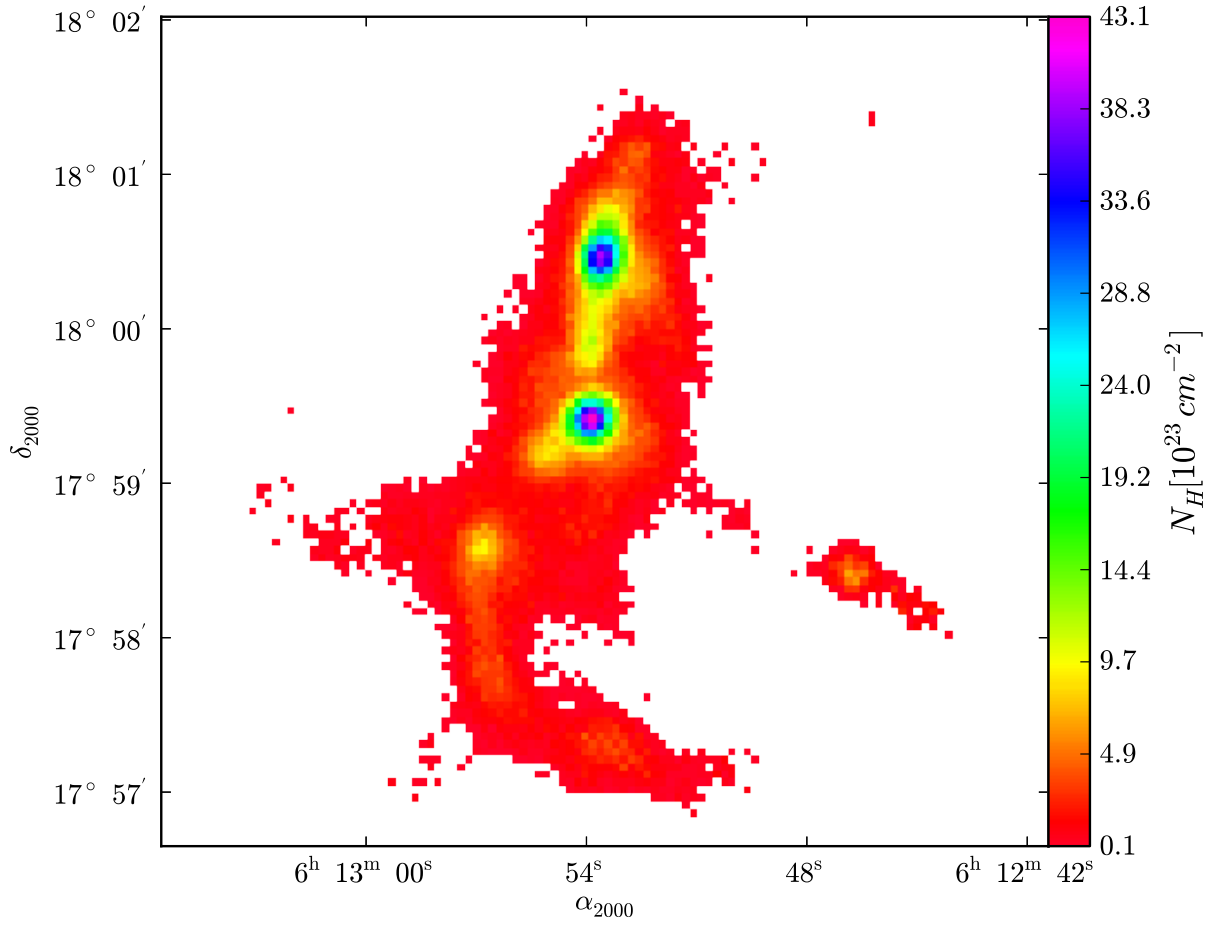

Figure 5.45: Column density plot of S254 obtained from 450 and 850 μm SCUBA-2 observations by assuming a β of 2.

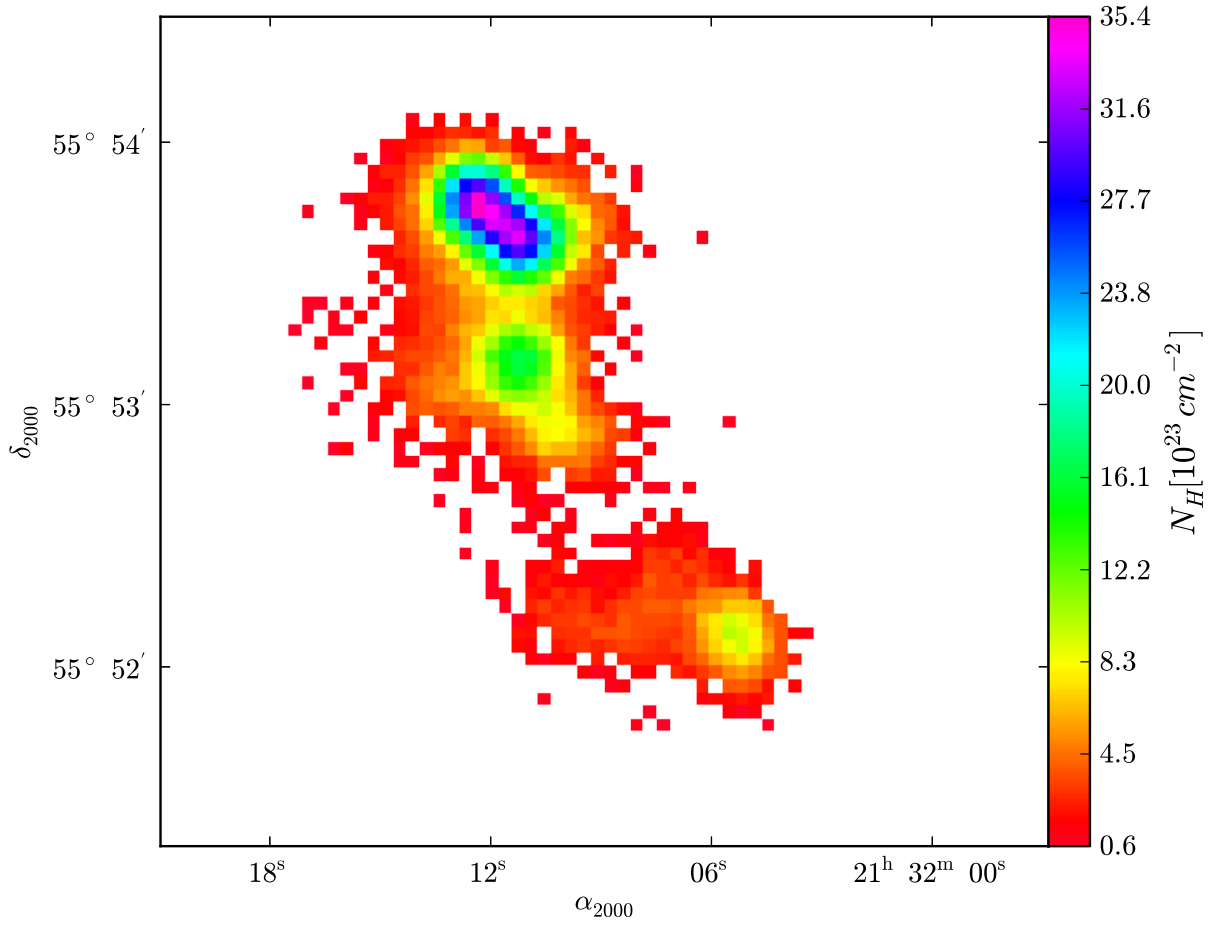

Figure 5.46: Column density plot of S128 obtained from 450 and 850 μm SCUBA-2 observations by assuming a β of 2.

5.6.5 Visual extinction maps

Visual extinction maps of the complexes are obtained from their derived column density maps and displayed in Figures 5.47 to 5.52. All the cores except S148 show peak extinction values above 100. In S254S, S254N, S128N, the peak A_V values are above 1000. The other complexes in the sample (S159, S305, an BFS15) are characterized by peak A_V between 100 and 1000.

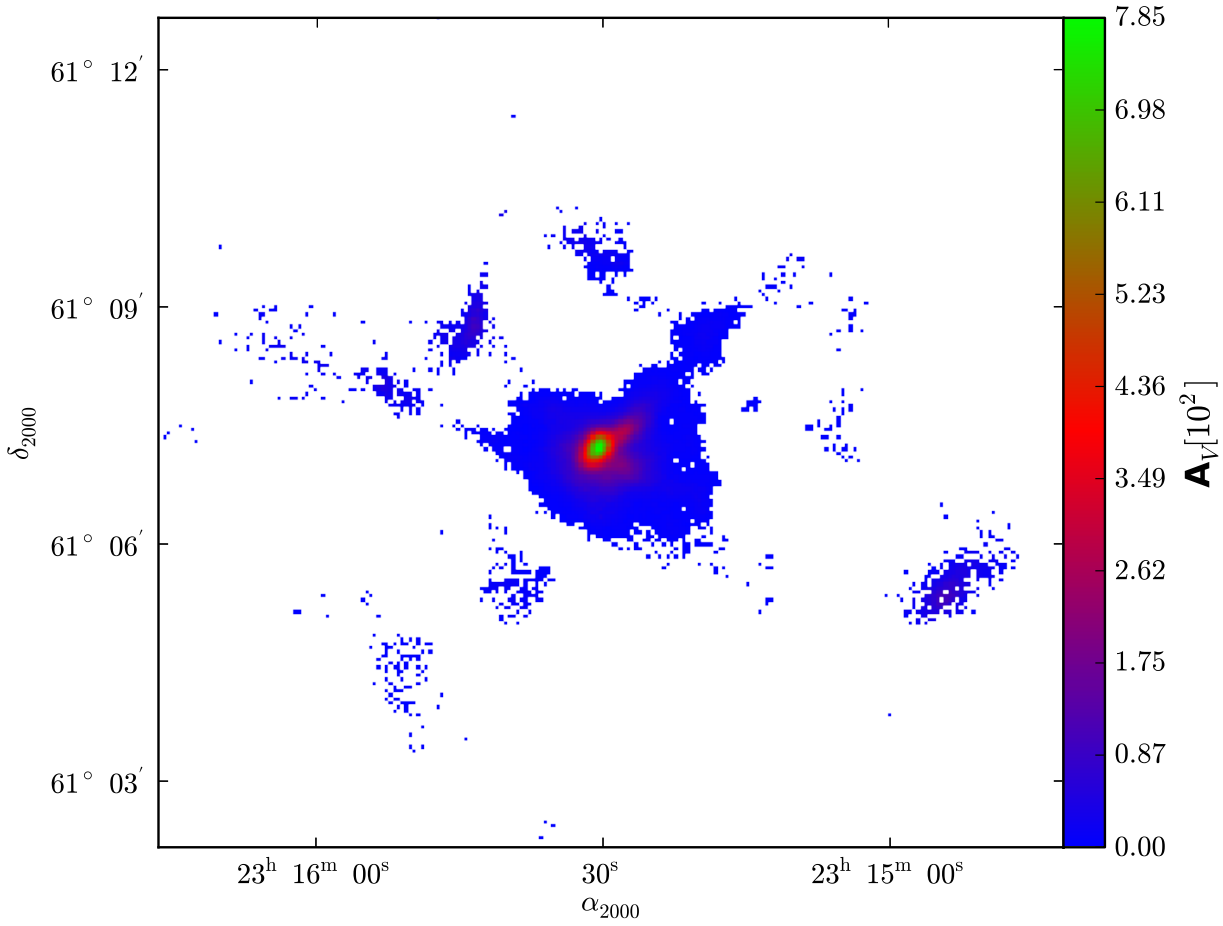

Figure 5.47: A_V plot of S159 at 850 μm using an assumed β of 2 in the temperature derivation.

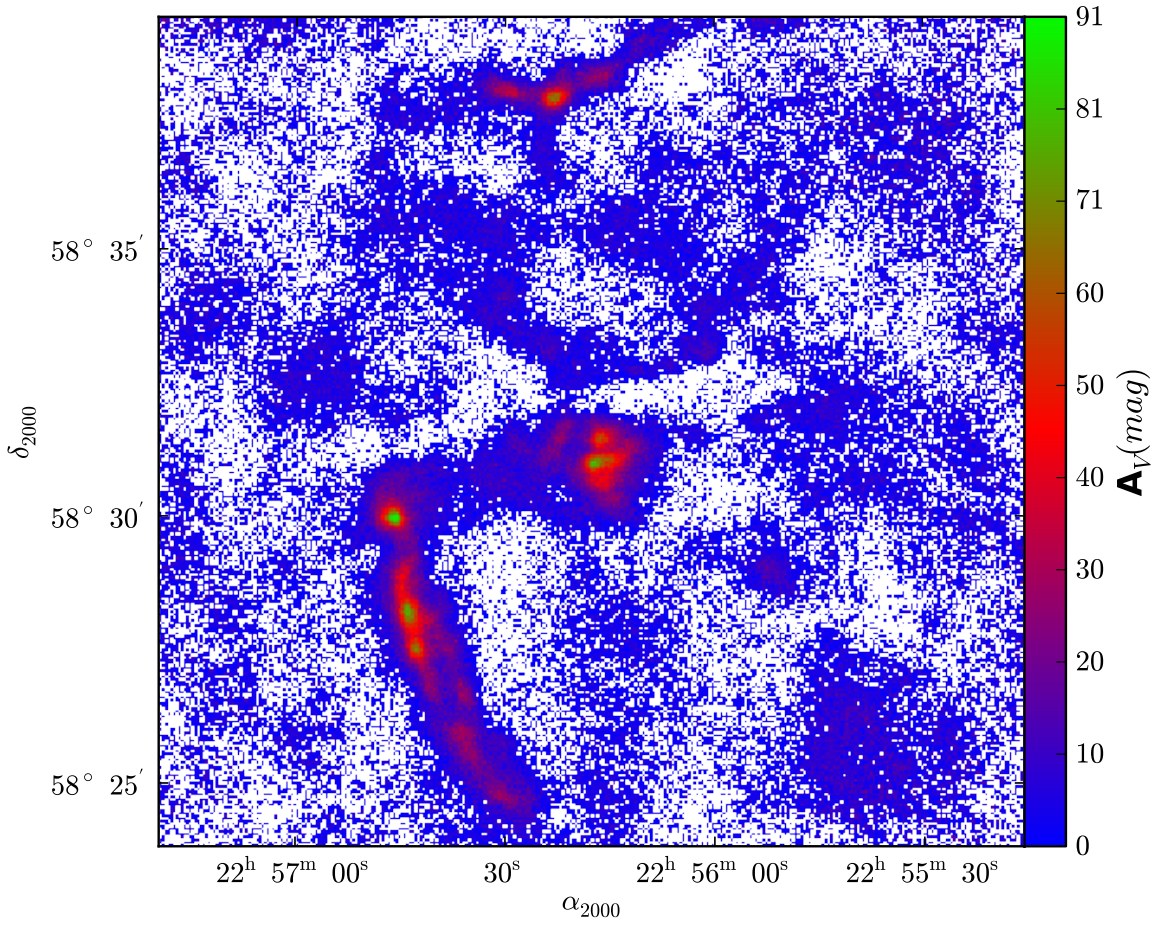

Figure 5.48: A_v plot of S148 at 850 μm using temperature derived from assuming a T_d of 10 K.

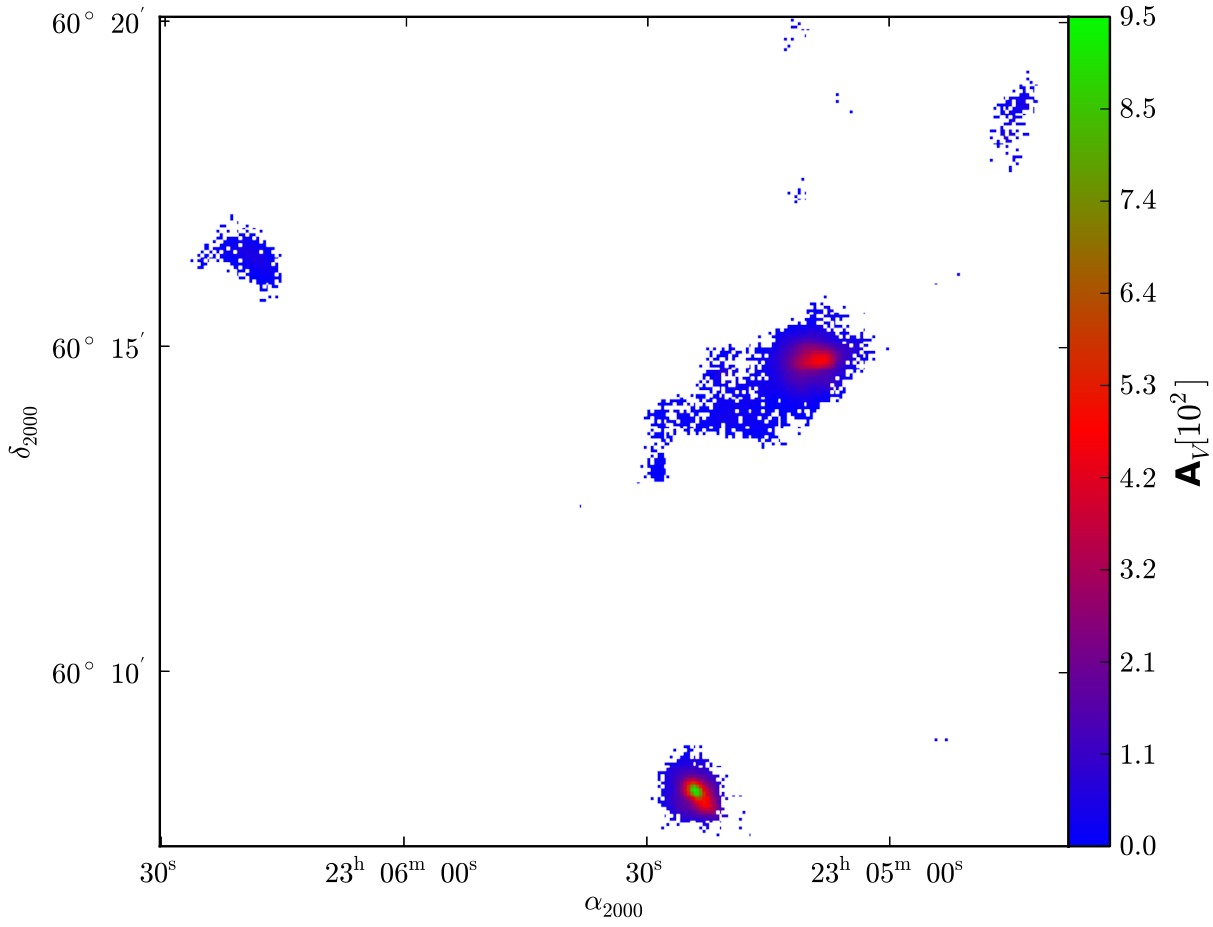

Figure 5.49: A_V plot of S156 at 850 μm using an assumed β of 2 in the temperature derivation.

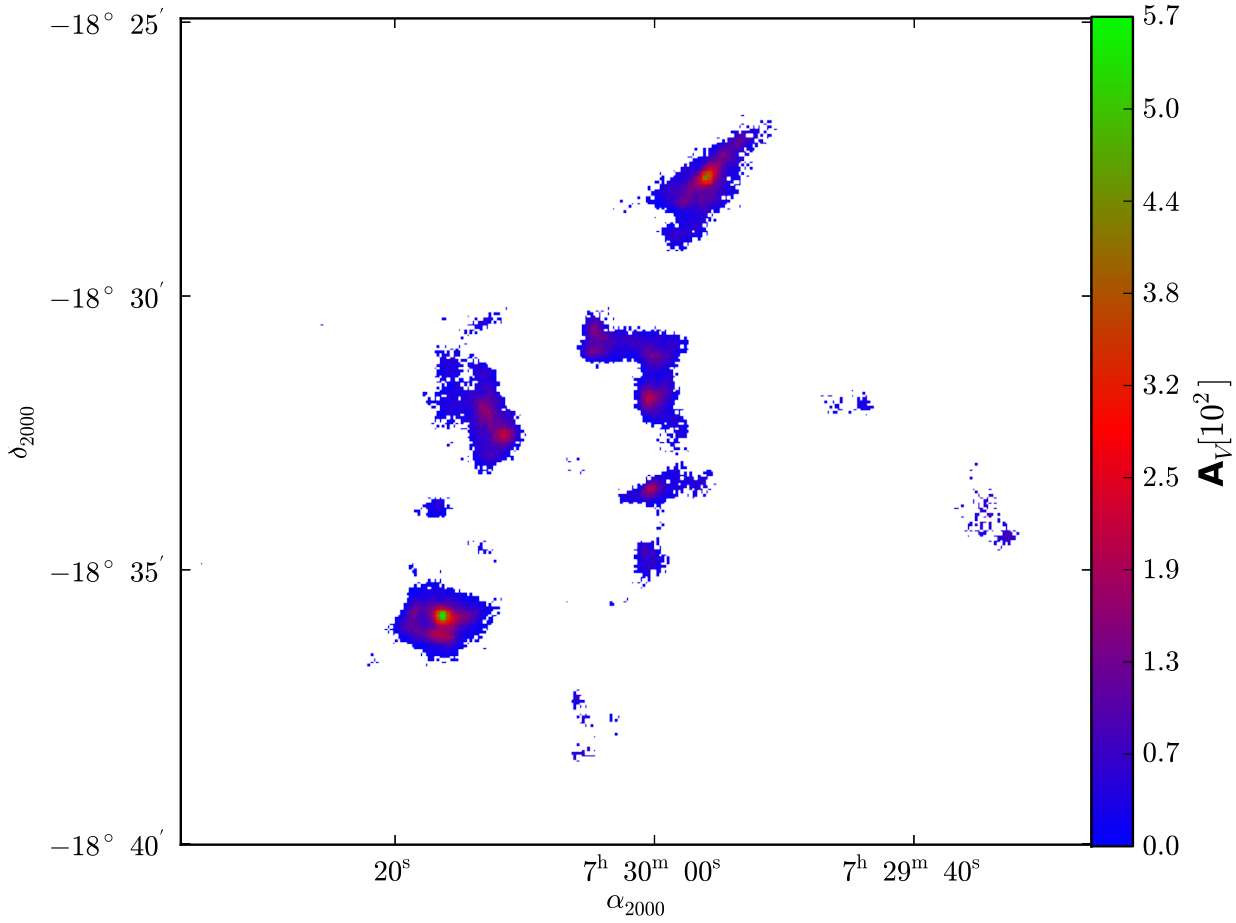

Figure 5.50: A_V plot of S305 at 850 μm using an assumed β of 2 in the temperature derivation.

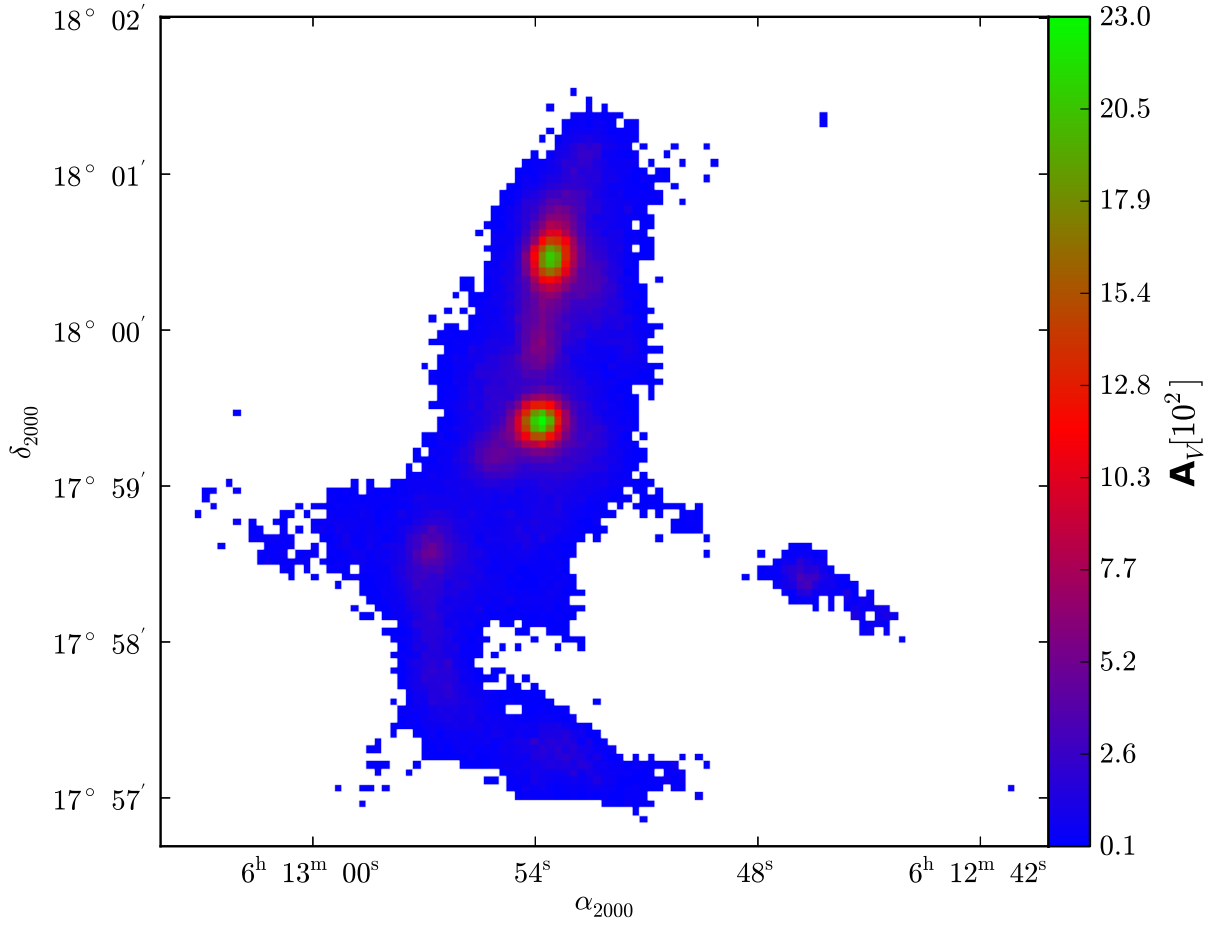

Figure 5.51: A_V plot of S254 at 850 μm using an assumed β of 2 in the temperature derivation.

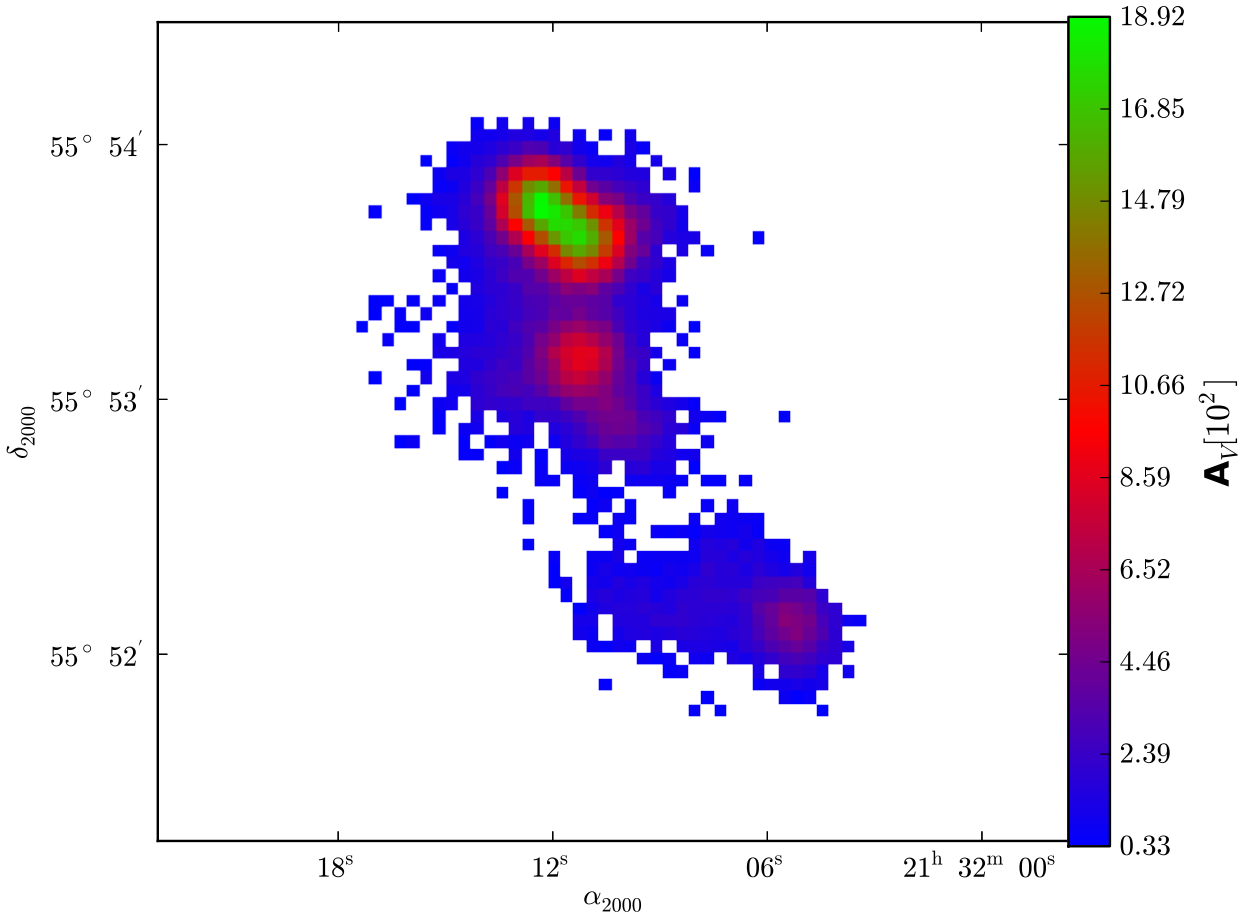

Figure 5.52: A_V plot of S128 at 850 μm using an assumed β of 2 in the temperature derivation.

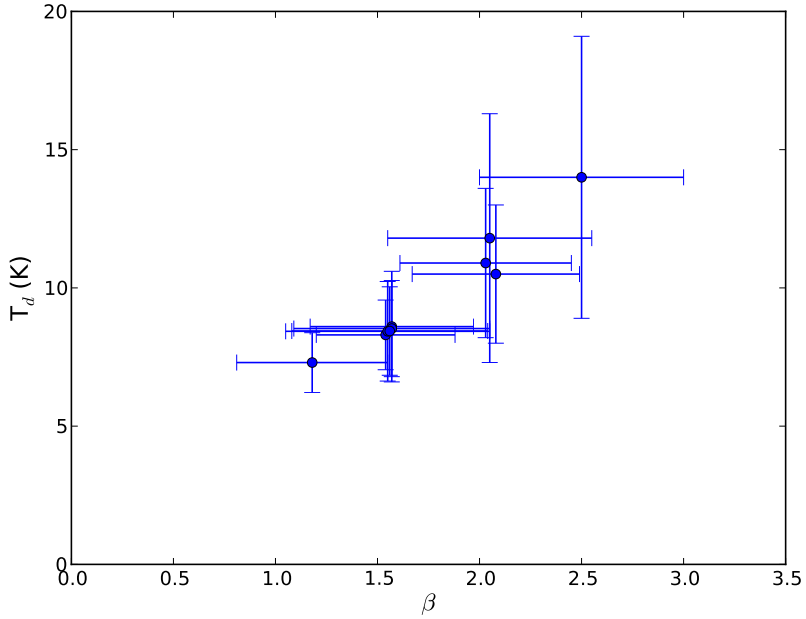

Figure 5.53: Plot of average values of T_d vs. average values of β of all the sample clouds.

The derived cloud properties are listed in Table 5.3. The first column gives the source names, and the second and third columns provide the average values of dust temperatures and dust emissivity indices for each core. Note that we counted the cores and their envelopes in calculating the average. The fourth, fifth, and sixth columns list the peak values of the optical depth at 850 μm, column densities and visual extinction at the centres of the cores. The average central number densities are given in the last column. The uncertainties in the mean temperatures and mean β are their $1-\sigma$ standard deviations attributed to the shape of the cloud core. Note that this uncertainty far exceeds the effect of the uncertainty in the flux due to the background. Uncertainties in the diameter and number densities of the clouds are primarily due to uncertainties in the distances to the clouds, and on average this is 18% and is not given in the table. Additional calibration errors of 50% at 450 and 20% at 850 μm in the SCUBA-2 fluxes also contribute uncertainties in the τ_{850}, N_H, A_V and $\bar{n_c}$ and are not shown in the table.

The mean values of the temperatures and the β for the clouds shown in Figure 5.53, show a strong positive correlation and has a correlation coefficient of 0.97. Note that β and T_d are interdependent: lower (higher) values of dust temperatures correspond to lower (higher) values of β. See Figure 5.53.

Table 5.3: Derived properties of the cores: Column 1 lists the core names associated with the Galactic H II regions; columns 2 and 3 list the mean colour temperature and mean β of the cores derived from the 450 and 850 μm fluxes. Columns 4, 5, and 6 list the peak values of the optical depth, column density, and visual extinction detected towards the centres of the respective cores. The central number densities of the cores are listed in the last column.

Source	$\bar{T_d}$ (K)	$\bar{\beta}$	τ_{850}	N_H cm^{-2}	A_V (mag)	Diameter (pc)	$\bar{n_c}$ cm^{-3}
S159	14.0±5.1	2.50±0.50	0.06	1.5×10^{24}	785	1.62	2.9×10^{5}
S156	11.8±4.5	2.05±0.50	0.04	9.0×10^{23}	482	3.06	2.1×10^{5}
BFS15	8.6±2.0	1.57±0.40	0.07	1.8×10^{24}	953	1.80	5.5×10^{5}
BFS18	15.8±5.3	2.48±0.33	4.7×10^{-3}	1.2×10^{23}	64.3	0.75	5.2×10^{4}
S148	–	–	6.29×10^{-3}	2×10^{23}	86.1	3.56	1.5×10^{4}
S305S	8.30±1.26	1.54±0.34	0.04	1.1×10^{24}	565	2.31	1.5×10^{5}
S305N	7.30±1.08	1.18±0.37	0.03	8.0×10^{23}	429	1.62	1.6×10^{5}
S254S	10.9±2.7	2.03±0.42	0.17	3.9×10^{24}	2303	0.90	1.6×10^{6}
S254N	10.5±2.5	2.08±0.41	0.15	4.3×10^{24}	2088	0.76	1.7×10^{6}
S128N	8.53±1.74	1.57±0.48	0.14	3.5×10^{24}	1892	1.98	5.8×10^{5}
S128S1	8.43±1.80	1.55±0.50	0.06	1.6×10^{24}	874	1.67	3.2×10^{5}
S128S2	8.44±1.60	1.56±0.48	0.04	1.0×10^{24}	537	1.27	2.6×10^{5}

5.7 Gas Masses from Dust Emission

There are many ways to derive the dust masses and hence the gas masses from submillimeter thermal emission. The hydrogen column density maps can be turned into gas masses. Furthermore, one can fit spectral energy distribution models to submillimeter continuum emission and can derive the gas masses assuming a gas-to-dust ratio. A third method is to assume a constant dust temperature, derive the dust masses and then derive the gas masses. Note that in the first case, we are not assuming the presence of a constant dust temperature throughout the cloud. However, in the second and third method, we assume isothermal dust temperature throughout the cloud.

The gas masses derived from the column densities of the clouds are listed below. The uncertainties in the masses are due to the uncertainty from the shape of the clouds and far exceed the uncertainties due to uncertainties in the flux. Note that uncertainties in the distances are the largest source of uncertainties on the observed SCUBA-2 flux densities. The uncertainties in the derived masses do not include any uncertainties due to distance and calibration on the fluxes. In the sample clouds, the average uncertainty contribution due to distance to the observed flux densities is $\approx 36\%$. The clouds show a large range in the distance uncertainties: S148 shows the smallest uncertainty of $\approx 11\%$ in the distance, the uncertainty in the distance to S305 contributes the largest, $\approx 54\%$, uncertainty in their observed fluxes. Note that additional flux calibration uncertainties are 50% at 450 and 20% at 850 μm.

All the individual clouds in the complexes are massive with the values of gas masses ranging from 2.81×10^2 $M_\odot$ to 6.4×10^4 $M_\odot$. The least massive cloud is BFS18 with a gas mass of 281 $M_\odot$. The most massive cloud is one of the farthest clouds S128N, associated with the compact H II region S128N. Note that all the clouds in the complex S128 show much higher masses, with masses above 10^4 $M_\odot$, than the clouds in other complexes.

The gas masses derived by other methods are discussed in Chapter 6.

Table 5.4: Cloud masses

Source	M_{gas} ($M_\odot$)
S159	$(6.2\pm0.1)\times10^3$
S159C	$(7.20\pm0.03)\times10^3$
S156	$(4.8\pm0.2)\times10^3$
BFS15	$(4.2\pm0.2)\times10^3$
BFS18	$(2.81\pm0.14)\times10^2$
S148	$(7.3\pm1.3)\times10^3$
S305S	$(1.13\pm\ 0.04)\times10^4$
S305N	$(1.17\pm\ 0.03)\times10^4$
S305C	$(4.45\pm0.02)\times10^4$
S254S	$(5.48\pm\ 0.02)\times10^3$
S254N	$(6.68\pm0.03)\times10^3$
S254N&S	$(1.52\pm0.04)\times10^4$
S254C	$(1.74\pm0.14)\times10^4$
S128N	$(6.4\pm0.1)\times10^4$
S128S1	$(3.28\pm0.06)\times10^4$
S128S2	$(1.87\pm0.04)\times10^4$
S128C	$(1.11\pm0.06)\times10^5$

5.8 Chapter Summary

In this chapter, we presented the dust continuum maps of six molecular complexes associated with Galactic H II regions. From the surface brightness maps of the clouds, different physical properties such as the dust temperature, dust emissivity index, optical depth, column density and visual extinction of the clouds were derived. The major results are outlined below:

• All the clouds are colder at the centre and warmer towards the periphery.
• The dust emissivity index values at a constant dust temperature of 10 K range from 0.5 to 3-3.5 in all the target clouds.
• The optical depth maps show that dust is optically thin at sub-millimeter wavelengths.
• Peak hydrogen column densities in all the complexes range from 10^{23} to 10^{24} cm^{-2}.
• Peak extinction at visual wavelengths is very high and varies from around 100 to over thousand.
• The column-density derived masses indicate that clouds are massive with gas masses ranging from around 100 to over 10^4 M$_\odot$.

Chapter 6

Analysis: Cold Dust from SCUBA-2 Observations

In this chapter, we analyze the results obtained from the SCUBA-2 observations of Galactic H II regions presented in Chapter 5. In the first section we discuss the two-dimensional maps that represent different physical properties of the clouds. We construct dust temperature and number density radial profiles of all the clouds in Section 6.2. The third section deals with the effect of possible line contamination on the SCUBA-2 fluxes. We also consider the presence of low density materials along the line-of-sight and their influence on SCUBA-2 data. In the last section we provide composite colour images of some of our clouds, which reveal the spatial distributions of different emission components accompanying the sample Galactic H II regions.

Thermal emission from dust at sub-millimeter wavelengths is very effective in tracing the gas column densities (if we know the dust temperature distribution) since the continuum emission from dust is optically thin at long wavelengths. The SCUBA-2 observations reveal that the dust grains in molecular clouds near massive star-forming regions can have very low temperatures, as low as 6K in the centres of the clouds, for a dust emissivity index of 2.0. Dust temperatures progressively rise from the centres of the cloud cores to the outer envelopes of the clouds.

Stars usually form in locations of dense molecular gas at high densities, over 10^4 cm^{-3}, and giant molecular clouds (GMCs) are ideal sites for such dense concentrations of gas. However, the star formation efficiency in GMCs is found to be very low, less than 3% [Myers et al., 1986; Lada, 1987], compared to the star formation efficiency in low-mass star-forming regions. The efficiency of isolated star formation is 9-15% [Swift and Welch, 2008] and 30-50% [Matzner and McKee, 2000] for clustered low-mass star formation. However, in regions of proto-stellar outflows, the low-mass star formation efficiency can be 25-70% [Matzner

and McKee, 2000]. Analyzing the cores within GMCs is therefore important to better understand the star formation processes.

The mean central densities of our sample cores is typically close to a value of 5×10^5 cm^{-3}. However, the central densities of the sample cores range over two orders of magnitude, from 10^4 to 10^6 cm^{-3}. In order to investigate the probable internal dynamics of the cloud cores, we need more than the average over the entire core. For this we construct temperature and density profiles and discuss their implications for the star formation.

6.1 Dust Temperature Radial Profiles

Dust temperature profiles of all the cloud cores are derived by assuming that each core has a spherical structure. The profile values are obtained by averaging the line-of-sight observed temperatures over 6″ wide concentric spherical annuli from the object centre, and the uncertainties in the temperature values are the standard deviation of temperature values from the mean in each annulus. The observed temperature profiles of the cloud cores are shown in Figures 6.1 to 6.7. The majority of the cloud cores are cold with temperatures ranging from 6K (in the centre) to ≈ 14K (at the core edges) except the core BFS18, where the temperatures are higher with 10 K at the centre and 22 K at the core boundary.

Nearly all the temperature profiles show a conspicuous trend: a break in their shape, with a 2-3 K increase in temperature up to a certain distance from the core centre, and then a couple of degrees of upswing in temperatures until the core boundary. The radius at which this break takes place is different in different cores. Cores such as S159, S156, BFS15, BFS18, and S254N show this tendency, especially between 0.2 and 0.4 pc. The shape of the observed temperature profiles in this study reveals interesting similarities to that obtained from the starless core TMC-1C in the Taurus molecular cloud: for a β of 1.5, they observe dust temperatures ranging from 6K to 22K from the centre to the outer envelope [Schnee and Goodman, 2005]. However, note that the TMC1-C is a low-mass star-forming core.

The observed temperature distribution shows a rise in the temperature from the centre of the core to the outer envelope, indicative of a less heating in the centre, for a constant value of the emissivity index. This feature in our sample cores is most likely to be attributed to the lack of any central heating source, since cores with increasing temperatures towards smaller radii depict cores that enclose central heating sources [van der Tak et al., 2000].

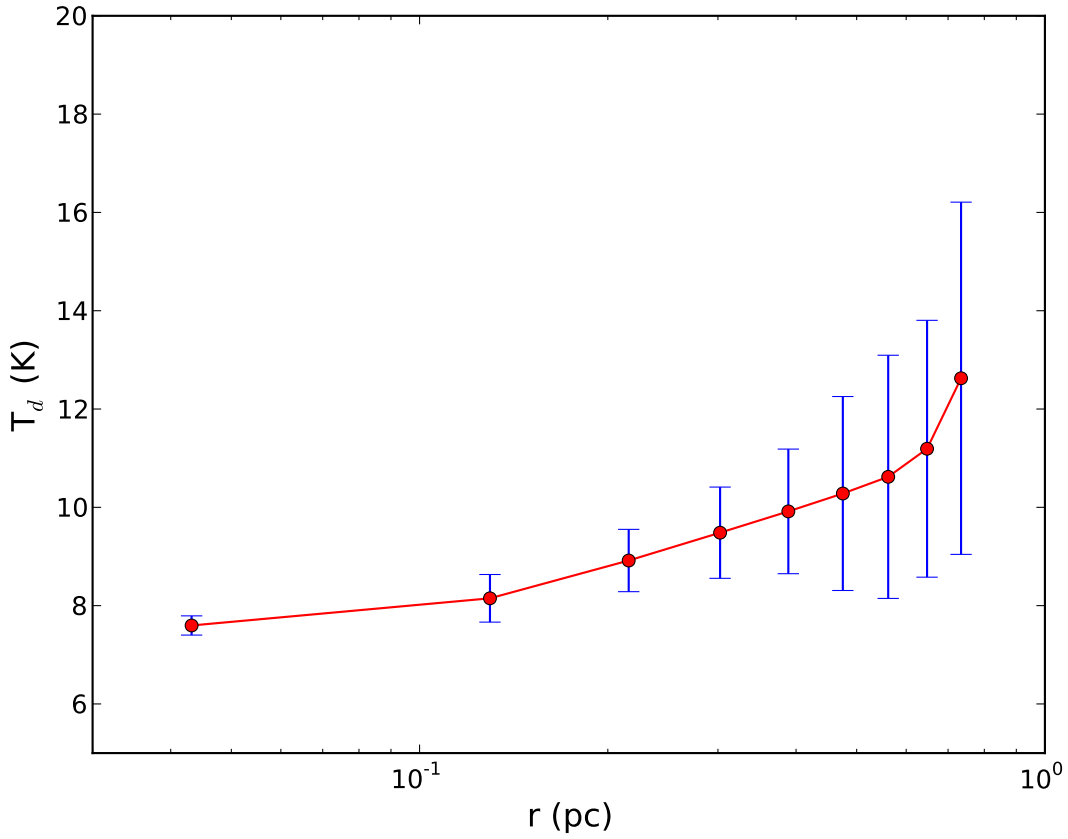

Figure 6.1: Dust temperature profile of the S159 core. Error bars indicate standard deviation of temperature distribution in each radial annulus.

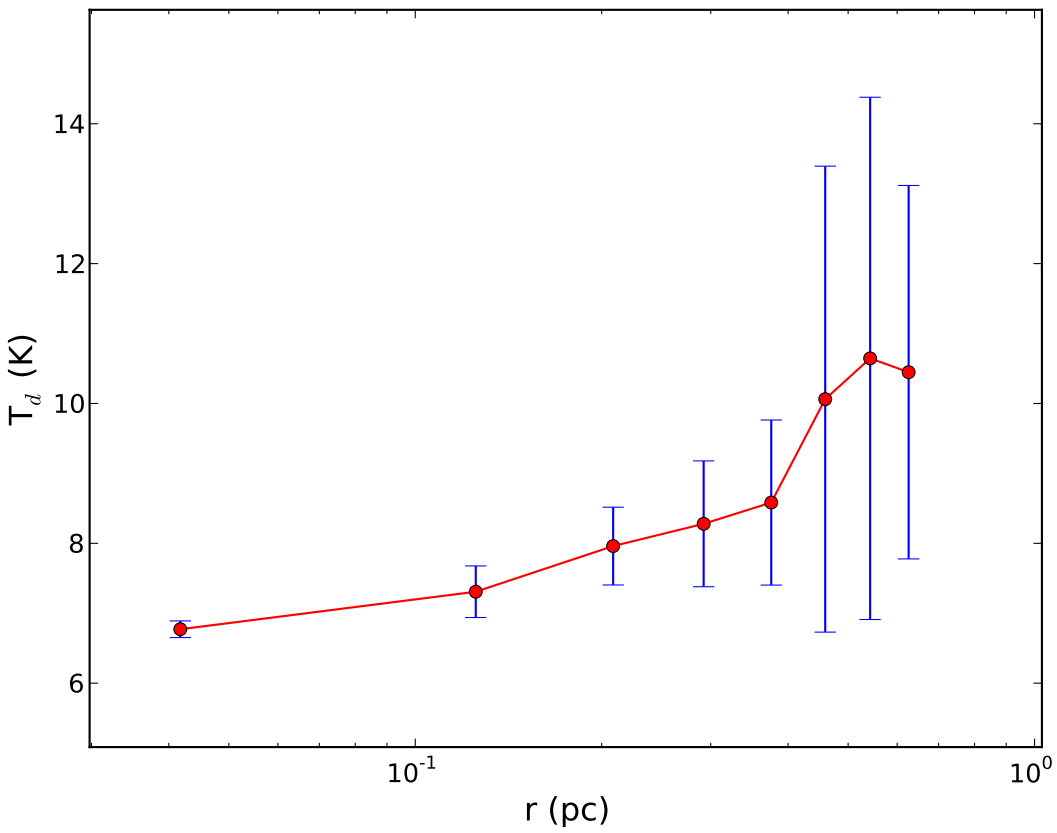

Figure 6.2: Dust temperature profile of the S156 core. Error bars indicate standard deviation of temperature distribution in each radial annulus.

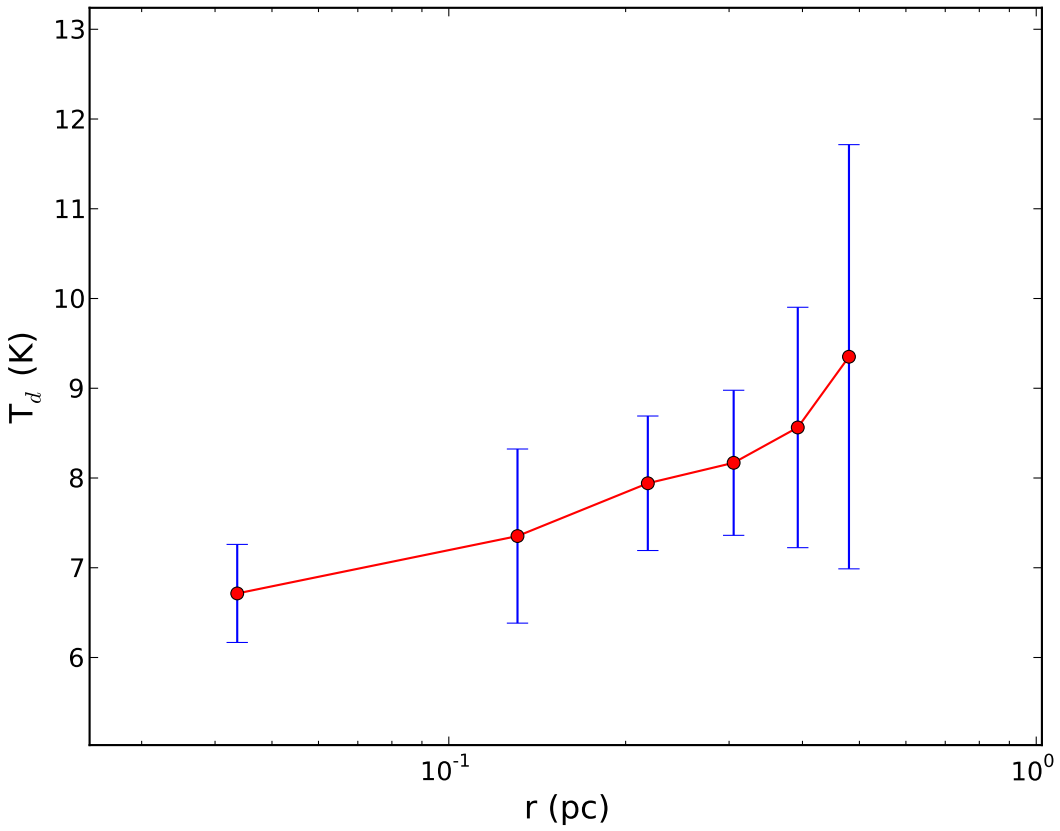

Figure 6.3: Dust temperature profile of the BFS15 core. Error bars indicate standard deviation of temperature distribution in each radial annulus.

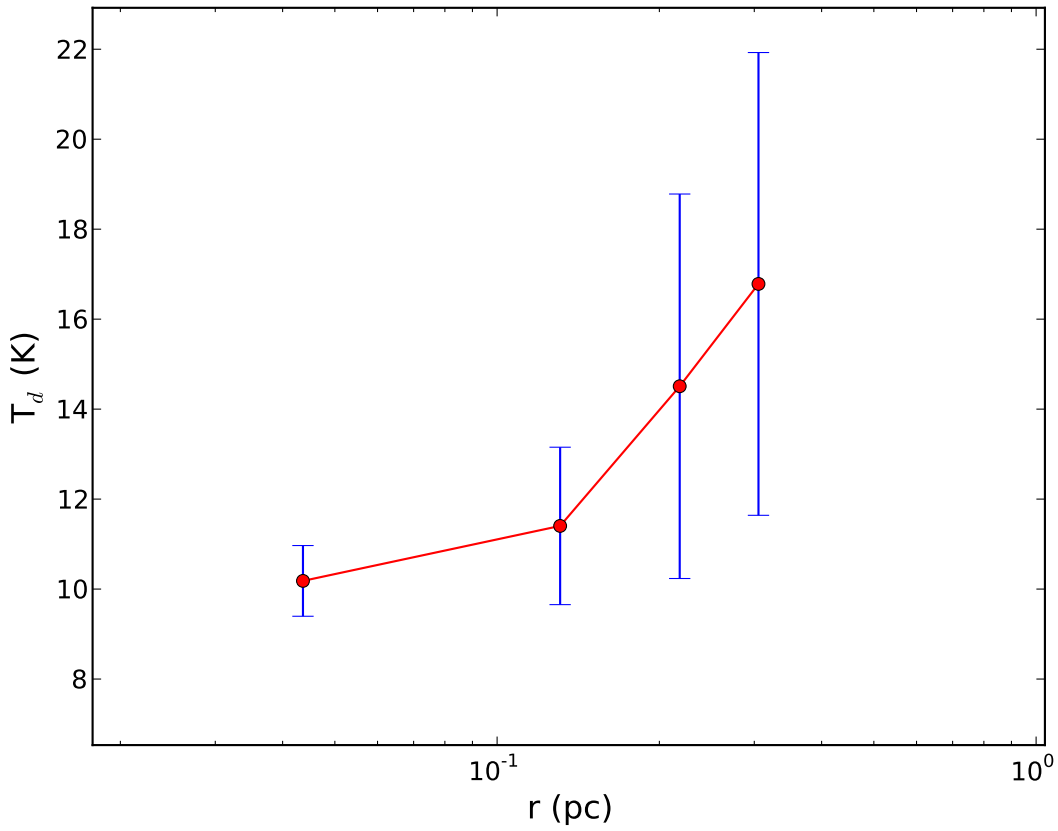

Figure 6.4: Dust temperature profile of the BFS18. Error bars indicate standard deviation of temperature distribution in each radial annulus.

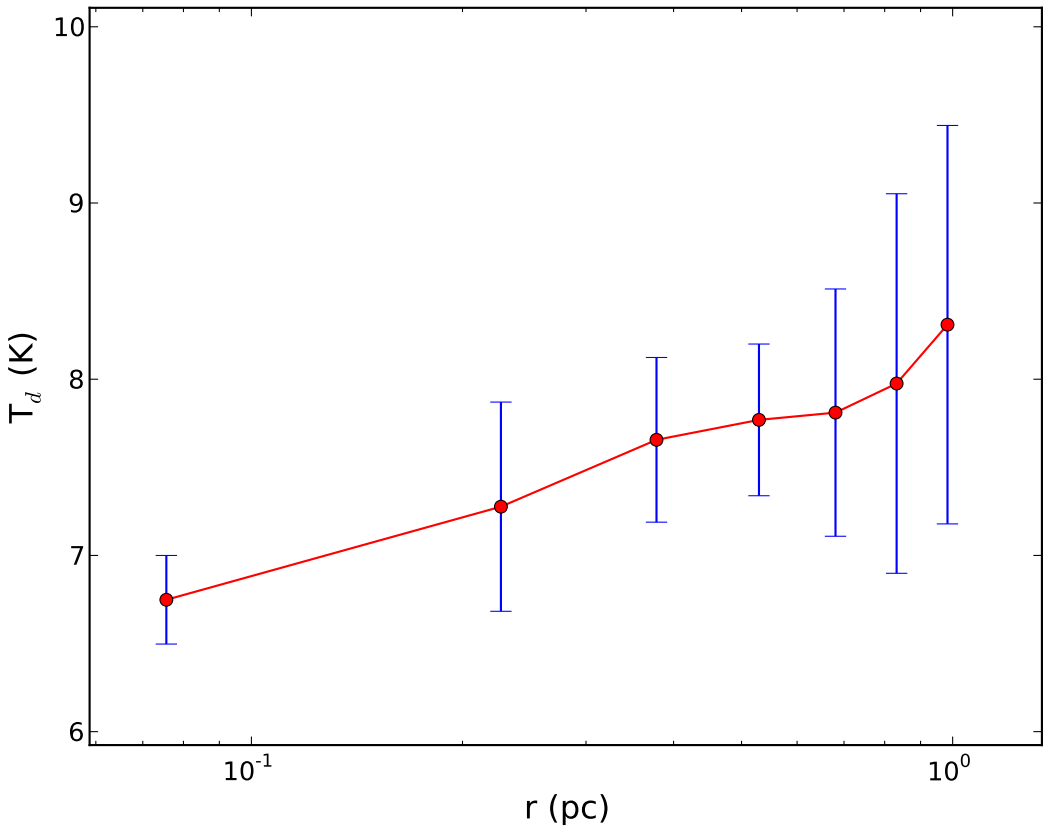

Figure 6.5: Dust temperature profile of the S305S. Error bars indicate standard deviation of temperature distribution in each radial annulus.

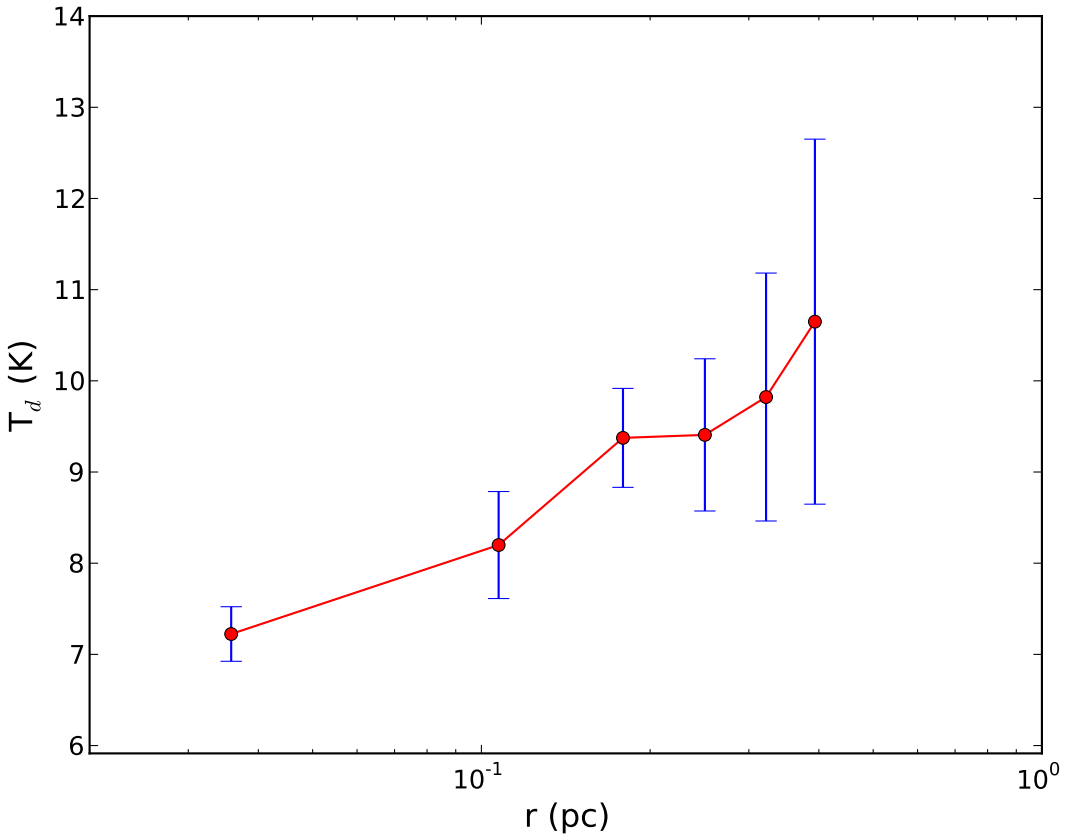

Figure 6.6: Dust temperature profile of the S254S. Error bars indicate standard deviation of temperature distribution in each radial annulus.

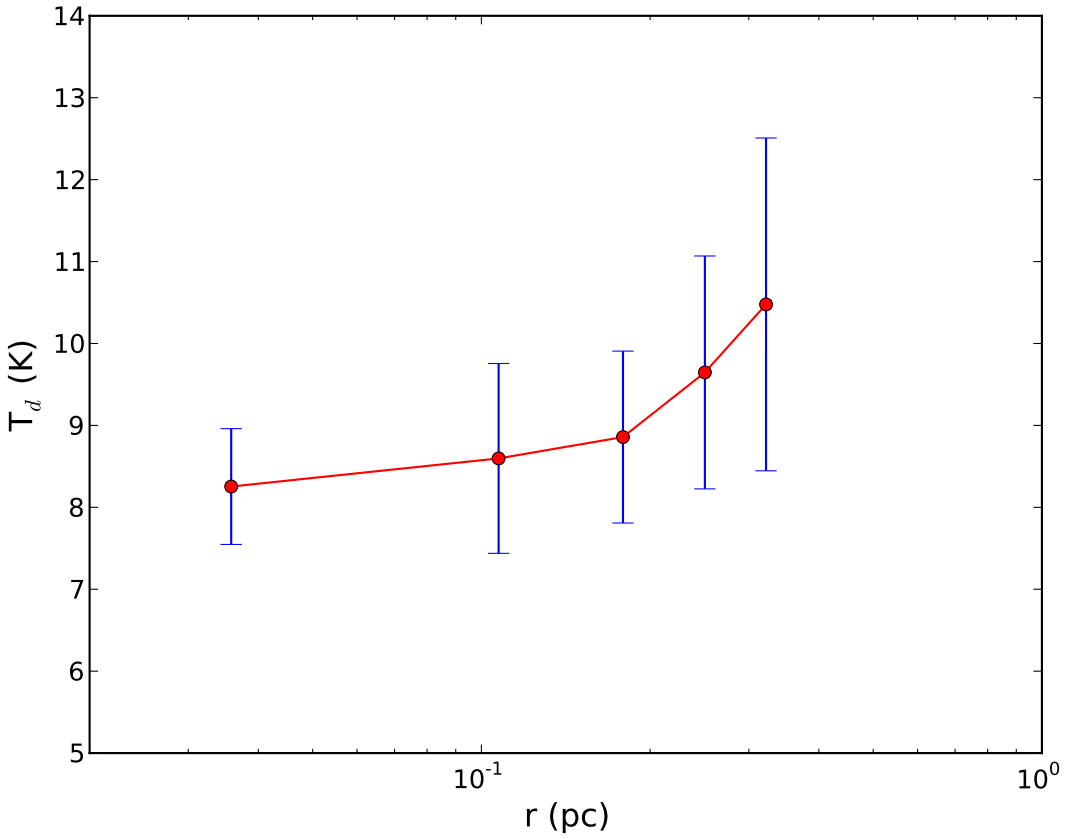

Figure 6.7: Dust temperature profile of the S254N. Error bars indicate standard deviation of temperature distribution in each radial annulus.

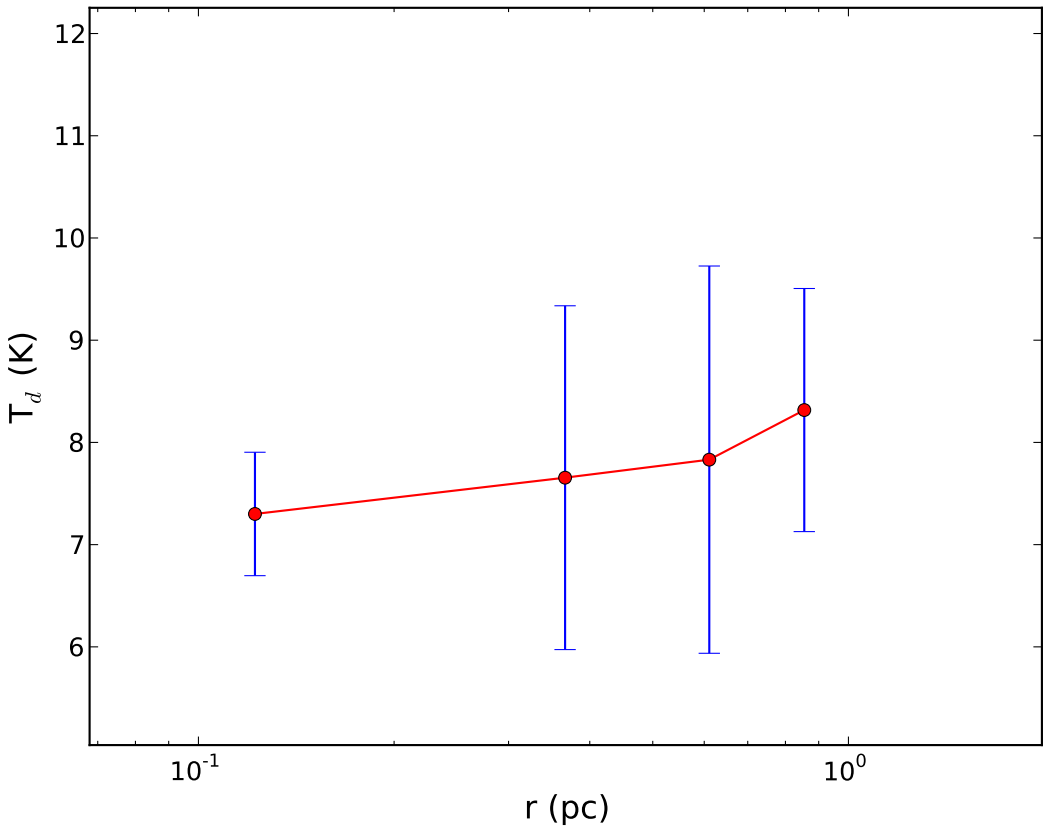

Figure 6.8: Dust temperature profile of the S128N. Error bars indicate standard deviation of temperature distribution in each radial annulus.

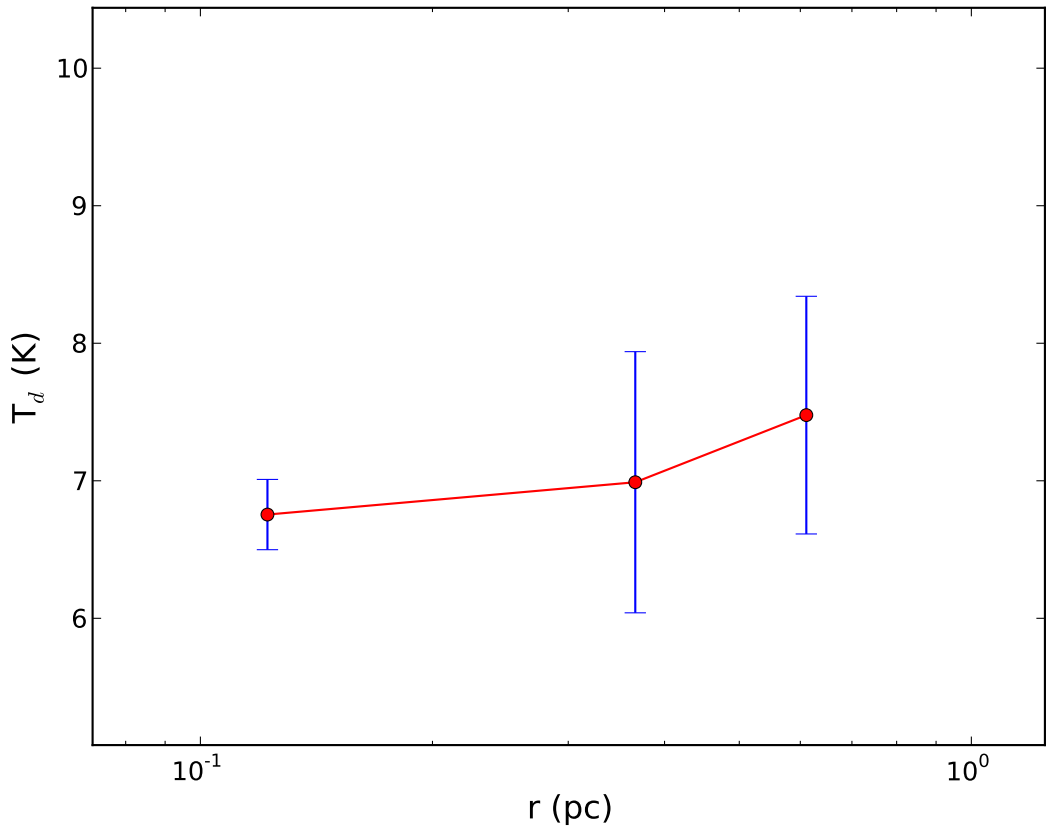

Figure 6.9: Dust temperature profile of the S128S1. Error bars indicate standard deviation of temperature distribution in each radial annulus.

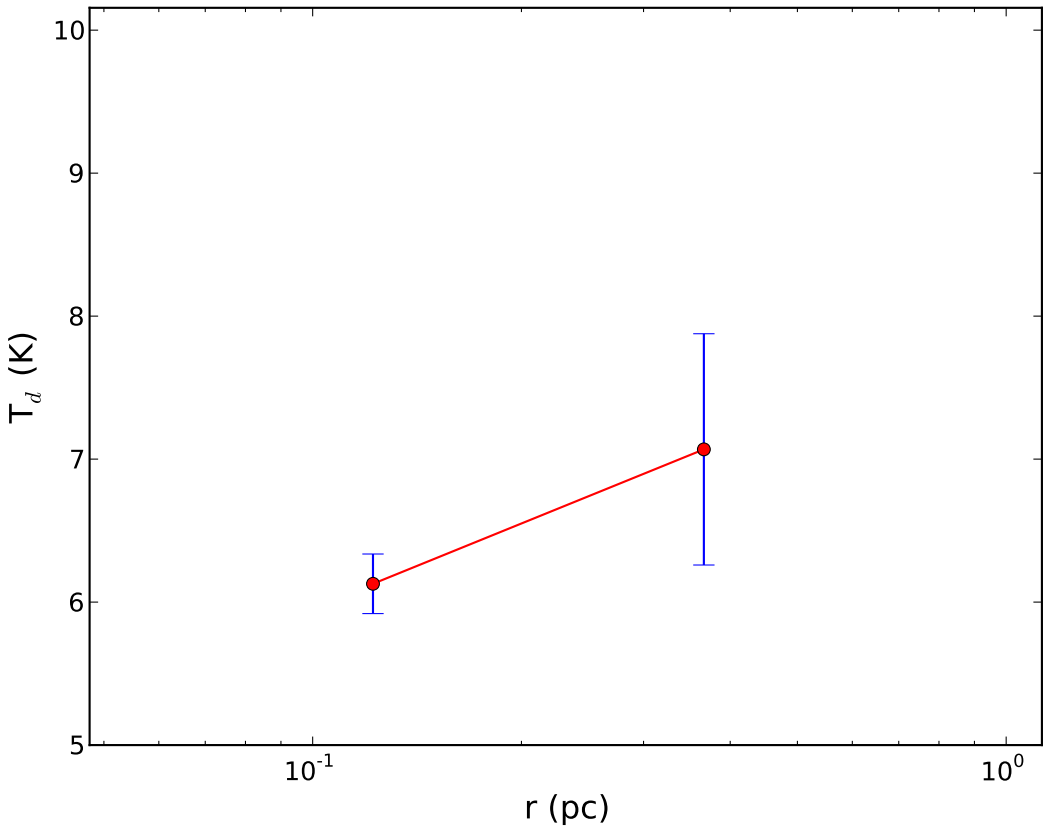

Figure 6.10: Dust temperature profile of the S128S2. Error bars indicate standard deviation of temperature distribution in each radial annulus.

6.2 Number Density Radial Profiles

Knowing the form of the density distribution in cores associated with massive star-forming regions is very important for understanding the future of star formation processes in cloud cores, primarily because this is a principal parameter that determines the initial conditions of star formation and dynamical state of the cores. Furthermore, massive star-forming zones are usually found to host clusters of young stars and thereby are an ideal place to search for the early stages of star formation.

From the observed column density maps of our clouds, the radial number density profiles are calculated assuming that the cloud cores are spherically symmetric and the data points are the mean values from 6″ wide (the same annular width used to calculate the temperature profiles) concentric spherical shells from the map centre. Note that the uncertainties in the mean values denote the standard deviation of the number density values about the mean.

In order to understand the core physical conditions we fitted the observed density profiles using a power law model density distribution of the form:

$$n(r) = n_0(r/r_0)^{-\alpha}, \tag{6.1}$$

where n_0 is the number density at which the distance $r = r_0$, and α is the power law index.

The observed radial density profiles of the cloud cores are then compared with different power law model profiles (see Figures 6.11 to 6.17). Note that we are unable to plot number density values from the innermost regions of the core, as the observational data from SCUBA-2 do not cover these regions. The observed density profiles of most of the target cores are consistent with single power law models where the power law index α ranges from -0.08 to -0.9. However the cores S159, S156, and BFS15 show a clear break in the observed density profile and a dual power law model is needed to describe the observations.

In S159, a flattened density profile best fits the observed data towards the inner region of the cloud core, whereas a relatively steeper profile is required to explain the observed density profile towards the outer core layers in this cloud. Note that the flat density profile ($n(r) \propto r^{-0.6}$) exists only up to distances that extend out to 0.18 pc from the core centre and the power law index for the outer density profile in S159 is -1.4. Much shallower values of the power law index for the inner (-0.37, and -0.52) and outer (-0.72, -0.88) profiles are needed to fit the observations of S156 and BFS15 (see Figures 6.12 and 6.13)

Several models are reviewed to test the prevailing dynamics of our sample molecular cloud cores. The density profiles in cloud cores associated with massive as well as low-mass star-forming regions have long been a subject of study and many studies put forward power laws to explain their density profiles. An r^{-2} law for the density profile is assumed outside the infall radius of a singular isothermal sphere in the classical theory of low-mass star formation named the 'inside-out' collapse model [Shu, 1977]. In his model, the free falling

material inside the collapse radius follows a power law of $r^{-1.5}$. However, our observations are not consistent with this model since we find lower values of the power law indices at both inside and outside regions. Therefore, the sample cores in our study are most likely not in an inside-out collapse mode. Most of the studies on low-mass cores are observed to follow a power law density profile that favour Shu's 'inside out' model [Motte and André, 2001; Jørgensen et al., 2002; Young et al., 2003].

Another possible explanation is the presence of a pressure-truncated isothermal gas sphere in hydrostatic equilibrium, generally known as the Bonnor-Ebert (BE) sphere [Bonnor, 1956; Ebert, 1955], which can be well described by an alternate form of the Lane-Emden equation:

$$\frac{1}{\xi^2}\frac{d}{d\xi}(\xi^2\frac{d\phi}{d\xi}) = e^{-\phi}, \tag{6.2}$$

where $\xi = \frac{r\sqrt{4\pi G\rho_c}}{C_s}$ is a scaled radius and $\phi(\xi) = -\ln(\frac{\rho}{\rho_c})$ and $C_s = \sqrt{\frac{kT}{\mu m_H}}$ is the sound speed and k, T, μ, and m_H are respectively the Boltzmann constant, kinetic temperature, mean molecular mass, and the mass of hydrogen. The above ordinary differential equation can be solved using the boundary conditions (ϕ and $\frac{d\phi}{d\xi} = 0$ at $r = r_0$).

A BE sphere model for a gas kinetic temperature of 10 K is plotted in Figure 6.21 for one of our sample cores, S159. A BE configuration at an isothermal temperature of 10 K fails to reproduce the observed density profile of the S159 core (and is true for all the other cores) and probably implies that our sample cores are not in a pressure equilibrium.

Some of the massive star-forming regions show density indices that are close to the indices found in low-mass cores. Studies on 31 molecular clouds linked to massive star-forming regions [Mueller et al., 2002] suggest an average density profile that varies as $r^{-1.8}$. A closer value of the power law index (-1.6) is obtained as an outer core power law index in cores with ongoing associated massive star formation [Pirogov, 2009]. The density profiles of the envelopes of 69 massive star-forming regions in the early stages of evolution support an inner density profile index of -1.6 [Beuther et al., 2002] and the value is comparable to those obtained in other studies of massive star-forming regions explained above. Note that as opposed to our target cores, all the mapped regions in these massive star-forming envelopes had embedded hot cores with increasing temperatures toward the centres of the cores.

Other theories, such as pressure-truncated gas spheres with a logotropic density profile, whose equilibrium profile varies as r^{-1} in the outer regions of the cores, predict a shallower α in the core outer envelopes in giant molecular clouds [McLaughlin and Pudritz, 1996]. Note that the equation of state for a logotrope has the form $\frac{P}{P_c} = 1 + A\ln\frac{\rho}{\rho_c}$, where P_c and ρ_c are the pressure and densities at the centre of the core. A is a free parameter, and its value is estimated to be $\simeq 0.2 \pm 0.02$ in clumps of both low- and high-mass stars

inside giant molecular clouds [McLaughlin and Pudritz, 1996]. Power law indices in the range from around -1 to -1.5 have a bias towards logotropic density distributions. The cores of high-mass proto-stellar objects modelled using power law density profiles where the mean value of α is -1.3 [Williams et al., 2005] are assumed to be logotropes. The flatter power law indices of the majority of our cloud cores are more consistent with the indices predicted by the logotropic profile. Figure 6.22 shows an $A = 0.22$ logotrope profile on the S159 number density profile.

According to many previous studies, the mode of pressure that supports against gravity is proposed to be decided by the power law indices of the density profiles. A flatter value of the power law index may represent a core where the pressure due to gravitational force is supported by pressure due to non-thermal forces (for example, turbulence) and is the dominant mechanism in massive cores. Note that the more massive the core is, the more small the α will be [Zhou et al., 1994]. However, larger values of α are characterized by cores that are purely supported by thermal pressure against gravity. Furthermore, regions with flatter density distributions tend to produce more numbers of stars probably attributed by fragmentation and thus eventual formation of stellar clusters [Zhou et al., 1994]. The shallow power law indices of our study fall much lower than the typical indices of the low-mass cores, and this most likely suggests that the cores near to massive-star-forming regions are supported by some sort of non-thermal pressure against gravity such as the pressure due to turbulence or magnetic field.

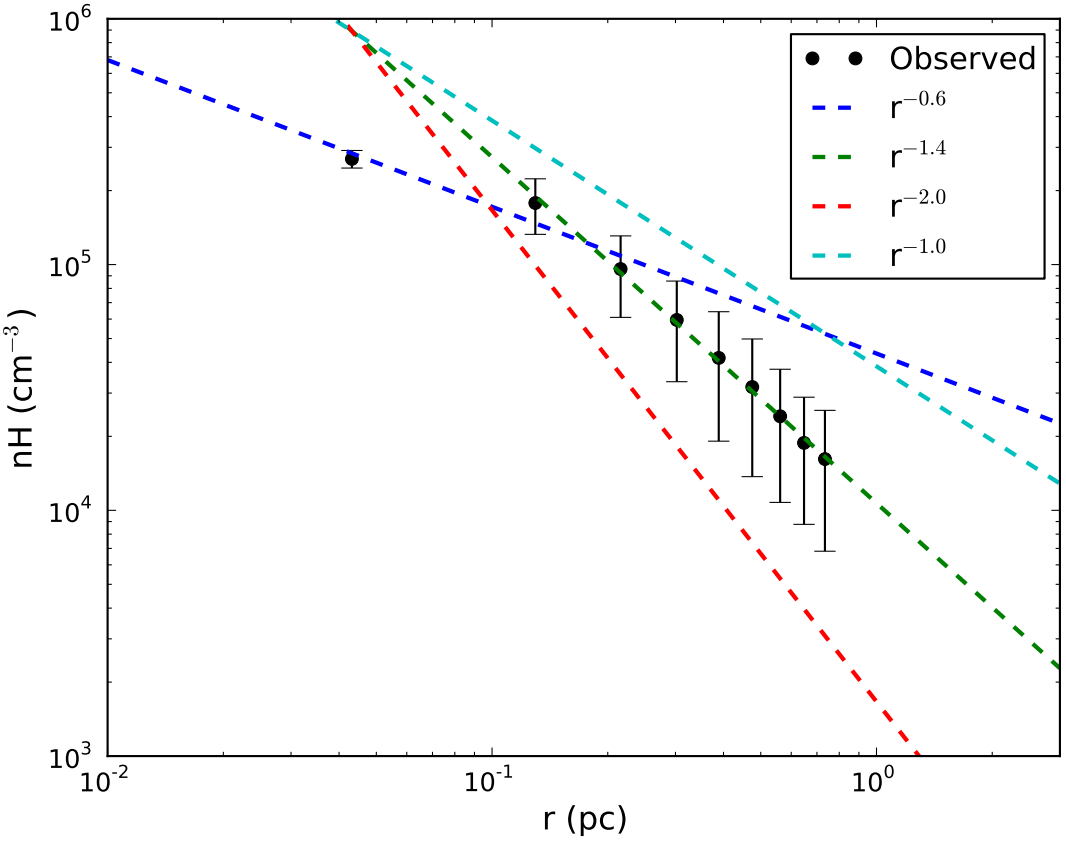

Figure 6.11: Hydrogen number density profile of S159. Error bars indicate standard deviation of density distribution in each radial annulus.

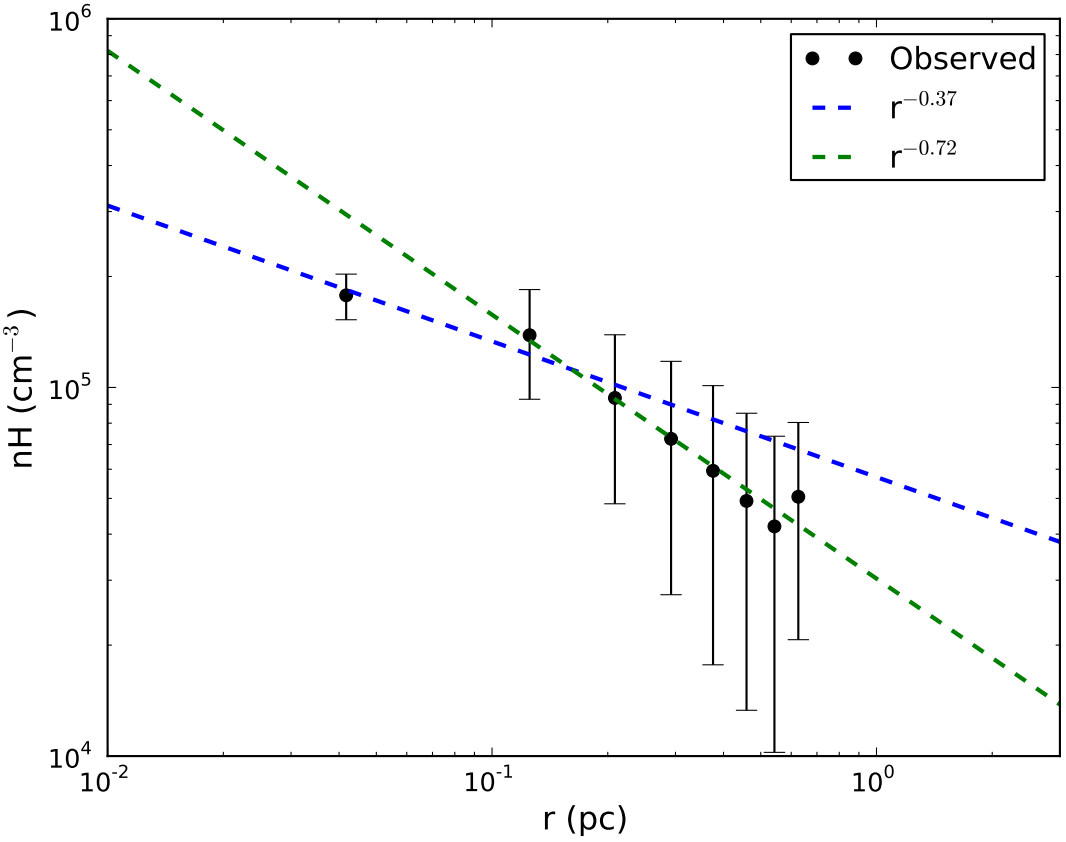

Figure 6.12: Hydrogen number density profile of S156. Error bars indicate standard deviation of density distribution in each radial annulus.

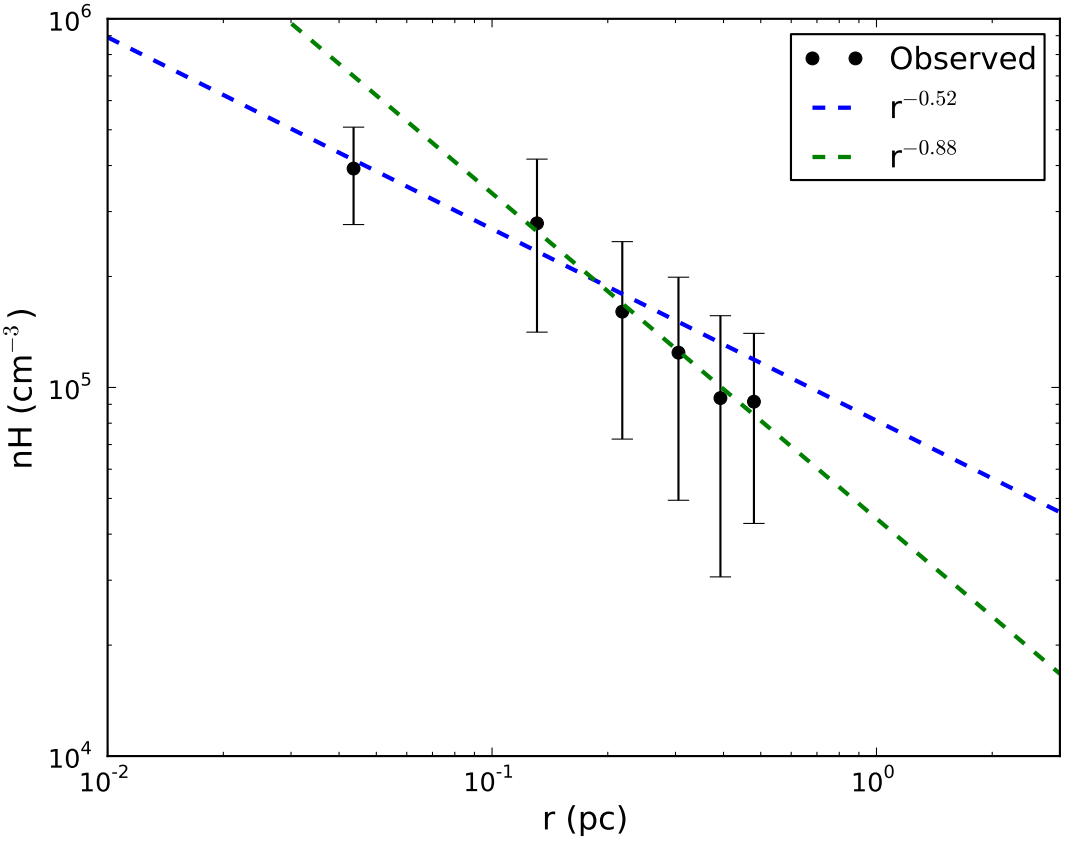

Figure 6.13: Hydrogen number density profile of BFS15. Error bars indicate standard deviation of density distribution in each radial annulus.

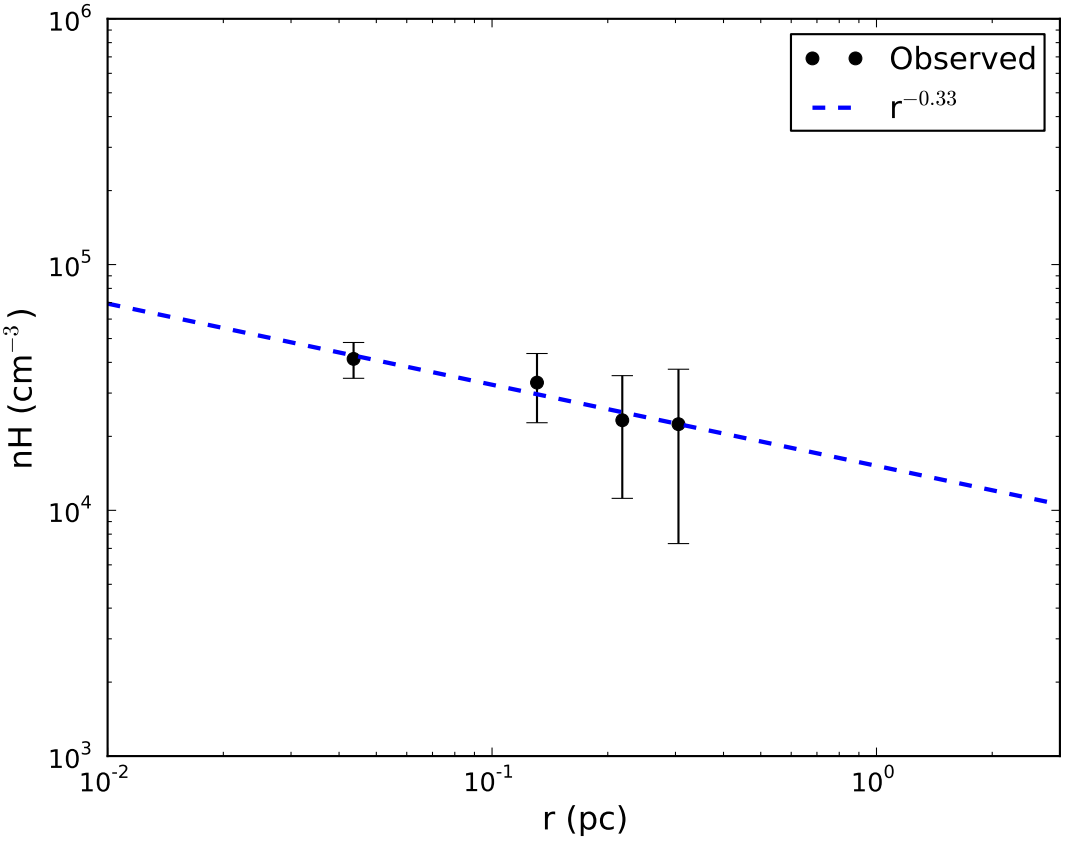

Figure 6.14: Hydrogen number density profile of BFS18. Error bars indicate standard deviation of density distribution in each radial annulus.

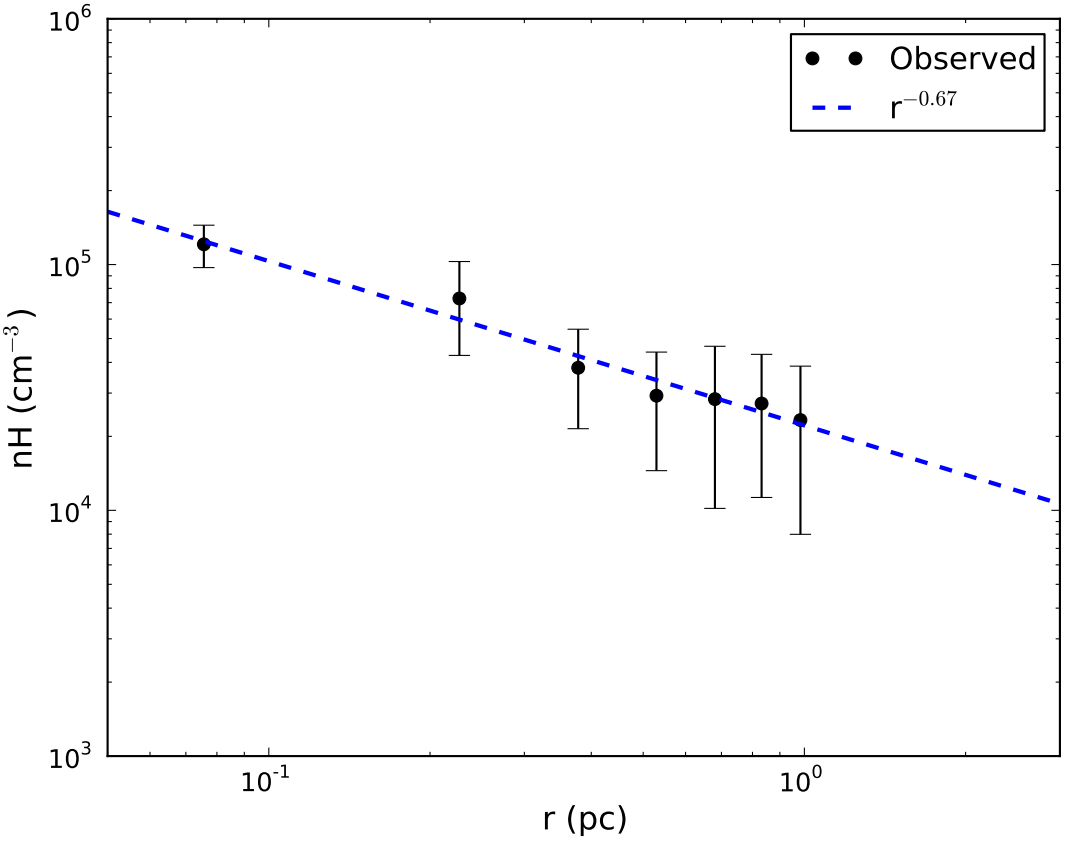

Figure 6.15: Hydrogen number density profile of S305. Error bars indicate standard deviation of density distribution in each radial annulus.

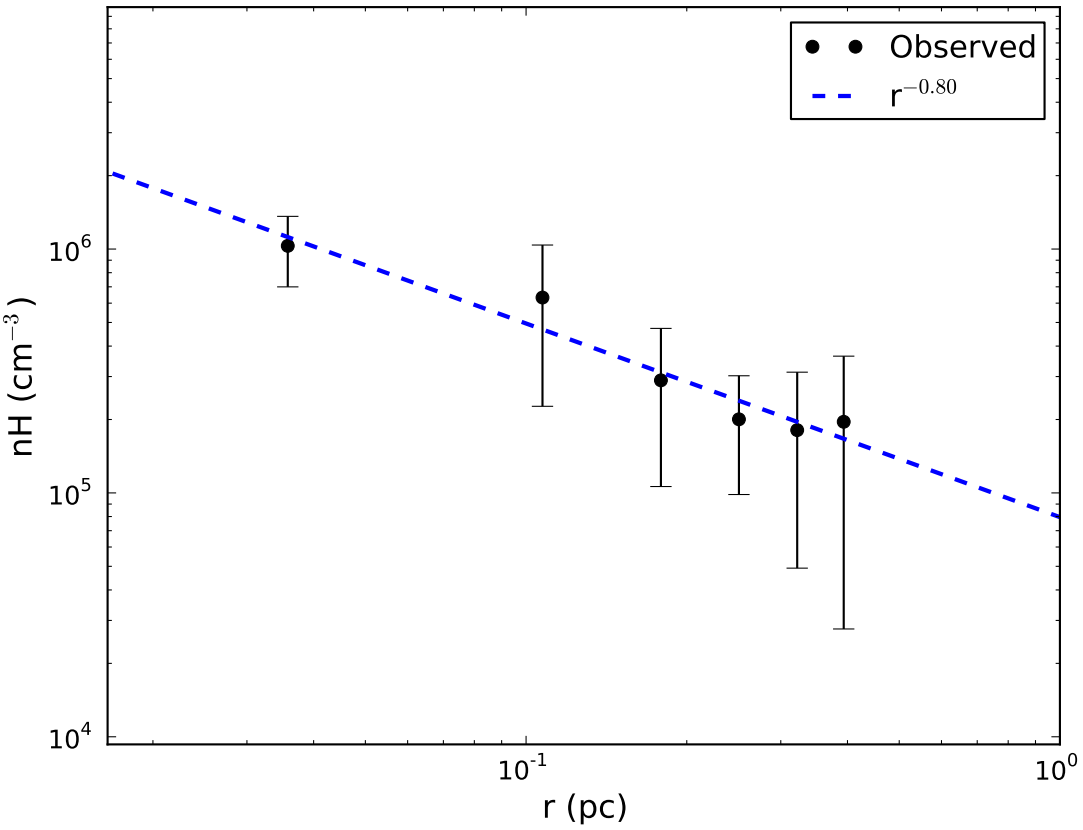

Figure 6.16: Hydrogen number density profile of S254S. Error bars indicate standard deviation of density distribution in each radial annulus.

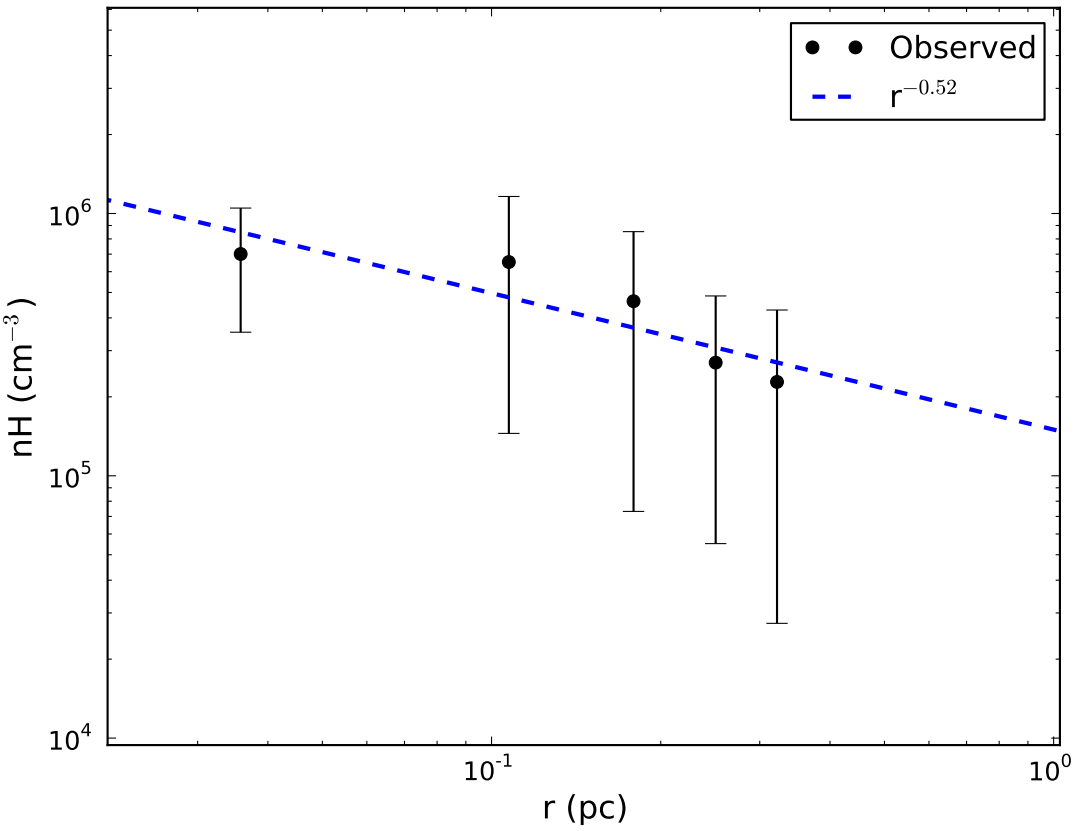

Figure 6.17: Hydrogen number density profile of S254N. Error bars indicate standard deviation of density distribution in each radial annulus.

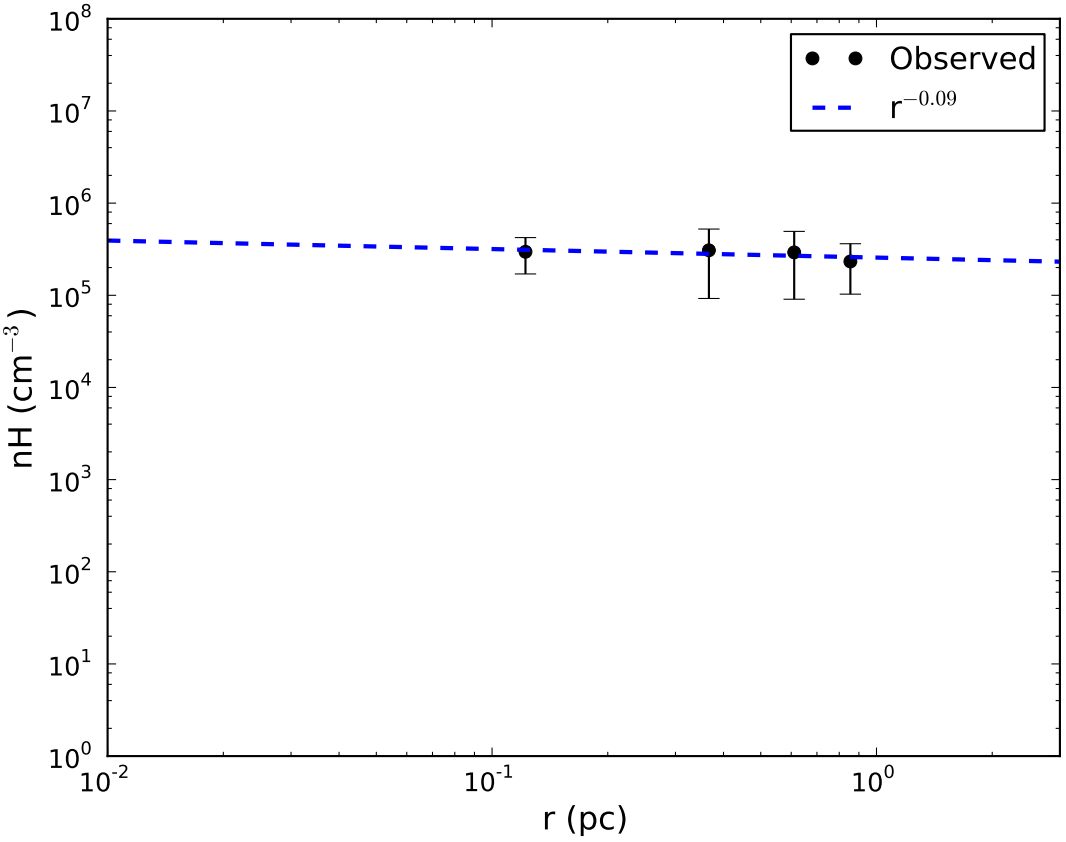

Figure 6.18: Hydrogen number density profile of S128N. Error bars indicate standard deviation of density distribution in each radial annulus.

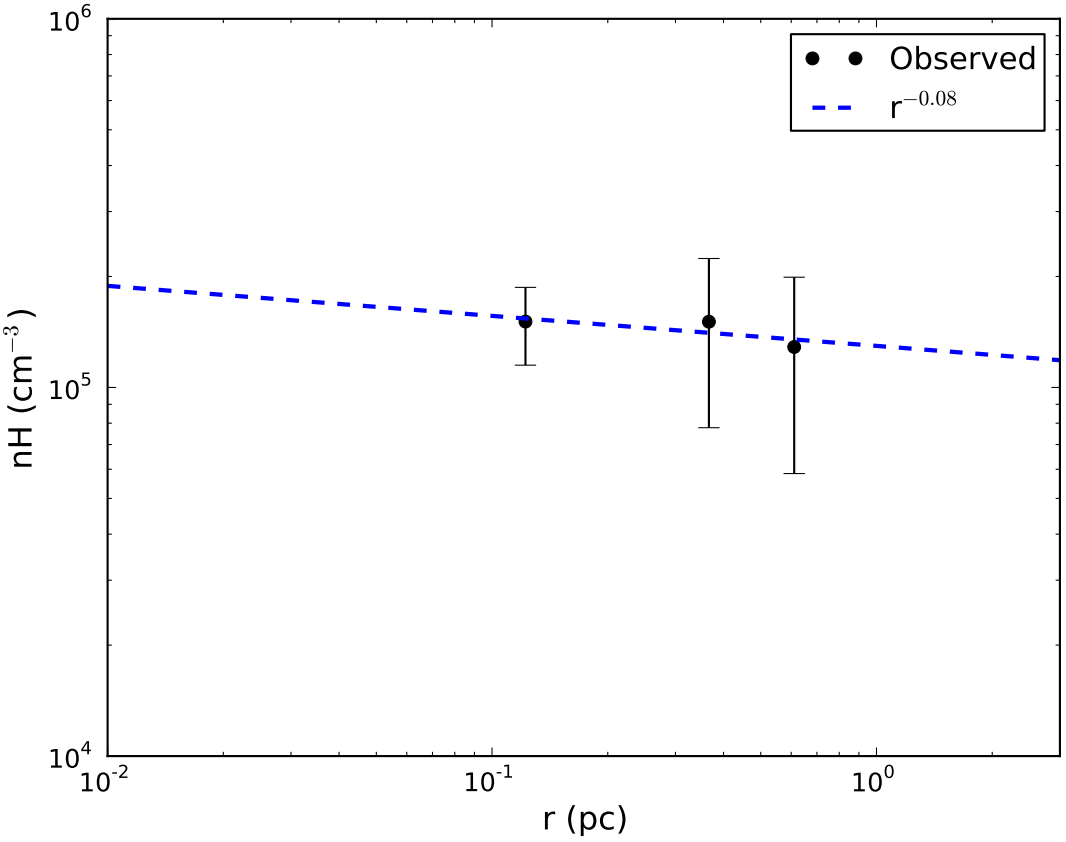

Figure 6.19: Hydrogen number density profile of S128S1. Error bars indicate standard deviation of density distribution in each radial annulus.

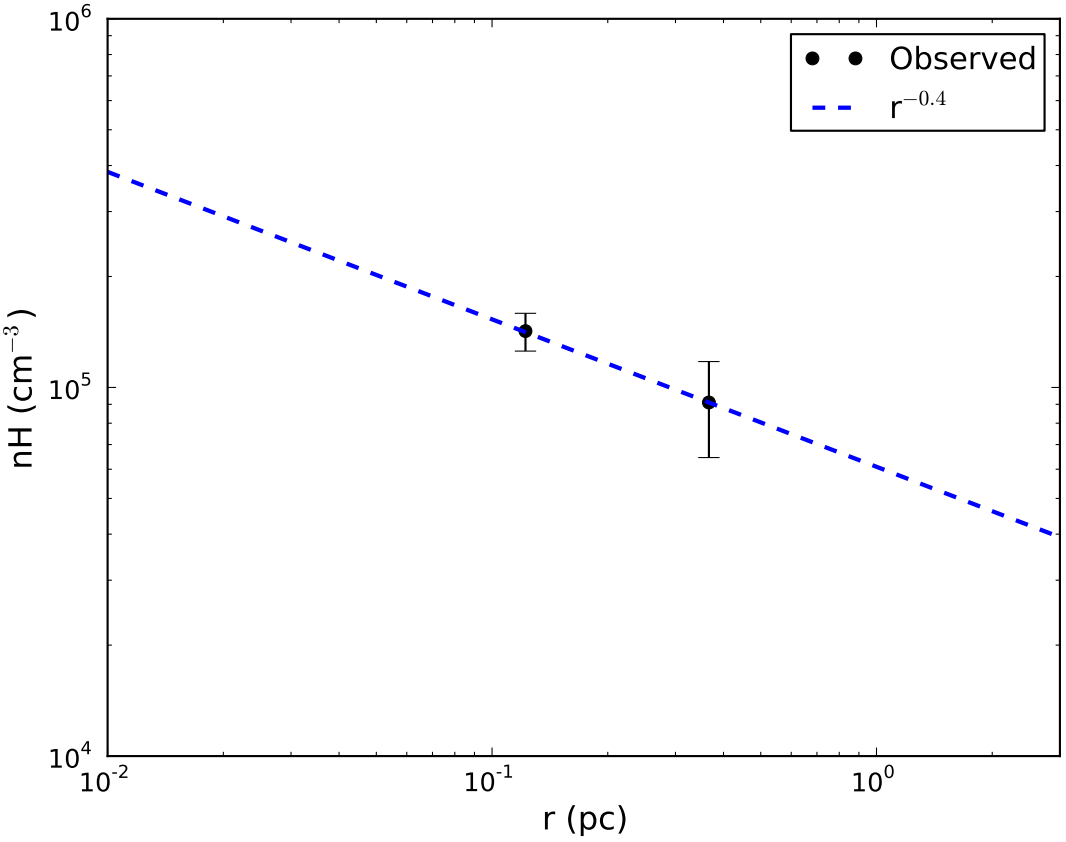

Figure 6.20: Hydrogen number density profile of S128S2. Error bars indicate standard deviation of density distribution in each radial annulus.

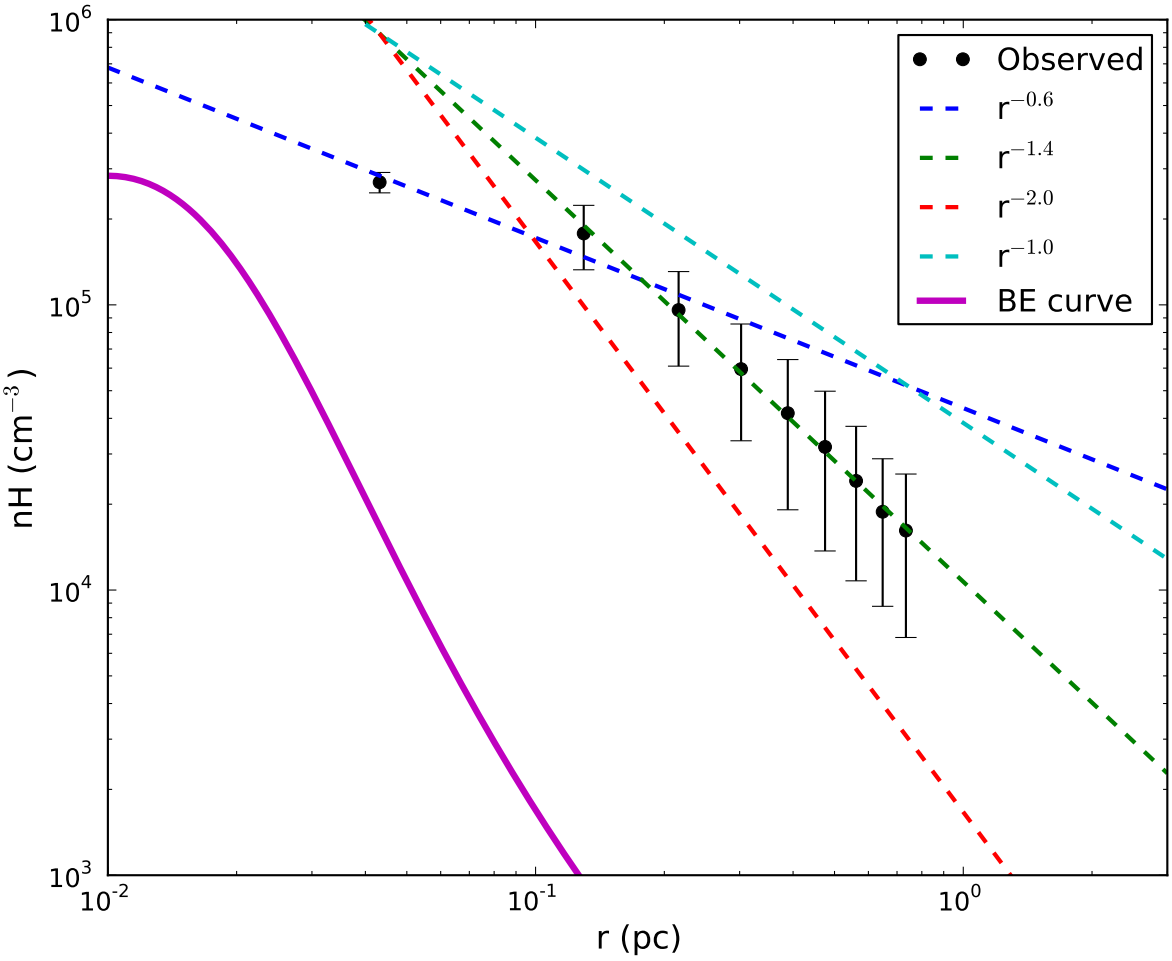

Figure 6.21: Hydrogen number density profile of S159 along with a Bonnor-Ebert profile corresponding to a kinetic temperature of 10 K.

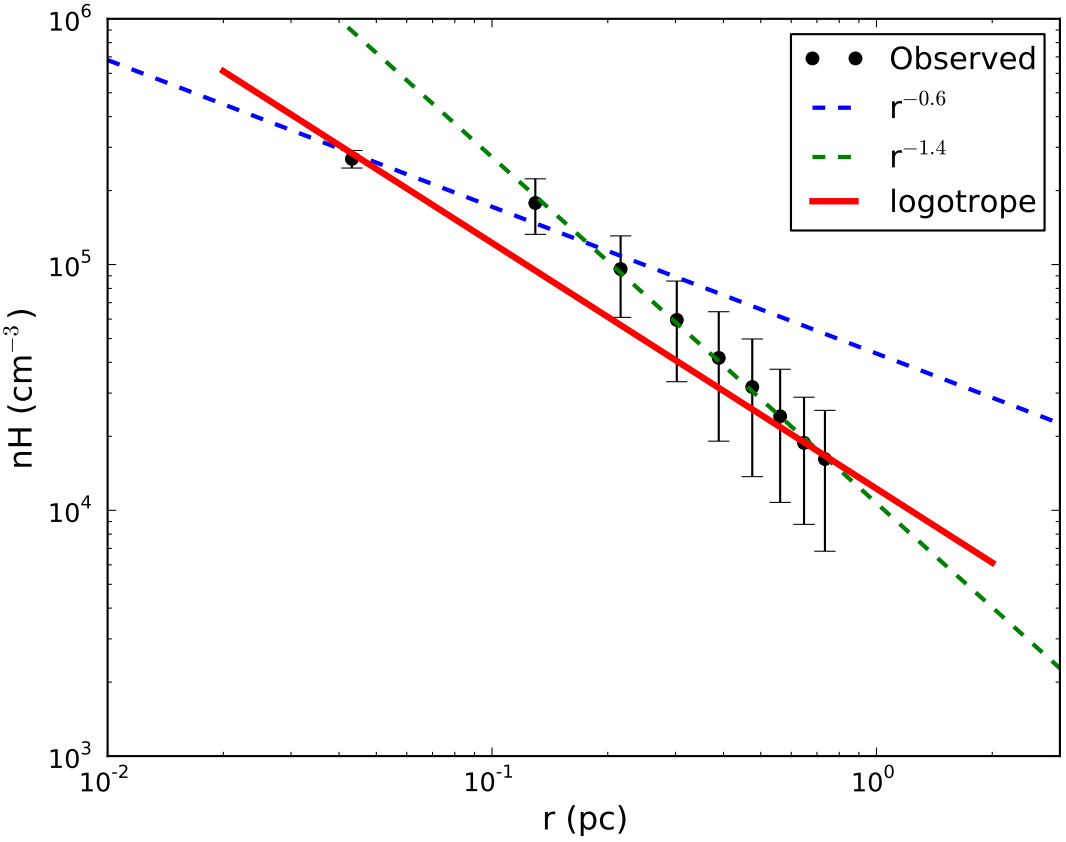

Figure 6.22: Hydrogen number density profile of S159 along with a logotrope profile corresponding to $A = 0.22$ and a kinetic temperature of 10 K.

6.3 Line Contamination

The observed fluxes from sub-millimeter thermal emission can suffer from a number of uncertainties and they can influence the observed dust temperatures and number densities. These uncertainties include (1) spectral line contamination, (2) projection of line-of-sight contamination by low density materials, and (3) variations of the value of β.

Spectral line contamination to the SCUBA-2 bolometer band passes is a prominent source of uncertainty in the measured masses. The abundant molecules such as CO and its isotopes embedded in dust clouds are one of the primary sources of dust continuum pollutants at sub-millimeter wavelengths. A number of studies have focused on the contribution of different spectral line emissions on the 450 and 850 μm SCUBA bands. Continuum flux densities are overestimated, by up to 40%, caused by the additional emission from molecular spectral lines at mm wavelengths; the tendency usually decreases with decreasing wavelengths [Gordon, 1995]. Line emission from CO is the major source of continuum flux pollution at sub-millimeter wavelengths: CO(3-2) lines at 850 μm and CO(6-5) lines at 450 μm. The rest frequency of the CO(3-2) line is close to the centre of the SCUBA-2 850 μm passband. The CO(3-2) emission in the 850 μm filter adds up to 40% in starburst galaxies [Papadopoulos and Allen, 2000]. About 25% of CO(3-2) contribution to the SCUBA 850 μm emission is observed in a sample of IR galaxies [Seaquist et al., 2004], which in turn affect the calculated dust masses of galaxies.

However, the effect of CO(6-5) line emission on the 450 μm bandpass is considered insignificant—perhaps due to the fact that the 6-5 emission is weaker than 3-2 emission and the rest frequency of the transition falls much farther away from the central 450 μm passband. In addition to CO, other possible contaminants that can affect emission from the SCUBA-2 pass bands include SO, SO_2, methanol, etc. For example, emission from SO and SO_2 spectral lines together contributes 28% and 24% of the continuum flux at SCUBA 850 and 450 μm wavelengths, respectively, in a warm Orion cloud core [Johnstone and Bally, 1999].

According to a recent study by Drabek et al. [2012], the ^{12}CO 3-2 line contamination factors on the 850 continuum bandpass are dependent on the weather band of the SCUBA-2 observations; contamination is minimum in band 1 weather. Their study on a number of nebulae in the Perseus and Orion cloud complexes confirmed less than 20% contribution from the CO(3-2) line emission on the SCUBA-2 850 μm flux in regions without outflows and an insignificant contribution from CO(6-5) lines at 450 μm dust emission.

In our analysis, we assume that spectral line emissions from all the molecules at 850 μm amount to 30% and there are negligible contributions from all the lines including CO(6-5) at 450 μm. To test the effect of the line contamination on the SCUBA-2 results, we subtracted 30% flux from the 850 μm flux. Using S159 as our test cloud, we re-calculated

the temperature and number density profiles after subtracting the line contamination at 850 μm (see Figures 6.23 and 6.24).

The removal of line-contaminated fluxes from the SCUBA-2 850 μm data has a noticeable effect on the dust temperatures. Core temperatures increased by around 2K at the centre, and 7K at the periphery of the S159 core after this procedure to eliminate the spectral contribution. However, the line contamination removal has only a minimal effect on the slope of the density profiles. The power law index becomes slightly steeper (from 1.4 to 1.5) in the outer region and the slope of the inner density profile shows only a minute variation. Reducing the 850 μm flux affected the peak-averaged central number densities: peak number densities decreased by a factor of 2.5 upon the removal of spectral line pollution. The line contamination removal, therefore, has a negligible effect on the slopes of the density profile; however, the process moderately increased the central temperatures and decreased the peak densities.

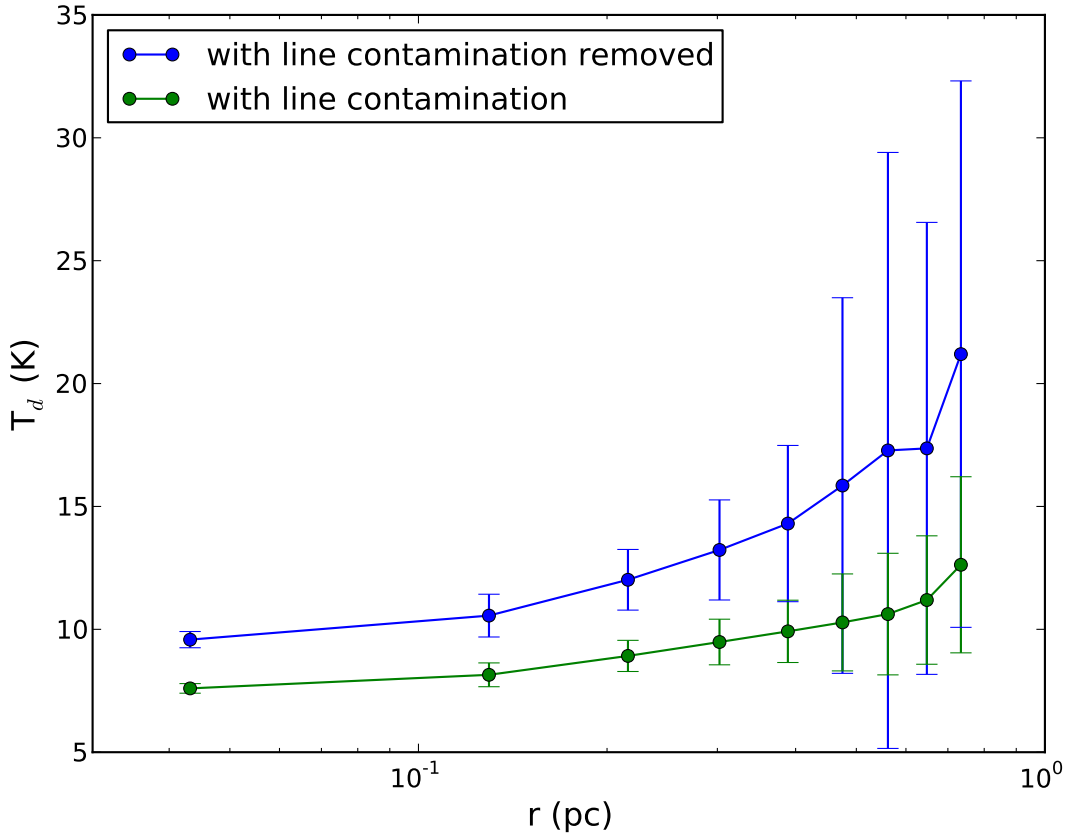

Figure 6.23: Dust temperature profiles of the cloud S159 with (green curve) and without (blue curve) line contamination at 850 μm.

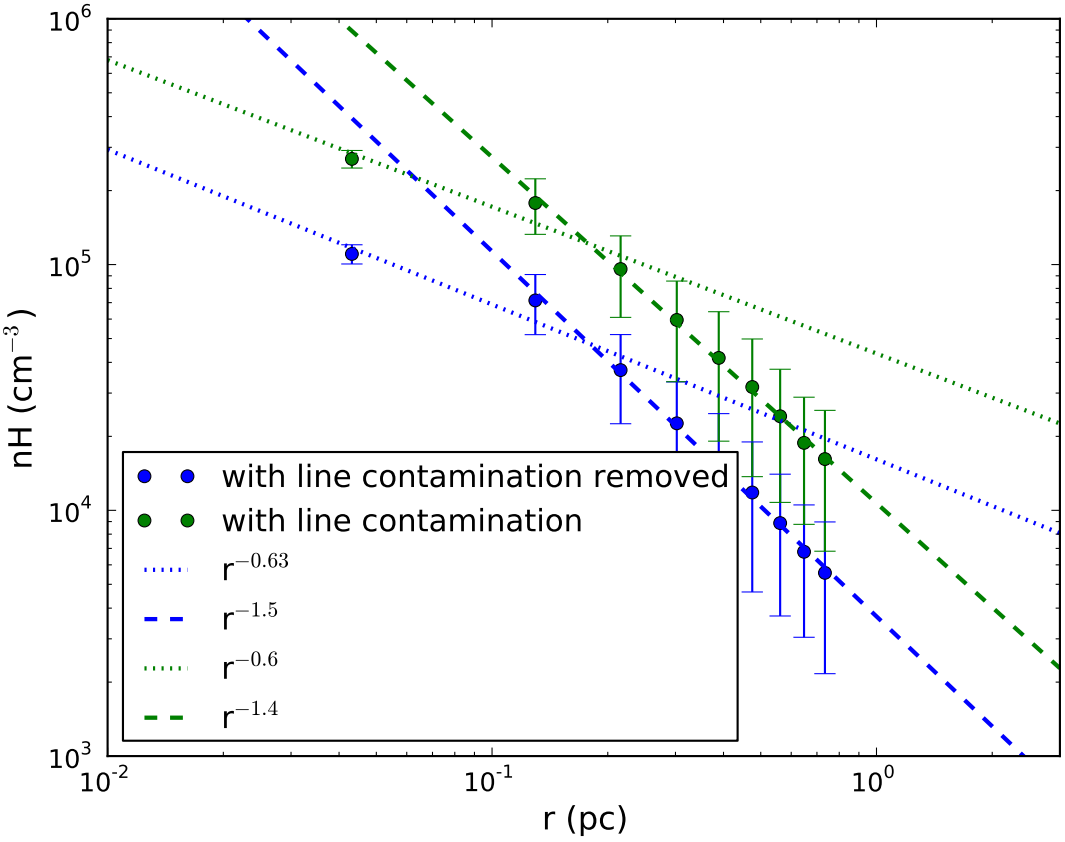

Figure 6.24: Hydrogen number density profile of S159 with (green) and without (blue) line contamination at 850 μm.

6.4 Effect of Low Density Materials along the Line Of Sight

The masses obtained from the column density maps using the observed sub-millimeter data could be an overestimation of the true cloud masses. Recent research on star-forming clumps, using simulations that model the gravitational collapse of molecular clouds, argue that the existence of low density materials along the sightline can increase the real mass of a cloud by a factor of three, which always results in an overestimation of the cloud mass during mass calculations (Ward, R.L et al. 2012, private communication). Note that all our sample clouds are vulnerable to this condition, and there can be a factor of three decrease in the observed cloud masses. This effect is dependent on the mass: towards massive regions, this effect is more pronounced due to the influence of much higher density materials along the line of sight.

6.5 Emissivity Spectral Index

The dust emissivity spectral index maps of all the complexes (Chapter 5, Figures 5.28 to 5.32) are derived from the long and short wavelength SCUBA-2 surface brightness maps by adopting a constant temperature of 10 K throughout each target complex. A radial variation of β is observed in all the complexes with very low values ($\beta = 0.5$) towards the centres of cloud cores and high values ($\beta \approx 3 - 3.5$) towards the outer cloud boundaries.

Much lower values ($\beta = 0.2$) are detected in the direction of the isolated low-mass star-forming core TMC-1C's centre [Schnee and Goodman, 2005]. A low value of β in cloud centres is perhaps an indication of an immensely dense region, which favours grain growth by coagulation, generating evolved dust grains of mm sizes [Miyake and Nakagawa, 1993; Testi et al., 2003].

Increasing the temperature from 10 K to 15 K decreases the values of the emissivity index (Chapter 5, Figure 5.33). Note that if we employ a temperature of 10 K to derive β, the β at the centres of the clouds drops to values close to zero, indicating a very dense, cold centre (for example, around 7 K for S159). A lower β at the centre due to a higher temperature (15 K) therefore indicates a much colder and denser centre. At 15 K, the centres of the fragments associated with the main cloud show negative values of β and it is very unlikely to get negative values of β in real clouds at sub-millimeter wavelengths.

The exterior cloud regions are often more sparsely populated than the interiors and due to insufficient mutual collisions, grains seldom grow to large sizes. The rare collision events are also a consequence of the low column densities and visual extinctions at the outer edges of the clouds and can be the most likely interpretation of the high β values at

the cloud borders. Note that the sample clouds show another conspicuous feature: regions of higher column densities are at lower temperatures if β is uniform throughout the cloud. This feature, perhaps, implies that the dust grains at the densest regions of the clouds are effectively shielded from the stellar radiation field and retain a colder temperature, which assists in grain growth.

6.5.1 Impact of a lower β on the dust physical property maps

In this section, we analyze the impact of a lower β ($\beta = 1.5$) on the two-dimensional dust physical property maps. Reducing the value of the emissivity spectral index from 2.0 to 1.5 increases dust temperatures throughout the cloud (see Figure 6.25). The bulk of the core is below 20 K (9-20 K) in the $\beta = 1.5$ case, whereas the same region is below 12 K (7-12 K) when $\beta = 2.0$. With a β of 1.5, a 23% decrease is observed in the peak values of optical depth, column density and visual extinction in the core of S159 (Figures 6.26 to 6.28).

Variations in the dust temperature profiles of the S159 core corresponding to different values of β are displayed in Figure 6.29. As the value of β gets larger from 1.0 to 2.0, the temperature profile shifts from top to bottom denoting an anti-correlation between temperature profiles with the values of β. This implies that the temperature structure is dependent on the grain opacity—which in turn relies on the chemistry in cloud cores, density structure, luminosity etc. Note that the central core temperatures shift from 7.5 K to 12.2 K as we decrease the value of β from 2.0 to 1.0.

Using β values of 1.0, 1.5, and 2.0, we plotted the number density profiles of the core of S159 in Figure 6.30. The higher the value of β, the higher the number density profile will be; nevertheless, the slope of the curves remains the same. Note that changing the values of the β therefore does not influence the overall shape of the number density profiles. At higher values of β, the result is consistent with the fact that grains are more abundant as the regions get colder, which in effect is responsible for the growth of grains.

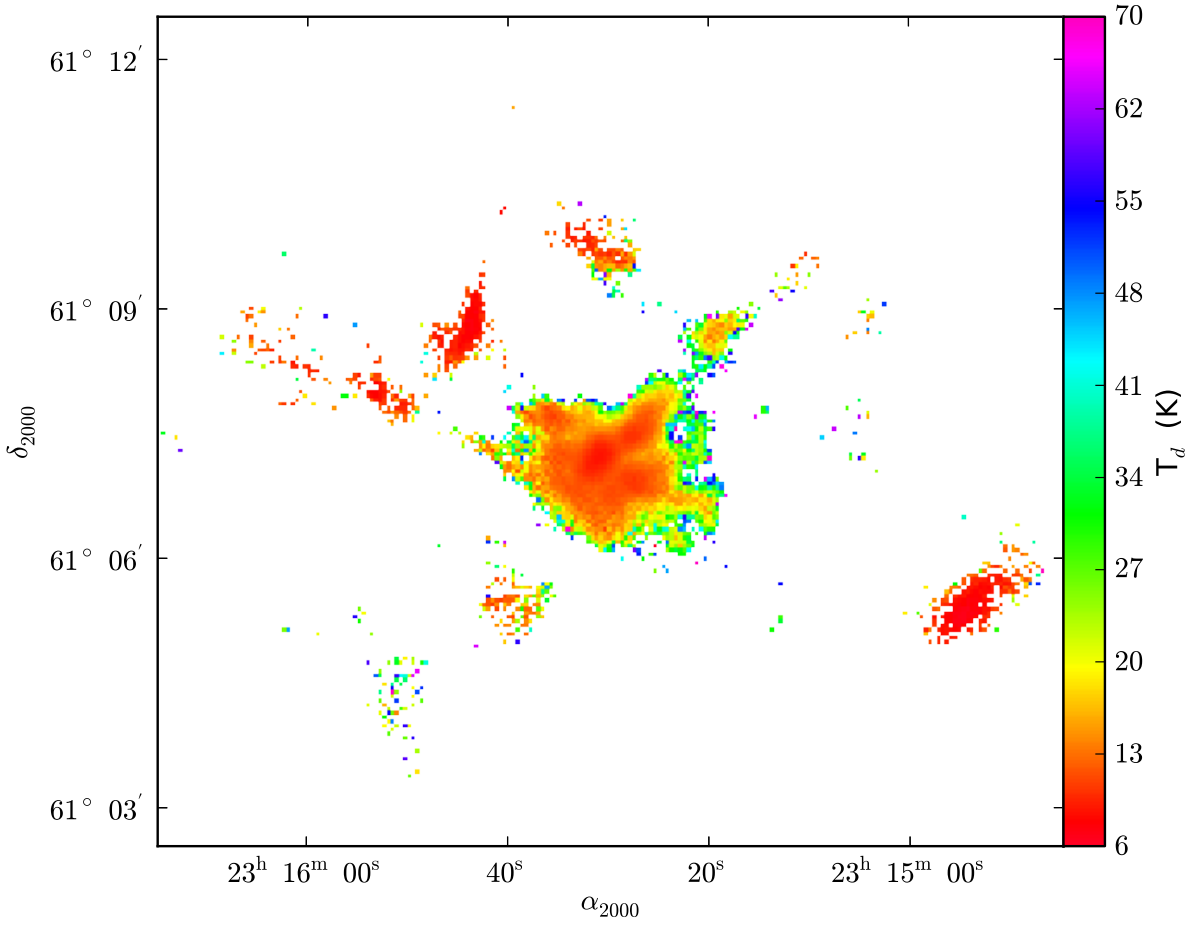

Figure 6.25: Derived dust temperature using SCUBA-2 450 and 850 μm maps of S159 with β =1.5.

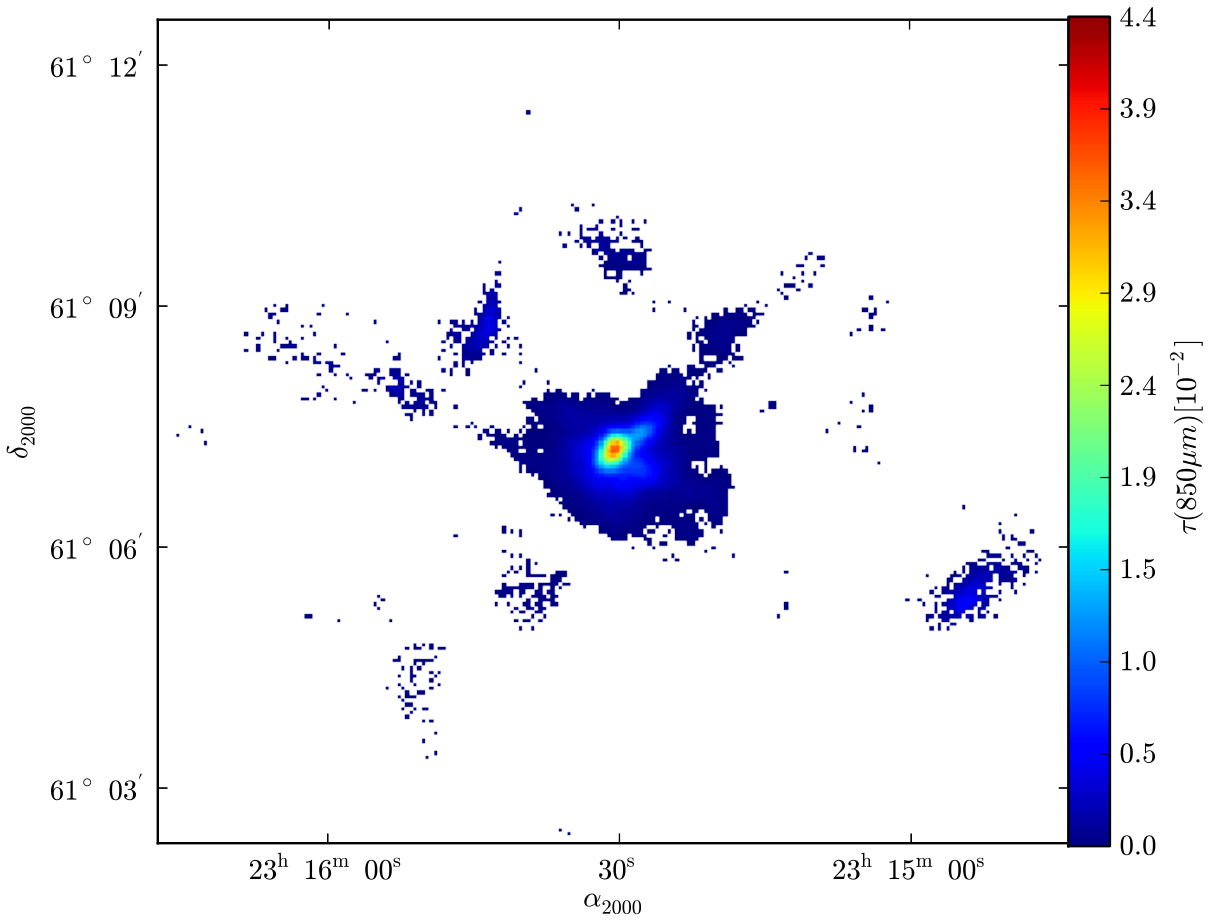

Figure 6.26: Optical depth plot of S159 at 850 μm using temperature derived from assuming β =1.5.

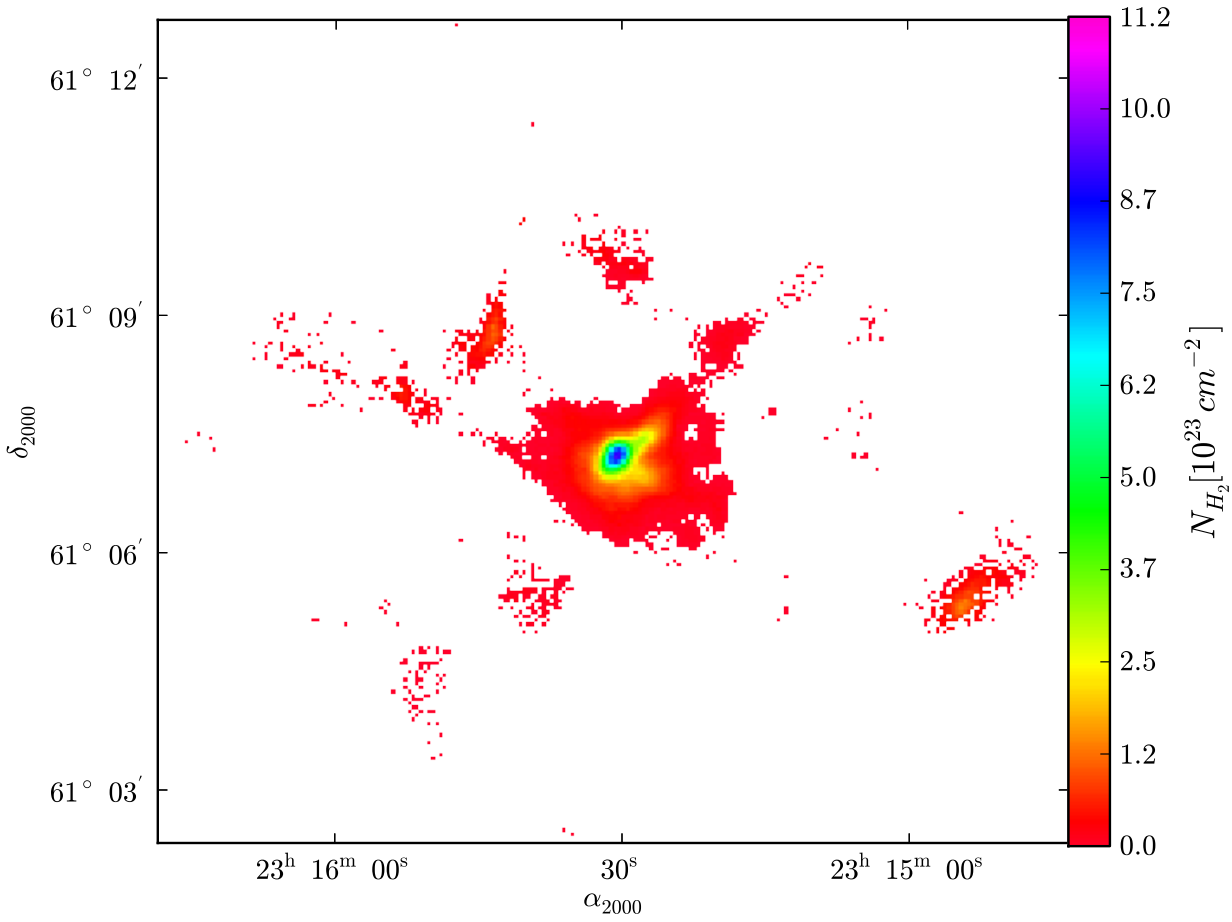

Figure 6.27: Column density plot of S159 at 850 μm using temperature derived from assuming β =1.5.

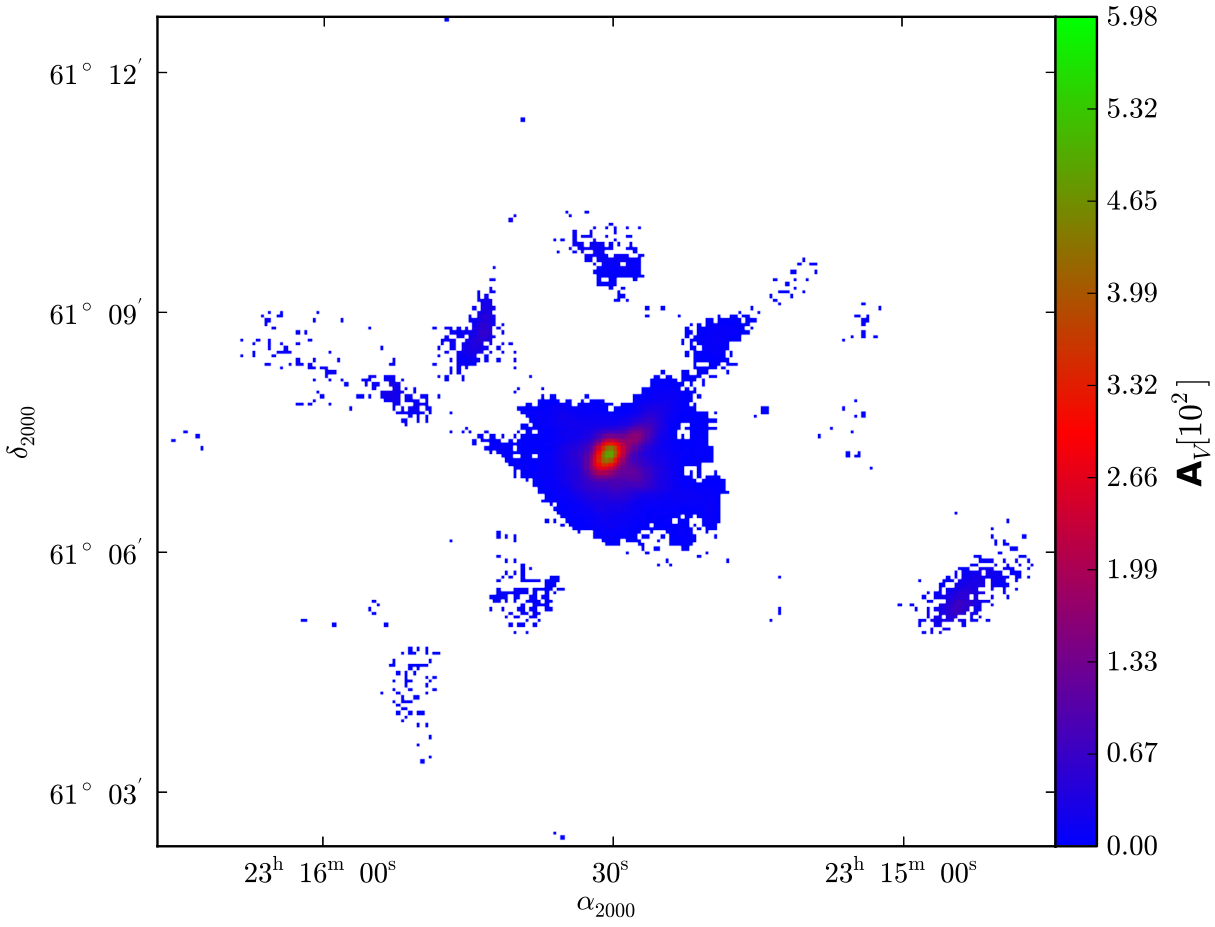

Figure 6.28: A_V plot of S159 at 850 μm using an assumed β of 1.5 in the temperature derivation.

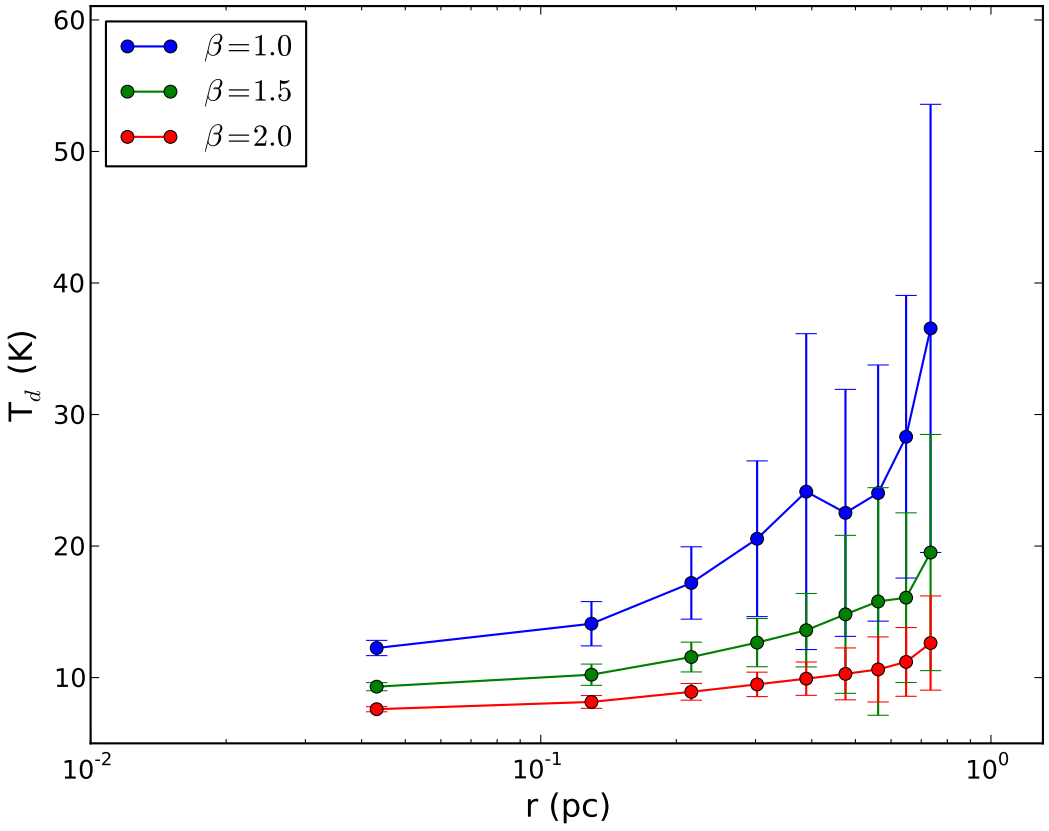

Figure 6.29: Variations in dust temperature profile with different β—S159 core.

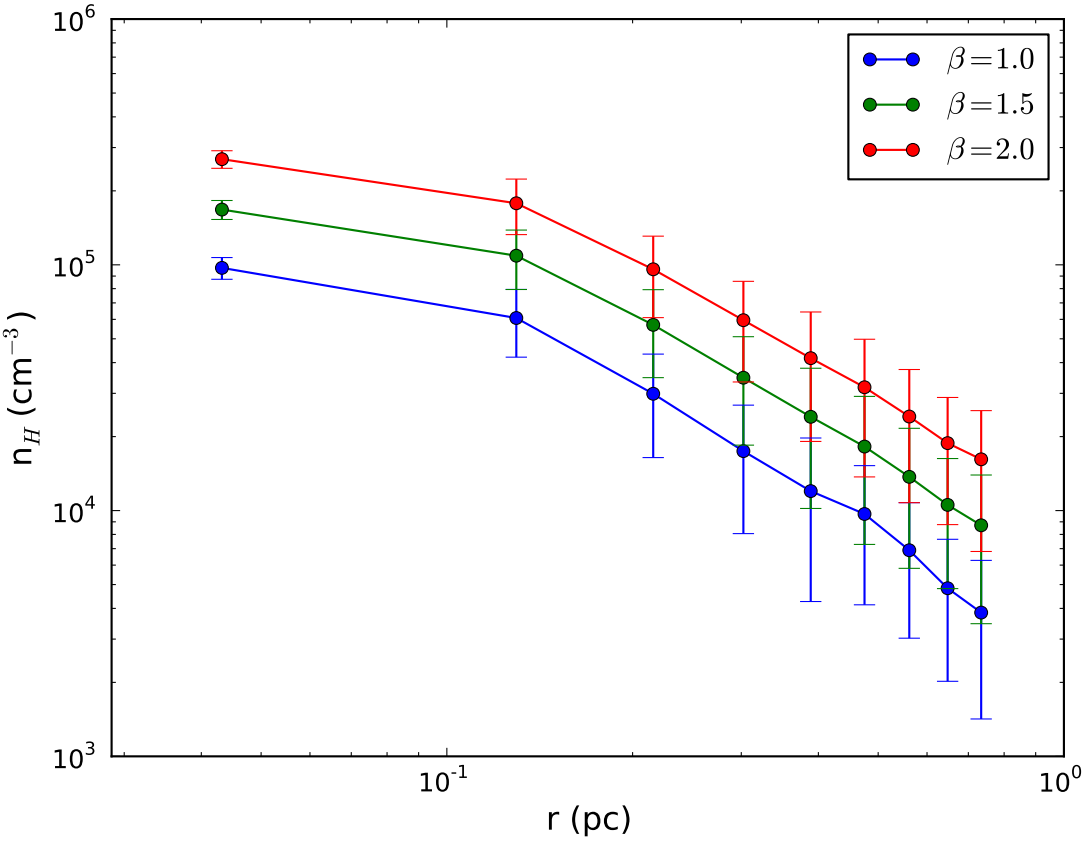

Figure 6.30: Variations in number density profile with different β—S159 core.

6.5.2 Gas masses

The gas masses given in Table 5.4 (Chapter 5) are derived from the column density maps, which are generated from the 850 μm dust emission, employing the dust temperature distribution assuming an emissivity index of 2.0. All the clouds in the target complexes are massive with masses higher than 10^3 $M_\odot$. Gas masses can also be calculated by fitting the SED.

A three-component model SED of hot, cool and cold dust is used to fit IRAS and SCUBA-2 observations of the molecular clouds and complexes. In some clouds, a discrepancy is observed between the values of the masses derived from the spectral energy distribution and from the column density distribution. The column density and SED derived gas masses are shown in Table 6.1.

The SED derived mass (M_{SED}) of the complex S305 is found to be four times lower than the column density derived masses (M_{NH}). This is because by assuming a constant dust temperature throughout the cloud, we are underestimating M_{SED}. The cold dust temperature obtained from the fit is $23.2^{+1.2}_{-8.6}$. However, the temperatures of the clouds obtained from the two-dimensional maps are much lower at the centres of clouds (around 5 K) compared to the warmer edges (14 K). Note that the column density maps are derived from the 850 μm optical depth maps and from the maps of the dust temperature distribution. The colder cloud centres therefore contribute to higher masses, which in turn enhanced M_{NH} compared to M_{SED} in the S305 complex.

The column density derived mass of the cloud S156 is within the uncertainty limits of M_{SED}. However BFS15 show twice as high M_{SED} than M_{NH}. On the other hand, M_{SED} is lower than M_{NH} by a factor of 17 in S128N, most likely due to the fact that we considered only the S128N core in calculating the fluxes from this cloud, and this must have reduced the M_{SED}, whereas the M_{NH} is from the whole S128N cloud. Due to the lack of a good 450 μm SCUBA-2 observation of cloud S148, we supplied a constant temperature of 10 K to calculate the mass and the calculated M_{SED} is within the error limits of M_{NH}.

For the rest of the clouds, a good three-component fit cannot be found. Note that for all these clouds, the 450/850 μm ratio is beyond 10 and an emissivity index of 2 is not sufficient to obtain masses of cold dust which radiate below 20 K. We require higher large grain dust temperatures, above 30 K, to fit such a larger ratio. Note that for a lower β, ($\beta = 1$), dust temperatures attain even very high values (above 500 K) at lower values of the 450/850 ratio (~ 7). The resultant temperatures are greater than those found for the hot dust from IRAS observations. Such high values of dust temperatures are very unlikely for the large grains at sub-millimeter wavelengths.

Table 6.1: Gas masses

Source	M_{N_H} $M_\odot$	M_{SED} $M_\odot$	T_{SED} (K)	M_{CO} $M_\odot$
S156	$(4.8\pm0.2)\times10^3$	$6.7^{+8.4}_{-3.0}\times10^3$	$6.6^{+1.5}_{-1.6}$	
BFS15	$(4.2\pm0.2)\times10^3$	$9.0^{+2.7}_{-2.3}\times10^3$	$9.3^{+1.0}_{-0.9}$	
S148	$(7.3\pm1.3)\times10^3$	7.6×10^3 [1]	10.0 [2]	7.9×10^3
S305C	$(4.45\pm0.02)\times10^4$	$1.07^{+0.28}_{-0.27}\times10^4$	$23.2^{+1.2}_{-8.6}$	3.8×10^3
S128N	$(6.4\pm0.1)\times10^4$	$0.37^{+1.51}_{-0.20}\times10^4$	$14.0^{+11.0}_{-7.5}$	

[1]Gas mass derived by assuming a constant dust temperature of 10 K.
[2]Assumed a constant T_d of 10 K throughout the cloud due to the absence of good quality 450 μm SCUBA-2 data.

Mass-size diagram

The mass vs. size of the target clouds is plotted in Figure 6.36. No correlation between the mass and size is observed and most likely we require a large sample of objects to determine whether there is correlation between the mass and size.

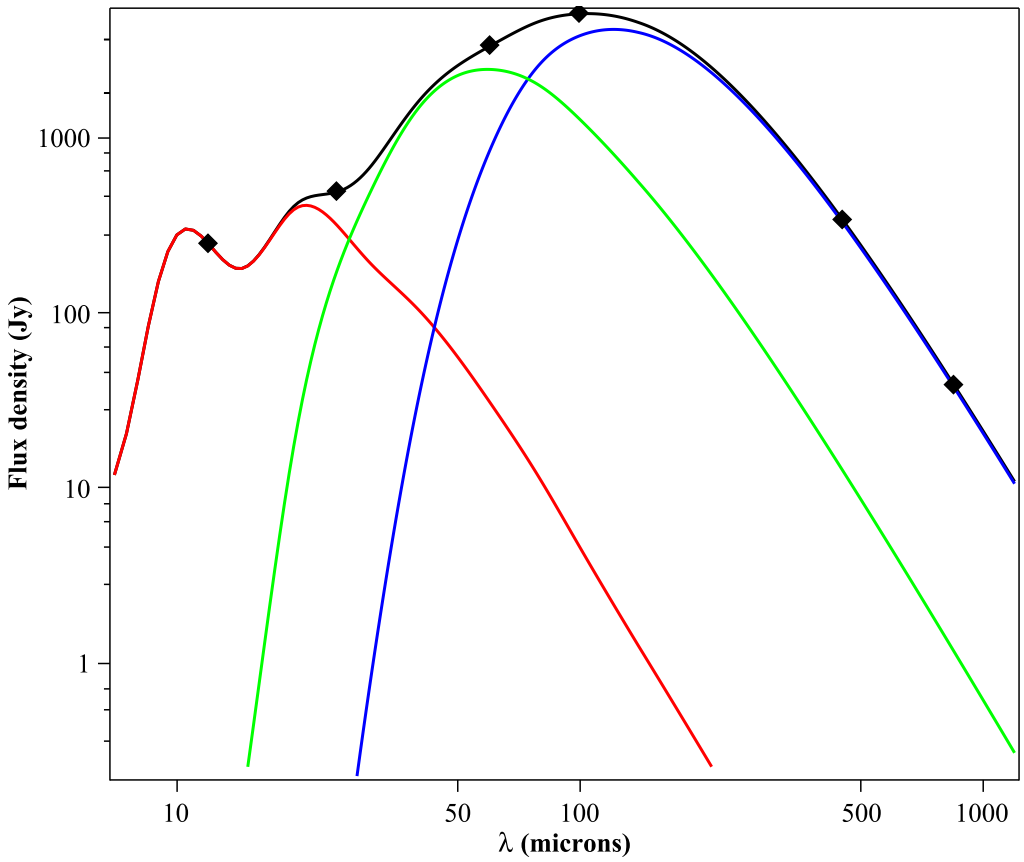

Figure 6.31: Illustration of the Spectral Energy Distribution of the Galactic H II region complex S305 from both the IRAS and SCUBA-2 observations (solid diamonds mark the observed flux densities) along with the three-component optimal model fit. The solid red line shows the contribution from hot dust, the solid green line represent the contribution from the cool dust, and the solid blue line displays the contribution from the cold dust, whereas the black solid line denotes the combined spectrum of all the three components.

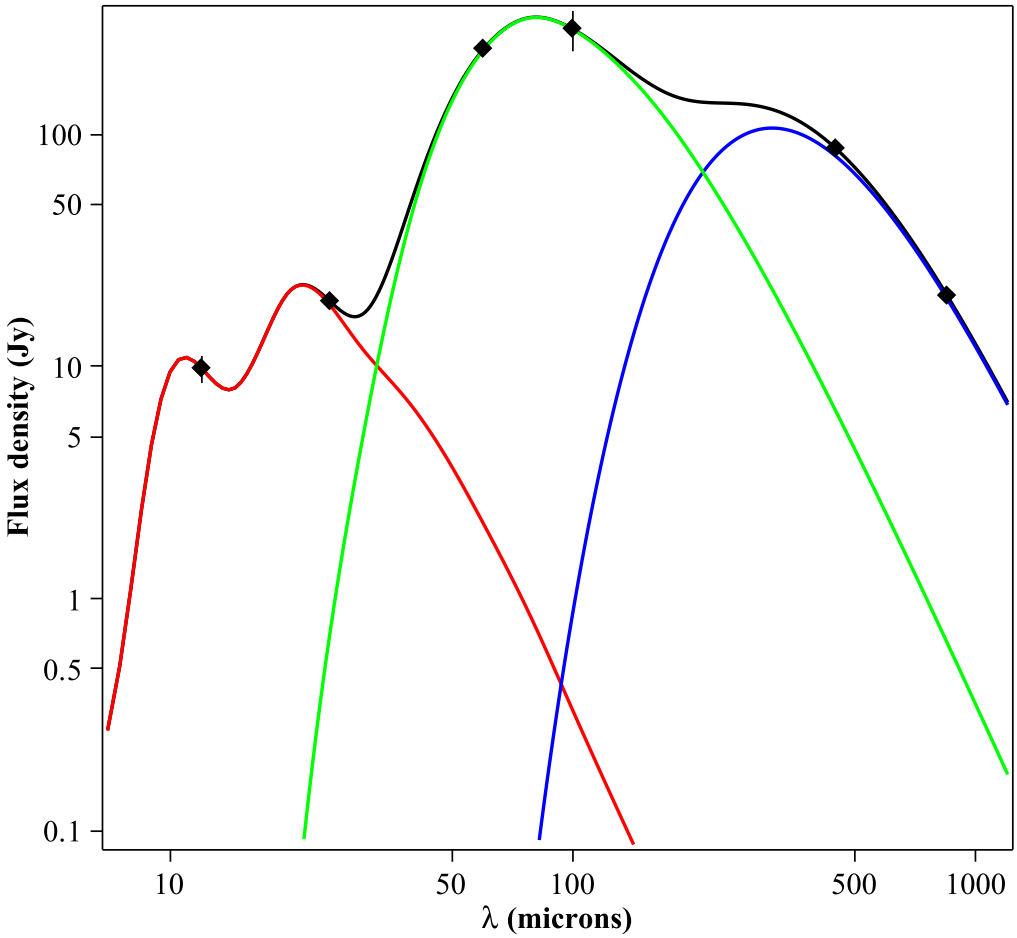

Figure 6.32: Illustration of the Spectral Energy Distribution of the BFS15 cloud from both the IRAS and SCUBA-2 observations (solid diamonds mark the observed flux densities) along with the three-component optimal model fit. The solid red line shows the contribution from hot dust, the solid green line represent the contribution from the cool dust, and the solid blue line displays the contribution from the cold dust, whereas the black solid line denotes the combined spectrum of all the three components.

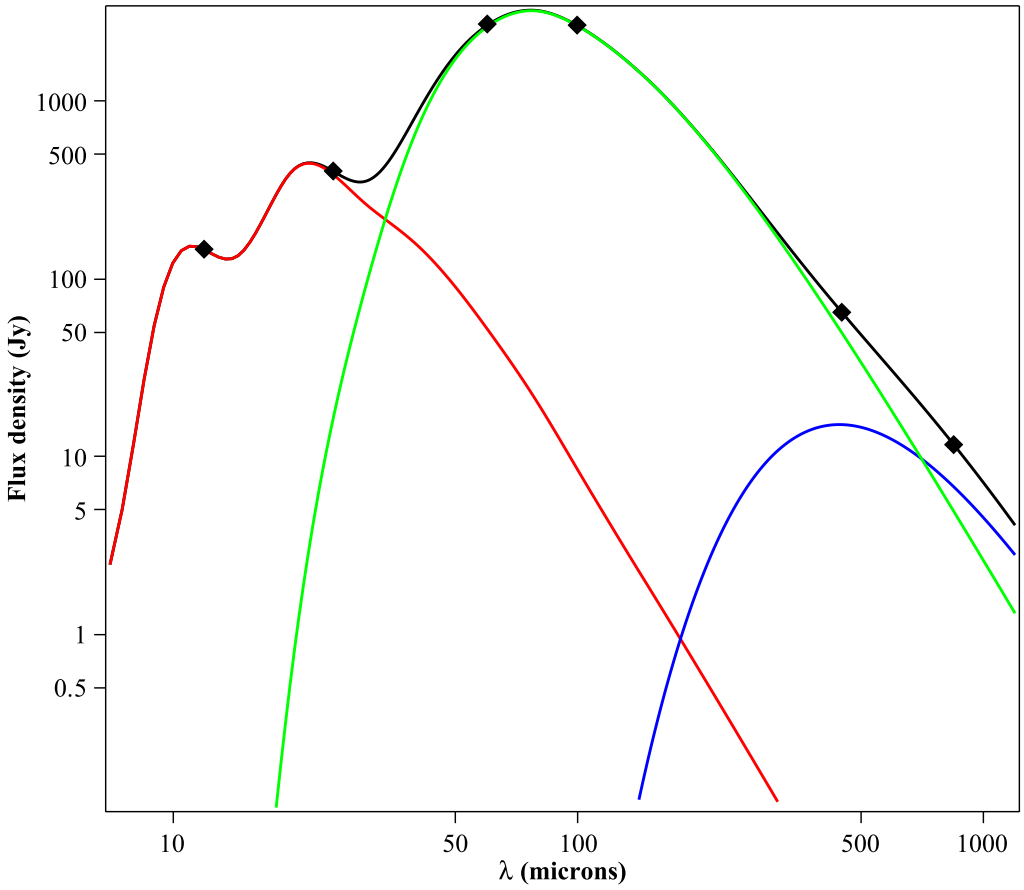

Figure 6.33: Illustration of the Spectral Energy Distribution of the S156 cloud from both the IRAS and SCUBA-2 observations (solid diamonds mark the observed flux densities) along with the three-component optimal model fit. The solid red line shows the contribution from hot dust, the solid green line represent the contribution from the cool dust, and the solid blue line displays the contribution from the cold dust, whereas the black solid line denotes the combined spectrum of all the three components.

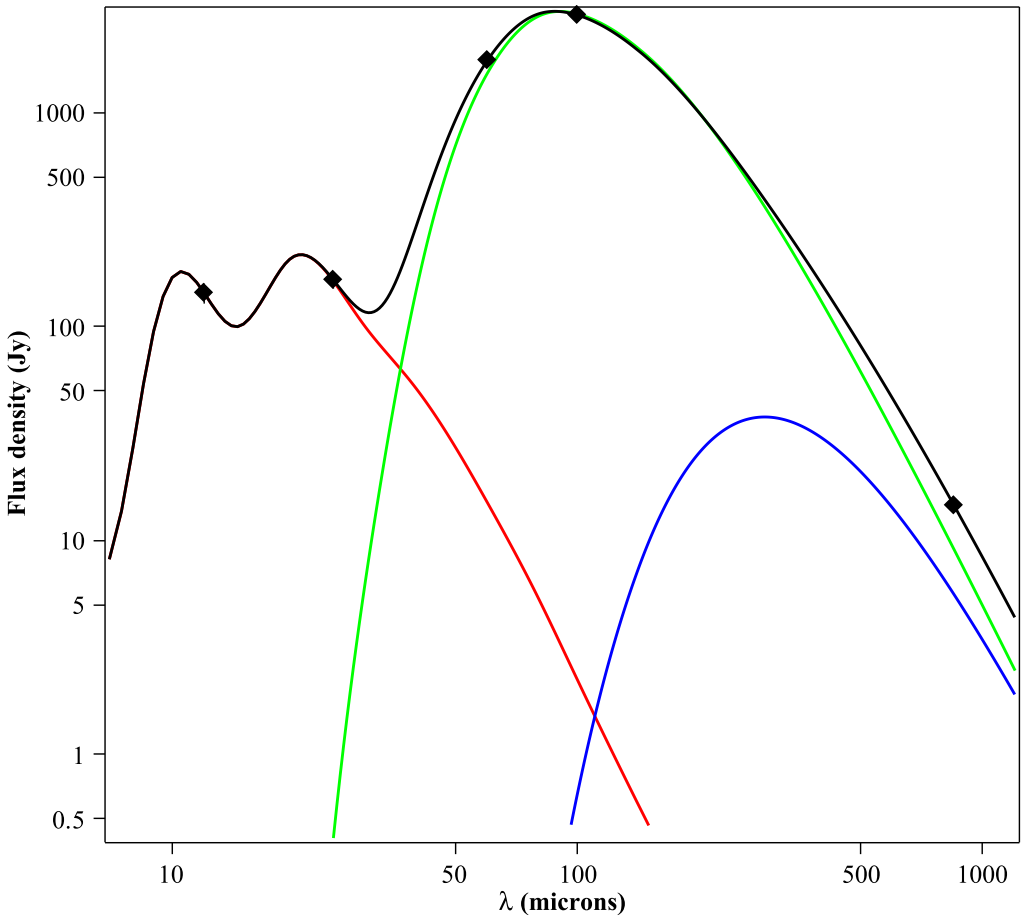

Figure 6.34: Illustration of the Spectral Energy Distribution of the S148 cloud from both the IRAS and SCUBA-2 observations (solid diamonds mark the observed flux densities) along with the three-component optimal model fit. The solid red line shows the contribution from hot dust, the solid green line represent the contribution from the cool dust, and the solid blue line displays the contribution from the cold dust, whereas the black solid line denotes the combined spectrum of all the three components.

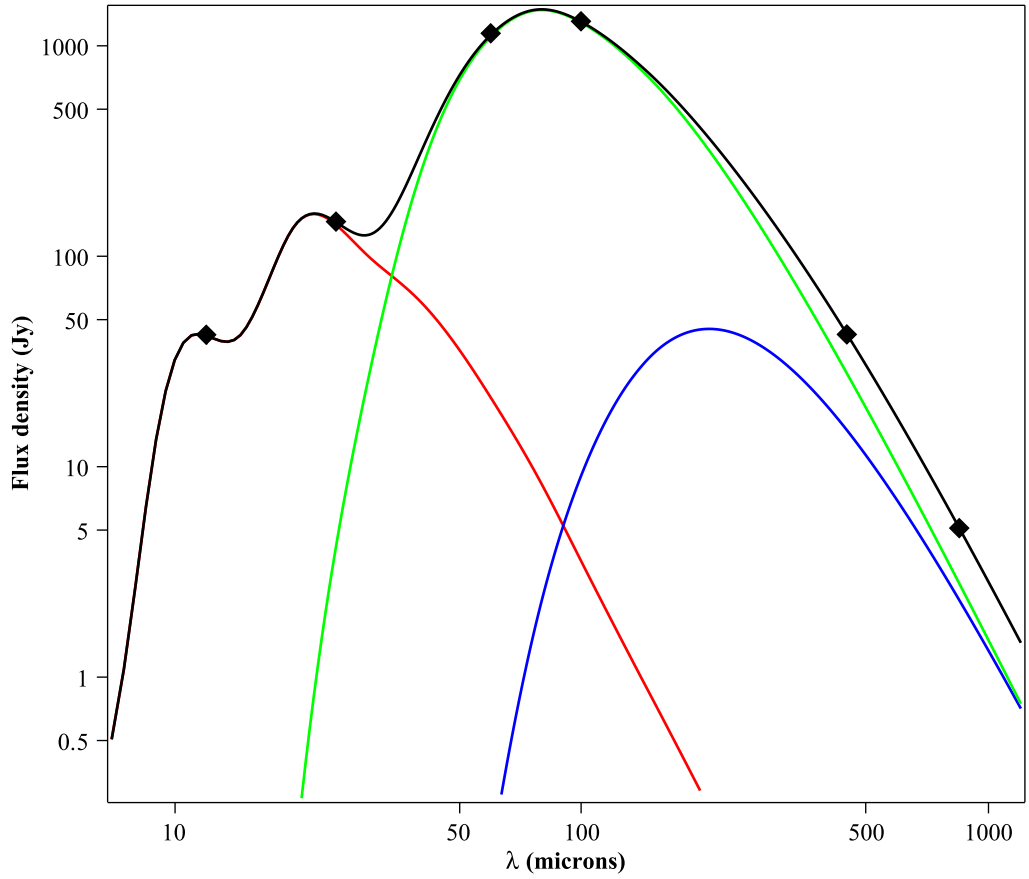

Figure 6.35: Illustration of the Spectral Energy Distribution of the S128N cloud from both the IRAS and SCUBA-2 observations (solid diamonds mark the observed flux densities) along with the three-component optimal model fit. The solid red line shows the contribution from hot dust, the solid green line represent the contribution from the cool dust, and the solid blue line displays the contribution from the cold dust, whereas the black solid line denotes the combined spectrum of all the three components.

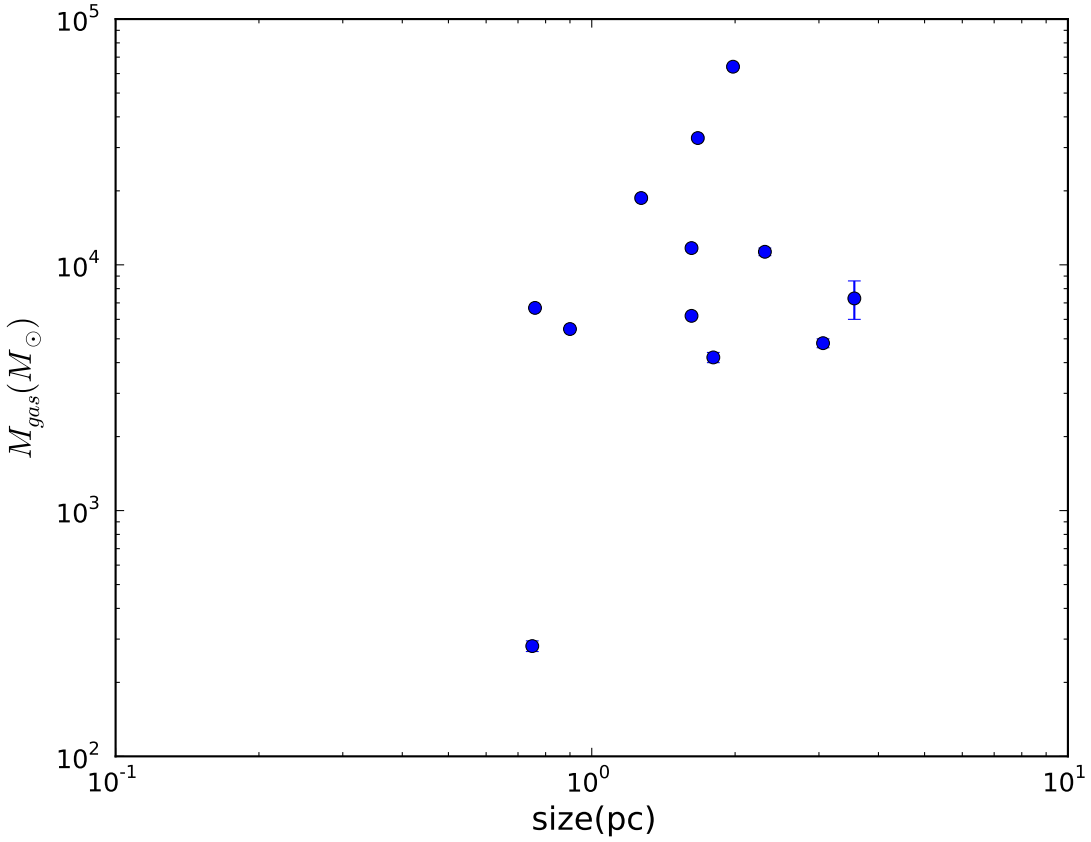

Figure 6.36: Mass-size diagram of the target cores.

6.6 Chapter Summary

In this chapter, we analyzed the results gained from the SCUBA-2 observations of the molecular clouds associated with outer Galaxy H II regions. Assuming a spherical geometry for all the cloud cores, dust temperature and gas number density profiles of the target cores are constructed and analyzed. Probable contamination from the spectral lines at SCUBA-2 wavelengths and its effect on the number density and temperature profiles of the cloud cores are examined. The dependence of the number density profiles and temperature profiles on the dust emissivity index are investigated. The major conclusions drawn from this chapter are as follows:

• The sub-millimeter continuum emission from SCUBA-2 reveals high number density regions of the clouds and the number density profiles follow a power law density distribution.

• The density profiles of the cloud cores are consistent with a logotropic density distribution.

• Removal of line contamination at 850 μm shifted the temperatures to higher values and slightly increased the steepness of the density profile.

• Increasing the value of the emissivity index from 1.0 to 2.0 decreases the overall temperatures of the clouds showing an anti-correlation between T_d and β. However, the number density profiles show a correlation with β: number densities increase with increasing values of β.

Chapter 7

Discussion, Conclusions and Future work

7.1 Discussion

Dust in molecular clouds associated with Galactic massive star-forming regions has been studied in detail using far-infrared and sub-millimeter observations. Fitting a two-component dust model to the IRAS observations shows that the grains near H II regions can be at two different temperatures, namely hot and cool: the hot dust is at temperatures above 100 K, and the cool dust is at temperatures between 20-40 K. The mass of the cool dust is observed to be four to five orders of magnitude higher than the hot dust. We found that the ratio of the bolometric luminosities (2.8) at the two different temperatures (cool and hot) is uniform in all the sample clouds. The calculation of the bolometric luminosity ratio required several steps, including an automated fitting procedure. However, directly using the observed dust emission from the sample clouds at the four different effective wavelengths of the IRAS bands, we noticed that the observed flux density ratio, $F_{100}/(F_{12} + F_{25})$, also appeared to be unvarying and this confirmed the above result. The observed flux density ratio of all the molecular clouds associated with the Galactic H II regions is confined to a very narrow band compared to all the objects in the IRAS PSC. However, dust in clouds without any H II regions displays a higher flux density ratio, i.e., a lack of short wavelength emission from hot dust, indicating the absence of any strong heating source near them. Using the observed flux density ratios, we also presented a formula to estimate the total infrared luminosity of Galactic H II region clouds from the flux density at any one IRAS wavelength. Note that these results are useful for estimating gas masses in extragalactic regions with active massive star formation.

The dust masses derived from the two-component model fits to the IRAS data show

that most of the mass resides in the cool dust compared to the hot dust. These results are compared with the results obtained from a subsample (11) of the target clouds examined using CO molecular line observations [Azimlu and Fich, 2011]. The gas masses obtained from the CO observations span a wide range from 124 $M_\odot$ (S175A) to 7961 $M_\odot$ (S148-S149). The ratio of the CO derived gas masses and cool dust derived gas masses (assuming a gas-to-dust ratio of 100) in 10 of the sample clouds on average is 2.95, and ranges from 0.31 to 5.4. In S196 and S192-S194, the gas masses derived from cool dust exceed the gas masses obtained from CO. In all other clouds, the ratio varies from 1.3 to 5.4, and S175B shows the highest ratio among all these clouds.

The gas masses derived from the CO molecular line observations are $\sim$3 times higher on average than the cool dust derived gas masses. Similar studies to trace gas masses using thermal emission from dust at millimeter (mm) wavelengths and CO observations by Bot et al. [2007] provide a ratio (ratio of virial mass from CO to the mass of gas deduced from mm dust emission) of $\sim$2 for Galactic GMCs. The cool dust mass in our study is derived using IRAS data and therefore the gas masses deduced from thermal dust emission can in effect increase, with a subsequent reduction in the ratio, if we consider sub-millimeter emission from dust. If the ratio is 1, then it indicates that the CO is a good tracer of molecular gas. If the ratio is less than 1, then it may be either due to the presence of "CO dark H_2 gas", the molecular gas component that cannot be traced by CO, or due to the fact the dust emission better probes the denser gas than the CO. The dust masses were calculated using the data from IRAS observations and we did not have sub-millimeter data for most of the objects observed using CO. A value higher than 1 as obtained in the above study is most likely caused by the lack of continuum data at longer wavelengths in deriving the dust masses.

Using a sub-sample of the target observations obtained from the SCUBA archive, we analyzed the cold dust (< 20 K), since IRAS is insensitive to the emission from dust at sub-millimeter wavelengths where the peak of the cold dust emission lies. Most of the clouds showed the presence of very cold dust ($6 \text{ K} < T_d < 10$ K) revealing the evidence of very cold dust even in the extreme environments near high-mass stars. The masses of the cold dust derived from SCUBA observations showed that they far exceed the masses of the cool and hot dust derived from IRAS observations. The M_{cold} to the M_{cool} ratio spans a wide range from 12 to 260 and the large amount of dust at very low temperatures such as 6 K can also be attributed by factors such as line contamination, variations in dust emissivity index, and galactic spinning dust emission on the sub-millimeter flux from the clouds.

The hot and cool dust interface in molecular clouds near the Galactic H II regions was modeled using different plausible number density distributions, assuming that the heating and cooling of dust grains are in equilibrium in our sample clouds. The modeled clouds are exposed to plane parallel stellar radiation from a massive star on one side and, in

addition, they are also subjected to internal heating such as heating by Galactic cosmic rays. A uniform number density distribution throughout the length of the cloud does not reproduce the observed normalized IRAS fluxes, and therefore it is expected that the uniform density cloud model is not suitable to represent typical Galactic H II region molecular clouds. Varying the incident stellar fluxes could not replicate the observations, and therefore we tested a number of other distributions such as linear, power law, and step function density distributions. None of these models could reproduce all the observed normalized flux densities at the four IRAS wavelengths. We, therefore, artificially raised the internal heating inside the cloud in a step function density distribution and the model is found to be well matched with the observational data.

In the above modelling of IRAS emission, we did not examine grain heating along the distance of the cloud by the absorption of near-infrared radiation originating from the hot dust located close to the surface layer facing the star. However

> "In a blister H II region, dust at the ionized surface of a dense cloud and in the immediate vicinity of the stars may be a source of this radiation. However, like the emission-line radiation discussed above, the flux of near-infrared radiation is low, and it is insufficiently absorbed. Heating by this mechanism may be significant in the interiors of dense clouds, however the grains there are so cold that they cannot be detected in contrast to the dust at the cloud surface except perhaps at millimeter or sub-millimeter wavelengths (Natta et al.1981; Walker 1982); no such contrast is expected at the wavelengths observed by IRAS."

[Leisawitz, 1991]

SCUBA fluxes of our sample clouds always suffered from a number of inadequacies such as sky chopping and spacing in the bolometer arrays, which always reduced the observed fluxes. In addition, the 450 μm SCUBA data were affected by large scale sky variations. Furthermore, most of the maps that we gathered from the SCUBA archive were small area jiggle maps, which could not provide the large-scale extended flux from the target objects. The emission from extended regions is very relevant to study the clouds near H II regions because it is essential to complete the breadth of dust temperatures at the edges of the cold clouds. Knowing these temperatures is vital to make predictions of the structure of the cores in clouds.

With the use of SCUBA-2 data, we were able to elude the impact of sky chopping and bolometer spacing on the emission from dust at sub-millimeter wavelengths. We could also obtain good quality data at 450 and 850 μm SCUBA-2 wavelengths. For larger complexes, we were able to use wider Pong maps, which always covered the total angular size of the target objects and this also enabled us to recover the cloud edges. A total of six Galactic H II region complexes were studied using the SCUBA-2 camera.

Sub-millimeter thermal dust emission from all six complexes near to Galactic H II regions displays the presence of cold dust ($T_d < 20$ K). The dust temperature distribution is calculated from the SCUBA-2 450 and 850 μm wavelengths. The two-dimensional temperature maps of all the clouds show very cold, on average 6.7 K, core centres. The average temperatures of the clouds range from 7.30±1.08 K to 15.8±5.3 K. We assumed a constant value (2.0) of the emissivity index β in deriving these temperatures. Progressively decreasing temperatures from the envelope of the cloud to the centres suggests less heating in the core centres, most likely due to the absence of any central heating source. The observed low temperatures at the centres of the cloud cores are compatible with the central temperatures (< 10 K) of low mass prestellar cores based on both observations [Schnee and Goodman, 2005] and theory [Galli et al., 2002].

It is important to note that each cloud is composed of regions at different temperatures, typically a warmer zone is close to the side facing the star and a colder, denser zone is farther away from the star. The coldest regions of our clouds are deeply embedded in the warmer and less dense envelope. The dust grains emitting at shorter mid- and far-infrared wavelengths are warmer than the grains emitting at sub-millimeter wavelengths. The 30 K dust emission (if internal heating is present) is most likely arising from the moderately shielded regions where most of the 60 μm emission originates. This result is consistent with the warmest dust grain temperatures of ∼30 K, observed in a thin layer at the H II region-molecular cloud interface in the Rosette molecular cloud, derived using *Herschel* PACS 70, 160, and SPIRE 250, 350, and 500 μm fluxes [Schneider et al., 2010]. The 6 K dust observed at sub-millimeter wavelengths of our study, however, emerges from the region where the visual extinction is very high. Therefore the 30 K and the 6 K dust emission originates from spatially different zones.

There are very few existing observations of cold dust in the environments of H II regions, but cold dust at 20 K is found in S106 [Mezger et al., 1987]. One of the best studied GMC H II regions is the Orion Molecular Cloud (OMC), which is located at a distance of 420 pc. Dust at temperatures down to 15 K is identified in a clump associated with Orion A [Mookerjea et al., 2000] from far infrared observations. They also found signatures of dust at temperatures between 15 and 20 K, corresponding to cold dust, in a number of Orion clumps. Recent observations using BLAST and *Herschel* on clouds near massive star forming sites confirm temperatures as low as 10 K [Roy et al., 2011b; Giannini et al., 2012; Schneider et al., 2010].

The obtained temperatures from our study are dependent on the values of the dust emissivity index and reducing the value of β increases the core temperatures. At a uniform β, the cloud shows a temperature gradient which is increasing towards the edge. The coldest temperature in the interior probably refers to a region shielded from the external radiation field, both the direct stellar radiation field and the diffuse interstellar radiation field. The β maps (at constant temperature) show a gradient from the centre to the

edge. The lowest values of β are at the cloud centres, probably suggesting the presence of grain growth at the centres where density is highest. If we raise the temperature by 5 K, the resultant β maps show much lower values of the emissivity index towards the cloud interiors.

The optical depths of the clouds at 850 μm indicate that they are optically thin at 850 μm (peak τ_{850} span from 6.7×10^{-3} to 0.17). The column densities of the clouds derived from the 850 μm optical depth show very high values (ranging from 1.2×10^{23} to 4.3×10^{24}) towards the centres. The observed column densities of all the cloud cores exceed 10^{22} cm^{-2}, the typical limit for safe equilibrium at very cold temperatures against pure thermal pressure. The visual extinctions toward the core centres are very high, above 100, in most cases, indicating the presence of a highly opaque zone shielded from external radiation at the centre.

Not only temperature but also density structures are important to characterize the earliest stages of star formation. The constructed density profiles demonstrate a power law dependence; some clouds show dual, broken, power laws and most other clouds follow single power laws. The density power law index α is a parameter that often illustrates the conditions present inside the cores. A power law index of 2.0 at the outer regions and 1.5 towards the inner regions corresponds to the inside-out collapse model. However, flatter values of the observed cores' power law indices do not agree with this model. The observed density profiles are wider than a typical Bonnor-Ebert model at an isothermal temperature of 10 K. This signifies the absence of the hydrostatic equilibrium condition in our sample cores. A logotropic profile better represents the observed density profiles of our cores and may indicate the presence of turbulent pressure support against gravity.

The gas masses of the clouds obtained from hydrogen column density distributions represent the cloud masses better than do SED derived masses. This is because of the presence of the temperature gradients in the clouds. The derived masses from SED fitting assuming that dust is at three different temperatures—namely hot, cool and cold—do not always designate the real cloud masses. Three of our complexes, namely S254 [Heyer et al., 1989], S305, and S148 [Azimlu and Fich, 2011] were studied previously using CO observations. The gas mass obtained from CO observations (2.7×10^4 $M_\odot$) for the S254 complex is close to the gas mass obtained from our studies (1.74×10^4 $M_\odot$), indicating that cold dust is a good tracer of gas mass. Similarly, the gas mass of the S148 complex calculated from CO studies (7.9×10^3 $M_\odot$) is close to our results (7.3×10^3 $M_\odot$). However the mass of the S305 complex from CO studies (3.8×10^3 $M_\odot$) is an order of magnitude smaller than the mass obtained from our studies (4.45×10^4 $M_\odot$), perhaps due to insufficient coverage of the complex during the CO observations.

At visual extinctions above $\sim$3.2 [Whittet et al., 2001] and at temperatures below $\sim$ 90 K, H_2O freeze-out occurs on bare dust grains creating water ice mantles. The threshold A_v for the formation of ice mantles depends on the local UV radiation field of the cloud.

The chemical reactions which produce water subsequently diminish as the cloud becomes denser and colder converting most of the H to H_2 [Whittet, 2003]. At very high densities and cold conditions (temperatures less than 20 K), the molecules, especially CO—due to its high abundance in the gas phase, can freeze-out on to dust grains and can develop CO ice mantles [Henning, 1998] over the H_2O ice mantle layers. Water ice is the chief ingredient of ice mantles with a minor contribution from the CO [Chiar et al., 1995]. The accretion of ice mantles alters the optical properties of the dust components and thus increases the opacities of the dust grains present in the denser regions of the clouds. An increase in the opacity at sub-millimeter wavelengths reduces the temperatures of the dust grains slightly.

The temperatures of the clouds determine the the initial stages of star formation. To verify the conditions of the cloud cores, we calculated the Jeans mass of the cloud cores using central average number densities, assuming that the gas and the dust temperatures are coupled inside the cores. At regions of high densities, higher than $\approx 10^4$ cm^{-3}, the gas and the dust temperatures share the same value [Galli et al., 2002]. The derived Jeans masses of the clouds are significantly smaller than the mass of the clouds calculated from the dust emission suggesting that gravitational attraction overwhelms the thermal pressure and in effect, the cloud cores are undergoing a contraction which in turn is responsible for an eventual collapse.

Assuming that the clouds are spherical and no other forces are acting against gravity, the free-fall time scales were calculated and were found to be much less than the sound crossing times in the clouds. The free fall collapse times in our sample cores range from 10^3 to 10^4 years. The cloud cores S254N, S254S, BFS15, and S128N will collapse quickly in 10^3 years. However all other clouds have longer free fall time scales, of the order of 10^4 years.

In the previous calculation, we considered the simplest case, where the force due to thermal pressure opposes the gravitational force. But in a real cloud, there may be additional turbulence caused by kinetic pressure due to non-thermal motions. However we do not have observational non-thermal velocity dispersion information of these cores to estimate the turbulent pressure. The clouds considered in the previous calculation were stationary and unmagnetized. If the cloud cores possess non-zero angular momentum, or a considerable magnetic field, then the conditions inside the cores will be more complex. If rotation are large enough, it can oppose gravity. If the magnetic energy is comparable to the gravitational energy, it can also balance gravity. Polarimetric studies are required to find the value of the magnetic flux threading these regions.

High visual extinction, high mass, high column densities and cold temperatures of our sample cores favour an infalling state over an equilibrium state. At visual extinctions greater than 100 and column densities higher than 10^{23} cm^{-2} at very high masses, the cloud cores are unstable to collapse [Kauffmann and Bertoldi, 2004]. All the observed cores come under the category of potential High Mass Starless Cores (HMSCs), which by

definition do not host any massive protostars at the centre and are the probable precursors of high-mass proto-stellar objects. HMSCs represent initial conditions of high-mass star formation and are the least studied objects in the field of star formation. This is because these objects' peak emission falls in the sub-millimeter regime and until recently, we were unable to probe their evidence due to the lack of sufficient instruments that operate at these wavelengths.

Very few HMSCs are known todate and probing the properties of HMSCs is central to understanding the massive star formation processes. Because these regions evolve fast, they most likely generate massive stars which live for around million years without clearing out their dust cocoon. Most of the known HMSCs [Sridharan et al., 2005] have masses ranging from 10^2 to 10^3 $M_\odot$ and are at multiple evolutionary stages.

Typical molecular clouds of our samples possess total IR luminosities ranging from 10^3 to 10^6 $L_\odot$ and some of the clouds are identified with young stellar populations and open stellar clusters—primarily the main sequence stars associated with them [Azimlu Shanjani, 2010], and are at multiple evolutionary stages. One of our SCUBA-2 targets, S254, is a multiple star forming complex and Class I and Class II YSOs, which represent stars with infalling envelope and disk respectively, are detected in the region [Chavarría et al., 2008]. Thus even in such complexes, we can find high-mass starless cores.

The derived results from IRAS, SCUBA, and SCUBA-2 observations suggest the following geometry for the clouds near Galactic H II regions. Temperatures of the hot dust obtained in this study range from $\sim$ 100 K-300 K and is from large grains at thermal equilibrium that cannot radiate at very high temperatures. Most of the complexes observed with SCUBA-2 have associated emission in most of the IRAC wavebands (see Sections 7.1.1 and 7.1.2) implying the presence of PAHs and VSGs. Due to transient heating, PAHs and VSGs radiating at mid-IR wavelengths can raise the dust temperatures above a $\sim$ 1000 K for a short while. The hottest dust component is therefore associated with PAHs and VSGs located at the periphery of the H II regions. The cool dust temperatures reflect the equilibrium temperatures of large grains, which are the most likely sources of far infrared radiation from IRAS. The hot and cool dust emission is most likely from the surface layer, which is the interface between the ionized and molecular regions. The modeled interface shows the presence of a step function density distribution. The derived temperature of the cold dust is less than 20 K, implying the absence of any external radiation field in those regions. The cold dust is buried deep inside the molecular cloud and there exists a temperature gradient, which is decreasing toward the centre.

The large grains, PAHs, and VSGs do not affect the main result: the constant bolometric luminosity ratio of the cool dust to the hot dust. The PAHs and VSGs do affect the masses of the clouds, but still their contribution to the total mass of the clouds will be very small and insignificant.

An overall the Galactic H II region cloud geometry predicted from the observations is

presented below (see Figure 7.1). The H II region with an exciting star in the centre is shown on the left and an associated molecular cloud on the right. The radiation from the massive star heats up the cloud region close to the star to temperatures above 100 K shown in the green. The short wavelegth IRAS emission originates from this region. The white pale-blue region depicts the cool zone with typical temperatures between 20 and 40 K, and most of the long wavelength IRAS emission has its origin from here. The solid blue colour corresponds to the coldest region ($<$ 20 K) of the cloud, which is probably undergoing contraction. A gradient in temperature is shown towards the centre of the clouds, consistent with the SCUBA-2 result.

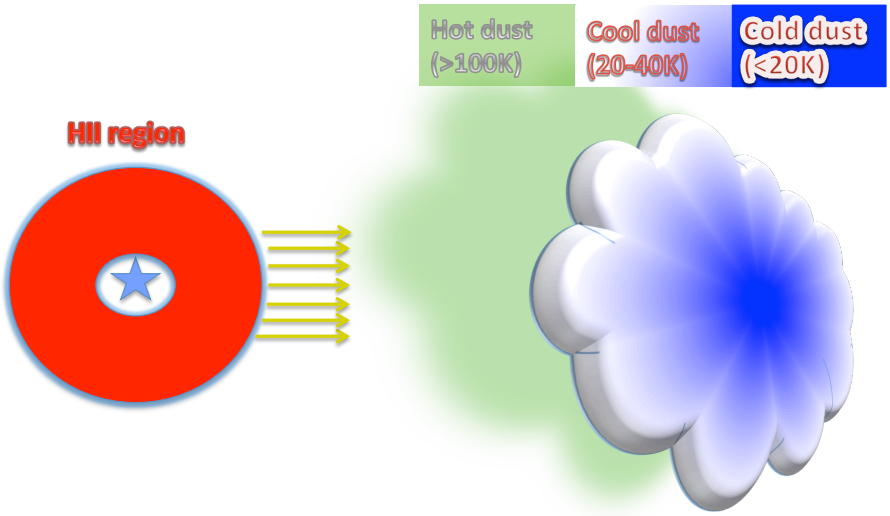

Figure 7.1: The predicted Galactic H II region cloud geometry from observations.

The overall cloud temperatures and predicted structure are consistent with the observed

morphology of the clouds in complexes associated with Galactic H II regions. To illustrate the morphology of hot dust near H II regions, we present the mid-infrared (mid-IR) configurations, employing Infrared Array Camera (IRAC) data, of a sub-sample of the objects observed using SCUBA-2. To emphasize the validity of the results derived in this thesis, we show the morphology of the ionized gas, the hot dust, and the cold dust, in another subsample of the SCUBA-2 targets, in the next section.

7.1.1 Mid-IR emission morphology

To present the mid-IR features of the target clouds, we used data obtained from the Spitzer Space Telescope Infrared Array Camera (IRAC) [Fazio et al., 2004]. The IRAC basic calibrated data (BCD) frames of the clouds S159, S156, and S254 were extracted from the Spitzer Heritage Archive (SHA) and processed using MOPEX software. For all other clouds, post BCD products from the SHA were used to generate the Spitzer images. For S159, S148, S156, and S254 colour composite images were constructed from the IRAC 3.6, 5.8 and 8.0 μm images. Due to the lack of data at 5.6 and 8.0 μm, IRAC colour composite images were not created for the complexes S305 and S128. Note that IRAC 3.6 μm emission is dominated by photospheric emission from stars and emission at IRAC 5.8 and 8 μm are dominated by PAHs.

Figure 7.2 shows the IRAC emission from the H II region S159 and it is apparent that the cloud centre represents emission from all three wavelengths. The red dots designate the young stellar objects associated with the S159 star forming region and a large number of such objects are present close to the centre of the cloud. The presence of a filament (or wind) emerging out of the cloud is clearly visible in the NW direction of the cloud.

Emission from longer IRAC wavelengths (5.6 and 8.0 μm) is predominant in the complex S148 (See Figure 7.3). However, the centre of the complex furnishes concurrent emission from all three wave bands. The bright stellar emission on the NE side of the complex is probably from a star along the line of sight. Similar to S159, the S148 complex has existing stellar clusters associated with its field.

The S156 cloud shows a roughly circular PAH emission structure with central concentrations of young stellar objects (see Figure 7.4) accompanied by a diffuse PAH envelope extending towards the south. The transparent central region of the cloud most likely suggests the presence of a central zone of ionized gas corresponding to the H II region.

S254, which is a molecular cloud complex containing 5 H II regions, is a well studied H II region in all the IRAC wave bands [Chavarría et al., 2008]. The IRAC RGB colour image of the S254 complex is presented in Figure 7.5 with the 3.6 μm in red, 5.8 μm in green, and the 8.0 μm in blue. The young stellar objects are in red colour and the diffuse PAH emission is in pale white colour.

The mid-IR emission morphologies of all sub-sample clouds disclose the presence of a large number of young stellar objects associated with the molecular clouds near H II regions in addition to the diffuse PAH emission features.

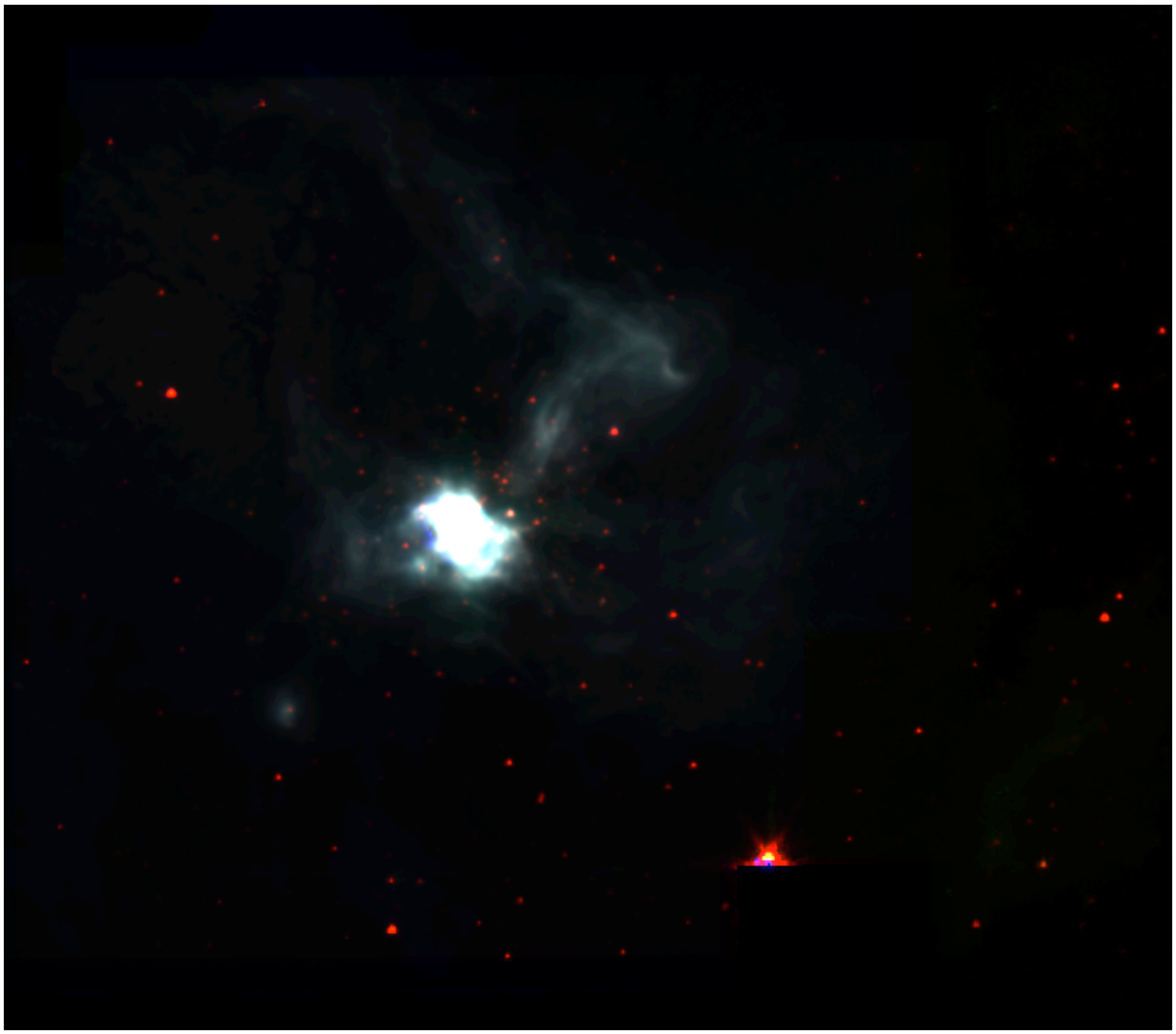

Figure 7.2: S159 SPITZER IRAC RGB colour composite image, with the 3.6 μm in red, 5.8 μm in green, and the 8.0 μm in blue.

Figure 7.3: S148 SPITZER IRAC RGB colour composite image, with the 3.6 μm in red, 5.8 μm in green, and the 8.0 μm in blue.

Figure 7.4: S156 SPITZER IRAC RGB colour composite image, with the 3.6 μm in red, 5.8 μm in green, and the 8.0 μm in blue.

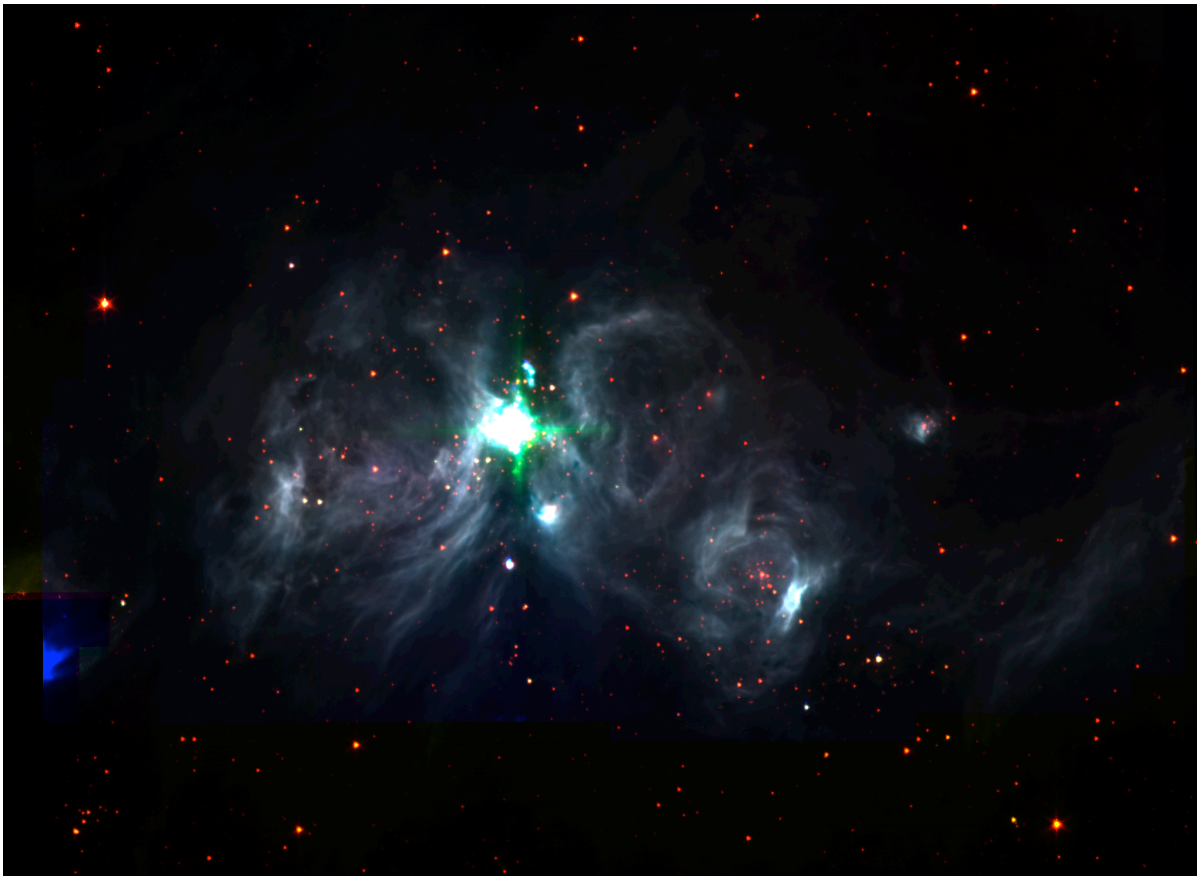

Figure 7.5: S254 SPITZER IRAC RGB colour composite image, with the 3.6 μm in red, 5.8 μm in green, and the 8.0 μm in blue.

7.1.2 Spatial distributions of H II regions, PDRs and cold dust

In this section we present the spatial distribution of four of our sample molecular clouds with respect to the sites of associated ionized gas from the H II regions. The polycyclic aromatic hydrocarbon (PAH) emission from Spitzer IRAC 1st (3.6 μm) or 4th (8 μm) band (depending on the availability and quality of the IRAC data at different bands) and cold dust at 850 μm SCUBA-2 wavelengths are used to display the very hot and cold dust components in these molecular clouds. The maps of the ionized components of the four H II regions are obtained from the VLA studies of the outer galaxy H II regions [Fich, 1986, 1993].

The 8 μm PAH feature (green) is well defined and located in the outer borders of the ionized gas (red colour) from the H II regions S148 and S149. At some locations, the ionized and the PAH emission coexist and are visible in yellow. The pink-coloured emission appears to originate from a blend of the ionized and the cold dust emissions. From the image (see Figure 7.6) it is evident that the emission from PAHs, which is generally associated with photodissociation regions (PDRs) near hot stars, and the cold dust are discrete. Note that the PDRs near massive stars are the borderlines isolating the ionized and the molecular components of the gas. The cold dust is most likely positioned along the line of sight to the H II region.

The S305 complex has the layout of a typical bubble H II region (Figure 7.7). The ionized gas is shown in red and the IRAC 3.6 μm in green, and the cold dust emission at 850 μm from SCUBA-2 is in blue. Two H II regions are visible in the map field, with the major one surrounded by the cold dust in the centre and compact H II region south-east of S305S. The 3.6 μm IRAC emission is associated with the photospheric emission from young stars in the field. A very faint 3.6 μm emission layer, most likely due to the continuum emission from very small grains, is present encircling the ionized gas. In addition, a very strong PAH nebulosity is present in the core centre of the cloud S305S.

The four spheres of ionized hydrogen (in red) around massive young stars accompanying the S254 complex are displayed in Figure 7.8. The PAH emission in green is primarily surrounding the H II regions and is largely concentrated in the area between the H II regions S255 and S257. Furthermore, the cold dust is mostly condensed on the same zone between these two H II regions and is almost absent in or near the diffuse H II region S254.

The diffuse and the compact H II regions in S128 are shown in red (Figure 7.9). The emission from IRAC 3.6 μm is represented in green and the cold dust emission in blue. The diffuse H II region on the south is bordered by a web-like bubble of PAHs and no cold dust is present in the location of this H II region. Bright PAH emission is found in the northern region coincident with the compact H II region.

In all cases, the composite RGB images reveal that the spherical H II regions (Stromgren spheres) corresponding to the ionized gas are always enclosed by the emission from PAHs

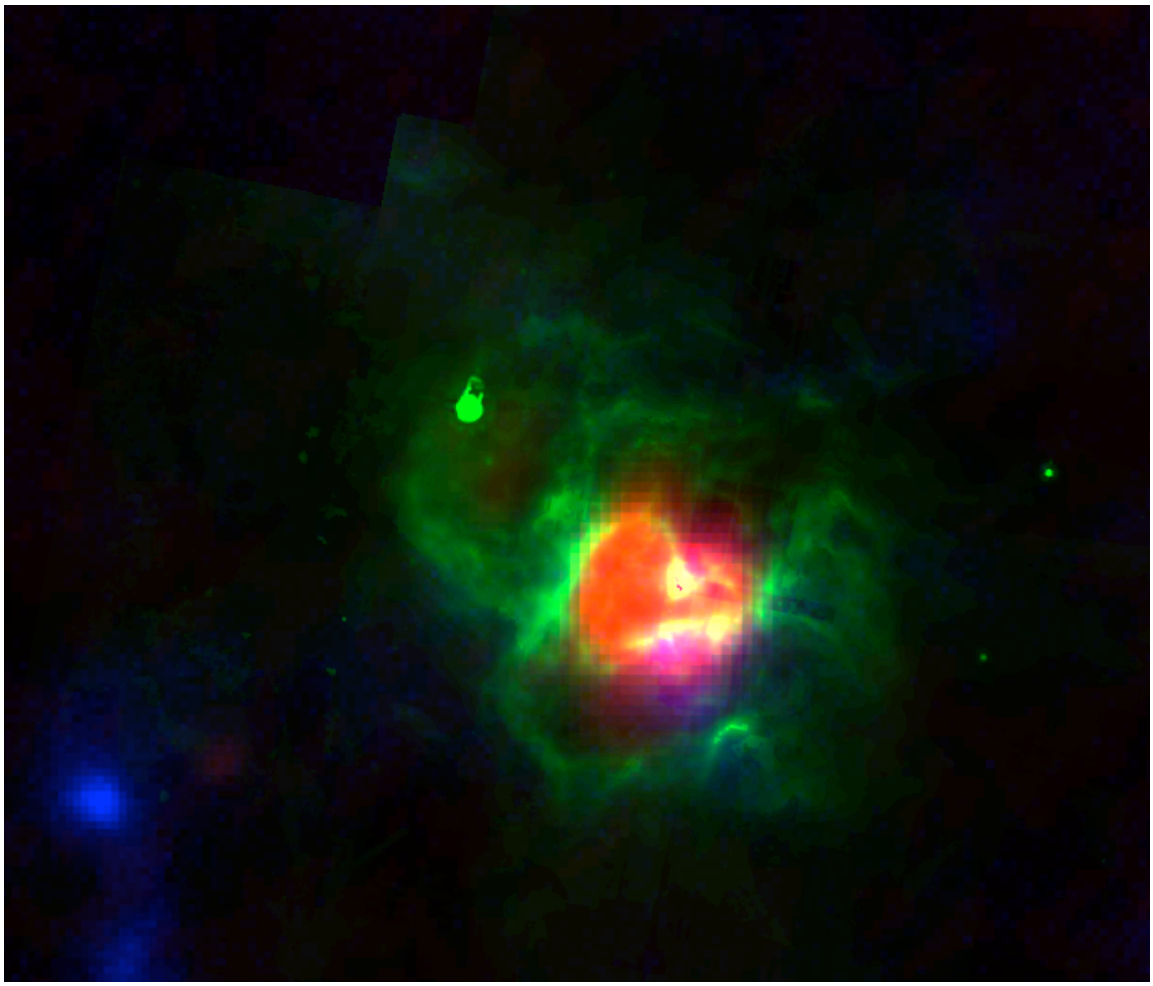

Figure 7.6: Colour composite image of S148, with the VLA radio emission corresponding to the H II region in red, the 8.0 μm PAH emission emphasizing the emission from PDR surrounding the ionized gas in green, and the cold dust emission from 850 μm SCUBA-2 wavelengths in blue.

(or continuum emission from very small grains) and cold dust. The PAH emission arising from the PDRs represent the boundaries of the ionized gas. In most cases, there is an anti-correlation between the spatial distributions of the cold dust and the ionized gas. The case is similar with emission from PAHs and the cold dust. However, a correlation between PAH and ionized gas is observed in the compact H II region of S128 and in the region between H II regions S255 and S257.

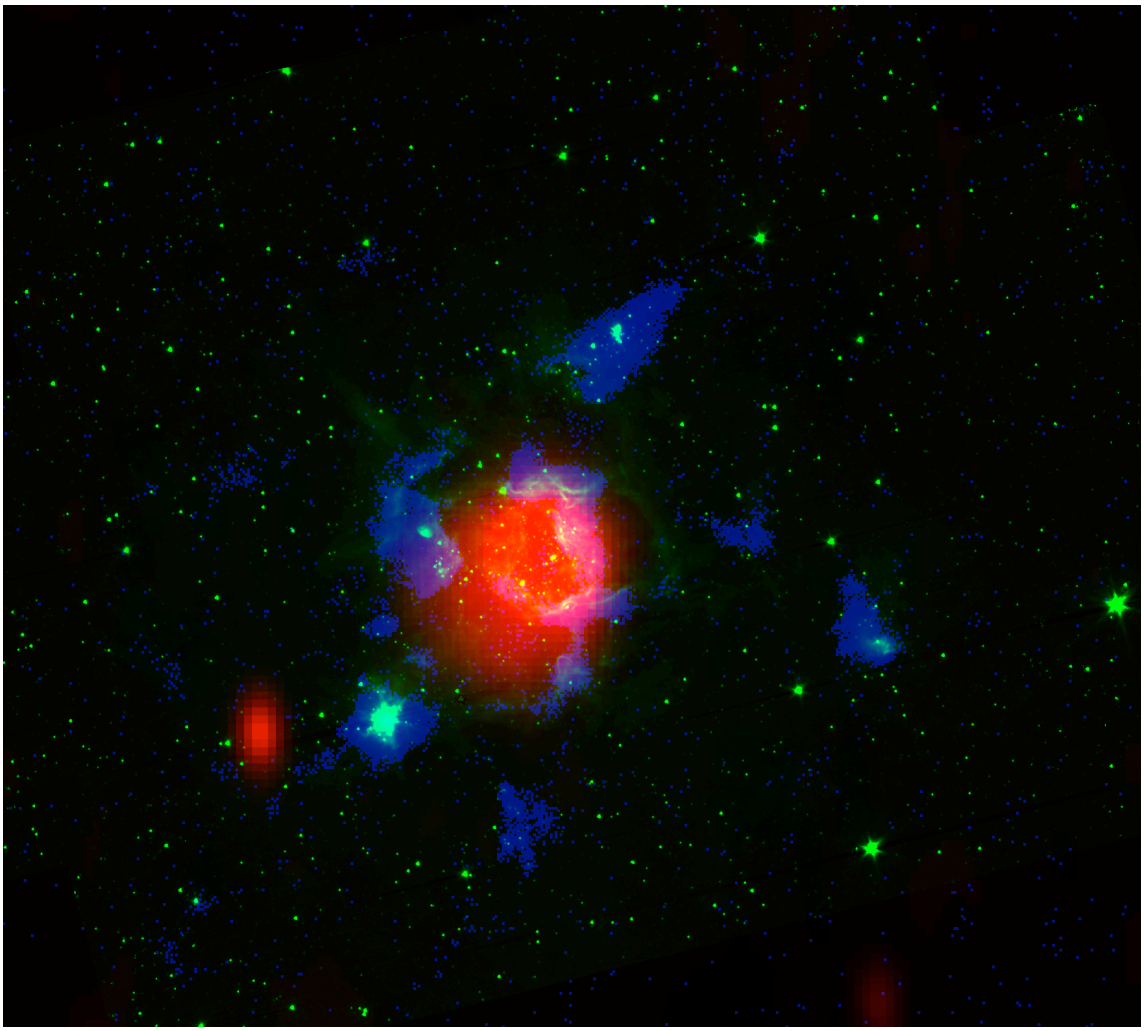

Figure 7.7: Colour composite image of S305, with the VLA radio emission corresponding to the H II region in red, the 3.6 μm IRAC emission emphasizing the emission from PDR surrounding the ionized gas in green, and the cold dust emission from 850 μm SCUBA-2 wavelengths in blue.

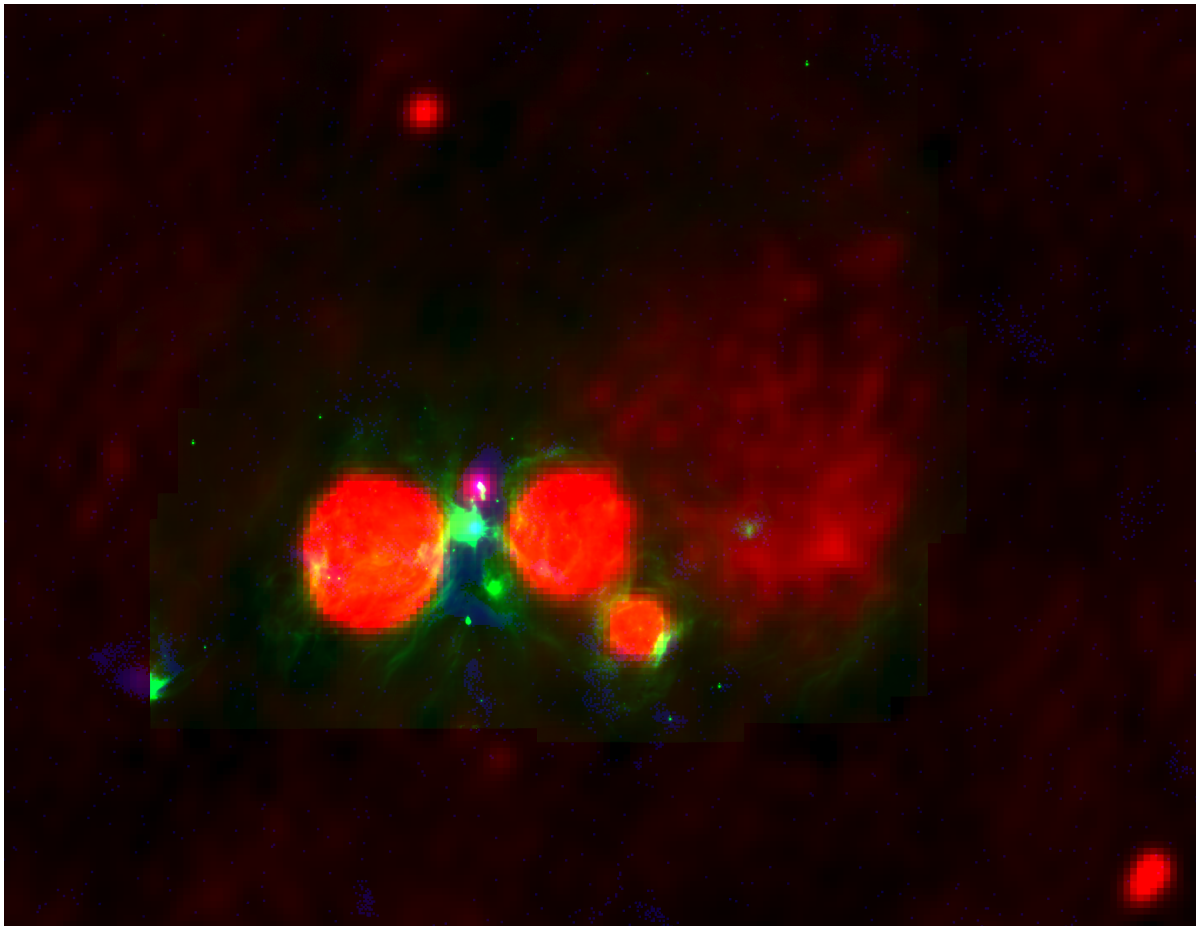

Figure 7.8: Colour composite image of S254, with the VLA radio emission corresponding to the H II region in red, PAH emission at 8 μm from SPITZER IRAC (green), and 850 μm dust emission from SCUBA-2 (blue).

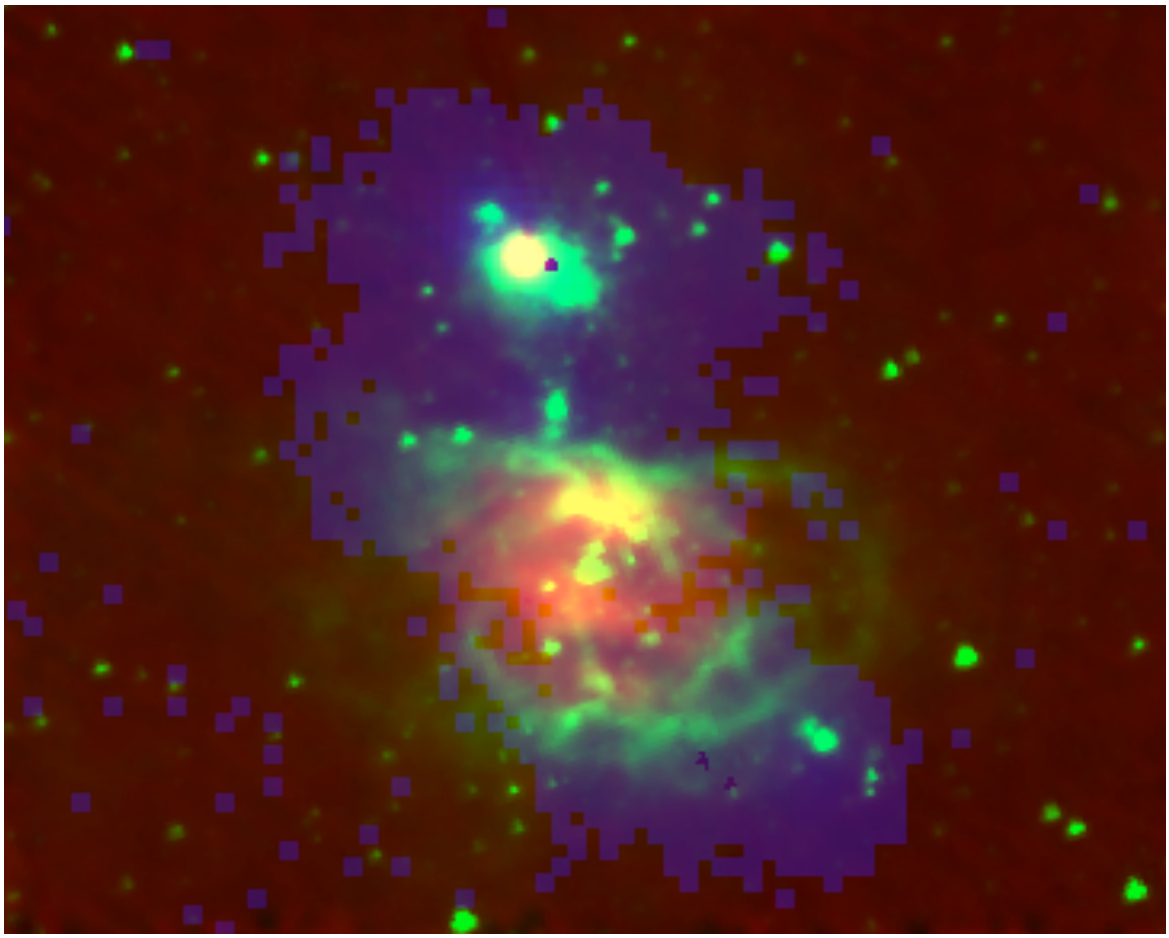

Figure 7.9: Colour composite image of S128, with the VLA radio emission corresponding to the H II region in red, the 3.6 μm IRAC emission emphasizing the emission from PDR surrounding the ionized gas in green, and the cold dust emission from 850 μm SCUBA-2 wavelengths in blue.

7.2 Conclusion

In this thesis I have presented studies of molecular clouds near Galactic H II regions using dust continuum observations, primarily employing IRAS, SCUBA, and SCUBA-2 instruments. A total of 83 clouds associated with Galactic H II regions were studied using IRAS data. A subsample (10) of the clouds were analyzed using SCUBA, and another subsample containing six Galactic H II region complexes were examined using SCUBA-2. The central goal of this thesis has been to obtain an insight into the physical properties, such as the temperature and mass, of the dust in molecular clouds associated with Galactic H II regions, and thereby to understand the effect of the dust on the process of massive star formation.

• Using a two-component model SED of hot and cool dust fitted to the IRAS data, we derived the temperatures and masses of the hot and cool dust components and found that the hot dust temperatures exceed 100 K and cool dust temperatures fall between 20 and 40 K. The obtained masses of cool dust are typically four to five orders of magnitude higher than the hot dust.

•The bolometric luminosity ratio and the observed flux density ratio are found to be roughly a constant in all the Galactic H II region clouds.

•The three-component model SED of hot, cool and cold dust fitted to IRAS and SCUBA data indicates the presence of very cold dust, less than 20 K, in clouds near H II regions. The cold dust component dominates the masses, even though it is not a very good source of total bolometric luminosity.

• Modeling of the IRAS data using different density distributions in molecular clouds near Galactic H II regions could not reproduce all the observed normalized IRAS flux densities, since the clouds required a higher heating at the interiors where most of the 60 μm originates. Artificially raising the internal heating by 30 K could reproduce the IRAS observations.

•The dust temperature distribution in molecular cloud complexes near Galactic H II regions was examined using data obtained from the new SCUBA-2 camera. We find that the central cloud regions are very cold, with temperatures around 6 K. Towards larger radii, the dust temperatures increase.

• The detected clouds are very massive, with masses ranging from 10^2 to 10^5 $M_\odot$, and they belong to the category of HMSCs and are most likely collapsing.

• The derived properties and the inferred geometry from the IRAS and SCUBA-2 observations are consistent with the mid-IR morphology of a subsample of clouds from SPITZER IRAC observations and the radio morphology from VLA observations. Mid-IR emission also points to the presence of young stellar objects inside them. An anti-correlation in the

spatial distributions between the cold dust and ionized gas is observed towards the target clouds: A cold dust layer surrounds the ionized hydrogen regions in the target objects, and the hot dust is located in between the ionized and the molecular regions, at the borders of the molecular clouds.

7.3 Summary

The three most important results of this thesis are: (1) the constant value of the bolometric luminosity ratio of the cool dust to the hot dust, indicates that, although the clouds most probably receive very different amounts of radiation from their exciting stars, a constant value for the bolometric luminosity ratio is found in all of the 83 clouds. This implies that the ratio is dependent on some properties of the dust and the structure of the interface region, and not on the intensity of the radiation field of the exciting star or the size of the clouds. (2) none of the density models and models including varying amounts of stellar radiation could reproduce the IRAS SED, pointing to the presence of some other phenomenon in H II region clouds such as near-infrared heating; this is discussed in the section "Future Research." (3) the cloud cores are cold and massive and are potential candidates of HMSCs, precursors of massive pre-stellar objects—some of the least studied objects in the area of star formation.

The presented results in this thesis can also act as a template for observations made with the forthcoming high spatial resolution instruments such as the Atacama Large Millimeter Array (ALMA) and James Webb Space Telescope (JWST) on extragalactic star forming regions.

7.4 Future Work

We have recently obtained SCUBA-2 data from a seventh Galactic H II region complex and have received further observation time for a number of Galactic H II regions in the upcoming term. Using these data, we expect to complete the SCUBA-2 survey of our outer Galaxy H II regions that I started as part of my thesis project, and eventually the general physical properties of the molecular clouds near massive star forming environments will be provided.

Modelling of the IRAS data for clouds near H II regions could not reproduce the observations. I found that raising the 60 μm emission by supplying a higher value of internal heating (around 30 K) could best match the observations, but there were no obvious physical reasons behind this. However according to a recent proposition by my supervisor Dr. Mike Fich, the hot dust at the surface layers, emitting in the near- and mid-infrared,

could be a good source of heating for the cloud interiors, especially at regions from where most of the 60 μm IRAS emission originates, and his initial models put forward a higher degree of internal heating by the near-infrared than the heating of the same region by the attenuated stellar radiation field. We plan to pursue this work to provide a probable interior heating mechanism that can complement our IRAS observations.

We speculated on the presence of centrally-heated cloud cores associated with our sample H II regions and developed radiative transfer modelling code using DUSTY. However, we could not test the code on our samples because of the presence of very cold cloud centres. If we can find the presence of internal heating sources inside cloud cores in our future SCUBA-2 observations, we plan to do the modelling using DUSTY.

To better understand star formation associated with Galactic H II regions, we need to examine the influence of environmental triggering on the core-to-star conversion. Several Galactic H II regions appear to show triggered star formation [Brand et al., 2011]. Massive stars can trigger core collapse via radiative or mechanical feedback. We will estimate the prevalence of triggering by looking for extremely young stellar objects associated with H II regions. SPITZER IRAC colour-colour diagrams and colour-magnitude diagrams of star clusters present near H II regions can be used to identify the youngest stars [Allen et al., 2005]. A number of young stellar populations have already been visually identified in a subsample of our target clouds and we are currently inspecting the data for further analysis. Furthermore, massive stars usually form in clusters and the localities near Galactic H II regions are ideal places to study their formation and evolution.

The overall star formation efficiencies in giant molecular clouds are found to be very low. Using the total stellar masses from our sample H II regions and the gas masses from the SCUBA-2 observations, we can determine the efficiency of star formation in our target regions. Note that better mass estimations of the clouds using sub-millimeter data will definitely provide more accurate measurements of the efficiencies of star formation.

The mass distribution of molecular cloud cores (the number of cores per logarithmic mass interval) in the ISM is called the core mass function (CMF). The CMF may provide a hint to the origin of the stellar initial mass function (IMF), which is a fundamental question yet to be resolved in the field of star and galaxy formation, evolution and feedback. A careful comparison of the CMF of the dense cores with the IMF of stars should indicate whether the dense core's mass completely pre-sets the star's birth mass. A similarity between the CMF and the IMF might imply that core mass largely determines stellar mass in a simple way whereas a dissimilarity would indicate there are other factors involved (e.g., environment). Once we finish the observations, we will examine the CMFs of our cloud cores and will compare these results to the stellar IMF to understand its physical origin.

Dust continuum observations are inadequate to elucidate the existing dynamics of the clouds and we require spectral line observations to get more deep insight into these regions.

The spectral line maps of the molecular clouds near H II regions will be used to compare the results obtained in this thesis. Note that spectral line observations are essential to better interpret the star formation. The standard value of the gas-to-dust ratio in the Milky Way ISM is 100 and there can be variations in this ratio, especially in the dense molecular cloud cores, due to different chemistry prevailing in cloud cores, particularly at low temperatures. We intend to calculate radial variations of the gas-to-dust ratios in each cloud and the overall mean values from cloud to cloud.

7.5 Acknowledgements

I acknowledge several important discussions with Dr. Carolyn McCoey. The suggestions from Dr. Gerald H. Moriarty-Schieven (NRC), Dr. Tim Jenness (JAC, Hawaii), Dr. Ed Chapin (UBC), Dr. Andy Gibb (UBC) and Dr. David Berry (JAC, Hawaii), about SCUBA and SCUBA-2 data reduction are greatly appreciated. I would like to acknowledge the use of APLPY and pywcsgrid2 in this research.

Bibliography

Allen, L. E., Hora, J. L., Megeath, S. T., Deutsch, L. K., Fazio, G. G., Chavarria, L., and dell, R. W. (2005). A Spitzer/IRAC survey of massive star-forming regions. In Cesaroni, R., Felli, M., Churchwell, E., and Walmsley, M., editors, *Massive Star Birth: A Crossroads of Astrophysics*, volume 227 of *IAU Symposium*, pages 352–357. 313

Anderson, L. D., Zavagno, A., Deharveng, L., Abergel, A., Motte, F., André, P., Bernard, J.-P., Bontemps, S., Hennemann, M., Hill, T., Rodón, J. A., Roussel, H., and Russeil, D. (2012). The dust properties of bubble H II regions as seen by Herschel. *A&A*, 542:A10. 21

Anderson, L. D., Zavagno, A., Rodón, J. A., Russeil, D., Abergel, A., Ade, P., André, P., Arab, H., Baluteau, J.-P., Bernard, J.-P., Blagrave, K., Bontemps, S., Boulanger, F., Cohen, M., Compiègne, M., Cox, P., Dartois, E., Davis, G., Emery, R., Fulton, T., Gry, C., Habart, E., Huang, M., Joblin, C., Jones, S. C., Kirk, J. M., Lagache, G., Lim, T., Madden, S., Makiwa, G., Martin, P., Miville-Deschênes, M.-A., Molinari, S., Moseley, H., Motte, F., Naylor, D. A., Okumura, K., Pinheiro Gonçalves, D., Polehampton, E., Saraceno, P., Sauvage, M., Sidher, S., Spencer, L., Swinyard, B., Ward-Thompson, D., and White, G. J. (2010). The physical properties of the dust in the RCW 120 H II region as seen by Herschel. *A&A*, 518:L99. 21

Andre, P., Ward-Thompson, D., and Barsony, M. (2000). From Prestellar Cores to Protostars: the Initial Conditions of Star Formation. *Protostars and Planets IV*, page 59. 20

Arvidsson, K., Kerton, C. R., Alexander, M. J., Kobulnicky, H. A., and Uzpen, B. (2010). A sample of intermediate-mass star-forming regions: Making stars at mass column densities <1 g cm^{-2}. *AJ*, 140:462–479. 82

Azimlu, M. and Fich, M. (2011). Study of Molecular Clouds Associated with H II Regions. *AJ*, 141:123. 96, 293, 296

Azimlu Shanjani, M. (2010). *Star Formation in Molecular Clouds Associated with H II Regions*. PhD thesis, University of Waterloo. 298

Beichman, C. A., Neugebauer, G., Habing, H. J., Clegg, P. E., and Chester, T. J. (1988). Infrared Astronomical Satellite (IRAS) Catalogs and Atlases, Explanatory Supplement. *NASA RP-1190 (Washington, DC: GPO)*, 1. 29

Beuther, H., Schilke, P., Menten, K. M., Motte, F., Sridharan, T. K., and Wyrowski, F. (2002). High-Mass Protostellar Candidates. II. Density Structure from Dust Continuum and CS Emission. *ApJ*, 566:945–965. 257

Bieging, J. H., Peters, W. L., Vila Vilaro, B., Schlottman, K., and Kulesa, C. (2009). Sequential Star Formation in the Sh 254-258 Molecular Cloud: Heinrich Hertz Telescope Maps of CO J = 2-1 and 3-2 Emission. *AJ*, 138:975–985. 172

Black, J. H. (1994). Energy Budgets of Diffuse Clouds. In Cutri, R. M. and Latter, W. B., editors, *The First Symposium on the Infrared Cirrus and Diffuse Interstellar Clouds*, volume 58 of *Astronomical Society of the Pacific Conference Series*, page 355. 92

Blitz, L., Fich, M., and Stark, A. A. (1982). Catalog of CO radial velocities toward galactic H II regions. *ApJS*, 49:183–206. 171, 194

Bohigas, J. and Tapia, M. (2003). Sh 2-128: An H II and Star-forming Region in the Galactic Outback. *AJ*, 126:1861–1870. 173

Bohlin, R. C., Savage, B. D., and Drake, J. F. (1978). A survey of interstellar H I from L-alpha absorption measurements. II. *ApJ*, 224:132–142. 187

Bonnor, W. B. (1956). Boyle's Law and gravitational instability. *MNRAS*, 116:351. 257

Bösch, M. A. (1978). Anomalous Absorption in Amorphous Solids at Low Temperature. *Physical Review Letters*, 40:879–882. 86

Bot, C., Boulanger, F., Rubio, M., and Rantakyro, F. (2007). Millimeter dust continuum emission revealing the true mass of giant molecular clouds in the Small Magellanic Cloud. *A&A*, 471:103–112. 293

Bot, C., Ysard, N., Paradis, D., Bernard, J. P., Lagache, G., Israel, F. P., and Wall, W. F. (2010). Submillimeter to centimeter excess emission from the Magellanic Clouds. II. On the nature of the excess. *A& A*, 523:A20. 86

Boudet, N., Mutschke, H., Nayral, C., Jäger, C., Bernard, J., Henning, T., and Meny, C. (2005). Temperature Dependence of the Submillimeter Absorption Coefficient of Amorphous Silicate Grains. *ApJ*, 633:272–281. 86

Brand, J. and Blitz, L. (1993). The Velocity Field of the Outer Galaxy. *A&A*, 275:67. 169, 170

Brand, J., Massi, F., Zavagno, A., Deharveng, L., and Lefloch, B. (2011). Triggered star formation at the borders of the H ii region Sh 2-217. *A&A*, 527:A62. 313

Brand, J. and Wouterloot, J. G. A. (1998). A multi-wavelength study of the Sharpless 151 region. *A& A*, 337:539–557. 20

Caplan, J., Deharveng, L., Peña, M., Costero, R., and Blondel, C. (2000). Oxygen and helium abundances in Galactic Hii regions - I. Observations. *MNRAS*, 311:317–328. 26, 170, 172

Chan, G. and Fich, M. (1995). An IRAS Survey of H II Regions. *AJ*, 109:2611. 25, 26, 27, 36, 79, 170

Chavarría, L. A., Allen, L. E., Hora, J. L., Brunt, C. M., and Fazio, G. G. (2008). Spitzer Observations of the Massive Star-forming Complex S254-S258: Structure and Evolution. *ApJ*, 682:445–462. 172, 298, 301

Chen, N. (1990). Modified Möbius inverse formula and its applications in physics. *Physical Review Letters*, 64:1193–1195. 18

Chiar, J. E., Adamson, A. J., Kerr, T. H., and Whittet, D. C. B. (1995). High-Resolution Studies of Solid CO in the Taurus Dark Cloud: Characterizing the Ices in Quiescent Clouds. *ApJ*, 455:234. 297

Chini, R., Kruegel, E., Kreysa, E., and Gemuend, H. (1989). The submillimeter continuum of active galaxies. *A&A*, 216:L5–L7. 83, 84

Chini, R., Kruegel, E., and Wargau, W. (1987). Dust emission and star formation in compact H II regions. *A&A*, 181:378–382. 82

Chini, R. and Wink, J. E. (1984). The galactic rotation outside the solar circle. *A&A*, 139:L5–L8. 169, 171

Cichowolski, S., Romero, G. A., Ortega, M. E., Cappa, C. E., and Vasquez, J. (2009). Unveiling the birth and evolution of the H II region Sh2-173. *MNRAS*, 394:900–915. 20

Clayton, G. C., Wolff, M. J., Sofia, U. J., Gordon, K. D., and Misselt, K. A. (2003). Dust Grain Size Distributions from MRN to MEM. *ApJ*, 588:871–880. 162

Cox, P., Deharveng, L., and Caplan, J. (1987). Extinction and reddening towards compact Galactic H II regions. *A&A*, 171:277–288. 170

Crampton, D., Georgelin, Y. M., and Georgelin, Y. P. (1978). First optical detection of W51 and observations of new H II regions and exciting stars. *A&A*, 66:1–11. 170

Deane, J. R., Ladd, E. F., and Sanders, D. B. (1994). Spatially-Resolved L sub-ir/M(H2) Ratios in the W3 GMC. In D. P. Clemens & R. Barvainis, editor, *Clouds, Cores, and Low Mass Stars*, volume 65 of *Astronomical Society of the Pacific Conference Series*, page 46. 84

Deharveng, L., Zavagno, A., Anderson, L. D., Motte, F., Abergel, A., Andre, P., Bontemps, S., Leleu, G., Roussel, H., and Russeil, D. (2012). Interstellar matter and star formation in W5-E - A Herschel view. *ArXiv e-prints*. 21

Dempsey, J. T., Holland, W. S., Chrysostomou, A., Berry, D. S., Bintley, D., Chapin, E. L., Craig, S. C., Coulson, I. M., Davis, G. R., Friberg, P., Jenness, T., Gibb, A. G., Parsons, H. A. L., Scott, D., Thomas, H. S., Tilanus, R. P. J., Robson, I., and Walther, C. A. (2012). A new era of wide-field submillimetre imaging: on-sky performance of SCUBA-2. *ArXiv e-prints*. 176

Désert, F. and et al. (2008). Submillimetre point sources from the Archeops experiment: very cold clumps in the Galactic plane. *A& A*, 481:411–421. 86

Di Francesco, J., Johnstone, D., Kirk, H., MacKenzie, T., and Ledwosinska, E. (2008). The SCUBA Legacy Catalogues: Submillimeter-Continuum Objects Detected by SCUBA. *ApJS*, 175:277–295. 36, 199

Drabek, E., Hatchell, J., Friberg, P., Richer, J., Graves, S., Buckle, J. V., Nutter, D., Johnstone, D., and Di Francesco, J. (2012). Molecular line contamination in the SCUBA-2 450 {\mu}m and 850 {\mu}m continuum data. *ArXiv e-prints*. 271

Draine, B. T. (1985). Tabulated optical properties of graphite and silicate grains. *ApJS*, 57:587–594. 28

Draine, B. T. (2003). Interstellar Dust Grains. *ARA& A*, 41:241–289. 14

Draine, B. T. (2009). Interstellar dust models and evolutionary implications. In T. Henning, E. Grün, . J. S., editor, *Astronomical Society of the Pacific Conference Series*, volume 414 of *Astronomical Society of the Pacific Conference Series*, page 453. 2, 4

Draine, B. T. and Anderson, N. (1985). Temperature fluctuations and infrared emission from interstellar grains. *ApJ*, 292:494–499. 14

Draine, B. T., Dale, D. A., Bendo, G., Gordon, K. D., Smith, J. D. T., Armus, L., Engelbracht, C. W., Helou, G., Kennicutt, Jr., R. C., Li, A., Roussel, H., Walter, F., Calzetti, D., Moustakas, J., Murphy, E. J., Rieke, G. H., Bot, C., Hollenbach, D. J., Sheth, K., and Teplitz, H. I. (2007). Dust Masses, PAH Abundances, and Starlight Intensities in the SINGS Galaxy Sample. *ApJ*, 663:866–894. 186

Draine, B. T. and Fraisse, A. A. (2009). Polarized Far-Infrared and Submillimeter Emission from Interstellar Dust. *ApJ*, 696:1–11. 162

Draine, B. T. and Lee, H. M. (1984). Optical properties of interstellar graphite and silicate grains. *ApJ*, 285:89–108. 5, 6, 7, 182

Draine, B. T. and Li, A. (2007). Infrared Emission from Interstellar Dust. IV. The Silicate-Graphite-PAH Model in the Post-Spitzer Era. *ApJ*, 657:810–837. 162

Duley, W. W. (1973). Fluctuations in Interstellar Grain Temperatures. *ApSS*, 23:43–50. 14

Dupac, X., Bernard, J., Boudet, N., Giard, M., Lamarre, J., Mény, C., Pajot, F., Ristorcelli, I., Serra, G., Stepnik, B., and Torre, J. (2003). Inverse temperature dependence of the dust submillimeter spectral index. *A& A*, 404:L11–L15. 11, 86

Ebert, R. (1955). Über die Verdichtung von H I-Gebieten. Mit 5 Textabbildungen. *Z.Astrophys.*, 37:217. 257

Evans, II, N. J., Beckwith, S., and Blair, G. N. (1977). The energetics of molecular clouds. I - Methods of analysis and application to the S255 molecular cloud. *ApJ*, 217:448–451. 172

Evans, II, N. J., Rawlings, J. M. C., Shirley, Y. L., and Mundy, L. G. (2001). Tracing the Mass during Low-Mass Star Formation. II. Modeling the Submillimeter Emission from Preprotostellar Cores. *ApJ*, 557:193–208. 17, 19

Fazio, G. G., Hora, J. L., Allen, L. E., Ashby, M. L. N., Barmby, P., Deutsch, L. K., Huang, J.-S., Kleiner, S., Marengo, M., Megeath, S. T., Melnick, G. J., Pahre, M. A., Patten, B. M., Polizotti, J., Smith, H. A., Taylor, R. S., Wang, Z., Willner, S. P., Hoffmann, W. F., Pipher, J. L., Forrest, W. J., McMurty, C. W., McCreight, C. R., McKelvey, M. E., McMurray, R. E., Koch, D. G., Moseley, S. H., Arendt, R. G., Mentzell, J. E., Marx, C. T., Losch, P., Mayman, P., Eichhorn, W., Krebs, D., Jhabvala, M., Gezari, D. Y., Fixsen, D. J., Flores, J., Shakoorzadeh, K., Jungo, R., Hakun, C., Workman, L., Karpati, G., Kichak, R., Whitley, R., Mann, S., Tollestrup, E. V., Eisenhardt, P., Stern, D., Gorjian, V., Bhattacharya, B., Carey, S., Nelson, B. O., Glaccum, W. J., Lacy, M., Lowrance, P. J., Laine, S., Reach, W. T., Stauffer, J. A., Surace, J. A., Wilson, G., Wright, E. L., Hoffman, A., Domingo, G., and Cohen, M. (2004). The Infrared Array Camera (IRAC) for the Spitzer Space Telescope. *ApJS*, 154:10–17. 301

Felli, M. and Churchwell, E. (1972). Radio emission at 1400 MHz from galactic H II regions. *A&AS*, 5:369. 170, 172

Felli, M. and Harten, R. H. (1981). A High Resolution Search for Small-Scale Structure in Sharpless HII Regions at 4.995-GHZ - Part Three - Description of Selected Sources. *A&A*, 100:42. 170

Fich, M. (1986). A complete VLA survey in the outer galaxy. *AJ*, 92:787–804. 170, 172, 306

Fich, M. (1993). A VLA survey of optically visible galactic H II regions. *ApJS*, 86:475–497. 171, 194, 306

Fich, M. and Blitz, L. (1984). Optical H II regions in the outer galaxy. *ApJ*, 279:125–135. 26, 169, 171

Fich, M., Blitz, L., and Stark, A. A. (1989). The rotation curve of the Milky Way to 2 R(0). *ApJ*, 342:272–284. 169, 171

Fich, M., Dahl, G. P., and Treffers, R. R. (1990). Fabry-Perot H-alpha observations of Galactic H II regions. *AJ*, 99:622–637. 171

Fich, M. and Hodge, P. (1991). Continuum emission at 1 millimeter from the elliptical galaxy NGC 205. *APJL*, 374:L17–L20. 28

Fich, M. and Terebey, S. (1996). IRAS Observations of the Outer Galaxy. I. Discrete Sources and Large-Scale (Diffuse) Emission. *ApJ*, 472:624. 91

Galli, D., Walmsley, M., and Gonçalves, J. (2002). The structure and stability of molecular cloud cores in external radiation fields. *A&A*, 394:275–284. 295, 297

Giannini, T., Elia, D., Lorenzetti, D., Molinari, S., Motte, F., Schisano, E., Pezzuto, S., Pestalozzi, M., di Giorgio, A. M., André, P., Hill, T., Benedettini, M., Bontemps, S., di Francesco, J., Fallscheer, C., Hennemann, M., Kirk, J., Minier, V., Nguyen Luong, Q., Polychroni, D., Rygl, K. L. J., Saraceno, P., Schneider, N., Spinoglio, L., Testi, L., Ward-Thompson, D., and White, G. J. (2012). The Herschel view of the on-going star formation in the Vela-C molecular cloud. *A&A*, 539:A156. 21, 295

Gordon, M. A. (1995). Dust emission as a quantitative probe of star-forming regions. *A&A*, 301:853. 271

Greenberg, J. M. (1968). *Interstellar Grains*, page 221. University of Chicago Press, Chicago, ILL USA, 1968, p.221. 14

Habart, E., Abergel, A., Walmsley, C. M., Teyssier, D., and Pety, J. (2005). Density structure of the Horsehead nebula photo-dissociation region. *A&A*, 437:177–188. 123

Habing, H. J. and Israel, F. P. (1979). Compact H II regions and OB star formation. *ARA&A*, 17:345–385. 13

Haschick, A. D. and Ho, P. T. P. (1985). Formation of OB clusters - CO, NH3, and H2O observations of the distant H II region complex in S128. *ApJ*, 292:200–205. 173

Henning, T. (1998). Chemistry and physics of cosmic nano-and micro-particles. *Chem. Soc. Rev.*, 27(5):315–321. 297

Heske, A. and Wendker, H. J. (1982). Formaldehyde absorption in S 128. *A&A*, 113:170–172. 172

Heydari-Malayeri, M., Testor, G., and Lortet, M. C. (1980). Interaction of hot stars and the interstellar matter. X - Morphology, excitation, and structure of the bright galactic nebula Sh2-156 /IC 1470/. *A&A*, 84:154–166. 170

Heyer, M. H., Snell, R. L., Morgan, J., and Schloerb, F. P. (1989). A CO and far-infrared study of the S254-S258 region. *ApJ*, 346:220–231. 172, 296

Hildebrand, R. H. (1983). The Determination of Cloud Masses and Dust Characteristics from Submillimetre Thermal Emission. *QJRAS*, 24:267. 9, 11, 16, 187

Hildebrand, R. H., Whitcomb, S. E., Winston, R., Stiening, R. F., Harper, D. A., and Moseley, S. H. (1977). Submillimeter photometry of extragalactic objects. *ApJ*, 216:698–705. 9, 16

Ho, P. T. P., Haschick, A. D., and Israel, F. P. (1981). OB star formation in the S128 region. *ApJ*, 243:526–532. 172

Hobson, M. P. and Padman, R. (1994). A Maximum Entropy Method for Reconstructing Dust Temperature Distributions from Millimetre and Submillimetre Fluxes. *MNRAS*, 266:752. 18

Hobson, M. P. and Ward-Thompson, D. (1994). Maximum Entropy Mapping of IRAS Data - Part Three - Evidence for Hot Dust in M17. *MNRAS*, 267:141. 20

Holland, W., MacIntosh, M., Fairley, A., Kelly, D., Montgomery, D., Gostick, D., Atad-Ettedgui, E., Ellis, M., Robson, I., Hollister, M., Woodcraft, A., Ade, P., Walker, I., Irwin, K., Hilton, G., Duncan, W., Reintsema, C., Walton, A., Parkes, W., Dunare, C., Fich, M., Kycia, J., Halpern, M., Scott, D., Gibb, A., Molnar, J., Chapin, E., Bintley, D., Craig, S., Chylek, T., Jenness, T., Economou, F., and Davis, G. (2006). SCUBA-2: a 10,000-pixel submillimeter camera for the James Clerk Maxwell Telescope. In *Society of Photo-Optical Instrumentation Engineers (SPIE) Conference Series*, volume 6275 of *Society of Photo-Optical Instrumentation Engineers (SPIE) Conference Series*. 164

Holland, W. S., Robson, E. I., Gear, W. K., and Cunningham (1999). SCUBA: a common-user submillimetre camera operating on the James Clerk Maxwell Telescope. *MNRAS*, 303(4):659–672. 35

Hoyle, F. and Wickramasinghe, N. C. (1962). On graphite particles as interstellar grains. *MNRAS*, 124:417. 5

Hughes, V. A. and MacLeod, G. C. (1989). The use of IRAS data to define H II regions. *AJ*, 97:786–800. 79

Hunter, D. A., Thronson, Jr., H. A., and Wilton, C. (1990). Small Galactic H II regions. II - The molecular clouds and star formation. *AJ*, 100:1915–1926. 171

Hunter, T. R., Churchwell, E., Watson, C., Cox, P., Benford, D. J., and Roelfsema, P. R. (2000). 350 Micron Images of Massive Star Formation Regions. *AJ*, 119:2711–2727. 173

Israel, F. P. (1977). Aperture synthesis observations of galactic H II regions. IV - New observations of H II regions around L = 111 deg. *A&A*, 59:27–41. 170

Israel, F. P., Habing, H. J., and de Jong, T. (1973). Aperture synthesis observations of H II regions. I. A group of H II regions around l = 111 . *A&A*, 27:143–160. 169

Jenness, T., Berry, D., Chapin, E., Economou, F., Gibb, A., and Scott, D. (2011). SCUBA-2 Data Processing. In I. N. Evans, A. Accomazzi, D. J. Mink, & A. H. Rots, editor, *Astronomical Data Analysis Software and Systems XX*, volume 442 of *Astronomical Society of the Pacific Conference Series*, page 281. 175

Jenness, T. and Economou, F. (1999). The SCUBA Data Reduction Pipeline: ORAC-DR at the JCMT. In Mehringer, D. M., Plante, R. L., and Roberts, D. A., editors, *Astronomical Data Analysis Software and Systems VIII*, volume 172 of *Astronomical Society of the Pacific Conference Series*, page 171. 36, 176

Jenness, T., Lightfoot, J. F., and Holland, W. S. (1998). Removing sky contributions from SCUBA data. In T. G. Phillips, editor, *Society of Photo-Optical Instrumentation Engineers (SPIE) Conference Series*, volume 3357 of *Society of Photo-Optical Instrumentation Engineers (SPIE) Conference Series*, pages 548–558. 36

Johnstone, D. and Bally, J. (1999). JCMT/SCUBA Submillimeter Wavelength Imaging of the Integral-shaped Filament in Orion. *ApJL*, 510:L49–L53. 271

Jones, A. P. (2004). Dust Destruction Processes. In A. N. Witt, G. C. Clayton, & B. T. Draine, editor, *Astrophysics of Dust*, volume 309 of *Astronomical Society of the Pacific Conference Series*, page 347. 2, 3, 14

Jørgensen, J. K., Schöier, F. L., and van Dishoeck, E. F. (2002). Physical structure and CO abundance of low-mass protostellar envelopes. *A&A*, 389:908–930. 257

Joy, M., Harvey, P. M., Evans, II, N. J., and Wilking, B. A. (1984). Infrared and millimeter-wave observations of the Sharpless 156 molecular cloud. *ApJ*, 284:161–175. 171

Juvela, M., Ristorcelli, I., Pelkonen, V., Marshall, D. J., Montier, L. A., Bernard, J., Paladini, R., Lunttila, T., Abergel, A., André, P., Dickinson, C., Dupac, X., Malinen, J., Martin, P., McGehee, P., Pagani, L., Ysard, N., and Zavagno, A. (2011). Galactic cold cores. II. Herschel study of the extended dust emission around the first Planck detections. *A& A*, 527:A111. 11

Kauffmann, J. and Bertoldi, F. (2004). Structure and Stability of Prestellar Cores. *ArXiv Astrophysics e-prints*. 297

Kemper, F., Vriend, W. J., and Tielens, A. G. G. M. (2004). The Absence of Crystalline Silicates in the Diffuse Interstellar Medium. *ApJ*, 609:826–837. 4

Kerton, C. R. (2002). Detecting Embedded Intermediate-Mass Stars Using Mid-Infrared and H I 21 Centimeter Emission. *AJ*, 124:3449–3464. 79

Kirk, J. M. and et al. (2010). Herschel-SPIRE spectroscopy of G29.96-0.02: Fitting the full SED. *A& A*, 518:L82. 87

Kirk, J. M., Ward-Thompson, D., and André, P. (2005). The initial conditions of isolated star formation - VI. SCUBA mappingof pre-stellar cores. *MNRAS*, 360:1506–1526. 36, 81

Kothes, R. and Kerton, C. R. (2002). Expanding shells of shocked neutral hydrogen around compact H II regions. *A&A*, 390:337–350. 169, 173

Kozasa, T., Nozawa, T., Tominaga, N., Umeda, H., Maeda, K., and Nomoto, K. (2009). Dust in Supernovae: Formation and Evolution. In Henning, T., Grün, E., and Steinacker, J., editors, *Cosmic Dust - Near and Far*, volume 414 of *Astronomical Society of the Pacific Conference Series*, page 43. 2

Kramer, C., Richer, J., Mookerjea, B., Alves, J., and Lada, C. (2003). Dust properties of the dark cloud IC 5146. Submillimeter and NIR imaging. *A&A*, 399:1073–1082. 182

Krügel, E. (2003). *The Physics of Interstellar Dust*. Institute of Physics, Bristol and Philadelphia. 9, 10, 18, 91, 92

Kurtz, S. (2002). Ultracompact HII Regions. In P. Crowther, editor, *Hot Star Workshop III: The Earliest Phases of Massive Star Birth*, volume 267 of *Astronomical Society of the Pacific Conference Series*, page 81. 13

Lada, C. J. (1978). The locations of newly formed stars in molecular clouds. *Moon and Planets*, 19:157. 89

Lada, C. J. (1987). Star formation - From OB associations to protostars. In Peimbert, M. and Jugaku, J., editors, *Star Forming Regions*, volume 115 of *IAU Symposium*, pages 1–17. 244

Lebrón, M. E., Rodríguez, L. F., and Lizano, S. (2001). Observations of the Ionized, Neutral, and Molecular Components Associated with an Expanding H II Region. *ApJ*, 560:806–820. 169

Leisawitz, D. (1991). A model for the infrared emission from an OB star cluster environment. *ApJS*, 77:451–471. 89, 294

Leung, C. M. (1975). Radiation transport in dense interstellar dust clouds. I - Grain temperature. *ApJ*, 199:340–360. 16, 17

Li, D., Goldsmith, P., and Xie, T. (1999). A new method for determining the dust temperature distribution in star-forming regions. *ApJ*, 522(2, Part 1):897–903. 18, 19

Mampaso, A., Gomez, P., Sanchez-Magro, C., and Selby, M. J. (1984). Infrared observations of H II regions - S128 and G134.2+0.8 (GL 333). *MNRAS*, 207:465–470. 173

Mathis, J. S. (1990). Interstellar dust and extinction. *ARA&A*, 28:37–70. 187

Mathis, J. S., Rumpl, W., and Nordsieck, K. H. (1977). The size distribution of interstellar grains. *ApJ*, 217:425–433. 5, 27

Matzner, C. D. and McKee, C. F. (2000). Efficiencies of Low-Mass Star and Star Cluster Formation. *ApJ*, 545:364–378. 244

McCarthy, J. F., Forrest, W. J., Briotta, Jr., D. A., and Houck, J. R. (1980). The galactic center - 16-30 micron observations and the 18 micron extinction. *ApJ*, 242:965–975. 4

McCutcheon, W. H., Sato, T., Purton, C. R., Matthews, H. E., and Dewdney, P. E. (1995). Millimeter and Submillimeter Wavelength Continuum Observations of Massive Young Stellar Objects. *AJ*, 110:1762. 20

McGlynn, T., Scollick, K., and White, N. (1996). *SkyView: The Multi-Wavelength Sky on the Internet, McLean, B.J. et al.*, volume 179, p465 of *New Horizons from Multi-Wavelength Sky Surveys*. Kluwer Academic Publishers, au symposium edition. 36

McLaughlin, D. E. and Pudritz, R. E. (1996). A Model for the Internal Structure of Molecular Cloud Cores. *ApJ*, 469:194. 257, 258

Mennella, V., Brucato, J. R., Colangeli, L., Palumbo, P., Rotundi, A., and Bussoletti, E. (1998). Temperature Dependence of the Absorption Coefficient of Cosmic Analog Grains in the Wavelength Range 20 Microns to 2 Millimeters. *ApJ*, 496:1058. 86

Mennella, V., Colangeli, L., and Bussoletti, E. (1995). The absorption coefficient of cosmic carbon analogue grains in the wavelength range 20 - 2000 microns. *A& A*, 295:165–170. 11

Mezger, P. G., Chini, R., Kreysa, E., and Wink, J. (1987). Observations of cold dust in S 106. *A& A*, 182:127–136. 20, 295

Miyake, K. and Nakagawa, Y. (1993). Effects of particle size distribution on opacity curves of protoplanetary disks around T Tauri stars. *Icarus*, 106:20. 275

Moffat, A. F. J., Jackson, P. D., and Fitzgerald, M. P. (1979). The rotation and structure of the galaxy beyond the solar circle. I - Photometry and spectroscopy of 276 stars in 45 H II regions and other young stellar groups toward the galactic anticentre. *A&AS*, 38:197–225. 171

Mookerjea, B., Ghosh, S. K., Rengarajan, T. N., Tandon, S. N., and Verma, R. P. (2000). Distribution of Cold Dust in Orion A and B. *AJ*, 120:1954–1962. 295

Mooney, T. J. and Solomon, P. M. (1988). Star formation rates and the far-infrared luminosity of Galactic molecular clouds. *APJL*, 334:L51–L54. 84

Motte, F. and André, P. (2001). The circumstellar environment of low-mass protostars: A millimeter continuum mapping survey. *A&A*, 365:440–464. 257

Motte, F., Zavagno, A., Bontemps, S., Schneider, N., Hennemann, M., di Francesco, J., André, P., Saraceno, P., Griffin, M., Marston, A., Ward-Thompson, D., White, G., Minier, V., Men'shchikov, A., Hill, T., Abergel, A., Anderson, L. D., Aussel, H., Balog, Z., Baluteau, J.-P., Bernard, J.-P., Cox, P., Csengeri, T., Deharveng, L., Didelon, P., di Giorgio, A.-M., Hargrave, P., Huang, M., Kirk, J., Leeks, S., Li, J. Z., Martin, P., Molinari, S., Nguyen-Luong, Q., Olofsson, G., Persi, P., Peretto, N., Pezzuto, S., Roussel, H., Russeil, D., Sadavoy, S., Sauvage, M., Sibthorpe, B., Spinoglio, L., Testi, L., Teyssier, D., Vavrek, R., Wilson, C. D., and Woodcraft, A. (2010). Initial highlights of the HOBYS key program, the Herschel imaging survey of OB young stellar objects. *A&A*, 518:L77. 21

Mueller, K. E., Shirley, Y. L., Evans, II, N. J., and Jacobson, H. R. (2002). The Physical Conditions for Massive Star Formation: Dust Continuum Maps and Modeling. *APJS*, 143:469–497. 173, 257

Myers, P. C., Dame, T. M., Thaddeus, P., Cohen, R. S., Silverberg, R. F., Dwek, E., and Hauser, M. G. (1986). Molecular clouds and star formation in the inner galaxy - A comparison of CO, H II, and far-infrared surveys. *ApJ*, 301:398–422. 244

Natta, A. and Panagia, N. (1976). Model calculations of dusty H II regions. *A&A*, 50:191–211. 89

Nenkova, M., Ivezić, Ž., and Elitzur, M. (2000). DUSTY: a Publicly Available Code for Modeling Dust Emission. *Thermal Emission Spectroscopy and Analysis of Dust, Disks, and Regoliths*, 196:77–82. 19

Ney, E. P. and Hatfield, B. F. (1978). The isothermal dust condensation of Nova Vulpeculae 1976. *ApJL*, 219:L111–L115. 2

Ney, E. P., Strecker, D. W., and Gehrz, R. D. (1973). Dust emission nebulae around Orion O and B stars. *ApJ*, 180:809–816. 4

Ojha, D. K., Samal, M. R., Pandey, A. K., Bhatt, B. C., Ghosh, S. K., Sharma, S., Tamura, M., Mohan, V., and Zinchenko, I. (2011). Star Formation Activity in the Galactic H II Complex S255-S257. *ApJ*, 738:156. 172

Pagani, L. and et al. (2003). L183 (L134N) Revisited. I. The very cold core and the ridge. *A& A*, 406:L59–L62. 20

Pagani, L. and et al. (2004). L183 (L134N) Revisited. II. The dust content. *A& A*, 417:605–613. 20

Papadopoulos, P. P. and Allen, M. L. (2000). Gas and Dust in NGC 7469: Submillimeter Imaging and CO J=3-2. *ApJ*, 537:631–637. 271

Paradis, D. and et al. (2011). A Statistical Study of Dust Properties in Large Magellanic Cloud Molecular Clouds. *AJ*, 141:43. 84

Pascale, E., Ade, P. A. R., Bock, J. J., Chapin, E. L., Chung, J., Devlin, M. J., Dicker, S., Griffin, M., Gundersen, J. O., Halpern, M., Hargrave, P. C., Hughes, D. H., Klein, J., MacTavish, C. J., Marsden, G., Martin, P. G., Martin, T. G., Mauskopf, P., Netterfield, C. B., Olmi, L., Patanchon, G., Rex, M., Scott, D., Semisch, C., Thomas, N., Truch, M. D. P., Tucker, C., Tucker, G. S., Viero, M. P., and Wiebe, D. V. (2008). The Balloon-borne Large Aperture Submillimeter Telescope: BLAST. *ApJ*, 681:400–414. 21

Pilbratt, G. L., Riedinger, J. R., Passvogel, T., Crone, G., Doyle, D., Gageur, U., Heras, A. M., Jewell, C., Metcalfe, L., Ott, S., and Schmidt, M. (2010). Herschel Space Observatory. An ESA facility for far-infrared and submillimetre astronomy. *A&A*, 518:L1. 21

Pirogov, L. E. (2009). Density profiles in molecular cloud cores associated with high-mass star-forming regions. *Astronomy Reports*, 53:1127–1135. 257

Pismis, P. and Hasse, I. (1976). Study of a triple emission nebula in Orion. *AP&SS*, 45:79–85. 171

Pismis, P. and Mampaso, A. (1991). Infrared studies of H II regions - The Sharpless regions S148, 184, 198, 206 and 269. *MNRAS*, 249:385–403. 170

Platt, J. R. (1956). On the Optical Properties of Interstellar Dust. *ApJ*, 123:486. 5

Recillas-Cruz, E. and Pismis, P. (1979). Internal motions in H II regions. VII - The emission nebulae complex S 147, 148 and 149. *RMxAA*, 4:337–340. 170

Rivera-Ingraham, A., Ade, P. A. R., Bock, J. J., Chapin, E. L., Devlin, M. J., Dicker, S. R., Griffin, M., Gundersen, J. O., Halpern, M., Hargrave, P. C., Hughes, D. H., Klein, J., Marsden, G., Martin, P. G., Mauskopf, P., Netterfield, C. B., Olmi, L., Patanchon, G., Rex, M., Scott, D., Semisch, C., Truch, M. D. P., Tucker, C., Tucker, G. S., Viero, M. P., and Wiebe, D. V. (2010). The BLAST View of the Star-forming Region in Aquila (ell = 45°, b = 0°). *ApJ*, 723:915–934. 21

Robson, I. and Holland, W. (2007). SCUBA-2: The Submillimeter Mapping Machine. In A. J. Baker, J. Glenn, A. I. Harris, J. G. Mangum, & M. S. Yun , editor, *From Z-Machines to ALMA: (Sub)Millimeter Spectroscopy of Galaxies*, volume 375 of *Astronomical Society of the Pacific Conference Series*, page 275. 164

Rodón, J. A. and et al. (2010). Physical properties of the Sh2-104 H II region as seen by Herschel. *A& A*, 518:L80. 21, 38

Romero, G. A. and Cappa, C. E. (2008). Sh2-205 - I. The surrounding interstellar medium. *MNRAS*, 387:1080–1092. 20

Roy, A., Ade, P. A. R., Bock, J. J., Brunt, C. M., Chapin, E. L., Devlin, M. J., Dicker, S. R., France, K., Gibb, A. G., Griffin, M., Gundersen, J. O., Halpern, M., Hargrave, P. C., Hughes, D. H., Klein, J., Marsden, G., Martin, P. G., Mauskopf, P., Netterfield, C. B., Olmi, L., Patanchon, G., Rex, M., Scott, D., Semisch, C., Truch, M. D. P., Tucker, C., Tucker, G. S., Viero, M. P., and Wiebe, D. V. (2011a). Deconvolution of Images from BLAST 2005: Insight into the K3-50 and IC 5146 Star-forming Regions. *ApJ*, 730:142. 21

Roy, A., Ade, P. A. R., Bock, J. J., Chapin, E. L., Devlin, M. J., Dicker, S. R., France, K., Gibb, A. G., Griffin, M., Gundersen, J. O., Halpern, M., Hargrave, P. C., Hughes, D. H., Klein, J., Marsden, G., Martin, P. G., Mauskopf, P., Morales Ortiz, J. L., Netterfield,

C. B., Noriega-Crespo, A., Olmi, L., Patanchon, G., Rex, M., Scott, D., Semisch, C., Truch, M. D. P., Tucker, C., Tucker, G. S., Viero, M. P., and Wiebe, D. V. (2011b). The Balloon-borne Large Aperture Submillimeter Telescope (BLAST) 2005: A 10 deg^2 Survey of Star Formation in Cygnus X. *ApJ*, 727:114. 21, 295

Russeil, D., Adami, C., and Georgelin, Y. M. (2007). Revised distances of Northern H II regions. *A& A*, 470:161–171. 26, 169, 170, 171

Russeil, D., Georgelin, Y. M., Georgelin, Y. P., Le Coarer, E., and Marcelin, M. (1995). Galactic HII regions at l= 234deg. *A&AS*, 114:557. 171

Scaife, A. M. M. and et al. (2008). AMI limits on 15-GHz excess emission in northern H II regions. *MNRAS*, 385:809–822. 35

Schnee, S., Enoch, M., Noriega-Crespo, A., Sayers, J., Terebey, S., Caselli, P., Foster, J., Goodman, A., Kauffmann, J., Padgett, D., Rebull, L., Sargent, A., and Shetty, R. (2010). The Dust Emissivity Spectral Index in the Starless Core TMC-1C. *ApJ*, 708:127–136. 11

Schnee, S. and Goodman, A. (2005). Density and Temperature Structure of TMC-1C from 450 and 850 Micron Maps. *ApJ*, 624:254–266. 245, 275, 295

Schneider, N., Motte, F., Bontemps, S., Hennemann, M., di Francesco, J., André, P., Zavagno, A., Csengeri, T., Men'shchikov, A., Abergel, A., Baluteau, J.-P., Bernard, J.-P., Cox, P., Didelon, P., di Giorgio, A.-M., Gastaud, R., Griffin, M., Hargrave, P., Hill, T., Huang, M., Kirk, J., Könyves, V., Leeks, S., Li, J. Z., Marston, A., Martin, P., Minier, V., Molinari, S., Olofsson, G., Panuzzo, P., Persi, P., Pezzuto, S., Roussel, H., Russeil, D., Sadavoy, S., Saraceno, P., Sauvage, M., Sibthorpe, B., Spinoglio, L., Testi, L., Teyssier, D., Vavrek, R., Ward-Thompson, D., White, G., Wilson, C. D., and Woodcraft, A. (2010). The Herschel view of star formation in the Rosette molecular cloud under the influence of NGC 2244. *A&A*, 518:L83. 21, 295

Scoville, N. Z. and Good, J. C. (1989). The far-infrared luminosity of molecular clouds in the Galaxy. *ApJ*, 339:149–162. 20

Seaquist, E., Yao, L., Dunne, L., and Cameron, H. (2004). Revised masses of dust and gas of SCUBA Local Universe Survey far-infrared bright galaxies based on a recent CO survey. *MNRAS*, 349:1428–1434. 87, 271

Sharpless, S. (1959). A Catalogue of H II Regions. *ApJS*, 4:257. 169

Shetty, R., Kauffmann, J., Schnee, S., and Goodman, A. A. (2009a). The Effect of Noise on the Dust Temperature-Spectral Index Correlation. *ApJ*, 696:676–680. 11

Shetty, R., Kauffmann, J., Schnee, S., Goodman, A. A., and Ercolano, B. (2009b). The Effect of Line-of-Sight Temperature Variation and Noise on Dust Continuum Observations. *ApJ*, 696:2234–2251. 11, 12

Shirley, Y. L., Nordhaus, M. K., Grcevich, J. M., Evans, II, N. J., Rawlings, J. M. C., and Tatematsu, K. (2005). Modeling the Physical Structure of the Low-Density Pre-Protostellar Core Lynds 1498. *ApJ*, 632:982–1000. 11

Shu, F. H. (1977). Self-similar collapse of isothermal spheres and star formation. *ApJ*, 214:488–497. 256

Sievers, A. W., Mezger, P. G., Bordeon, M. A., Kreysa, E., Haslam, C. G. T., and Lemke, R. (1991). Dust emission from star forming regions. I - The W49A and W51A complexes. *A& A*, 251:231–244. 20

Sreenilayam, G. and Fich, M. (2011). Hot and Cold Dust near H II Regions. *AJ*, 142:4. 26

Sridharan, T. K., Beuther, H., Saito, M., Wyrowski, F., and Schilke, P. (2005). High-Mass Starless Cores. *ApJL*, 634:L57–L60. 298

Stecher, T. P. (1965). Interstellar Ectinction in the Ultraviolet. *ApJ*, 142:1683. 5

Stecher, T. P. and Donn, B. (1965). On Graphite and Interstellar Extinction. *ApJ*, 142:1681. 5

Stein, W. A. and Gillett, F. C. (1969). Spectral Distribution of Infrared Radiation from the Trapezium Region of the Orion Nebula. *ApJL*, 155:L197. 4

Swift, J. J. and Welch, W. J. (2008). A Case Study of Low-Mass Star Formation. *ApJS*, 174:202–222. 244

Testi, L., Natta, A., Shepherd, D. S., and Wilner, D. J. (2003). Large grains in the disk of CQ Tau. *A&A*, 403:323–328. 275

Tielens, A. G. G. M. (2005). *The physics and chemistry of the interstellar medium*. Cambridge University Press. 14

Trumpler, R. J. (1930a). Absorption of light in the galactic system. *PASP*, 42:214. 1

Trumpler, R. J. (1930b). Preliminary results on the distances, dimensions and space distribution of open star clusters. *Lick Observatory Bulletin*, 14:154–188. 1

van der Tak, F. F. S., van Dishoeck, E. F., Evans, II, N. J., and Blake, G. A. (2000). Structure and Evolution of the Envelopes of Deeply Embedded Massive Young Stars. *ApJ*, 537:283–303. 245

Weingartner, J. C. and Draine, B. T. (2001). Dust Grain-Size Distributions and Extinction in the Milky Way, Large Magellanic Cloud, and Small Magellanic Cloud. *ApJ*, 548:296–309. 162

Whittet, D. C. B., editor (2003). *Dust in the galactic environment*. 3, 4, 297

Whittet, D. C. B., Gerakines, P. A., Hough, J. H., and Shenoy, S. S. (2001). Interstellar Extinction and Polarization in the Taurus Dark Clouds: The Optical Properties of Dust near the Diffuse/Dense Cloud Interface. *ApJ*, 547:872–884. 296

Williams, S. J., Fuller, G. A., and Sridharan, T. K. (2005). The circumstellar environments of high-mass protostellar objects. II. Dust continuum models. *A&A*, 434:257–274. 258

Wood, D. O. S. and Churchwell, E. (1989a). Massive stars embedded in molecular clouds - Their population and distribution in the galaxy. *ApJ*, 340:265–272. 79, 80

Wood, D. O. S. and Churchwell, E. (1989b). Massive stars embedded in molecular clouds - Their population and distribution in the galaxy. *ApJ*, 340:265–272. 89

Wood, D. O. S., Myers, P. C., and Daugherty, D. A. (1994). IRAS images of nearby dark clouds. *ApJS*, 95:457–501. 20

Wright, E. L., Harper, D. A., Loewenstein, R. F., and Moseley, H. (1981). Far-infrared observations of the H2O masers in NGC 281, NGC 2175, and S255/257. *ApJ*, 246:426–429. 172

Xie, T., Goldsmith, P. F., Snell, R. L., and Zhou, W. (1993). Dust temperature distributions in star-forming condensations. *ApJ*, 402:216–225. 18

Yang, M. and Phillips, T. (2007). 350 μm Observations of Local Luminous Infrared Galaxies and the Temperature Dependence of the Emissivity Index. *ApJ*, 662:284–293. 11

Young, C. H., Shirley, Y. L., Evans, II, N. J., and Rawlings, J. M. C. (2003). Tracing the Mass during Low-Mass Star Formation. IV. Observations and Modeling of the Submillimeter Continuum Emission from Class I Protostars. *ApJS*, 145:111–145. 257

Zhou, S., Butner, H. M., Evans, II, N. J., Guesten, R., Kutner, M. L., and Mundy, L. G. (1994). CS multitransitional study of density distribution in star-forming regions. 2: The S140 region. *ApJ*, 428:219–232. 258

Zinchenko, I., Forsstroem, V., Lapinov, A., and Mattila, K. (1994). Studies of dense molecular cores in regions of massive star formation. CS J=2-1 and HCN J=1-0 observations of 11 northern cores. *A&A*, 288:601–616. 169

Zubko, V., Dwek, E., and Arendt, R. G. (2004). Interstellar Dust Models Consistent with Extinction, Emission, and Abundance Constraints. *ApJS*, 152:211–249. 162